Mechanisms and Machine Science

Doina Pisla
Giuseppe Carbone
Daniel Condurache
Calin Vaida *Editors*

Advances in Service and Industrial Robotics

RAAD 2024

IFToMM

Springer

Mechanisms and Machine Science

Volume 157

This book series establishes a well-defined forum for monographs, edited Books, and proceedings on mechanical engineering with particular emphasis on MMS (Mechanism and Machine Science). The final goal is the publication of research that shows the development of mechanical engineering and particularly MMS in all technical aspects, even in very recent assessments. Published works share an approach by which technical details and formulation are discussed, and discuss modern formalisms with the aim to circulate research and technical achievements for use in professional, research, academic, and teaching activities.

This technical approach is an essential characteristic of the series. By discussing technical details and formulations in terms of modern formalisms, the possibility is created not only to show technical developments but also to explain achievements for technical teaching and research activity today and for the future.

The book series is intended to collect technical views on developments of the broad field of MMS in a unique frame that can be seen in its totality as an Encyclopaedia of MMS but with the additional purpose of archiving and teaching MMS achievements. Therefore, the book series will be of use not only for researchers and teachers in Mechanical Engineering but also for professionals and students for their formation and future work.

The series is promoted under the auspices of International Federation for the Promotion of Mechanism and Machine Science (IFToMM).

Prospective authors and editors can contact Mr. Pierpaolo Riva (publishing editor, Springer) at: pierpaolo.riva@springer.com

Indexed by SCOPUS and Google Scholar.

Doina Pisla · Giuseppe Carbone ·
Daniel Condurache · Calin Vaida
Editors

Advances in Service and Industrial Robotics

RAAD 2024

Springer

Editors
Doina Pisla
CESTER
Technical University of Cluj-Napoca
Cluj-Napoca, Romania

Giuseppe Carbone
DIMEG
University of Calabria
Rende, Italy

Daniel Condurache
Department of Theoretical Mechanics
Technical University of Iasi
Iasi, Romania

Calin Vaida
CESTER
Technical University of Cluj-Napoca
Cluj-Napoca, Romania

ISSN 2211-0984 ISSN 2211-0992 (electronic)
Mechanisms and Machine Science
ISBN 978-3-031-59256-0 ISBN 978-3-031-59257-7 (eBook)
https://doi.org/10.1007/978-3-031-59257-7

This Springer imprint is published by the registered company Springer Nature Switzerland AG
The registered company address is: Gewerbestrasse 11, 6330 Cham, Switzerland

Organization

General Chair

Doina Pisla, Technical University of Cluj-Napoca, Romania

Co-Chairs

Giuseppe Carbone, University of Calabria, Italy
Daniel Condurache, “Gheorghe Asachi” Technical University of Iasi, Romania
Calin Vaida, Technical University of Cluj-Napoca, Romania

International Scientific Committee (RAAD ISC)

Nikos A. Aspragathos, University of Patras, Greece
Karsten Berns, University of Kaiserslautern, Germany
Theodor Borangiu, Polytech. University of Bucharest, Romania
Mathias Brandstötter, Carinthia University of Applied Sciences, Austria
Ivana Budinská, Slovak Academy of Sciences, Bratislava, Slovakia
Giuseppe Carbone, University of Calabria, Italy
Karol Dobrovodský, Slovak Academy of Sciences, Bratislava, Slovakia
Carlo Ferraresi, Polytech. of Turin, Italy
Alessandro Gasparetto, University of Udine, Italy
Nick Andrei Ivanescu, Polytech. University of Bucharest, Romania
Kosta Jovanović, University of Belgrade, Serbia
Roman Kamnik, Univ. of Ljubljana, Slovenia
Gernot Kronreif, ACMIT, Wiener Neustadt, Austria
Med Amine Laribi, University of Poitiers, France

Andreas Müller, Johannes Kepler University, Linz, Austria
Tadej Petrič, Jožef Stefan Institute, Ljubljana, Slovenia
Ivan Petrović, University of Zagreb, Croatia
Doina Pisla, Technical University of Cluj-Napoca, Romania
Aleksandar Rodić, Institute Mihailo Pupin, Belgrade, Serbia
Marko Švaco, University of Zagreb, Croatia
József K. Tar, Óbuda University, Budapest, Hungary
Said Zeghloul, University of Poitiers, France
Leon Žlajpah, Jožef Stefan Institute, Ljubljana, Slovenia

Preface

The 33rd International Conference on Robotics in Alpe-Adria-Danube Region, RAAD 2024, is organized by the Technical University of Cluj-Napoca, Romania, June 5–7, 2024. The conference offers an international and cooperative platform to exchange and discuss recent research results and future trends about robotic technology, engineering, and science. RAAD represents an event on robotics that is organized yearly by a community of robotic specialists in the Alpe-Adria-Danube Region of Europe. The first event was held in 1992, organized by the Jozef Stefan Institute, Ljubljana, Slovenia. It was named the 1st International Meeting on Robotics in Alpe-Adria Region. In the following years, the event was named International Workshop on Robotics in Alpe-Adria Region (RAA) until 1996, when the denomination was changed into International Conference on Robotics in Alpe-Adria-Danube Region (RAAD). RAAD 2024 conference brought together robotics researchers in academy and industry from 17 countries, mainly in the Alpe-Adria-Danube Region, but also from other countries worldwide. Discussion of current trends and exchange of recent results in robotics research in an open and collegial atmosphere is a key aspect of the RAAD conference, and besides the technical sessions, plenary talks by renowned experts are a key component of the conference. We are thankful and honored that we have three plenary speakers sharing their ideas on current topics—Manfred Husty (University of Innsbruck, Austria) on “Local versus global Kinematics”; Damien Chablat (Centre National de la Recherche Scientifique (CNRS), Laboratoire des Sciences du Numérique de Nantes and Agence Nationale de la Recherche (ANR), France) on “Assistance Robot for Otological and Sinus Endoscopic Surgery: Advancing Surgical Innovation”; and José Machado (University of Minho, Campus of Azurém, Portugal) on “A Global Overview on Designing and Using Mechatronic Healthcare Assistive Devices”. According to its tradition, RAAD 2024 covers all major areas of research, development, and innovation in robotics, including new applications and trends related to new theories, advanced design of robot mechanics and control architectures, and development of intelligent robotic applications. After a careful and accurate peer-review process, with at least two reviews for each paper, 63 papers, authored by researchers from the RAAD community but also from other European countries, were considered suitable for publication in this book. The evaluation process has considered the relevance, novelty, and clarity of the papers which guaranteed the high-quality level of this collection. We would like to thank all the reviewers for allocating their valuable time and effort for their outstanding work in reviewing the assigned papers. We are also very grateful to all the authors for their effort and excellent work to improve their papers. According to the planned conference sessions, this book is organized in seven parts, covering the major research areas of the conference: I. Perception and Learning, II. Medical Robotics and Biomechanics, III. Industrial Robots and Education, IV. Kinematics and Dynamics, V. Motion Planning and Control, VI. Service Robotics and Applications, and VII. Mobile Robots and Innovative Robot Design.

We thank the Technical University of Cluj-Napoca, Romania, for its availability to host the RAAD 2024 event. We acknowledge the support of the International Federation for the Promotion of Mechanism and Machine Science (IFToMM, https://iftomm-world.org/), Ministry of Education of Romania and the Technical Sciences Academy of Romania. The Technical Science Academy of Romania. Special thanks go to the RAAD Scientific Conference Committee for support and advertisement of the conference. We thank the publisher Springer and its editorial staff for accepting and helping in the publication of this proceedings volume within the book series on Mechanism and Machine Science (MMS).

June 2024

Doina Pisla
Giuseppe Carbone
Daniel Condurache
Calin Vaida

Contents

Kinematics and Dynamics

Motion Planning and Control

Service Robotics and Applications

Part I
Perception and Learning

Determining Sample Quantity for Robot Vision-to-Motion Cloth Flattening

Peter Nimac and Andrej Gams

Abstract It is not clear how much data is needed to train a neural network efficiently. The "more is better" approach is not necessarily true for a multitude of reasons, especially when data is expensive to obtain in terms of time and effort, as is the case with robots in the real world. In this paper, we describe a method for determining the sample quantity for training a vision-to-motion DNN (Deep Neural Network). The training task is to straighten a single crumpled corner on a white towel in a simulated environment. For this purpose, the neural network was trained to identify a correct grab point for the simulated fabric as well as the direction and length of the movement to straighten the towel. We have trained it multiple times with datasets differing in the amount of samples. Comparisons show that the results hardly improve above a certain number of samples. In our experiments, datasets with 1000 and 2000 samples proved to be the most promising by striking a good balance between training time and desired accuracy. These models had a median error in predicting grab point position of 1.095 px and 0.977 px, respectively. Both reached or just exceeded the median error threshold of 1 px, which corresponds to an error of about 2.4 mm in the simulated environment. The study serves as a basis for transferring the movement to the real world, where Sim-2-Real approaches must be employed. Creating a dataset using only real world data with these sample quantities is not feasible.

Keywords Vision-to-motion · Deep neural network · Cloth flattening · Sample quantity

Supported by young researcher grant (PR-11324), research grant Robot Textile and Fabric Inspection and Manipulation—RTFM (J2-4457) and program group Automation, Robotics, and Biocybernetics (P2-0076), all by ARIS.

P. Nimac (✉) · A. Gams
Jožef Stefan Institute, Jamova cesta 39, SI-1000 Ljubljana, Slovenia
e-mail: peter.nimac@ijs.si

P. Nimac
Jožef Stefan International Postgraduate School, Jamova cesta 39, SI-1000 Ljubljana, Slovenia

D. Pisla et al. (eds.), *Advances in Service and Industrial Robotics*, Mechanisms and Machine Science 157, https://doi.org/10.1007/978-3-031-59257-7_1

1 Introduction

There is no question that the best way to train a neural network is to use a dataset with diverse data [2]. But it is not clear how much data we need to train a neural network efficiently. The "more is better" approach is not necessarily true for several reasons. Firstly, we do not want the neural network overfitting to the training data. And secondly, when we generate our own datasets, we do not want to waste time generating unnecessary data. It has been shown that direct data acquisition for real-world robotics experiments requires enormous amounts of data [4]. Therefore, the question of data acquisition is also extremely important when we want to use and retrain our neural network in different use cases with similar data domains. The answer to how many data samples are needed can also provide a rough estimate of how much data we need if we want to perform domain adaptation with additional training on a pre-trained neural network. This has been discussed before, for example in Sim-2-Real scenarios where different methods have been applied [5, 6]. Meta-learning as an approach for the adaptation of deep networks was reported in [1].

2 Dataset

We used the MuJoCo simulation environment to collect the data samples. The simulated textile, i.e. the towel, was rectangular, with the size of the edges at $t_a = 50$ cm and $t_b = 29$ cm. The thickness of the simulated textile was $t_c = 6$ mm. The simulation of the textile was implemented with a matrix of capsule nodes of a size 29×17, as shown in Fig. 1. The nodes were flexibly connected. The towel was placed on a light-coloured wooden board to mimic the real-world experimental setup.

Our database consisted of 4000 simulated towel deformation experiments. In every experiment the towel was initialised in the original, flattened state. The robot was used to linearly push at the corner of the towel, pushing it towards its centre, thus crumpling it. For every experiment the robot linear motion was random in the distance and the angle of the push. The distance was between 3 and 30 cm and the angle ranged from 20° to 70° as depicted also in (Fig. 2a). The final, deformed state of the towel was recorded along with the initial and final points of the robot motion when in contact with the towel.

In addition, we have introduced domain randomization with a random hue shift in each image. Since the pixels representing the towel are predominantly white with different shades of grey in certain shaded areas, the hue shift had no effect on them. This is because the hue shift only affects the pixels with unequal values for the red, green and blue channels. It therefore only affected the light brown wood surface. The colour shift was random for each image and ranged between 0° and 360°. This was done to introduce more variation to our dataset. We have already tested this approach on a similar set of data end described it in more detail in [8].

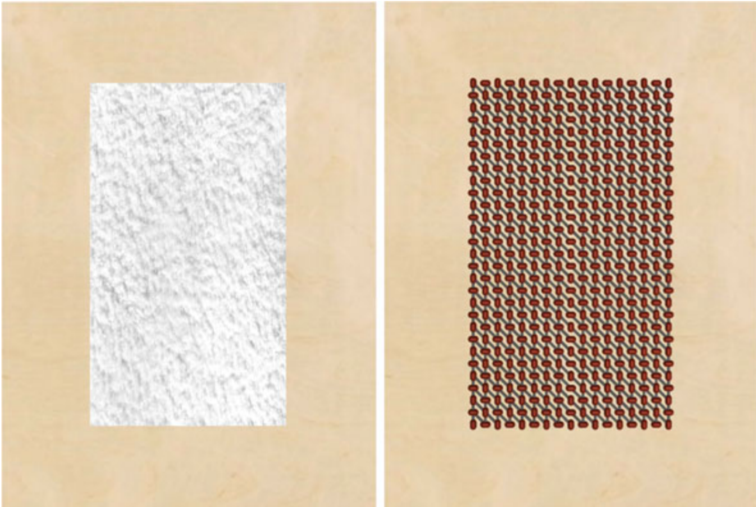

Fig. 1 Cloth raster representation inside the simulation

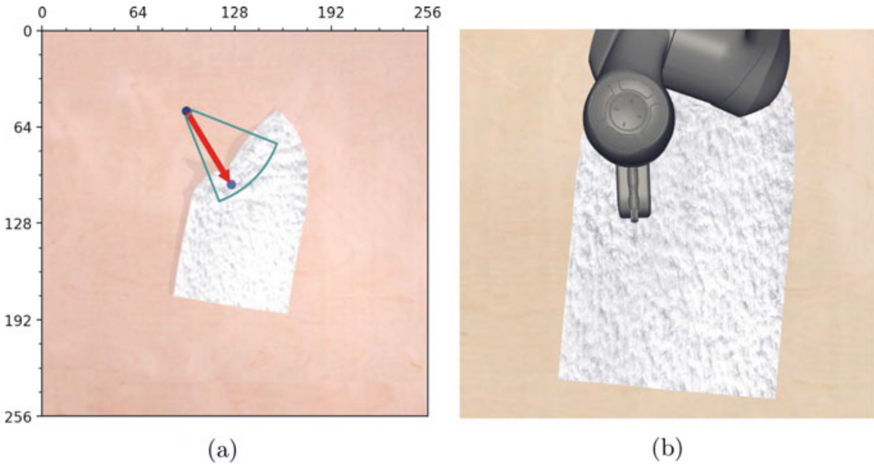

Fig. 2 Subfigure 2**a** shows the deformation area into which the robot pushed the upper left corner during data acquisition. The dark dot marks the point where the robot started the deformation movement and the light dot marks the point where the robot ended the movement. Subfigure 2**b** shows the robot during the deformation movement

The data pairs D in each dataset are mathematically expressed as

$$D = \{C_j,\ M_j\}_{j=1}^{P}. \tag{1}$$

P is the total number of samples, which consist of images $C_j \in \mathbb{R}^{3\times H\times W}$ with height H and width W and the corresponding grab point and manipulation motion vector pair of the linear smoothing motions

$$M_j = \{\mathbf{g}_j,\ \mathbf{m}_j\}. \tag{2}$$

In the above equation, vectors $\mathbf{g}_j$ and $\mathbf{m}_j$ are defined as

$$\mathbf{g}_j = \{g_{x,j},\ g_{y,j}\}, \tag{3}$$

$$\mathbf{m}_j = \{m_{r,j},\ m_{\varphi,j}\}, \tag{4}$$

where $g_{x,j}$ and $g_{y,j}$ represent the x and y pixel coordinates of the grab point respectively, the starting point of the smoothing movement. While r (Euclidean distance in pixels) and φ (in degrees) are components of the smoothing motion vector $\mathbf{m}_j$, expressed in polar coordinates. The values for r and φ were calculated from recorded pairs of grab points $\mathbf{g}_j$ and drop points $\mathbf{d}_j$.

3 DNN Architecture for Vision-to-Motion Skill Encoding

As in our previous work [7], we used an image-to-motion network based on [9]. We kept the architecture almost unchanged, which is composed of three convolutional layers and three fully connected layers. The first convolutional layer takes an RGB image with an image size of $3 \times 256 \times 256$ pixels as the input. After the input data is convolved, ReLU and max-pool operations follow on each convolution layer. After the last convolution layer, adaptive pooling is performed and then followed by flattening into a one-dimensional vector. The flattened output is passed through three layers that are fully connected. The final result is a linear motion smoothing vector M_j in a 2D plane (Fig. 3).

3.1 Training

To find the required sample quantity to achieve our target accuracy, or about 1px for the grab point, we ran the training with different sample sizes of the generated dataset. We performed the first training with a dataset of 4000 samples, followed by training with 2000 samples, 1000 samples and finally 500 samples. All these datasets are

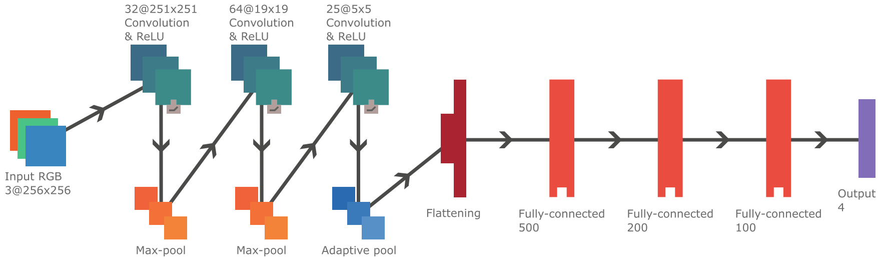

Fig. 3 The architecture of image-to-motion DNN that was used to generate grab point and smoothing motion vector pairs

subsets of the dataset with the most samples to speed up the generation of samples. For each training, we evaluated the accuracy of the predicted grab and drop point pairs. The evaluation was performed on a separate dataset with 500 samples. The test dataset was generated in the same way as the training dataset.

3.2 Learning Parameters

For each training, we set the maximum training period to 3500 epochs, setting the learning rate to 1×10^{-5} and the weight decay rate to 1×10^{-4}. The network was trained with batches of size 10. To determine the training loss, we calculated it as the mean squared error (MSE) between the predicted and target values of a motion vector M_j. If the validation loss did not decrease further in 100 consecutive epochs, the training was cancelled. In this way, we attempt to mitigate the overfitting of the network to training data with a high sample quantity, although the number of parameters that are trained is very high. We used Adam optimiser [3] to dynamically adjust the parameters of the network during training.

3.3 Results

For each batch of training, we evaluated the achieved accuracy of the model, expressed as absolute pixel error, in predicting grab and drop points of the flattening motion. The statistical values of the results are shown in Fig. 4. Our training goal is to find the sample number at which the median value of the error in the grab point falls to ∼1 px. For an image with a size of 256×256 px^2, we can approximate this error to 1 px ≈ 2.4 mm in a simulated environment. The model trained with 2000 samples just reaches this threshold with a median value of $g_{err2000,med} = 0.977$ px. We have chosen the median value as the threshold value because we expect our model to have an error of $g_{err,med} \leq 1$ px no more than 50 % of the time. The model

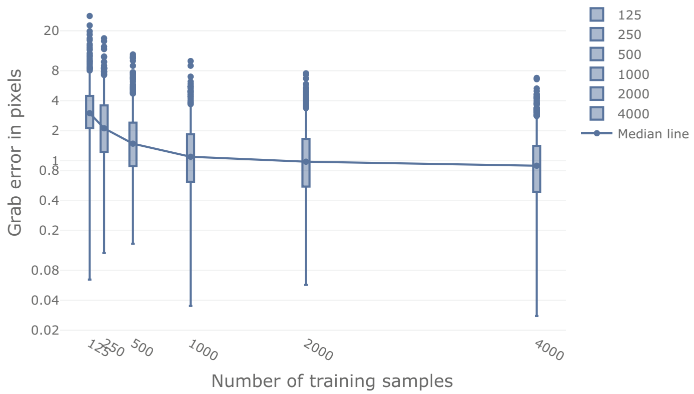

(a) Grab point error distribution

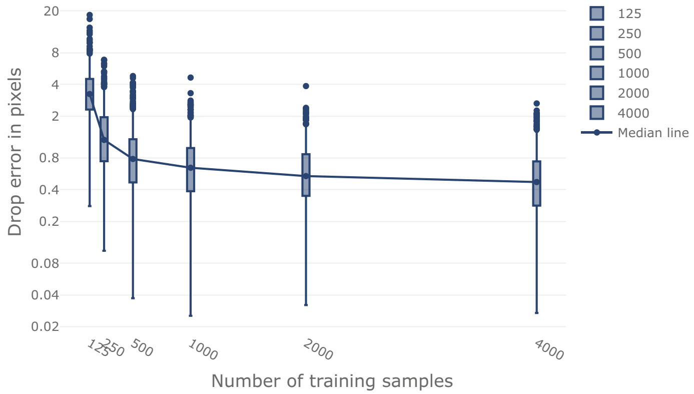

(b) Drop point error distribution

Fig. 4 The distribution of drop point and grab point errors is shown with box-and-whisker plots for different training samples count. Overlaid is a line plot of error median values. The points that fall outside the whiskers are statistical outliers. Samples that fall within the boxes represent 50 % of all samples in the test set

trained on 1000 samples comes close to this threshold with $g_{err1000,med} = 1.095$ px. Both models also exceed the threshold $g_{err,q3} \leq 2$ px ($g_{err2000,med} = 1.653$ px and $g_{err1000,med} = 1.842$ px respectively). In practise, 75 % of the cases of one of these two models will have an error less than 4.8 mm in simulation. If we also consider the training times ($t_{2000} = 320$ min and $t_{1000} = 90$ min), as shown in Fig. 5, the model trained on 1000 samples trains more than 3 times faster, which might outweigh the slightly lower accuracy. Of course, if higher accuracy were required, we can always increase the training dataset, but in this case the yields decrease due to the steep increase in training times.

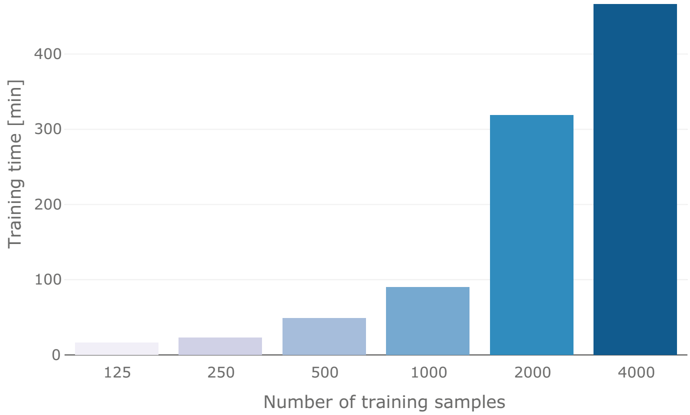

Fig. 5 Image of cloth manipulation setup in reality

4 Discussion

This article describes our research progress in manipulation of textiles with robots, where predict flattening motion of a rectangular towel. In our previous work [7], the fabric model we used in MuJoCo was coarser and less realistic. One of the main limitations in our experiments is simulation computational speed. The used size of the simulated textile raster (29×17) was computationally so expensive that the simulation speed was on average around ~ 15 % of the real-time speed. However, this raster size was needed for the simulation accuracy, even though it severely reduced the simulation speed and increased the duration of the experiments. On the other hand, the smaller perceptual gap to the real world is expected to accelerate our transfer to the real world.

However, it should be noted that these results apply to this particular example. Should we have a dataset with more variability, it is reasonable to expect that we will need more samples for optimal training. Further statistical comparisons are also required. The results in Fig. 4b are the average results for training with 2 initial seeds. To obtain more accurate results, we would also need to repeat our training several more times with different random initial seeds for each dataset size to account for the result variability due to the initialisation of the neural network weights.This amount of samples is also attainable in practise. Therefore, we estimate that we only need about 100 samples (maybe less) from the real world setup and include them in the training of more accurate models to achieve the desired accuracy.

Fig. 6 Image of cloth manipulation setup in reality

5 Conclusion

The results show that training a neural network, which we used in our experiments, requires about 1000 samples to deliver results with the desired accuracy. Creating a dataset with this many samples in the real world is a large and complex endeavour that is not practically feasible. If we want to apply the use of this neural network to a real-world example (as in Fig. 6), we need to use different methods for Sim-2-Real transfer. One possible approach is meta-learning, as described in [1], or other methods, as described in [6]. We can observe in Fig. 4a, that the model trained with the lowest training sample count already achieves reasonable accuracy. This amount of samples is also attainable in practise. Therefore, we estimate that we only need about 100 samples (maybe less) from the real world setup and include them in the training of more accurate models to achieve the desired accuracy.

References

1. Finn, C., Abbeel, P., Levine, S.: Model-agnostic meta-learning for fast adaptation of deep networks. In: International Conference on Machine Learning, pp. 1126–1135. PMLR (2017)
2. Gawlikowski, J., Tassi, C.R.N., Ali, M., Lee, J., Humt, M., Feng, J., Kruspe, A., Triebel, R., Jung, P., Roscher, R., et al.: A survey of uncertainty in deep neural networks. Artif. Intell. Rev. **56**(Suppl 1), 1513–1589 (2023)
3. Kingma, D.P., Ba, J.: Adam: a method for stochastic optimization. In: The International Conference on Learning Representations (ICLR) (2015)
4. Levine, S., Pastor, P., Krizhevsky, A., Ibarz, J., Quillen, D.: Learning hand-eye coordination for robotic grasping with deep learning and large-scale data collection. Int. J. Robot. Res. **37**(4–5), 421–436 (2018)
5. Lončarević, Z., Simonič, M., Ude, A., Gams, A.: Combining reinforcement learning and lazy learning for faster few-shot transfer learning. In: 2022 IEEE-RAS 21st International Conference on Humanoid Robots (Humanoids), pp. 285–290 (2022)

6. Muratore, F., Ramos, F., Turk, G., Yu, W., Gienger, M., Peters, J.: Robot learning from randomized simulations: a review. Front. Robot. AI **9** (2022)
7. Nimac, P., Gams, A.: Cloth flattening with vision-to-motion skill model. In: Advances in Service and Industrial Robotics, RAAD 2023, 32nd International Conference on Robotics in Alpe-Adria-Danube Region, pp. 367–374. Springer (2023)
8. Nimac, P., Gams, A.: Vpliv parametrov barvnega modela pri robotskem ravnanju tekstila. In: Zbornik dvaintridesete mednarodne Elektrotehniške in računalniške konference ERK 2023, pp. 189–192. Društvo Slovenska sekcija IEEE (2023)
9. Pahič, R., Ridge, B., Gams, A., Morimoto, J., Ude, A.: Training of deep neural networks for the generation of dynamic movement primitives. Neural Netw. Official J. Int. Neural Netw. Soc. **127**, 121–131 (2020)

Outliers—Do Image and Feature Domain Outliers Coincide in Robotic Applications?

Axel Vierling, Urooj Iltifat, and Karsten Berns

Abstract In this work, robotic application data is taken and quantitatively analyzed if outliers in the image domain correlate with outliers in the feature space of CNNs used for the detection of objects. This is necessary to ensure that commonly given reasons for perception failures such as overexposure are valid for any object detection robustness analysis. The outlier detection is done with an encoder-decoder network on images and different layers of different object detection networks. Last, a qualitative analysis of what makes an image an outlier and how this relates to the experience from the application is done.

Keywords Robotic vision · Explainability · Outliers

1 Introduction and Related Work

In recent years autonomous driving has been of steady interest. The applications if an adequate level of autonomy could be reached are vast. They range from public transport [8], via automated construction processes like road compaction [19], to autonomous fire fighting [18], to give just a few examples. While the past years have shown good results and capabilities under defined conditions one of the main problems which is not yet covered in a substantial amount is the robustness of driving approaches in different conditions. Weather effects like e.g. rain or a low sun leading to sun glares can have tremendous implications and have even led to

http://agrosy.cs.uni-kl.de.

A. Vierling (✉) · U. Iltifat · K. Berns
Robotics Research Lab, Department of Computer Science, University of Kaiserslautern-Landau, 67663 Kaiserslautern, Germany
e-mail: axel.vierling@cs.rptu.de

K. Berns
e-mail: karsten.berns@cs.rptu.de

D. Pisla et al. (eds.), *Advances in Service and Industrial Robotics*, Mechanisms and Machine Science 157, https://doi.org/10.1007/978-3-031-59257-7_2

fatal accidents before.[1] A robustness to changing conditions is paramount to reach widespread deployment of autonomous vehicles. Oftentimes the most vulnerable part of an autonomous vehicle with respect to changing weather is the image processing. Nowadays most used image processing approaches are based on neural networks, and more specifically on Convolutional Neural Networks (CNNs). While there has been some research to measure the robustness of CNNs with respect to changing weather [9, 11, 16], it has not yet been solved. Most approaches try to tackle the problem on the level of the features represented in a CNN [10, 21], as this is most relevant for the output of the network. However, most robotic and autonomous driving applications try to identify problems on the image level [2, 13, 17]. So, there seems to be a discrepancy. This paper tries to overcome this gap, by identifying outliers in different levels of the feature domain, and in the image domain for autonomous driving. Then a statistical analysis of the outliers in all domains is done to see if there is a correlation and how strong this correlation is. Such a correlation is required to even attempt to identify complicated weather conditions with the help of the feature space of a CNN. Extending the common approach of outliers in the image domain to the feature domain, and analyzing the statistical correlation as well as a visual analysis is the main contribution of this paper.

2 Outlier Detection Approaches

The idea of outlier detection is simple, to find data points that deviate significantly from the majority of data. There exists a multitude of different approaches to achieve this. Common for all approaches is a mapping function $\boldsymbol{f}$ which can be expressed as $f(p) \rightarrow q$. Where $\boldsymbol{p}$ represents a data point and $\boldsymbol{q}$ denotes its outlier-ness score, representing the intensity of the outlier-ness of $\boldsymbol{p}$. Outlier detection algorithms belong to one of two groups based on the mapping function [20] and the task: (1.) Find the top $\boldsymbol{k}$ outliers with the highest outlier-ness score. (2.) Find all outliers above a threshold value.

For both approaches, various techniques exist and can be grouped into three categories [14]: Supervised Outlier Detection (SOD), Semi-supervised Outlier Detection (SSOD), and Unsupervised Outlier Detection (UOD). For detecting outliers efficiently multiple techniques have been proposed [3]. For instance, the Transformation Invariant Autoencoder (TIAE) proposed by Cheng et al. [4] is an unsupervised outlier detector based on a deep neural network to mitigate the impact of noise induced by outliers. In [1], a novel approach for open-set recognition and dense outlier detection is introduced by discriminating the inlier dataset examples specific to some domain from a diverse dataset containing general-purpose examples whose pixels represent negative noisy samples.

[1] https://www.theguardian.com/technology/2018/mar/19/uber-self-driving-car-kills-woman-arizona-tempe.

While classical approaches exist nowadays deep learning-based outlier detection techniques are more popular and exhibit significant benefits [4]. Among unsupervised outlier detection techniques, autoencoders are considered to be very effective tools. Therefore, in this work, the focus is on a UOD-approach with a deep autoencoder implemented with and as in [15]. Autoencoders are usually used for other applications such as image denoising or dimensionality reduction, however, they can also be used for the detection of outliers. In this work, the convolutional autoencoder (CAE) reconstructs an output similar to the input, if the difference between the reconstructed output and input, measured by the pixelwise Mean Squared Error, is high then the image/feature is flagged as an outlier. This reconstruction error is used in this work as the dimensionless outlier score.

3 Concept and Experiments

The general overview of this work is given in Fig. 1. As discussed before, outliers in the image domain as well as in the feature domain are detected. Then, it should be seen, if these outliers correlated and finally if any or both types of these outliers correlate with the object detection quality. Therefore, first, the images are taken and preprocessed for object detection and outlier detection. The object detection starts with the feature extraction. These feature maps are then extracted, preprocessed and then outliers are detected. Meanwhile, the object detection network continues normally and yields the detection result.

For object detection two different networks are used, Faster-RCNN [12] and Mask-RCNN [6] in both cases with ResNet [7] as feature extractor and a Feature Pyramid Network (FPN). To ensure independence of the overall architecture. The features

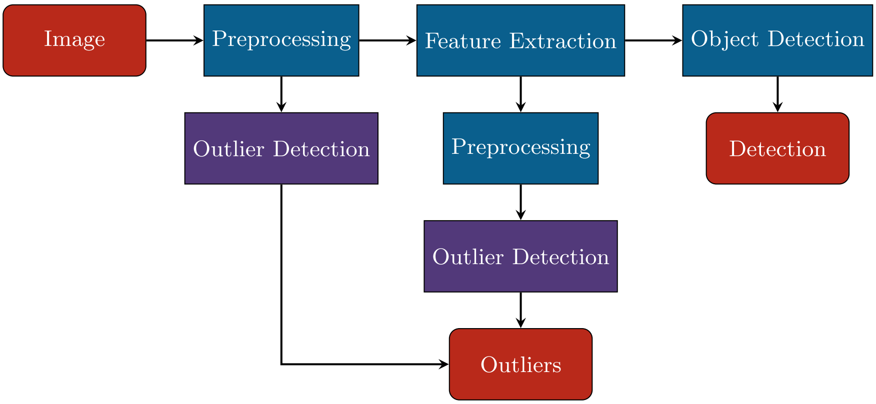

Fig. 1 Overview outlier detection approach. In- and Outputs are denoted in red, common object detection parts in blue, and the outlier detection in purple

for the outlier detection are extracted in two places, layer 3 (P3) and layer 6 (P6) of ResNet or rather the corresponding FPN. This way it can be checked if earlier layers, which usually are related to lower-level features, and deeper layers usually related to more abstract higher-level concepts, behave differently with respect to outlier detection.

The architecture of the CAE for the outlier detection consists of an encoder network with three convolutional layers that compress the input image to its latent representation, and a decoder network also with three convolutional layers that reconstruct the input image from the latent embedding. In both the encoder and decoder a stride of 2 is used in convolutional layers and in between the convolutional layers, the ReLu activation function is used. For the output layer of the decoder network, however, a sigmoid activation function is utilized.

The training of the object detection was done on 2000 images of the KITTI [5] dataset with 600 epochs of training, a learning rate of 0.00025 and a batch size of 64. The training of CAE was done on the same 2000 images and on their features to detect outliers in both image space and feature space, also with 600 epochs and a learning rate of 0.00025. The P3 and P6 features acquired from the object detection models are taken as input for the training of CAE. Feature representation of layers was preprocessed to make it compatible with the CAE algorithm. In both cases, 4 GeForce RTX 2080 Ti GPUs were utilized for the training and testing. Additionally, the dataset was extended by adding Salt and Pepper noise to check how robust the correlation is concerning small perturbations to the images. This gives 8 experimental setups, Faster RCNN versus Mask RCNN, layer P3 versus P6, and clean versus noisy data. These experiments are denoted as Mask-6, Mask-3, Faster-6, Faster-3, Mask-6-Noise, Mask-3-Noise, Faster-6-Noise, and Faster-3-Noise.

In the evaluation phase, 327 images and their features consisting of both inliers and outliers are fed to the CAE, trying to reconstruct the image. A larger reconstruction error, also referred to as the instance score or outlier score, indicates that an instance is an outlier. A threshold value is set to identify which examples are regarded as outliers. The outliers are data points that dramatically deviate from the patterns the autoencoder learned during training and have instance scores over the chosen threshold.

The outlier-ness scores for the different experimental setups can be seen in Fig. 3 without noise and in Fig. 4 with noise. The covariance values of all experiments are depicted in Table 1. Assuming outliers in the image and feature domain coincide, then there should be a positive outlier-ness correlation between the two, and object detection should perform worse for outliers in both domains. Taking a look at the experimental values, one can see that this is true if the features in the 6th layer are considered, but the assumption does not seem to hold for outliers in the 3rd layer. This implies that indeed outliers in the image domain are outliers in higher-level abstract features where complex shapes are considered, but not for lower-level features. This coincides with the common observation that deeper networks can better represent the original image as a whole, but it also means that image preprocessing to smooth outliers can not only be based on low level features as classical image processing techniques in robotic applications often do.

Table 1 Correlation between different metrics for all experiments

Experiment	Fig. 3a	Fig. 3b	Fig. 3c	Fig. 3d	Fig. 3e	Fig. 3f
covariance	0.002863	−0.005272	−0.0031	−0.002195	−0.005272	0.011642
Experiment	Fig. 3g	Fig. 3h	Fig. 3i	Fig. 3j	Fig. 3k	Fig. 3l
covariance	0.000649	−0.006145	−0.007002	0.020269	−0.006311	−0.010936
Experiment	Fig. 4a	Fig. 4b	Fig. 4c	Fig. 4d	Fig. 4e	Fig. 4f
covariance	0.004053	−0.007338	−0.008813	−0.0023	−0.007338	0.004006
Experiment	Fig. 4g	Fig. 4h	Fig. 4i	Fig. 4j	Fig. 4k	Fig. 4l
covariance	0.000643	−0.007905	−0.005206	−0.003132	−0.007338	0.000948

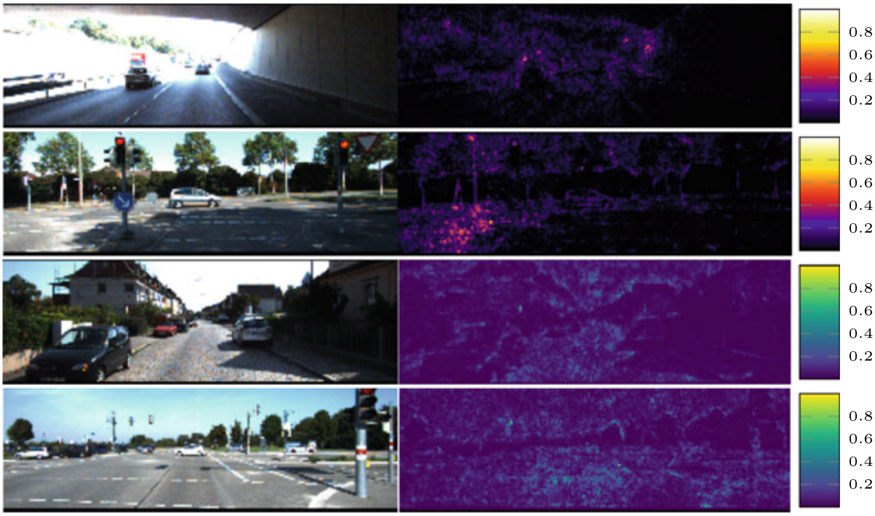

Fig. 2 Original image (left) versus attribution masks (right). The influence of the pixels in the attribution mask is mentioned on the right in each row

However, even more interesting for robotic applications is, what makes images outliers. To answer this, the attribution masks of the outlier score of some exemplary outliers are analyzed in Fig. 2, so which regions contribute the most to the outlier-ness score. One can see, that in the first row, the top-left and top-middle area pixels which are overexposed are highlighted in the attribution mask. Similarly, in the second row, the overexposed area which is bottom-left is highlighted most in the attribution mask. Therefore, it could be concluded that these images are considered outliers by the CAE due to *overexposure*. However, in the third row, the attribution mask highlights the over-exposed area which is the top-middle, but it also highlights the bottom-middle which is not so much exposed. Therefore, the analysis is inconclusive. Furthermore, in the last row, the cause of the image being an outlier is vague because the salient features from the attribution mask are selected from all over the image. So it seems

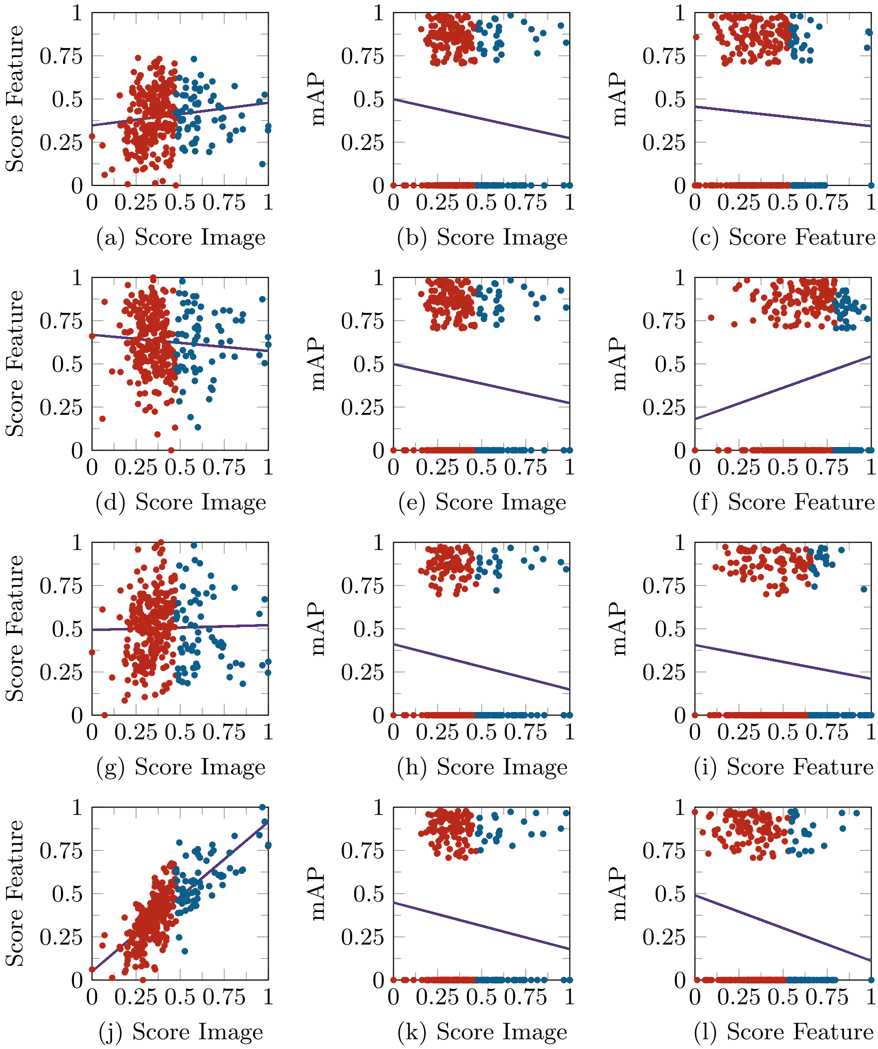

Fig. 3 Correlation between outlier score in the image and feature domain, as well as the object detection accuracy. The plots depicted show experiments Mask-6 (first row), Mask-3 (second row), Faster-6 (third row), and Faster-3 (fourth row), the comparison between the instance score in the image domain and the feature domain (first column), the correlation between the instance score in the image domain and the object detection accuracy (second column), and the correlation between the instance score in the feature domain and the object detection accuracy (third column). In blue outliers are represented, red represents non-outliers, and purple the regression line

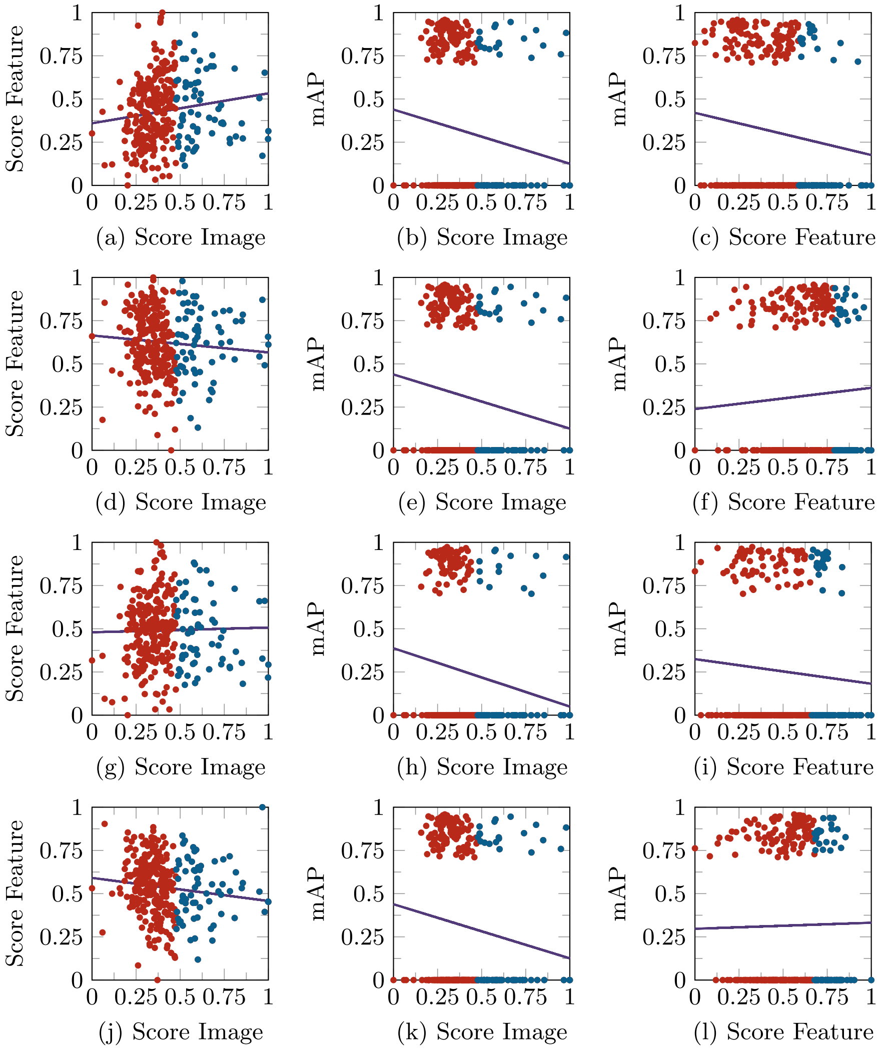

Fig. 4 Setup and colors same as in Fig. 3, added Salt and Pepper noise in the data

that clear disturbances in the robotic application domain like overexposure are indeed reasons for outliers, but they do not cover all cases of outliers.

4 Conclusion

In this work, the correlation between outliers of different domains was analyzed. The domains are robotic application images with outliers due to human visible disturbances such as overexposure, as well as outliers in the image and feature domain, determined by the outlier-ness score of an encoder-decoder network (Figs. 3 and 4). It could be seen that outliers in deeper layers and outliers in the image domain correlate, but they do not correlate with outliers in lower layers. This partially follows common theory but gives further new hints on how potential preprocessing for robotic applications must look like.

References

1. Bevandić, P., Krešo, I., Oršić, M., Šegvić, S.: Dense outlier detection and open-set recognition based on training with noisy negative images. arXiv preprint arXiv:2101.09193 (2021)
2. Brophy, T., Mullins, D., Parsi, A., Horgan, J., Ward, E., Denny, P., Eising, C., Deegan, B., Glavin, M., Jones, E.: A review of the impact of rain on camera-based perception in automated driving systems. IEEE Access **11**, 67040–67057 (2023)
3. Chen, Z., Yeo, C.K., Lee, B.S., Lau, C.T., Jin, Y.: Evolutionary multi-objective optimization based ensemble autoencoders for image outlier detection. Neurocomputing **309**, 192–200 (2018)
4. Cheng, Z., Zhu, E., Wang, S., Zhang, P., Li, W.: Unsupervised outlier detection via transformation invariant autoencoder. IEEE Access **9**, 43991–44002 (2021)
5. Geiger, A., Lenz, P., Urtasun, R.: Are we ready for autonomous driving? The kitti vision benchmark suite. In: Conference on Computer Vision and Pattern Recognition (CVPR) (2012)
6. He, K., Gkioxari, G., Dollár, P., Girshick, R.: Mask r-cnn (2018)
7. He, K., Zhang, X., Ren, S., Sun, J.: Deep residual learning for image recognition. In: Proceedings of the IEEE Conference on Computer Vision and Pattern Recognition, pp. 770–778 (2016)
8. Jan, Q.H., Klein, S., Berns, K.: Safe and efficient navigation of an autonomous shuttle in a pedestrian zone. In: Proceedings of the 28th International Conference on Robotics in Alpe-Adria-Danube Region, pp. 267–274. Springer (2019)
9. Khosravian, A., Amirkhani, A., Kashiani, H., Masih-Tehrani, M.: Generalizing state-of-the-art object detectors for autonomous vehicles in unseen environments. Expert Syst. Appl. **183**, 115417 (2021)
10. Li, J., Xu, R., Ma, J., Zou, Q., Ma, J., Yu, H.: Domain adaptive object detection for autonomous driving under foggy weather. In: Proceedings of the IEEE/CVF Winter Conference on Applications of Computer Vision (WACV) (2023)
11. Michaelis, C., Mitzkus, B., Geirhos, R., Rusak, E., Bringmann, O., Ecker, A.S., Bethge, M., Brendel, W.: Benchmarking robustness in object detection: autonomous driving when winter is coming. arXiv preprint arXiv:1907.07484 (2019)
12. Ren, S., He, K., Girshick, R.B., Sun, J.: Faster r-cnn: Towards real-time object detection with region proposal networks. CoRR **abs/1506.01497** (2015)
13. Roh, C.G., Kim, J., Im, I.J.: Analysis of impact of rain conditions on adas. Sensors **20**(23) (2020)
14. Singh, K., Upadhyaya, S.: Outlier detection: applications and techniques. Int. J. Comput. Sci. Issues (IJCSI) **9**(1), 307 (2012)

15. Van Looveren, A., Klaise, J., Vacanti, G., Cobb, O., Scillitoe, A., Samoilescu, R., Athorne, A.: Alibi detect: algorithms for outlier, adversarial and drift detection (2019), https://github.com/SeldonIO/alibi-detect
16. Vierling, A., Groll, T., Meckel, D., Heim, K., Walter, D., Scheidhauer, L., Körkemeyer, K., Berns, K.: Progress estimation of an excavation pit. In: Proceedings of the 39th ISARC (2022)
17. Wolf, P., Berns, K.: Data-fusion for robust off-road perception considering data quality of uncertain sensors. In: IEEE/RSJ International Conference on Intelligent Robots and Systems (IROS), pp. 6853–6860 (2021)
18. Wolf, P., Ropertz, T., Berns, K.: Behavior-based obstacle detection in off-road environments considering data quality. In: Informatics in Control, Automation and Robotics, vol. 495, pp. 786–809. Springer International Publishing (2020)
19. Wolf, P., Ropertz, T., Berns, K., Thul, M., Wetzel, P., Vogt, A.: Behavior-based control for safe and robust navigation of an unimog in off-road environments. In: Proceedings of the 5th Commercial Vehicle Technology Symposium (2018)
20. Zhang, J.: Advancements of outlier detection: a survey. ICST Trans. Scalable Inf. Syst. **13**(1), 1–26 (2013)
21. Zhu, Y., Zhou, G., Ren, J., Tian, J., Jia, Z.: Multi-task model based on vision task level for saliency object detection in foggy conditions. In: 2023 IEEE International Conference on Image Processing (ICIP), pp. 3055–3059 (2023)

An Algorithm for Determining the Coordinates of a Test Tube by a Robotic Aliquoting System Based on a Combination of the Hough Method and a Result Filtering Algorithm

Larisa Rybak, Vladislav Cherkasov, Dmitry Malyshev, Dmitry Dyakonov, and G. Carbone

Abstract The article considers the problem of determining the position of test tubes in a tripod during aliquoting using technical vision. To solve this problem, the Hough circle transformation method was used, supplemented by an algorithm for filtering the obtained values. Experimental investigation of this algorithm have been carried out, which have shown its high accuracy and the possibility of successful application for determining the position of test tubes by a vision system. The results of the investigation show the high efficiency and accuracy of the proposed algorithm in determining the coordinates of a test tube with a biological liquid, which makes it a promising tool for automating the aliquoting process.

Keywords Aliquoting system · Computer vision · Object detection · Gripper

1 Introduction

The fields of application of robots in medicine are expanding every day. This is facilitated by the development of robotics in the field of new mechanisms with advantages such as accuracy and high speed, as well as the development of new control algorithms.

One of the tasks of medicine, in which the use of robots can increase productivity, is to work with samples for laboratory research. The replacement of manual labor will reduce the risk of infection of medical personnel and increase the productivity

L. Rybak (✉) · V. Cherkasov · D. Malyshev · D. Dyakonov
Belgorod State Technological University Named After V.G. Shukhov, 46 Kostyukova Street, Belgorod 308012, Russia
e-mail: rlbgtu@gmail.com

G. Carbone
Department of Mechanical, Energy and Management Engineering, University of Calabria, 87036 Rende, Italy

D. Pisla et al. (eds.), *Advances in Service and Industrial Robotics*, Mechanisms and Machine Science 157, https://doi.org/10.1007/978-3-031-59257-7_3

of tests. Aliquoting is the process of dividing or splitting a certain volume of liquid or substance into smaller parts called aliquots. This process is often used in the laboratory to prepare identical samples or solutions for further analysis or experiments. Aliquots usually have the same volume and contain the same amount of substance, which allows you to get more accurate results and compare data with each other. The work [1] shows the effectiveness of automated aliquoting in comparison with the use of manual labor. Thus, in [2], an automated system based on the Tecan station for aliquoting the HIV pseudovirus is considered.

The automation and use of robots in medicine requires the use of vision systems. Currently, vision systems are based on the application of one of two approaches: machine learning or the creation of an algorithm based on color models. Each of the approaches has its advantages and disadvantages, so it is appropriate to use them together to solve complex problems. In [3], two methods for recognizing blood serum and determining its volume for aliquoting were considered, however, these methods did not allow accurate recognition of the position of the test tube in a tripod to perform grasp. The Hough circle method was used to solve this problem [4]. Hough circles (or Hough transform) are one of the most widely used methods in computer vision for detecting geometric shapes in an image. They were developed in 1962 by Paul Haf to detect lines in an image, but have since been expanded and used to detect circles and other geometric shapes [5].

The Hough transform is based on a mathematical theory that allows you to translate points in an image into a parametric space [6]. In the case of circles, each pixel of the image will be represented by a circle in a parametric space, which is determined by its center and radius. Then the number of intersections between the circles in the parametric space is calculated, which makes it possible to identify the most likely circles in the image [7, 8].

The advantage of using Hough circles for technical vision is their ability to detect circles of various sizes and orientations, as well as resistance to noise and distortion in the image. In addition, they can be used to detect not only circles, but also other geometric shapes such as ellipses, rectangles, etc. [9].

The current investigation examines the use of Hough circles to solve problems of determining the coordinates of the location of test tubes in a tripod. To do this, images from a camera mounted above a tripod are used, and the Hough circle detection algorithm is used to determine the coordinates of the test tube centers. This allows you to automate the aliquoting process and increase the accuracy and speed of this operation. This method can also be applied in other workspaces of machine vision, where it is necessary to detect and recognize geometric shapes in an image.

2 Application of the Hough Transform to Determine the Position of Test Tubes

The process of aliquoting the blood of various patients involves the excavation of biological material from a test tube with a divided fraction into small-volume test tubes. The aliquoting workspace is divided into clean and dirty zones. In the clean area, tripods are stored before being fed to the dirty area where aliquots are dispensed. The work [10] shows the effectiveness of automated aliquoting compared with the use of manual labor. Automation of the aliquoting process allows you to avoid errors and improve the quality of analysis results by increasing the accuracy and reliability of the aliquoting process; reduce the time spent on sample preparation; reduce the risk of contamination of samples and cross-contamination, as the automated system minimizes contact with personnel; improve working conditions for laboratory staff by reducing physical exertion and increasing safety.

The design of a robotic system for aliquoting biological fluid of various patients is proposed, shown in Fig. 1. The PC includes: case 1, in which a parallel delta manipulator 2 is located, moving the dosing device 3, fixed in the center of the movable manipulator platform and performing aliquoting of biomaterial. The replaceable tip 4 on the dosing head is fixed with a rubber O-ring. A serial manipulator with six degrees of freedom 5 is mounted on a fixed base 6 and ensures the movement of racks 8 using a gripper device within the workspace 7.

The technological process of sample preparation and aliquoting of blood serum includes two main stages: at the first stage, blood is taken from the patient and the sample is centrifuged. At the second stage, blood serum is collected and dosed (Fig. 2).

To manipulate the tubes, it is necessary to solve the problem of determining their position in order to grasp and move them. In this regard, it was decided to use an algorithm based on the definition of Hough circles, which allows you to analyze the image and save the obtained values, which can be transmitted to the manipulator.

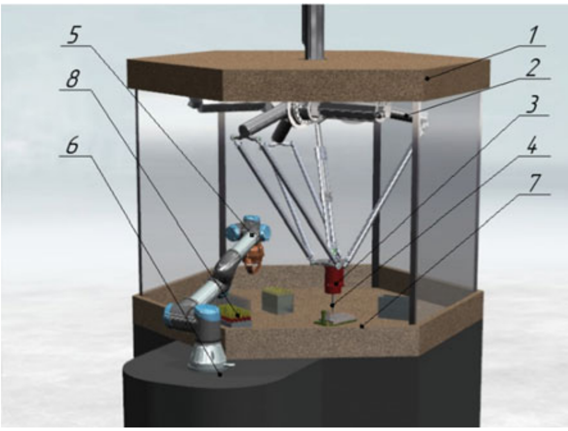

Fig. 1 Robotic system for aliquoting biosamples

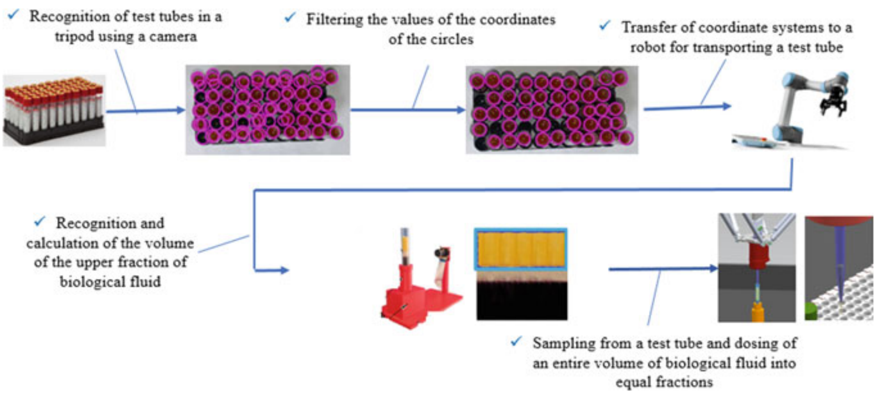

Fig. 2 Technological process of biomaterial aliquoting

This algorithm is easy to set up and, in comparison with the Yolo neural network, does not require a large set of training data. The result of the algorithm is an image with objects fixed in a circle. The results of recognition of various objects had high accuracy, however, incorrect results were obtained when recognizing test tubes. The algorithm either does not select all the tubes, or mistakenly selects workspace of the image where there are no tubes, depending on the selected values of the Hough transform parameters (Fig. 3).

To improve the accuracy of determining the coordinates of the tubes, the Hough circle transformation algorithm was supplemented with an algorithm for filtering the obtained values.

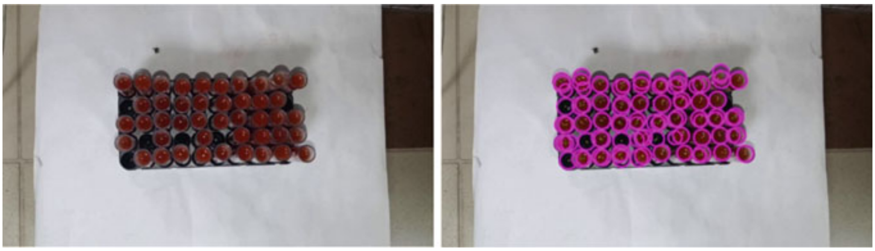

a) b)

Fig. 3 The result of tube recognition by the Hough algorithm. **a** The original image of the tripod with test tubes, **b** the image after the Hough transform

3 The Algorithm for Filtering the Results of the Hough Transform

The filtering algorithm made it possible to clear the array of coordinate values that are outside the area of the objects under consideration and filter the values to search for the necessary objects. The algorithm is configured to evaluate the attribute values of RGB and HSV models (Fig. 4).

The RGB format is an adaptive color model that forms any shades of the spectrum visible to the human eye, in which three colors are mixed: red, green and blue. The HSV format is a color model based on color parameters: hue, saturation, value.

Classifying a pixel by its position inside or outside the boundaries of the tube is possible due to the attributes of the models: R, G, B, H, S, V. Each attribute takes a value from 0 to 255 except for the H attribute, it takes values from 0 to 179.

The algorithm is shown in Fig. 5.

The input data for the algorithm is an image (I_{RGB}) and arrays of acceptable color ranges (R_{in}, R_{out}). The image is an array with information about the RGB attribute values for each pixel. The R_{in} array includes valid ranges of values for the 6 color attributes R, G, B, H, S and V pixels of the contents of the test tube. The R_{out} array includes valid values of the 4 color attributes R, G, B and V of the tube neck pixels. The H and S attributes are not included in the R_{out} array, since they can take any value for the neck pixels and cannot be limited.

In the first step (Fig. 5) of the algorithm, the input image is converted to an image (I_{GRAY}) in grayscale. In the second step, using the Hough transform in the image (I_{GRAY}), the values of the coordinates of the centers of m circles and their radiuses are determined and written to an array(c).

If the array(c) contains at least one circle, then the circles are filtered. To do this, an array (I_{HSV}) is formed based on the input image (I_{RGB}) with information about the value of HSV attributes for each of the pixels (the algorithm in Fig. 5, step 4). The first stage of filtering evaluates the color of pixels inside and on the contour of the circle. If this color does not match the color of the neck of the test tube or its contents, that is, if the number of false arrays ($P_{bool}^{(i)}$) is more than half the number of array elements ($P_{bool}^{(i)}$), then the circle corresponding to this element is removed from the array (c). With each the removed circle corrects the parameter m. Pixel color matching in step 8 is performed using the procedure (*Filter*), the pseudocode

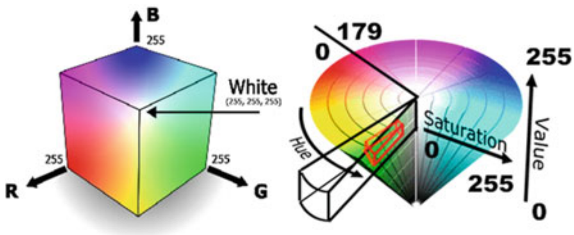

Fig. 4 HSV and RGB color palettes

Algorithm 1 Haugh circle detection

```
Input: I_RGB, R_in, R_out
Output: c = {c_1, c_2, ..., c_m}
I_GRAY = BGRTOGRAY(I_RGB)
c = {c_1, c_2, ..., c_m} = HoughCircles(I_GRAY)
if c ≠ ∅ then
    I_HSV = RGBTOHSV(I_RGB)
    for i=1 to m do
        c_coord = {c_i^(0), c_i^(1)}                ▷ c_coord – array of two coordinates
        r = c_i^(2)                                  ▷ r – radius of the circle
        P_bool^(i) = {p_1, p_2, ..., p_k} = Filter(c_coord, r, I_RGB, I_HSV)
        if Boolarray(P_bool^(i)) < size(P_bool^(i))/2 then
            c = c \ c_i
            m = m - 1
        end if
    end for
    for i=1 to m-1 do
        x_i = c_i^(0), y_i = c_i^(1), r_i = c_i^(2)
        for j= i to m do
            x_j = c_j^(0), y_j = c_j^(1), r_j = c_j^(2)
            d = ((x_j - x_i)^2 + (y_j - y_i)^2)^0.5
            if d < 0.9 * (r_j + r_i) then
                if Boolarray(P_bool^(i)) > Boolarray(P_bool^(j)) then
                    c = c \ c^(j)
                else
                    c = c \ c^(i)
                end if
            end if
        end for
    end for
end if
```

Fig. 5 Pseudocode of the result filtering algorithm

of which is shown in Fig. 6. For each i-th element of the array (c) in the procedure (*Filter*), an array ($P_{bool}^{(i)}$) consisting of two parts is formed. For the first part of the procedure (*Filter*), pixels in the inner circle are considered in increments of t and their coordinates are calculated:

$$x_{pi} = x_c + 0.7 * r * \cos(\alpha_i), \tag{1}$$

$$y_{pi} = y_c + 0.7 * r * sin(\alpha_i), \tag{2}$$

where x_c, y_c, r are the values obtained during the operation of the algorithm based on the Hough circle transformation. α_i is the angle of rotation in increments of t, α_i is the angle of rotation in increments of t.

Algorithm 2 Filter

function FILTER($c_{coord}, r, I_{RGB}, I_{HSV}$)
  $P_{bool} = \varnothing$
  $t = 30$ $\triangleright$ *t – step angle*
  for $a_t = 0$ **to** 360 **do**
    $x_{pi} = \left[c^{(1)}_{coord} + 0.7 * r * \cos(a_t)\right]$
    $y_{pi} = \left[c^{(2)}_{coord} + 0.7 * r * \sin(a_t)\right]$
    $W = \{W^{(R)}, W^{G)}, W^{(B)}, W^{(H)}, W^{(S)}, W^{(V)}\} = \{I^{(x_{pi})(y_{pi})}_{RGB}, I^{(x_{pi})(y_{pi})}_{HSV}\}$
    $W_{bool} = \varnothing$
    for $j = 1$ **to** 6 **do** $\triangleright$ $1 - R, 2 - G, 3 - B, 4 - H, 5 - S, 6 - V$
      if $W^{(j)} \in R^{(j)}_{in}$ **then**
        $W_{bool} \cup true$
      else
        $W_{bool} \cup false$
      end if
    end for
    if $Boolarray(W_{bool}) \geq size(W_{bool})/2$ **then**
      $P_{bool} \cup true$
    else
      $P_{bool} \cup false$
    end if
  end for
  for $a_t = 0$ **to** 360 **do**
    $x_{pi} = \left[c^{(1)}_{coord} + r * \cos(a_t)\right]$
    $y_{pi} = \left[c^{(2)}_{coord} + r * \sin(a_t)\right]$
    $W = \{I^{(x_{pi})(y_{pi})}_{RGB}, I^{(x_{pi})(y_{pi})}_{HSV}\}$
    $W = W \setminus W^{(5)}$
    $W = W \setminus W^{(4)}$
    $W_{bool} = \varnothing$
    for $j = 1$ **to** 4 **do** $\triangleright$ $1 - R, 2 - G, 3 - B, 4 - V$
      if $W^{(j)} \in R^{(j)}_{out}$ **then**
        $W_{bool} \cup true$
      else
        $W_{bool} \cup false$
      end if
    end for
    if $Boolarray(W_{bool}) \geq size(W_{bool})/2$ **then**
      $P_{bool} \cup true$
    else
      $P_{bool} \cup false$
    end if
  end for
  return P_{bool}
end function

Fig. 6 Pseudocode of the filter algorithm procedure

Algorithm 3 Boolarray

```
function BOOLARRAY(W_bool)
    a = size(W_bool)
    trueC = 0
    for n = 0 to a do
        if W_bool^(n) = true then
            trueC = trueC + 1
        end if
    end for
    return trueC
end function
```

Fig. 7 The pseudocode of the Boolarray algorithm procedure

For filtering (Fig. 6), an array W is formed from the color attributes R, G, B, H, S and V of the pixel with coordinates $x_{pi}, y_{pi}.$. The resulting array (W) is compared with the R_{in} array, which has the maximum and minimum values of the color attributes). If the color attribute lies within the acceptable ranges specified in R_{in}, then the value true is entered into the W_{bool} array, otherwise false (the algorithm in Fig. 6, steps 9–15). The number of corresponding and false values of color attributes is calculated in the procedure (*Boolarray*) (Fig. 7). If the number of true values is greater than or equal to half the number of array elements (W_{bool}), then the value true is entered into the array (P_{bool}), otherwise false.

The second part of the *Filter* procedure (Fig. 6, steps 22–41) is similar to the first, but it considers pixels on a circle corresponding to the contour of the neck:

$$x_{pi} = x_c + r * \cos(\alpha_i), \tag{3}$$

$$y_{pi} = y_c + r * sin(\alpha_i), \tag{4}$$

The pseudocode of the Filter procedure is shown in Fig. 6.

At the second stage of filtering the results (Fig. 6, steps 14–27), neighboring circles are compared. If one of the circles does not match the color of the neck of the test tube or its contents, the filtering algorithm removes this circle. For each element of the array (c), the distance (d) between the centers of two adjacent circles and 90% of the sum of the radii of the two circles is compared:

$$(\left(x_j - x_i\right)^2 + \left(y_j - y_i\right)^2)^{0.5} < 0.9 * \left(r_j + r_i\right),$$

where x_i, y_i, r_i are the coordinates of the center and radius of the circle in question, x_j, y_j, r_j are the coordinates of the center and radius of the neighboring circle.

If the comparison is correct, then for each of the two circles, a check is performed in the procedure (*Boolarray*) and the number of pixels that do not correspond to the allowed range of color attributes is determined. If the number of such pixels of the first circle is greater than the number of non-matching pixels of the second circle, then the first circle is removed from the array (c), otherwise the second one. As a result of the algorithm, the array(c) contains only filtered circles.

4 Experimental Investigation

Experimental studies of the developed algorithm for determining the position of test tubes and comparison of the proposed algorithm with the basic one have been performed. The comparison was performed on the same set of images of a tripod with test tubes. The analysis of the results of determining the circles obtained during the processing of 100 images of tripods with test tubes (Fig. 8).

Indicators such as accuracy and recall were used to determine accuracy. The accuracy indicator represents the proportion of the corresponding instances among the extracted instances.

$$accuracy = \frac{TP}{TP + FP + FN}, \tag{5}$$

where TP are correctly recognized objects (test tubes), FP are incorrectly recognized objects, and FN are unrecognized objects.

The Recall metric represents the proportion of recognized object instances in the total number of object instances in the image:

$$recall = \frac{TP}{TP + FP}, \tag{6}$$

The graph (Fig. 9) shows a graph of the normal distribution of accuracy and repeatability of results (dimensionless value) during the recognition of test tubes in 100 images.

Based on the test results of the basic and proposed algorithm, it was concluded that with the same configured parameters, the accuracy of the proposed algorithm

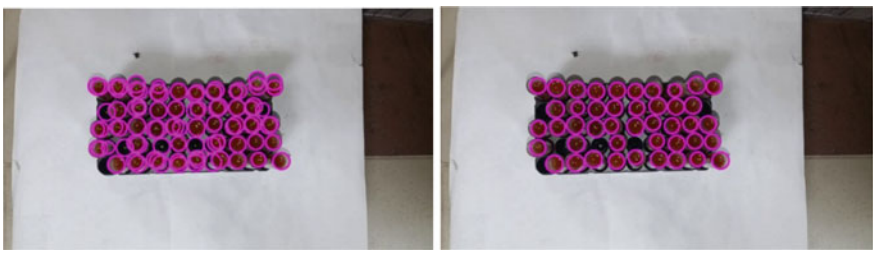

a) b)

Fig. 8 The results. **a** Before filtering, **b** after filtering

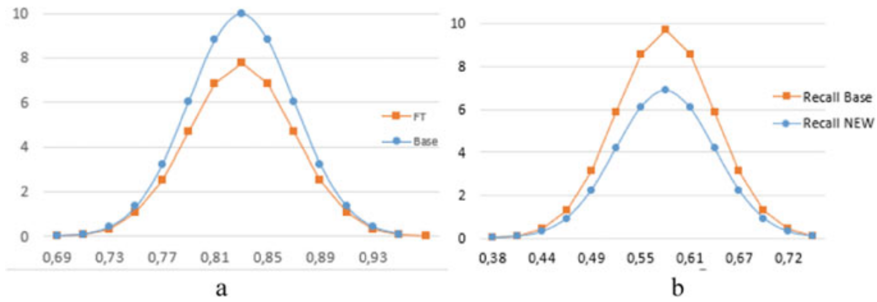

Fig. 9 Comparison of the accuracy and repeatability of the basic and proposed algorithms

was 96.3%, and the accuracy of the basic algorithm was 54.4%. The repeatability of the results of the proposed algorithm was 99.7%, and the basic one was 54.4%.

To conduct experimental studies as part of the robotic system, a 1080p webcam, a tripod for test tubes and 50 test tubes for storing blood samples were used in the collaborative work of the AUBO i5. To grasp test tubes, a gripping device has been developed and manufactured using 3D printing, the design of which is shown in Fig. 10.

The gripping device consists of a housing 1, in which a stepper motor is installed, a gear wheel 2, rails 3 and fingers 4. An Arduino nano is used as a controller to control the movement of the gripper device. The stepper motor receives a signal from the controller and rotates a gear wheel 2 mounted on its shaft, which transmits motion through a gear engagement to rails 3 moving in a circular groove translationally in opposite directions. 4 fingers are attached to the slats, which move along with the slats, grasp and move the object.

The algorithm for determining the position of test tubes is written in the python programming language and integrated into the robot's control program. The algorithm was tested as part of the aliquotation system (Fig. 11).

Fig. 10 Gripping device

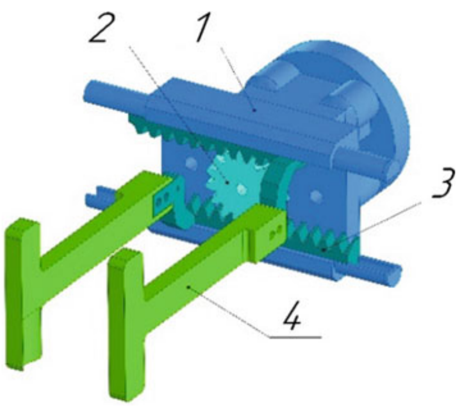

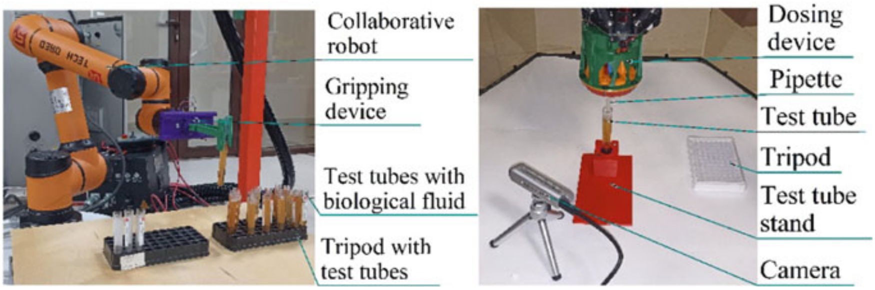

Fig. 11 Experimental investigations of the grasping of the transfer of test tubes by the robot according to the coordinates determined by the proposed algorithm

50 test tubes have been moved, the coordinates of which are determined by the proposed algorithm. The results showed that all 50 test tubes were successfully grasped and transferred from the tripod to the aliquotation workspace.

5 Conclusion

The application of the proposed Hough transform algorithm made it possible to determine the position of the test tube in the aliquoting system with an accuracy of 96.3%. The repeatability of the results when using the filtering algorithm increased from 54.4 to 99.7%. This allows you to automatically configure the system for a specific test tube and reduces the likelihood of errors during aliquoting. In addition, the Hough transform can be used to analyze images of other objects, for example, to recognize samples or to determine the boundaries of objects in an image. Thus, the Hough transform is a powerful tool for image processing and analysis and can be applied in various fields, including biology, medicine, robotics and computer vision.

Acknowledgements This work was supported by the state assignment of Ministry of Science and Higher Education of the Russian Federation under Grant FZWN-2020-0017.

References

1. Malyshev, D., Rybak, L., Carbone, G., Semenenko, T., Nozdracheva, A.: Adv. Serv. Industr. Robot. **102**, 31–38 (2021)
2. Schultz, A., Germann, A., Fuss, M., Sarzotti-Kelsoe, M., Ozaki, D., Montefiori, D., Zimmermann, H., Briesen, H.: PLoS ONE **13**, 1 (2018)
3. Khalapyan, S., Rybak, L., Nebolsin, V., Malyshev, D., Nozdracheva, A., Semenenko, T., Gavrilov, D.: Machines **11**(3), 349 (2023)
4. Tropin, D.V., Ilyuhin, S.A., Nikolaev, D.P., Arlazarov, V.V.: Comput. Vis. Patt. Recogn. 9689–9695 (2020)

5. Hough, P.V.C.: US 3069654 A (1962)
6. Bezmaternykh, P.V., Nikolaev, D.P.: SPIE **11433**, 132–137 (2019)
7. Jacobs, L., Weiss, J., Dolan, D.: EIT 1–6 (2013)
8. Aminuddin, N.S., et al.: J. Inform. Commun. Technol. **16**(2), 244–260 (2017)
9. Panfilova, E.I., Shipitko, O.S., Kunina, I.A.: SPIE **11605**, 671–680 (2021)
10. Malm, J., Végvári, A., Rezeli, M., Upton, P., Danmyr, P., Nilsson, R., Steinfelder, E., Marko-Varga, G.J.: Proteomics.Large scale biobanking of blood——the importance of high density sample processing procedures. 5;76 Spec No.:116–24 (2012). https://doi.org/10.1016/j.jprot.2012.05.003. Epub 2012 May 9

Deployment of Algorithms for Autonomous Drone Racing in a Real Environment

Marko Šušnjar and Kosta Jovanović

Abstract Autonomous drone racing (ADR) has proven to be a good training ground for developing and testing algorithms for autonomous drones. It usually requires specific conditions not available to many researchers. In this paper, we use the affordable Tello drone with support for ROS to implement and deploy computationally efficient algorithms for ADR. We propose the use of a control system based on a combination of the Feedback Linearization and the Model Predictive Control, localization and gate detection using a convolutional neural network and images from the drone's front camera as inputs, and a motion planning algorithm described by a state machine. We tested our system in simulations and in an adapted outdoor environment, demonstrating the system is capable of flying through all gates without collisions.

Keywords Autonomous drone racing · Deep learning · Model predictive control · Feedback linearization · Tello drone

1 Introduction

Together with the rising popularity of unmanned aerial vehicles and drone racing competitions, there has been a significant increase in interest in autonomous drone racing (ADR). The goal of these competitions is to build a drone capable of autonomously detecting gates on the track and flying through them in the shortest time possible. To achieve this, teams of engineers have to develop effective and time-efficient algorithms for perception, motion planning and control of autonomous drones. So far, ADR has proven to be a good motivation for improving these algorithms and trying out novel methods, as well as a good polygon for testing them in practice. Discoveries in the ADR may find applications in search and rescue missions, delivery in urban areas and other time-critical tasks.

In case of the ADR, it is common to use a custom-made drone with certain characteristics (such as great maneuverability and adequate computational power

M. Šušnjar (✉) · K. Jovanović
School of Electrical Engineering, University of Belgrade, Belgrade, Serbia
e-mail: marko0898@hotmail.com

D. Pisla et al. (eds.), *Advances in Service and Industrial Robotics*, Mechanisms and Machine Science 157, https://doi.org/10.1007/978-3-031-59257-7_4

and set of sensors onboard) and test its behaviour in large indoor areas suitable for this purpose. However, this setting is often not accessible to many researchers. In this paper, we opted for a different approach. We used an affordable DJI Ryze Tello drone and created simple environments convenient for testing our system both in simulations and in the real world.

We proposed a combination of computationally efficient algorithms to safely navigate the drone along the track. For the control system, we adapted Feedback Linearization and linear Model Predictive Control (MPC) for use in ADR, the localization system is based on a deep Convolutional Neural Network (CNN) optimised for quick predictions and trained on our inputs, while the motion planing algorithm is a simple and intuitive state machine. All methods are deployed on the real drone and tested in a real environment. To present our approach, we will first discuss related work in Sect. 2, then describe our methodology in Sect. 3, provide results and discussion in Sect. 4, and finally conclude in Sect. 5.

2 Related Work

The first international ADR competition was organised in 2016. In the first few years, numerous ideas for gate detection, drone localization, control, and path planning were presented [1, 2]. High-frequency localization can be enabled by using CNNs for estimation of the drone's position based on the image from the front camera. A modification of PoseNet architecture has been tested in simulations [3] and in a real-world indoor scenario [4] and has shown good precision. Using a sequence of consecutive greyscale images together with the Kalman filter for prediction smoothing has been proposed in [5], with promising results. The Kalman filter has been used to fuse measurements from multiple sensors in similar applications with other mobile robots in [6].

Neural networks have shown the potential to solve other problems in ADR as well. In [7], the network has been trained to replace classical control methods, while in [8] the end-to-end network has been used to predict control commands for inner controller directly from camera inputs. However, in many applications, a control system based on MPC has been used [9, 10], since it exploits the knowledge of the system dynamics. A combination of MPC and Feedback Linearization has demonstrated a great ability to follow the given trajectory in [11].

When positions of all gates are known, the trajectory can be found as a solution that minimises the time needed to fly through the given sequence of points [7]. Instead, if only the position of the closest gate is known, planning based on a state machine and piecewise trajectories has been proposed [5, 12]. In more complex environments and in case of multi-robot systems, multi-criteria decision making can be used [13]. Although mass-produced drones cannot achieve noticeable results in official racing competitions, they can be used for various research purposes, which was demonstrated with the DJI Tello drone [12, 14].

3 Methodology

In this paper, we used the DJI Ryze Tello drone, a small and affordable programmable quadrotor. It is equipped with a 5MP front camera, IMU sensor, a height sensor and a vision positioning system. There are packages for the integration of the Tello drone with the Robot Operating System (ROS) [15], while more advanced logic can be implemented using the Python programming language. Algorithms used for drone control, localization and motion planning, along with the implementation details, are presented in this section.

3.1 Testing Environments

To test our system in simulations, we created an environment similar to the ADR tracks using the Gazebo simulator in ROS, containing several brown gates of inner dimension $0.8\,\text{m} \times 0.8\,\text{m}$ placed on a homogeneous green ground, which should prevent the localization system from learning patterns on the floor. We used the RotorS package [16] to create a model of the Tello drone and trustworthy represent the real drone in simulations.

For real-world experiments, we built a polygon similar to the environment in simulations outdoors and we used a real Tello drone. The polygon was $10\,\text{m} \times 4\,\text{m}$ space enclosed on three sides by grey nylon up to a height of 3 m, in order to hide external objects and have nearly single-color background. Brown gates with a $1\,\text{m} \times 1\,\text{m}$ square opening were placed on a grassy surface. Algorithms described in this paper were run on a separate laptop with ROS and tello-driver package [17] for communication with the Tello drone via wireless network. Since the Tello drone is designed to fly indoors and is sensitive to external disturbances due to its size, experiments were run in dry weather without strong wind.

3.2 Control System

The control system consists of two parts: an outer loop based on the Feedback Linearization for position control, and an inner loop based on the Model Predictive Control for attitude (Fig. 1). The desired trajectory is forwarded from the path planner to the control system in form of reference coordinates, velocities, accelerations (X_R, Y_R, Z_R and their derivatives) and yaw angle ψ_R. Similar designs have already been applied in literature [11].

Drone's coordinates in the laboratory frame are defined with its position (X, Y, Z) and orientation (φ, θ, ψ). Drone's acceleration in the laboratory frame is described with the following equations:

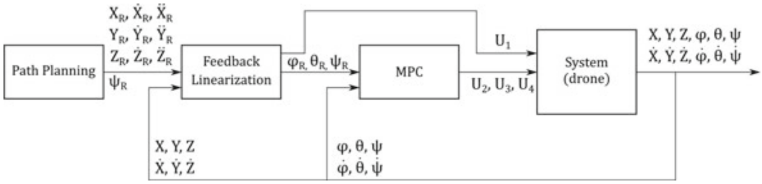

Fig. 1 Schematic representation of the control system

$$
\begin{aligned}
\ddot{X} &= (\cos\psi \sin\theta \cos\varphi + \sin\psi \sin\varphi)\tfrac{U_1}{m},\\
\ddot{Y} &= (\sin\psi \sin\theta \cos\varphi - \cos\psi \sin\varphi)\tfrac{U_1}{m},\\
\ddot{Z} &= -g + \cos\theta \cos\varphi \tfrac{U_1}{m}.
\end{aligned} \tag{1}
$$

Feedback Linearization controller determines appropriate thrust U_1 and sets target roll φ_R and pitch θ_R angles for the MPC controller. The inner loop regulates the drone's orientation with four times higher frequency than the outer loop. Around the hovering position, the transformation matrix between the body and the laboratory frame can be approximated by an identity matrix, and angular accelerations can be calculated as:

$$
\begin{aligned}
\ddot{\varphi} &= \tfrac{I_{yy}-I_{zz}}{I_{xx}}\dot{\theta}\dot{\psi} - \tfrac{J_P}{I_{xx}}\dot{\theta}\Omega + \tfrac{U_2}{I_{xx}},\\
\ddot{\theta} &= \tfrac{I_{zz}-I_{xx}}{I_{yy}}\dot{\psi}\dot{\varphi} + \tfrac{J_P}{I_{yy}}\dot{\varphi}\Omega + \tfrac{U_3}{I_{yy}},\\
\ddot{\psi} &= \tfrac{I_{xx}-I_{yy}}{I_{zz}}\dot{\varphi}\dot{\theta} + \tfrac{U_4}{I_{zz}},
\end{aligned} \tag{2}
$$

where U_2, U_3 and U_4 are torques generated by drone's rotors around X, Y and Z axes, $I = \text{diag}(I_{xx}, I_{yy}, I_{zz})$ is the diagonal inertia tensor of the drone's body, J_P is the moment of inertia of a rotor around Z axis, and $\Omega = \Omega_1 - \Omega_2 + \Omega_3 - \Omega_4$ is a function of angular velocities of all four rotors.

Equation (2) can be rearranged into the state space representation, so that parameters in matrices vary over time (LPV form, as in [11]). These matrices can be discretized and used to describe the current model of the drone for the Linear MPC controller, which finds the control inputs that minimise the cost function

$$
J = \tfrac{1}{2}\Delta\mathbf{u}^T\bar{\bar{\mathbf{H}}}\Delta\mathbf{u} + \mathbf{f}^T\Delta\mathbf{u}, \tag{3}
$$

where $\bar{\bar{\mathbf{H}}}$ and $\mathbf{f}$ depend on the model, initial conditions, reference given, and provided cost ratios for optimisation, and $\Delta\mathbf{u}$ defines incremental changes for control inputs U_2, U_3, U_4. If no additional constrains are set, there is an analytical solution for the optimal inputs $\Delta\mathbf{u} = -\bar{\bar{\mathbf{H}}}^{-1}\mathbf{f}$ based on the Eq. (3).

In contrast to the numerical optimisation of the cost function, with this approach all control inputs can be calculated directly, which reduces the overall time complexity. It is important to tune the cost parameters to get feasible values for the rotors speed due to physical limitations of the system. Also, the modular architecture shown in Fig. 1 is convenient for the transition to the real system. Since the Tello drone has its own low-level controller, only the outer loop needs to be implemented in that case.

3.3 Localization

The localization process is primarily based on a convolutional neural network, which utilizes the drone's front camera image to estimate the drone's position relative to the closest gate. This approach has already demonstrated good precision in ADR [3–5]. The drone has additional sensors whose measurements will be fused with the CNN prediction to obtain a more accurate estimation. The architecture of the CNN is inspired by [5] and modified for our use case to achieve faster estimations (Fig. 2a). An input of the CNN is a single greyscale image of size 224×224 pixels, while there are three output channels, one for each coordinate, describing the distance between the drone and the centre of the gate.

In the simulation, we generated 15869 greyscale images for training, 5442 images for validation, and testing on completely new inputs was done as part of the full-system evaluation. For the training set, the drone moved along a path parallel to the gate at various distances from the gate and at various heights in the region of interest, and collected images from the front camera and ground truth position with respect to the closest gate. For the validation set, we used a trajectory of a similar shape, but with different key points. Images were generated in environments with one gate and with three gates, in order to cover cases when the camera captures only the closest gate and multiple consecutive gates.

In real world, the CNN was trained independently, keeping the same architecture. Camera inputs were created similarly, but we used only one environment with three

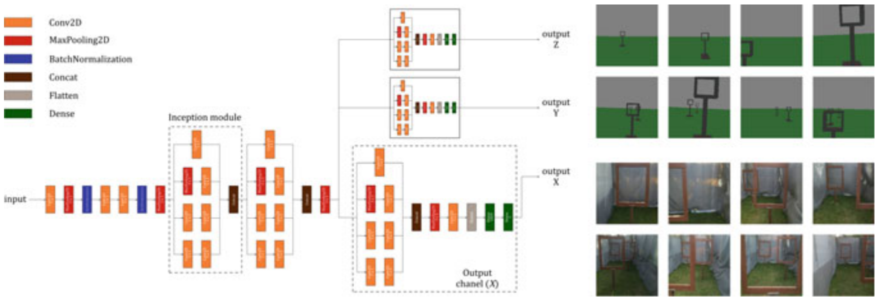

(a) CNN architecture

(b) Training sets examples

Fig. 2 Localization system: CNN used for the estimation of relative position of the drone with respect to the gate **a**, and example images from training sets in the simulation and in the real-world experiment **b**

gates, and collected 5453 images for training and 1378 for validation, scaled to the input size. Examples from training sets are shown in Fig. 2b.

Tello drone has its own estimation of the current velocity, based on measurements from IMU sensor. It is particularly useful when the drone is close to the gate and the camera does not capture its edges. Therefore, the Kalman filter was used to predict the next position of the drone, fuse outputs from the CNN and velocity estimations, and provide the final estimation of the localization system.

3.4 Motion Planning

The goal of the motion planning algorithm is to set an appropriate reference trajectory in the laboratory frame for the control system in order to navigate a drone to fly safely through the closest gate. The trajectory is divided into several segments and can be represented by a state machine. First, the drone approaches the gate and aligns with its centre at the distance of around 1 m from the gate. Next, the drone flies through the gate, close to the centre, and continues the motion for a certain length, during which it detects the next gate and repeats the process, i.e., returns to the initial state. Values are calculated with respect to the gate, based on the estimation of localization algorithms.

Reference trajectory for each segment is a polynomial function of fifth order, defined by the boundary conditions: desired positions, velocities and accelerations at the beginning and the end of the segment.

4 Results

The system was tested in simulations and in the real world. The CNN was trained separately in both cases on corresponding training sets for 100 epochs with a batch size of 32, minimising the mean squared error of predictions on the validation set. As a result, it was capable of calculating 80–90 predictions per second on a laptop with Intel i7-9750H processor and NVidia GeForce GTX1050 graphics card. Since the frequency of receiving new camera inputs is lower, and there are other calculations in the cycle, we opted to run CNN predictions with the frequency of 10 Hz in the simulation.

We created two different tracks in Gazebo. The first one had three gates of the same height and was similar to the environment used for collecting images for the training set (Fig. 3a). The drone started its motion from three different starting positions. In each case, drone successfully detected all gates and finished its motion without collisions. Trajectories in the horizontal plane are shown in Fig. 3c. They illustrate the state-machine approach - the drone moves towards the gate, aligns with its centre, flies through it and detects the next gate.

(a) 3-gates track (b) 7-gates track

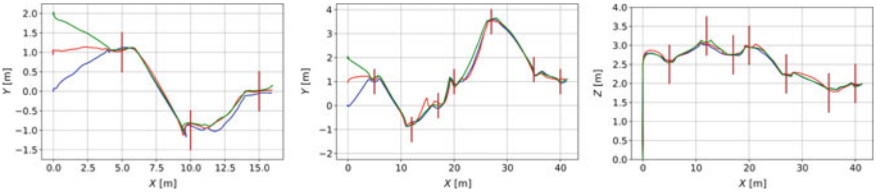

(c) Trajectory in horizontal plane with 3 gates (d) Trajectory in horizontal plane with 7 gates (e) Trajectory in vertical plane with 7 gates

Fig. 3 Simulation environments with three and seven gates in Gazebo and realised trajectories starting from three different initial positions

The second track consisted of seven gates of variable height (Fig. 3b), satisfying the condition that the next gate had to be in the camera field of view after flying through the previous one. Again, the drone was capable of flying safely through all gates in the track starting from three different initial positions, which can be seen from trajectories in horizontal and vertical plane in Figs. 3d, e. The total time required to complete the 40-meter-long track was about 35 s. A better result could have been accomplished with a more aggressive motion planning, but it is important to keep in mind limitations of the control system, which was derived under the small angles assumption.

While working with a real Tello drone, thanks to the ROS architecture and the use of tello-driver package, algorithms tested in simulations were reused to a great extent. As stated above, it was needed to adjust the control algorithm to use only the outer loop based on the Feedback Linearization and to retrain the CNN with inputs from a real-world environment. One major issue we experienced with a real system is a delay in communication between the drone and the laptop, especially in receiving images from the front camera. Also, since the error of IMU measurements accumulates with integration over time, that was not a reliable method for position and velocity tracking over longer distances. Hence, the front camera remained the main sensor for localization, but we reduced velocity of the drone and working frequencies to calculate CNN predictions twice per second.

The polygon with three gates used for testing is shown in Fig. 4a. Due to the limitations, achieving the shortest time was not the main quest and we focused on completing the track safely. In majority of tests, the drone was capable to detect all three gates and fly through them without collisions in around 70 s, which is approximately 8 times slower compared to the simulations. One example trajectory recorded as a sequence of images from the drone's camera is given in Fig. 4b. However, the

(a) Polygon

(b) Trajectory

Fig. 4 A polygon for the real-world experiment **a** and realised trajectory as a sequence of images from the drone's front camera **b**

real system did not demonstrate the same level of robustness as in simulations. In some occasions, after flying through the first gate, the second one was not in the camera's field of view, so the drone missed it and flew directly to the third one. An accompanying video with the results in simulations and the experiment can be found at: https://youtu.be/Ze2n9H0tL7U.

5 Conclusion

In this paper, we implemented a system for ADR using computationally efficient algorithms for control, localization and motion planning, and presented an affordable method for testing both in a simulation and in the real world. Our system demonstrated the ability to fly autonomously through the sequence of gates without collisions, achieving good flying time in the simulations. The speed in the real world was lower and not good enough for authentic ADR competitions, but the experiment provided valuable insights into the limitations of the system and the outdoor environment. For better results, the delay in the communication needs to be reduced, ideally by doing all processing onboard. Also, the existence of external motion capturing system for ground truth measurements would be beneficial during the training process. The use of the ROS and the corresponding driver for the Tello drone enabled a simple transition from the simulation to the real hardware, without a need for much effort and adaptations. A similar procedure could be repeated for any other drone with the support for ROS.

Acknowledgements This research was partly supported by the Horizon Europe grant #101070421, MUSAE: A Human-Centred Factory for a Future Technological Sustainable Development Driven by Arts.

References

1. Moon, H., Martinez-Carranza, J., Cieslewski, T., et al.: Challenges and implemented technologies used in autonomous drone racing. Intell. Serv. Robot. **12**, 137–148. Springer (2019)
2. Li, S., Ozo, M.M.O.I., De Wagter, C., De Croon, G.C.H.E.: Autonomous drone race: a computationally efficient vision-based navigation and control strategy. Robot. Auton. Syst. **133**, 103621 (2020)
3. Cocoma-Ortega, J.A., Martinez-Carranza J.: A CNN-based drone localisation approach for autonomous drone racing. In: Proceedings of the 11th International Micro Air Vehicle Competition and Conference, vol. 30 (2019)
4. Cocoma-Ortega J.A., Martinez-Carranza J.: Towards high-speed localisation for autonomous drone racing. In: Advances in Soft Computing: 18th Mexican International Conference on Artificial Intelligence (MICAI 2019), pp. 740–751. Springer (2019)
5. Cocoma-Ortega, J.A., Martinez-Carranza, J.: A compact CNN approach for drone localisation in autonomous drone racing. J. Real-Time Image Process. **19**(1), 73–86 (2022)
6. Gokhale, V., Barrera, G.M., Prasad, R.V.: FEEL: fast, energy efficient localization for autonomous indoor vehicles. In: ICC 2021-IEEE International Conference on Communications, pp. 1–6. IEEE (2021)
7. Penicka, R., Song, Y., Kaufmann, E., Scaramuzza, D.: Learning minimum-time flight in cluttered environments. IEEE Robot. Autom. Lett. **7**(3), 7209 (2022)
8. Rojas-Perez, L.O., Martinez-Carranza, J.: DeepPilot: a CNN for autonomous drone racing. Sensors **20**(16), 4524 (2020)
9. Kamel, M., Stastny, T., Alexis, K., Siegwart, R.: Model predictive control for trajectory tracking of unmanned aerial vehicles using robot operating system. In: Robot Operating System The Complete Reference, vol. 2, pp. 3–39. Springer (2017)
10. Kaufmann, E., Gehrig, M., Foehn, P., et al.: Beauty and the beast: Optimal methods meet learning for drone racing. In: 2019 International Conference on Robotics and Automation (ICRA), pp. 690–696. IEEE (2019)
11. Misin, M., Puig, V.: LPV MPC control of an autonomous aerial vehicle. In: 2020 28th Mediterranean Conference on Control and Automation, pp. 109–114 (2020)
12. Cyba, A., Szolc, H., Kryjak, T.: A simple vision-based navigation and control strategy for autonomous drone racing. In: 2021 25th International Conference on Methods and Models in Automation and Robotics, pp. 185–190. IEEE (2021)
13. Zagradjanin, N., Pamucar, D., Jovanovic, K.: Cloud-based multi-robot path planning in complex and crowded environment with multi-criteria decision making using full consistency method. Symmetry **11**(10), 1241 (2019)
14. Maalouf, A., Gurfinkel, Y., Diker, B., Gal, O., Rus, D., Feldman, D.: Deep learning on home drone: searching for the optimal architecture. In: 2023 IEEE International Conference on Robotics and Automation, pp. 8208–8215. IEEE (2023)
15. Quigley, M., Conley, K., Gerkey, B., et al.: ROS: an open-source robot operating system. In: ICRA Workshop on Open Source Software, vol. 3 (2009)
16. Furrer, F., Burri, M., Achtelik, M., Siegwart, R.: RotorS—a modular gazebo MAV simulator framework. In: Robot Operating System (ROS) The Complete Reference, vol. 1, pp. 595–625. Springer (2016)
17. ROS Documentation, Tello driver. https://wiki.ros.org/tello-driver

Contactless Assembly of a Pi and a Plug Micropart with Electrostatic Force Fields

Georgia Kritikou, Vassilis Moulianitis, and Nikos Aspragathos

Abstract The assembly of a plug and a pi micropart with electrostatic force fields on a micro-manipulation platform is studied. The operational principle of the platform is based on its electrodes activations that result in interacting with the neighboring microparts' electrodes. The components are conveyed on the device with transfer lines reaching random configurations and their micro-manipulation begins with their centralization on a platform electrode. Then, a new heuristic method searches for the best place on the platform where they will be assembled while the presence of the undesired electrostatic stack phenomena is avoided. Based on the heuristic's results, the microparts are reoriented and move towards their assembly configuration. At the final stage of the process, a stabilizing activation method is applied for assembling the microparts effectively. The steps of the assembly method are described and simulated and the results are shown and discussed.

Keywords Automated contactless assembly · Electrostatic force fields · Stabilizing activation

1 Introduction

The MEMS assembly is an outstanding ongoing research area. Nowadays, micro-grippers are mostly used in industry for the MEMS built [1] increasing significantly the production time and cost [2]. Contactless micro-manipulation methods using force fields promise the automated mass parallel assembly of multiple components.

The assembly of a pi and a rectangular component using programmable planar force fields for the components' centralization, aligning and transfer was firstly designed in [3]. The mass parallel assembly exclusively with force fields has been

G. Kritikou (✉) · V. Moulianitis
Department of Mechanical Engineering, University of Peloponnese, Tripoli, Greece
e-mail: g.kritikou@go.uop.gr

N. Aspragathos
Department of Mechanical Engineering and Aeronautics, University of Patras, Patras, Greece

D. Pisla et al. (eds.), *Advances in Service and Industrial Robotics*, Mechanisms and Machine Science 157, https://doi.org/10.1007/978-3-031-59257-7_5

achieved in bio-systems industry where bio-cells and nano/micro-polymer beads can be assembled with dielectrophoresis [4]. In micro-robotics manufacturing adhesive forces have been applied to micro-components using droplets achieving the built of micro-vehicles and snake shaped structures [5].

The electrostatic force fields have been used for the micro-components handling and positioning to pallets using vibrating and ultrasound plates [6, 7]. In our research team's previous publications the contactless electrostatic micro-manipulation of plastic or plexiglass convex components has been proposed [8]. The components' handling is implemented on a platform of a micro-factory where they are placed with conveyors. The platform is a PCB with conductive pads whose activation induces electrostatic force fields concluding to interact with the electrodes underneath the microparts' bottom surface. The components' micro-handling begins with their simultaneous centralization [9] and keeps on with their motion and rotation due to the automated activation methods that are applied to them [10].

In this work, the micro-manipulation and the assembly of two non-convex microparts (a plug and a pi), is proposed. The goal is to assemble the components automatically avoiding simultaneously the electrostatic stack phenomena. Firstly, the platform's and microparts' initial state is described and the microparts' electrodes layout underneath their bottom is presented. Then the micropart's free configuration space is calculated and the microparts feasible rotations and motions on the platform are determined. Considering that the microparts are centralized, a new heuristic method finds where they will be assembled on the platform decreasing simultaneously the possibility of the electrostatic stack phenomena presence. Based on the resulting assembly configuration the microparts are rotated and then move towards it. Finally, a stabilizing activation technique is proposed that contributes to assemble the microparts.

The Sect. 2 is dedicated to present the platform's and micropart's layout, their initial state and the stabilizing activation method for the components' assembly. The automated plug–pi assembly method is described step–by–step in Sect. 3 and the conclusions and the future work are discussed in Sect. 4.

2 The Platform and Two Non-convex Micro-components

2.1 The Platform

The platform is a MEMS device that has on its surface a square area with N × N electrodes where the center of the electrode number 1 coincides with the origin (x, y) = (0,0) of the platform's Global Coordinate System (GCS) (Fig. 1). The micro-manipulation processes on the platform's surface are detected with vision systems and the microparts are manipulated on the platform due to its electrodes activations [10].

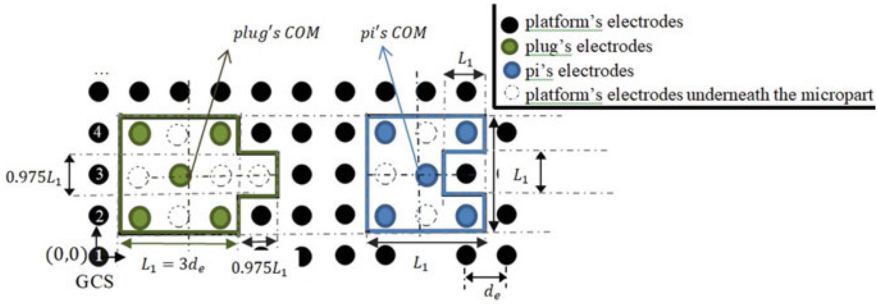

Fig. 1 A plug and a pi micropart centralized on the platform's surface with orientation $\theta_1 = \theta_2 = 0^o$

2.2 *The Configuration Space, the Action Space and the Activation Methods for the Manipulation of a Pi and a Plug Micropart on the Platform*

The plug and the pi microparts are both made from the same insulating material. In this work, it is not significant how they are conveyed on the platform however; it is taken into account that at the end of their conveyance they reach random configurations. The microparts' electrodes are positioned underneath their bottom surface according to the layout that is illustrated in Fig. 1. The components are centralized when their central electrode totally coincides with a platform electrode as in Fig. 1.

The microparts' configuration on the platform is given by $q_i = (x_i, y_i, \theta_i)\ \forall i \in \{1, 2\}$ where x_i, y_i the position of their central electrode on the platform and θ_i their orientation with respect to the GCS where i = 1 the plug and i = 2 the pi micropart. The collision free parallel micro-manipulation of randomly positioned components is achieved since the constraints $|\Delta x| \geq 6d_e$ or $|\Delta y| \geq 6d_e$ are satisfied [9], where $|\Delta x| = |x_1 - x_2|$ and $|\Delta y| = |y_1 - y_2|$ where d_e the horizontal/vertical distance between the centers of two neighboring platform's electrodes. The components' Free Configuration Space is equal to:

$$C_{free} = X \times Y \times \Theta, \forall x_i \in X = [d_e, (N-1)\cdot d_e], \\ \forall y_i \in Y = [d_e, (N-1)\cdot d_e] \forall i \in [1, 2] \text{ and} \forall \theta_i \in \Theta = \left[-180^o, 180^o\right] \quad (1)$$

Since the microparts are centralized and $\theta_i \in \{0°, \pm 90°, \pm 180°\}$ they can move automatically making actions that are included in the Actions Space:

$$U^c = \{v_1, v_2, v_3, v_4, v_5\} \\ = \{(d_e, 0, 0), (-d_e, 0, 0), (0, d_e, 0), (0, -d_e, 0), (0, 0, 0)\} \quad (2)$$

The centralized micro-components can be oriented and accomplish an action $v\lambda \in U_c\ \forall \lambda \in \{1,2,3,4,5\}$ since the platform electrodes are activated properly [10].

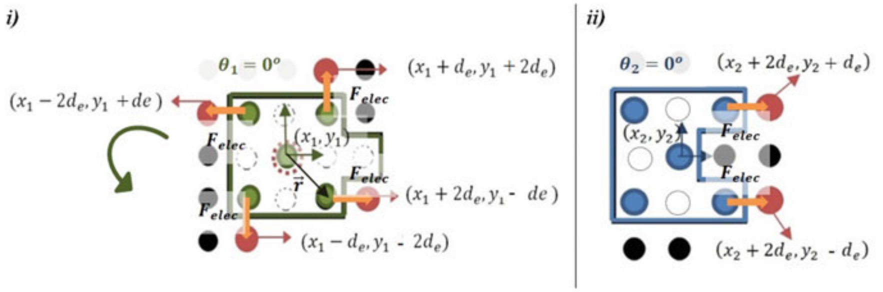

Fig. 2 The (i) Activation methods for the rotation of a plug (ii) activation methods for the motion of a pi micropart in parallel with the x axis applying a v_1 action

Figure 2 illustrates two activation examples where in Fig. 2(i) the rotation of a plug micropart and in 2(ii) the action v1 of a pi component are presented.

2.3 *Simulating Activation Methods for the Components' Efficient Assembly*

The differential equations for the motion and the rotation of the microparts from their current position and orientation to the next are equal to:

$$m_i \cdot du/dt + b \cdot u = \sum F_{elec} \tag{3}$$

$$I_i \cdot d\omega/dt + b/m_i \cdot \omega = \sum \tau_{elec} \tag{4}$$

where m_i the components mass, b the damping coefficient that depends on the microparts dimensions and the liquid dielectric's viscosity, Ii the components' moment of inertia, $\sum F_{elec}$ the total electrostatic force that is applied to each micropart's COM due to each single interactions F_{elec} and $\sum \tau_{elec}$ the micropart's total torque where each $\tau_{elec} = F_{elec} \times r$ where $|r| = \sqrt{2}d_e$ (see Fig. 2i).

A 90° rotation of a plug component is simulated on a 10 × 10 electrodes platform where $d_e = 1.08\bullet10^{-4}$m and the plug's start configuration is equal to the $(x_1, y_1, 0°) = (3.24\bullet10^{-4}$ m, $4.32 \bullet10^{-4}$m,0°). The simulation results are illustrated in Fig. 3 showing that for the plug's rotation four platform activation steps are applied. The microparts' electrode layout design and the activation methods contribute to keeping the plug's central electrode constant while its COM, which does not coincide with the pivot point center, is successfully rotated by 90°.

An assembly example is shown in Fig. 4i where a pi micropart implements a v_1 action to come closer to the plug however such activation concludes in plug's v_2 action which is undesired during components' assembly. Therefore, all the platform electrodes underneath the plug's electrodes (see Fig. 4i) are also activated to

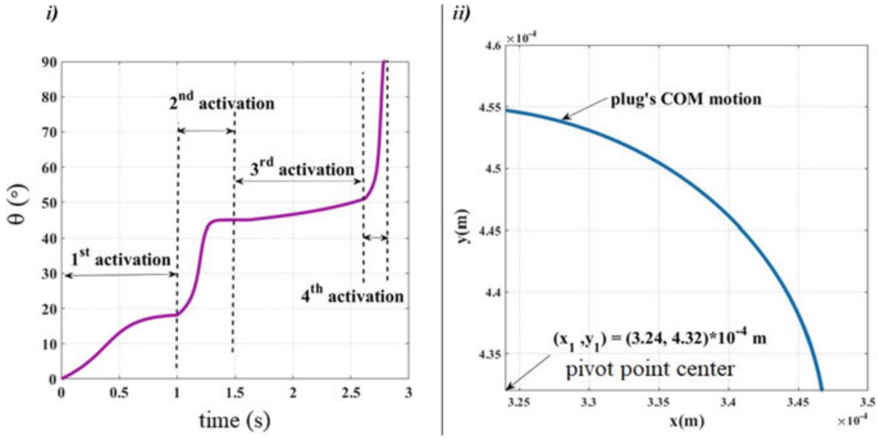

Fig. 3 Simulation results (i) the plug is rotated by 90° (ii) the plug's COM is rotated by 90° around the micropart's central electrode

stabilize the component hence the assembly is accomplished in secure (see Fig. 4ii). The assembly process of Fig. 4 is simulated on the 10 × 10 electrodes platform where the components start configurations are equal to: $(x_1, y_1, \theta_1) = (5.4\bullet 10^{-4}$ m, $2.16\bullet 10^{-4}$ m, 180°) and $(x_2, y_2, \theta_2) = (1.08\bullet 10^{-4}$ m, $0.54\bullet 10^{-4}$ m, 0°).The simulation results are illustrated in Fig. 5 where it is shown that the stabilization of the plug contributes to keeping it constant accomplishing the components' assembly while without the stabilization the plug moves towards pi.

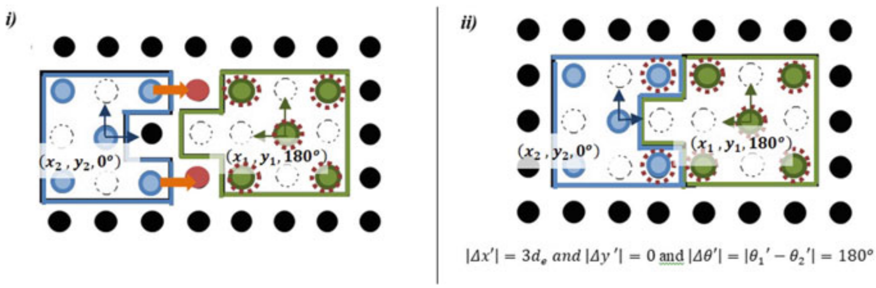

Fig. 4 Pi—plug final assembly stage (i) pi moves towards plug (ii) successive assembly because of the stabilizing activations

3 Assembly of a Pi and a Plug Micropart

3.1 An Automated Method for the Plug—Pi Assembly

The plug and the pi are considered as assembled when their coordinates satisfy the constraints: $|\Delta x'| = |x_1' - x_2'| = 0$ and $|\Delta y'| = |y_1' - y_2'| = 3d_e$ or $|\Delta x'| = 3d_e$ and $|\Delta y'| = 0$ and $|\Delta\theta'| = |\theta_1' - \theta_2'| = 180^o$ (see Fig. 4ii) where x_1', x_2', y_1', y_2', θ_1' and θ_2' the components' coordinates at the end of their assembly. The plug has bigger mass than the pi ($m_1 > m_2$) hence, bigger potential is requested when the v_λ $\forall\lambda \in \{1, 2, 3, 4\}$ actions are implemented. Therefore, in order to limit the platform's electrostatic force fields' magnitude limiting simultaneously the possibility for undesired stack phenomena the assembly process is built considering that the plug has to move less and the pi more.

The assembly process is divided in the following steps: (1) centralize simultaneously both components (2) reorient in parallel the components so that $|\Delta\theta'| = 180^o$ (3) drive them to the configurations where either $|\Delta x'| = 0$ and $|\Delta y'| = 3d_e$ or $|\Delta x'| = 3d_e$ and $|\Delta y'| = 0$. Therefore, the randomly positioned components are centralized in parallel to one of the platform electrodes that is closer to their central electrode. Then, a heuristic is proposed to search the best place where the components will be assembled considering how the pi will better approach the plug. Specifically, the distances $|\Delta x|$ and $|\Delta y|$ are computed, and since $|\Delta x| \geq |\Delta y|$ the x axis is selected to implement the final stage of the components assembly shown in Fig. 4; in case, $|\Delta x| < |\Delta y|$ then *y* axis is preferred. According to their start configuration and the selected assembly axis their final assembly configurations are computed using the method that is shown in Table 1. Finally, the number of the needed activation steps is calculated taking into account the computed assembly configuration.

3.2 An Example of a Plug—Pi Assembly on the Platform

A plug–pi assembly example is presented in Fig. 6. Figure 6i) shows a non-centralized plug and pi component with random orientations just conveyed on the platform's surface where $|\Delta x| = 6d_e$. According to the proposed method each component is centralized to the platform electrode that is closer to its central electrode (see Fig. 6ii).

Since the microparts' centralization is accomplished the distances $|\Delta x|$ and $|\Delta y|$ are calculated. Considering the configurations in Fig. 6ii) $\Delta x| = 6d_e$ and $|\Delta y| = 0$ therefore, the x axis is selected for the components assembly. According to the method shown in Table 1: $x_1 < x_2$ ($d_e < 7d_e$) and $y_1 = y_2$ ($2d_e = 2d_e$) hence: $x_1' = d_e + 6d_e - 3d_e = 4d_e$, $y_1' = y_1 - 0 = 2d_e$, $x_2' = x_2 = 7d_e$, $y_2' = y_2 = 2d_e$, $\theta_1' = 0^o$ and $\theta_2' = 180^o$. Taking into account the computed θ_1' and θ_2', 7 activation steps have to be applied to the plug and 2 to the pi respectively. Therefore, the pi will reach $\theta_1' = 0^o$ sooner than the plug the orientation $\theta_2' = 180^o$ hence, while the plug keeps on its rotation a v_5 action is applied to the reoriented pi. Figure 6(iii)

Table 1 A calculation method for the assembly configuration considering the centralized components' position

Assembly axis	Assembly configuration calculation method
x axis|	If $x_1 < x_2$ and $y_1 \leq y_2$ then $x_1' = x_1 + \|\Delta x\| - 3d_e$, $y_1' = y_1 + \|\Delta y\|$, $x_2' = x_2$, $y_2' = y_2$, $\theta_1'0^o$ and $\theta_2' = 180^o$
	If $x_1 > x_2$, and $y_1 \leq y_2$ then $x_1' = x_1 - \|\Delta x\|+3de$, $y_1' = y_1 + \|\Delta y\|$,$x_2' = x_2$, $y_2' = y_2$, $\theta_1' = 180^o$ and $\theta_2' = 0^o$
	If $x_1 < x_2$ and $y_1 \geq y_2$ then $x_1' = x_1 + \|\Delta x\| - 3d_e$, $y_1' = y_1 - \|\Delta y\|$, $x_2' = x_2$, $y_2' = y_2$, $\theta_1' = 0^o$ and $\theta_2' = 180^o$
	If $x_1 > x_2$, and $y_1 \geq y_2$ then $x_1' = x_1 - \|\Delta x\|+3d_e$, $y_1' = y_1 - \|\Delta y\|$, $x_2' = x_2$, $y_2' = y_2$, $\theta_1' = 180^o$ and $\theta_2' = 0^o$
y axis	If $y_1 < y_2$ and $x_1 \leq x_2$ then $x_1' = x_1 + \|\Delta x\|$, $y_1' = y_1 + \|\Delta y\| - 3d_e$, $x_2' = x_2$, $y_2' = y_2$, $\theta_1' = -90^o$ and $\theta_2' = 90^o$
	If $y_1 > y_2$ and $x_1 \geq x_2$ then $x_1' = x_1 + \|\Delta x\|$, $y_1' = y_1 - \|\Delta y\| + 3d_e$, $x_2' = x_2$, $y2' = y_2$, $\theta_1' = 90^o$ and $\theta_2' = -90^o$
	If $y_1 < y_2$ and $x_1 \geq x_2$ then $x_1' = x_1 - \|\Delta x\|$, $y_1' = y_1 + \|\Delta y\| - 3de$, $x_2' = x_2$, $y_2' = y_2$, $\theta_1' = -90^o$ and $\theta_2' = 90^o$
	If $y_1 > y_2$ and $x_1 \leq x_2$ then $x_1' = x_1 - \|\Delta x\|$, $y_1' = y_1 - \|\Delta y\|+3de$, $x_2' = x_2$, $y_2' = y_2$, $\theta_1' = 90^o$ and $\theta_2' = -90^o$

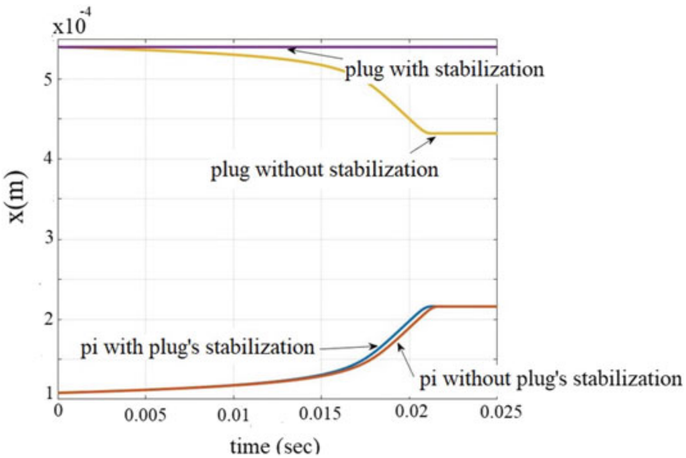

Fig. 5 Simulation results for the pi—plug assembly final stage on a *10* × *10* electrodes platform

illustrates the microparts' rotation and Fig. 6(iv) their configuration at the end of this step.

Finally, the number of the v_1 and v_5 actions according which the pi will approach the plug are equal to $(|\Delta x|/d_e) - 3 = 3$. The motion of pi towards plug begins since both are reoriented (Fig. 6iv). Figure 6(v) illustrates the accomplishment of

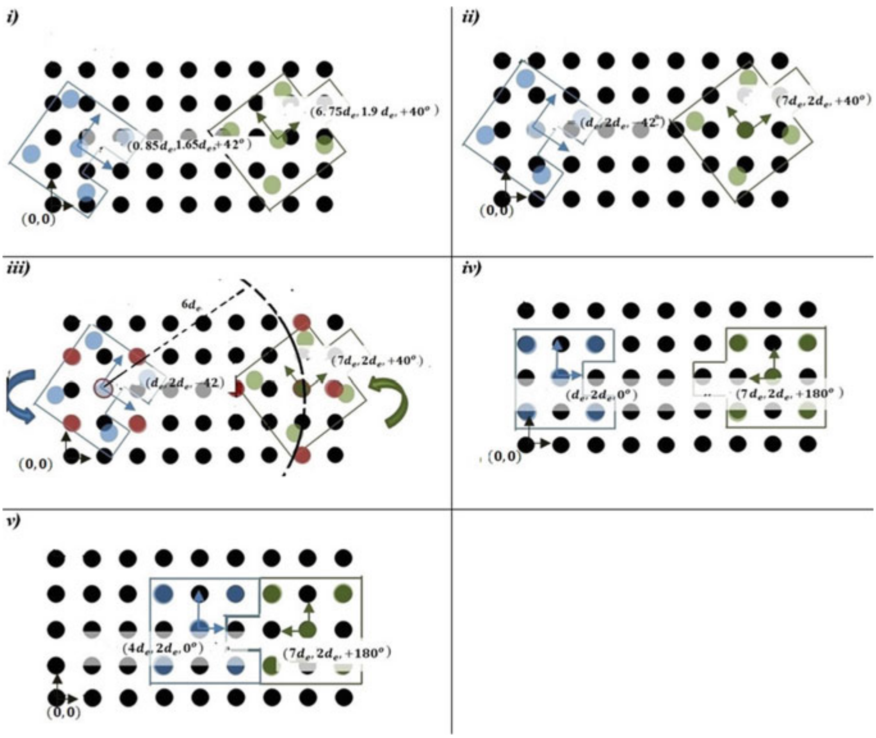

Fig. 6 A plug—pi assembly example (i) the components' first conveyance reaching random configurations (ii) the microparts are centralized simultaneously to the closer platform electrode (iii) the microparts are rotated to reach the computed orientation showing that the distance 6d_e is sufficient for such micro-manipulation (iv) the pi starts moving towards the plug (v) the components are assembled

the process showing that the proposed automated method succeeds to assemble the components effectively.

4 Conclusions—Future Work

A method for the automated contactless assembly of a pi and a plug micropart with electrostatic force fields on a platform was presented in this work. The simulation results showed that the pi and the plug geometries can be manipulated successfully applying the proposed electrodes layout and the appropriate activation methods. The proposed heuristic finds successfully a single assembly position on the platform considering how the pi will come closer to the plug avoiding the stack phenomena presence. Finally, the stabilization of the plug micropart contributes to the effective components assembly.

As future work, the mass parallel assembly of multiple convex and non–convex microparts on the platform will be investigated. The goal of our research team is to propose an automated global method able to compute the activations that will be applied to each micropart considering its geometry and its goal configuration on the platform. Finally, the platform's construction to apply the manipulation methods that we have proposed to our relevant publications is an ongoing project.

References

1. Mehrabi, H., Hamedi, M., Aminzahed, I.: A novel design and fabrication of a micro-gripper for manipulation of micro-scale parts actuated by a bending piezoelectric. Microsyst. Technol. **26**, 1563–1571 (2020)
2. Yang, S., Xu, Q.: A review on actuation and sensing techniques for MEMS-based microgrippers. J. Micro-Bio. Robot **13**, 1–14 (2017)
3. Luo, J., Kavraki, L.: Part assembly using static and dynamic force fields. In: Proceedings of the 2000 IEEE/RSJ, pp. 1468–1473 (2000)
4. Zhou, T., Chen, J., Kropp, E., Kulinsky, L.: Guided electrokinetic assembly of polystyrene microbeads onto photopatterned carbon electrode arrays. ACS Appl. Mater. Interf. **12**(31), 35647–35656 (2020)
5. Dai, L., Lin, D., Wang, X., Jiao, N., Liu, L.: Integrated assembly and flexible movement of microparts using multifunctional bubble microrobots. ACS Appl. Mater. Interf. (2020)
6. Fang, J., Karl, F.B.: Wafer-level packaging based on uniquely orienting self-assembly (The DUO-SPASS Processes). J. Microelectromech. Syst. **15**(3) (2006)
7. Ardanuç, S.M., Lal, A.: Ultrasound enhanced electrostatic batch assembly for MEMS. Sens. Act. A **197**, 136–149 (2013)
8. Kritikou, G., Lamprianidis, N., Aspragathos, N.: A modified cooperative A* algorithm for the simultaneous motion of multiple microparts on a "smart platform" with electrostatic fields. Micromachines **9**, 548 (2018)
9. Kritikou, G., Aspragathos, N., Moulianitis, V.: Algorithms for the motion of randomly positioned hexagonal and square microparts on a "smart platform" with electrostatic forces and a new method for their simultaneous centralization and alignment. Micromachines **10**, 874 (2019)
10. Kritikou, G., Aspragathos, N.: Micro-manipulation methods and assembly of hexagonal microparts on a programmable platform with electrostatic forces. Int. J. Mech. Control **20**, 71–80 (2019)

Modern Quality Control: Integrating Computer Vision in Inspection of PCB Elements

Luka Šiktar, Filip Šuligoj, Marko Švaco, and Branimir Ćaran

Abstract This study introduces a computer vision application for the automated detection, localization, and inspection of microcontroller boards and Single Board Computers, generally referred to as Printed Circuit Boards (PCBs), as part of the quality control process. Given the key role of quality control in product pricing for systems with automated and robotized production, there is an imperative to enhance its speed and cost-effectiveness. To address this, we propose the utilization of computer vision tools, particularly deep neural networks. The proposed system encompasses several modules: PCB detection and component verification using YOLOv8 convolutional neural network (CNN), targeted image extraction of components, solder joint quality assessment via adaptive thresholding and optical character recognition (OCR) on selected images. The overreaching goal is to devise a practical industry application of computer vision for adaptable quality control. This system's development involved PCB dataset creation, neural network training, and the development of final implementation. The trained YOLOv8 neural network achieves Mean Average Precision (mAP) of 99.5%, the proposed inspection system scores 96.1% precision and 97.8% recall. The OCR model scores 95.6% true positive character predictions.

Keywords Computer vision · PCB · Adaptive thresholding · YOLOv8 · OCR

1 Introduction

PCBs, critical components in electronic devices, face a booming market demanding swifter and more precise manufacturing. With PCBs evolving into compact, complex forms, quality control challenges intensify. This necessitates highly flexible inspection methods in tune with robotic manufacturing systems. Researchers are thus motivated to develop innovative approaches annually. Current research predominantly

L. Šiktar (✉) · F. Šuligoj · M. Švaco · B. Ćaran
Faculty of Mechanical Engineering and Naval Architecture, University of Zagreb, Zagreb, Croatia
e-mail: luka.siktar@fsb.hr
URL: https://fsb.unizg.hr

D. Pisla et al. (eds.), *Advances in Service and Industrial Robotics*, Mechanisms and Machine Science 157, https://doi.org/10.1007/978-3-031-59257-7_6

focuses on enhancing Automated Optical Inspection (AOI), a prevalent method for PCB inspection. Janczki et al. [1] adopted AOI for solder paste inspection instead of solder joint inspection to achieve significantly better outcome. Given AOI's limited adaptability, a wide range of research works concentrate on replacing the system by proposing solutions for specific areas like object detection, soldering joint inspection, optical character recognition or end-to-end solutions. One such example showcases usage of image subtraction and blob detection [2] for effective PCB inspection. In another research, Crispin and Rankov [3] proposed a template-matching approach for object recognition. In [4] PCB defect detection was performed using Otsu thresholding and Hough transformations for feature extraction and matching algorithms. Proposed solutions are evaluated in research studies [5, 6] which recommend using Computer Vision and deep learning methods to improve inspection performance. Additionally, the inspection process is divided into four main steps: classification of images, image processing, object detection and defect detection [5]. Latter research [6] proposes a methodology for data collection, feature extraction and selection for optimized PCB component detection.

While traditional approaches in research have predominantly focused on custom algorithms and methods within computer vision, a significant shift is observed towards more advanced techniques, specifically deep neural networks like CNNs. This transition to deep learning is driven by its improved flexibility and robustness in object detection and quality control, stemming from its ability to learn from large datasets. In terms of creating an enhanced dataset, Huang et al. [7] proposed a PCB dataset HRIPCB with 1386 images with 6 types of common PCB defects. Ulger et al. [8] introduced a dataset for PCB solder joint inspection and alternative inspection approaches: reference-based, computer vision, deep learning, and 3D reconstruction-based models. Sathiaseelan et al. [9] proposed ECLAD-Net CNN and addressed the problem of a limited dataset and the risk of model overfitting. CNN models trained on precise datasets can surpass expensive conventional PCB quality control solutions. It is stated that CNNs are more flexible and faster than AOI [9]. Akhyar et al. [10] examined deep learning object recognition methods for PCB surface inspection and obtained robust results using ResNeSt that achieved the mean Average Precision of 99.2% and average recall of 99.5%. The innovative detection approach started with Redmon et al. [11] and You Only Look Once (YOLO), the state-of-the-art model for real-time object detection. Furthermore, Li et al. [12] proposed a dataset that incorporates real and virtual PCB images. It uses a YOLOv3 modified algorithm to detect tiny PCB components. Lim et al. [13] presented a deep learning-based model for detection of tiny and varying defects in real-time by adapting YOLOv5 model and modifying it for higher detection accuracy.

Current computer vision solutions can be ineffective for flexible and rapidly evolving PCB production due to system limitations on strict and predefined PCB quality control parameters. Furthermore, SOA research addresses specific quality control tasks, either detection, inspection, or OCR, which do not provide automated end-to-end and rapid single-step inspection, crucial for real-time quality control.

To address this challenge, we introduced the use of CNNs for flexible PCB detection combined with thresholding techniques for precise inspection. The development involves creating a custom PCB dataset and training YOLOv8 model, which is deployed for PCB component detection system. Relevant PCB components are further analyzed using adaptive thresholding technique and contour detection for pin and soldering point pattern assessment. The OCR, performed on PCB designations validates YOLOv8 detection performance. Scientific contributions of the research include training dataset creation, YOLOv8 CNN model training, and the end-to-end automated system development.

2 Methodology

The research workflow consists of the dataset creation using Roboflow, YOLOv8 model training using PyTorch, experiment stage for creating a system that detects PCB components, performs inspection and OCR. To capture images for detection purposes, a special setup, easily integrable into a robotic manufacturing process is constructed. The setup consists of a LUCID Vision Labs PHX064S-CC industrial camera and two CSS HLDL2-450X45SW industrial lights, shown in Fig. 1(g).

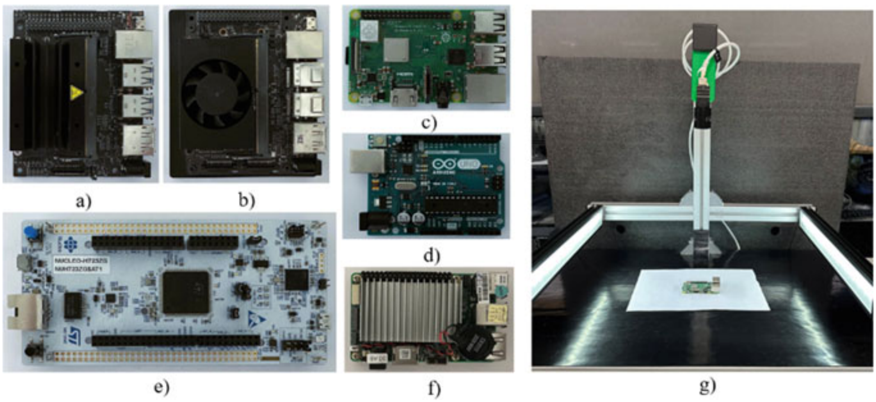

Fig. 1 PCBs: **a** Jetson nano, **b** Jetson NX Xavier, **c** Raspberry Pi 3, **d** Arduino Uno, **e** STM32, **f** Up board, **g** Inspection setup

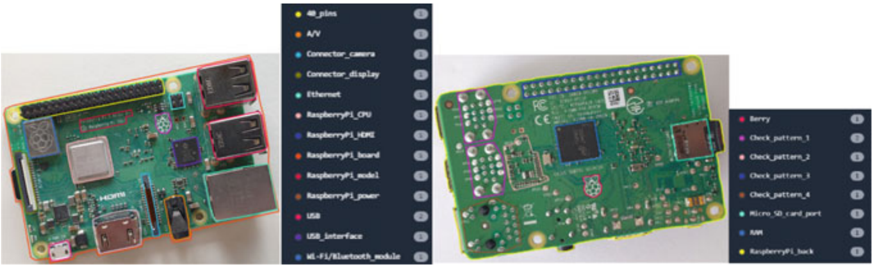

Fig. 2 Image annotations and list of annotated classes

2.1 *Creation of a Custom Dataset*

To train the YOLOv8 CNN model for PCB detection, 'PCB_detector_main_dataset',[1] a custom dataset is created to obtain full control over annotating and system's capability to detect, inspect and perform OCR tasks effectively. The dataset originally consisted of 1,200 images captured under different angles and lightning environments to provide a variety, crucial for detection performance. The created dataset consists of six different PCBs annotated using the Roboflow, with the example shown in Fig. 2.

Annotated images are then pre-processed by applying auto-orientation and image resizing to 640 $\times$ 640 pixels, the optimal size for YOLOv8 training. After preprocessing, the augmentation is performed. The custom dataset is augmented by rotating $\pm 4°$, and hue, saturation, brightness, and exposure variations of $\pm 8\%$. Additionally, for better detection performance, a blur of 0.75px and salt and pepper noise for 0.5% of image pixels are added. The final augmented dataset contains 2895 training images, 135 validation and 100 test images.

2.2 *YOLOv8 Model Training*

YOLOv8 is the state-of-the-art CNN model that enables fast and accurate object detection on images with a single pass of a model. The model is pre-trained on the COCO dataset [14, 15] that provides standard metrics to evaluate the quality of trained models, mean Average Precision (mAP). Metric mAP measures detection quality by using standard precision and recall metrics.

The model in our research, trained using PyTorch, is separated into three segments, backbone, neck, and head, where backbone is a pre-trained model "Darknet-53" [16]. To train the model for the detection of 83 different labels/objects from created dataset, medium size YOLOv8 model with 295 layers and 25,903,798 parameters is used. For the training process, maximum of 100 epochs is anticipated, with provisions

[1] https://github.com/lukasiktar/PCB_Quality_Control_with_ArenaSDK.

Table 1 Training and test results

Training losses		Training and test metrics	Training results	Test results
Box_loss	0.3505	Precision	0.994	0.934
Cls_loss	0.2116	Recall	0.998	0.997
Dfl_loss	0.8262	mAP	0.995	0.995

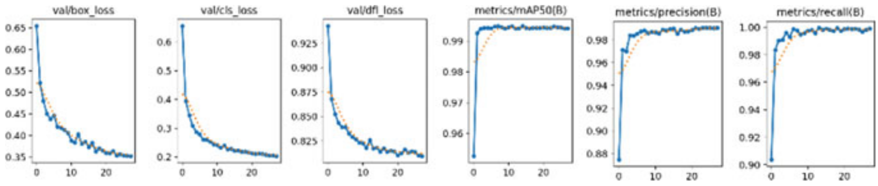

Fig. 3 Training and results of Raspberry Pi 3

for early stopping after a patience threshold of 4 epochs to prevent overfitting. The batch size is 8, the image size is 640 × 640, the optimizer is AdamW, the specified learning rate is 0.001 and the momentum is 0.937. The training was completed after 51 epochs with the results shown in Table 1.

A loss is separated into a Bounding Box Regression loss (box loss), a Classification loss (cls loss) and a Detection Focal loss (dfl loss) [17]. Box loss uses Mean Squared Error to measure the difference between real and predicted coordinates of bounding boxes. Cls loss is caused by not predicting the right classification of an object in created bounding boxes. It uses Cross-Entropy loss. Dfl loss is caused by underrepresented classes. The mentioned losses give the information of model capability to create bounding boxes, classify the elements in those boxes and give the accent to the specific and underrepresented objects during training. To validate the performance of the trained model, mAP is used. The mAP [15] measures the detection and classification performance combining precision and recall values. A training results are shown in Fig. 3.

Descending losses and ascending mAP suggest the model does not overfit. The detection results on the Raspberry Pi 3 are presented on Fig. 4. The detection is stable under different lighting conditions and changes in PCB orientations due to performed augmentation and successful training. The trained PyTorch YOLO model is converted to the ONNX format, better suited for C + + development and robotic applications.

2.3 Inspection

PCBs have standard elements like USB, Ethernet and HDMI ports that have consistent shapes, so they do not undergo further inspection. The main goal is to inspect

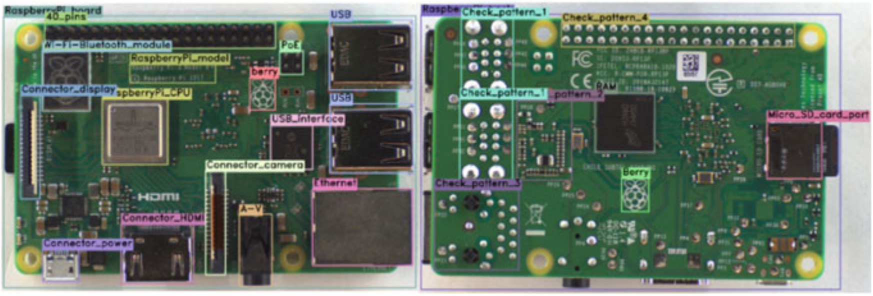

Fig. 4 Detection results of Raspberry Pi 3

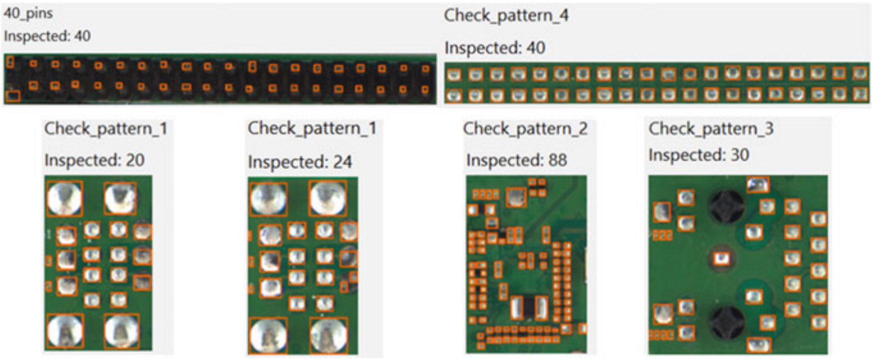

Fig. 5 Raspberry Pi 3 inspected elements

soldering joint points annotated in patterns that connect a specific element to the board. For example, Check_pattern_1 in Fig. 5 is the soldering connection for the USB port.

Inspection is performed on extracted images using adaptive thresholding, the method that computes the threshold for every pixel independently. Block size determines the size of the pixel neighbourhood that is used to calculate the threshold value for a specific pixel using OpenCV thresholding function. Additionally, constant C = 25, obtained experimentally, is subtracted from the calculated threshold to adjust the threshold. Adaptive threshold Gaussian C is used adaptive method and Thresh Binary is used threshold type for the function. The proposed method creates a binary image that is used to find contours. The contours are stored and filtered to get one contour for every pin or soldering point and then the bounding boxes around them are created. The inspections for Raspberry Pi 3 pins and soldering points are presented in Fig. 5. The method counts boxes and compares it to boxes number specified for every pattern.

Fig. 6 Raspberry Pi 3 OCR result

2.4 OCR

The OCR is performed on extracted PCB model designations to provide additional checks if the right PCB is detected. The Tesseract OCR engine with the Leptonica library is used for the OCR algorithm. Tesseract OCR engine uses convolutional neural network to detect and classify characters from the input image. It uses Leptonica for preprocessing data. Classified characters are connected to words and analysed by using language libraries with specific language rules. The resulting text is compared to the detected class names and predefined text expected on each board, to provide additional YOLOv8 detection check. One example of OCR is shown in Fig. 6.

3 Experiments

This chapter presents results of end-to-end quality control system. The detection results in Table 2 suggest the correctness of using CNN for detection purposes. The overall number of objects to detect is 127, that are successfully detected. The detection confidence of whole PCB boards (front and back side) is 97% and the calculated confidence of PCB boards and their components is 92.7% because of the low detection confidence for underrepresented classes as Dfl loss suggests. The confidences are obtained by trained YOLOv8 model detections.

Inspection is stable for industrial lighting conditions. For testing purposes, standard computer vision evaluation metrics that includes precision, and recall are calculated [12], with the results in Table 2. Excellent recall results suggest all the pins/soldering points are recognized and a precision suggests there is a small number of false positive predictions. The inspection performance on Arduino Uno and Jetson Nano are shown in Fig. 7. Given results justify the use of adaptive threshold algorithm for inspection.

OCR is used to check the model designations of detected PCB. The solution can be modified to read all text on boards, but it is not necessary for inspection purposes. The OCR performs well across a variety of text sizes, specific fonts, and diverse background colours. OCR detected text with character classification accuracy of 95.6%. The recognized text is compared to the expected output to provide validation of YOLOv8 model.

The proposed system, that consists of detection using YOLOv8 model, inspection using adaptive threshold and OCR using Tesseract OCR, can be performed on CPU or GPU. Because of relatively big model for real-time applications and image resolution

Table 2 YOLOv8 detection and inspection results

PCBs	No. objects (to detect)	No. detected objects	PCB detection confidence, front, and back side	Overall component detection confidence (%)	Inspection precision (%)	Inspection recall (%)
Raspberry Pi	25	25	98% (fr.), 97% (b.)	95.3	96.4	89.8
Arduino Uno	21	21	97% (fr.), 96% (b.)	92.9	96.8	100
Jetson Nano	22	22	98% (fr.), 97% (b.)	93.2	92.9	100
Jetson Xavier	22	22	97% (fr.), 98% (b.)	92.4	92.7	100
Up board	14	14	98% (fr.), 98% (b.)	93.2	98.1	99.8
STM32	23	23	95% (fr.), 95% (b.)	89.3	100	100

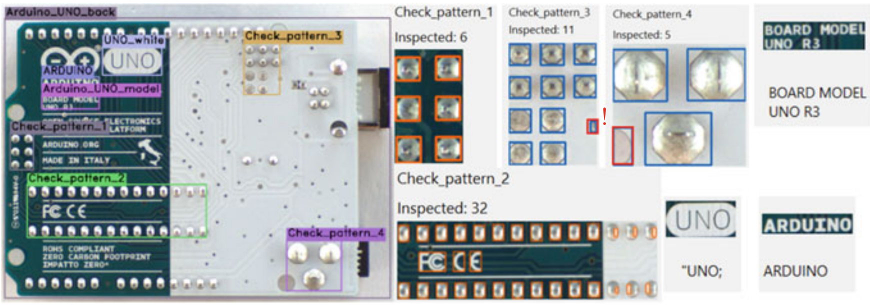

a) Arduino Uno back side

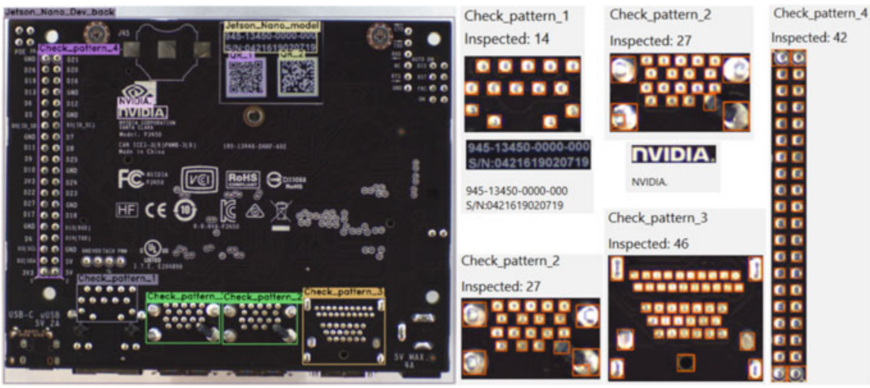

b) Jetson Nano back side

Fig. 7 Detection, inspection and OCR on Arduino Uno and Jeston Nano back of 3072 $\times$ 2048 pixels, the time required for quality control loop on GPU (GeForce GTX 1650), preferred for computer vision applications, is 255 ms. The achieved processing time enables using the system in real-time robotic production.

4 Conclusion

This research presented the approach to PCB quality control for robotic production systems that includes detection, inspection, and OCR. For detection purposes, the custom dataset is created and the YOLOv8 model is trained with an overall 97% detection confidence just for PCBs and 92.7% for PCBs with all components. The adaptive threshold and contour finding algorithms are used for inspection to visually inspect the quantity and quality of pins and soldering points. The overall precision of the algorithm is 96.1% and recall is 98.2%. The combination of CNN model and adaptive thresholding algorithm matches the results of AOI and related research works in this field. For the OCR, the Tesseract OCR engine is utilized, and the result is 95.6% classification accuracy on text characters. The complete system for quality control purposes is fast and fully automated, making it preferable for real time robotic applications. Given results confirmed the justification of using computer vision algorithms for quality control to improve reliability, reduce inspection time and reduce costs, that are the main requirements for modern quality control systems. The combination of state-of-the-art CNN with computer vision algorithms to perform end-to-end quality control represents the main innovation and foundation to address future quality control problems.

The main objective for future work is to implement the proposed system within robotic PCB production system to create fluent workflow from the initial board to the finalized, manufactured PCB. It is also required to reduce losses by increasing the dataset and achieve more stable detection, extraction, and inspection.

Acknowledgements The authors would like to acknowledge the support of the project CRTA Regional Centre of Excellence for Robotic Technology, funded by the ERDF fund.

References

1. Janczki, M., et al.: Automatic optical inspection of soldering. materials science—advanced topics. In: Mastai, Y. (ed.) InTech. https://doi.org/10.5772/51699 (2013)
2. Raihan, F., Ce, W.: PCB defect detection USING OPENCV with image subratction method. 2017 ICIMTech, pp. 204–209 (2017). https://doi.org/10.1109/ICIMTech.2017.8273538
3. Crispin, A.J., Rankov, V.: Automated inspection of PCB components using a genetic algorithm template-matching approach. Int. J. Adv. Manuf. Technol. **35**(3–4), 293–300 (2007). https://doi.org/10.1007/s00170-006-0730-0
4. Baygin, M. et al.: Machine vision based defect detection approach using image processing. 2017 IDAP, Malatya: IEEE, pp. 1–5 (2017). https://doi.org/10.1109/IDAP.2017.8090292

5. Bukhari, S., et al.: Automated PCB inspection system. TEM J. **6**, 380–390 (2017)
6. Zhao, W., et al.: PCB component detection using computer vision for hardware assurance. BDCC **6**(2), 39 (2022). https://doi.org/10.3390/bdcc6020039
7. Huang, W., et al.: HRIPCB: a challenging dataset for PCB defects detection and classification. J. Eng. **2020**, 303–309 (2020).https://doi.org/10.1049/joe.2019.1183
8. Ulger, F., et al.: Solder joint inspection on printed circuit boards: a survey and a dataset. IEEE Trans. Istrum. Meas. **72**, 1–21 (2023). https://doi.org/10.1109/TIM.2023.3277935
9. Sathiaseelan, M., et al.: Why is deep learning challenging for printed circuit board (pcb) component recognition and how can we address it?. Cryptography **5**(1), 9 (2021). https://doi.org/10.3390/cryptography5010009
10. Akhyar, F., et al.: Observation of attention mechanism baseline for PCB surface inspection system. APWiMob 1–6 (2022). https://doi.org/10.1109/APWiMob56856.2022.10014223
11. Redmon, J., et al.: You only look once: unified, real-time object detection. In: 2016 IEEE Conference on Computer Vision and Pattern Recognition, pp. 779–788 (2016)
12. Li, J., et al.: Application research of improved YOLO V3 algorithm in PCB electronic component detection. Appl. Sci. **9**(18), 3750. https://doi.org/10.3390/app9183750
13. Lim, J., et al.: A deep context learning based PCB defect detection model with anomalous trend alarming system. Results Eng. **17**, 100968 (2023)
14. Terven, J., Cordova-Esperanza, D.: A comprehensive review of YOLO: From YOLOv1 to YOLOv8 and beyond. arXiv (2023)
15. Solawetz, J., Francesco.: What is YOLOv8? The ultimate guide (2023)
16. Rdmon, J., Farhadi. A.: YOLOv3: an incremental improvement. arXiv (2023)
17. Official GitHub repository. https://github.com/ultralytics/, Ultralytics (2023)

Cost-Effective Robot Arm Teleoperation Via Human Pose Tracking with Monocular Camera

Bernard Parfaite, Luka Petrović, Vlaho-Josip Štironja, Ivan Marković, and Ivan Petrović

Abstract Robot teleoperation is an essential tool for performing complex tasks that require dexterity beyond the capabilities of state-of-the-art algorithms. Existing teleoperation methods are often non-intuitive for human operators or require special sensors and equipment, making them cost-ineffective and impractical in many scenarios. In this paper, we propose a robot arm teleoperation framework that relies on monocular camera images. The proposed framework first uses lightweight neural networks for estimating the human operator body pose and recognizing their hand gesture. An efficient inverse kinematics algorithm then finds the desired robot arm configuration, achieving end-effector motion that imitates operator's wrist movement. Our teleoperation framework can be executed on an average laptop using a web camera with any robotic arm that has a ROS interface. We verified its performance in real-world experiments with a Kinova Jaco robotic arm, demonstrating the ability to grasp and move an object in the environment.

Keywords Cost-effective robot · Robot teleoperation · Mediapipe pose

1 Introduction

In recent years, the development of robotic systems has witnessed significant advancements, revolutionizing various industries and sectors. One area of particular interest is robot arm teleoperation, where human operators can remotely control robotic arms to perform complex tasks in hazardous environments or situations requiring dexterity beyond the current capabilities of autonomous robots [1]. Existing teleoperation approaches [2–4] are often not intuitive and *natural* for human operators. Moreover, they are usually developed for a particular use case and may depend

B. Parfaite
Universite Paul Sabatier Toulouse III, Toulouse, France
e-mail: parfaite.bernard@gmail.com

L. Petrović (✉) · V.-J. Štironja · I. Marković · I. Petrović
Faculty of Electrical Engineering and Computing, University of Zagreb, Zagreb, Croatia
e-mail: luka.petrovic@fer.hr

D. Pisla et al. (eds.), *Advances in Service and Industrial Robotics*, Mechanisms and Machine Science 157, https://doi.org/10.1007/978-3-031-59257-7_7

on specific characteristics of the teleoperated robot or its environment. Teleoperation methods that imitate the movement of the human operator with a robotic arm are more intuitive [5, 6], but often require additional equipment which may be impractical. All of the mentioned properties limit usability of such teleoperation systems by increasing the deployment cost and requiring the operator to learn the control interface.

Some authors suggest using widely-available Android-based mobile devices as cheap teleoperation interfaces to increase cost-effectiveness [7, 8]. Mobile devices act as joystick controllers, which makes the teleoperation intuitive for the operator. However, it may be difficult for the operator to achieve complex robotic arm behavior, such as grasping an object and moving it to a different location. On the other hand, a cost-effective and intuitive teleoperation can be achieved by detecting the human full-body pose in RGB-D images and controlling the robot in a way that mimics the human operator [9–11]. These methods require depth sensing, which is usually not available on laptops and mobile devices, thus requiring an additional sensor.

To address these issues, in this paper we propose a cost-effective robot arm teleoperation framework that relies on monocular camera images. The proposed framework first detects the full-body pose of the human operator and their hand gesture, relying on lightweight open-source neural network models. An efficient inverse kinematics algorithm then finds the desired robot arm configuration that achieves end-effector motion which mimics the operator's wrist movement, enabling intuitive teleoperation. We make several deliberate choices to make the proposed framework as cost-effective as possible. First, we rely on a single monocular RGB camera, enabling teleoperation on virtually any laptop with a web camera or a mobile device. Second, for communication between all components in the system we utilize Robot Operating System (ROS), an open-source middleware framework that integrates control interface for many existing robots. Third, for human pose tracking and gesture recognition we use the open-source Mediapipe computer vision framework aimed at running in real-time on mobile devices and cheap hardware. The proposed teleoperation framework can thus be executed on an average laptop CPU with a web camera, using any robotic arm that has a ROS interface. We verified the performance of our framework in real-world experiments with the Kinova Jaco robotic arm, demonstrating the ability to grasp and move an object in the environment.

2 Robot Arm Teleoperation Framework

To achieve cost-effective robot arm teleoperation, we first take as input a monocular camera image of the human operator. The obtained image is processed to estimate the full-body pose of the operator, and also to recognize hand gestures. From the full-body pose, we extract the information about wrist joint position of the person's arm. The relative movement of operator's wrist between consecutive frames is used to compute the robot control commands that mimic the person's arm movement, which are then sent to the robot for execution. The proposed teleoperation framework is shown in Fig. 1.

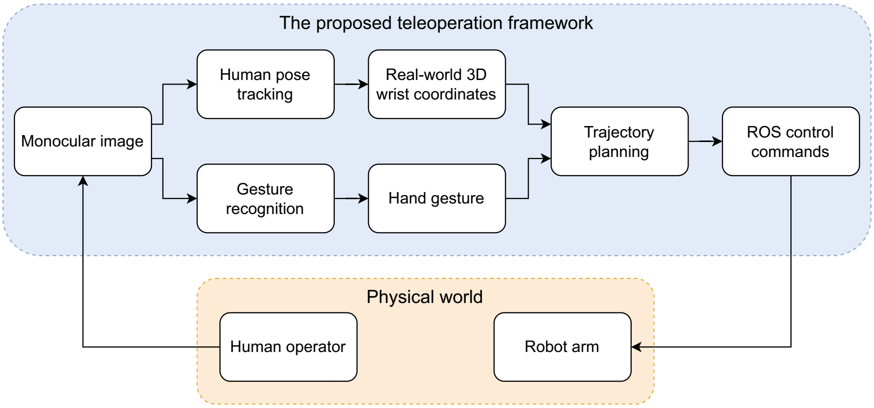

Fig. 1 The proposed teleoperation framework

2.1 Human Pose Tracking

Human pose estimation using a monocular camera refers to the process of estimating positions of human body joints and limbs based solely on the input from a single camera, without explicitly tracking the movement of the person over time. This is an inherently ill-posed problem due to the need of estimating depth from a single 2D image. State-of-the-art deep learning models are able to surmount this challenge, particularly if the intrinsic camera calibration parameters are known. In our framework, we employ the open-source pipeline called *Mediapipe*, a versatile platform designed to facilitate computer vision inferences over various sensory data, encompassing video and audio. Within this pipeline, we employ *MediaPipe Pose Landmark Detection*, a Google-developed open-source library based on deep learning that can accurately estimate 2D and 3D positions of human body keypoints (joints) in real-time, given a single monocular image. The implementation of Mediapipe enables high-fidelity body pose tracking, allowing the inference of 33 3D landmarks across the entire body from RGB video frames, as illustrated in Fig. 2.

The underlying deep model is a lightweight convolutional neural network BlazePose [12], tailored for real-time inference on mobile devices, allowing our teleoperation framework to work on low-power hardware. BlazePose first detects the human body from an image by employing an efficient face detector [13], under the assumption that a person's face is always visible for a single-person use case, such as the proposed teleoperation framework. Once a human body is detected, the model estimates positions of key body joints, often referred to as keypoints, including the head, shoulders, elbows, wrists, hips, knees, and ankles. Each keypoint is accompanied by a visibility score, signifying the likelihood of the keypoint being unobstructed and correctly positioned within the frame. BlazePose estimates the overall pose of the person by utilizing an encoder-decoder architecture to predict heatmaps for all

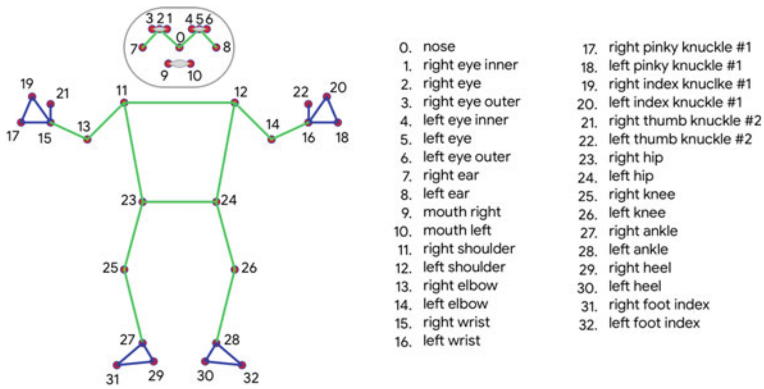

Fig. 2 The mediapipe pose landmark detection tracks 33 body landmarks that represent the approximate location of body parts [12]

joints, followed by another encoder that regresses directly to the coordinates of all joints [12]. The final output of the BlazePose human pose estimation system includes a set of 3D coordinates representing the positions of each joint.

We implement a ROS interface for Mediapipe in Python, where a monocular camera image is read from a ROS topic and the resulting human pose detection result can be published. After obtaining the human pose estimate, we extract the 3D position of the left hand (landmark 16 on Fig. 2), with the frame's origin positioned at the center between the hips. We denote this position with $\mathbf{p}_B^H$, indicating the hand position in the body frame. Our teleoperation framework only considers the relative change in the person's wrist position. Thus, our framework can operate even if the person is moving, while also circumventing the need for calibration between camera and robot arm frames, further enhancing simplicity and cost-effectiveness. Additionally, we utilize a hand gesture recognition classification model from the Mediapipe pipeline [14], enabling the detection of whether the human operator's hand is open or closed. The neural network model consists of 3 fully connected layers with 50 neurons each, acting as a lightweight real-time classifier.

2.2 Robot Arm Control

Once we acquire the real-world 3D coordinates of the person's left wrist in the body frame $\mathbf{p}_B^H$ and its corresponding hand gesture, we can plan the action to maneuver the robot arm's end effector to a desired location or control the gripper. We consider three high-level actions: teleoperation activation, robot arm movement, and gripper opening or closing. Before enabling arm movement teleoperation, we check that both wrists of the human operator are within the webcam's captured frame. Activation of teleoperation is achieved by the operator joining their hands.

To achieve the robot arm movement, we first compute the desired end-effector position in the robot base frame $\mathbf{p}_R^{EE}(k)$ for the k-th iteration by moving the arm proportionally to the detected wrist movement

$$\mathbf{p}_R^{EE}(t_k) = \mathbf{p}_R^{EE}(t_{k-1}) + \alpha\big(\mathbf{p}_B^{H}(t_k) - \mathbf{p}_B^{H}(t_{k-1})\big), \tag{1}$$

where α is the scaling factor. Then, we use Trac-IK [15] open-source library for efficient inverse kinematics to find the robot's configuration $\mathbf{q}(t_k)$ required to achieve the desired pose. We calculate the displacement between the desired and current configuration and compute a desired uniform joint space velocity that is passed to a PID velocity controller using ROS. Consequently, the robot arm's end effector mirrors the movement of the operator's hand.

The third action adjusts the state of the gripper based on *palm open* and *palm closed* gestures. Based on the detected gestures, we wither fully open or fully close the gripper fingers. The set of actions is modular and different actions can be derived from hand gestures and used for different robot arms depending on specific robot features. Our framework is applicable to all robot arms that have a ROS interface. Moreover, given that the pose tracking can be performed for both wrists, it is feasible to teleoperate two arms simultaneously using a single monocular camera.

3 Results

To evaluate the proposed teleoperation framework, we conducted a performance analysis in simulation and real-world demonstrations in a laboratory environment on the 6 degree-of-freedom Kinova Jaco robot arm. First we examined the conditions that enable teleoperation with a cheap web camera in a number of experiments with a simulated robot arm. For simulation, we used Gazebo and the Kinova Jaco robot arm URDF model, which exhibits the same behavior as the real-world arm due to the shared ROS interface. Then, we execute three real-world teleoperation scenarios that include grasping and moving a plastic bottle.

3.1 Simulation Performance Analysis

First, we investigated the human pose tracking accuracy given different light conditions and human posture. The precision of pose tracking is notably improved when the human operator is situated in well-illuminated surroundings and when the upper body is fully captured within the camera frame. Consequently, we choose to compute control commands only if the left wrist keypoint has visibility greater than 0.9. Next, we observed enhanced accuracy in hand gesture recognition when the palm faces the camera and maintains a distance of no more than 2 m, coupled with favourable lighting conditions. Note that the BlazePose model in poor light conditions sometimes erroneously classifies the *palm closed* gesture as the *thumbs up* gesture, leading to a missed gripper action.

We then investigated the robot arm motion, which was smooth and accurately tracked the calculated trajectory, in most cases achieving the intended movement commanded by the user's hand gestures. However, we found that the BlazePose depth estimation often lacked accuracy, which was expected due to the ill-posed problem of monocular depth estimation, especially using a cheap camera. To address this limitation and achieve teleoperation accurate enough for completing complex movements, such as grasping a bottle, we decided to restrict the movement of the end effector to a pre-specified distance of ± 0.1 m along the axis corresponding to the camera depth, if any change in the operator's arm movement along the camera depth axis is observed. In summary, given good lighting conditions and accurate human operator pose estimation, our simulation performance study indicates the feasibility of accomplishing pick and place tasks using the developed teleoperation framework.

3.2 *Real-World Demonstrations*

In order to test our teleoperation framework, three scenarios have been considered. In the first scenario, we verify that our framework enables the motion of the arm in free space that mimics the movement of the human operator. Moreover, we verify that the robot arm gripper closes in response to the operator's palm closure, and that it opens when the palm is extended, as shown in Fig. 3. The latency between operator's hand

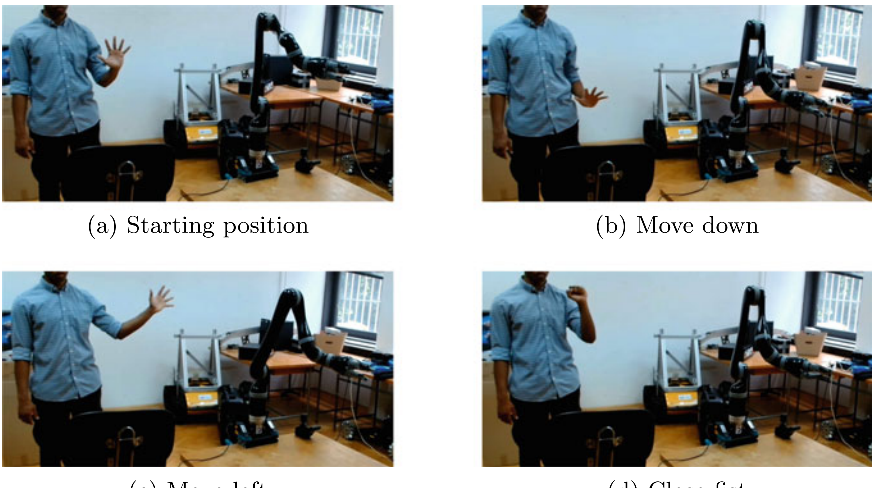

(a) Starting position (b) Move down

(c) Move left (d) Close fist

Fig. 3 Teleoperation in free space

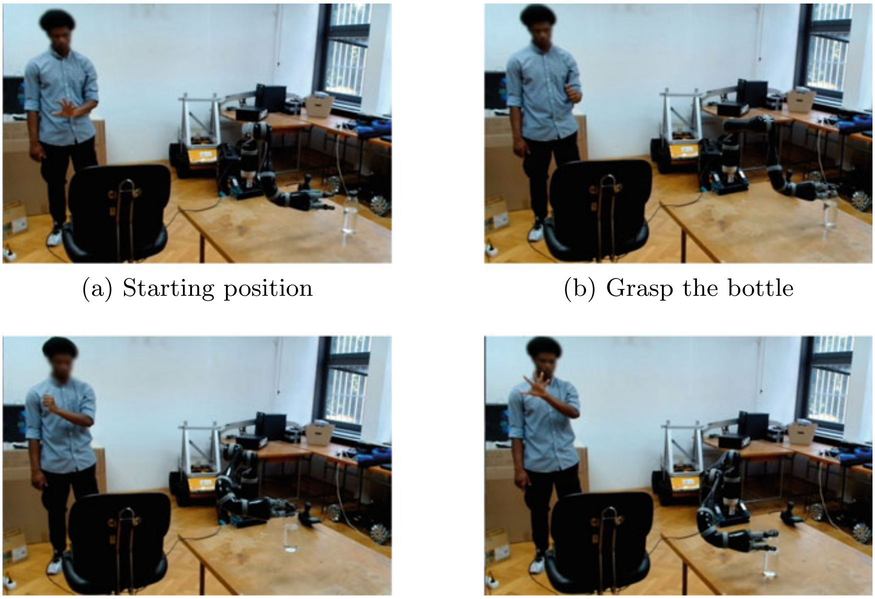

(a) Starting position (b) Grasp the bottle

(c) Move the bottle (d) Release the bottle

Fig. 4 Manipulating the plastic bottle

movement of about 0.3 m and robot's motion completion was around 1.2 s. Note that the robotic arm's speed was deliberately restricted during our testing phase for safety considerations.

In the second scenario, the goal is to teleoperate the robot to move an empty plastic bottle. The operator guides the robot to grasp the bottle from a table, move it in the air, and then return it on the same table without flipping, as shown in Fig. 4. We completed this process 5 times in a row to ensure repeatability.

The third scenario considered moving the plastic bottle from a table to a shelf. The operator guided the robotic arm towards the bottle on the table, grasped it using hand gestures, moved it towards the shelf and successfully released it, as depicted in Fig. 5.

4 Conclusion

In this paper, we developed a framework that enables intuitive robot arm teleoperation using a monocular camera. The proposed framework first uses lightweight neural networks for estimating the human operator body pose and recognizing their hand gesture. An efficient inverse kinematics algorithm is then utilized to find the robot arm configuration, achieving end-effector motion that mimics operator's wrist movement.

(a) Starting position

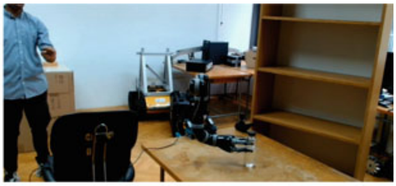

(b) Grasp the bottle

(c) Move to shelf

(d) Release the bottle

Fig. 5 Moving the plastic bottle from the table to the shelf

The proposed teleoperation framework can be executed on an average laptop with any robotic arm that has a ROS interface. We verified the performance of our teleoperation framework in real-world experiments with a Kinova Jaco robotic arm, demonstrating the ability to grasp and move an object in the environment.

Acknowledgements This research has been supported by the European Regional Development Fund under the grant PK.1.1.02.0008 (DATACROSS).

References

1. Vertut, J.: Teleoperation and Robotics: Applications and Technology, vol. 3. Springer Science & Business Media (2013)
2. Kofman, J., Wu, X., Luu, T.J., Verma, S.: Teleoperation of a robot manipulator using a vision-based human-robot interface. IEEE Trans. Ind. Electr. **52**(5), 1206–1219 (2005)
3. Hainsworth, D.W.: Teleoperation user interfaces for mining robotics. Auton. Rob. **11**(1), 19–28 (2001)
4. Birk, A., Schwertfeger, S., Pathak, K.: A networking framework for teleoperation in safety, security, and rescue robotics. IEEE Wireless Commun **16**(1), 6–13 (2009)
5. Artemiadis, P.K., Kyriakopoulos, K.J.: Emg-based control of a robot arm using low-dimensional embeddings. IEEE Trans. Robot. **26**(2), 393–398 (2010)
6. Gupta, G.S., Mukhopadhyay, S.C., Messom, C.H., Demidenko, S.N.: Master-slave control of a teleoperated anthropomorphic robotic arm with gripping force sensing. IEEE Trans. Inst. Measur. **55**(6), 2136–2145 (2006)
7. Szymańska, E., Petrović, L., Marković, I., Petrović, I.: Mobile robot teleoperation via android mobile device with udp communication. In: 2021 44th International Convention on Information, Communication and Electronic Technology (MIPRO), pp. 1143–1148. IEEE (2021)

8. Yepes, J.C., Yepes, J.J., Martinez, J.R., Pérez, V.Z.: Implementation of an android based teleoperation application for controlling a kuka-kr6 robot by using sensor fusion. In: Pan American Health Care Exchanges (PAHCE), pp. 1–5. IEEE (2013)
9. Syakir, M., Ningrum, E.S., Sulistijono, I.A.: Teleoperation robot arm using depth sensor. In: International Electronics Symposium (IES), pp. 394–399. IEEE (2019)
10. Marić, F., Jurin, I., Marković, I., Kalafatić, Z., Petrović, I.: Robot arm teleoperation via rgbd sensor palm tracking. In: 2016 39th International Convention on Information and Communication Technology, Electronics and Microelectronics (MIPRO), pp. 1093–1098. IEEE (2016)
11. Handa, A., Van Wyk, K., Yang, W., Liang, J., Chao, Y.W., Wan, Q., Birchfield, S., Ratliff, N., Fox, D.: Dexpilot: Vision-based teleoperation of dexterous robotic hand-arm system. In: 2020 IEEE International Conference on Robotics and Automation (ICRA), pp. 9164–9170. IEEE (2020)
12. Bazarevsky, V., Grishchenko, I., Raveendran, K., Zhu, T., Zhang, F., Grundmann, M.: Blazepose: On-device real-time body pose tracking. arXiv preprint arXiv:2006.10204 (2020)
13. Bazarevsky, V., Kartynnik, Y., Vakunov, A., Raveendran, K., Grundmann, M.: Blazeface: Submillisecond neural face detection on mobile gpus. ArXiv preprint arXiv:1907.05047 (2019)
14. Sung, G., Sokal, K., Uboweja, E., Bazarevsky, V., Baccash, J., Bazavan, E.G., Chang, C.L., Grundmann, M.: On-device real-time hand gesture recognition. ArXiv preprint arXiv:2111.00038 (2021)
15. Beeson, P., Ames, B.: Trac-ik: An open-source library for improved solving of generic inverse kinematics. In: 2015 IEEE-RAS 15th International Conference on Humanoid Robots (Humanoids), pp. 928–935. IEEE (2015)

Revolutionizing Speech Emotion Recognition: A Novel Hilbert Curve Approach for Two-Dimensional Representation and Convolutional Neural Network Classification

Suryakant Tyagi and Sándor Szénási

Abstract Emotions are integral to human existence, influencing psychological well-being and permeating various aspects of daily life. Speech emotion recognition (SER) stands as a pivotal branch of emotion detection, focusing on decoding the acoustic nuances embedded in speech signals. This study delves into the landscape of SER, addressing challenges related to feature extraction and classifier development. Inspired by the Hilbert curve, a novel approach is proposed, converting one-dimensional time series data into informative two-dimensional images. A convolutional neural network extracts features from these images, and a fully connected network processes these features for sentiment classification. The study comprehensively evaluates this method across four diverse datasets, namely RAVDESS, TESS, SAVEE, and EmoDB. The proposed algorithm demonstrates promising results, showcasing potential advantages in emotion recognition tasks. Comparative analyses with existing methodologies, including Gram Angle Fields (GAF) and CyTex, affirm the feasibility and effectiveness of the proposed algorithm. The study contributes to advancing sentiment recognition by transforming time-series data into two-dimensional images, thereby opening new avenues in speech emotion recognition with improved accuracy and performance. The paper outlines the algorithms employed, details the methodology, presents experimental results, and concludes with reflections on findings and potential future directions.

S. Tyagi (✉)
Doctoral School of Applied Informatics and Applied Mathematics, Óbuda University, Budapest 1034, Hungary
e-mail: suryakant.tyagi@phd.uni-obuda.hu

S. Szénási
John Von Neumann Faculty of Informatics, Óbuda University, Budapest, Hungary

Faculty of Economics and Informatics, J. Selye University, Komárno, Slovakia

S. Szénási
e-mail: szenasi.sandor@nik.uni-obuda.hu

D. Pisla et al. (eds.), *Advances in Service and Industrial Robotics*, Mechanisms and Machine Science 157, https://doi.org/10.1007/978-3-031-59257-7_8

Keywords Speech emotion recognition (SER) · Hilbert curve · TESS · Gram angle fields · CyTex

1 First Section

Emotions constitute a fundamental aspect of human existence, playing a pivotal role in psychological well-being [1]. The evolving landscape of emotion detection research spans the realms of psychology, cognitive science, machine learning, and natural language processing (NLP) [2]. Notably, speech emerges as a significant mode of emotional expression, contributing 38% to the intricate tapestry of emotional communication. As such, speech emotion recognition (SER) emerges as a crucial branch of emotion detection, focusing on unraveling the acoustic nuances embedded in speech signals to discern emotional states [3].

The implications of SER extend across diverse applications, including healthcare, education, and social interaction. From monitoring stress-induced changes in mental health to facilitating mental health assessments and predicting depression severity, SER actively contributes to holistic well-being [4]. Moreover, its role in decision-making within the tourism industry and gathering opinions on various topics underscores its societal impact, promoting social stability and harmony [5].

Integrating SER into real-life applications enhances human–computer interactions, offering the prospect of more intuitive and emotionally enriched engagements [6]. Previous studies have explored varied approaches, combining visual and auditory analyses, integrated learning, and advanced neural network architectures to bolster sentiment analysis and emotion recognition.

However, a primary challenge in SER lies in extracting relevant features from speech signals and developing suitable classifiers [7]. The multidimensionality and redundancy introduced by combining multiple affective features pose obstacles to machine-learning algorithms. Against this backdrop, innovative approaches have emerged, transforming one-dimensional speech time series into two-dimensional images, leveraging computer vision's efficiency and accuracy. Noteworthy among these are methods proposed by [8, 9] each introducing unique challenges and complexities.

In this context, our study builds upon these foundations, introducing a novel method addressing standardization, calibration, interpretability, and generalizability challenges in emotion recognition from speech signals. Inspired by the structure of a Hilbert curve, our approach converts one-dimensional time series data into informative two-dimensional images. A convolutional neural network extracts image features, and a fully connected network processes the extracted features for sentiment classification.

We analyze and compare the performance of our method across four diverse datasets: the Ryerson Audio-Visual Database of Emotional Speech and Song (RAVDESS) [10], Toronto Emotional Speech Set (TESS) [11], Emotional Database (EmoDB) [12], and Surrey Audio-Visual Expressed Emotion (SAVEE) [13]. These datasets offer a wide spectrum of vocal expressions, capturing diverse actors, natural and controlled environments, and various emotional categories. A comparative analysis with previous studies validates the feasibility and effectiveness of our proposed algorithm, showcasing potential advantages in emotion-recognition tasks. Emotion recognition in human–robot interactions, showcasing a novel approach employing emotion cards and emotional storytelling. Through meticulous experimentation, it underscores the pivotal role of emotion recognition in enhancing robot adaptivity and enriching the overall interaction experience [14].

This study contributes to the processing of one-dimensional time-series data and also underscores the potential applications of this approach in emotion recognition. By transforming time-series data into two-dimensional images, we open new avenues in speech emotion recognition, promising enhanced accuracy and performance. The success of this approach highlights the value of deep learning and computer vision in advancing sentiment recognition.

The subsequent sections of this paper detail the algorithms employed, outline the methodology, present and discuss experimental results, and conclude with reflections on the findings and potential future directions.

1.1 Background

Understanding the current landscape of methodologies for emotion recognition is essential for advancing innovative solutions. This section explores the work of Wang et al. [8] and Bakhshi et al. [9], shedding light on their respective contributions and the challenges encountered in their proposed approaches.

Wang et al. [8] introduced a novel methodology using Gram Angle Fields (GAF) to convert one-dimensional speech signals into two-dimensional images. The GAF algorithm, a time-series data coding method, preserves time-domain information by rescaling the time series to the interval [0, 1] or [−1, 1]. It represents the rescaled time series in polar coordinates, providing a unique perspective on temporal relationships. The algorithm utilizes triangular sum/difference calculations to generate a two-dimensional image, known as the Generalized Autocorrelation Matrix (GAF). Despite its innovation, challenges arise in emotion recognition, particularly in ensuring the accuracy and robustness of the conversion process and the dependence on GAF for capturing essential emotional features.

Bakhshi et al. proposed the CyTex method, focusing on leveraging the periodicity of speech signals for emotion recognition. CyTex transforms speech signals into structured images, representing each speech cycle as a row in the image. Challenges with CyTex relate to the generalizability of the conversion technique, as the periodicity of speech signals may not universally capture diverse emotional patterns.

1.2 Motivation

In response to these challenges, this study proposes an innovative approach to emotion recognition. The method involves mapping one-dimensional time series data, specifically speech signals, onto two-dimensional images following the trajectory of the Hilbert curve. The feature values of the resulting images are extracted through a convolution operation, flattened based on the Hilbert curve arrangement, and categorized by a classifier for speech emotion recognition.

This methodology capitalizes on the structural properties of the Hilbert curve, offering a unique and efficient means of representing and analyzing speech signals for emotion recognition. Advantages include preserving crucial information without downsampling and overcoming challenges associated with the periodicity of speech signals through a novel flattening technique along the Hilbert curve path. These innovations contribute significantly to addressing challenges within the emotion recognition domain.

2 Literature Review

Emotions are integral to human life [14] and play a crucial role in psychological survival [15]. Research in emotion detection is evolving through interdisciplinary collaboration across psychology, cognitive science, machine learning, and natural language processing (NLP) [16]. Early studies, including those by Darwin [17], considered emotional expression as a fundamental behavioral pattern preserved in human evolution. Speech signaling, contributing to 38% of emotional communication [18], is a crucial mode of emotional expression influencing emotion recognition and communication [19]. Speech emotion recognition (SER), with over two decades of research history [20], focuses on recognizing emotions in speech, excluding semantic content [21, 22]. SER finds diverse applications in healthcare, education, social interaction [23–25], mental health monitoring [26], assessments [27], depression severity prediction [28], and decision-making in the tourism industry [17, 22]. SER's convergence with real-life applications enhances human–computer interactions, offering the potential for more intuitive and emotionally rich experiences [25]. Previous studies [29–33] enriched SER knowledge, introducing various models and techniques. However, a primary challenge in SER is the extraction of relevant features [30, 34] and developing suitable classifiers [20, 35], leading to increased dimensionality and the risk of overfitting [13]. Noteworthy approaches include Wang et al.'s transformation of speech time series into two-dimensional images [8], leveraging computer vision, and another study using the quasiperiodic nature of speech signals to enhance emotion recognition [9]. These methods, while innovative, present challenges in accuracy and generalizability. Building on these foundations, our study proposes a novel method inspired by the Hilbert curve, addressing challenges in emotion recognition from speech signals [30]. By converting one-dimensional time series into two-dimensional images using convolutional neural networks and comparing them with existing studies [8, 9], our approach demonstrates potential advantages, showcasing the value of deep learning and computer vision in advancing sentiment recognition with improved accuracy and performance.

2.1 Proposed Approach

This study introduces an innovative method to overcome challenges identified in the approaches of Wang et al. and Bakhshi et al. Specifically, we present a novel technique for converting one-dimensional time series, such as speech signals, into two-dimensional images. Our method utilizes the Hilbert curve, mapping the speech signal onto an image. Through convolution, we extract feature values from the images and flatten them based on the Hilbert curve arrangement, resulting in a one-dimensional vector. A classifier is then applied to categorize the vector, achieving the goal of speech emotion recognition. Leveraging the structural properties of the Hilbert curve, our approach provides a unique and efficient way to represent and analyze speech signals for emotion recognition. Notably, our methodology avoids downsampling, preserving crucial information and addresses periodicity challenges by introducing a novel flattening method along the Hilbert curve path. These innovations significantly improve conversion accuracy and generalizability, addressing key challenges in emotion recognition.

3 Experimental Setup

In this section, we detail our methodology and experiments, focusing on a thorough analysis of one-dimensional time series using computer vision techniques.

3.1 Approach

Our innovative approach transforms one-dimensional time series, such as speech signals, into two-dimensional images. Specifically, we arrange the signal along the path of the Hilbert curve, mapping it onto an image to preserve temporal correlations. The Hilbert curve, a space-filling curve proposed by mathematician David Hilbert, proves instrumental in maintaining locality and facilitating localized access to spatial data. Two novel proposals based on Hilbert curve mapping and inverse mapping are presented to convert one-dimensional time series to two-dimensional images efficiently.

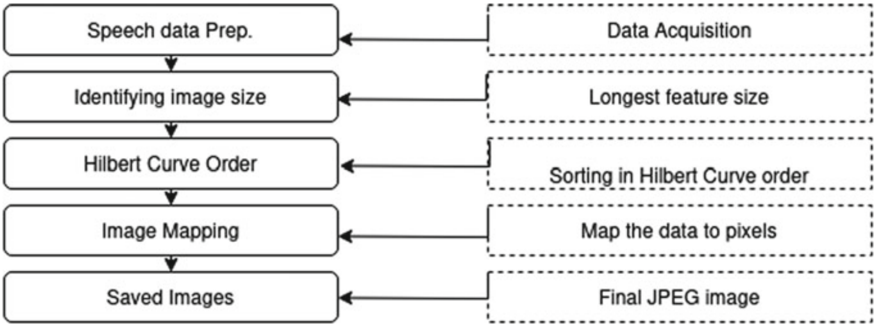

Fig. 1 Demonstration of the transition from one to two dimensions. In this experiment, speech data transforms into a structured image, aligning grayscale pixel values along the Hilbert curve. The image size is set at (640, 640), determined by the longest segment of speech data, and various padding techniques are employed to address incomplete regions

Conversion from One to Two Dimensions: This method employs Hilbert curves to upscale one-dimensional time series into two-dimensional images. Speech data is treated as grayscale pixel values, ordered according to the Hilbert curve to create an ordered image. Image dimensions are set to (640, and 640), accommodating different sizes with flexible padding methods. This process provides an innovative means of representing speech information as an image while handling incomplete regions.

Conversion from Two to One Dimension: This study introduces a novel 2D to 1D dimensionality reduction method based on the Hilbert curve to restore information. Inverse mapping unfolds feature maps along the Hilbert curve, forming a one-dimensional array. This method preserves temporal correlation, ensuring an accurate and ordered representation for further speech data analysis. These proposals optimize the data representation and reduction process, leveraging Hilbert curves to provide a reliable and powerful tool for emotion recognition tasks (Fig. 1).

3.2 Experiments

Commencing with the preprocessing of the speech signal, the experimental workflow transformed the preprocessed data into Hilbert curves. Subsequent stages involved an in-depth analysis employing a CNN, culminating in conclusive classification results.

The study employed four distinct datasets, including the RAVDESS, TESS, SAVEE, and EmoDB, each offering unique attributes for emotional speech analysis. RAVDESS provides diverse expressions with 24 actors, while TESS stands out for its comprehensive collection of 2,803 recordings, featuring various emotions portrayed by professional actors. SAVEE, designed for speech emotion recognition, features a single male actor portraying seven emotional states, and EmoDB, used for emotional speech recognition, involves recordings from ten professional German actors. However, limitations such as actor diversity, imbalanced classes, controlled recording conditions, limited contextual information, and language representation are acknowledged. The TESS dataset, despite dataset-specific considerations, excels with its diverse emotional expressions, large actor pool, natural recording conditions, high-quality data, detailed metadata, and multimodal features, making it a robust resource for emotional speech analysis research. The corpus was randomly divided into an 80% training set and a 20% test set.

In our experimental procedure, we first normalized and regularized the speech signals. This involved adjusting the values of the signals to ensure consistency and compatibility for further processing. Subsequently, we transformed the one-dimensional speech data into a two-dimensional format using Hilbert curves, facilitating spatial organization for analysis. For feature extraction and classification, convolutional neural networks were employed. During the preprocessing phase, the speech signals were initially normalized to a range of [0–1] to standardize their amplitude. Following this, regularization was performed to rescale the values to fit within the range [0–255], conforming to the specifications for an 8-bit image representation. The subsequent transformation of one-dimensional data into two-dimensional data is carried out based on the characteristics of the Hilbert curve. The correlation between the Hilbert curve dimensions and the time series length is outlined in Table 1. For speech data with a length of, the Hilbert curve typically adopts a dimension of, resulting in a Hilbert curve. In cases where the speech data lengths fall within the range of to, two distinct approaches are employed for data supplementation, ensuring compliance with Hilbert curve dimension requirements. Method one involves utilizing zero-padding, while method two entails iterative data replication to meet dimensionality criteria. The selection of zero-padding primarily stems from the translation invariance property inherent in the convolution operation.

The experimental process is delineated in Fig. 2, providing a visual depiction of the methodological steps undertaken in the experiment. This illustrative representation serves to elucidate the procedural intricacies involved. The approach employed in this method optimally leverages the capabilities inherent in computer vision and deep learning methodologies tailored for the analysis of one-dimensional time-series data.

Table 1 Hilbert curve dimension and time series length relationship

Dimensions	Length of time series	Image size
5	1024	(32, 32)
6	4096	(64, 64)
7	16,364	(128, 128)
8	65,538	(256, 256)
9	202,144	(512, 512)
10	409,600	(640, 640)

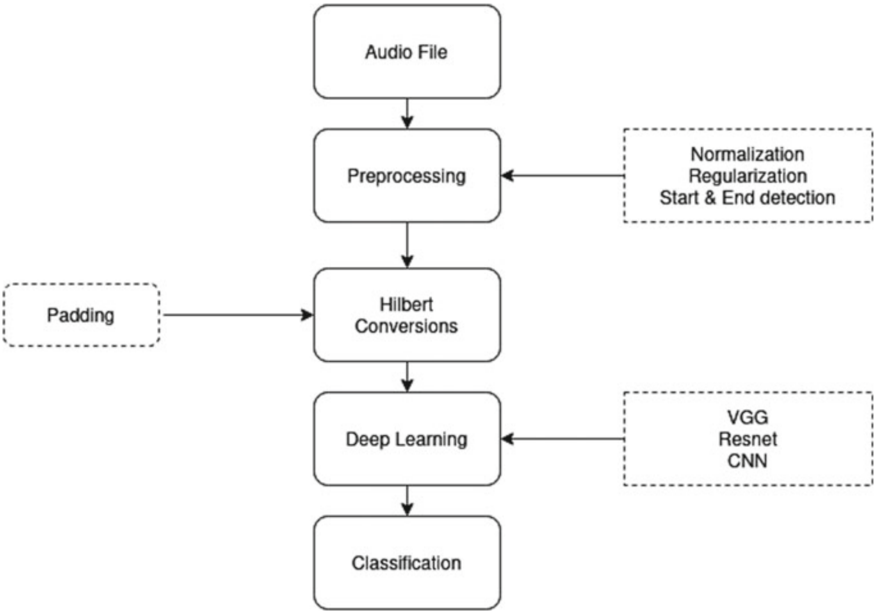

Fig. 2 The flowchart of the experiment

4 Results and Discussion

In this section, we examine the outcomes of transforming one-dimensional data into two-dimensional images and meticulously compare and analyze the performance of these approaches. The methodology employed in this study is predominantly grounded in the attributes of the Hilbert curve, known for its capacity to convert one-dimensional time series data into a more information-rich two-dimensional image format. To bolster the model's resilience and adaptability to diverse speech features, encompassing variations in speeds and speech rates, the training dataset is augmented with 1.5 acceleration and 0.5 deceleration. This augmentation aims to capture and process the nuanced characteristics of real-world speech more comprehensively. Evaluation is based on accuracy, the ratio of correctly predicted samples to the total samples, expressed as a percentage. A comparative analysis with related methods, detailed in Table 2, distinctly highlights the substantial improvement in accuracy achieved through the utilization of Hilbert curve-generated images. Instances in bold signify the data with the highest accuracy for each method.

The comprehensive results of our experiments utilizing ResNet for feature extraction from audio images generated through the Hilbert curve. This approach was applied to four diverse datasets: SAVEE, RAVDESS, EmoDB, and TESS. For the audio-to-image conversion, employing Hilbert curves, we transformed the audio into images sized 640 by 640. Subsequently, ResNet was utilized for extracting features from these images, and SVM served as the classification model. The outcomes

Table 2 Hilbert curve dimension and time series length relationship

Algorithm	Dataset	Accuracy (%)
CyTex	TESS	83.68%
	SAVEE	89.31%
	RAVEDESS	94.13%
	EmoDB	91.12%
GAF	TESS	81%
	SAVEE	86%
	RAVEDESS	91.43%
	EmoDB	90.81%
Hilbert (Ours)	TESS	91.31%
	SAVEE	95.97%
	RAVEDESS	98.37%
	EmoDB	97.81%

demonstrated promising accuracies, such as 81% for TESS, 86% for SAVEE, 91.43% for RAVDESS, and 90.81% for EmoDB.

In addition to ResNet, we explored dimensionality conversion using CyTex, GAF, and our proposed Hilbert Curve approach. Applying ResNet for feature extraction and SVM for classification, the results for GAF were consistent across datasets (TESS: 81%, SAVEE: 86%, RAVDESS: 91.43%, EmoDB: 90.81%). Notably, employing CyTex exhibited improved accuracies, with results of 83.68% for TESS, 89.31% for SAVEE, 94.13% for RAVDESS, and 91.12% for EmoDB. However, the most remarkable outcomes were observed with our Hilbert Curve approach: TESS achieved 91.32% accuracy, SAVEE reached an impressive 95.97%, RAVDESS demonstrated exceptional accuracy at 98.37%, and EmoDB yielded a commendable accuracy of 97.81%. These outstanding results highlight the efficacy of our proposed Hilbert Curve approach for one-dimensional to two-dimensional data conversion, showcasing its potential for robust emotion recognition across diverse datasets. If you have further inquiries or require additional details, please feel free to ask.

5 Conclusion

We introduced an inventive technique for converting one-dimensional time-series data into two-dimensional images, leveraging the temporal correlation through the utilization of Hilbert curve path scheduling. Employing a convolutional neural network, our approach extracts image features and conducts sentiment classification via Hilbert curve spreading. Results from experiments showcase the notable enhancements in SER accuracy achieved by our proposed method. Regarding SER accuracy, our method surpasses other techniques on the same dataset, particularly when employing the Hilbert data representation method, reaching an impressive accuracy rate of 98.37%. It's essential to note that our method's performance is contingent on the availability of large-scale, high-quality speech datasets, which may pose challenges in practical applications. Future research endeavors will concentrate on real-world robotic systems, allowing robots to better understand and respond to human emotions in various interaction scenarios. The proposed algorithm across different languages and cultural contexts could further enhance its applicability in diverse human–robot interaction settings. Exploring the potential synergies between speech emotion recognition and other modalities such as facial expressions or body language could lead to multimodal emotion detection systems, providing robots with more comprehensive insights into human emotions and intentions.

References

1. Hema, C., Fausto Pedro Garcia, M.: Emotional speech recognition using cnn and deep learning techniques. Appl. Acoust. **211**, 109492 (2023)
2. Vuong, N.A., Tran, T.M.: Unveiling the synergy: exploring the intersection of AI and NLP in redefining modern marketing for enhanced consumer engagement and strategy optimization. Q. J. Emerg. Technol. Innov. **8**(3), 103–118 (2023)
3. de Lacerda Pataca, C.: Speech-modulated typography (2023)
4. El Ayadi, M., Kamel, M.S., Karray, F.: Survey on speech emotion recognition: features, classification schemes, and databases. Patt. Recogn. **44**(3), 572–587 (2011)
5. Ujjwal, B.: Roles of AI in digital transformation of tourism business (2024)
6. Partarakis, N., Zabulis, X.: A review of immersive technologies, knowledge representation, and AI for human-centered digital experiences. Electronics **13**(2), 269 (2024)
7. Zmolikova, K., Marc, D., Tsubasa, O., Keisuke, K., Jan, Č, Dong, Y.: Neural target speech extraction: an overview. IEEE Sign. Process. Mag. **40**(3), 8–29 (2023)
8. Wang, Z., Tim, O.: Imaging time-series to improve classification and imputation. arXiv preprint arXiv:1506.00327 (2015)
9. Bakhshi, A., Harimi, A., Chalup, S.: CyTex: transforming speech to textured images for speech emotion recognition. Speech Commun. **139**, 62–75 (2022)
10. Livingstone, S.R., Russo, F.A.: The Ryerson audio-visual database of emotional speech and song (RAVDESS): a dynamic, multimodal set of facial and vocal expressions in North American English. PLoS ONE **13**(5), e0196391 (2018)
11. Dupuis, K., Fuller, K.P.: Toronto emotional speech set (TESS) Collection (2010)
12. Burkhardt, F., Paeschke, A., Rolfes, M., Sendlmeier, W.F., Weiss, B.: A database of German emotional speech. In Interspeech **5**, 1517–1520 (2005)
13. Jackson, P., SJUoSG, H.: Surrey audio-visual expressed emotion (savee) database. University of Surrey: Guildford, UK (2014)
14. Ashok, A., Pawlak, J., Paplu, S., Zafar, Z., Berns, K.: Paralinguistic cues in speech to adapt robot behavior in human-robot interaction. In: 2022 9th IEEE RAS/EMBS international conference for biomedical robotics and biomechatronics (BioRob). IEEE, pp 01–06 (2022)
15. Albanie, S., Nagrani, A., Vedaldi, A., Zisserman, A.: Emotion recognition in speech using cross-modal transfer in the wild. In: Proceedings of the 26th ACM International Conference on Multimedia, pp. 292–301 (2018, October)
16. Arun, A., Rallabhandi, I., Hebbar, S., Nair, A., Jayashree, R.: Emotion recognition in speech using machine learning techniques. In: 2021 12th International Conference on Computing Communication and Networking Technologies (ICCCNT), pp. 01–07. IEEE (2021, July)
17. Al-Talabani, A., Sellahewa, H., Jassim, S.A.: Emotion recognition from speech: tools and challenges. In: Mobile Multimedia/Image Processing, Security, and Applications 2015, vol. 9497, pp. 193–200. SPIE (2015, May)

18. France, D.J., Shiavi, R.G., Silverman, S., Silverman, M., Wilkes, M.: Acoustical properties of speech as indicators of depression and suicidal risk. IEEE Trans. Biomed. Eng. **47**(7), 829–837 (2000)
19. Vogt, T., André, E., Wagner, J.: Automatic recognition of emotions from speech: a review of the literature and recommendations for practical realisation. Affect Emot. Hum. Comput. Interact.: From Theor. Appl. 75–91 (2008)
20. Chen, L., Mao, X., Xue, Y., Cheng, L.L.: Speech emotion recognition: features and classification models. Digit. Sig. Proc. **22**(6), 1154–1160 (2012)
21. Jahan, M.S., Oussalah, M.: A systematic review of hate speech automatic detection using natural language processing. Neurocomputing. 126232 (2023)
22. Al-Dujaili, M.J., Ebrahimi-Moghadam, A.: Speech emotion recognition: a comprehensive survey. Wire. Pers. Commun. **129**(4), 2525–2561 (2023)
23. Boccanfuso, L., Wang, Q., Leite, I., Li, B., Torres, C., Chen, L., Salomons, N., Foster, C., Barney, E., Ahn, Y.A., Scassellati, B., et al.: A thermal emotion classifier for improved human-robot interaction. In: 2016 25th IEEE International Symposium on Robot and Human Interactive Communication (RO-MAN), pp. 718–723. IEEE (2016, August)
24. Kotha, M.: Advancements in speech based emotion identification models using deep learning: a comprehensive overview
25. George, S.M., Ilyas, P.M.: A review on speech emotion recognition: a survey, recent advances, challenges, and the influence of noise. Neurocomputing. 127015 (2023)
26. Geetha, A.V., Mala, T., Priyanka, D., Uma, E.: Multimodal emotion recognition with deep learning: advancements, challenges, and future directions. Inform. Fusion **105**, 102218 (2024)
27. Khan, U.A., Xu, Q., Liu, Y., Lagstedt, A., Alamäki, A., Kauttonen, J.: Exploring contactless techniques in multimodal emotion recognition: insights into diverse applications, challenges, solutions, and prospects. Multimedia Syst. **30**(3), 1–48 (2024)
28. Xu, S., Fang, J., Hu, X., Ngai, E., Wang, W., Guo, Y., Leung, V.C.: Emotion recognition from gait analyses: current research and future directions. IEEE Trans. Comput. Soc. Syst. **11**(1), 363–377 (2022)
29. Sönmez, Y.Ü., Varol, A.: In-depth investigation of speech emotion recognition studies from past to present. The importance of emotion recognition from speech signal for AI. Intell. Syst. Appl. 200351 (2024)
30. Wang, J., Yin, H., Zhou, Y., Xi, W.: Advancements and challenges in speech emotion recognition: a comprehensive review. In: Fourth International Conference on Signal Processing and Machine Learning (CONF-SPML 2024), vol. 13077, pp. 102–109. SPIE (2024, April)
31. Akçay, M.B., Oğuz, K.: Speech emotion recognition: emotional models, databases, features, preprocessing methods, supporting modalities, and classifiers. Speech Commun. **116**, 56–76 (2020)
32. Panda, R., Malheiro, R., Paiva, R.P.: Novel audio features for music emotion recognition. IEEE Trans. Affect. Comput. **11**(4), 614–626 (2018)
33. Kaur, K., Singh, P.: Trends in speech emotion recognition: a comprehensive survey. Multimedia Tools Appl. **82**(19), 29307–29351 (2023)
34. Madanian, S., Chen, T., Adeleye, O., Templeton, J.M., Poellabauer, C., Parry, D., Schneider, S.L.: Speech emotion recognition using machine learning—a systematic review. Intell. Syst. Appl. 200266 (2023)
35. Anagnostopoulos, C.N., Iliou, T., Giannoukos, I.: Features and classifiers for emotion recognition from speech: a survey from 2000 to 2011. Artif. Intell. Rev. **43**, 155–177 (2015)

Positioning of a Surgical Parallel Robot Using Artificial Intelligence

Florin Covaciu, Paul Tucan, Gabriela Rus, Adrian Pisla, Ionut Zima, and Bogdan Gherman

Abstract Virtual reality (VR) can serve as a revolutionary technology in surgery, where robotic systems are used to assist residents in training and accumulating knowledge without risk. In this article, a simulator was developed using virtual reality technology designed for a surgical robotic system used in the single-incision laparoscopic surgery (SILS) procedure. For this system, artificial intelligence is employed for the automatic positioning of the mobile platform of the parallel robot above the SILS port. On the mobile platform, there are two active instruments and a laparoscopic camera, which can be easily inserted through the SILS port by means of two controllers and voice commands.

Keywords Parallel robot · Surgery · Virtual reality · Simulator · Artificial intelligence · YOLOv8

F. Covaciu · P. Tucan (✉) · G. Rus · A. Pisla · I. Zima · B. Gherman
CESTER, Technical University of Cluj-Napoca, 400114 Cluj-Napoca, Romania
e-mail: paul.tucan@mep.utcluj.ro

F. Covaciu
e-mail: florin.covaciu@muri.utcluj.ro

G. Rus
e-mail: gabriela.rus@mep.utcluj.ro

A. Pisla
e-mail: adrian.pisla@muri.utcluj.ro

I. Zima
e-mail: ionut.zima@mep.utcluj.ro

B. Gherman
e-mail: bogdan.gherman@mep.utcluj.ro

D. Pisla et al. (eds.), *Advances in Service and Industrial Robotics*, Mechanisms and Machine Science 157, https://doi.org/10.1007/978-3-031-59257-7_9

1 Introduction

Using the da Vinci multi-arm robotic platform, the first series of successful interventions performed on humans was reported by the Cleveland Clinic (Cleveland, OH, USA) group led by Kaouk in 2009. These interventions include prostatectomy, pyeloplasty and nephrectomy [1]. Surgery employs robots due to their superior benefits, such as enhanced precision, elimination of tremors and other capabilities that surpass those of humans [2]. To implement robotic systems in tasks such as minimally invasive surgical procedures, effective control is essential [3, 4]. SILS is part of the minimally invasive revolution, representing a step forward in reducing surgical trauma and invasiveness [5].

Virtual reality technology is being used increasingly in the medical field as a tool to educate residents. Through this technology, residents can gain technical skills using various simulators. Surgical robotic systems and simulators developed using VR in conjunction with artificial intelligence (AI) have the potential to enhance patient safety in surgery and all its aspects, including resident education and training [6]. In [7], the authors use virtual reality and artificial intelligence to create a simulator for a surgical robotic system designed for use in the SILS procedure. Elessawy et al. evaluate the training benefit using the laparoscopic virtual reality simulator [8]. In [9], the authors conduct a study to determine whether laparoscopic nephrectomy training with a VR simulator improves porcine performance. To carry out this study, 12 urology residents were divided into two groups, a group that performs training and a group without training. The training group received preoperative training on the LapPASS® simulator for laparoscopic nephrectomy. Afterwards both groups performed laparoscopic nephrectomy using a porcine model and the results demonstrated that training with VR improved performance in a real operation, which means that VR-based procedural simulation could become a vital part of the laparoscopic resident training program. Rogers et al. describe the current state regarding the use of VR coupled with machine learning for surgical training, as well as future directions and existing limitations of this technology [10].

The present study aims to develop a virtual reality simulator for a SILS robotic system that uses artificial intelligence in object detection for the automatic positioning of a mobile platform. Through an automatic positioning of the mobile platform using artificial intelligence, a series of benefits are brought such as the reduction of human errors, increased precision and real-time efficiency. Automatic positioning assists the doctor in achieving precise positioning of the robotic module over the SILS port.

The article is structured as follows: after the introduction, the second section outlines the development of the robotic system, succeeded by a description of the steps for using the robotic system where AI is used to detect the SILS port in Sect. 3. Section 4 provides the conclusions.

2 Development of the Robotic System

Several programs were used in developing the control of the robotic system, as illustrated in the block diagram in Fig. 1.

The Siemens NX program was utilized to design the parallel robotic structure, after which the 3D CAD model of this structure was imported into the Unity program. To develop the virtual human patient, the MakeHuman [11] program was used, and its 3D CAD model was imported into the Unity [12] program. To develop the User Interface (UI), the Visual Studio program with the C-Sharp (C#) programming language was chosen. Communication between the UI is facilitated via the TCP/IP protocol. Real-time object detection was achieved using the YOLOv8 [13] program, which employs the Python programming language and the PyTorch [14] package. Communication between the UI and the python environment is established using the Python.NET library.

2.1 *Robotic Structure for Surgery and Virtual Human Model*

The robotic structure (Fig. 2a, 1) has 6 degrees of freedom (DOF) and features a modular construction consisting of three identical kinematic chains (Fig. 2a, 2) positioned along the sides of an equilateral triangle. These chains are connected to a mobile platform by three spherical joints. The mobile platform integrates three independent modules, each containing one instrument, as follows: two 3-DOF mechanisms (Fig. 2a, 3, 4) responsible for positioning, inserting and retracting two active instruments; in the center, there is a 1-DOF mechanism that performs the insertion and retraction of an endoscopic camera (Fig. 2a, 5). To enhance the realism of the simulation, the virtual human patient is characterized by the following attributes (Fig. 2b): a 47-year-old man with a height of 1.85 m and a weight of 100 kg.

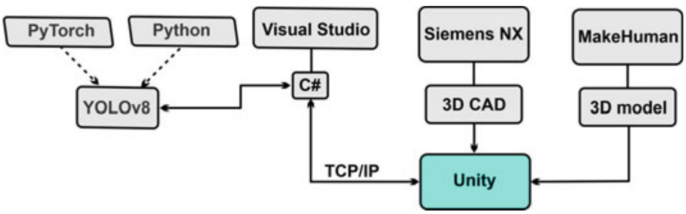

Fig. 1 Block diagram of the software programs used

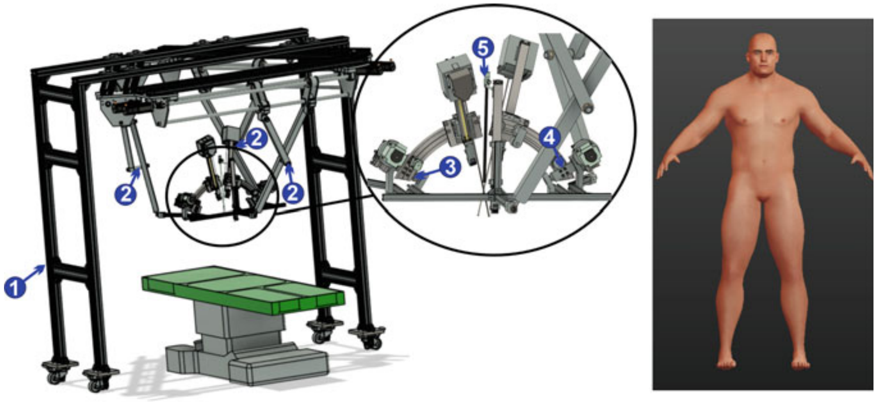

(a) (b)

Fig. 2 **a** Design of the parallel robotic system. **b** Development of the virtual human patient

2.2 Development of the Virtual Reality Application and the User Interface

The virtual reality application was designed using the Unity program, which supports desktop, mobile and console platforms. At the initial stages of the virtual reality application development, the operating room was created using the ProBuilder program. This program is a package that is installed in the Unity program, dedicated to creating prototype structures. Within the operating room, the virtual human patient is positioned on an operating table to facilitate access for the instruments located on the robotic structure to the intervention area. Various pieces of equipment are introduced in the operating room as follows: a surgical light suspended above the operating table for optimal illumination of the work area (Fig. 3, 1); a device for monitoring vital functions (Fig. 3, 2); a monitor for the endoscopic camera (Fig. 3, 3); a suction system (Fig. 3, 4) and sterilization equipment (Fig. 3, 5).

User Interface and Controllers

The user interface (Fig. 4) was developed using the Visual Studio environment with C#. To establish the connection between the User Interface and the virtual reality application, the user needs to press the "Connect" button first. Subsequently, the virtual reality application opens, and upon successful connection the button alters its state to "Disconnect" (1) in Fig. 4 on a red background. To initiate the data communication between the User Interface and the VR application, the user should press the "Start" button. After establishing communication, the button undergoes a state change and the text "Stop" appears on the button (Fig. 4, 1) against a red background. Since the laparoscopic camera is controlled by voice commands, the user must select a voice profile trained for this purpose (2) in Fig. 4. The introduction and retraction of instrument 1 and instrument 2 are facilitated by two controllers

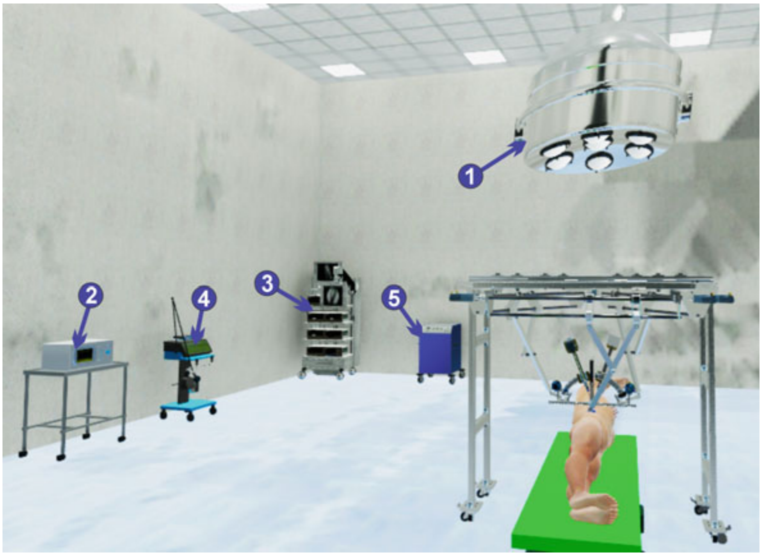

Fig. 3 Operating room

(Fig. 5). To insert instrument 1, the user needs to press button 1 on the right-hand controller (1) in Fig. 5, and to retract instrument 1, the user must press button 2 (2) in Fig. 5. Instrument 2 is inserted by pressing button 3 on the left-hand controller (Fig. 5, 3), and retraction is executed by pressing button 4 (Fig. 5, 4). Depending on the instruments chosen, the status of the pressed buttons is reflected on the user interface (Fig. 5, 3) (Fig. 4, 4) by a change in the background color, transitioning from blue to yellow. The insertion and retraction of the laparoscopic camera is controlled by voice command and the selected state is displayed on the user interface (Fig. 5, 5). To detect the SILS port from an image that was saved from the VR application, the user must press the "Upload" button (Fig. 4, 6). After uploading the image, the user should press the "Detect" button (Fig. 4, 7) to initiate the detection process. Once the SILS port is detected, it is displayed within a bounding box along with the confidence level of the detection (Fig. 4, 8).

2.3 Using the YOLOv8 Program for Real-Time Detection

YOLO (You Only Look Once) was developed by Joseph Redmon and Ali Farhadi at the University of Washington and was launched in 2015. This program quickly gained popularity due to its speed and accuracy [15]. YOLO has evolved into an important system for real-time object detection in various applications such as video monitoring, driverless cars and robotics. Since its inception, several versions of YOLO have been released, each aimed at improving the accuracy and speed of the algorithm.

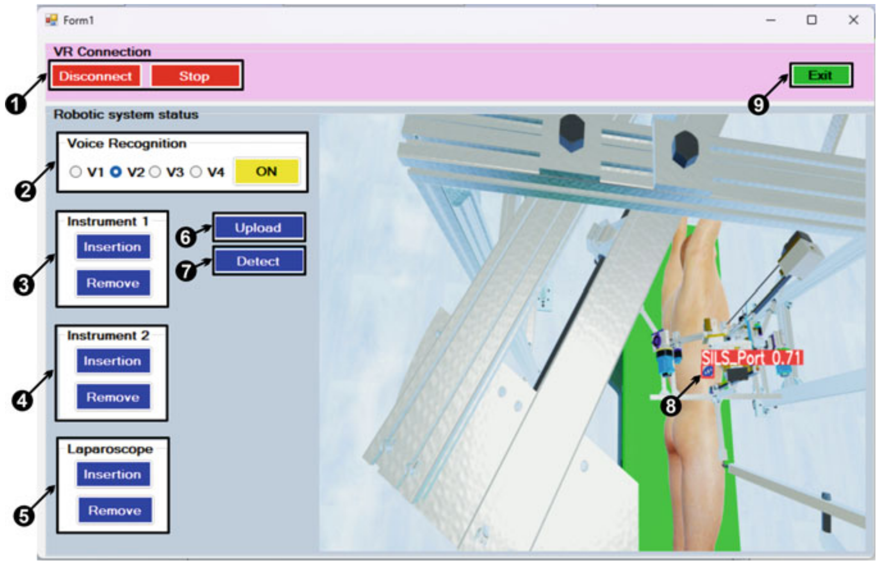

Fig. 4 User interface

Fig. 5 Controllers

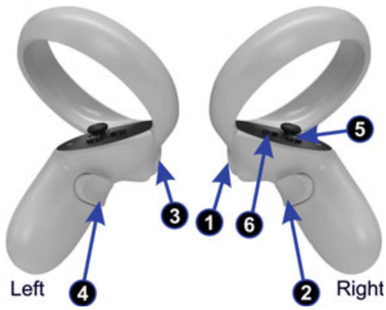

YOLOv8 is the latest version of the YOLO series of real-time object detection of objects in both images and videos. This version is renowned for its superior performance in terms of speed and accuracy. The YOLOv8 version introduces new features and optimizations compared to its predecessors, making it an ideal choice for a wide range of applications [16].

For the correct operation of the YOLOv8 program, several resources are required, which must be presented on the computer running the program neural network training. In the current application, a laptop (Lenovo Legion) with the following specifications was used for neural network training: Intel(R) Core(TM) i7-10875H CPU 2.3 GHz, NVIDIA GeForce RTX 2070 with Max-Q Design, 8 GB Graphics Card. The training was conducted in an Anaconda3 environment with Python 3.9.7,

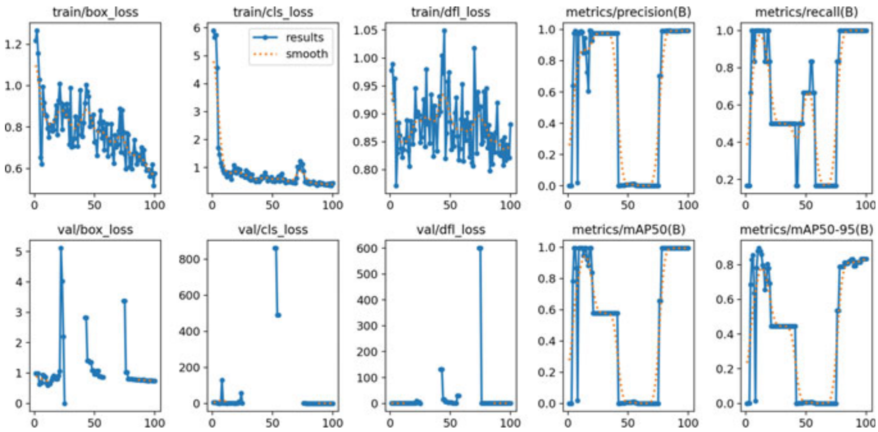

Fig. 6 Detection performance of YOLOv8

Pytorch 2.1.1 library and CUDA 11.8 for enhanced performance. The training session was conducted with a learning rate of 0.05, batch size 8 and 100 epochs.

To assess the training performance of the neural network, several informative graphs were generated, as illustrated in Fig. 6. The graphs highlight the following metrics:

- train/box_loss—is a loss function specifically addressing the loss associated with predictions related to the location of frames (bounding boxes) for objects present in the image;
- train/cls_loss—loss function that specifically deals with the loss associated with object classification;
- metrics/precision(B)—is the rate of correctly identified objects relative to all objects identified by the model;
- metrics/precision(B)—is the rate of correctly identified objects relative to all objects present in the dataset;
- val/box_loss—is the loss function associated with locating objects within the validation dataset;
- metrics/mAP50(B) is the average precision (mAP—Mean Average Precision) for object detection at an overlap threshold of 0.5 (B for IoU—Intersection over Union);
- metrics/mAP50-95(B)—mAP is calculated in the range of overlap thresholds (IoU) between 0.5 and 0.95 (B for IoU—Intersection over Union).

3 Using the Robotic System

The main purpose of the application is to accurately position the mobile platform housing two active instruments and the laparoscopic camera above the SILS port (Fig. 7, 1). Positioning is achieved using AI by detecting the SILS port using machine learning. In order to obtain the coordinates of the SILS port, images are initially saved using the view camera (Fig. 7, 2) in the VR application. Subsequently, these images, along with others containing models of SILS ports, are used to train the neural network using YOLOv8 program.

After training the neural network, an image from the VR application is captured using the viewing camera (Fig. 7, 2). The saved image is then loaded into the UI (Fig. 4, 6), and the "Detect" button (Fig. 4, 7) is pressed to detect the SILS port. To access the virtual environment, the user needs to wear the Oculus Quest 2 VR headset (Fig. 8, 1). To send the coordinates to the robotic system for the automatic positioning of the mobile platform above the SILS port (Fig. 9, 1) the user must press the controller button (Fig. 5, 5) held in the right hand. From this position, the two active instruments and the laparoscopic camera can be easily inserted. Instrument 1 can be inserted Through the SILS port by pressing the button (Fig. 5, 1) on the right-hand controller, instrument 2 is inserted by pressing the button (Fig. 5, 3) on the left-hand controller, and inserting the laparoscopic camera is accomplished through a voice command, using a microphone (Fig. 8, 2) attached to the VR headset.

To train the machine learning program, 30 images were used, with 6 of them allocated for testing. Upon completion of the training process, the program acquired the ability to analyze an image and identify the SILS port. When presented with an image, the program successfully detected the SILS port with a confidence level of 0.71. In some studies using the YOLOv8 program, a confidence level for detecting objects in images ranging from 0.34 to 0.96 was achieved [17]. The performance of

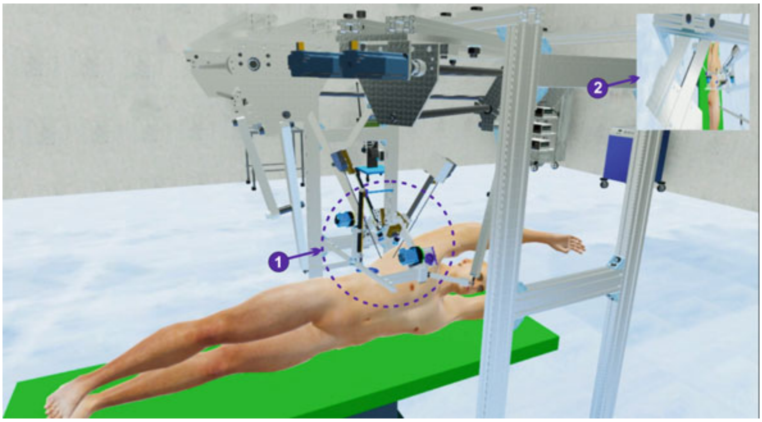

Fig. 7 Surgical robotic system

Fig. 8 VR headset

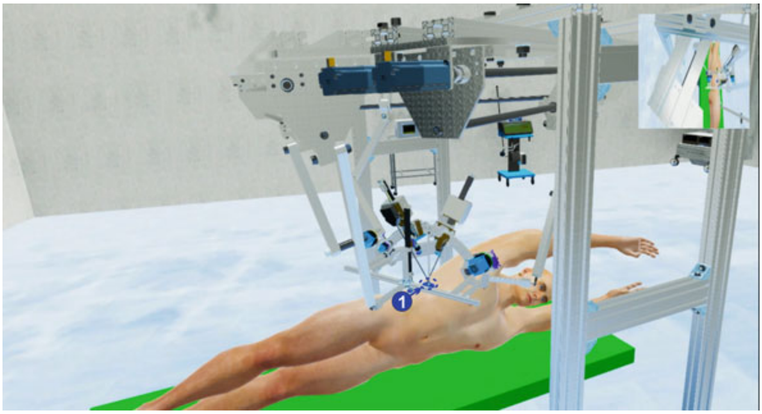

Fig. 9 Mobile platform positioning

the confidence level detection depends on the number of images given to the program for training.

4 Conclusions

This article presents a study in which a virtual reality simulator is developed for a robotic surgical system intended for use in the SILS procedure. User control over the active instruments and the laparoscopic camera is facilitated through two controllers and a microphone using voice commands. Artificial intelligence is employed for the automatic positioning of the mobile platform housing the instruments. The YOLOv8 artificial intelligence program is utilized for the automatic detection of the SILS port. By using this artificial intelligence program, significant benefits are brought, including increased accuracy, real-time efficiency, adaptability to different environments and reduction of human errors, thereby contributing to the overall improvement of the positioning process. Subsequently, the port coordinates are transmitted to the robotic system control program to achieve the automatic positioning of the mobile platform. Once the mobile platform is automatically positioned, the active instruments and the laparoscopic camera can be easily inserted through the SILS port.

Acknowledgements This work was supported by the project New smart and adaptive robotics solutions for personalized minimally invasive surgery in cancer treatment—ATHENA, funded by European Union—NextGenerationEU and Romanian Government, under National Recovery and Resilience Plan for Romania, contract no. 760072/23.05.2023, code CF 116/15.11.2022, through the Romanian Ministry of Research, Innovation and Digitalization, within Component 9, investment I8.

References

1. Nguyen, T.T., Basilius, J., Ali, S.N., Dobbs, R.W., Lee, D.I.: Single-port robotic applications in urology. J. Endourol. **37**(6), 688–699 (2023)
2. Pisla, D., Plitea, N., Gherman, B., Pisla, A., Vaida, C.: Kinematical analysis and design of a new surgical parallel robot. In: Proceedings of the 5th international workshop on computational kinematics, Duisburg, Germany, pp. 273–282 (2009)
3. Vaida, C., Pisla, D., Plitea, N., Gherman, B., Gyurka, B., Stancel, E., Hesselbach, J., Raatz, A., Vlad, L., Graur, F.: Development of a control system for a parallel robot used in minimally invasive surgery. IFMBE Proc. **26**, 171–176 (2009)
4. Pisla, D., Birlescu, I., Vaida, C., Tucan, P., Pisla, A., Gherman, B., Crisan, N., Plitea, N.: Algebraic modeling of kinematics and singularities for a prostate biopsy parallel robot. Proc. Rom. Acad. Ser. A **19**, 489–497 (2019)
5. Furukawa, K., Asaoka, T., Mikamori, M., et al.: Single-incision laparoscopic cholecystectomy: a single-centre experience of 1469 cases. J. Gastrointest. Surg. **26**, 831–836 (2022)
6. Moglia, A., Morelli, L., et al.: Ensemble deep learning for the prediction of proficiency at a virtual simulator for robot-assisted surgery. Surg. Endosc. **36**, 6473–6479 (2022)
7. Covaciu, F., N. Crisan, Vaida, C., Andras, I., Pusca, A., Gherman, B., Radu, C., Tucan, P., Al Hajjar, N., Pisla, D.: Integration of virtual reality in the control system of an innovative medical robot for single-incision laparoscopic surgery. Sensors **23**(12) (2023)
8. Elessawy, M., Mabrouk, M., et al.: Evaluation of laparoscopy virtual reality training on the improvement of trainees' surgical skills. Medicina **57**(2), 130 (2021)
9. Ohtake, S., Makiyama, K., Yamashita, D., Tatenuma, T., Yao, M.: Training on a virtual reality laparoscopic simulator improves performance of live laparoscopic surgery. Asian J. Endoscop. Surg. **15**(2), 313–319 (2022)
10. Rogers, M.P., DeSantis, A.J., Janjua, H., Barry, T.M., Kuo, P.C.: The future surgical training paradigm: virtual reality and machine learning in surgical education. Surgery **169**(5), 1250–1252 (2021)
11. https://static.makehumancommunity.org/makehuman/docs.html
12. https://docs.unity3d.com/Manual/index.html
13. https://docs.ultralytics.com/
14. https://pytorch.org/docs/stable/index.html
15. Redmon, J., Divvala, S., et al.: You only look once: unified, real-time object detection. Comput. Vis. Patt. Recogn. (CVPR) 779–788 (2016)
16. Hussain, M.: YOLO-v1 to YOLO-v8, the rise of YOLO and its complementary nature toward digital manufacturing and industrial defect detection. Machines **11**(7), 677 (2023)
17. Soylu, E., Soylu, T.: A performance comparison of YOLOv8 models for traffic sign detection in the Robotaxi-full scale autonomous vehicle competition. Multimedia Tools Appl. 1–31 (2023)

Effects of Increased Entropy on Robustness of Reinforcement Learning for Robot Box-Pushing

Zvezdan Lončarević and Andrej Gams

Abstract Deterministic reinforcement learning (RL) methods, which produce a single solution for a given system state, have shown impressive results in simulated environments with well-defined parameters. However, their performance often declines when applied to real-world systems, where parameters fluctuate. In contrast, probabilistic RL approaches, capable of generating a spectrum of potential solutions, demonstrate enhanced robustness to variations in parameters. Our study evaluates the performance of probabilistic RL in a robotic task of manipulating a box on a table. We investigate the robustness of policies trained with varying degrees of entropy by training them with one set of box mass and friction parameters and then testing their performance in a simulated environment with altered parameters. Our findings reveal that policies with lower entropy perform best in stable conditions, while those with higher entropy become more effective as parameter variability increases. Given that applying learned policies to real robots requires further transfer learning (TL), where the efficiency heavily depends on the quality of the initial policy, selecting the optimal entropy level for initial training could significantly enhance the TL process.

Keywords Reinforcement learning · Movement primitives · Probabilistic policy · Object manipulation

1 Introduction

Numerous review papers [1, 2, 9, 14] have shown the possibility of RL algorithms to obtain knowledge completely autonomously and from scratch. However, all the presented algorithms require huge amounts of data and therefore many learning

Z. Lončarević (✉) · A. Gams
Department of Automatics, Biocybernetics, and Robotics, Jožef Stefan Institute, Ljubljana, Slovenia
e-mail: zvezdan.loncarevic@ijs.si
URL: https://abr.ijs.si/

A. Gams
e-mail: andrej.gams@ijs.si

D. Pisla et al. (eds.), *Advances in Service and Industrial Robotics*, Mechanisms and Machine Science 157, https://doi.org/10.1007/978-3-031-59257-7_10

iterations in order to converge, so they can be applied only in simulation. The main problem is that the knowledge obtained in simulation cannot be directly applied in a real-world scenario, because the real-world has different sorts of non-linearities and irregularities and therefore cannot be perfectly modelled [8]. One of the possible solutions is to use transfer learning (TL) methods based on domain adaptation in order to adapt this knowledge. Transfer of the knowledge is heavily influenced by the initial policy obtained in simulation. Although deterministic methods work best in the source environment, where the agent is trained, the study presented in [3], has shown that the probabilistic methods with bigger diversity of solutions are more robust to the parameter changes of the environment. Therefore, we analyze the influence of the diversity of solutions to the robustness of the algorithm when the parameters are perturbed. We perform our experiments on the example of the robot pushing a box on the table. The task of box-pushing was introduced and described in [12] where trajectories were parametrized with ProMPs [13] and different learning algorithms and reward settings were considered. On the other hand, we use ProDMPs [4] that take into consideration current velocity of the robot's joints, thus allowing for the smooth transition between different trajectory segments. We also focus on the influence of the entropy on the robustness of the policy. Similar analysis was done for the case of the imitation learning, where the relation between the diversity of the solutions and quality of the trained policy has been already studied [6]. In that case, the dataset was acquired by a human demonstrator and the task was simplified so that some of the movement directions were fixed. For the ones that were not fixed, Cartesian coordinates were used.

The paper is structured as follows. In Sect. 2 we give a brief overview of the trajectory parametrization and the used algorithm. Section 3 presents the experimental setup. It is followed by the results in Sect. 4 and the conclusion in Sect. 5.

2 Trajectory and Learning

In order to perform the efficient RL and avoid curse of dimensionality of action parameters, it is common that we use parametric representation of the trajectories. One of the most commonly used in the probabilistic approaches are ProMPs [13]. However, the main drawback of this approach is that they cannot take initial velocity of the trajectory into account and therefore, if we apply replanning in our algorithm, they produce discontinuities in the resulting trajectory. In this section, we first give a brief recap of the ProDMPs that are able to take into account trajectory velocity and capturing the diversity of the solutions directly in their parametric representation. We proceed with presenting the algorithm that was used for learning the policy. The algorithm is based on Policy Gradient method, but the loss function is extended so that it takes into account entropy of the policy while also controlling the update step as described in [10].

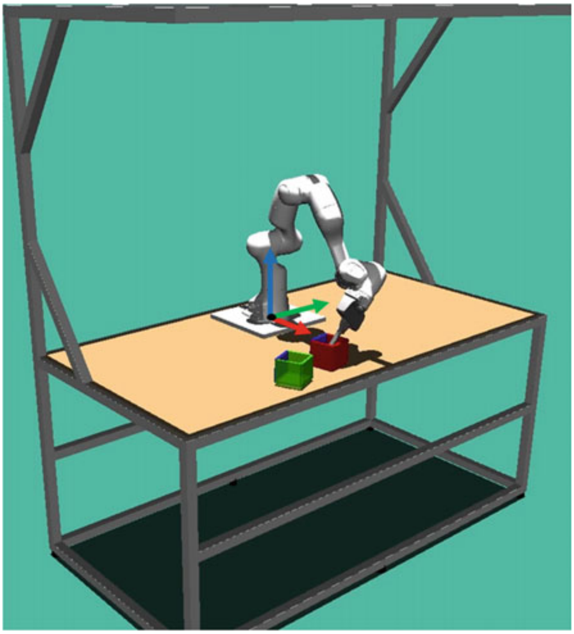

Fig. 1 Experimental setup with Franka Panda Robot moving the box in MuJoCo simulation

2.1 Probabilistic Dynamic Movement Primitives (ProDMPs)

The ProDMPs framework combines elements of Dynamic Movement Primitives (DMPs) and Probabilistic Movement Primitives (ProMPs), incorporating probabilistic modeling into the dynamic movement generation. The key idea is to represent the trajectory distribution in a way that captures both the dynamical properties of DMPs and the probabilistic nature of ProMPs. The positions y and velocities $\dot{y}$ of a trajectory for one Degree of Freedom (DoF) are formulated as:

$$\begin{aligned} y(t) &= c_1 y_1(t) + c_2 y_2(t) + \boldsymbol{\Phi}(t)^\top \boldsymbol{\omega}, \\ \dot{y}(t) &= c_1 \dot{y}_1(t) + c_2 \dot{y}_2(t) + \dot{\boldsymbol{\Phi}}(t)^\top \boldsymbol{\omega} \end{aligned} \tag{1}$$

where y_1 and y_2 are two linearly independent complementary functions of the ProDMP's homogeneous Ordinary Differential Equation (ODE). $\dot{y}_1$ and $\dot{y}_2$ are their respective time derivatives. The coefficients c_1 and c_2 are constants derived from the boundary conditions of the ODE. These coefficients are calculated based on the desired position and velocity at a specific time step, allowing for smooth transitions between action sequences, which is not typically possible with ProMPs alone. The basis functions for position and velocity, $\boldsymbol{\Phi}$ and $\dot{\boldsymbol{\Phi}}$, are computed once and then used as fixed functions. The weights $\boldsymbol{\omega}$ are a composite vector that merges the DMP's original weight vector with the goal attractor towards which the ODE converges. Similar to ProMPs, assuming the weights $\boldsymbol{\omega}$ follow a multivariate normal distribution $\boldsymbol{\omega} \sim \mathcal{N}(\boldsymbol{\omega}|\mu_{\boldsymbol{\omega}}, \Sigma_{\boldsymbol{\omega}})$, we can compute the trajectory distribution for one DoF over all timesteps $0:T$ as

$$p(\boldsymbol{\Lambda}; \boldsymbol{\mu}_{\boldsymbol{\omega}}, \boldsymbol{\Sigma}_{\boldsymbol{\omega}}, y_b, \dot{y}_b) = \mathcal{N}(\boldsymbol{\Lambda}|\boldsymbol{\mu}_{\boldsymbol{\Lambda}}, \boldsymbol{\Sigma}_{\boldsymbol{\Lambda}}), \tag{2}$$

where

$$\begin{aligned} \boldsymbol{\mu}_{\boldsymbol{\Lambda}} &= \boldsymbol{\xi}_1 y_b + \boldsymbol{\xi}_2 \dot{y}_b + \boldsymbol{H}_{0:T} \boldsymbol{\mu}_{\boldsymbol{\omega}}, \\ \boldsymbol{\Sigma}_{\boldsymbol{\Lambda}} &= \boldsymbol{H}_{0:T}^{\top} \boldsymbol{\Sigma}_{\boldsymbol{\omega}} \boldsymbol{H}_{0:T} + \sigma_n^2 \boldsymbol{I}, \\ \text{with } \boldsymbol{H}_{0:T} &= \boldsymbol{\xi}_3 \boldsymbol{\Phi}_b + \boldsymbol{\xi}_4 \dot{\boldsymbol{\Phi}}_b + \boldsymbol{\Phi}_{0:T}. \end{aligned}$$

In these equations, $\boldsymbol{\Lambda}$ represents the trajectory, $\boldsymbol{\mu}_{\boldsymbol{\Lambda}}$ and $\boldsymbol{\Sigma}_{\boldsymbol{\Lambda}}$ are its mean and covariance, $\boldsymbol{y}_b$ and $\dot{\boldsymbol{y}}_b$ are the boundary conditions (starting position and velocity of the robot usually), $\boldsymbol{\Phi}_b$ and $\dot{\boldsymbol{\Phi}}_b$ are basis functions, $\boldsymbol{\xi}_k$ are calculated using y_1 and y_2 at each time step and the boundary conditions, and $\sigma_n^2 \boldsymbol{I}$ represents the noise covariance. Details about the derivation are given in [4].

2.2 Policy Gradient

In Reinforcement Learning (RL) using Probabilistic Dynamic Movement Primitives (ProDMPs), the policy actions are represented by the parameters $\boldsymbol{\omega}$, which define the trajectories. The policy maps contexts, labeled as $\boldsymbol{c}$, to a specific set of parameters $\boldsymbol{\omega}$. In this setting, the reward structure can vary, and one approach is to use a dense reward structure, where a reward is provided at each time-step t. The advantage function is used in the policy update process.

1. **Surrogate Loss with Normalized Advantage**: In certain reinforcement learning approaches, the surrogate loss function may utilize normalized advantage. This normalization helps in reducing variance and improving the stability and efficiency of the learning process. The normalized advantage for each experience is calculated as:

$$A_{\text{norm}}(\boldsymbol{c}, \boldsymbol{\omega}) = \frac{A(\boldsymbol{c}, \boldsymbol{\omega}) - \mu_A}{\sigma_A + \epsilon_{\text{A}}} \tag{3}$$

where $A(\boldsymbol{c}, \boldsymbol{\omega})$ is the advantage function, μ_A is the mean, σ_A is the standard deviation of the advantage across the batch and ϵ_{A} is the small constant preventing the normalized advantage being infinity in the case when standard deviation drops to zero. The advantage function $A(\boldsymbol{c}, \boldsymbol{\omega})$ is calculated using the return and the value function $V(\boldsymbol{c})$, approximated by the critic:

$$A(\boldsymbol{c}, \boldsymbol{\omega}) = V_{\boldsymbol{\Phi}}(\boldsymbol{c}) - G_t \tag{4}$$

where G_t is the return from context $\boldsymbol{c}$, and $V(\boldsymbol{c}_t)$ is the estimated value given the context $\boldsymbol{c}_t$ as:

$$V_{\boldsymbol{\Phi}}(\boldsymbol{c}) = \mathbb{E}[G_t|\boldsymbol{c};\pi] \tag{5}$$

The advantage function provides a measure of how much better taking a particular action is compared to the average policy performance. The return, denoted as G_t, from a context $\boldsymbol{c}$ at time t, is given by:

$$G_t = \sum_{k=0}^{K} \gamma^k R_{t+k+1} \tag{6}$$

where R_{t+k+1} is the reward received at time $t+k+1$, and γ is the discount factor.Value function is obtained by training the critic network with minimizing loss:

$$L^{\text{Critic}} = \arg\min_{\boldsymbol{\Phi}} \mathbb{E}_{\pi_{\boldsymbol{\theta}_{\text{old}}}(\boldsymbol{c},\boldsymbol{\omega})}[G_t(\boldsymbol{\omega}|\boldsymbol{c}) - V_{\boldsymbol{\Phi}}(\boldsymbol{c})] \tag{7}$$

The surrogate loss is then defined as:

$$L^{\text{Surrogate}}(\boldsymbol{\theta}) = \mathbb{E}_{\pi_{\boldsymbol{\theta}_{\text{old}}}(\boldsymbol{\omega}|\boldsymbol{c})}\left[r(\boldsymbol{\theta})A_{\text{norm}}(\boldsymbol{c},\boldsymbol{\omega})\right] \tag{8}$$

where $r(\boldsymbol{\theta}) = \frac{\pi_{\boldsymbol{\theta}}(\boldsymbol{\omega}|\boldsymbol{c})}{\pi_{\boldsymbol{\theta}_{\text{old}}}(\boldsymbol{\omega}|\boldsymbol{c})}$ is the probability ratio.

2. **Entropy Loss**: The entropy loss for ProDMPs is defined over the distribution of parameter sets ω given a context:

$$L^{\text{Entropy}}(\boldsymbol{\theta}) = \mathbb{E}_{\pi_{\boldsymbol{\theta}_{\text{old}}}}[H(\pi_{\boldsymbol{\theta}_{\text{target}}}(\cdot|\boldsymbol{c}))] \tag{9}$$

where $H(\pi_{\boldsymbol{\theta}_{\text{target}}}(\cdot|\boldsymbol{c}))$ is the entropy of the parameter distribution for a given context $\boldsymbol{c}$.

3. **Trust Region Loss**: The trust region loss measures the divergence between the old policy and the target policy in the space of parameter sets θ for a given context:

$$L^{\text{TR}}(\boldsymbol{\theta}) = D_{KL}(\pi_{\boldsymbol{\theta}_{\text{old}}}(\cdot|\boldsymbol{c})||\pi_{\boldsymbol{\theta}_{\text{target}}}(\cdot|\boldsymbol{c})) \tag{10}$$

For the target policy $\pi_{\boldsymbol{\theta}_{\text{target}}}$, constraints are provided for both the mean and the covariance of the trajectory distributions. The trust region distance is calculated as the sum of the distances for both mean and covariance, ensuring that the new policy respects the trust region in terms of both central tendency and variability. Mathematical background and detailed explanation is given in [10].

The target policy $\pi_{\boldsymbol{\theta}_{\text{target}}}$ is obtained by solving an optimization problem that seeks to maximize performance while maintaining constraints manually given to the algorithm on both the mean ϵ_μ and covariance ϵ_Σ in the Kullback-Leibler (KL) divergence between $\pi_{\boldsymbol{\theta}_{\text{target}}}(\cdot|\boldsymbol{c})$ and $\pi_{\boldsymbol{\theta}_{\text{old}}}(\cdot|\boldsymbol{c})$.

The overall maximization problem in RL with ProDMPs is to find the parameter set θ that maximizes the following composite loss function:

$$\max_{\boldsymbol{\theta}} L(\boldsymbol{\theta}) = \max_{\boldsymbol{\theta}} \left[L^{\text{Surrogate}}(\boldsymbol{\theta}) - \beta L^{\text{Entropy}}(\boldsymbol{\theta}) + \lambda L^{\text{TR}}(\boldsymbol{\theta}) \right] \tag{11}$$

where β and λ are coefficients that balance the importance of the entropy and trust region loss terms, respectively. This formulation captures the direct mapping of contexts to parameter sets $\boldsymbol{\omega}$ that define the trajectories in the context of ProDMPs.

3 Experimental Evaluation

We evaluate our approach on the task where the simulated robot is moving a box on the table by using only a rod as an end-effector in MuJoCo simulation as shown in Fig. 1 that is part of FancyGym framework [11]. The task was to move the box in xy-plane, being set on the surface of the table, from the initial position being set at $\{x_s, y_s, \varphi_s\} = \{0.4 \text{ m } 0.3 \text{ m}, 0 \text{ rad}\}$ m to a randomly generated position $\{x_g, y_g, \varphi_g\}$ where $x_g \in [0.3, 0.6]$ m, $y_g \in [-0.45, 0.45]$ m and $\varphi_g \in [0, 2\pi]$. We use a model of 7-DoF Franka Panda robot that is redundant for executing this task and therefore provides an infinite number of possible solutions. Since the learning is done in joint space of the robot, this makes the learning problem even harder. We encoded trajectories using ProDMPs with $N = 5$ as the number of weights for each of the robot joints. The time for the trajectory was fixed to 2 s. We allowed our algorithm to make 4 replanning steps, and therefore, for each predicted part of the trajectory, τ was set to be 0.5 s. Distribution of ProDMP parameters was the output of the policy neural network that takes as the input context describing box position and orientation, as well as desired goal position and orientation. It was trained by maximizing the loss function given with Eq. 11, and it had two hidden layers with sizes of 128 neurons. The critic neural network for approximating value function had 2 hidden layers of 32 neurons and was trained by minimizing the loss function given with Eq. 7. Both of the networks used leaky-relu activation function. Coefficient λ in Eq. 11 was set to 0.5 and β was varied through the experiments. Regularization coefficient in Eq. 3 was set to $\epsilon_{\text{A}} = 10^{-8}$, discount factor in Eq. 6 to $\gamma = 0.99$ and coefficients for projecting the policy to the target policy (Eq. 10) were set to $\epsilon_\mu = 5 \cdot 10^{-2}$ and $\epsilon_\Sigma = 5 \cdot 10^{-4}$. Reward was given at a frequency of 50 Hz at time-steps t based on the difference between real and desired box position and orientation as well as the torques required to move robot joints. It was implemented in [11] and detailed description of the dense reward for this experimental setup is given in [12].

The original setup where the agent was trained consisted of the box with the mass of 2 kg and friction coefficient between the box and the table set at 0.3. We trained 6 different models with different entropy coefficients $e = [0, 0.01, 0.02, 0.03, 0.04, 0.05]$ respectively. In order to test behaviour of the learned agents, we varied the friction and mass separately and evaluated all 6 models. In experiments, we set the box mass to $m = [1, 1.5, 2, 2.5, 3]$ kg and friction coefficient to $\mu = [0.15,$

0.20, 0.25, 0.30, 0.35, 0.40, 0.45]. For each changed parameter, we evaluated errors in both position and orientation of the box at the end of the movement. For the completeness of the results, we repeated this for 100 different randomly generated final positions and orientations.

4 Results

In our experiments, all policies were trained with five different initial seeds. The reported results represent the outcomes of the best-performing policies, determined by the highest success rate when assessed in the original setup.

Figure 2 summarizes the position, orientation error results and the success rate of all policies. In our specific use-case, movement generated by the policy was

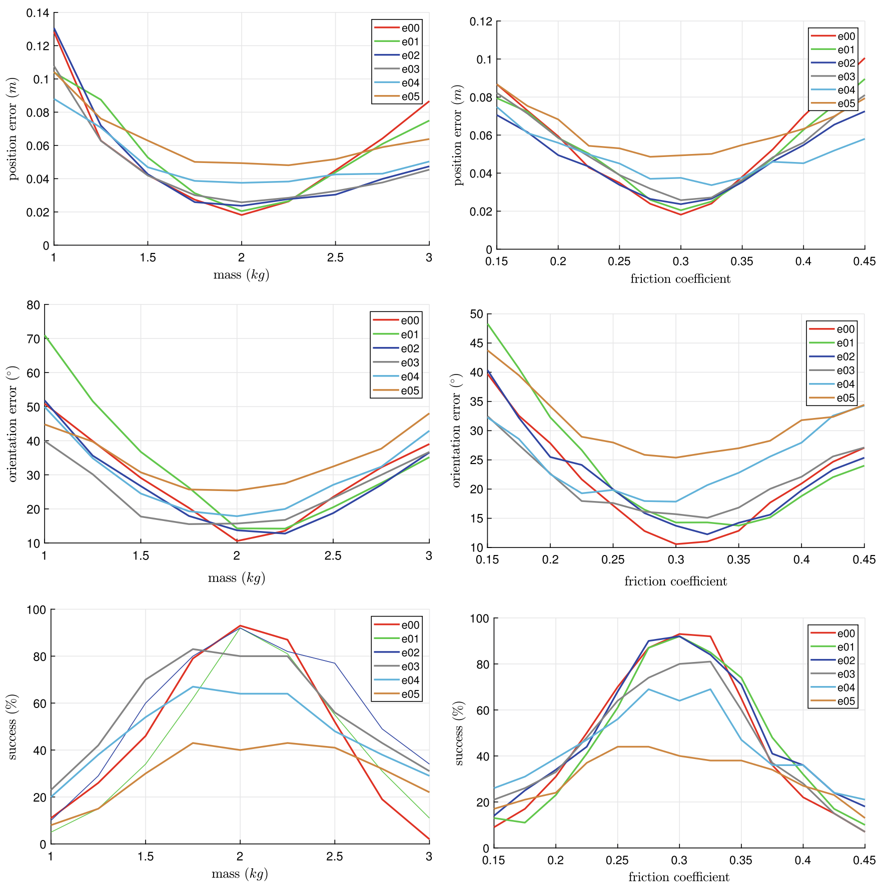

Fig. 2 Average position and orientation error of the trained agents when the box mass is varied

considered successful when the position error was below 0.05 m and the orientation error was less than 0.5 rad. We evaluated policy robustness based on varied mass of the box (Fig. 2-left) and friction coefficient between the table and the box (Fig. 2-right). From the figure, it can be noted that as the difference in mass or friction coefficients between the training and evaluation scenarios increased, policies with higher entropy demonstrated better performance.

5 Conclusion

Since the real-world application of any autonomous learning policies requires many iterations, the focus of our research is to reduce the number of the iterations to be executed on the real robot because this process is dangerous for the equipment and at the same time time-consuming. Using pretrained agents from the simulation accelerates this process, but with choosing the right policy, we believe it can be accelerated even further. In this paper, we have showed that each level of discrepancy between parameters in the training and execution has a policy of a certain entropy that works best for it. Testing different policy entropies on the real system in only few iterations could give us insights into which policy performs the best for the specific environment changes. With choosing that policy, we could accelerate the TL process, since the amount of the data needed to be acquired in the target environment would consequently drop.

The ability of probabilistic methods to provide the whole spectre of different solutions enables them to find the right solution quicker and therefore converge faster in the adaptation phase to the new domain. This is due to their exploration phase not being based on random sampling only, but also included in the probabilistic nature of the predicted trajectories. Moreover, since they are also trained on the same task in the different environment, they are not that much dependent on setting up the exploration noise, and therefore it is less probable that some parameters will produce a trajectory that is not executable.

In our future work, we plan to explore the possibility of implementing the policy learning method outlined in this paper and determining the most suitable entropy, identified by the highest success rate, for real-world applications. Once the optimal entropy is identified, our plan is to generate a simulation database and store the policy into a neural network, following a similar approach as presented in [6]. Using this neural network, we plan to apply TL, as demonstrated in our previous works [5, 7], thus closing the loop of learning from scratch.

Acknowledgements This research was funded by ARIS research grant Robot Textile and Fabric Inspection and Manipulation - RTFM (J2-4457), ARIS program group Automation, Robotics, and Biocybernetics (P2-0076) and DAAD Grant 57588366.

References

1. Arulkumaran, K., Deisenroth, M.P., Brundage, M., Bharath, A.A.: Deep reinforcement learning: a brief survey. IEEE Sig. Proc. Magaz. **34**(6), 26–38 (2017)
2. Elguea-Aguinaco, Íñ., Serrano-Muñoz, A., Chrysostomou, D., Inziarte-Hidalgo, I., Bøgh, S., Arana-Arexolaleiba, N.: A review on reinforcement learning for contact-rich robotic manipulation tasks. Robot. Comput.-Int. Manuf. (RCIM) **81**, 102517 (2023)
3. Eysenbach, B., Levine, S.: Maximum entropy RL (provably) solves some robust RL problems (2021). https://doi.org/10.48550/ARXIV.2103.06257
4. Li, G., Jin, Z., Volpp, M., Otto, F., Lioutikov, R., Neumann, G.: ProDMPs: a unified perspective on dynamic and probabilistic movement primitives (2022). https://doi.org/10.48550/ARXIV.2210.01531
5. Lončarević, Z., Simonič, M., Ude, A., Gams, A.: Combining reinforcement learning and lazy learning for faster few-shot transfer learning. In: IEEE-RAS 21st International Conference on Humanoid Robots (Humanoids), pp. 285–290 (2022)
6. Lončarević, Z., Li, G., Neumann, G., Gams, A.: An encoder-decoder architecture for smooth motion generation. In: Petrič, T., Ude, A., Žlajpah, L. (eds.) Advances in Service and Industrial Robotics, pp. 358–366. Springer Nature Switzerland, Cham (2023)
7. Lončarević, Z., Ude, A., Gams, A.: Accelerated robot skill acquisition by reinforcement learning-aided sim-to-real domain adaptation. In: 20th International Conference on Advanced Robotics (ICAR), pp. 269–274 (2021)
8. Muratore, F., Ramos, F., Turk, G., Yu, W., Gienger, M., Peters, J.: Robot learning from randomized simulations: a review. Front. Robot. AI **9** (2022). https://doi.org/10.3389/frobt.2022.799893
9. Nguyen, T.T., Nguyen, N.D., Nahavandi, S.: Deep reinforcement learning for multiagent systems: a review of challenges, solutions, and applications. IEEE Trans. Cybernet. **50**(9), 3826–3839 (2020)
10. Otto, F., Becker, P., Vien, N.A., Ziesche, H.C., Neumann, G.: Differentiable trust region layers for deep reinforcement learning (2021)
11. Otto, F., Celik, O., Roth, D., Zhou, H.: Fancy gym. https://github.com/ALRhub/fancy_gym
12. Otto, F., Celik, O., Zhou, H., Ziesche, H., Ngo, V.A., Neumann, G.: Deep black-box reinforcement learning with movement primitives. In: 6th Annual Conference on Robot Learning (2022)
13. Paraschos, A., Daniel, C., Peters, J., Neumann, G.: Probabilistic movement primitives. Neural Inf. Proc. Syst. 2616–2624 (2013)
14. Suomalainen, M., Karayiannidis, Y., Kyrki, V.: A survey of robot manipulation in contact. Robot. Autonomous Syst. (RAS) **156**, 104224 (2022)

Part II
Medical Robotics and Biomechanics

Dynamic Analysis of an Exoskeleton Robotic System for Stair Walking Assistance

Ionut Geonea and Daniela Tarnita

Abstract This paper presents aspects of motion simulation and dynamic analysis of an exoskeleton for assisting the gait of people with disabilities when using access stairs. The design of the exoskeleton is carried out in the computer design environment SolidWorks. The dynamic simulation is carried out in conditions as close to reality as possible, taking into account the friction in the kinematic couplings of the robot exoskeleton. The results of the dynamic simulation in the case of stair walking validate the engineering feasibility of the proposed solution and the next stage of development is the construction of a physical prototype of the exoskeleton. For this purpose, we have used additive manufacturing technology. The physically realized robot is tested for the situation of its use by a human subject when walking on stairs.

Keywords Robot · Exoskeleton · Dynamic analysis · Stair climbing · Rapid prototyping

1 Introduction

The motivation of robotic rehabilitation is the recovery of locomotor functions of a human subject, for this reason the study of human gait biomechanics is the starting point of research in rehabilitation robotics. Exoskeleton robotic systems are used for rehabilitation in two ways: treadmill-based exoskeleton for the lower limb rehabilitation; overground lower limb rehabilitation exoskeletons. A review of robotic rehabilitation systems is presented in [1]. According to this study, the control strategies of exoskeleton robotic systems are: position control, force controller, EMG based control, assist-as-needed control. In [2], a novel synthesis method for the multicriteria optimization of a lower limb exoskeleton is proposed. A six-bar Stephenson III type lower-limb mechanism is proposed for geometrical synthesis and multi-criteria optimization.

I. Geonea (✉) · D. Tarnita
Faculty of Mechanics, Department of Applied Mechanics and Civil Construction, University of Craiova, 215512 Craiova, Romania
e-mail: ionut.geonea@edu.ucv.ro

D. Pisla et al. (eds.), *Advances in Service and Industrial Robotics*, Mechanisms and Machine Science 157, https://doi.org/10.1007/978-3-031-59257-7_12

Closed kinematic chains designed to reproduce the legs of an exoskeleton robotic system are made by several researchers, as presented in papers [3–7]. Stephenson type I, II and III mechanisms are designed for use in a quadruped robot. In paper [8] a synthetic procedure is presented to guide a point along a specified trajectory. The analyzed synthesis example is proposed to produce a desired robot leg trajectory.

Another eight-bar mechanism is proposed for the foot of a walking robot in the paper [9]. The characteristic of these mechanisms is that they achieve an adequate walking trajectory, which has a linear portion corresponding to the drag phase.

Of particular interest in the category of active rehabilitation systems are exoskeleton systems. Parameterized gait planning methods [10] or multibody dynamic analysis methods [11] are described for these systems. The impact of robotic rehabilitation on the motor system in neurological diseases is studied in [12, 13].

The paper is structured in four parts. After, the "Introduction" part, an original constructive solution of an exoskeleton leg is presented in Sect. 2. Next, in Sect. 3, a dynamic analysis is performed when using the exoskeleton in two situations, namely stair and floor assistance. In the last Section, the physical prototype of the exoskeleton is manufactured by 3D printing and its motion analysis is carried out with the help of ultrafast camera-based equipment.

2 The Proposed Structural and Design Solution

The developed exoskeleton robot solution has the kinematic scheme shown in Fig. 1a. The solution has in its structure three kinematic chains of the articulated quadrilateral type, namely the kinematic chain ABDE, CDFH and FIJG. The motion is performed by a single motor, placed in the kinematic coupling A, of kinematic element 1. The kinematic elements modelling the structure of the human foot are numbered 4 and 7 (through the segment GM), whose construction is carried out in a modular manner (see Fig. 1b), which allows the length of the elements to be adjusted. An important role in the functionality of the proposed solution is played by the drive kinematic chain, consisting of kinematic elements 1, 2 and 4. In the present design, the actuation is done through the parallelogram mechanism formed with links 1, 2 and 4. It can be seen from Fig. 1a, that the structure consists of 7 bar-type kinematic elements, connected by rotating couplings, according to the scheme shown.

As a standard, the structure of the plane mechanism that shapes the human foot is based on kinematic chains of the articulated quadrilateral or parallelogram type. The actuation of this kinematic chain is very important because it imprints the right movement in the joints of the foot. The simplest method of actuation is with a kinematic element in rotational motion, but which does not assume human-like movements. Thus, in order to have anthropomorphic movements of the foot, kinematic chains such as Hoecken linkage, Peaucellier–Lipkin linkage or Chebyshev Lambda Linkage are used for actuation. In another design variant, this proposed kinematic chain for the human leg, is actuated by a Chebyshev Lambda linkage. In kinematics, the Chebyshev Lambda Linkage is a four-bar linkage that converts rotational motion to approximate

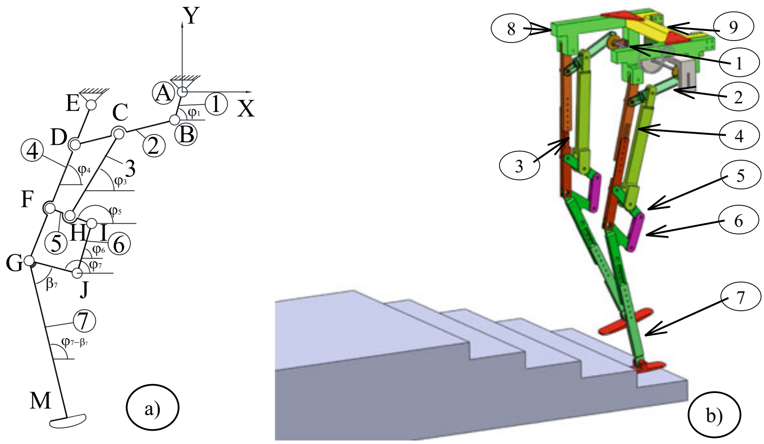

Fig. 1 Proposed kinematic scheme for the exoskeleton leg **a** and its virtual model **b**

straight-line motion with approximate constant velocity. It is so-named because it looks like a lowercase Greek letter lambda (λ). The linkage was first shown in Paris on the Exposition Universally (1878) as “The Plantigrade Machine”. The Chebyshev Lambda Linkage is a cognate linkage of the Chebyshev linkage, and usually, it is used in vehicle suspension mechanisms, walking robots and rover wheel mechanisms.

The design of the exoskeleton robot is shown in Fig. 1b. The component parts of the leg mechanism are designed as fork-shaped, which are subsequently joined using 10 mm diameter pins. An upper frame is designed, comprising two lateral elements (8), assembled at the rear with the yellow element (9).

The drive motor is mounted at the rear of the upper frame on a specially designed component, which is mounted by screwing it to the rear ends of the side components. Also mounted on this frame are two brackets, on which a shaft is mounted. This shaft is driven from the electric motor by means of a gear transmission with a transmission ratio of 1:2. This developed 3D model will be used in the first phase to perform a dynamic simulation of the robotic system’s gait with the help of a dynamic analysis software for multibody systems. The dynamic simulation will involve climbing stairs, walking on a flat portion as well as descending stairs. Accordingly, the virtual model was supplemented with a staircase model as shown in Fig. 2.

3 Dynamic Simulation of Exoskeleton Robotic System

The purpose of the dynamic simulation is to verify the technical feasibility of the design solution by checking the movements performed by the robot. In the first phase the dynamic simulation is performed with the robot with the upper frame fixed to the base. In this case the trajectory of the ankle joint M, must have the shape of a

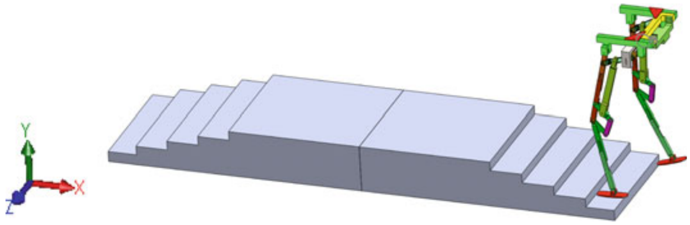

Fig. 2 Designed 3D model, positioned for climbing stairs and walking on a horizontal plane

"flattened D". In order to obtain this shape, an optimization of the solution is carried out, which consists of changing the length of the elements in the drive chain and the position of the rotating couplings at the base. The optimization is performed in ADAMS, very often used for simulation and dynamic analysis of multi-body systems [6, 14, 15], specifying, as design variables, the coordinates of the points defining the locations of the kinematic couplings, and as objective function, the maximization of the rotation angles in the E and G couplings. The constraint defined was the limit value of these angles, established from experimental analysis of human gait, namely 35° for the hip joint and 55° for the knee joint. The optimized model is simulated under the assumption of stair climbing, horizontal walking and stair descent. Figure 3 shows the successive positions of the robot on this path, as well as the trajectories performed by the robot's legs during the simulation in ADAMS.

An important advantage of dynamic simulation is to obtain the connection forces from kinematic couplings. These results are useful for verifying the structural integrity of the kinematic elements of the exoskeleton, transmission and drive train. Thus, in Figs. 4 and 5 are shown the resultant connection forces from the kinematic couplings E and G, found in the exoskeleton leg structure, being similar to the hip and knee joints of the human leg. These results are obtained, for the situation where the exoskeleton takes up the entire mass of the assisted human subject, i.e. 80 kg. It is observed that we have similar variations for the two legs. The spikes recorded in the graphs of the connection forces appear in the simulation due to the fact that we considered the contact between the sole and the ground with rigid type elements. In reality they do not appear, the contact shocks are damped.

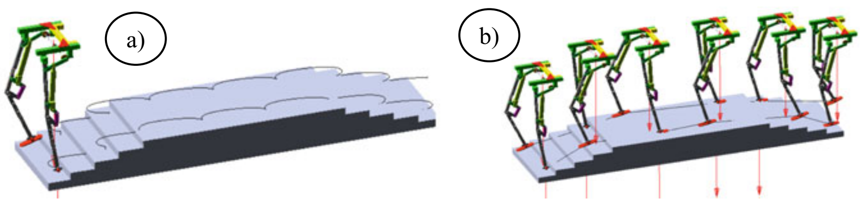

Fig. 3 Dynamic simulation in ADAMS of the robotic system, **a** ankle joint trajectories, **b** successive frames

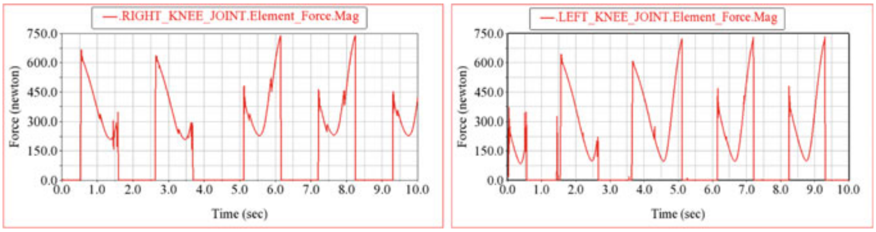

Fig. 4 Resultant connection forces, for the exoskeleton knee joints

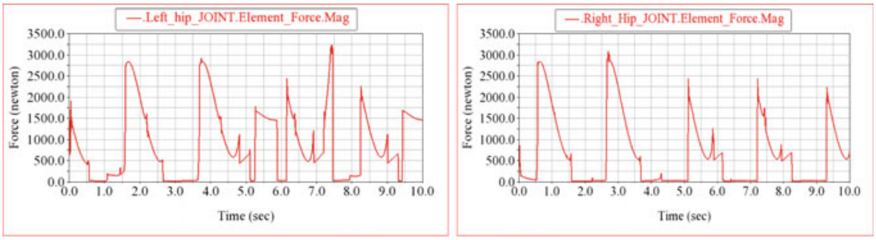

Fig. 5 Resultant connection forces, for the exoskeleton hip joint

A development of the dynamic model is to transform kinematic elements from rigid solids into deformable solids. We did this, and in the first phase we obtained a map of the distribution of elastic displacements in the structure. The maximum value recorded, is 0.8 mm, as can be seen in Fig. 6. In Fig. 7, we have shown the time variation of the deformations of the center of mass of element (4) for both legs.

If we consider previously determined connection forces as input data to check the structural integrity of the kinematic elements using the finite element method, the design solution is validated. For the finite element method analysis, we used ANSYS software, very useful in structural analysis and optimization problems [14–16]. A structural analysis is carried out in static mode. The kinematic element is subjected to

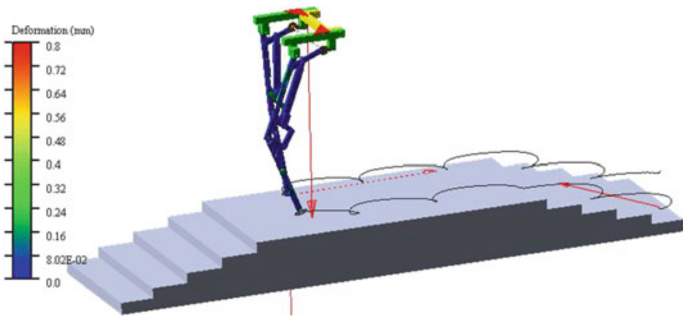

Fig. 6 Dynamic simulation performed considering kinematic elements as deformable solids

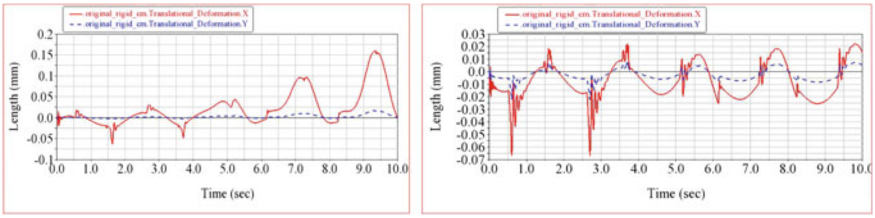

Fig. 7 Linear deformations of the center of mass of element (7), for the left and right leg

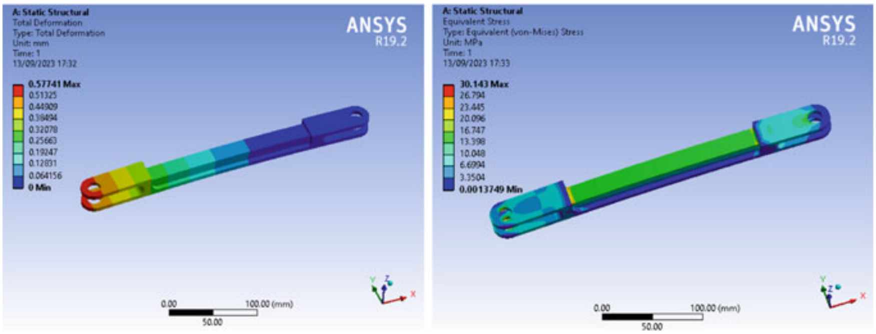

Fig. 8 Results obtained for the verification of the structural integrity of kinematic element 4

tension/compression by the maximum force of 2000 N. Thus, we presented in Fig. 8, the distribution maps of total displacements and equivalent mechanical stresses. It is noticed that the total displacements have small values not exceeding 0.6 mm, and this result confirms the correct operation of the mobile mechanical system. As regards the verification of the structural integrity, the solution is optimally designed, the maximum values of the mechanical stresses being 30 MPa, a value which is within the permissible limits, being below the flow limit of the material from which the kinematic element is made. According to literature data, the mechanical strength of PLA + material is 50–70 MPa [17].

In Fig. 9 the horizontal and vertical displacements of the M point, from the left leg are shown. The graphs obtained for the displacements have no sharp variations, this demonstrating the stable functioning of the robotic system.

4 Experimental Study of the Motion of the Physical Prototype of the Exoskeleton

The optimized elements of the exoskeleton robot were printed on the Anycubic 3D printer. The size of the 3D printer's print bed (400 × 400 × 400 mm) allowed the printing of elements with a maximum length of 331 mm. The assembly of the robot's

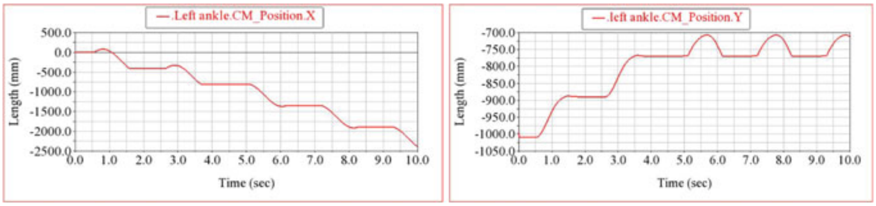

Fig. 9 Displacement of M-point (corresp. to the ankle joint)—horizontal and vertical directions

component parts was carried out, and the assembled physical model is detailed in Fig. 10.

Experimental analysis of robot motion was performed using ultrafast video cameras. The trajectories described by the exoskeleton right leg joints markers, obtained with a motion analysis software, namely CONTEMPLAS, are shown in Fig. 11.

In Fig. 12, a comparison of the angular variations in the kinematic couplings related to the hip (E) and knee (G) obtained by dynamic simulation in ADAMS and experimentally determined by camera motion analysis in CONTEMPLAS is shown. Similar variations obtained by simulation and experiment are observed. The overlapping differences of the two plots, are related to the synchronization of the physical model motion with the simulation.

The results obtained for the rotation angles in the knee and hip kinematic joints obtained by simulation are close to those obtained in normal gait. Thus, in the exoskeleton hip joint we have an angular amplitude of 35 degrees, similar to that of a human subject. In contrast, in the knee joint we have an angular amplitude of 40°, less than that achieved by a human subject, which reaches 55°. So the solution should be kinematically optimized.

Fig. 10 Physical model of the exoskeleton robot

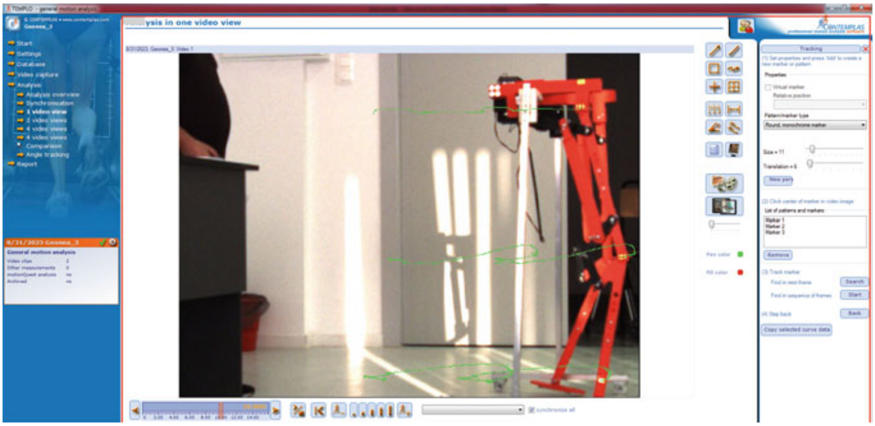

Fig. 11 Trajectories described by the right leg joints of the exoskeleton

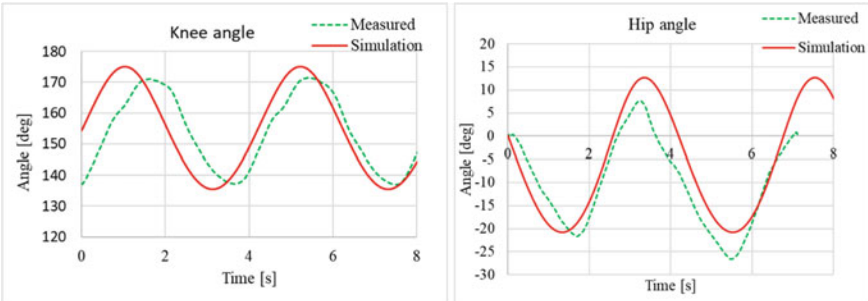

Fig. 12 Angular variations for hip and knee obtained by simulation and experiment

5 Conclusions

In this paper, we have presented an original structural solution for a mechanism used to an exoskeleton robot leg. The aspects addressed in the paper are multiple, namely firstly we have achieved an optimal design of the mechanical assembly, from a structural point of view. The structural solution has been kinematically and dynamically optimized for safe use. The motion simulation is performed in three hypostases, namely climbing up and down stairs, and walking on a horizontal floor. The CAD model is finally used for additive manufacturing of component parts. These elements were assembled and the physical model was used for the study of the movement, by means of ultra-fast video camera equipment.

References

1. Shi, D., Zhang, W., Zhang, W., Ding, X.: A review on lower limb rehabilitation exoskeleton robots. Chin. J. Mech. Eng. **32**, 1–11 (2019)
2. Ibrayev, S., Ibrayeva, A., et al.: Multicriteria optimization of lower limb exoskeleton mechanism. Appl. Sci. **13**(23), 12781 (2023)
3. Copilusi, C., Dumitru, S., Geonea, I., Ciurezu, L.G., Dumitru, N.: Design approaches of an exoskeleton for human neuromotor rehabilitation. Appl. Sci. **12**, 3952 (2022)
4. Geonea, I., Dumitru, N., Tarnita, D., Rinderu, P.: Design and kinematics of a new leg exoskeleton for human motion assistance. In: Advances in Mechanism and Machine Science: Proceedings of the 15th IFToMM World Congress, 15, pp. 165–174. Springer, Berlin (2019)
5. Shen, Z., Allison, G., Cui, L.: An integrated type and dimensional synthesis method to design one degree-of-freedom planar linkages with only revolute joints for exoskeletons. J. Mech. Des. **140**, 092302 (2018)
6. Geonea, I., Tarnita, D., Carbone, G., Ceccarelli, M.: Design and simulation of a leg exoskeleton linkage for human motion assistance. In: New Trends in Medical and Service Robotics: Advances in Theory and Practice, pp. 93–100. Springer, Berlin (2019)
7. Plecnik, M., McCarthy, J.: Dimensional synthesis of six-bar linkage as a constrained RPR chain. In: New Trends in Mechanism and Machine Science: Theory and Applications in Engineering, pp. 273–280. Springer, Berlin, Heidelberg, Germany (2013)
8. Plecnik, M.M., McCarthy, J.M.: Design of Stephenson linkages that guide a point along a specified trajectory. Mech. Mach. Theory **96**, 38–51 (2016)
9. Desai, S.G., Annigeri, A.R., et al.: Analysis of a new single degree-of-freedom eight-link leg mechanism for walking machine. Mech. Mach. Theory **140**, 747–764 (2019)
10. Jiang, J., Chen, P., Peng, J., Qiao, X., Zhu, F.: Design and optimization of lower limb rehabilitation exoskeleton with a multiaxial knee joint. Biomimetics **8**(2), 156 (2023)
11. Ren, H., Shang, W., Li, N., Wu, X.: A fast parameterized gait planning method for a lower-limb exoskeleton robot. Intern. J. Adv. Robot. Syst. **17**(1), 2020 (2020). https://doi.org/10.1177/1729881419893221
12. Major, Z.Z., Vaida, C., et al.: The impact of robotic rehabilitation on the motor system in neurological diseases. a multimodal neurophysiological approach. Int. J. Environ. Res. Public Health. **17**(18), 6557 (2020)
13. Pisla, D., Tarnita, D., et al.: A parallel robot with torque monitoring for brachial monoparesis rehabilitation tasks. Appl. Sci. **11**, 9932 (2021)
14. Tarnita, D., et al.: Experimental characterization of human walking on stairs applied to humanoid dynamics, In: Advances in Robot Design and Intelligent Control, RAAD16, pp. 293–301. Springer, Berlin (2017)
15. Geonea, I.D., et al.: Dynamic analysis of a spherical parallel robot used for brachial monoparesis rehabilitation. Appl. Sci. **11**(24), 11849 (2021)
16. Tarnita, D., Catana, M., et al.: Design and simulation of an orthotic device for patients with osteoarthritis. New Trends Med. Serv. Robots **38**, 61–77 (2016)
17. Travieso-Rodriguez, J.A., Jerez-Mesa, R., Llumà, J., Traver-Ramos, O., Gomez-Gras, G., Roa Rovira, J.J.: Mechanical properties of 3D-printing polylactic acid parts subjected to bending stress and fatigue testing. Materials **12**(23), 3859 (2019)

A Compact Low-Frequencies Vibrational Bioreactor to Induce Cellular Response

Luca Ragno, Alberto Borboni, Paola Serena Ginestra, Elena Laura Mazzoldi, Rosalba Monica Ferraro, and Gabriele Benini

Abstract The production of functional tissues, as well as ensuring cells viability, differentiation and proliferation, is mainly related to the biomimicking degree of the culture chamber, that aims to reproduce the same conditions that occur in-vivo. For this reason, bioreactors able to mimic and provide specific signals or a combination of them, are used to improve tissue formation and biological results. Specifically, literature widely reports that external stimulation can deeply influence cells behavior. This paper presents the design of a compact vibrational bioreactor, operating at low frequencies. The device is based on a voice-coil actuator connected to a bioreactor chamber. Firstly, the system design process is demonstrated, motivated by the necessity for 10^1–10^2 Hz vibrational stimulation, and then the electro-mechanical model is established. The obtained system allows to investigate cellular response to extremely low-frequency of vibrations, and it is used in combination to a peristaltic pump to realize a perfusion-based system obtaining a continuous flow of culture medium during mechanical excitation.

Keywords Vibration · Subwoofer · Shaker · Mechanotransduction · Biomimetic · Bioreactor

1 Introduction

Tissue engineered grafts are now emerging as a potential solution to treat different clinical conditions, overcoming limitations of traditional artificial prostheses. Furthermore, principles of this discipline can be used to develop biologically representative and accurate in-vitro models. Various factors are taken into account

L. Ragno (✉) · A. Borboni · P. S. Ginestra · G. Benini
University of Brescia, 25123 Brescia, BS, Italy
e-mail: luca.ragno@unibs.it

E. L. Mazzoldi · R. M. Ferraro
Angelo Nocivelli Institute for Molecular Medicine, University of Brescia, 25123 Brescia, BS, Italy

D. Pisla et al. (eds.), *Advances in Service and Industrial Robotics*, Mechanisms and Machine Science 157, https://doi.org/10.1007/978-3-031-59257-7_13

during the design process of these cell cultures. Biomimetics refers to the collective endeavors in technology and procedures aimed at achieving conditions that closely resemble physiological ones. Firstly, according to the tissue that has to be obtained, the primary cell culture is identified. Secondly, a proper scaffold can be produced, towards proper material selection and manufacturing process [1]. Finally, in order to mimic physiological conditions in the growing chambers (i.e., bioreactors, petri dishes, multi-well plates), obtain desired cellular adhesion, differentiation, and allow cells to produce new extracellular matrix, scaffolds have to be combined with active external biosignaling [2]. For instance, vibrations can induce biochemical events inside the cells, which affects tissue growth and cellular behavior. This process leads to the conversion of external mechanical signals into biochemical and electrical ones for the cells. In this context, a vibrational bioreactor prototype is presented. This device has been developed starting from a DAYTON AUDIO BST-1 bass shaker (https://www.daytonaudio.com), a particular type of exciter used to reproduce low-frequency (LF) sounds. Although they are voice-coil actuator-based systems as subwoofers, bass shakers can oscillate far below resonance frequency of them. Thus, it can be possible to investigate the cellular behavior when subjected to extremely-low frequency of vibration. Despite significant advancements in the development of devices aimed at enhancing cell culturing techniques and outcomes, the study of hyalocytes and vitreous body tissue remains relatively underexplored. In this particular case, the device, designed to be integrated on a perfusion bioreactor has been developed to provide biomimetic stimuli to a human hyalocytes cell culture and eye movements that occur every day in vitreous body [3].

2 Problem Statement

The utilization of mechanical stimulation plays a crucial role in modulating cell physiology by facilitating the transmission of specific signals among them. Depending on the application area, ranging from industrial and automotive to acoustic and sensing, various devices have been utilized as vibratory systems to generate the required amplitudes and frequencies. However, in biological and tissue engineering fields, the definition of vibrational generators remains elusive due to the wide array of use cases and the need for device customization to produce specific frequencies and amplitudes tailored to each unique application. In this context, it has been demonstrated that a customized bioreactor with the addition of a low-intensity pulsed ultrasound (LIPUS) generator, can improve osteogenesis, emulating the in-vivo process and avoiding thermal effects [4]. In the case of LF stimulation (i.e., 25 Hz) a customized acoustic-derived voice coil actuator (VCA) has allowed to observe that oscillations stimulate proliferation and osteogenic differentiation [5]. In another case a subwoofer-based device has been adopted to evaluate blackberries susceptibility to red drupelet reversion [6]. Specifically, subwoofers are linear voice coil actuated, and use a permanent magnet and an alternating current-driven metal coil to reproduce sounds. The current flow passing through the coil, temporary generates an electromagnetic field and consequently an induced force. The polarity of the magnetic field follows the current direction and, as a result, the VCA is able to move linearly expanding and contracting the diaphragm. Finally, these acoustic devices are characterized by a resonance frequency below which they cannot be effectively utilized; bass shakers represent a novel and effective approach for delivering LF stimuli that mimic the characteristics of saccadic eye movements and produce biologically relevant oscillations. The device presented in this work has been designed to be implemented in a bioreactor system, that is involved in in-vitro hyalocytes culturing and stimulation. The main advantage of the proposed solution is the possibility to provide vibrations close to and above vitreous body model resonance frequency [3].

3 Materials and Methods

3.1 Vibration System

The system (see Fig. 1) is composed by a Krieger 150 W transformer to connect the Dayton Audio SA70 70 W Subwoofer Amplifier (https://www.daytonaudio.com) to the European power grid. The amplifier is connected to an FG-100 DSS function generator as low-level input signal source, while the Dayton Audio BST-1 High Power Pro Tactile Bass Shaker 50 W (https://www.daytonaudio.com) is connected as end effector of the system, interfacing directly to the 3D printed parts that sustain and immobilize the bioreactor. Thiele-Small parameters of the BST-1 are essential to describe the behavior and frequency response of the system, particularly referring to Electromechanical force factor (K_{Bl}), Mechanical stiffness of suspension (K), Moving Mass (m) and Resonance Frequency (F_s). Finally, a damped harmonic oscillator linear model, for LF time-invariant and low-amplitude excitations, has been used.

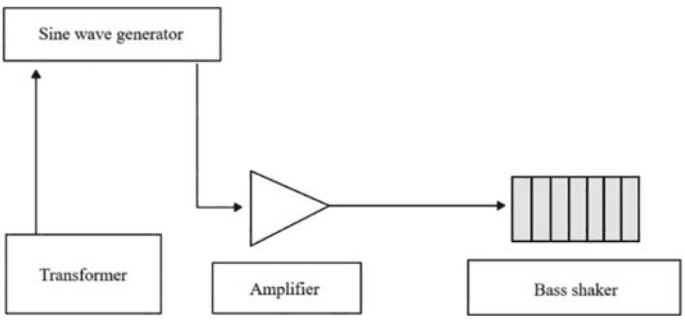

Fig. 1 Schematic representation of the vibrational generator

3.2 Biological Model

Human Vitreous Body (HVB) is a transparent gel substance for the most part composed of water (about 99%) entrapped in a network made of collagen and hyaluronic acid [7]. During eye movements inside ocular cavity, the vitreous body is supportive and adherent with the retina, this generates deformation inside the three-dimensional structure of the gel leading to the stimulation of the vitreous body and the retina themselves. These mechanical stresses have been proposed as possible causes of vitreous diseases. According to studies on a synthetic model of the HVB, examining eye bulb velocity field components (specifically, azimuthal and radial velocities) has revealed a connection between biological damage and mechanical phenomena [3]. Bonfiglio et al. demonstrates that in the HVB, when resonance conditions are achieved, azimuthal velocity is more pronounced in the central area than near the periphery. This leads to significant stress levels within the vitreous body, impacting the retina and causing internal changes in the ocular organ. In this context, the model primarily focuses on the azimuthal velocity (Eq. 1) to determine the resonance frequency, beyond which the proposed vibrational generator can operate:

$$v_\theta = \frac{-v_x^* \sin(\theta) + v_y^* \cos(\theta)}{A\omega R} \tag{1}$$

where v_θ corresponds to the azimuthal velocity, scaled by $A\omega R$. The scaling factor is determined by multiplying eye rotation amplitude (A), the angular frequency (ω) and the model's cavity radius (R).

3.3 Electrodynamical Model

According to Ampère equation, when an electric current flows through VCA coil, it generates a magnetic field, and as a result of interaction of this magnetic field with the permanent magnet's one, Lorentz force is produced and guarantees actuator motion. This mechanism converts electrical energy into mechanical energy, enabling precise linear movements based on current direction. In order to control VCA position as well as bioreactor chamber movement on the top of it, the combination of an electrical model and a dynamical model has been required. According to Kirchhoff's Law the balance of VCM equivalent electrical circuit (see Fig. 2a) can be written as follow (Eq. 2):

$$e_{act}(t) = R \cdot i(t) + L \cdot \frac{di(t)}{dt} + e_{back}(t) \tag{2}$$

where e_{act} represents the electrical alternating input signal for a voltage-driven circuit; R and L are respectively the equivalent resistance and inductance; $i(t)$ represents the current flow through the circuit, while e_{back} (i.e., back electromotive force) from Faraday law can be expressed for a moving coil as follow (Eq. 3):

$$e_{back}(t) = B \cdot l \cdot \frac{dx(t)}{dt} \tag{3}$$

where B represents the magnetic field intensity; l represents the length of the coil; $x(t)$ and its derivatives represent the fundamental kinematic equations. Since the proposed vibration generator operates a very LF (i.e., below 10^2 Hz) the circuit can be considered as purely resistive. From a mechanical point of view the vibration generator can be considered equivalent to a spring-mass-damper dynamical positioning system (see Fig. 2b), and the balance of forces can be written as follow (Eq. 4):

$$B \cdot l \cdot i(t) = m\frac{d^2x(t)}{dt^2} + DF\frac{dx(t)}{dt} + Kx(t) \tag{4}$$

where $B{\cdot}l$ represents the force factor; m the mass of the moving part; DF represents the damping factor; K represents the stiffness of the system. Moreover, assuming $i(t)$ as a sinusoidal input (Eq. 5) and applying the Laplace transformation to Eq. 4, the relationship between input and output signals in the frequency domain has been obtained (Eq. 6):

$$i(t) = i_0 sin(\omega t) \tag{5}$$

$$Y(s) \cdot \left(m \cdot s^2 + DF \cdot s + K\right) = \frac{K_{Bl} \cdot i_0 \cdot \omega}{\left(s^2 + \omega^2\right)} \tag{6}$$

K_{Bl} is used to synthesize the force factor represented by $B{\cdot}l$; ω represents the angular velocity. Finally, using appropriate mathematical steps and applying the Inverse Laplace transformation to $Y(s)$ (Eq. 7) have allowed to obtain $y(t)$ (Eq. 8), that represent the vertical displacement in the time domain (i.e., equation of motion $x(t)$):

$$\mathcal{L} - 1[Y(s)] = \mathcal{L}^{-1}\left[\frac{K_{Bl} \cdot i_0 \cdot \omega}{\left(s^2 + \omega^2\right)\left(m \cdot s^2 + DF \cdot s + K\right)}\right] \tag{7}$$

$$A = \begin{pmatrix} 2m\left(m\omega^2 - K\right)\left(e^{\frac{t\sqrt{DF^2-4Km}}{m}} - 1\right) + DF^2\left(e^{\frac{t\sqrt{DF^2-4Km}}{m}} - 1\right) \\ +DF\sqrt{DF^2 - 4Km}\left(e^{\frac{t\sqrt{DF^2-4Km}}{m}} + 1\right) \end{pmatrix} \tag{8}$$

$$B = 2\sqrt{DF^2 - 4Km}\left(K - m\omega^2\right)\sin(t\omega) - 2DF\omega\sqrt{DF^2 - 4Km}\cos(t\omega)$$

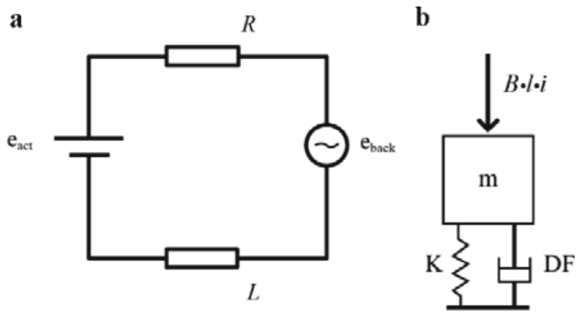

Fig. 2 Electrical equivalent circuit of VCA (**a**). Mass-damper-spring dynamical model of VCA (**b**)

$$y(t) = \frac{i_0 K_{Bl}\left(A \cdot \left(we^{-\frac{t\left(\sqrt{DF^2-4Km}+DF\right)}{2m}}\right) + B\right)}{2\sqrt{DF^2-4Km}\left(DF^2\omega^2 + K^2 - 2Km\omega^2 + m^2\omega^4\right)}$$

4 Result and Discussion

Despite advances in cell culturing devices, research on eye cells and vitreous body tissue is still limited due to the difficulties related to the simulation of the body mechanical stimuli typical of this biological district. This work introduces a VCA-based mechatronic system designed for usage in bioreactors for in-vitro cultures LF stimulation [8]. It mainly consists of an oscillating platform that can be installed on a bioreactor (see Fig. 3a) and its primary function lies in the capability to produce vibrations at, or above, the resonance frequency of a vitreous body model. This feature allows the analysis of stress impacting the interior structures of the eye bulb and relative damages. Initially, aiming to develop the present compact vibration generator, commercially available devices and scientific literature have been analyzed. In this context, linear resonant actuators have been considered, but limits in frequency modulation affect this solution [9]. Furthermore, cam systems based on eccentric rotor coupled to DC motor, has been reported as effective solution to obtain oscillatory motion [10]. This approach is susceptible to performance issues due to the dimensional tolerances of the components and the precision required in assembly practices. In the same way, piezoelectric materials have been widely used to provide and control vibrations, but limited to high frequencies [11, 12]. In addition, although shape memory actuators (SMA) constitute promising systems to provide vibrational simulations, cell cultures require specific temperature conditions and incubators, as a consequence temperature-driven SMA cannot be involved into biological field [13]. Assuming frequency as pivotal factor in the selection criteria, a voice coil actuator, from a bass shaker, has been selected here as an optimal and simple solution to apply

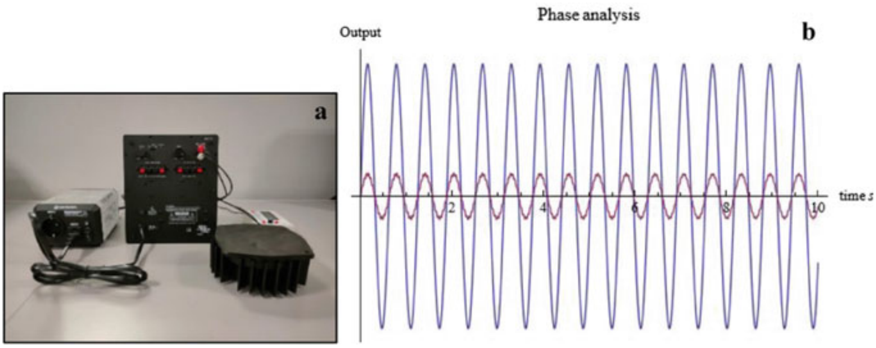

Fig. 3 Output phase analysis. Output represents the electrical current signal $i(t)$ that has been scaled to be visualized along with linear vertical displacement $y(t)$. They are respectively the blue line and the red one (**a**). Vibrational generator based on BST-1 Bass shaker, Dayton Audio (**b**)

LF mechanical stimulation to human eye models and in-vitro eye cells cultures. The fundamental lumped parameter model used to describe vibrations generated includes a spring (i.e., potential energy storing element), a mass (i.e., kinetic energy storing element) and a damper (i.e., dissipating energy element). Therefore, it has been used to perform a phase analysis between current $i(t)$ and the linear vertical displacement $y(t)$ (Eq. 9). The simulation of biological analysis performed at the angular frequency identified by Bonfiglio et al. [3] (i.e., 62.83 rad/s, equivalent to 10 Hz), confirms the phase relationship between the two quantities. In conclusion, this VCA-based vibratory system emerges as an effective experimental tool for achieving HVB resonance conditions. It enables the exploration of the roles played by biological and dynamical triggers, specifically eye cell contractions and eye movements, in causing network collapse and vitreous liquefaction. In this case, gap in research is notable considering the critical role these cells and tissue play in ocular health. The proposed vibrational bioreactor could not only facilitate a deeper understanding of hyalocytes biology and function, but also potentially lead to breakthroughs in treating a range of ocular pathological conditions, such as floaters, macular diseases (i.e., hole and pucker) and posterior vitreous detachment [7]. In conclusion, multi-dimensional mechanical stimulation may play a vital role in regulating cellular physiology and enhancing communication between cells across various tissues, in this context multi-axis vibrational platforms development can further improve biomimetic stimulation [14, 15].

5 Conclusions

The gel-like viscoelastic vitreous body oscillates with eye movement. When aroused, eye cells can cause internal inflammation and stress, despite the longtime reputation as an inert tissue with just structural and supporting roles of the vitreous body. These mechanical and biological stimuli can cause floaters, posterior vitreous separation, macular holes, and other eye disorders. The main purpose of this work aimed to present a device involved in human vitreous body cells analysis and simulation of the in-vivo conditions. The main points demonstrated by this tailored vibrational generator are reported here:

- The low frequency vibrational generator applicable to perfusion-based bioreactors here presented is not commercially available;
- Bass shakers have been used here as innovative tools to be involved in the vibrations field;
- The device can be fully modular, in a second phase of the development, 3D printed supports, allow to implement UV light source in the compact vibrational system.

References

1. Ginestra, P., Pandini, S., Ceretti, E.: Hybrid multi-layered scaffolds produced via grain extrusion and electrospinning for 3D cell culture tests. Rapid Prototyp. J. **26**(3) (2020). https://doi.org/10.1108/RPJ-03-2019-0079
2. Campsie, P., et al.: Design, construction and characterisation of a novel nanovibrational bioreactor and cultureware for osteogenesis. Sci. Rep. **9**(1) (2019). https://doi.org/10.1038/s41598-019-49422-4
3. Bonfiglio, Lagazzo, A., Repetto, R., Stocchino, A.: An experimental model of vitreous motion induced by eye rotations. Eye Vision **2**(1) (2015). https://doi.org/10.1186/s40662-015-0020-8
4. Cha, J.M., Hwang, Y.S., Kang, D.K., Lee, J., Cooper, E.S., Mantalaris, A.: Development of a novel perfusion rotating wall vessel bioreactor with ultrasound stimulation for mass-production of mineralized tissue constructs. Tissue Eng. Regen. Med. **19**(4) (2022). https://doi.org/10.1007/s13770-022-00447-3
5. Marędziak, M., Lewandowski, D., Tomaszewski, K.A., Kubiak, K., Marycz, K.: The effect of low-magnitude low-frequency vibrations (LMLF) on osteogenic differentiation potential of human adipose derived mesenchymal stem cells. Cell. Mol. Bioeng. **10**(6), 549–562 (2017). https://doi.org/10.1007/s12195-017-0501-z
6. Flores-Sosa, R., Fabela-Gallegos, M.J., Cruz-Acevedo, M.E., Rivera-Pastrana, D.M., Nava, G.M., Mercado-Silva, E.M.: A portable vibration system to induce and evaluate susceptibility to red drupelet reversion in blackberry cultivars. Horticulturae **8**(7) (2022). https://doi.org/10.3390/horticulturae8070631
7. Mazzoldi, E.L., Riva, L., Ferraro, R.M., Ginestra, P.S., Giliani, S.C.: 3D printing of biocompatible scaffolds for eye tissue engineering. In: Procedia CIRP, pp. 214–219. Elsevier B.V. (2022). https://doi.org/10.1016/j.procir.2022.06.039
8. Aggogeri, F., Borboni, A., Faglia, R.: Reliability roadmap for mechatronic systems. In: Applied Mechanics and Materials, pp. 130–133 (2013). https://doi.org/10.4028/www.scientific.net/AMM.373-375.130
9. Liu, S.H., Kao, Y.C., Feng, G.H.: Linear resonator actuator-constructed wearable haptic system with the application of converting remote grinding force to vibratory sensation. Actuators **12**(9) (2023). https://doi.org/10.3390/act12090359
10. Borboni, Aggogeri, F., Pellegrini, N., Faglia, R.: Precision point design of a cam indexing mechanism **590** (2012). https://doi.org/10.4028/www.scientific.net/AMR.590.399
11. Aggogeri, F., Borboni, A., Merlo, A., Pellegrini, N., Ricatto, R.: Real-time performance of mechatronic PZT module using active vibration feedback control. Sensors (Switzerland) **16**(10) (2016). https://doi.org/10.3390/s16101577

12. DeVoe, D.L., Pisano, A.P.: Modeling and optimal design of piezoelectric cantilever microactuators. J. Microelectromech. Syst. **6**(3) (1997). https://doi.org/10.1109/84.623116
13. Borboni, Aggogeri, F., Pellegrini, N., Faglia, R.: Innovative modular SMA actuator **590** (2012). https://doi.org/10.4028/www.scientific.net/AMR.590.405
14. 2019 15th International Wireless Communications & Mobile Computing Conference (IWCMC). IEEE (2019)
15. Guzman, Leon, C., Vuelvas, J., Manrique, M.: Earthquake simulator. In: Proceedings of the 2021 IEEE 5th Colombian Conference on Automatic Control, CCAC 2021, Institute of Electrical and Electronics Engineers Inc., pp. 268–273 (2021). https://doi.org/10.1109/CCAC51819.2021.9633272

Design of Wearable Prostheses: A New Approach

Pedro Moreira, José Machado, Calin Vaida, Doina Pisla, Daniel Miranda, Nuno Martins, Vítor Carvalho, and Demétrio Matos

Abstract In this paper an approach for assistance with a limb amputee is described. Amputations represent a severe alteration of an individual's physical capabilities; however, their body image is equally affected. The field of prosthetic development has continuously evolved over the years, but it is noticeable that often users' needs are not fully met—this is because the main focus during the development process is oriented solely towards functional issues, relegating aesthetic and usability concerns to a secondary position. The present work aims at the design and development of a wearable prosthetic device for an upper limb using additive manufacturing. The

P. Moreira · N. Martins · D. Matos
ID+ Research Institute in Design, Media and Culture, School of Design, Polytechnic University of Cávado and Ave (IPCA), 4750-810 Barcelos, Portugal
e-mail: pmoreira@ipca.pt

N. Martins
e-mail: nmartins@ipca.pt

D. Matos
e-mail: dmatos@ipca.pt

J. Machado (✉)
MEtRICs Research Center, University of Minho, Campus of Azurém, 4800-058 Guimarães, Portugal
e-mail: jmachado@dem.uminho.pt

J. Machado · C. Vaida · D. Pisla
CESTER Research Center, Technical University of Cluj-Napoca, Muncii Ave. 103-105, 400641 Cluj-Napoca, Romania
e-mail: Calin.Vaida@mep.utcluj.ro

D. Pisla
e-mail: Doina.Pisla@mep.utcluj.ro

D. Miranda · V. Carvalho
2Ai, School of Technology, Polytechnic University of Cávado and Ave (IPCA), 4750-810 Barcelos, Portugal
e-mail: damiranda@ipca.pt

V. Carvalho
e-mail: vcarvalho@ipca.pt

D. Pisla et al. (eds.), *Advances in Service and Industrial Robotics*, Mechanisms and Machine Science 157, https://doi.org/10.1007/978-3-031-59257-7_14

goal is for the device to meet the needs and characteristics of each user. An interventionist research methodology was applied in parallel with the Double Diamond design process. Theoretical foundations were established, and data collection tools such as observation, interviews, and user questionnaires were employed. The current phase of the work, which is ongoing, represents the entire practical development, with the participation of a rehabilitation and prosthetics production center. Preliminary results of this research indicate that through additive manufacturing it is possible to reduce the final cost of the device, allowing for greater customization and, consequently, better acceptance by users. It is also evident that the use of additive manufacturing, combined with the incorporation of the prosthesis, facilitates an improvement in the rehabilitation process.

Keywords Prosthetic devices · Medical devices design · Prosthesis embodiment · Wearable prosthesis

1 Introduction

1.1 Amputation

The increasing demand for solutions to treat disorders or dysfunctions in the health sector has been intensifying the development of products with the aim of providing a better quality of life. This applied and exploratory research falls within the scientific field of design and focuses on the investigation, design, development, and testing of the use of medical devices, specifically myoelectric wearable prostheses for upper limbs.

In addition to the use of sophisticated systems for healthcare and rehabilitation improvement [1, 2], it is important to consider several dimensions in the increasing the quality of life of populations.

Driven by population growth, aging, chronic pathologies, wars, domestic injuries, and other causes often related to poverty, the disabled population has been increasing for decades [3]. In 2005, over half a million people in the United States alone experienced some form of upper limb amputation, with an expected doubling of this number by 2050 [4].

The amputation of an upper limb is defined by the International Organization for Standardization as the "surgical removal of all or part of an upper limb" [5]. The loss of a limb represents a drastic change in a person's life. It is responsible for altering their interaction with the social environment and their perception of body image [6], potentially causing fear and insecurity in the use of a prosthesis [7]. Therefore, prostheses play a significant role in the rehabilitation process for an amputee, allowing them to reintegrate into society and resume activities [8]. The prosthesis should be seen as a product designed to fulfill the function of the missing limb; however, it cannot be expected to entirely replace the lost function.

1.2 Prosthesis

Prostheses are medical devices designed to replace a missing bodily function resulting from traumatic loss or congenital malformation of a body part. Various categories have been defined, and they can be further classified into two main groups: (i) exoskeletal prostheses and (ii) endoskeleton prostheses [9]. Exoskeletal prostheses have a volumetric shape similar to the real limb, resulting in a higher weight compared to endoskeleton prostheses. The latter consist of central supports, like bones, with the addition of cosmetic coverings on the outside.

A Mechanical Prosthesis provides its user with slightly reduced mobility as limb movement is controlled by nerve impulses. On the other hand, a prosthesis referred to as Bionic offers much more control and is developed with the patient's comfort and convenience in mind. Gesture control allows for automated and straightforward movement alterations, providing more degrees of freedom.

Here, it is crucial to emphasize that each patient will have their adaptation time to the prosthesis. Marketed as state-of-the-art prostheses, bionic prostheses require an extended period of adaptation and training to begin performing basic daily tasks. This process remains a hurdle for the patient's rehabilitation and satisfaction with the product. The cost of an upper limb prosthesis can vary significantly depending on various factors, such as the type of prosthesis, the materials used, and the complexity of the prosthesis. According to a statement made by the American Orthotics and Prosthetics Association, the average prosthetic costs between $1500 to $8000. This expense is often paid out of pocket rather than covered by insurance. By contrast, a 3D printed prosthetic costs as little as $50. We agree that cost is not just about the price; however, even with indirect costs, this type of product is important for the user.

1.3 Embodiment

Part of the state of the art focuses solely on the development of various myoelectric and biomechanical control methods, limiting research to complex daily tasks involving prosthetic manipulation, such as gripping and releasing [10]. This approach does not consider the aesthetic and psychological dimensions in the interaction between the user and the product. The use of a prosthesis is a key component of the rehabilitation process for individuals with limb amputation. The literature allows us to assert that the incorporation of the prosthesis facilitates an improvement in the rehabilitation process. Whether the prosthesis is used for basic mobility or for more demanding activities, it can offer profound psychological benefits and improve quality of life. Several studies have shown a direct correlation between prosthetic locomotor capabilities and increased levels of autonomy, self-esteem, and improvement in social life.

According to Abraham Maslow [11], human needs follow a logical sequence, where it is possible to identify those that emerge first in a person's life. An amputation can provide an experience that prevents a human from ever feeling fulfilled because they cannot satisfy their basic needs [12]. On the other hand, socialization with others is facilitated through hand movements, serving as a means of communication. Thus, the loss of a limb requires adaptation on the part of the amputee, directly affecting their daily actions as well as their professional and social life [13].

"Embodiment" is a term used to define the incorporation or personification, representing the effect of embodying, or integrating something into the body. It is employed in various domains such as psychology, cognitive sciences, neuroscience, and, above all, technology. This bodily experience is central when associated with the concept of medical devices or technical aids in healthcare. The acceptance of a medical device by a human is a consequence of physiological response and perception. The term embodiment has become ubiquitous in research and is frequently used as a metric of progress as well as a measure of user acceptance [14].

The embodiment framework is based on bodily representations, and the appropriation model proposed by Manos Tsakiris [15] introduces sensory feedback related to the prosthesis, which is consecutively confronted in a three-step comparison process. Figure 1 contextualizes and explores the relationship between the various stages.

The similarity between the prosthesis and the residual limb, feedback obtained solely through visual observation, is explored in the initial phase. It is compared with the persistent representation of how a biological limb should be in the body model, the socially acceptable norm. Subsequently, the postural and anatomical feedback from the prosthesis is compared with the current estimated body posture, stored in the body schema. The last step is the sensory integration of the remaining feedback. If there is consistency in the three comparison phases, the property emerges, which is then used to update the body representation [14, 15]. The most common aids are feedback sensors used at the fingertips, aiming to provide some depth to the user's

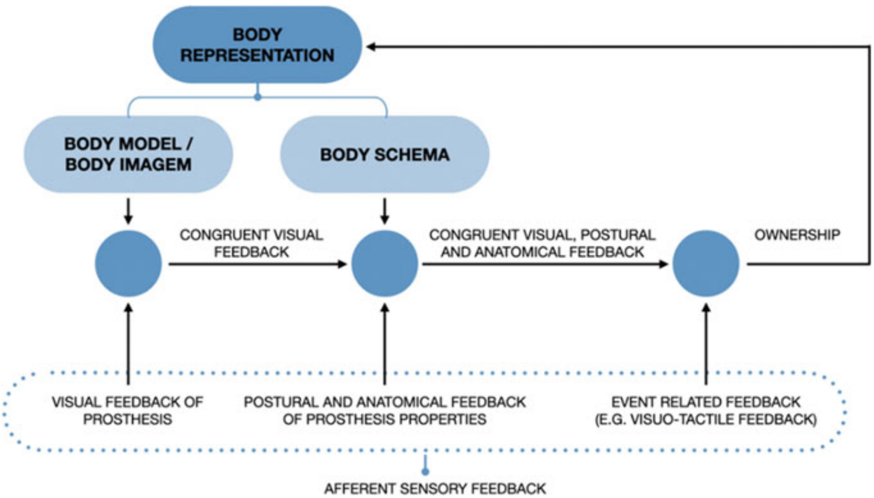

Fig. 1 Neurocognitive schema of the emergence of ownership, adapted from [15]

experience. When the user feels tactile feedback on the stump, the sense of body extension will be greater.

This paper is organized in 4 sections. After Sects. 1 and 2 presents the Materials and Methods employed, Sect. 3 describes the Preliminary Results obtained and finally, Sect. 4 draws the Final Remarks and points out further developments.

2 Materials and Methods

The methodology used in this work involves exploratory studies and action research, considering our intention to analyze what is being developed and propose a new approach to the use of prostheses. The aesthetic-formal function aims to assess how the cosmetic covering, with this new configuration, can contribute to reducing the existing stigma regarding medical devices. The symbolic function aims to explore the possibility of personalizing the prosthesis, blending it with clothing to make it more appealing and contribute to stigma reduction. The objectives were problem resolution across various dimensions to ensure effectiveness, safety, and comfort of the solutions. Tasks included technical aspects, such as acquiring a myoelectric signal to operationalize the prosthesis through a wearable device. On a functional level, it involved incorporating the prosthetic element printed with the textile element.

2.1 Digitalization

To begin, it was necessary to obtain the geometry of the amputee's residual limb. The equipment used for digitalization was an iPad, and the application used for scanning the limb was Orten3DCam. It is a free scanning software widely used for such applications, given its user-friendly interface and the ability to achieve accurate results with a scanner precision of up to $\pm$ 0.3 mm. To obtain a more detailed result, the "Structure Sensor Pro Specs" was used, attached to the back of the iPad, to capture the geometry (see Fig. 2.). To ensure a product with the most precise geometry, the healthy arm was also digitized.

This process (Fig. 2) requires making corrections after obtaining the 3D mesh since irregularities were present in its geometry. It was immediately evident that the entire limb exhibited the highest number of irregularities in the hand area, requiring the use of digital modeling tools to make the necessary corrections. Blender was the software utilized to carry out the mesh corrections.

Fig. 2 Process of digitizing the stump

2.2 Customization and Printing

For the study of fittings with the stump and the examination of geometry, the functional requirement was considered. After defining the limits, the first fitting was modeled and printed, allowing us to assess whether it fit correctly with the stump (see Fig. 3). A 3 mm spacing was provided between the fitting and the stump, as foam is intended to be placed in this space to increase comfort. To adjust the fitting and secure it to the stump, the “BOA Fit System” tightening system from the company was chosen.

This version of the myoelectric upper limb prosthesis consists of four main elements: the socket, the mechanism for the wrist, the hand, and the cosmetic covering, which is secured by magnets. In total, this device is composed of 39 components printed in 3D. The mentioned components do not include the magnets, internal

Fig. 3 Fitting development process

Fig. 4 Wrist mechanism and printed component assembly

components for the operation of a myoelectric device, the "BOA" tightening system, or the foam for the socket. The final weight of the device, excluding electronic components, remained below 500 g (see Fig. 4).

3 Preliminary Results

After analyzing the obtained data and the first version of an additively manufactured prosthesis, it became possible to define the product requirements. These were divided into two groups: (i) functional requirements and (ii) user requirements. This division allowed for a separation between the necessary requirements for the correct operation of a myoelectric device and the requirements that add value to the product, ensuring that it meets the needs and characteristics of the user.

The use of body-integrated devices is becoming increasingly common, promoting an interaction between the body and devices that can result in a sustained experience, where technology becomes an extension of the body, cognition, and even the self, recently conceptualized as the incorporation of wearable technology [16]. As wearable technologies evoke deep connections and feelings in people, the process has now transitioned to exploring the concept of wearable prosthetics.

While several studies have been conducted on receiving and using a physical prosthesis, it is unknown whether similar subjective experiences arise with technology [17], a factor that should be observed in the interaction with end-users. We will now leverage the inherent geometric freedom of this 3D printing approach (see Fig. 5) and develop an interface between the prosthesis and clothing to maximize strength and minimize the weight of the prosthetic arm. Transforming this set of components into a wearable.

The compatibility between the prosthesis, clothing, and technology is crucial for the progress of the project. The processes of modeling and printing the upper limb

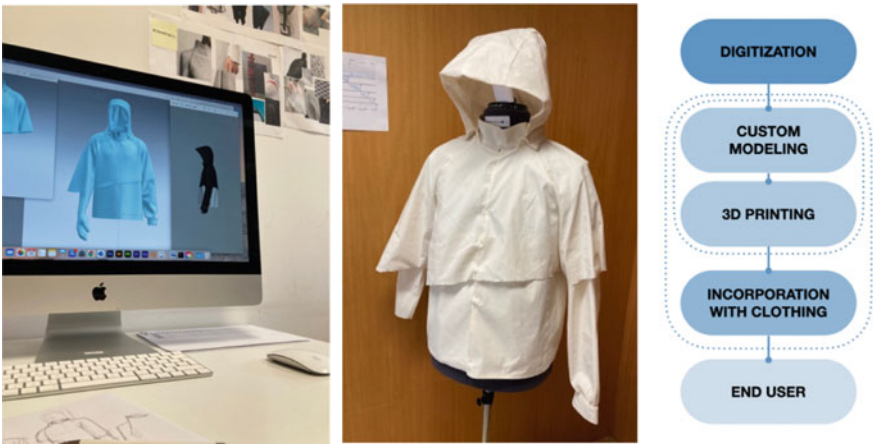

Fig. 5 Planning the textile component for introduction into the process

prosthesis are carefully analyzed, as well as the processes and potential solutions for clothing that are most suitable for this project. The possibility of placing or finding an alternative for myoelectric sensors is also explored. Once these dimensions are thoroughly examined, the identification of all connection points and compatibility issues is carried out.

4 Final Remarks

The initial experiments have yielded promising results. Considering that the development of user-centric medical devices allows for better responsiveness to the final consumer's expectations and better satisfaction of their needs, both physical and psychological. Considering the ongoing development and research to understand the applicability of 3D printing in prosthetic creation, improvements in cost-effectiveness have been observed with the use of this technology, along with the potential to design more versatile products. Although the project is still in the validation phase, it proves to be a promising field with a facilitating resource for the rehabilitation process.

In terms of future work, based on a functional prototype, usability tests will be conducted to verify the effectiveness of the chosen options and simultaneously gather information about possible improvements. The proof of concept will help ascertain whether the results obtained with the use of the new prosthesis align with the requirements. Collaborating with the orthopedic center will enable us to understand the real user's perception of this new concept and discover new insights for final validation. The goal is to achieve universality in products, creating accessible solutions for as many people as possible.

Acknowledgements This research has been partially supported by the project *New frontiers in adaptive modular robotics for patient-centered medical rehabilitation*—ASKLEPIOS, funded by European Union—NextGenerationEU and Romanian Government, under National Recovery and Resilience Plan for Romania, contract no. 760071/23.05.2023, code CF 121/15.11.2022, with Romanian Ministry of Research, Innovation and Digitalization, within Component 9, investment I8; and partially supported by national portuguese funds through FCT—*Fundação para a Ciência e a Tecnologia*, I.P., in the framework of the project «Ref: PeX_2022.09053.PTDC». DOI https://doi.org/10.54499/2022.09053.PTDC.

References

1. Pisla, D., Plitea, N., Vidrean, A., Prodan, B., Gherman, B., Lese, D.: Kinematics and design of two variants of a reconfigurable parallel robot. In: Proceedings of the 2009 ASME/IFToMM International Conference on Reconfigurable Mechanisms and Robots, London, UK, 22–24 June, pp. 624–631 (2009)
2. Pisla, D., Tarnita, D., Tucan, P., Tohanean, N., Vaida, C., Geonea, I.D., Bogdan, G., Abrudan, C., Carbone, G., Plitea, N.: A parallel robot with torque monitoring for brachial monoparesis rehabilitation tasks. Appl. Sci. **11**, 9932 (2021). https://doi.org/10.3390/app11219932
3. World Health Organization, Guidelines for training personnel in developing countries for prosthetics and orthotics services. WHO publications, Geneva (2005)
4. Ziegler-Graham, K., MacKenzie, E.J., Ephraim, P.L., Travison, T.G., Brookmeyer, R.: Estimating the prevalence of Limb Loss in the United States: 2005 to 2050. Arch. Phys. Med. Rehabil. **89**(3), 422–429 (2008). https://doi.org/10.1016/j.apmr.2007.11.005
5. ISO: Prosthetics and orthotics-Vocabulary-Part 4: terms relating to limb amputation (ISO 8549-4). www.iso.org (2020)
6. Moreira, P., Matos, D., Miranda, D., Carvalho, V.: O contributo dos fatores humanos no design de produtos para a reabilitação de amputados produzidos por fabricação aditiva. In: Arezes, P., Baptista, J.S., Melo, R., Barroso, M., Branco, J.C., Carneiro, P., Colim, A., Costa, N., Costa, S., Duarte, J., Guedes, J., Perestrelo, G. (Eds) International Symposium on Occupational Safety and Hygiene: Proceedings Book of the SHO2023. Sociedade Portuguesa de Segurança e Higiene Ocupacionais (SPOSHO), pp. 278–284. (in portuguese) (2023)
7. Matos, D.: Contributo do Design no processo de desenvolvimento de dispositivos médicos. Projeto de um elemento protésico segundo uma abordagem centrada no utilizador. [Ph.D.]. (in portuguese) (2016)
8. O'Keeffe, B., Rout, S.: Prosthetic rehabilitation in the lower limb. Indian J. Plast. Surg. **52**(1), 134–143 (2019). https://doi.org/10.1055/s-0039-1687919. Epub 2019 Apr 29. PMID: 31456622; PMCID: PMC6664837
9. Carvalho, J.A.: Amputações de membros inferiores: Em busca da plena reabilitação (2_a edição). (in portuguese)
10. Bilyy, R.I.: Review of research towards the myoelectric method of controlling bionic prosthesis. Optoelectron. Inf. Power Technol. **46**(2), 142–149 (2023). https://doi.org/10.31649/1681-7893-2023-46-2-142-149
11. Maslow, A.: Motivation and Personality (Second). Harper & Row (1970)
12. Matos, D.F., Ferreira, A.M., Pinho, A.M., Martins, J.P.: Design de Dispositivos Médicos Contributo do Design para o Desenvolvimento de uma Pró-tese Externa de um Membro Inferior. E-Revista Logo **4**(2238–2542), 73–90 (2015). (in portuguese)
13. Cordella, F., Ciancio, A.L., Sacchetti, R., Davalli, A., Cutti, A.G., Guglielmelli, E., Zollo, L.: Literature review on needs of upper limb prosthesis users. Front. Neurosci. **10**(5). Frontiers Media S.A (2016). https://doi.org/10.3389/fnins.2016.00209

14. Zbinden, J., Lendaro, E., Ortiz-Catalan, M.: Prosthetic embodiment: systematic review on definitions, measures, and experimental paradigms. J. Neuroeng. Rehabil. **19**(1), 37 (2022). https://doi.org/10.1186/s12984-022-01006-6
15. Tsakiris, M.: My body in the brain: a neurocognitive model of body-ownership. Neuropsychologia **48**(3), 703–712 (2010). https://doi.org/10.1016/j.neuropsycholo-gia.2009.09.034
16. Nelson, E., Verhagen, T., Vollenbroek-Hutten, M., Noordzij, M.: Is wearable technology becoming part of us? Developing and validating a measurement scale for wearable technology embodiment. JMIR Mhealth Uhealth **7**(8), e12771 (2019). https://doi.org/10.2196/12771
17. Nelson, E.C., Sools, A.M., Vollenbroek-Hutten, M.M.R., Verhagen, T., Noordzij, M.L.: Embodiment of wearable technology: qualitative longitudinal study. JMIR Mhealth Uhealth **8**(11), e16973 (2020). https://doi.org/10.2196/16973

Workspace Analysis for Laparoscopic Rectal Surgery: A Preliminary Study

Alexandra Thomieres, Dhruva Khanzode, Emilie Duchalais, Ranjan Jha, and Damien Chablat

Abstract The integration of medical imaging, computational analysis, and robotic technology has brought about a significant transformation in minimally invasive surgical procedures, particularly in the realm of laparoscopic rectal surgery (LRS). This specialized surgical technique, aimed at addressing rectal cancer, requires an in-depth comprehension of the spatial dynamics within the narrow space of the pelvis. Leveraging Magnetic Resonance Imaging (MRI) scans as a foundational dataset, this study incorporates them into Computer-Aided Design (CAD) software to generate precise three-dimensional (3D) reconstructions of the patient's anatomy. At the core of this research is the analysis of the surgical workspace, a critical aspect in the optimization of robotic interventions. Sophisticated computational algorithms process MRI data within the CAD environment, meticulously calculating the dimensions and contours of the pelvic internal regions. The outcome is a nuanced understanding of both viable and restricted zones during LRS, taking into account factors such as curvature, diameter variations, and potential obstacles. This paper delves deeply into the complexities of workspace analysis for robotic LRS, illustrating the seam-

A. Thomieres · E. Duchalais
Centre Hospitalier Universitaire, 44000 Nantes, France
e-mail: alexandra.thomieres@chu-nantes.fr

E. Duchalais
e-mail: emilie.dassonneville@chu-nantes.fr

D. Khanzode · R. Jha
CSIR-Central Scientific Instruments Organisation, 160030 Chandigarh, India
e-mail: dhruva.csio20a@acsir.res.in

R. Jha
e-mail: ranjan.jha@csio.res.in

Academy of Scientific and Innovative Research (AcSIR), 201002 Ghaziabad, India

D. Khanzode · D. Chablat
UMR 6004, École Centrale Nantes, Nantes Université, CNRS, LS2N, 44000 Nantes, France

D. Chablat (✉)
Research Center for Industrial Robots Simulation and Testing, Technical University of Cluj-Napoca, 400114 Cluj-Napoca, Romania
e-mail: damien.chablat@cnrs.fr

D. Pisla et al. (eds.), *Advances in Service and Industrial Robotics*, Mechanisms and Machine Science 157, https://doi.org/10.1007/978-3-031-59257-7_15

less collaboration between medical imaging, CAD software, and surgical robotics. Through this interdisciplinary approach, the study aims to surpass traditional surgical methodologies, offering novel insights for a paradigm shift in optimizing robotic interventions within the complex environment of the pelvis.

Keywords Laparoscopic rectal surgery · Magnetic resonance imaging · Workspace analysis

1 Introduction

In the field of minimally invasive surgical procedures, the fusion of medical imaging, computational analysis, and robotic technology has significantly advanced the precision and efficacy of the procedures. Despite the implementation of robotic assistance, laparoscopic rectal surgery (LRS) remains one of the most difficult procedure due to the narrowness of the workspace into the pelvis. Understanding the spatial dynamics and complexity of the human pelvic workspace is important for optimizing the performance of robotic systems used in these procedures. This requires a comprehensive workspace analysis, where Magnetic Resonance Imaging (MRI) scans serve as the foundational data source, providing detailed anatomical information.

The use of pelvic MRI before LRS has progressively become the gold standard of analysis, surpassing other techniques like endorectal ultrasound and CT-scanning [3, 6]. Over the past two decades, the consistent improvement in MRI quality has positioned it as one of the most effective examination procedures for the anatomical analysis of pelvic tissues. The integration of MRI slices into Computer-Aided Design (CAD) software could stand as a pivotal step in understanding the complex geometry of the pelvis. This integration allows for the creation of three-dimensional (3D) reconstructions that faithfully replicate the patient's anatomy. These reconstructions, derived from high-resolution MRI scans, serve as the virtual models upon which the subsequent workspace analysis could be carried out for robotic surgical equipment and tools.

The workspace analysis, a critical feature of this study, involves differentiating the feasible and restricted zones within the pelvis that can be crossed by robotic instruments during a LRS. By employing advanced computational algorithms within the CAD environment, the software processes the comprehensive MRI data to precisely calculate the dimensions and contours of the pelvis area. This computational procedure facilitates a better understanding of the workspace, considering factors such as dimensions, curvature, diameter variations, and potential obstacles.

This paper describes the methodology of the fusion of medical imaging, CAD modeling, and robotic apparatus utilising raw MRI data from the patients and using it to generate a virtual 3D CAD model. The aim is to facilitate the analysis and optimisation of available workspace for a robotic surgical tool during minimally invasive laparoscopic surgery [7, 11].

2 Medical Imaging

Medical imaging allows us for a clear visualization of the muscles of the pelvic floor, blood vessels, and a distinct identification of the soft tissues surrounding the rectum [5]. Numerous studies have investigated whether 2D pelvimetry could predict the difficulty of total mesorectal excision in patients operated for rectal resection [14]. The narrowness of the pelvis can be estimated by several measurements obtained from MRI imaging, including obstetric conjugate, pelvic depth, sacral curvature angle, sacral depth, transverse diameter, interspinous distance, and intertuberous distance. These measurements are associated with intraoperative difficulty, in terms of operative duration or intraoperative blood loss [1, 2, 8, 9, 12].

Three-dimensional reconstruction could improve pelvic evaluation and facilitate pelvimetry and is frequently performed in gynecology and urology, but it remains uncommon in colorectal surgery [4, 10]. Virzi et al. explored the mapping of pelvic tumors in children using 3D Slicer software [13]. It could provide improved visibility of the pelvic space by delineating the bony structure, soft tissues, and the genitourinary system. Such visualization could enhance the understanding of challenges encountered during surgery and better estimate the area available to maneuver surgical instruments.

3 Methodology

This retrospective study included patients with rectal cancer (within 15 cm of the anal verge) who had undergone preoperative MRI with the T2 sequence available on our software and surgical resection by laparoscopy between 2020 and 2023. Patients were informed that their data could be used for research.

Radiological study: For pelvic and rectal imaging, T2-weighted MRI images were acquired in the Axial, Coronal, and Sagittal planes. The images were exported using the CHU Nantes radiology software, CARESTREAM Vue PACS (version 12.1.6.1005, CARESTREAM Health, New York, USA). For pelvic volumetry, DICOM data from selected patients were analyzed using open-source software, 3D Slicer image computing platform (version 5.4.0). In the Axial section, the region studied is delimited cranially by the promontory and caudally by the top of the anal canal. The distal limit of stapling was located 1 cm above the superior pole of the internal sphincter.

The pelvic cavity was divided into six zones, as depicted in Fig. 1:

- The working area (green), is the most accessible, the stapler can run smoothly by compressing the fatty mesorectal tissue.
- Bones (blue), are hard and incompressible in nature.
- Genito-urinary system (red): The bladder was considered empty due to the presence of a urinary catheter during surgery. In men, prostate and seminal vesicles were included in this zone. In women, since the uterus can be fully mobilized

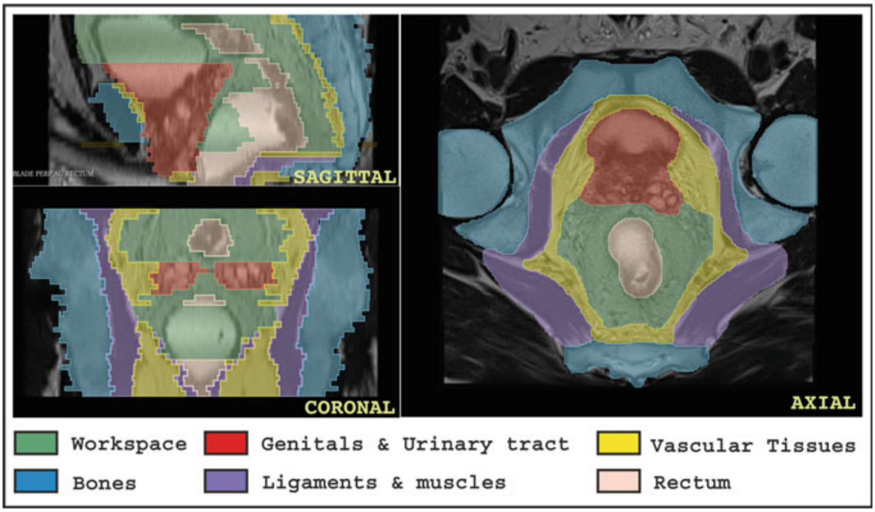

Fig. 1 Marked MRI with differentiation of tissues in Axial, coronal, and Sagittal plane

anteriorely during surgery, we opted to neglect it and instead used the cervix to delineate the upper part of the female genitourinary tract.

- Vasculo-fatty tissues (yellow) encompass the ureters, iliac vessels, pre-sacral fascia, and certain nerves. This area exhibits low compressibility.
- Muscles and ligaments (purple) are hardly compressible.
- The rectum is represented in the color beige. In some MRI, rectal gel was used to facilitate the intraluminal visualization of the tumor. To mitigate any bias associated with rectal filling, we intentionally reduced the size of the rectum to mimick an empty rectum (no intraluminal space) as during surgery.

The tumour was not separately delimited but rather included within the rectum area. Contours of the areas were manually traced on all available axial images only for each patient. After axial delimitation, the contours were reviewed and adjusted as needed in sagittal and coronal planes. Section thickness varied among patients, ranging between 3 and 4.20 mm based on MRI specifications. The overall data was analyzed based on the patient's gender and BMI of the particular patient.

Subsequently, a 3D reconstruction of the pelvic cavity based on the marked MRI data was generated, as represented in Fig. 2, and the workspace area (green) was isolated within the cluster of various marked zones, as depicted in Fig. 3. The data was then exported in the CAD-compatible *.stl* format for analysis by the experienced design engineers.

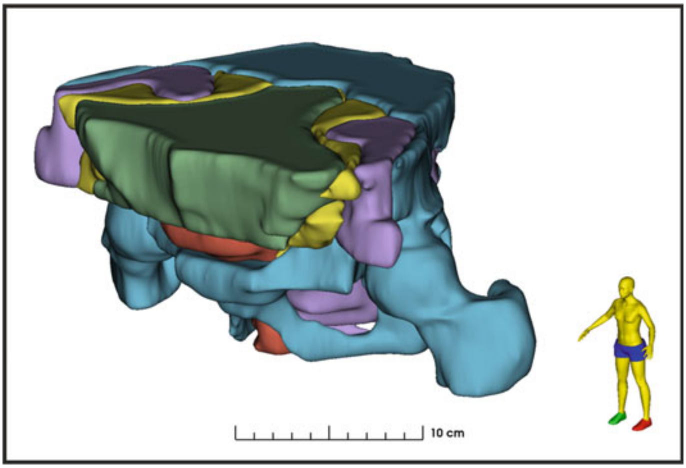

Fig. 2 3D representation of pelvic cavity using MRI data showing all the six zones

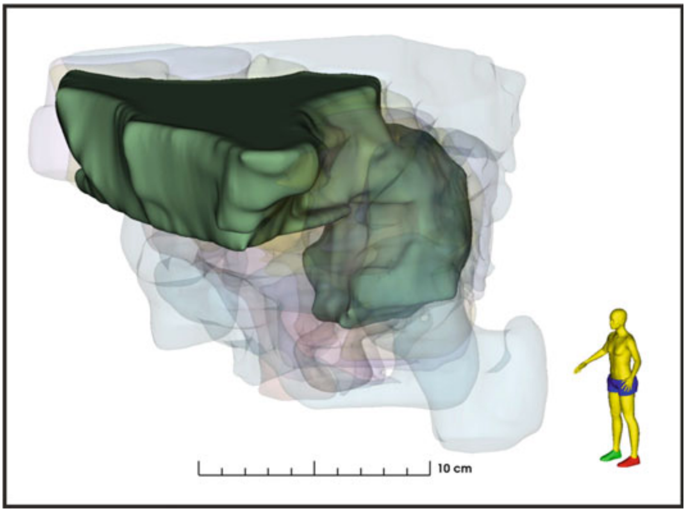

Fig. 3 3D representation of pelvic MRI data highlighting solely the working area

4 Workspace Analysis

In this section, the *.stl* files generated in the previous step are put to work. In this step, we use Computer-Aided Design (CAD) software, SOLIDWORKS (version 2023, Dassault systems, Paris, France) to carry out design analysis and workspace evaluation.

In the virtual design domain, the *.stl* files are imported into SOLIDWORKS and are converted into a modifiable *.sldprt* file format. Once the file is in *.sldprt* format, we

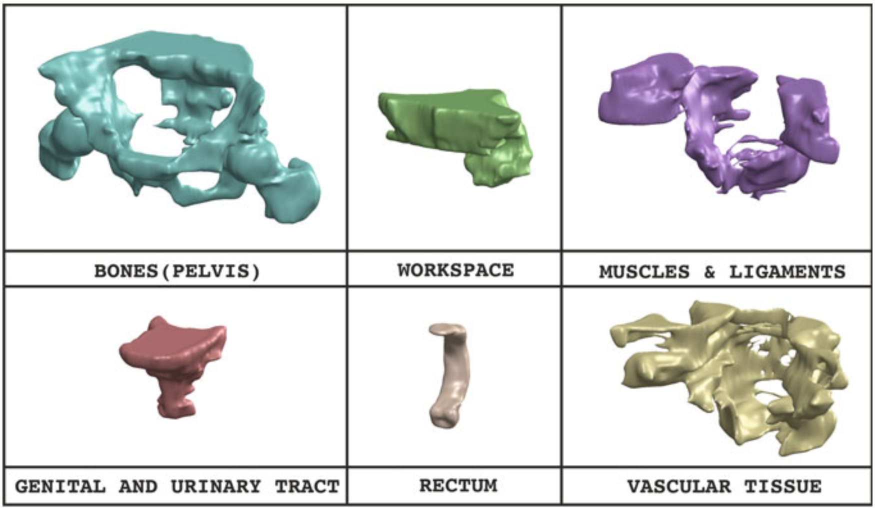

Fig. 4 3D CAD models depicting the six distinct zones within the surgical site

can perform various design operations, feature alterations, and dimensional analysis in a much effortless manner. In the previous step, when *.stl* files were generated for each and every tissue type, like Bones, Ligament, Vascular Tissue etc. that each file is to be imported and inspected carefully, for some isolated parts that needed to be removed before analysis. The 3D digital models of each and every tissue type in SOLIDWORKS are depicted in Fig. 4. Once all the parts are inspected and converted successfully, all parts are to be combined to generate a mechanical assembly of the system. After the assembly is successfully carried out, we need to compare it with the 3D representation generated by the 3D Slicer software in the previous step.

After this step, we mainly focus on the "workspace" or the "working area" 3D CAD model as depicted in Fig. 5. The internal dimensional tools of SOLIDWORKS software can be used to calculate the dimensional data such as centre of mass, overall surface area, and total volume of the model body. This dimensional data, specifically the volumetric data can be utilized to determine the workspace for the robotic tool during minimally invasive surgical procedures. The dimensional and structural data obtained provided us with valuable insights into anatomical constraints and variations in the workspace due to differences in patient types. In this study, we included both male and female patients with diverse body shape. Our observations highlighted that, from a workspace perspective, the total available workspace is greater in female patients than in male patients, suggesting anatomical constraints that differ between genders. Furthermore, we concluded that the actual site for maneuvering the robotic surgical tool is constrained to the lower half of the total available free workspace, and the shape of the functional workspace is similar to a concentric cylindrical structure.

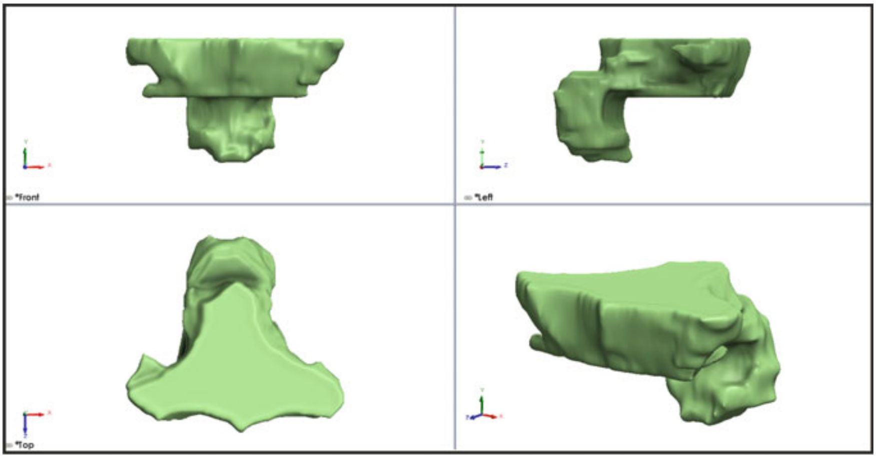

Fig. 5 Front, Left, Top, and Isometric views of 3D workspace from CAD software

5 Conclusions and Future Work

In summary, this article presents a methodology that involves utilizing raw MRI data to construct a functional 3D CAD model. This process includes precise tissue identification, marking, and data refinement to develop a CAD model that can be analyzed both dimensionally and volumetrically. Additionally, our preliminary findings indicate a greater total workspace in female patients compared to male patients, although other physiological parameters also probably contribute to workspace availability. Looking ahead, our future plans will involve studying of the anatomical properties of 40 patients representative of the epidemiological data for both female and male groups in our hospital. Then, a more in-depth analysis of the CAD model will be conducted to precisely determine the available workspace for robotic surgical tools near the surgical site and allow the surgeon to anticipate the surgical strategy. This analysis will contribute to the development of a robotic surgical tool specifically designed to facilitate minimally invasive LRS.

Acknowledgements This research was supported by CSIR-Central Scientific Instruments Organization, Chandigarh, India, Centre Hospitalier Universitaire de Nantes, and Centrale Nantes, France. This research is funded by the Indian Council of Medical Research, New Delhi, India under the "Senior Research Fellowship" (File no.5/3/8/46/ITR-F/2022) and Centrale Nantes, Nantes, France under Contrat doctoral privé (décret 2021–1233) awarded to Mr. Dhruva Rajesh Khanzode & by AMI CHU /Centrale Nantes financing, awarded to Ms. Alexandra Thomieres. This research was supported by the project New Smart and Adaptive Robotics Solutions for Personalized Minimally Invasive Surgery in Cancer Treatment - ATHENA, funded by the European Union - NextGenerationEU and Romanian Government, under National Recovery and Resilience Plan for Romania, contract no. 760072 /23.05.2023, code CF 16/15.11.2022, through the Romanian Ministry of Research, Innovation and Digitalization, within Component 9, investment I8.

References

1. Akiyoshi, T., Kuroyanagi, H., Oya, M., Konishi, T., Fukuda, M., Fujimoto, Y., Ueno, M., Miyata, S., Yamaguchi, T.: Factors affecting the difficulty of laparoscopic total mesorectal excision with double stapling technique anastomosis for low rectal cancer. Surgery **146**(3), 483–489 (2009)
2. Atasoy, G., Arslan, N.C., Elibol, F.D., Sagol, O., Obuz, F., Sokmen, S.: Magnetic resonance-based pelvimetry and tumor volumetry can predict surgical difficulty and oncologic outcome in locally advanced mid-low rectal cancer. Surgery Today **48**(12), 1040–1051 (2018)
3. Brown, G., Davies, S., Williams, G., Bourne, M., Newcombe, R., Radcliffe, A., Blethyn, J., Dallimore, N., Rees, B., Phillips, C., et al.: Effectiveness of preoperative staging in rectal cancer: digital rectal examination, endoluminal ultrasound or magnetic resonance imaging. British J. Cancer **91**(1), 23–29 (2004)
4. Doumouchtsis, S.K., Nazarian, D.A., Gauthaman, N., Durnea, C.M., Munneke, G.: Three-dimensional volume rendering of pelvic models and paraurethral masses based on MRI cross-sectional images. Int. Urogynecology J. **28**(10), 1579–1587 (2017)
5. Hong, J.S., Brown, K.G., Waller, J., Young, C.J., Solomon, M.J.: The role of MRI pelvimetry in predicting technical difficulty and outcomes of open and minimally invasive total mesorectal excision: a systematic review. Tech. Coloproctol **24**(10), 991–1000 (2020)
6. Jhaveri, K.S., Sadaf, A.: Role of mri for staging of rectal cancer. Expert Rev. Anticancer Therapy **9**(4), 469–481 (2009)
7. Khanzode, D., Jha, R., Thomieres, A., Duchalais, E., Chablat, D.: Surgical staplers in laparoscopic colectomy: a new innovative flexible design perspective. Robotics **12**(6), 156 (2023)
8. Killeen, T., Banerjee, S., Vijay, V., Al-Dabbagh, Z., Francis, D., Warren, S.: Magnetic resonance (MR) pelvimetry as a predictor of difficulty in laparoscopic operations for rectal cancer. Surg. Endosc. **24**(12), 2974–2979 (2010)
9. Kim, J.Y., Kim, Y.W., Kim, N.K., Hur, H., Lee, K., Min, B.S., Cho, H.J.: Pelvic anatomy as a factor in laparoscopic rectal surgery: a prospective study. Surgical Laparoscopy, Endosc. Percutaneous Tech. **21**(5), 334–339 (2011)
10. Lenhard, M., Johnson, T., Weckbach, S., Nikolaou, K., Friese, K., Hasbargen, U.: Three-dimensional pelvimetry by computed tomography. Radiologia Medica **114**(5), 827–834 (2009)
11. Pisla, D., Plitea, N., Gherman, B., Pisla, A., Vaida, C.: Kinematical analysis and design of a new surgical parallel robot. In: Computational Kinematics: Proceedings of the 5th International Workshop on Computational Kinematics, pp. 273–282. Springer (2009)
12. Teng, W., Liu, J., Chen, M., Zang, W., Wu, A.: BMI and pelvimetry help to predict the duration of laparoscopic resection for low and middle rectal cancer. BMC Surgery **22**(1), 1–7 (2022)
13. Virzì, A., Muller, C.O., Marret, J.B., Mille, E., Berteloot, L., Grévent, D., Boddaert, N., Gori, P., Sarnacki, S., Bloch, I.: Comprehensive review of 3D segmentation software tools for MRI usable for pelvic surgery planning. J. Digital Imaging **33**(1), 99–110 (2020)
14. Zhang, Q., Wei, J., Chen, H.: Advances in pelvic imaging parameters predicting surgical difficulty in rectal cancer. World J. Surg. Oncol. **21**(1), 1–9 (2023)

An Analysis of Virtual Reality Applications in Rehabilitation Engineering

Cosmin-Ilie Coția and Silviu-Dan Mândru

Abstract The application of science and technology for more efficient medical rehabilitation processes has led to the inclusion of new fields such as Virtual Reality (VR) and Augmented Reality (AR) among specific approaches of Rehabilitation Engineering and Assistive Technology. The primary goal of this paper is to identify what are the most common VR solution in rehabilitation engineering, and suggest directions for the future research. In terms of research methodology, this paper involved identification of relevant publications through keyword searches and bibliometric analysis. As results we identified the key medical domains where virtual reality has a significant impact with measurable results. In this paper, the Virtual Reality impact on research in the rehabilitation engineering field is emphasized and analyzed. Representative examples of VR and AR systems are studied and future research and development topics are identified.

Keywords Virtual reality · Augmented reality · Rehabilitation engineering · 3D visualization · Body tracking

1 Introduction

Rehabilitation Engineering is an interdisciplinary component of Biomedical Engineering dealing with the study of mechanical, electronic, electrical and computer systems and their integration in the area of motor, sensorial and cognitive rehabilitation equipment [1–3]. Its role is to enable individuals with special needs to be more independent, self-confident, and integrated into society. To the traditional

C.-I. Coția (✉) · S.-D. Mândru
Technical University of Cluj-Napoca, Memorandumului Str. No. 28, Cluj-Napoca, Romania
e-mail: cosmin.cotia@mdm.utcluj.ro

S.-D. Mândru
e-mail: dan.mandru@mdm.utcluj.ro

C.-I. Coția
SC RehabVR SRL, Bună Ziua Str. No. 35D, Cluj-Napoca, Romania

D. Pisla et al. (eds.), *Advances in Service and Industrial Robotics*, Mechanisms and Machine Science 157, https://doi.org/10.1007/978-3-031-59257-7_16

rehabilitation products and systems (prostheses, orthoses, wheelchairs/ mobility aids, exercisers, aids for daily living, augmentative/alternative communication, rehabilitation robotics, aids for hearing and vision impaired), new opportunities given by new fields such as Virtual Reality (VR) and Augmented Reality (AR) are added.

The definition of virtual reality has many forms. Still, the most representative description refers to simulation in an environment generated by a computer system, hardware, and software being composed of images and videos, so instead of looking at a screen, the user can interact with a 3D world, [4]. Are many scientifically papers that presenting concrete applications of VR in rehabilitation engineering [3, 5, 6], from perspective of an original approach the analysis of these results is relatively small.

Stroke is one of the main causes leading to disability, so people who suffer a stroke are affected both at the cognitive and motor levels [5]. Neurorehabilitation following a stroke is important for the recovery of motor activities, conventional rehabilitation is occupational therapy that has the role of directing the patient toward participation in activities that help them restore mobility [1, 7]. Virtual reality opens up new opportunities in the recovery process, VR can increase neuroplasticity, which is the brain's ability to adapt to certain situations, experiences, and new environments, but also to sudden changes or trauma [1]. The composition of this paper is structured as it follows: Chapter Two, "Research Strategy" we make an examination of pertinent papers that are required for our research. Subsequently, Chapter Three, "Analysis of Virtual Reality Impact on Rehabilitation", at the end we close with extracting the final conclusion and establish the following directions for our research.

2 Research Strategy

In the process of data, the acquisition the keywords in English as "*virtual reality*", and "*augmented reality*" were associated with "*rehabilitation engineering*", or "*medical recovery*", thus, approximately 7000 articles were collected from 1993 until this research began, and only the most relevant research will be extracted from them.

Figure 1 shows the type of scientific papers and publications analyzed and the number of publications per year, the main types of publications being articles, reviews, books, editorials, corrections, or republicans.

To extract the most relevant articles we analyze the keywords of the title (Fig. 2). It can be seen the pathology that is addressed and the average age of patients, which is for all age categories from children to elderly people. Some pathologies that are addressed are: stroke, limb rehabilitation, gait rehabilitation cerebral palsy, etc. [8]. To ensure that the results are as relevant as possible, close cooperation between the research fields is needed [4, 7].

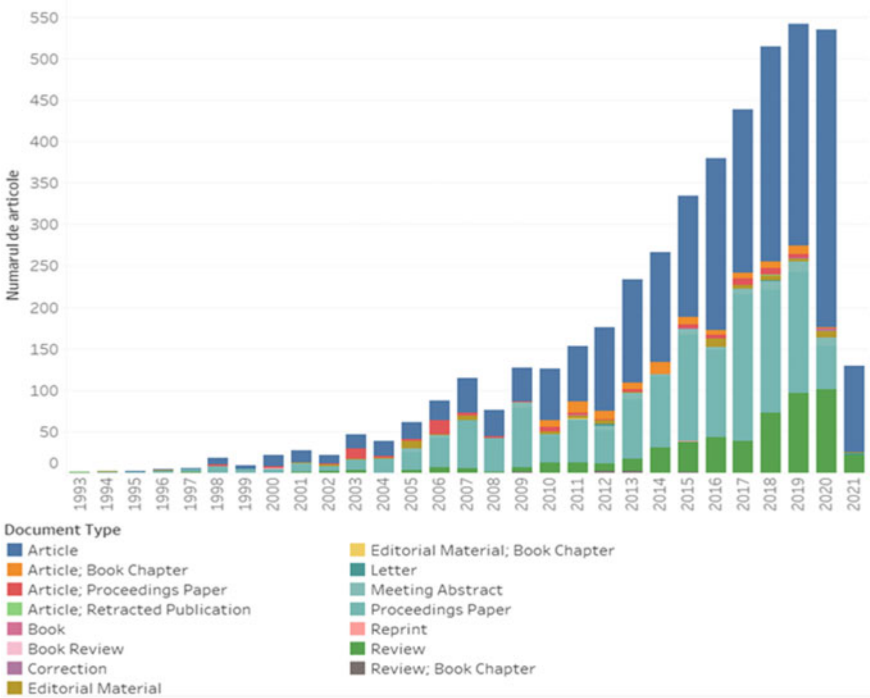

Fig. 1 Distribution of papers based on the number of publications and trend evolution in years

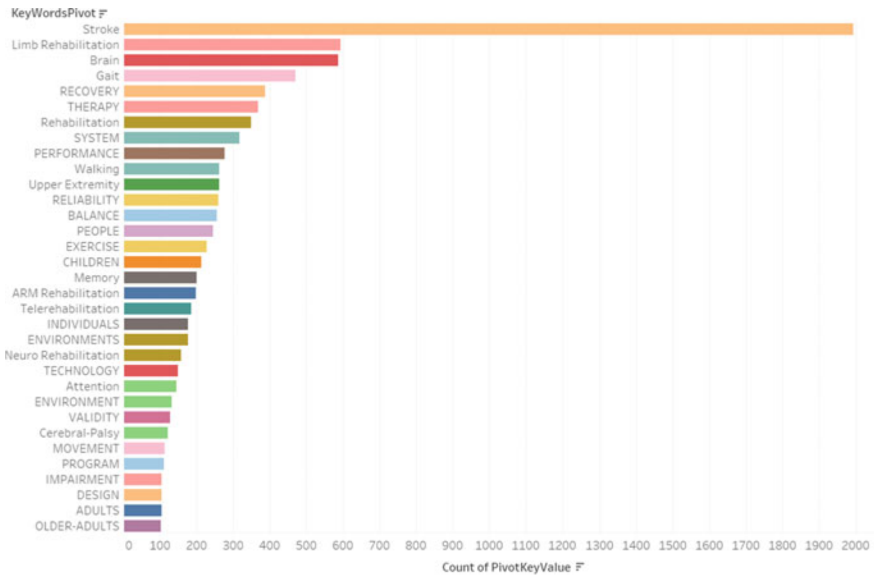

Fig. 2 Analysis of pathology research in the context of virtual reality

3 Analysis of Virtual Reality Impact on Rehabilitation

Virtual reality is defined as experiencing a virtual environment and is the easiest achieved by introducing a participant in the entire peripheral vision in a virtual environment through a head-mounted display (HMD).

The area where virtual reality is most present today is the video game industry according to a study it was valued at $11.56 billion in 2019 with a 30% growth forecast between 2020 and 2027, [1, 2, 7].

Table 1 gives an analysis of the main applications of virtual reality and augmented reality in the context of rehabilitation approaches [5, 7, 9].

In the following, we will analyze several applications that use virtual and augmented reality in rehabilitation processes.

The research presented in [10] aims to use the MIRA software platform to investigate the effectiveness of the immersive and non-immersive virtual environment in neuromotor rehabilitation for people who have had a stroke, with a study duration of 9 months on a total of 55 patients, [10]. The technology used is composed of a 55-inch TV, a PC running Mira Rehab limited (software component specialized in virtual recovery), and sensors from Microsoft Kinetic that allow the detection of body movements, and movement of the wrists on the 3 axes. The Mira system is a system for telerehabilitation, which helps to improve the effectiveness and interaction between physiotherapists and patients in the recovery process, Microsoft Kinect sensors are used to calibrate the patient's position at the beginning of VR sessions, and the application requires the presence of a physiotherapist to evaluate AROM

Table 1 Analysis of applied medical applications of virtual reality and augmented reality

Medical application	Assessment criteria	Virtual/Augmented reality component	Keywords
Stroke	Motor function	Virtual reality and augmented reality	Stroke, heart attack
Clinical psychology	Impact of personal change	Virtual reality	VR, psychology
Mental illness	Reducing depression, anxiety	Virtual reality	Depression, anxiety
Orthopedic rehabilitation	Motor/muscle rehabilitation	Virtual reality and augmented reality	Orthopedic
Neuro-rehabilitation	Recovery of motor activities	Virtual Reality	Neurological
Neuropathy	Improvement of the nervous system	Virtual Reality	Plexopathy
Geriatrics and gerontology	Everyday activities	Improvement of the nervous system	Neurology
Osteoporosis	Skeletal system	Virtual Reality	Bones
Pediatric	Playing motor	Augmented Reality	Mobility

(Active Range of Motion) the selection of motion type and exercise for VR therapy will be made, [10].

The application of virtual reality in the context of mental illness and depression shows that VRET (Virtual reality Expo Therapy) can be effective in both directions both for reducing depression caused by phobias or fears and for investigating the psychological processes and mechanisms associated with psychosis, [3]. Virtual reality is an articular medium that contains sensory information, the scope in the context of psychological or psychological recovery being a fairly broad one we will remember only some of them such as PTSA, anxiety, phobias, schizophrenia, ADHD, autism or pain management as an alternative to pharmacological treatments, [3].

The effectiveness of individuals performing certain exercises in the virtual environment has been analyzed, so adaptability leads to improved motor functions, if the virtual reality system is allowed to adapt to the needs of the individual; there are both mental and physical stimulation, interactivity helps improve levels of involvement in the execution of tasks, the feedback components and the purpose of pregnancy did not produce significant motor performance results, [11].

The paper [5] examined the effects of video games in virtual reality and the introduction of positive emotions over negative ones, as well as the assessment of anxiety states of players. The study was conducted on 36 young people. Video games are applied the fastest technology of virtual reality due to the experience of digital information that video game developers possess. Positive emotions are those that increase self-esteem and improve quality of life, which is the main reason people buy digital video games, the difference between classic games and those in the virtual environment is that the user's involvement in virtual reality is much higher, the body is the main interface between the virtual environment and the user.

Occupational therapy plays an important role in rehabilitation, the paper [6] focuses on assessing the effectiveness of virtual reality in occupational therapy for patients who have suffered a cardiovascular attack, so studies have been analyzed that have examples of rehabilitation systems with virtual reality components. Principles have been extracted that have shown efficiency in motor recovery, these being: Large-scale executions, the possibility of increasing the intensity of exercises, the structure of the contents of exercises, specific exercises for patients according to the need, the possibility of variation of exercises, much sensory stimulation, increased level of difficulty, feedback both implicitly and explicitly, human representation in the form of avatar in the virtual reality environment, so these principles integrated into a system can have a significant impact on motor recovery in the upper arms.

Clinical psychology is often used to facilitate changes at the personal level when individuals do not have this ability to change such as in critical illness situations. The paper [12] is based on the impact of virtual reality and augmented reality components in the external transformation of human experience focusing on personal efficiency, meditating and generating a sense of fulfillment and emotional involvement. The ultimate goal is to generate new experiences with the ability to transform and generate knowledge that otherwise would be inaccessible only if they lived a real-world experience. Throughout human experience, individuals go through several stages of change (we change homes, schools, workplaces, sometimes even friends or life partners), and all of these changes affect us as individuals. but studies show that in some situations, subjects cannot change even if they really want to.

In their research [3], the author makes a selection of the main current VR applications for improving the quality of life here we can list: immersing individuals in a virtual reality environment with the help of HDM glasses and experimenting with various games that involve walking attention but also memory; another application is the navigation of a street in VR environment, but also music therapy with the help of VR environment. The main results were the prevention of falls, elimination or reduction of anxiety, depression, improvement of daily activities, improvement of cognitive functions such as memory. In all cases, individuals were completely immersed in the VR environment so HDM glasses and auxiliary elements for tracking body movements were used. The results are recorded in cognitive aspects such as memory or psychological aspects, but also in the prevention of falls where the use of a virtual environment immersed with the help of HDM glasses has a significant impact, VR experiences prevent or eliminate fear of falling and increase individuals' level of confidence in real experiences [3].

4 Conclusions

Virtual reality has a broad range of applications when it comes to rehabilitation, bringing together knowledge from different industries like Gaming, Rehabilitation Engineering, and Health. Thus, complex systems can be created to solve and help people to recover much faster and treat them with a more holistic approach.

The main advantages when it comes to virtual reality in the context of rehabilitation are instant feedback, the possibility to give patients a real context, simulation activities in a safe environment, and an impact on multiple sides neurological and motor. Also, a main advantage that is worth to be mentioned is Virtual Reality will allow remote rehabilitation. Disadvantages of virtual reality in rehabilitation are related to the complexity of the development and hardware limitations in some cases, but also a very high percentage of people are affected by virtual reality (especially the first time they use it, the effect is called "cybersickness" and affect roundabout 40% of users). We have seen a big interest in virtual reality also in the hardware industry in the last 10 years we have a lot of innovation in this field, and this will be for sure very beneficial for those who want to apply VR in rehabilitation.

The integration of Virtual Reality in rehabilitation practices offers innovative and effective ways to improve patient recovery. Also, it‘s important to consider the cost and hardware limitations when designing and implementing VR solutions in clinical applications.

According to our research, we choose to start with virtual reality non-immersive for the following milestone, the main goal is to investigate state-of-the-art hardware and software solutions in rehabilitation engineering and start working on a functional prototype that can be tested in the first phase with healthy people afterward we will try to identify rehabilitation centers that can help us to test with real patients. Future research will focus on iterative development, and get deeper in applications using virtual reality with a non-immersive approach for rehabilitation. We aim to architect and develop an application dedicated to upper limb rehabilitation, for this our plan is to make a non-immersive virtual reality framework that can be extended later on and can be applied on different use cases for upper limb rehabilitation. The scope is to create a user experience much different from traditional rehabilitation and fill the gap between digital interaction and physical rehabilitation exercises. By doing this we aim to change rehabilitation processes and making more engaging, intuitive, and effective. This approach is not only to enhance the effectiveness of rehabilitation exercises but also how patients will interact with their rehabilitation journey. The main objective of future research is to develop, optimize, and integrate an real-time arm motion tracking with correlation of virtual scenarios, also in the end we plan to conduct clinical trials to evaluate the efficacy and overall user experience of our application.

References

1. Berton, A., Longo, U.G., Candela, V., Fioravanti, S., Giannone, L., Arcangeli, V., Alciati, V., Berton, C., Facchinetti, G., Marchetti, A., Schena, E., De Marinis, M.G., Denaro, V.: Virtual reality, augmented reality, gamification, and telerehabilitation: psychological impact on orthopedic patients' rehabilitation. PMCID: PMC7465609 (2020)
2. ReportLinker: Homepage. [Website]. Available: https://www.reportlinker.com/p05819727/Global-Mixed-Reality-Industry.html?utm_source=GNW. Accessed (2021)
3. Felsberg, D.T., Maher, J.P., Rhea, C.K.: The state of behavior change techniques in virtual reality rehabilitation of neurologic populations. PubMed.gov, PMID: 31139106 (2019)
4. Kim, W.-S., Cho, S., Ku, J., Kim, Y., Lee, K., Hwang, H.-J., Paik, N.-J.: Clinical application of virtual reality for upper limb motor rehabilitation in stroke: review of technologies and clinical evidence. PMID: 33096678 (2020)
5. Maier, M., Ballester, B.R., Duff, A., Oller, E.D., Verschure, P.F.M.J.: Effect of specific over nonspecific VR-based rehabilitation on poststroke motor recovery: a systematic meta-analysis. Web of Science (2019)
6. Riva, G., Baños, R.M., Botella, C., Mantovani, F., Gaggioli, A.: Transforming experience: the potential of augmented reality and virtual reality for enhancing personal and clinical change (2016)
7. Perez-Marcos, D.: Virtual reality experiences, embodiment, videogames and their dimensions in neurorehabilitation. PubMed.gov, PMCID: PMC6258149 (2018)
8. Clarivate: Homepage. [Website]. Available: https://clarivate.libguides.com/webofscienceplatform/coverage. Accessed (2021)
9. Weber, L.M., Nilsen, D.M., Gillen, G., Yoon, J., Stein, J.: Immersive virtual reality mirror therapy for upper limb recovery after stroke: a pilot study. PubMed.gov, PMCID: PMC6697203 (2019)
10. Miclaus, R., Roman, N., Caloian, S., Mitoiu, B., Suciu, O., Onofrei, R.R., Pavel, E., Neculau, A.: Non-immersive virtual reality for post-stroke upper extremity rehabilitation: a small cohort randomized trial. PubMed.gov, PMCID: PMC7563455 (2020)
11. Pallavicini, F., Pepe, A.: Virtual reality games and the role of body involvement in enhancing positive emotions and decreasing anxiety: within-subjects pilot study. PubMed.gov, PMCID: PMC7330737 (2020)

12. Dermody, G., Whitehead, L., Wilson, G., Glass, C.: The role of virtual reality in improving health outcomes for community-dwelling older adults: systematic review. PubMed.gov, PMCID: PMC7296414 (2020)

Low-Cost Functional Infrared Spectroscopy Based System as a Brain-Computer Interface

Ana Cristina Feneşan, Alexandru Ianoşi-Andreeva-Dimitrova, and Dan Silviu Mândru

Abstract Functional infrared spectroscopy is a non-invasive, non-ionizing imaging method for measuring the functional hemodynamic response to brain activity. This study aims to explore the method, proposing the development of a functional prototype to measure hemodynamic activity on the scalp. At first, we outlined the application of functional infrared spectroscopy in scalp hemodynamic monitoring. The state-of-the-art section delves into the theoretical foundations of photoplethysmography, its functioning, physiological aspects, and clinical importance. Also, it discusses the current state of scalp hemodynamic monitoring systems, the principles of infrared spectroscopy, advantages, limitations, and relevant literature examples. We aimed to create an experimental demonstrator, from modeling to circuit design, assembly, and testing. The conclusions present the need for a non-invasive neuronal interfacing method, personal contributions, and potential future research directions.

Keywords Infrared spectroscopy · Hemodynamic · Non-Invasive · Photoplethysmography · Oxygen saturation

1 Introduction

Functional infrared spectroscopy is a non-invasive, non-ionizing imaging method used to measure the functional hemodynamic response to brain activity. The fundamental principle of photoplethysmography technology involves the use of a limited set of optoelectronic components, such as a light source illuminating the tissue and a

A. C. Feneşan (✉) · A. Ianoşi-Andreeva-Dimitrova · D. S. Mândru
Department of Mechatronics and Machine Dynamics, Technical University of Cluj-Napoca, Cluj-Napoca, Romania
e-mail: Ana.Fenesan@campus.utcluj.ro

A. Ianoşi-Andreeva-Dimitrova
e-mail: Alexandru.Ianosi@mdm.utcluj.ro

D. S. Mândru
e-mail: Dan.Mandru@mdm.utcluj.ro

D. Pisla et al. (eds.), *Advances in Service and Industrial Robotics*, Mechanisms and Machine Science 157, https://doi.org/10.1007/978-3-031-59257-7_17

photodetector measuring small variations in light intensity correlated with changes in the volume of blood vessels based on arterial pulsation.

Arterial and venous blood, having different colors, absorb light differently, facilitating the determination of the amount of oxygen in the blood through photoplethysmography techniques. Infrared light possesses remarkable penetration capabilities, reflecting the blood pulse from deeper tissue layers, making it a preferred choice in various medical and monitoring applications.

By utilizing infrared light, physiological parameters such as blood pressure, hepatic clearance, and blood sugar levels can be non-invasively and accurately detected. Functional infrared spectroscopy thus becomes an accessible technique, not entailing high costs and providing precise results, proving valuable in determining cerebral hemodynamic activity.

This technique holds significant potential in diagnosing neuropsychiatric and neurological disorders, offering the ability to monitor cerebral activity without inducing physiological stress. Through this work, the proposal is to research, model, and develop a functional demonstrator based on functional infrared spectroscopy to monitor cerebral hemodynamic activity and provide real-time results related to oxygen supply based on various activities.

In this paper we present the process in which a low-cost non-invasive near-infrared spectroscopy system was created and preliminary explored if it could serve as a Brain-Computer Interface instead of the traditional method that makes use of electroencephalography.

2 State of the Art

The principle of photoplethysmography is based on measuring the amount of light absorbed or reflected by the blood vessels in living tissue. Photoplethysmography is most commonly utilized in clinical settings for pulse oximetry. This technique relies on the use of a pulse oximeter, a device that measures the oxygen saturation in the blood. This technology is becoming increasingly available, user-friendly, cost-effective, and more easily integrated into the portable devices we commonly use.

Recent market advancements include the development of smartphones and devices such as watches or bracelets that collect pulse oximeter signals [1].

The photoplethysmography waveform is generated by the pulsatile changes in the optical density of tissue, primarily induced by arterial pulsations, which are notably robust and influential [2].

Photoplethysmography employs the arterial pressure wave to assess the patient's response to fluid levels in the body, enabling the computation of cardiac output based on the volume of fluid within the circulatory system. The optical absorption or reflection of light is contingent upon the quantity of oxygenated blood within the optical path, particularly within the blood vessels, causing the photoplethysmogram signal to predominantly capture variations in blood volume rather than the pressure within the blood vessels.

Consequently, photoplethysmography detects changes in blood volume through photoelectric techniques, whether they be transmissive or reflective. It generates a signal by recording the blood volume within the sensor's coverage area [3].

As oxygenated and deoxygenated hemoglobin exhibit different light absorption characteristics, the level of tissue oxygenation can be assessed by illuminating the tissue and measuring the quantity of unabsorbed light that emerges. The infrared light used in functional spectroscopy, chosen for its ability to penetrate tissue more deeply, is instrumental in measuring cerebral oxygenation [4].

The most cost-effective spectroscopy technique for tracking hemodynamic activity on the scalp is infrared spectroscopy, offering an optimal balance between quality and price. Inexpensive LED sources have limited light penetration into tissue and are employed at shorter distances from the source to the detector (20–35 mm). Conversely, pricier laser-based sources offer greater tissue penetration, enabling imaging at deeper brain levels with larger separations between the detector and source. However, they come with considerably higher costs compared to infrared sources [5].

A significant constraint of functional infrared spectroscopy lies in its limited spatial resolution, both in depth and area of interest. A related method is diffuse optical tomography, which rely on augmenting the density of infrared light sources on the scalp and using more photosensitive detectors to improve sensitivity to overlapping signals. Subsequently, tomographic algorithms facilitate the reconstruction of 3D images depicting brain activation [6].

Prominent instances in the literature showcasing functional infrared spectroscopy recordings substantiate the method's capability to discern localized cerebral hemodynamic activity associated with events across various stimulation protocols [7].

3 Materials and Methods

In the development of a prototype device aimed at monitoring cerebral hemodynamic activity, several components were used, including LEDs, phototransistors, electrical conductors, an Arduino board, and a swimming cap for their integration. Firstly, the TCRT5000 Optical Sensor assemblies, featuring an infrared emitter and a phototransistor in close proximity were used to capture the pulsatile oxygenated blood flow at the scalp.

The TCRT5000 assemblies were positioned within a custom-designed plastic holder, modeled inside the Catia v5 CAD program, and subsequently 3D printed with a biodegradable plastic material using the Original Prusa Mk3 i3 printer. This design process ensured precise placement at the required distances for the sensor components.

For the physical integration onto the user, the plastic holders were fixed to a swim cap, chosen for its economic efficiency and its fabric's elastic properties, providing a comfortable and secure fit. The incorporation of these plastic components into the textile material of the swim cap was achieved by sewing them in place, reinforcing the structural integrity of the entire assembly.

With the sensors and LED securely in place on the plastic holders, the next phase involved the assembly of the electrical circuit. In this stage in the demonstrator's development the different components were soldered in place, without a dedicated printed circuit board, as the aim at this point was to have an operational device capable of monitoring cerebral hemodynamic activity for testing.

Subsequently, a Biomedical Measuring Unit KL7001 was utilized in conjunction with the Photoplethysmogram Measuring Unit KL75006 to amplify the signal, which was then read using an oscilloscope. The signal captured originated from capillaries on the scalp, which was the expected result given the small distance between the IR source and receptor; next, an assembly was devised where the LED and transistor are positioned at a greater distance from each other, allowing infrared light to penetrate deeper through the skull. To this end, a support structure was designed that ensures both a 35 mm distance from the IR source to the IR receptor, as well as the ability to conform for the curved surface of the head (Fig. 1). Following the fabrication of the support structure, the electrical circuit was completed. This consists of an 5 V 800 mA supply, a 33 Ω resistor to limit the current through the 4 IR LEDs, 4470 Ω pull-up resistors and 4 IR sensitive transistors. Each collector was connected to an ADC pin of an Arduino Leonardo board, which features a 10-bit precision. The radiant intensity of each IR LED is 21 mW/sr, concentrating 63% of it in a 2.1 mm diameter; the peak wavelength is at 940 nm, at which the molar extinction coefficient of oxygenated hemoglobin is 1300, respectively 700 M^{-1} cm^{-1} for deoxygenated hemoglobin. The sensing part consists of 4 silicon NPN transistor BPV11F; these have a 450 gain, 15° angle of half sensitivity and a collector light current of 9 mA at an illumination power of 1 mV/cm^2. Peak sensitivity is at 930 nm, with a spectral range between 900 and 980 nm. It features a very fast response time, it's 110 kHz cutoff frequency being more than enough to monitor hemodynamic changes.

4 Results

After the physical completion of the demonstrator, the testing phase commenced. Figure 1 illustrates the placement of the optode on the scalp, within the precentral gyrus area: The IR LEDs illuminates the C4 position, and the backscattered elliptical optical path closes at C2, C6, FC4 and CP4 positions (the nomenclature used is the same as the one used for 10–10 EEG electrode positioning system). This particular region was chosen to evaluate the demonstrator's ability to capture limb movement.

An Arduino Leonardo board was used as a capture device; each ADC channel was sampled at 200 Hz and the DC bias given by the tissue reflectivity was subtracted from the raw signal. To obtain an initial set of data, in older to highlight the movement of the left hand, the subject was instructed to remain seated, the demonstrator was placed at the designated area, and subsequently, the subject initiated movement of the upper limb, yielding the results as depicted in Fig. 2: the green areas represents

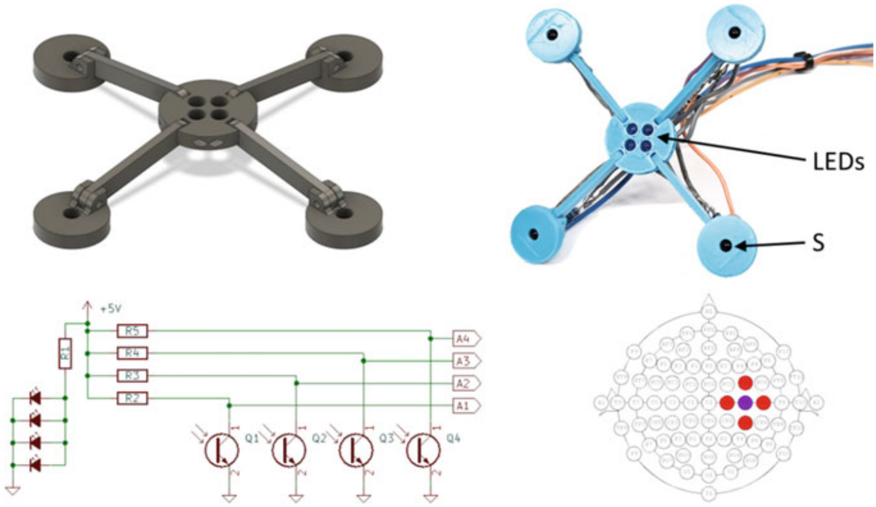

Fig. 1 The 3D modeling of the support, the electrical scheme, and the positioning of the optode on the scalp

changes in tissue opacity correlated with movement of the upper limb, whereas the red regions are uncorrelated (possibly electrical artifacts). The changes in tissue opacity are due to the increased level of metabolic activity of the neurons involved in the control of the hand movement; this increased level generates a lot more CO_2, which is captured and transported by the hemoglobin, which in turn absorbs more of the incident IR radiation.

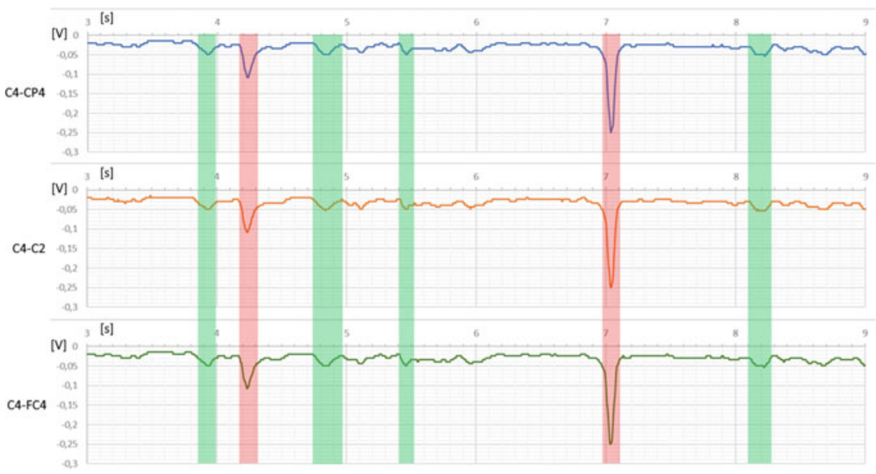

Fig. 2 The signal recorded during the movement of the left hand

Only 3 channels are shown because due to some build errors, the 4th was unusable. These signals reflect the brain hemodynamic activity between C4-CP4, C4-C2 and C4-FC4, which, due to its proximity to the motor cortex, is associated with upper limb movement at these particular positions.

Because the electrical artefacts, highlighted with red, exhibit a very sudden change in voltage with respect to time, they can be detected by computing the first and second order derivatives. The acquired signal is in discrete time domain, therefore, these derivatives are approximated using the central difference formula, as shown in Eqs. (1) and (2), for the first derivative:

$$f'(x_i) \approx \frac{f(x_{i+1}) - f(x_{i-1})}{2h} \tag{1}$$

and for the second derivative:

$$f''(x_i) \approx \frac{f(x_{i+1}) - 2f(x_i) + f(x_{i-1})}{h^2} \tag{2}$$

where $f'(x_i)$, $f''(x_i)$ are the estimated first, respectively second derivative, $f(x_{i+1})$, $f(x_i)$, $f(x_{i-1})$ are the values of the function at neighboring points and h is the constant sampling interval, equal to 0.005 s.

Despite of the small amount of noise in the acquired signal, numerically approximating the first and second derivatives in this manner greatly amplify it, therefore, before computing the first derivative, the signal was filtered with a moving average window of 5 samples, respectively before computing the second derivative, the signal was filtered with a moving average window of 17 samples. Figure 3 illustrates the result of this process for the signal acquired at the C4-CP4 location, for the same interval as the one used to picture the signals in Fig. 2. It can be observed that the electrical artifacts can be easily identified, meanwhile the natural changes in tissue opacity due to the limb movement become almost invisible. Accordingly, by comparing both the original signal and the derivative of it, a classifier can be constructed for a reliable detection of upper limb movement.

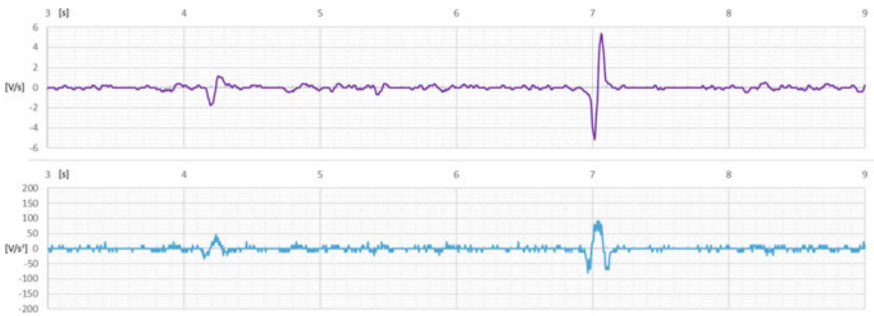

Fig. 3 Approximation of first (top) and second (bottom) derivatives of the signal at C4-CP4

5 Conclusions

This paper presented the modeling and construction process with minimal resources of a low-cost non-invasive demonstrator that shows the potential of being used as a Brain-Computer Interface, along with the testing phase that yielded preliminary results illustrated by the recorded data during upper limb movement.

Future research is needed to further assess the viability of a low-cost near-infrared spectrograph as a Brain-Computer Interface; another research avenue is incorporating multiple optodes with additional LEDs and receptors positioned at varying distances to record a more intricate dataset from different regions of the brain, as well as experimenting with different frequencies from the tissue transparency window.

Gathering detailed information about hemodynamic activity at the cranial level has important meaning for monitoring the released oxygen supply and assessing the adequacy of cerebral perfusion correlated with the brain functions.

References

1. Elgendi, M., Fletcher, R., Liang, Y., Howard, N., Lovell, N.H., Abbott, D., Lim, K., Ward, R.: The use of photoplethysmography for assessing hypertension. NPJ Digit. Med. **2**, 1–11 (2019). https://doi.org/10.1038/s41746-019-0136-7
2. Kamshilin, A.A., Nippolainen, E., Sidorov, I.S., Vasilev, P.V., Erofeev, N.P., Podolian, N.P., Romashko, R.V.: A new look at the essence of the imaging photoplethysmography. Sci. Rep. **5**(1), 1–9 (2015)
3. Alian, A.A., Shelley, K.H.: Photoplethysmography. Best Pract. Res. Clin. Anaesthesiol. **28**(4), 395–406 (2014)
4. Pinti, P., Aichelburg, C., Lind, F., Power, S., Swingler, E., Merla, A., Hamilton, A., Gilbert, S., Burgess, P., Tachtsidis, I.: Using fiberless, wearable fNIRS to monitor brain activity in real-world cognitive tasks. JoVE (J. Visualized Exp.) (106), e53336 (2015)
5. Tsow, F., Kumar, A., Hosseini, S.H., Bowden, A.: A low-cost, wearable, do-it-yourself functional near-infrared spectroscopy (DIY-fNIRS) headband. HardwareX **10**, e00204 (2021)
6. Yucel, M., Selb, J.J., Huppert, T.J., Franceschini, M.A., Boas, D.A.: Functional near infrared spectroscopy: enabling routine functional brain imaging. Curr. Opin. Biomed. Eng. **4**, 78–86 (2017). https://doi.org/10.1016/j.cobme.2017.09.011
7. Saager, R., Berger, A.: Measurement of layer-like hemodynamic trends in scalp and cortex: implications for physiological baseline suppression in functional near-infrared spectroscopy. J. Biomed. Opt. **13**(3), 034017–034017 (2008)

Phenomenological Modelling of the Nonlinear Flexion–Extension Movement of Human Lower Limb Joints

Marius Georgescu, Daniela Tarniță, Cosmin Berceanu, Ionuț Geonea, and Danut-N. Tarniță

Abstract In this paper we obtain a mathematical model for the flexion–extension (flex-ext) motion of the human lower limb joints in the sagittal plane. This model is composed of a system of differential equations based on quadratic polinoms, obtained from the experimental data collected during walking. Numerical integrations of the mathematical model and the construction of the state space by utilizing numerical solutions and the comparison with the state space obtained from experimental data are obtained. The trajectories of the solution of the phenomenological model are very close to the result of the measurements of the flex-ext angles of the Subject's joints before the pre-processing stage, but they are narrower, more similar with those obtained after pre-processing.

Keywords Phenomenological modelling · Lower limb joints · Flexion–extension · Electrogoniometers · Nonlinear movement

1 Introduction

Phenomenological models rely on data. These models are an intermediary valuable instrument, which connects the empirical observations with the theory describing, by the aid of mathematics, the observed behaviour, without necessarily offering an explanation for the mechanisms which constitute the foundation of such behaviour [1]. By utilizing one or more time series of certain variables of a dynamic system, through phenomenological modeling, one can obtain equations which describe the dynamics, enabling us to extrapolate beyond the atractor from which they were measured [2]. In the context of nonlinear analysis of time series, the phenomenological models are systems of differential equations of first order, usually expressed as

M. Georgescu · D. Tarniță (✉) · C. Berceanu · I. Geonea
University of Craiova, Craiova, Dolj County, Romania
e-mail: daniela.tarnita@edu.ucv.ro

D.-N. Tarniță
Emergency Hospital of Dolj County, Craiova, Dolj County, Romania

D. Pisla et al. (eds.), *Advances in Service and Industrial Robotics*, Mechanisms and Machine Science 157, https://doi.org/10.1007/978-3-031-59257-7_18

polynomial expansions of some interdependent variables of the analyzed system [2–4]. The purpose of this paper is to obtain a mathematical model for the flex-ext motion of the human lower limbs joints in the sagittal plane. This model is composed of a system of differential equations based on polinoms, that govern a dynamic biomechanical system, only from data measurements collected during walking, balancing the complexity of the model with its descriptive character. Numerical integrations of this mathematical model, the construction of the state space by utilizing numerical solutions and the comparison with the state space obtained from experimental data is another goal. For critical data-driven problems, such as predicting and eradicating the spread of diseases, data-driven dynamics discovery will continue to play an important role in these efforts.

2 Experimental Protocol

A number of 7 experimental trials of walking with normal speed (5 km/h) was performed during 30 s/each by a healthy subject, male, age 35, height 1.78 m, weight 72 kg. The experimental data, obtained as time series of the lower limb joint angles, was collected using the Biometrics data acquisition system, at a frequency of 500 Hz, often used in biomechanical and clinical research [5–10]. Six wearable twin-axes electrogoniometers were used for hip, knee and ankle human joints of both lower limbs. Each twin-axes electrogoniometer has 2 outputs that simultaneously collect a movement in one of two perpendicular planes: sagittal plane and, respectively, the frontal plane. The DataLOG acquisition unit allows the data collection from 8 sensors simultaneously. 3 units can be used simultaneously, i.e. up to 24 series of synchronized biomechanical data can be acquired. In Fig. 1 the schema block of the acquisition process, the sensors mounted on a subject, the DataLOG and the electrogoniometers are shown, while in Fig. 2 the variation of the right human joints angles during the experimental test are shown.

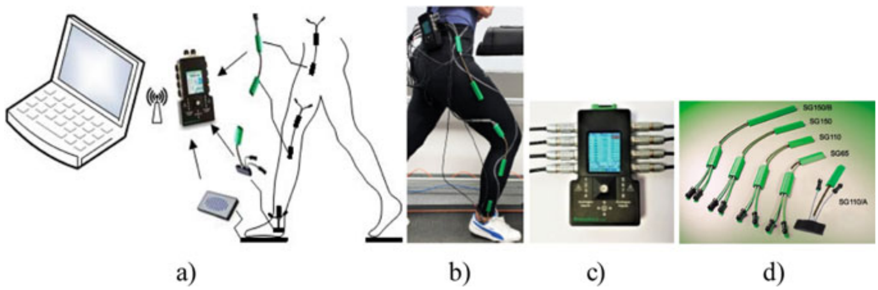

Fig. 1 **a** Biometrics data acquisition block schema; **b** mounted sensors on the subject; **c** DataLOG unit; **d** twin-axes electrogoniometers

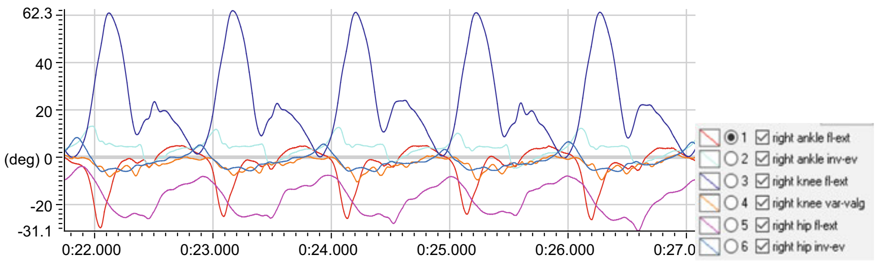

Fig. 2 Consecutive cycles of the flex-ext movements and rotation movement (in frontal plane) of the right lower limb joints during experimental test (5 km/h), function of time (s)

3 Method

The procedure is based on the analysis of time series of experimental measurements of a variable of the dynamic system. We consider that we have a time series composed of the following measurements:

$$s_1, s_2, s_3, \ldots, s_n \tag{1}$$

In a state space reconstructed in ***m*** dimensions, with a time lag ***d***, a point at time t is represented by a vector $\mathrm{x_t}$ with the following components:

$$x_t = \left(s_t, s_{t+d}, s_{t+2d}, \ldots, s_{t+(m-1)d}\right), \quad t = 1, \ldots, n \tag{2}$$

The state space reconstruction theories [11, 12], ensure that the geometrical object defined by the vector x_t is „equivalent" with the trajectory defined by the variables which characterize the dynamic system in the original state space. The embedding dimension ***d*** must be large enough so that the reconstructed orbit does not overlap with itself. When this happens, d is called the proper embedding dimension. In order to reconstruct the state space one could use the "Time delay method" proposed by Takens [11]. According to this method, is necessary to previously choose the right parameters for the reconstruction like: time delay and embedded dimension. The calculation of time delay is done by selecting the first minimal value of the function AMI (average mutual information), as proposed in [13]. An example of AMI function for the knee flex-ext is shown in Fig. 3. One of the most frequent methods used for the embedded dimension calculation was first proposed by Kennel [14], and is called FNN (False-Nearest Neighbors), often used [6, 10, 15]. According to this method, one could adopt the value for which the false neighbors proportion decreases under 10% (Fig. 4).

By utilizing the two parameters we are able to reconstruct the state space by using the Time Delay Method. Starting from the time series obtained for the flex-ext angles of the right knee joint of the human subject 1, shown in Fig. 2, we present in Fig. 5 the the reconstructed state space.

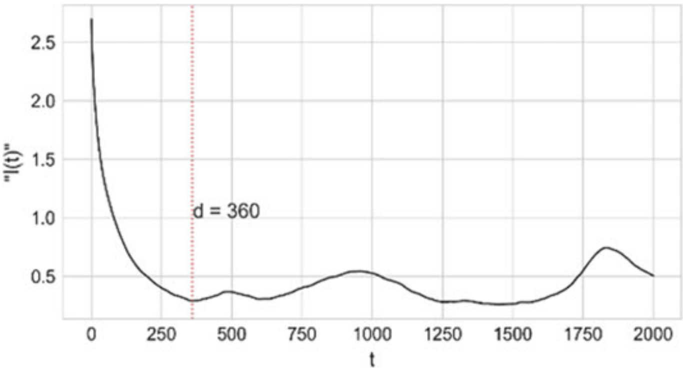

Fig. 3 The AMI function obtained for the knee flex-ext motion during normal walking

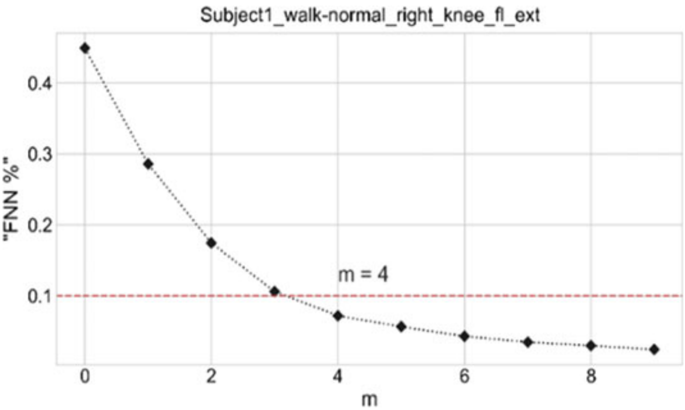

Fig. 4 The graph showing the FNN' percent for the knee joint. Using FNN we adopt m = 4

Fig. 5 The first three dimensions of the reconstructed state space starting from the time series of the right knee joint angle, flex-ext motion, normal walking

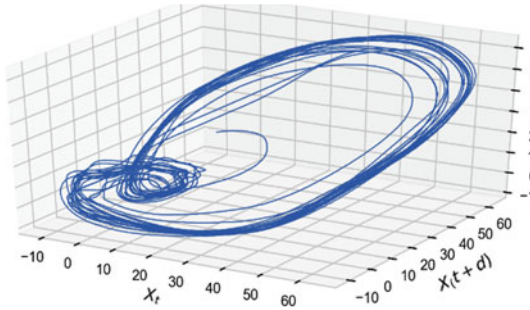

One important step in the nonlinear analysis of time series is the reconstruction of the system dynamics in the real world by using one single cronolological series of measurements of a system variable. We aim to identify which component of the observed dynamics has a deterministic nonlinear behavior or should be explained by a linear behavior affected by noise. One signal pre-processing technique is Singular Spectrum Analysis (SSA) [16, 17]. The analysis of the unic spectrum, SSA, will transform the data from the time series into structured variations (signal), including some oscilatory components and residual variations (noise). In oder to pre-process the time series, we employed the RSSA package [16, 17] available for the programming language R. After the pre-processing stage we obtained graphs with the original series, isoleted signal, and residual noise. Thereby, in Fig. 6, we show the graph for the human right knee during normal walking, for the motion in the sagittal plane [18]. In this graph, with black color is shown the original time series, with green color the isolated signal, and with red the residual noise. The horizontal axis shows the number of data points, while the vertical axis the knee angular amplitude, in degrees.

One example of a sistem of equations for three variables: x, y and z, composed of three differential equations of the first order, expressed in the form of polynomials, is presented in Eq. (3).

$$\begin{cases} \dfrac{dx}{dt} = \dot{x} = \alpha_1 + \alpha_2 z + \alpha_3 y + \alpha_4 yz + \alpha_5 x + \alpha_6 xz + \alpha_7 xy + \alpha_8 xyz \\ \dfrac{y}{dt} = \dot{y} = \beta_1 + \beta_2 z + \beta_3 y + \beta_4 yz + \beta_5 x + \beta_6 xz + \beta_7 xy + \beta_8 xyz \\ \dfrac{dz}{dt} = \dot{z} = \gamma_1 + \gamma_2 z + \gamma_3 y + \gamma_4 yz + \gamma_5 x + \gamma_6 xz + \gamma_7 xy + \gamma_8 xyz \end{cases} \tag{3}$$

where $x(t)$, $y(t)$, $z(t)$ are isolated signals of the time series corresponding to the three variables, and α_i, β_i, γ_i, $(i = 1, 2, 3, 4, 5, 6, 7, 8)$ are unknown fixed coefficients.

Starting from one or more time series of certain variables, one could obtain a phenomenological model based on the following algorithm [18]:

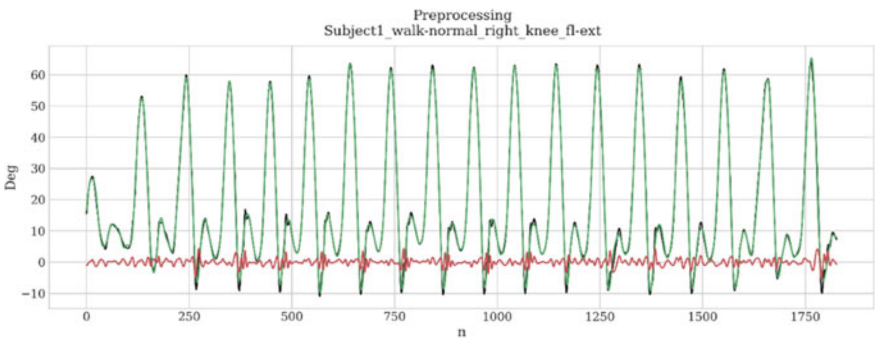

Fig. 6 The isolated signal (green), and removed residual noise (red) obtained for the time series corresponding to right knee joint during flex-ext, normal walking, Trial 2

1. The time derivatives are approximated by numerical derivation of $x(t)$, $y(t)$, $z(t)$ time series;
2. Depending of the number of time series (variables) and a selected order, we calculate polynomial expansions using time series data;
3. For each polynomial expansion we estimate the unknown coefficients of the monomial terms (α_i, β_i and γ_i,) using linear regression techniques, where the dependent variable is the numerical derivative of the time series, and the independent variables are the time series;
4. We check the accuracy of the first order differential equations by predicting the numerical derivatives approximated using finite differentiation;
5. We find (by numerical integration) the solution of the first order differential equations.

3.1 The Time Derivatives Approximation

The numerical derivation of the time series is done by approximating the derivatives with fourth order centered differences [19]:

$$\dot{x}_t = \frac{8(x_{t+1} - x_{t-1}) - (x_{t+2} - x_{t-2})}{12\delta} + \vartheta\left(\delta^4\right) \tag{4}$$

where δ is the integration step, and $\vartheta\left(\delta^4\right)$ is the truncation error.

3.2 The Polynomial Expansion

A regular polynomial function with multiple variables [20, 21] is given by:

$$F(x_1, x_2, \ldots, x_m) = \sum_{n=1}^{N_P} A_n x_1^{\alpha_1} x_2^{\alpha_2} \ldots x_m^{\alpha_m} \tag{5}$$

where A_n are unknown fixed coefficients, and N_P the number of expansion monoms given by $N_p = \left(M_p\right)^m$, in which m is the number of variables from the expansion, while M_p is the individual terms power interval [22]. The powers of the monomial terms from Eq. (3) are to be calculated using Eqs. (6) or (7):

$$\alpha_m = Int\left\{(n-1) - \alpha_1 M_P^{m-1} - \alpha_2 M_P^{m-2} - \ldots - \alpha_{m-1} M_p\right\} \tag{6}$$

$$\alpha_m = \left\lfloor (n-1) - \sum_{i=1}^{m-1} \alpha_i M_P^{m-i} \right\rfloor \tag{7}$$

Table 1 The monomial terms populated with experimental data of human motion [18]

Monom series	1	2	3
z	3.309927	3.412728	3.423657
z^2	10.95562	11.64671	11.72143
z^3	36.26229	39.74706	40.13015
y	2.797644	3.345265	3.837491
yz	9.259997	11.41648	13.13825
yz^2	30.64992	38.96134	44.98087
y^2	7.826812	11.1908	14.72634
y^2z	25.90618	38.19115	50.41793
x	0.179875	0.390724	0.693182
xz	0.595373	1.333435	2.373217
xy	0.503226	1.307075	2.66008
xyz	1.665642	4.460693	9.1072
x^2	0.032355	0.152665	0.480501
x^2z	0.107093	0.521005	1.645072

For example, in order to create a phenomenological model starting from the time series of the experimental data obtained for the right joints (hip, knee, and ankle) movements, in the sagittal plane, we will adopt $m = 3$ and $M_p = 4$ for numerical stability. Thus, we will obtain a system of three polynomial equations with $4^3 = 64$ monoms each. For each of the generated monoms, the monomial terms powers were calculated using Eq. (7). Afterwards, the resulted monoms have been populated with data from the time series corresponding to the hip, knee and akle of the human subject. In order to express the monomial terms we have used the Rmpoly package [20]. The resulted monoms for the first three values are depicted in Table 1. The values are not published in previous papers, they being extracted from the reference [18], the PhD thesis elaborated by the first author.

3.3 *The Estimation of the Coefficients*

The coefficients estimation is possible by applying linear regression methods, taking as dependent variable the numerical derivative of the time series, and as independent variables, the time series of the variables. By applying a method of linear regression which minimizes the value of MSE function (Mean Squared Error), given by Eq. (8).

$$MSE(p, \hat{p}) = \sum_{i=1}^{n} (\hat{p} - p)^2 \tag{8}$$

where p is the numerical derivative of the time series, and $\hat{p}$ is the result of the polynomial expansion, is not enough.

In order to obtain models which balance precision and complexity, and can be used to extrapolate the dynamics beyond the measured sample, one could employ regression techniques like the Ridge Regression which reduces the variability of the coefficients by decreasing these, adding to the cost function a penalty (the L_2 norm of the coefficients) [23, 24]. In Eq. (9), the α parameter controls how small the weights W will be.

$$cost_{RIDGE}(p, \hat{p}) = \sum_{i=1}^{n} (\hat{p} - p)^2 + \alpha \|W\|_2 \tag{9}$$

Alternaltively, the LASSO Regression (Least Absolute Shrinkage and Selection Operator) [25–27], adds the L_1 norm to the cost function, creating a scattered representation of the weights. The LASSO coefficients are estimated by Eq. (10):

$$\hat{\beta}(lasso) = \arg\min_{\beta} \left\| y - \sum_{j=1}^{p} x_j \beta_j^2 \right\| + \lambda \sum_{j=1}^{p} |\beta_j| \tag{10}$$

The second term of Eq. (8) is known as ℓ_1 constraint. The "adaptive.weights" routine from the R MESS [28] package outputs the weights as:

$$\frac{1}{|\hat{\beta}|^{\mathrm{nu}}} \tag{11}$$

In order to calculate the coefficients using LASSO regression we employed R glmnet package [29] which uses Eq. (12):

$$\min_{\beta_0 \beta} \frac{1}{N} \sum_{i=1}^{N} w_i l\left(y_i, \beta_0 + \beta^T x_i\right) + \lambda \left[\frac{(1-\alpha)\beta_2^2}{2} + \alpha \beta_1 \right] \tag{12}$$

The tuning parameter λ determines in which measure the coefficients calculated with the ℓ_1 constraint relate to the coefficients estimated by a simple linear regression. The routine R cv.glmnet, from the R glmnet [29] package, uses cross-validation to select the value of λ that provides the best fit to the data based on the mean squared deviations (MSE) between the finite differences calculated from the data and those predicted by the equation of regression, with estimated coefficients, where n is the sample size. In Fig. 7 we show the cross-validation curves for dx and dy (the curve for dz is similar), along with the upper and lower standard deviation values for each λ. The vertical dotted lines indicate the value of λ that gives the minimum cross-validated MSE and the value of λ that gives the most regularized model such that the cross-validated MSE is within one standard error of the minimum MSE. The model obtained for the sagittal plane movement of the Subject's right leg joints (knee, hip

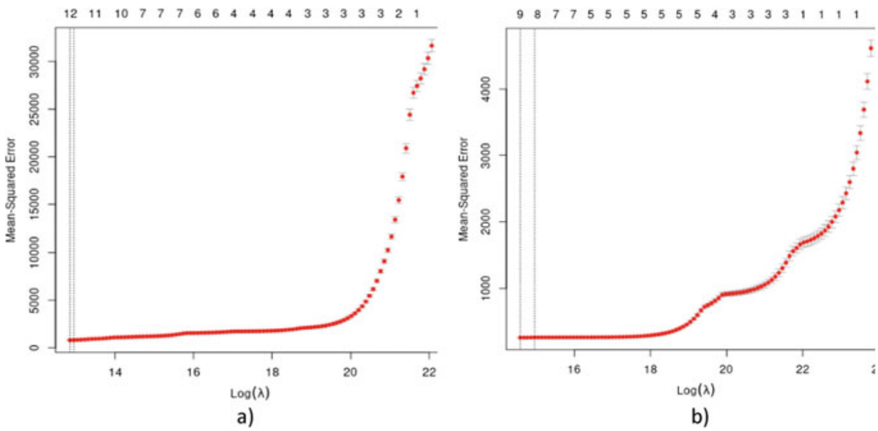

Fig. 7 The cross validation curve **a** dx; **b** dy

and ankle), in the normal walking test, is composed of only a part of the 64 possible terms.

$$
\begin{aligned}
F(x, y, z) = {} & A_1 x^0 y^0 z^1 + A_2 x^0 y^0 z^2 + A_3 x^0 y^0 z^3 + A_4 x^0 y^1 z^0 \\
& + A_5 x^0 y^1 z^1 + A_6 x^0 y^1 z^2 + A_8 x^0 y^2 z^0 + A_9 x^0 y^2 z^1 + A_{16} x^1 y^0 z^0 \\
& + A_{17} x^1 y^0 z^1 + A_{20} x^1 y^1 z^0 + A_{21} x^1 y^1 z^1 + A_{32} x^2 y^0 z^0 + A_{33} x^2 y^0 z^1
\end{aligned} \tag{13}
$$

3.4 *The Numerical Solution of the Phenomenological Model Extracted from Three Observed Variables*

From Eq. (11) we obtain the system of equations for the derivatives of the flex-ext angles of the subject's knee (dx), hip (dy) and ankle (dz) in the normal walking test (Eq. (12)). The solutions of the differential equations were determined with the *ode* routine from the R package, *deSolve* [30], based on the lsodes integration method [30]. The initial conditions are: the model, the estimated coefficients, the integration step $delta = 0.01$, and the first values of theseries.

$$
\begin{aligned}
\frac{dx}{dt} &= \dot{x} = 14.77 - 8.48z - 1.02z^2 + 0.02z^3 + 13.63y + 1.07yz \\
&\quad - 0.09yz^2 + 4.86x - 0.95xz + 0.37xy - 0.04xyz \\
&\quad + 0.02x^2 + 0.01x^2 z \\
\frac{dy}{dt} &= \dot{y} = 75.79 + 2.47z - 3.42y - 8.41x - 0.02x + 0.09x^2
\end{aligned}
$$

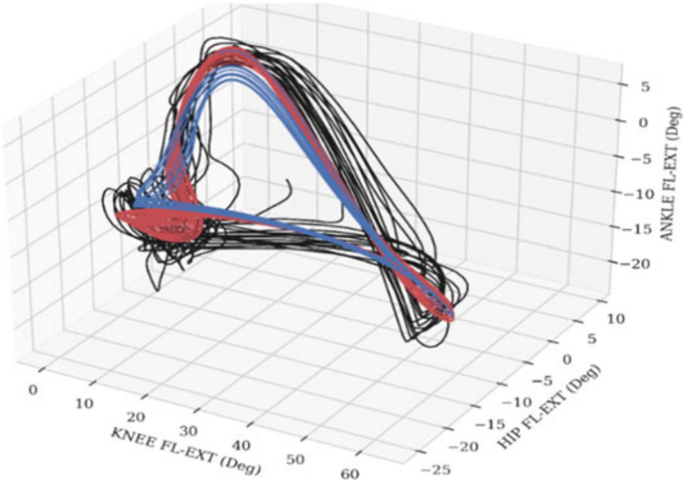

Fig. 8 The state space of the experimental (original) flex-ext angles (black); the isolated signal after pre-processing (red); the solution of the phenomenological model (blue)

$$\frac{dz}{dt} = \dot{z} = 38.62 - 2.45z - 0.33z^2 - 6.01y + 0.11 + 0.04yz^2 - 0.78y^2 \\ - 0.01y^2z - 6.7x - 0.44xz - 0.69xy - 0.09x^2 \tag{14}$$

Figure 8 shows the state space built with the time series related to the experimental flex-ext angles of the Subject's joints (red), the signals isolated after pre-processing (blue) and the solution of the phenomenological model (black). It can be seen that the trajectories of the state space constructed from the isolated signals are more stable compared to those of the state space constructed from the measured time series. At the same time, the trajectories of the solution of the phenomenological model are very close to the result of the measurements of the flex-ext angles of the Subject's joints before and after the pre-processing stage, the allures of the curves are similar, but they are narrower, more similar with those obtained after pre-processing.

4 Conclusions

The paper presents the experimental measurements of the flex-ext angles of the human lower limb joints as well as the numerical integrations of the mathematical model and the construction of the state space by utilizing numerical solutions. Then a comparison of the state space obtained by solving the phenomenological model with the state space obtained from experimental data are obtained. The trajectories of the solution of the phenomenological model are very close to the result of the measurements of the flex-ext angles of the Subject's joints before the pre-processing stage, but they are narrower, similar with those obtained after pre-processing. Future developments will focus on conducting experimental tests and phenomenological modelling for different other experimental tests and for a greater number of subjects.

References

1. Hilborn, R., Mangel, M.: The ecological detective: confronting models with data **28** (1997)
2. Brunton, S., et al.: Discovering governing equations from data: sparse identification of nonlinear dynamical systems. Proc. Natl. Acad. Sci. **113**, 3932–3937 (2015)
3. Breeden, J., Hübler, A.: Reconstructing equations of motion from experimental data with unobserved variables. Phys. Rev. A **42**, 5817–5826 (1990)
4. Baker, G., Gollub, J., Blackburn, J.: Inverting chaos: extracting system parameters from experimental data. Chaos **6**, 528–533 (1997)
5. Tarnita, D., et al.: Applications of nonlinear dynamics to human knee movement on plane &inclined treadmill. In: New Trends in Medical & Service Robots, vol. 39. Springer, pp. 59–73 (2016)
6. Tarnita, D., Geonea, I.: Numerical Simulations and Experimental Human Gait Analysis Using Wearable Sensors, pp. 289–304. New Trends in Medical and Service Robots, Springer (2018)
7. Major, Z.Z. et al.: The impact of robotic rehabilitation on the motor system in neurological diseases. A multimodal neurophysiological approach. Int. J. Environ. Res. Public Health **17**, 6557 (2020)
8. Pisla, D., et al.: A parallel robot with torque monitoring for brachial monoparesis rehabilitation tasks. Appl. Sci. **11**, 9932 (2021)
9. Pisla, D., et al.: Development of a control system and functional validation of a parallel robot for lower limb rehabilitation. Actuators **10**, 277 (2021)
10. Tarnita, D. et al.: Experimental characterization of human walking on stairs applied to humanoid dynamics. In: Advances in Robot Design and Intelligent Control, RAAD16, pp. 293–301. Springer (2017)
11. Takens, F.: Detecting strange attractors in turbulence. In: Dynamical Systems and Turbulence, 1981, pp. 366–381. Warwick (1980)
12. Broomhead, D.S., King, G.P.: Extracting qualitative dynamics from experimental data. Phys. D Nonlinear Phenom. **20**(2–3), 217–236 (1986)
13. Fraser, A.M., Swinney, H.L.: Independent coordinates for strange attractors from mutual information. Phys. Rev. A **33**(2), 1134–1140 (1986)
14. Kennel, M.B., et al.: Determining embedding dimension for phase-space reconstruction using a geometrical construction. Phys. Rev. A **45**(6), 3403–3411 (1992)
15. Tarnita, D., Marghitu, D.-B.: Nonlinear dynamics of normal and osteoarthritic human knee. In: Proceedings of the Romanian Academy, pp. 353–360 (2017)
16. Golyandina, N. et al.: Singular Spectrum Analysis with R (2018)
17. Golyandina, N., Korobeynikov, A.: Basic singular spectrum analysis and forecasting with R. Comput. Stat. Data Anal. **71**, 934–954 (2014)
18. Georgescu, M.: Contributions on the human gait stability. Ph.D. thesis, Craiova (2021)
19. Hershey, D.: Finite Difference Calculus Transport Analysis, pp. 299–326. Springer, Boston (1973)
20. Kahle, D.: Mpoly: multivariate polynomials in R. R J. **5**, 181–187 (2013)
21. Mourrain, B., Pan, V.Y.: Multivariate polynomials, duality, and structured matrices. J. Complex. **16**(1), 110–180 (2000)
22. Wei-Dong, L., et al.: Global vector-field reconstruction of nonlin dynamical systems from a time series with SVD method validation with Lyap exp. Chinese Phys. **12**, 1366 (2003)
23. Huffaker, R., Bittelli, M., Rosa, R.: Nonlinear time series analysis with R (2018)

24. Zhang, T., Yang, B.: An exact approach to ridge regression for big data. Comput. Stat. **32**(3), 909–928 (2017)
25. Tibshirani, R.: Regression shrinkage and selection via the lasso. J. R. Stat. Soc. Ser. B. R. Stat. Soc. Ser. B **58**, 267–288 (1996)
26. Gauraha, N.: Introduction to the LASSO. Resonance **23**(4), 439–464 (2018)
27. Yazdi, M., Golilarz, N.A., Nedjati, A., Adesina, K.A.: An improved lasso regression model for evaluating the efficiency of intervention actions in a system reliability analysis. Neural Comput. Appl. **33**(13), 7913–7928 (2021)
28. Ekstrøm, C.T.: MESS: miscellaneous esoteric statistical scripts (2020). https://cran.r-project.org/web/packages/MESS/index.html. Accessed 10 Jan 2020
29. Hastie, T., Qian, J., Tay, K.: An Introduction to glmnet (2020). https://glmnet.stanford.edu, https://glmnet.stanford.edu/articles/glmnet.html. Accessed 12 Jan 2020
30. Soetaert, K., Petzoldt, T., Setzer, R.: Package deSolve: solving initial value differential equations in R. R J. **2**, 5–15 (2010)

Continuous-Time Robust Control for Cancer Treatment Robots

Vlad Mihaly, Iosif Birlescu, Mircea Şuşcă, Damien Chablat, and Petru Dobra

Abstract The control system in surgical robots must ensure patient safety and real time control. As such, all the uncertainties which could appear should be considered into an extended model of the plant. After such an uncertain plant is formed, an adequate controller which ensures a minimum set of performances for each situation should be computed. As such, the continuous-time robust control paradigm is suitable for such scenarios. However, the problem is generally solved only for linear and time invariant plants. The main focus of the current paper is to include m-link serial surgical robots into Robust Control Framework by considering all nonlinearities as uncertainties. Moreover, the paper studies an incipient problem of numerical implementation of such control structures.

Keywords Robust control · Nonlinear systems · Cancer treatment robots

1 Introduction

Robotic-assisted cancer treatment was introduced in the 20th century, showing distinct advantages over classical interventions (whether we refer to surgical or percutaneous interventions), such as better accuracy, better ergonomics, and safety [1–4]. The cancer treatment robotics field is still in continuous development, with more state-of-the-art and emerging technologies being implemented into the surgical robotic systems such as Artificial Intelligence (AI), advanced vision, smart safety features and control modules [1]. One trend in the emerging cancer treatment robotic systems is to provide better surgical outcomes through personalized instrumentation and intervention [2].

V. Mihaly · M. Şuşcă · P. Dobra
Department of Automation, Technical University of Cluj-Napoca, Cluj-Napoca, Romania

I. Birlescu (✉) · D. Chablat
CESTER,Technical University of Cluj-Napoca, Cluj-Napoca, Romania
e-mail: iosif.birlescu@mep.utcluj.ro

D. Chablat
École Centrale Nantes, Nantes Université, CNRS, LS2N, Nantes, France

D. Pisla et al. (eds.), *Advances in Service and Industrial Robotics*, Mechanisms and Machine Science 157, https://doi.org/10.1007/978-3-031-59257-7_19

Continuous-time robust control synthesis has found extensive applications in various practical scenarios due to its high flexibility, and should be suitable for implementation in cancer treatment robotic systems. This approach offers a versatile framework for extending nominal models described by transfer matrix or state-space representations with model uncertainties and performance specifications through open-loop [5] and closed-loop shaping [6]. To design unstructured regulators, two approaches are the most common: algebraic Riccati equations [7] and linear matrix inequalities [8]. However, these controllers have the same order as the plant, leading to implementation issues. To design fixed-structure controllers, a nonsmooth optimization method has been presented in [9]. Commonly used performance metrics are the $\mathcal{H}_2$ and $\mathcal{H}_\infty$ norms, employed to quantify system performance, both in continuous and discrete cases [10]. The $\mathcal{H}_2/\mathcal{H}_\infty$ norms have been further extended by incorporating the structured singular value (SSV), which efficiently captures uncertainty in plant dynamics [11].

This framework has been used in [12] as an extra layer to guarantee the robustness of a nonlinear systems with polytopic approximation. The m-link serial robots studied in this paper have polytopic approximation. The main contribution of the current paper consists in removing the inner layer of the control structure proposed in [12], to simplify the design. The matrices from the polytopic approximation will be considered as uncertainties against a nominal plant obtained at the equilibrium point. As such, the contributions of the paper are: (1) obtaining a polytopic differential inclusion representation of an m-link serial robot; (2) representing an m-link serial robot (as a generic robot for cancer treatment) using polytopic differential inclusions; (3) including the nonlinearities into additive uncertainties against a linearized model around a given equilibrium point; (4) applying the generalized Robust Control Framework on the given problem; (5) illustrating the proposed control structure on a 2R serial robot (illustrating the possibility of integration in surgical robots).

The rest of the paper is organized as follows: Sect. 2 presents the problem to be solved, along with the available solutions and how to adapt them for our problem; in Sect. 3 the case of 2R serial robot is presented into an end-to-end manner, while Sect. 4 presents conclusions and further research directions.

Notations: $\mathrm{Co}(S)$ is the convex hull of the set S. The sets of symmetric and positive-(semi)definite matrices of order m are $\mathbb{S}_m^{\geq 0}$ and $\mathbb{S}_m^{+}$. The variable s is the complex frequency used in the Laplace Transform.

2 Problem Formulation

Consider a general m-link serial robot (that manipulates a surgical instrument for cancer treatment) as in Fig. 1 described by the following dynamic model:

$$M(\mathbf{q})\ddot{\mathbf{q}} + C(\mathbf{q}, \dot{\mathbf{q}})\dot{\mathbf{q}} + D\dot{\mathbf{q}} + g(\mathbf{q}) = \mathbf{u}, \tag{1}$$

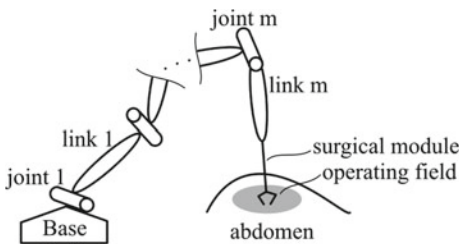

Fig. 1 General m-link cancer treatment serial robot

where $\mathbf{q} \in \mathcal{D}_q \subset \mathbb{R}^m$ is the vector of generalized coordinates representing joint positions, $\mathbf{u} \in \mathbb{R}^m$ is the control input vector, while $M(\mathbf{q})$ is the inertia matrix, $C(\mathbf{q}, \dot{\mathbf{q}})\dot{\mathbf{q}}$ encompasses the centrifugal and Coriolis forces, $D\dot{\mathbf{q}}$ is the viscous damping term, and $g(\mathbf{q})$ is the gravity term. The gravity term is given by:

$$g(\mathbf{q}) = \left(\frac{\partial P(\mathbf{q})}{\partial \mathbf{q}}\right)^\top, \tag{2}$$

where $P(\mathbf{q})$ is the total potential energy of the links due to gravity.

Assumption 1 For each $\mathbf{q} \in \mathcal{D}_q$ we assume that the following conditions are satisfied: $M(\mathbf{q}) \in \mathbb{S}_m^+$, $\dot{M} - 2C$ is skew-symmetric, and $D \in \mathbb{S}_m^{\geq 0}$.

The state vector $\mathbf{x} \in \mathcal{D}_x \subset \mathbb{R}^{n_x}$ contains the generalized coordinates $\mathbf{x}_1 = \mathbf{q}$ and velocities $\mathbf{x}_2 = \dot{\mathbf{q}}$, so $n_x = 2 \cdot m$. The state-space model is given by:

$$\begin{cases} \dot{\mathbf{x}}_1 = \mathbf{x}_2; \\ \dot{\mathbf{x}}_2 = -M^{-1}(\mathbf{x}_1)\left(C(\mathbf{x}_1, \mathbf{x}_2) + D\right)\mathbf{x}_2 - M^{-1}(\mathbf{x}_1)g(\mathbf{x}_1) + M^{-1}(\mathbf{x}_1)\mathbf{u}, \end{cases} \tag{3}$$

which could be viewed as an input-affine nonlinear system [13]:

$$(\Sigma) : \dot{\mathbf{x}} = f_0(\mathbf{x}) + \sum_{i=1}^{m} f_i(\mathbf{x})u_i \equiv f(\mathbf{x}, \mathbf{u}), \tag{4}$$

where:

$$f_0(\mathbf{x}) = \begin{pmatrix} \mathbf{x}_2 \\ -M^{-1}(\mathbf{x}_1)\left(C(\mathbf{x}_1, \mathbf{x}_2) + D\right)\mathbf{x}_2 - M^{-1}(\mathbf{x}_1)g(\mathbf{x}_1) \end{pmatrix}; \tag{5a}$$

$$\mathbf{f}(\mathbf{x}) = \begin{pmatrix} f_1(\mathbf{x}) & \ldots & f_m(\mathbf{x}) \end{pmatrix} = \begin{pmatrix} O_m \\ M^{-1}(\mathbf{x}_1) \end{pmatrix}. \tag{5b}$$

To include the said control problem into the generalized integer-order Robust Control Framework, we consider a polytopic approximation of the system (3). The positions $\mathbf{q}$ and the velocities $\dot{\mathbf{q}}$ are bounded, forming a compact domain $\mathcal{D}_x$. Therefore, there exist matrices $A_i^{(j)} \in \mathbb{R}^{n_x \times n_x}$, $i = \overline{1, n_{A^{(j)}}}$, $j = \overline{0, m}$ such that:

$$\frac{\partial g_j}{\partial \mathbf{x}} \in \mathrm{Co}\left(\mathcal{A}^{(j)} \equiv \left\{A_i^{(j)},\ i = \overline{1, n_{A^{(j)}}}\right\}\right),\ \forall \mathbf{x} \in \mathcal{D}_x, \tag{6}$$

for each index $j = \overline{0, m}$.

Now, the following polytopic linear differential inclusion (PLDI) will cover the behaviour of the given process:

$$(\Sigma_\delta) : \begin{cases} \dot{\mathbf{x}}(t) = A(\delta)\mathbf{x}(t) + B(\delta)\mathbf{u}(t); \\ \mathbf{y}(t) = \begin{pmatrix} I_m & O_m \end{pmatrix} \mathbf{x}(t), \end{cases} \tag{7}$$

where $\mathbf{x} \in \mathbb{R}^{n_x}$, $\mathbf{u} \in \mathbb{R}^{n_u}$, $\delta \in U_\delta \subset \mathbb{R}^{n_\delta}$ is the uncertainty from the state and input matrices, and U_δ is closed and bounded. The PLDI should be characterized by the following L-vertex convex hull, according to (6):

$$\{(A(\delta), B(\delta)) | \delta \in U_\delta\} \subset \Omega \equiv \mathrm{Co}\left\{(A_i, B_i), i = \overline{1, L}\right\}. \tag{8}$$

Assumption 2 Each pair $(A(\delta), B(\delta))$ with $\delta \in U_\delta$ is stabilizable.

The nominal plant G_n=$(A(\mathbf{0}), B(\mathbf{0}), C, O)$ has as interface the set of control inputs $\mathbf{u} \in \mathbb{R}^{n_u}$ and the set of control outputs $\mathbf{y} \in \mathbb{R}^{n_y}$. The uncertain plant $G_{\mathbf{\Delta}} \equiv G$ presents an additional set of disturbance inputs $\mathbf{d} \in \mathbb{R}^{n_d}$ and an additional set of disturbance outputs $\mathbf{v} \in \mathbb{R}^{n_v}$ and it can be written as a function of the structured normalized uncertainty block $\mathbf{\Delta}$ of corresponding dimension with an adequate mapping:

$$\mathcal{T} : \mathcal{G}^2 \to \mathcal{G},\ G = \mathcal{T}\left(G_n, U\right),\ \Delta \in \mathbf{\Delta},\ \|\Delta\|_\infty \leq 1, \tag{9}$$

having the transfer matrix U partitioned in a similar manner with the structured uncertainty set $\mathbf{\Delta} = \{\mathrm{diag}(\delta_1 I_{n_1}, \ldots, \delta_s I_{n_s})\}$, where $\delta_i I_{n_i}$ is used to encompass the parametric uncertainties from U_δ.

To impose a set of performances, an input performance vector $\mathbf{w} \in \mathbb{R}^{n_w}$ and an output performance vector $\mathbf{z} \in \mathbb{R}^{n_z}$ should be considered, the augmented plant P being written based on the uncertain plant G through an adequate mapping $\mathcal{A}$ as $\mathcal{A} : \mathcal{G} \times \mathcal{G} \to \mathcal{G},\ P = \mathcal{A}\left(G, W\right)$, with a transfer matrix W hosting the performance filters. The resulting continuous-time plant has the structure:

$$P : \begin{pmatrix} \dot{\mathbf{x}}(t) \\ \hline \mathbf{v}(t) \\ \mathbf{z}(t) \\ \mathbf{y}(t) \end{pmatrix} = \left(\begin{array}{c|ccc} A & B_d & B_w & B_u \\ \hline C_v & D_{vd} & D_{vw} & D_{vu} \\ C_z & D_{zd} & D_{zw} & D_{zu} \\ C_y & D_{yd} & D_{yw} & D_{yu} \end{array}\right) \begin{pmatrix} \mathbf{x}(t) \\ \hline \mathbf{d}(t) \\ \mathbf{w}(t) \\ \mathbf{u}(t) \end{pmatrix}, \tag{10}$$

where $\mathbf{x} \in \mathbb{R}^{n_x}$ is the state vector. The interconnections between the plant P, the controller K, and the uncertainties block $\mathbf{\Delta}$ are illustrated in Fig. 2.

Fig. 2 The generalized plant P and its interconnections with the uncertainty block $\mathbf{\Delta}$ and the controller K

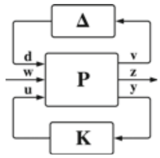

To compensate the uncertainty block, the structured singular value (SSV) of the closed-loop system given by the lower linear fractional transform interconnection between the plant P and the controller K according to the block $\mathbf{\Delta}$, denoted by $\mu_{\mathbf{\Delta}}(\text{LLFT}(P, K))$, can be used:

$$\mu_{\mathbf{\Delta}}(\text{LLFT}(P, K)) = \sup_{\omega \in \mathbb{R}_+} \frac{1}{\min\limits_{\Delta \in \mathbf{\Delta}}\{\overline{\sigma}(\Delta),\ \det(I - M_\omega \Delta) = 0\}},$$

where $M_\omega := \text{LLFT}(P, K)(j\omega)$. The Main Loop Theorem states that a controller K ensures robust stability and robust performance if $\mu_{\mathbf{\Delta}}(\text{LLFT}(P, K)) < 1$. Additionally, if a controller structure described by a family $\mathcal{K}$ is desired, the resulting optimization problem is:

$$\inf_{K \in \mathcal{K}} \mu_{\mathbf{\Delta}}(\text{LLFT}(P, K)). \tag{11}$$

However, the computational problem regarding SSVs is non-deterministic polynomial-time (NP) hard. There are several approaches available to solve this problem, the most common being the so-called D–K iteration approach, being based on an upper bound convexification procedure. The fixed-structure μ-synthesis requires a possibility to solve a fixed-structure $\mathcal{H}_\infty$ control problem, which has been successfully solved [9].

3 Numerical Example

In this section we present the proposed control methodology (for cancer treatment robots) on a 2R serial robot without friction (i.e. $D = 0$). The functions involved in the state-space model (3) are:

$$M(q_1, q_2) = \begin{pmatrix} a_1 + 2a_3\cos(q_2) & a_2 + a_3\cos(q_2) \\ a_2 + a_3\cos(q_2) & a_2 \end{pmatrix}; \tag{12a}$$

$$C(q_1, q_2, \dot{q}_1, \dot{q}_2) = a_3\sin(q_2)\begin{pmatrix} -\dot{q}_2 & \dot{q}_1 + \dot{q}_2 \\ \dot{q}_1 & 0 \end{pmatrix}. \tag{12b}$$

The gravity term will be also $g = 0$, because the gravity acts along the Z axis. The parameters of the above-mentioned model are: $a_1 = 48.125, a_2 = 13.125, a_3 = 6.25$.

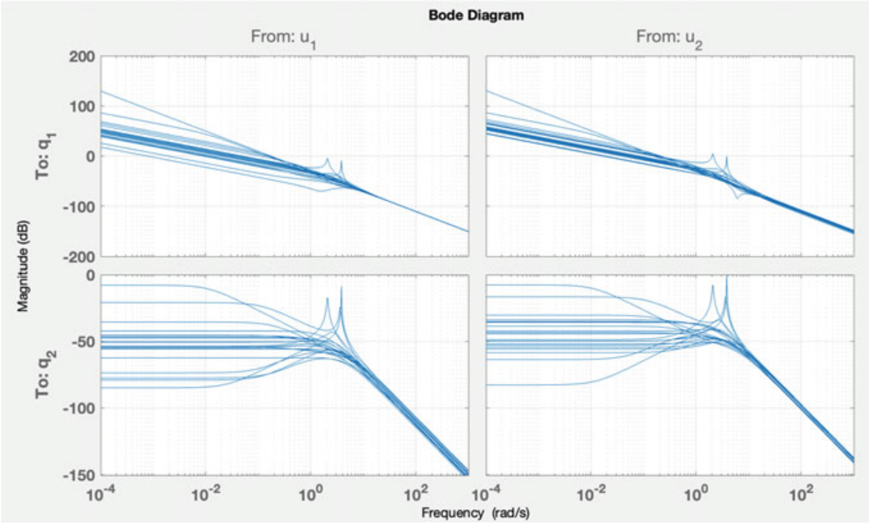

Fig. 3 Magnitude Bode diagram of the linear polytopic differential inclusion $G_\Delta(s)$

The state-space model can be viewed as the following linear polytopic differential inclusion:

$$G_\Delta(s): \begin{cases} \dot{\mathbf{x}} = \begin{pmatrix} 0 & 0 & 1 & 0 \\ 0 & 0 & 0 & 1 \\ 0 & a_{32} & a_{33} & a_{34} \\ 0 & a_{42} & a_{43} & a_{44} \end{pmatrix} \mathbf{x} + \begin{pmatrix} 0 & 0 \\ 0 & 0 \\ b_{31} & b_{32} \\ b_{41} & b_{42} \end{pmatrix} \mathbf{u}; \\ \mathbf{y} = \begin{pmatrix} 1 & 0 & 0 & 0 \\ 0 & 1 & 0 & 0 \end{pmatrix} \mathbf{x}, \end{cases} \tag{13}$$

where: $a_{32} \in [-19.127, 19.6402]$, $a_{33} \in [-1.58, 1.58]$, $a_{34} \in [-3.56, 3.56]$, $a_{42} \in [-13.9637, 28.2362]$, $a_{43} \in [-5.42, 5.42]$, $a_{44} \in [-3.95, 3.95]$, $b_{31} \in [0.0286, 0.0312]$, $b_{32} \in [-0.0461, -0.0164]$, $b_{41} \in [-0.0461, -0.0164]$, $b_{42} \in [0.0848, 0.144]$. The magnitude Bode diagram of the given process is described in Fig. 3. Such magnitude Bode diagrams are used to represent the frequency response of linear systems. In Control Engineering, these are great substitutes for studying both stability and performance aspects simultaneously.

To impose a set of desired performances which should be met by each process form $G_\Delta(s)$, we consider an augmentation using the sensitivity and the complementary sensitivity functions. We consider the following shapes of the weighting functions used for augmenting the plant [6]:

$$W_S(s) = \frac{1/M_S \cdot s + \omega_B}{s + \omega_B \cdot A} \quad \text{and} \quad W_T(s) = \frac{s + \omega_{BT}}{A_T s + \omega_{BT} \cdot M_T}. \tag{14}$$

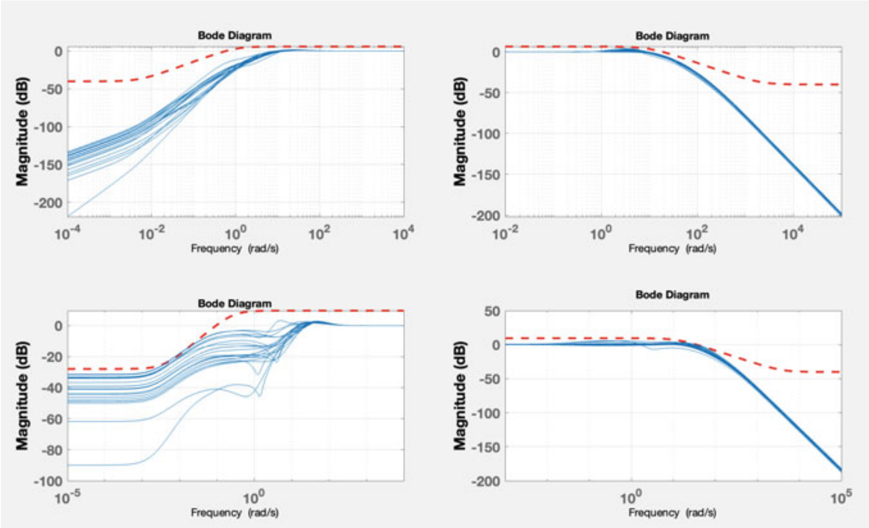

Fig. 4 The evolution of the sensitivity and the complementary sensitivity functions for both nominal model and 20 Monte Carlo simulations, along with the imposed shapes via the augmentation process (red line)

The rise time can be imposed using the minimum allowed bandwidth ω_B, the maximum overshoot can be imposed via the maximum amplitude of the sensitivity function M_S, while the maximum allowed steady-state error is imposed by the magnitude at low frequencies of the sensitivity function A_S. Similarly, for the complementary sensitivity we consider $\omega_{BT} > 10\omega_B$, $M_T \approx M_S$ and $A_T \approx A_S$.

For the proposed use-case we consider the following hyperparameters, one for each input-output pair: $\omega_{B,1} = 0.5[rad/s], \omega_{B,2} = 0.1[rad/s], M_{S,1} = 2, M_{S,2} = 3,$ $A_{S,1} = 10^{-2}$, and $A_{S,2} = 2 \cdot 10^{-2}$. As such, for complementary sensitivity we have: $\omega_{BT,1} = 10[rad/s],\ \omega_{BT,2} = 12[rad/s],\ M_{T,1} = 2.1,\ M_{T,2} = 3,\ A_{T,1} = A_{T,2} = 10^{-2}$. The resulting weighting functions are given by the following block-diagonal transfer matrices:

$$W_S(s) = \begin{pmatrix} \frac{0.5\,s+0.5}{s+0.005} & 0 \\ 0 & \frac{0.3333\,s+0.1}{s+0.002} \end{pmatrix} \text{ and } W_T(s) = \begin{pmatrix} \frac{s+10}{0.01\,s+21} & 0 \\ 0 & \frac{s+12}{0.01\,s+36} \end{pmatrix}. \tag{15}$$

Initially, the unstructured case has been considered. Using the `musyn` routine from MATLAB, a controller K which ensures both robust stability and robust performance is obtained after 22 D–K iterations. The mathematical guarantee of the robustness is given by the upper bound of the structured singular value of the closed-loop system according to the uncertainty set $\mu_{\mathbf{\Delta}(\mathrm{LLFT}(P,K))} \leq 0.9998 < 1$. An illustrative plot which certifies that the controller ensures the robustness properties is presented in Fig. 4.

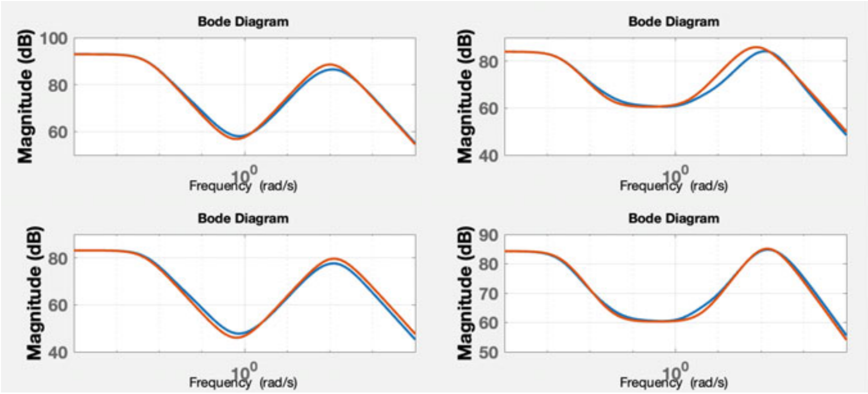

Fig. 5 Bode magnitude representations of the robust high-order controller (blue) and of the fixed-structure robust controller (orange)

However, the main drawback of the unstructured approach consists in the high order of the resulting controller, which could represent a major issue for the numerical implementation process [14]. In the above illustrated case the regulator is of order 132. A solution is to impose a fixed-structure controller:

$$K(s) = \begin{pmatrix} K_{11}(s) & K_{12}(s) \\ K_{21}(s) & K_{22}(s) \end{pmatrix} \in \mathcal{K}. \tag{16}$$

For the purpose of this paper we impose each component of $K(s)$ to be of third order. Solving the fixed-structure μ-synthesis control problem using `musyn` routine, a robust controller has been obtained in 25 D–K iterations, with an upper bound of the structured singular value $\mu_{\Delta}(\text{LLFT}(P, K)) \leq 0.9999 < 1$. The resulting controller is:

$$K^{\star}(s) = \begin{pmatrix} \frac{1.07\cdot10^5\,s^2+1.392\cdot10^5\,s+44157}{0.02\,s^3+4\,s^2+200\,s+1} & \frac{264150\,s^2+5.362e05s+15849}{0.08333\,s^3+13.33\,s^2+500\,s+1} \\ \frac{3.421\cdot10^4\,s^2+4.447\cdot10^4\,s+14454}{0.01422\,s^3+3.556\,s^2+222.2\,s+1} & \frac{1.172\cdot10^5\,s^2+4.728\cdot10^5\,s+16406}{0.02319\,s^3+6.494\,s^2+454.6\,s+1} \end{pmatrix}. \tag{17}$$

A comparison between the initial high-order robust controller and the fixed-structure robust controller is depicted in Fig. 5. As noticed, the differences are small, with a significant benefit regarding the implementation. Moreover, there is no need of an integrative effect, so the controller is stable. It allows one to perform a discretization and a quantization analysis in a straightforward manner.

4 Conclusions

Cancer treatment robotic systems require adequate control techniques to achieve patient safety in personalized therapies. The paper proposes a method to include the nonlinear model of a general m-link serial surgical robot into the generalized Robust Control Framework. Even if the linear polytopic differential inclusion could be conservative, a mathematical guarantee for an imposed set of performances is still fulfilled. The great advantage of the proposed method against the available solutions, such as robust passivity-based control, is the ability to reduce the control structure to a single layer. Numerical examples showed an incipient implementation issue regarding the order of the approximation, and an fixed-structure robust controller has been computed, without losing the robustness guarantee.

Further work is required to implement the proposed control techniques into existing medical robots and novel cancer treatment robots. Another research direction will be to extend the proposed control structure for parallel robots, which are usually described using input-affine descriptor nonlinear systems, presenting additional algebraic constraints.

Acknowledgements This research was supported by the project New smart and adaptive robotics solutions for personalized minimally invasive surgery in cancer treatment—ATHENA, funded by European Union—NextGenerationEU and Romanian Government, under National Recovery and Resilience Plan for Romania, contract no. 760072/23.05.2023, code CF 116/15.11.2022, through the Romanian Ministry of Research, Innovation and Digitalization, within Component 9, investment I8.

References

1. Haidegger, T., et al.: Robot-assisted minimally invasive surgery-Surgical robotics in the data age. Proceedings of the IEEE **110**(7), 835–846 (2022)
2. European Partnership for Personalised Medicine EP PerMed Version 2, Jan. 2022
3. Pisla D., et al.: Kinematical analysis and design of a new surgical parallel robot. In: Proceedings of the 5th International Workshop on Computational Kinematics, Duisburg, Germany, pp. 273–282 (2009)
4. Pisla, D., et al.: Algebraic modeling of kinematics and singularities for a prostate biopsy parallel robot. Proc. Rom. Acad. Ser. A **19**, 489–497 (2019)
5. McFarlane, D., Glover, K.: A loop-shaping design procedure using H_∞ synthesis. IEEE Trans. Autom. Control **37**(6), 759–769 (1992). June
6. Skogestad, S., Postlethwaite, I.: Multivariable Feedback Control: Analysis and Design. Wiley, Hoboken NJ, USA (2005)
7. Zhou, K., Doyle, J.C., Glover, K.: Robust and Optimal Control. Prentice Hall, Englewood Cliffs, New Jersey (1995)
8. Liu, K.Z., Yao, Y.: Robust Control-Theory and Applications. Wiley (2016)
9. Apkarian, P.: The $\mathcal{H}_\infty$ control problem is solved. Design and validation of aerospace control systems. Aerospace Lab 1–11, Alain Appriou (2017)
10. Tudor, S.F., Oară, C.: $\mathcal{H}_\infty$ control problem for generalized discrete-time LTI systems. In: American Control Conference (ACC), pp. 4640–4645 (2015)
11. Apkarian, P.: Nonsmooth μ synthesis. Int. J. Robust Nonlinear Control **21**, 1493–1508 (2011)
12. Mihaly, V., Şuşcă, M., Morar, D., Dobra, P.: Polytopic robust passivity cascade controller design for nonlinear systems. Proc. of 2022 Eu. Ctrl. Conf. (2022)
13. Khalil, H.,: Nonlinear Control, Global Edition, 1st edn. Pearson Education Limited (2015)
14. Şuşcă, M., Mihaly, V., Dobra, P.: Fixed-point uniform quantization analysis for numerical controllers. In: IEEE Conference on Decision and Control (2022)

Accuracy and Repeatability of a Parallel Robot for Personalised Minimally Invasive Surgery

Doina Pisla, Paul Tucan, Damien Chablat, Nadim Al Hajjar, Andra Ciocan, Alexandru Pusca, Adrian Pisla, Corina Radu, Grigore Pop, and Bogdan Gherman

Abstract The paper presents the methodology used for accuracy and repeatability measurements of the experimental model of a parallel robot developed for surgical applications. The experimental setup uses a motion tracking system (for accuracy) and a high precision measuring arm for position (for repeatability). The accuracy was obtained by comparing the trajectory data from the experimental measurement with a baseline trajectory defined with the kinematic models of the parallel robotic system. The repeatability was experimentally determined by moving (repeatedly) the robot platform in predefined points.

Keywords Parallel robot · Robotic assisted surgery · Measurement · Accuracy · Repeatability

D. Pisla · P. Tucan · D. Chablat · A. Pusca · A. Pisla · G. Pop · B. Gherman (✉)
CESTER, Technical University of Cluj-Napoca, 400114 Cluj-Napoca, Romania
e-mail: Bogdan.Gherman@mep.utcluj.ro

N. Al Hajjar · A. Ciocan
Department of Surgery, "Iuliu Hatieganu" University of Medicine and Pharmacy, 400347 Cluj-Napoca, Romania

C. Radu
Department of Internal Medicine, "Iuliu Hatieganu" University of Medicine and Pharmacy, 400347 Cluj-Napoca, Romania

D. Chablat
École Centrale Nantes, Nantes Université, CNRS, LS2N, UMR 6004, F-44000, Nantes, France

D. Pisla
Technical Sciences Academy of Romania, 26 Dacia Blvd, 030167 Bucharest, Romania

D. Pisla et al. (eds.), *Advances in Service and Industrial Robotics*, Mechanisms and Machine Science 157, https://doi.org/10.1007/978-3-031-59257-7_20

1 Introduction

The advancements of classical surgery have seen notable progress due to the development of multiport or single -port surgical techniques. These techniques represent a transition from traditional surgery, where the patient undergoes an incision ranging between 150 and 250 mm, to performing a reduced number of incisions (3 or 4) with a range varying between 10 and 25 mm in the case of multiport surgery, or a single incision varying between 10 and 25 mm in the case of single-port surgery (SILS) [1, 2]. These two techniques offer several advantages compared to classical surgery: the patient's recovery time is reduced, postoperative ileus experienced by the patient are significantly diminished, better cosmetics and there's a considerable reduction in blood loss [3, 4]. Alongside these advantages, these two techniques come with a series of limitations such as: collisions between instruments, the working space is reduced, lack of tactile feedback, low precision, visualizing the operative field using an endoscopic camera, diminished ergonomics and surgical hand dexterity, instrument crossing (in SILS) and, the surgeon's inability to manipulate more than two instruments simultaneously, and the position of the surgeon above the patient, culminating with prolonged intraoperative time [5, 6]. To reduce or eliminate these disadvantages, a series of robotic mechanical structures have been developed since 2000 when the first robot with FDA (Food and Drug Administration) approval is introduced in the field of surgery (da Vinci—developed by Intuitive Surgery). Intuitive Surgery holding a market monopoly with the structure such as: da Vinci S, da Vinci Si, and da Vinci SP until 2017 when a significant competitor emerged with the commercialization of a new multi-arm robot named Senhance, developed by Asensus Surgical [7, 8]. These structures are come with a series of advantages such as: improved medical ergonomics due to the use of the master–slave concept [9] (the surgeon controls the robot from a seated position through a master console), the surgeon's hand tremor elimination, reduced collisions between instruments, ability to control multiple instruments, improved accuracy and safety in medical procedures. The disadvantages of these system are: high cost of medical procedures, reduced intraoperative workspace, arm collisions, occupying a large volume in the operating room, the need to design new operating rooms adapted to the system's specifications, and the lack of tactile feedback need for out of sight instrument recognition [10].

To mitigate some of the previously mentioned disadvantages a new parallel robot for robotic assisted-surgery (PARA-SILSROB) [11] was developed. To validate the feasibility of the PARA-SILSROB robot experimental model, the robotic system accuracy and repeatability must be measured to determine if these parameters are within the values required for the medical tasks (to ensure safety and adequate control).

The paper presents the experimental assessment of PARA-SILSROB robot accuracy and repeatability using two methods: optical motion tracking and coordinate measuring. Starting from these methods, the accuracy, and the repeatability of the PARA-SILSROB robot is determined using the OptiTrack system [13] for optical detection and Stinger II [14] robotic arm for coordinate measuring. The robot's accuracy and repeatability are determined by comparing the trajectory of the robot's end-effector obtained using optical tracking and the coordinate measuring system with the trajectory generated in MATLAB using the kinematic model of the robot, thus functionally validating the mathematical model of the robot.

Following the Introduction section, the paper is structured as follows: Sect. 2, Materials, and methods, presents the experimental setup of the PARA-SILSROB robot, the preliminary setup of the tracking equipment and methodology used to determinate the accuracy and repeatability of the system. Section 3 presents the results of experimental assessment and Section 4 presents the conclusions and future work.

2 Materials and Methods

There are different techniques and systems of tracking, acquisition and processing biomechanical data, often used in clinical research, as the systems based on wearable sensors [15, 16] or systems based on video cameras. To determine the accuracy and repeatability of the PARA-SILSROB, optical motion tracking and Stinger II measuring arm were used.

2.1 The Experimental Setup

The experimental model of the PARA-SILSROB robot was designed with respect to the medical protocol and surgeon's requirements [2, 12, 17], to control the laparoscopic camera and two active instruments used in minimally invasive surgery. The detailed presentation of the PARA-SILSROB robot's functionality, the experimental model, and the mechanical design of the robot are described in [2, 11, 18] where the authors describe the robotic structure compose of three identical kinematic chains and the mobile platform developed to manipulate the active instruments and the laparoscopic camera necessary to perform the surgery. The experimental model of PARA-SILSROB robot is shown in Fig. 1. Master–Slave concept [9] is used to control the robot, the main console can be equipped with two haptic devices or two 3D Space Mouses.

The OptiTrack [13, 19] motion tracking system contains 6 cameras connected to a common switch controller that collaborates with a windows application installed on the computer. The cameras are placed around the robotic structure in positions that could achieve images of the optical markers placed on the mobile platform of the robot (Fig. 2). This calibration of the system is performed with the help of the CWM 125 calibration device, guided manually in the OptiTrack visual field, each one recording the number of points based on which the workspace of the measurement system is generated. After the system calibration, a fixed reference frame (OXYZ) is defined using the CS-400 calibration square (Fig. 2).

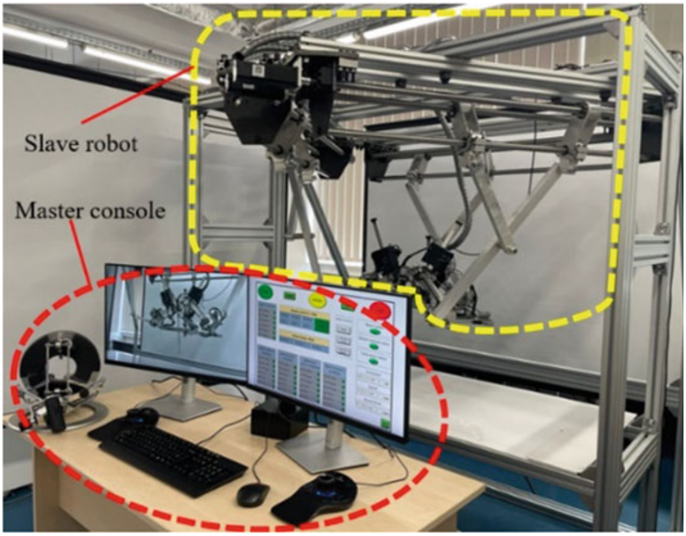

Fig. 1 The experimental model of the PARA-SILSROB

Fig. 2 Experimental setup for optical motion tracking

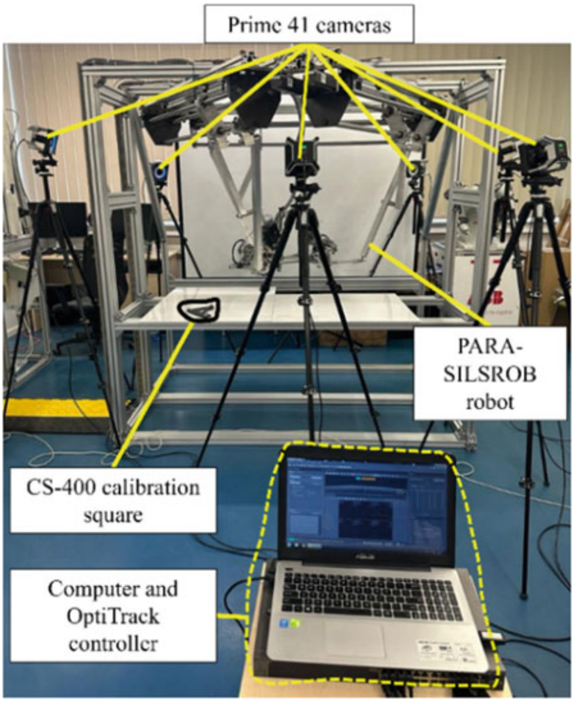

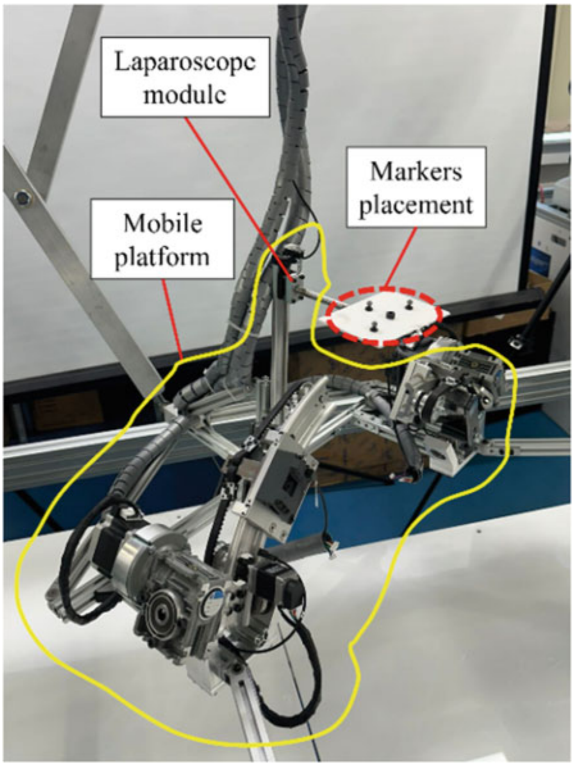

Fig. 3 Optical markers position during the experimental trials

Before placing the optical markers on the mobile platform of the PARA-SILSROB, the robot is initialized and placed in "Home" position (where the orientation angle on each axis is zero). Four markers were used for the measurements, placed on a smooth surface attached to the mobile platform; each marker has a diameter of 6.4 mm. The placement of the markers is shown in Fig. 3.

Figure 4 shows the position of the reference frame and the markers placed on the mobile platform of the robot within the application window of OptiTrack software.

The experimental setup used to determinate the repeatability for coordinate measuring is presented in Fig. 5. The repeatability of the robotic system is determined by using the Stinger II measuring arm [14]. The advantage of this setup used for measurement is the fact that the Stringer II measuring arm does not require calibration, it becomes active after reading the positions on the axes.

2.2 *Methodology*

Figure 6 illustrates the methodology defined for determining the accuracy, and Fig. 7 illustrates the methodology of determining the repeatability of the parallel

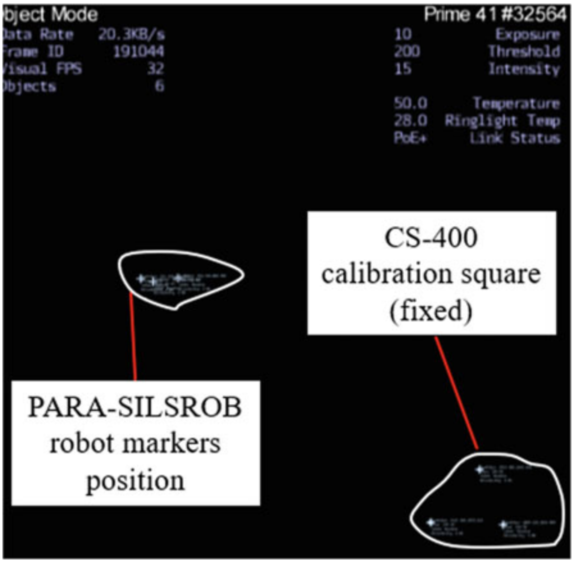

Fig. 4 PARA-SILSROB robot markers placement via motive software

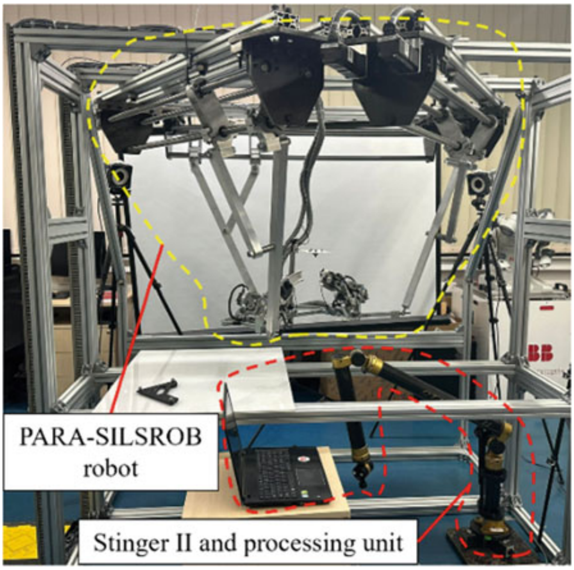

Fig. 5 Experimental setup for coordinate measuring

robotic system. After performing the experimental measurements using the optical tracking system, results were extracted from the systems database and imported in MATLAB for further processing. The OptiTrack system provides an exportable CSV file containing time-based values of the optical markers coordinates (X, Y and Z). In order to allow an accurate reading of the coordinates, a 2 s delay was imputed between the motion command and the motion start of PARA-SILSROB, to assure that the starting time of the optical tracking system is the same with the starting time of the motion. The robot performs a motion using three points, from the starting point, the mobile platform is moved to point 1 then to point 2 from where it moved back to starting position. Three sets of coordinates are obtained for each marker placed on the mobile platform (X, Y and Z). The markers are placed on the mobile platform so that they form a tringle with the centroid (computed using Eq. 1) coinciding with the tool center point (TCP) of the mobile platform. Using MATLAB, the same motion characteristics used in the experimental setup for the robot motion are imputed in a trajectory computation program based on the kinematic modelling of the robot in order to obtain the virtual trajectory of the TCP. The results obtained after processing the data from OptiTrack are compared with the data from the trajectory computation algorithm from MATLAB and graphically represented using the same reference system.

The repeatability of the robot was determined using the coordinate measuring system. For this experiment the evolution of the mobile platform was observed using 5 sets of measurements. The robot was moved from starting position to a selected point 5 times consecutively. Using the Stinger II measurement system, the position of the mobile platform was determined by touching three planes on the mobile platform using the measuring arm, after moving the robot to the second point, the same three planes were measured. In the end 5 sets of coordinates resulted for 4 points. After measurements, data was further processed to determine the repeatability of the robotic system.

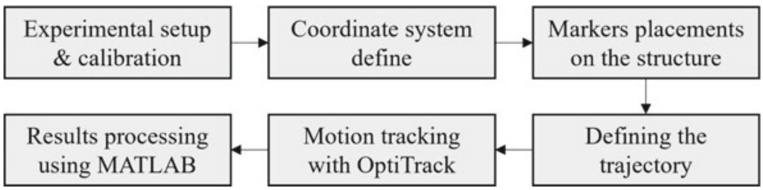

Fig. 6 Methodology used for accuracy of the PARA-SILSROB robot

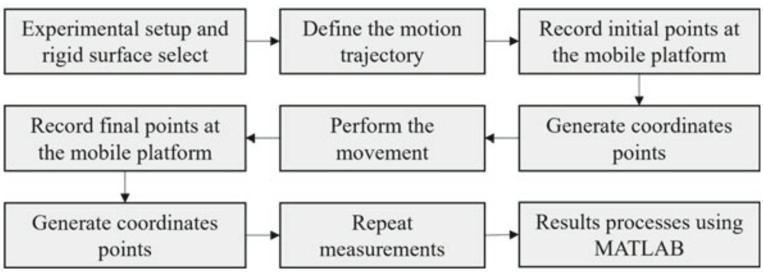

Fig. 7 Methodology used for repeatability of the PARA-SILSROB robot

3 Results

The velocity and acceleration of the PARA-SILSROB used to determine accuracy and repeatability is 20 mm/s and 50 mm/s^2, these parameters are chosen according to the medical protocol and the surgeon requirements [2, 10].

The accuracy was determined for a specific trajectory used to move the mobile platform (RCM) near the insertion point and the results are presented in Fig. 8. When comparing the centroid trajectory and the trajectory obtained using the kinematic model of the robot the Root-Mean-Square Error (RMSE) on the three axes was determined. For X axis RMSE was 0.2866 mm, for Y axis RMSE was 0.4052 and for the Z axis the RMSE was 0.1161. Analyzing the result obtained, the accuracy of the system for this specific trajectory was determined using the RMSE between the RMSE of OptiTrack and the RMSE of values extracted from the experimental model during the experimental run and the result is 0.3 mm, this accuracy is influenced by the OptiTrack system limitation and the light sources, according to the technical requirement of this system the accuracy is 0.1 mm in ideal conditions.

$$C(x, y) = \left(\frac{x_1 + x_2 + x_3}{3}, \frac{y_1 + y_2 + y_3}{3} \right) \quad (1)$$

The repeatability of the PARA-SILSROB was determined according to ISO 21748 [20] and based on the trajectory presented above the data was recorded using the Stinger II robotic arm and the results of data are presented in Fig. 9. In the end the repeatability for point 1 was 0.37 mm, for point 2 was 0.25 mm, for point 3 was 0.31 mm and for point 4 was 0.23 mm. The repeatability standard deviation for the

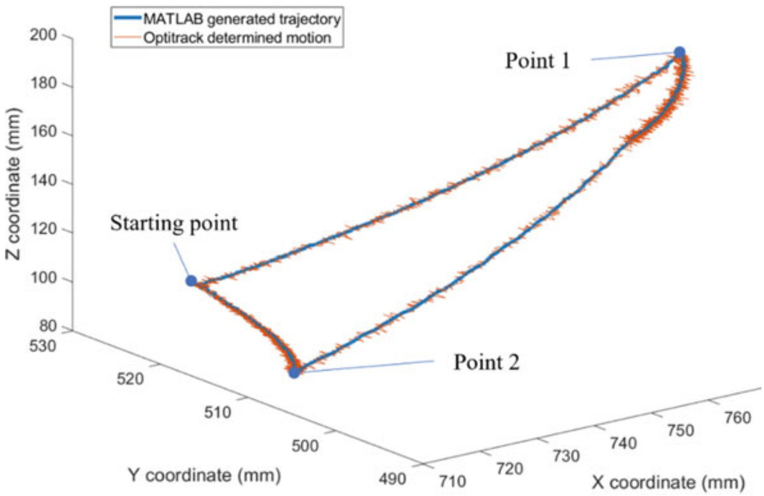

Fig. 8 MATLAB generated trajectory compared with measured trajectory

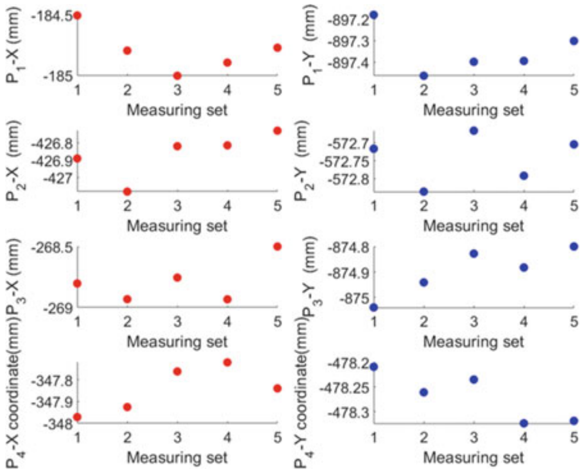

Fig. 9 Stinger II determined repeatability

entire robotic system on the trajectory defined above is 0.18. Based on the studies presented in [21, 22] the accuracy of the robots used in surgery (da Vinci) is 1.02 mm and the repeatability in classical surgery is 1.66 mm, this depends on the experience of surgeon, being also influenced by the hand tremors.

4 Conclusions

The paper presents the experimental assessment of the accuracy and repeatability for the specified trajectory (moving the mobile platform from an arbitrary position near by the insertion point) of the PARA-SILSROB robot, using OptiTrack measurement system for accuracy assessment and Stinger II measuring arm for repeatability assessment. This robot and the experimental test were developed according to the actual requirements used in this field and the medical protocol used in SILS surgery. The experimental measuring was carried out in laboratory conditions and an accuracy of 0.3 mm was obtained and a repeatability standard deviation of 0.18 was also obtained for this trajectory, the results being promising for the first iteration of the robot. Taking into account the fact that the active instruments are manipulated in the intraoperative field based on the images of the laparoscopic camera and in the case of robotic assisted surgery the margin of error is relatively higher due to the elasticity of the tissue, compared to other surgical interventions, the results obtained were considered acceptable.

Future developments will focus on extended this study for different trajectories and the experimental tests on human phantom in relevant medical conditions.

Acknowledgements This work was supported by the project New smart and adaptive robotics solutions for personalized minimally invasive surgery in cancer treatment—ATHENA, funded by European Union—NextGenerationEU and Romanian Government, under National Recovery and Resilience Plan for Romania, contract no. 760072/23.05.2023, code CF 116/15.11.2022, through the Romanian Ministry of Research, Innovation and Digitalization, within Component 9, investment I8 and by a grant of the Ministry of Research, Innovation and Digitization, CNCS/CCCDI—UEFISCDI, project number PN-III-P2-2.1-PED-2021-2790 694PED—Enhance, within PNCDI III.

References

1. Chen, S., et al.: Single-port laparoscopy versus conventional laparoscopy of benign adnexal masses during pregnancy: a retrospective case-control study. J. Int. Med. Res. **50**(10), 3000605221128153 (2022)
2. Pisla, D., et al.: Safety issues in the development of an innovative medical parallel robot used in renal single-incision laparoscopic surgery. J. Clin. Med. **12**(14), 4617 (2023)
3. Kiblawi, R., et al.: Laparoscopic versus open pediatric surgery: three decades of comparative studies. Eur. J. Pediatr. Surg. **32**, 9–25 (2022)
4. Antoniou, S.A., et al.: Past, present, and future of minimally invasive abdominal surgery. JSLS. **19**(3) (2015)
5. Pisla, D., el al.: Algebraic modeling of kinematics and singularities for a prostate biopsy parallel robot. Proc. Rom. Acad. Ser. A **19**, 489–497 (2019)
6. Cepolina, F., et al.: An introductory review of robotically assisted surgical systems. Int. J. Med. Robot. **18**(4), e2409 (2022)
7. Pisla, D., et al.: Kinematical analysis and design of a new surgical parallel robot. In: Proceedings of the 5th International Workshop on Computational Kinematics, pp. 273–282. Duisburg, Germany (2009)
8. Leal, G.T., et al.: 30 years of robotic surgery. World J. Surg. **40**(10):2550–7 (2016)
9. Low, S.C., et al.: A review of master–slave robotic systems for surgery. Int. J. Humanoid Rob. **03**(04), 547–567 (2006)
10. Pisla, D., et al.: Singularity analysis and geometric optimization of a 6-DOF parallel robot for SILS. Machines **10**(9), 764 (2022)
11. Pusca, A., et al.: On the development of an innovative surgical parallel robotic system. In: 11th IEEE International Conference on E-Health and Bioengineering Nov. 2023-in press (2023)
12. Koivukangas, T., et al.: Accuracy assessment phantom for surgical devices. In: 2010 5th Cairo International Biomedical Engineering Conference, pp. 57–60. Cairo, Egypt (2010)
13. Pisla, D., et al.: On the accuracy assessment of a parallel robot for the minimally invasive cancer treatment. J. Eng. Sci. Innov. Z-ASTR 2023-in press (2023)
14. Pop, G.M., et al.: On the association of datums and measurements using conventional measuring devices—topics within the GPS toolbox project. In: Majstorovic, V., Durakbasa, N. (eds.) Proceedings of the 12th—IMEKOTC14, pp. 209–216 (2019)
15. Tarnita, D., et al.: Applications of nonlinear dynamics to human knee movement on plane & inclined treadmill. New Trends in Med. and Service Robots, vol. 39, pp. 59–73. Springer (2016)
16. Tarnita, D., et al.: Contributions on the modeling and simulation of the human knee joint with applications to the robotic structures, pp. 283–297 (2014)
17. Vaida, C., et al.: Development of a control system for a parallel robot used in minimally invasive surgery. IFMBE Proc. **2009**(26), 171–176 (2009)
18. Pisla, D., et al.: Design and functional analysis of a new parallel modular robotic system for single incision laparoscopic surgery. In: New Trends in Medical and Service Robotics. MESROB 2023. Mechanisms and Machine Science, vol. 133. Springer (2023)

19. Ameler, T., et al.: A comparative evaluation of SteamVR tracking and the OptiTrack system for medical device tracking. In: 2019 41st Annual International Conference of the IEEE-EMBC, pp. 1465–1470. Berlin, Germany (2019)
20. ISO 21748:2017 Guidance for the Use of Repeatability, Reproducibility and Trueness Estimates in Measurement Uncertainty Evaluation (2017)
21. Ferguson, J.M., et al.: Comparing the accuracy of the da Vinci Xi and da Vinci Si for image guidance and automation. Int. J. Med. Robot. **16**(6):1–10 (2020)
22. Podsędkowski, L., et al.: Quality in medicine. Polish J. Cardio-Thoracic Surg. **1**(1), 90–101 (2014)

A Concise Review of Upper Limb Prostheses

Radu-Octavian Sandu, Ioan Doroftei, and Cristina-Magda Cazacu

Abstract Upper arm amputations typically result in partial limb loss, thus involving the development of various devices in order to aid the hand function rehabilitation. The trend concerning medical advancements for these types of devices is permanently growing and it is characterized by complex designs and precise constrains regarding mass and size. The main goal of these mechanisms is to replicate normal human limb functions, ensuring a proper reproduction of basic actions. This paper provides a succinct overview of upper limb prosthetic devices, examining various classification criteria.

Keywords Rehabilitation · Prosthetic devices · Upper limb

1 Introduction

Amputation refers to the removal of a limb due to trauma, medical illness or surgery. This surgical procedure is used in order to control pain or to treat a condition such as malignancy or gangrene. The increase number in amputation cases is due to the continuous growth of the industry and a lack of awareness regarding safety measures.

Limp amputation has a profound effect, causing emotional trauma due to the loss of the body part, preventing normal/daily activities, limiting work opportunities, increasing the physical dependence on another person and many other problems. In such cases prostheses become essential for everyday life. These prostheses are artificial body parts designed to restore functional abilities and to facilitate basic movements without manual support. Prosthetic arms are especially needed for subjects that lost an upper limb due to an accident or were born with a physical disability, in order to increase their quality of life.

R.-O. Sandu · I. Doroftei (✉) · C.-M. Cazacu
"Gheorghe Asachi" Technical University of Iasi, 43 D. Mangeron Blvd, 700050 Iasi, Romania
e-mail: idorofte@mail.tuiasi.ro

I. Doroftei
Technical Sciences Academy of Romania, 26 Dacia Blvd, 030167 Bucharest, Romania

D. Pisla et al. (eds.), *Advances in Service and Industrial Robotics*, Mechanisms and Machine Science 157, https://doi.org/10.1007/978-3-031-59257-7_21

Many criteria are considered when selecting an appropriate prosthesis. Considerations influencing this decision involve several factors, including (but not limited to): extent of limb difference, integrity of the remaining limb, functional objectives, work and home requirements, the nature and intensity of activities and aesthetic preferences.

A key criterion when considering prosthetic option is the level of limb difference (see Fig. 1). Generally accepted terminology for classifying upper limb disarticulation is as follows: glenohumeral (shoulder) disarticulation, elbow disarticulation, styloid/wrist disarticulation (for amputation starting with the respective joint) and transhumeral (above elbow), transradial (below elbow) and transcarpal or partial hand/finger [1].

Another key criterion for prosthetic devices is regarding the functional anatomy of the human torso, shoulder and upper extremity, more specific the range of motion of these parts. The movements with respect to the tri-orthogonal axis system of the upper limb are complex, but a few movements are essential for each case (the others resulting by combining these basic ones). Therefore, for a shoulder disarticulation the range of motion is 20° for flexion/15° for extension and also 40° for elevation/10° for depression. For a transhumeral amputation was recorded a range of motion of 180° flexion/60° extension, 180° elevation/20° depression and a rotation of 90° medial/20° lateral. The last case, for a transradial amputation a range of motion of 140° flexion/0° extension and 80° supination/90° pronation was noted [2].

Current prosthetic options vary both functionally and cosmetically, and meet a wide range of user needs and lifestyles. Some of these options and their classification are discussion in the following paragraph.

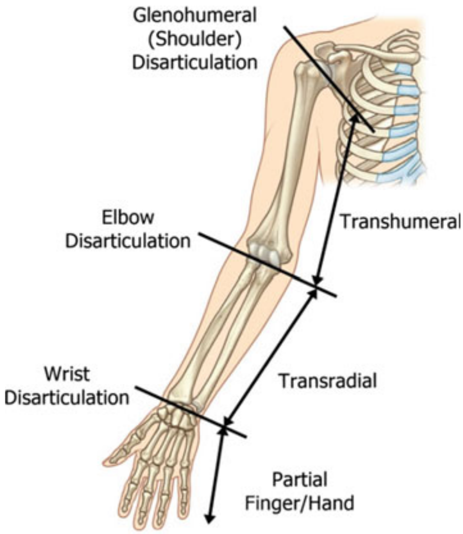

Fig. 1 Levels of amputation

2 Classification of Upper Limb Prostheses

In recent years, several proposals for upper limb prostheses have emerged. Currently available prosthetic devices can be classified according to different criteria. The first criteria will be, of course, the category of upper limb disarticulation (see Fig. 2). Moving forward they can be classified as passive prosthetics that do not provide any function and are related to physical appearance and active prosthetics that focus on the functionality of the patient. In the active prosthetics category will find externally powered devices, body powered devices and hybrid devices.

The classification of upper limb prosthetics could also take into consideration materials, type of control and any other design specific requirements. In the following paragraphs a succinct overview of upper limb prosthetic devices is presented, examining various classification criteria.

2.1 Control-Based Classification

Regarding the control systems for these devices, they can be divided as follows:

- body-powered prosthetics, which utilize cables, harnesses, and body movements to control the movements, this is achieved through residual movements of the user and the limb, such as shoulder shrugs or arm contractions, which activate mechanical linkages to manipulate the prosthetic limb;
- myoelectric prosthetic systems, which are using electromyographic (EMG) signals generated by residual muscle contractions to control a prosthetic limb;
- brain-machine interface devices, when electroencephalography (EEG) systems detect and analyze the electrical activity generated by the user's brain, translating it into commands for the device;

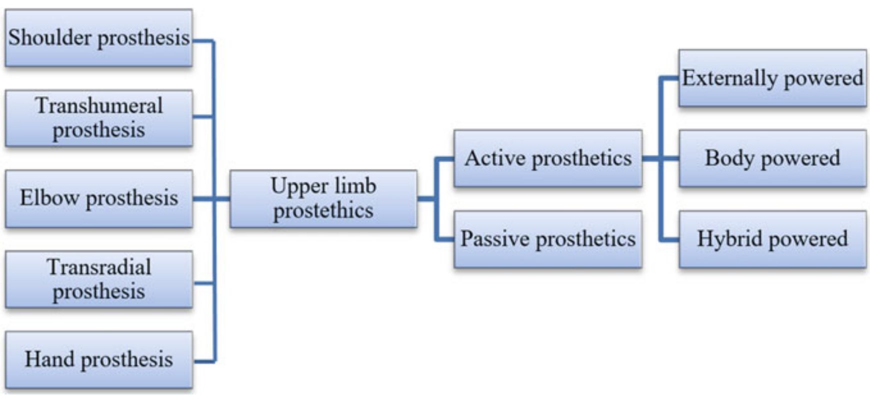

Fig. 2 Classification of prosthetic devices

- hybrid prosthetic systems, combining elements of both body power and myoelectric control methods to provide users with greater flexibility and functionality;
- pattern recognition systems, which analyze patterns in EMG signals to predict the user's intended movements and converting them into control commands for the prosthetic limb.

All these control strategies can be enhanced with sensory feedback from sensors such as accelerometers, gyroscopes, force sensors, or pressure sensors, to detect user movements and gestures for prosthetic control. These sensors provide real-time feedback on the position, orientation, and force exerted by the prosthetic limb, enabling precise and responsive control.

The Victoria Hand (Fig. 3a) is an affordable upper extremity prosthetic solution designed for transradial or transhumeral amputations. Using 3D printing and 3D scanning technologies during the manufacturing process, the system incorporates stainless steels to improve strength. The Voluntary Close Hand remains open until the user shrugs their shoulders to actuate the hand, and close the fingers [3].

Another type of control is based on electromyography data. The prosthetic from Fig. 3b operates through muscular contractions based on the patient's intention. A specially designed EMG surface sensor records muscle contraction signals from the residual forearm of amputees [4]. This prosthetic design includes an underactuated 3D printed hand with a socket assembly to attach to the remaining upper limb of the patient. The control system utilizes input from the EMG sensor and feedback input from a force sensor in order to allow users to control the grasp force of the hand fingers.

In order to experimentally investigate design features and control strategies of transhumeral prostheses a myoelectric prototype was developed [5]. This device (Fig. 3c) owns a powered wrist rotator, a powered elbow joint and a multi-grasp hand. This prosthesis allows different range of motions of the joints and provides a

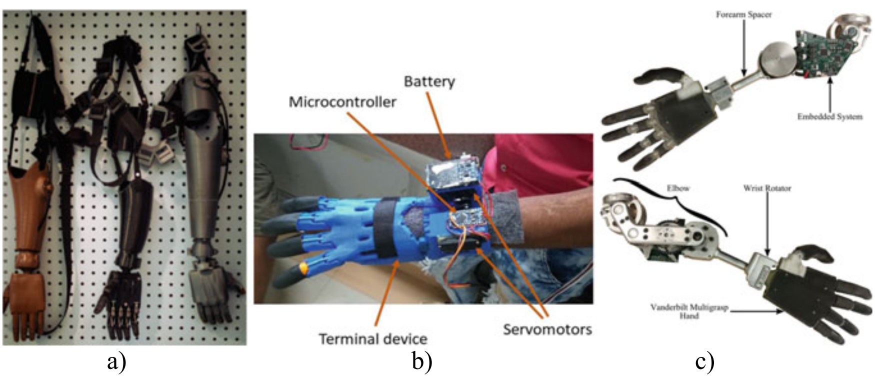

Fig. 3 Prosthesis with different control strategies: **a** transhumeral prosthesis—body powered [3]; **b** transradial prosthesis—myoelectric control [4]; **c** transhumeral prosthesis—myoelectric control [5]

satisfactory torque in order to safely operate. Transhumeral prostheses are necessary to restore independence and function to people who have suffered the loss of an upper limb. The constant development of materials and technology improves the design and properties of these prostheses, offering users an increasingly realistic and versatile solution to manage their daily activities.

MataPro-1 is a novel biomemitic transradial prosthetic arm that incorporates a 3D printed hand bone structure, assuring a close imitation of the morphology of human fingers and hand (see Fig. 4a). This prosthetic device has flexible elastic joints, artificial muscles and a silicone coating that assures a realistic appearance [6]. The artificial muscles that drive this prosthesis consist of shape memory alloy (SMA) wires, ensuring an effective grip strength for daily activities. These shape memory alloy wires are spooled in the forearm, actively cooled by a fan and are connected further to steel wires that actuate the phalanges.

A smart prosthesis controlled by electroencephalography (EEG) signals is presented in Fig. 4b [7]. The device is equipped with smart sensors and actuators in order to provide the user intelligent feedback about the environment. The sensors system includes sensors for temperature, pressure, proximity, accelerometers, potentiometers, strain gauges and gyroscopes. In the headset are included 14 EEG sensors that are converted into digital signals. The processing unit, consisting in a Rasberry PI II microcomputer and an Arduino Mega microcontroller, compares the signals received with different prerecorded tasks, providing feedback to the user on an LCD display.

In Fig. 5a, a dynamic arm externally powered is presented. This device can open and close almost three times faster than other hands, reaching 300 mm per second. In addition, it has an automatic grip function that includes sensor technology that detects when the object begins to slip. The electric motor allows the elbow to move twice as fast as other electric elbows, turning extension to full flexion in just 0.5 s [8, 9].

The transradial prosthetic arm with multiple degrees of freedom presented in Fig. 5b is capable of generating forearm supination/pronation, wrist flexion/

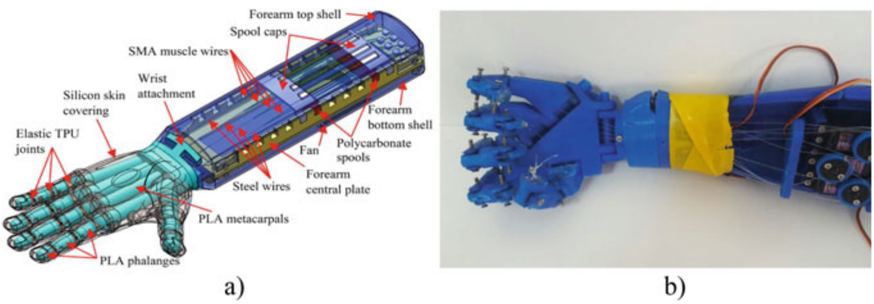

Fig. 4 Transradial prosthesis: **a** MataPro-1-shape memory alloy actuation [6]; **b** EEG mind-controlled ARM [7]

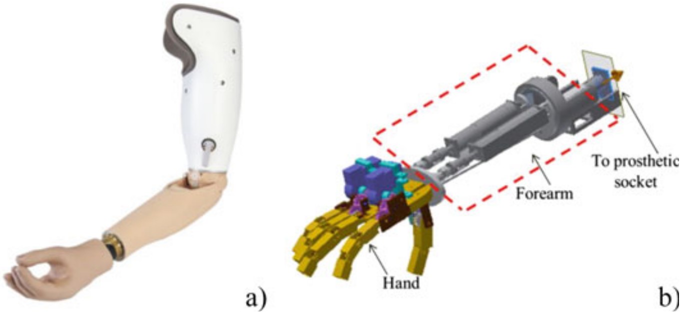

Fig. 5 Externally powered prosthesis: **a** transhumeral prosthesis-dynamic arm [8]; **b** transradial prosthesis-electric actuation [10]

extension, wrist ulnar/radial deviation, and finger motions [10]. The wrist mechanism utilizes one passive link to ensure rigidity and two linear actuators connected to the wrist plate through universal joints. These actuators correspond to the ulna and radial bones of the forearm, contributing to forearm motion, namely supination/pronation. The terminal section of the transradial prosthetic arm is an anthropomorphic hand, featuring separate actuation modules for the thumb, index finger, and the remaining three fingers, collectively providing 7 degrees of freedom.

The field of upper body prostheses is characterized by various control systems adapted to the specific needs of users. From body-based devices that use residual movements to advanced brain-machine interfaces that convert nerve signals into commands, these systems offer amputees greater functionality and independence.

2.2 Materials-Based Classification

The materials that have been used for upper body prosthetic devices have evolved through time. Several materials can be used for these devices as follows [11]:

- metals, used mainly for the skeletal design, such as titanium, aluminum and stainless steel;
- polymers such as acrylic resin (PMMA), that are often used to fabricate prosthetic sockets due to its moldability, transparency, and ability to form a customized fit for the user's residual limb;
- silicone that offers flexibility, elasticity and a skin-like structure that improves user comfort and aesthetics;
- carbon fiber is light, durable and has a high tensile strength, making it an ideal material for structural components such as prosthetic sockets, frames or supports;
- 3D printed materials, when additive manufacturing techniques allow the use of different materials, including thermoplastics, resins or metals, to create custom prosthetic components with complex geometries and tailored features.

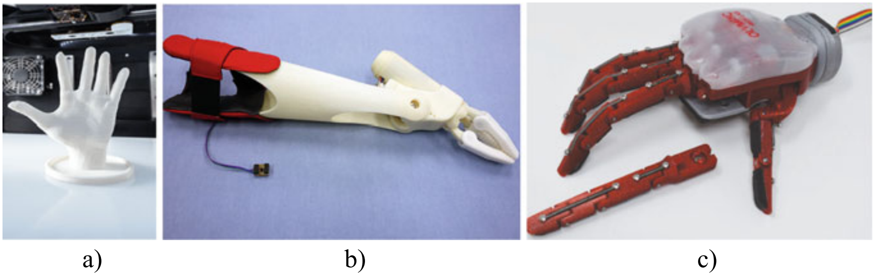

Fig. 6 3D printed prosthesis: **a** passive hand prosthesis [12]; **b** active transradial prosthesis [13]; **c** OLYMPIC-modular prosthesis [14]

An innovative approach to hand prosthesis is to utilize the precision and versatility of 3D printing technology to create custom, cost-effective prostheses tailored to each individual's unique needs (Fig. 6a). One of the main advantages of 3D printed prosthetic arms is their accessibility [12]. The cost-effectiveness of 3D printing will make these prostheses more affordable, potentially increasing access to a wider population.

The myoelectric prosthetic presented in Fig. 6.b is designed to be used in work environments. The device has a natural appearance, similar to the human hand, and the myoelectric control system makes it easy to use. The three fingers of the device are controlled by a linear actuator and a simple mechanism, making it lightweight and low-cost [13]. The prosthetic is 3D printed, this ensures a total weight of the hand and socket of only 300 g.

In Fig. 6c a prosthesis with a completely modular structure both at the level of fingers and wrists is presented. This design makes it easy to remove and attach tendon-driven fingers without tools, rewiring or wires. This approach allows the motors to be placed behind the hand, resulting in a remote control of the tendons. The hand prototype was fabricated using PLA (Polylactic Acid) and PETG (Polyethylene Terephthalate) through 3D printing. PETG was specifically selected for its enhanced strength and durability, attributed to the frequent loading experienced by the fingers and hand frame. Various household and food items of different shapes, sizes and weights can be safely grasped with the prosthetic hand without the risk of the fingers becoming detached [14].

Hybrid devices can use passive modules as well as body-powered ones, like the prosthesis presented in Fig. 7a. The shell is made from carbon fiber while the fingers are made from steel with a soft silicone inner socket. This prosthesis uses the power of the wrist movement to move the finger in order to grasp and release objects [15] and it's customed tailored for the patient.

The MANUS-HAND introduces a prosthetic design featuring ten joints, with three of them being autonomously driven (Fig. 7b). The remaining joints are interconnected to the driven ones through various mechanisms, in accordance with the underactuated principle. This allows the grasping modes to be activated with only

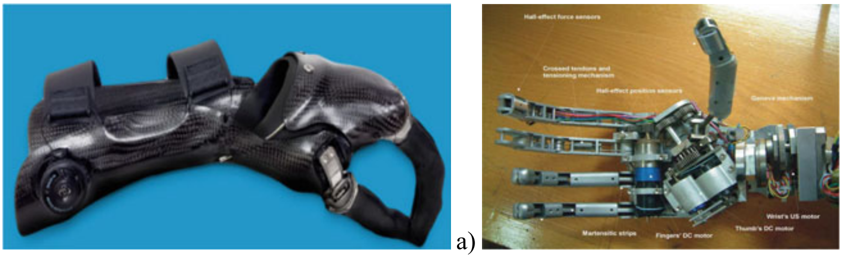

a) b)

Fig. 7 Hand prosthesis: **a** body powered prosthesis [15]; **b** MANUS-HAND [16]

two actuators. Ultrasonic motors were used to drive the wrist pronation and supination. The materials used for this prototype are a combination of metals-aluminum alloy and stainless steel, with martensitic strips used for fingers. Within the MANUS-HAND prototype, three distinct independent mechanisms are incorporated: the finger mechanism, the thumb mechanism and the wrist mechanism. This innovative design that triples the performance of currently existing commercial hand prosthesis [16].

The Boston Elbow [17, 18] (Fig. 8a) is a myoelectric elbow prosthesis with one active degree of freedom, namely elbow flexion. It attaches to the upper arm via surface electrodes and can be connected as a final device to the Otto Bock Myoelectric Hand. The prosthetist begins by layering foam downwards from the above-elbow socket and then affixes a prosthetic elbow unit containing a battery-powered motor. Within the forearm of the Boston Elbow, the batteries and electronics are housed. The materials used are a combination of silicon, polymers and metals. The weight of this prosthesis is 1020 g, providing the user a comfortable operation.

The Espire Elbow is a revolutionary prosthesis that places importance on user experience by combining function and design. Espire Hybrid (Fig. 8b) offers myoelectric control of the elbow lock and terminal device with mechanical flexion

a) b) c)

Fig. 8 Elbow prosthesis: **a** Boston Elbow-myoelectric control [17]; **b** Espire Hybrid [19]; **c** Utah Arm-externally powered [20] and extension control. The prosthetic is laminated in polyester with toughened integrated side steels and contains different elements. This device features an adjustable forearm counterweight mechanism designed to evenly distribute the weight of the forearm, wrist and handset. It effectively neutralizes the effect of gravity, allowing the user to position the forearm with as little effort as possible [19].

The Utah Arm 3+ (Fig. 8c) is a light weight, microprocessor-controlled electric elbow. It offers precise and responsive electronic elbow control and the ability to simultaneously control the arm or ETD (Electrical Terminal Device). The structural components of this device are made from high-strength plastic and other metallic materials. With a double locking system that includes a friction lock and a locking pin for heavier loads, the U3+ ensures safe operation. The Silent Freeswing function turns off the motor, saving battery life and providing a more natural arm movement during rest. An advantage is represented by the fact that the U3+ is compatible with almost all other manufacturers [18, 20].

The field of upper body prosthetics has seen significant advances in materials and design, enabling more functional and easier to use solutions for individuals with limb loss. Advances in materials, including metals, polymers, carbon fibers and 3D-printed materials, have provided prosthetic wearers with options that offer strength, durability, customization and cost-effectiveness. Innovative approaches such as 3D printing have revolutionized the production of prosthetic limbs, making them more affordable and accessible to the general population.

3 Conclusions

Amputation due to trauma, medical illness or surgery has a profound effect on people, causing emotional trauma and interfering with daily activities. Prostheses play a crucial role in restoring the functional abilities of lost limbs and improving the quality of life. Various considerations are taken into account when choosing an appropriate prosthesis, including the level of limb disparity, functional goals, job requirements, and aesthetic preferences. Advances in prosthetic technology have led to the development of various options, from passive to active devices, each of them offering different levels of functionality and control. Control systems such as body-powered, myoelectric, brain-machine interface and hybrid systems offer users greater flexibility and responsiveness. In addition, the materials used in prosthetic fabrication have evolved over time to provide strength, durability and adaptability. Innovations such as 3D printing have made prosthetics more accessible and cost-effective, expanding the availability of prosthetics to a wider population.

Although the revised upper limb prostheses offer significant advances and benefits, they also have certain disadvantages. One of these disadvantages is the cost because many advanced prosthetic devices, especially those with electronic components or complex structures, can be expensive. These high costs can limit access for those with limited financial resources, leading to inequalities in access to health care. Regular maintenance and occasional repairs are required for prosthetics, especially those with complex mechanisms or electronic components. This can be time-consuming and expensive, and individuals may lose their prosthesis during maintenance. Another problem is that adapting and learning how to use them effectively can be difficult and time consuming. Individuals may require extensive training and rehabilitation to maximize use of the devices, and some may have difficulty adapting to their functionality. Addressing these disadvantages requires ongoing research and development in prosthetic technology, as well as efforts to improve affordability, accessibility, and user experience for individuals with limb loss.

Future work will investigate energy-efficient actuation systems for prosthetic devices in order to extend battery life and enhance user autonomy. Research could also focus on integrating tactile sensors and haptic feedback mechanisms for the purpose of improving users' ability to interact with their environment.

The continuous development of materials, technology and design in the field of prosthetics offers users more and more realistic and versatile solutions. Prosthetic options are evolving to meet different needs, ultimately allowing amputees to live fuller lives.

References

1. Trent, L., Intintoli, M., Prigge, P., Bollinger, C., Walters, L.S., Conyers, D., Miguelez, J., Ryan, T.: A narrative review: current upper limb prosthetic options and design. Disabil. Rehabil. Assistive Technol. (2019)
2. Taylor, C.L.: The biomechanics of control in upper-extremity prostheses. National Academy of Sciences, Washington, DC, USA (1955)
3. Victoria Hand project. https://www.victoriahandproject.com/vhp-hands. Accessed 24 Jan 2024
4. Bennett, D.A., Mitchell, J.E., Truex, D., Goldfarb, M.: Design of a myoelectric transhumeral prosthesis. IEEE/ASME Trans. Mechatron. **21**(4), 1868–1879 (2016)
5. Prakash, A., Sharma, S.: A low-cost transradial prosthesis controlled by the intention of muscular contraction. Phys. Eng. Sci. Med. **44**(1), 229–241 (2021)
6. Bishay, P.L., Fontana, J., Raquipiso, B., Rodriguez, J., Borreta, M.J., Enos, B., Gay, T., Mauricio, K.: Development of a biomimetic transradial prosthetic arm with shape memory alloy muscle wires. Eng. Res. Express **2**(3), 035041 (2020)
7. Taha Beyrouthy, S.A.K., Korbane, J., Abouelela, M.: EEG mind controlled smart prosthetic arm–a comprehensive study. Adv. Sci. Technol. Eng. Syst. J. **2**(3), 891–899 (2017)
8. Otto Bock Arm Prostheses. https://www.ottobock.com/en-us/home. Accessed 24 Jan 2024
9. Kulkarni, T., Uddanwadiker, R.: Overview: mechanism and control of a prosthetic arm. Mol. Cell. Biomech. **12**(3), 147–195 (2015)
10. Bandara, D.S.V., Gopura, R.A.R.C., Hemapala, K.T.M.U., Kiguchi, K.: A multi-DoF anthropomorphic transradial prosthetic arm. In: 5th IEEE RAS/EMBS International Conference on Biomedical Robotics and Biomechatronics, pp. 1039–1044. IEEE (2014)
11. Brack, R., Amalu, E.H.: A review of technology, materials and R&D challenges of upper limb prosthesis for improved user suitability. J. Orthop. **23**, 88–96 (2021)
12. Amazing Real-World Examples of 3D Printing. https://bernardmarr.com/7-amazing-real-world-examples-of-3d-printing. Accessed 24 Jan 2024
13. Yoshikawa, M., Taguchi, Y., Sakamoto, S., Yamanaka, S., Matsumoto, Y., Ogasawara, T., Kawashima, N.: Trans-radial prosthesis with three opposed fingers. In: 2013 IEEE/RSJ International Conference on Intelligent Robots and Systems, pp. 1493–1498. IEEE (2013)

14. Liow, L., Clark, A.B., Rojas, N.: Olympic: a modular, tendon-driven prosthetic hand with novel finger and wrist coupling mechanisms. IEEE Robot. Autom. Lett. **5**(2), 299–306 (2019)
15. Arm Dynamics. https://www.armdynamics.com/upper-limb-library/what-is-a-hybrid-upper-limb-prosthesis. Accessed 24 Jan 2024
16. Pons, J.L., Rocon, E., Ceres, R., Reynaerts, D., Saro, B., Levin, S., Van Moorleghem, W.: The MANUS-HAND dextrous robotics upper limb prosthesis: mechanical and manipulation aspects. Auton. Robot. **16**, 143–163 (2004)
17. The Boston Elbow, Health Technology Case Study 29, November 1984. https://www.princeton.edu/~ota/disk3/1984/8405/8405.PDF. Accessed 24 Jan 2024
18. Bandara, D.S.V., Gopura, R.A.R.C., Hemapala, K.T.M.U., Kiguchi, K.: Upper extremity prosthetics: current status, challenges and future directions. In: The Seventeenth International Symposium on Artificial Life and Robotics (2012)
19. Espire Hybrid. https://www.thelondonprosthetics.com/prosthetic-solutions/upper-limb/bionics/espire-elbow. Accessed 24 Jan 2024
20. Uttah Arm 3+. https://fillauer.com/products/utah-arm-3-2/. Accessed 24 Jan 2024

Analysis Study of Working Modes Within a Redundant Architecture for a Spherical Parallel Manipulator (SPM)

Jasser Enbaya, Juan Sandoval, Moncef Ghiss, Zoubeir Tourki, Marc Arsicault, Said Zeghloul, and Med Amine Laribi

Abstract In this study, we focus on a 3DOF (RRR) spherical parallel manipulator (SPM) employed as haptic interface (HI) for teleoperation application. We started by presenting the kinematic model of the interface, its different working modes and identifying singularity zones within the operational workspace (WS). As a solution, a redundant architecture is proposed where we used a fourth motor to enhance the dexterity of the device. Subsequently, our study takes a closer look at the comparative analysis of working modes in the purpose of selecting the optimal starting configuration for our interface. This selection ensures an optimized torque distribution across various WS configurations where we respect the limit of torques for every motor in order to stay in a safe zone of control.

J. Enbaya · M. Ghiss · Z. Tourki
Mechanical Laboratory of Sousse (LMS), National Engineering School of Sousse, University of Sousse, 4000 Sousse, Tunisia
e-mail: jasser.embaya@eniso.u-sousse.tn

M. Ghiss
e-mail: moncef.ghiss@eniso.u-sousse.tn

Z. Tourki
e-mail: zoubeir.tourki@mesrs.tn

M. Arsicault · S. Zeghloul · M. A. Laribi (✉)
Department of GMSC, Pprime Institute CNRS, ENSMA, University of Poitiers, UPR 3346, Poitiers, France
e-mail: med.amine.laribi@univ-poitiers.fr

M. Arsicault
e-mail: marc.arsicault@univ-poitiers.fr

S. Zeghloul
e-mail: said.zeghloul@univ-poitiers.fr

J. Sandoval
Nantes Université, École Centrale Nantes, CNRS, LS2N, UMR 6004, F-44000, Nantes, France
e-mail: Juan.sandoval@ls2n.fr

D. Pisla et al. (eds.), *Advances in Service and Industrial Robotics*, Mechanisms and Machine Science 157, https://doi.org/10.1007/978-3-031-59257-7_22

Keywords Haptic interface · Redundancy · Dexterity · Working modes · Torque control · Optimal torque distribution · Spherical parallel manipulator · Teleoperation

1 Introduction

The collaboration between humans and robots has proven its efficiency in various domains, including manufacturing, industry, logistics, agriculture, and notably in the healthcare field. For instance, the integration of robots has significantly enhanced surgeons' precision [1] and expanded their ability to perform intricate procedures such as minimally invasive surgery (MIS) [2], which are characterized by the use of smaller incisions that leads to faster healing times and improved aesthetic outcomes for patients.

Haptic interfaces [3] amplify these benefits by allowing surgeons to conduct operations from a distance. This capability is particularly beneficial in operations with a limited field of view or a high risk of contamination, as observed during the COVID-19 pandemic [4]. Additionally, these interfaces contribute positively to the ergonomic posture of surgeons, particularly addressing musculoskeletal disorders among older practitioners [5]. Having an ideal haptic interface has been quite a challenge so far, requiring low inertia and friction values, along with a spacious workspace and high stiffness and dexterity. That's why numerous interfaces have been developed to meet these demands, employing various architectures [6] and control strategies [7] to achieve optimal results. Parallel architectures have proven superiority over the serial ones, in terms of stiffness and precision [8]. Many parallel manipulators have been developed [6] for various purposes, but when it comes to MIS the spherical parallel manipulator remains one of the most suitable architecture since its joint axes converge to a common point called the center of rotation (CoR). Tanio and al. [9] have proposed a novel spherical parallel manipulator with nonidentical limbs for MIS applications, and Li et al. [10] have utilized spherical parallel mechanisms for laparoscopic surgery. However, parallel spherical manipulator come with drawbacks, such as the potential occurrence of singularity at the center of the workspace for specific configurations, like when all the legs of the manipulator are parallel, this type of singularity is referred to as parallel singularity. Various methods have been proposed to overcome this drawback, Lee et al. [11] proposed a specific algorithm in the zone near singularity and Arsenault et al. [12] by proposing a design method that is capable of avoiding the presence of parallel singularities inside the WS. Indeed, the behavior of the parallel manipulator can be enhanced or deteriorated by the operating mode. Two aspects can impact the behavior of the structure, the assembly modes and the working modes linked to forward kinematic modal (FKM) and inverse kinematic model (IKM), respectively [13, 14]. So once the choice of architecture is made the issue of the way that the structure will be operated becomes important.

This paper focuses on a spherical parallel manipulator [15] with 3 degrees of freedom (DOF) RRR (R: revolute) (refer to Fig. 1). The manipulator is composed of

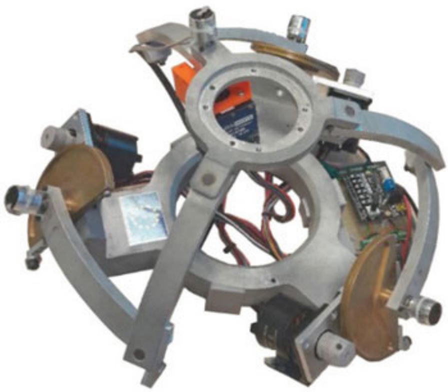

Fig. 1 Spherical parallel manipulator (SPM)

three identical legs denoted as A, B, and C. Linking the base to the mobile platform, each leg consists of two segments (proximal and distal) and three pivot joints.

The axes of the three revolute joints of the base form an orthonormal reference frame (X, Y, Z). The geometrical parameters of the SPM are defined by the angles α, β, and γ that equal respectively 39.3°, 34.1° and 18.2° (see Fig. 2a). These values have been selected based on the SPM geometry parameter optimization work conducted by Chaker et al. [16]. To provide haptic feedback, a motorized joint is present at the base level for each leg, the motors used are from simplex motion type SC040B providing a maximum torque of 0.8 Nm and a maximum speed of 6000 rpm. Additionally, four absolute encoders have been implemented on different joints to enhance the forward kinematic model (FKM) resolution (refer to Fig. 2b). The kinematic model will be further discussed in the next part of the article.

The paper is organized as follows: In Sect. 2, we introduce the kinematic model of the SPM, covering the eight potentials working modes, and we discuss the appearance of singularity zones within the workspace (WS). Section 3 outlines a redundant

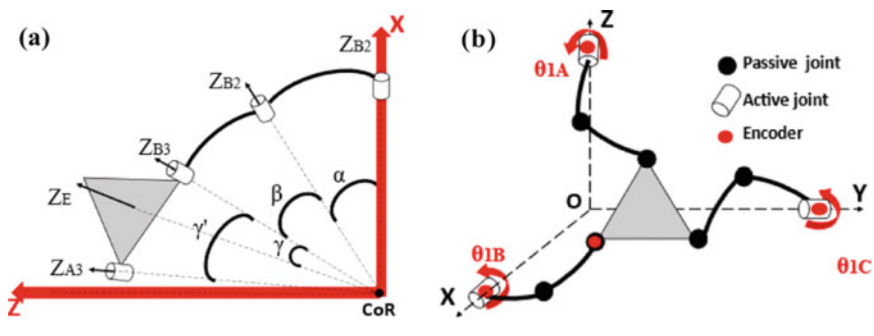

Fig. 2 **a**: Geometrical parameters of the SPM, **b**: motors and encoders emplacement

architecture with a fourth motor to overcome singularity issues in the classic SPM. Section 4 includes an analysis study of all the modes aiming to show the need for the selection of a suitable one. Criterion are introduced in this section based on dexterity and torque distribution for the motors.

2 SPM Presentation

2.1 Kinematic Model

The purpose of the inverse kinematic model (IKM) is to express the values of the actuated joints ($\theta_{1A}, \theta_{1B}, \theta_{1C}$) in function of the end effector (EE) configuration (ψ, θ, ϕ) all referenced to the base frame (X, Y, Z) (refer to Fig. 3).

The IKM of our manipulator can be resolved through this geometrical relation:

$$\mathbf{Z}_{2k} \cdot \mathbf{Z}_{3k} = \cos\beta \tag{1}$$

where $\mathbf{Z}_{2k}$ and $\mathbf{Z}_{3k}$ represent respectively the rotation axis of the second and the third articulation of leg k, where k ∈ {A, B, C}.

$$\mathbf{Z}_{2k} = \mathbf{R}_{0k} \cdot \mathbf{R}_Z(\theta_{1k}) \cdot \mathbf{R}_X(\propto) \cdot \mathbf{Z} \tag{2}$$

$$\mathbf{Z}_{3k} = \mathbf{R}_E \cdot \mathbf{R}_Z\left(\frac{2\pi}{3}(i-1)\right) \cdot \mathbf{R}_X(\gamma) \cdot \mathbf{Z}, \text{ for } i \in \{1, 2, 3\} \tag{3}$$

With R_E is the transformation matrix from the base to the EE,

$$\mathbf{R}_E = \mathbf{R}_Z(\psi) \cdot \mathbf{R}_X(\theta) \cdot \mathbf{R}_Z(\phi) \tag{4}$$

After substituting $\mathbf{Z}_{2k}$ and $\mathbf{Z}_{3k}$ with their expressions in Eq. (1) and differentiating the result, we obtain the following system:

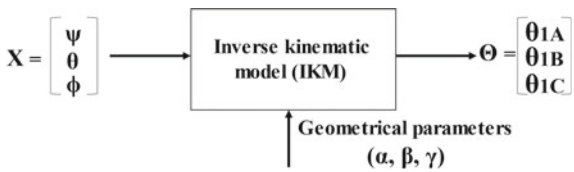

Fig. 3 IKM logic: inputs/ outputs

$$\begin{cases} A_1 \cos\theta_{1A} + B_1 \sin\theta_{1A} + C_1 = 0 \\ A_2 \cos\theta_{1B} + B_2 \sin\theta_{1B} + C_2 = 0 \\ A_3 \cos\theta_{1C} + B_3 \sin\theta_{1C} + C_3 = 0 \end{cases} \tag{5}$$

where A_i, $B_i endC_i$ are variables depend on α, β, γ, ψ, θ and ϕ.

In order for Eq. (5) to have solutions:

$$\frac{C_i^2}{A_i^2 + B_i^2} \leq 1, \text{ for i} \in \{1, 2, 3\} \tag{6}$$

After resolving Eq. (5), we derived the final expression for the relationship between the values of the actuated joints (θ1A, θ1B, θ1C) and the orientation values of the EE (ψ, θ, ϕ).€

$$\begin{cases} \theta_{1A} = \begin{cases} a\tan 2\left(y_1^1, x_1^1\right) \\ a\tan 2\left(y_1^2, x_1^2\right) \end{cases} \\ \theta_{1B} = \begin{cases} a\tan 2\left(y_2^1, x_2^1\right) \\ a\tan 2\left(y_2^2, x_2^2\right) \end{cases} \\ \theta_{1C} = \begin{cases} a\tan 2\left(y_3^1, x_3^1\right) \\ a\tan 2\left(y_3^2, x_3^2\right) \end{cases} \end{cases} \tag{7}$$

With $x_{1,2}$ and $y_{1,2}$ are variables depend on α, β, γ, ψ, θ and ϕ.

2.2 Working Modes

The IKM of our SPM has 8 solutions which are referred to as working modes. The table above summarizes all the possible modes (Table 1).

Table 1 All possible modes of the SPM

Modes	θ_{1A}	θ_{1B}	θ_{1C}
1	$a\tan 2(y_1^1, x_1^1)$	$a\tan 2(y_2^1, x_2^1)$	$a\tan 2(y_3^1, x_3^1)$
2	$a\tan 2(y_1^1, x_1^1)$	$a\tan 2(y_2^1, x_2^1)$	$a\tan 2(y_3^2, x_3^2)$
3	$a\tan 2(y_1^1, x_1^1)$	$a\tan 2(y_2^2, x_2^2)$	$a\tan 2(y_3^1, x_3^1)$
4	$a\tan 2(y_1^1, x_1^1)$	$a\tan 2(y_2^2, x_2^2)$	$a\tan 2(y_3^2, x_3^2)$
5	$a\tan 2(y_1^2, x_1^2)$	$a\tan 2(y_2^1, x_2^1)$	$a\tan 2(y_3^1, x_3^1)$
6	$a\tan 2(y_1^2, x_1^2)$	$a\tan 2(y_2^1, x_2^1)$	$a\tan 2(y_3^2, x_3^2)$
7	$a\tan 2(y_1^2, x_1^2)$	$a\tan 2(y_2^2, x_2^2)$	$a\tan 2(y_3^1, x_3^1)$
8	$a\tan 2(y_1^2, x_1^2)$	$a\tan 2(y_2^2, x_2^2)$	$a\tan 2(y_3^2, x_3^2)$

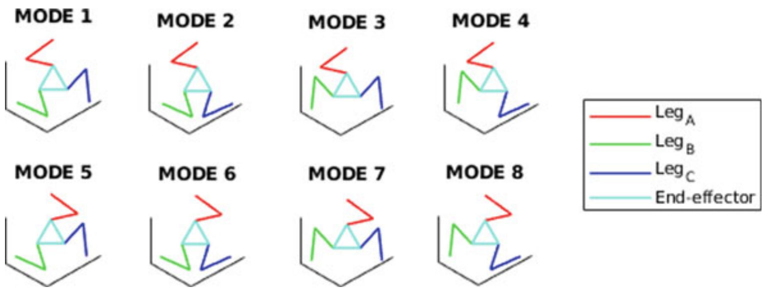

Fig. 4 The SPM work modes in the configuration ($\psi = 135°$, $\theta = 54.7°$, $\phi = 90°$)

Selecting one of those modes (refer to Fig. 4) as the starting configuration for our manipulator is crucial as it directly affects both dexterity and torque distribution for the motors across all configurations within the workspace (WS). A comparative study of these modes will be conducted in Sect. 4, considering criteria formulated on dexterity, the distance between the center of the WS and the singularity zones, and on the optimal torque distribution.

2.3 Singularity

As we mention in the introduction, the parallel singularity is significant drawback of the parallel structure interfaces, causing singular zones within the useful workspace for certain configurations. To identify these zones, we must first calculate the Jacobian matrix of our manipulator. The Jacobian matrix can be expressed as the product of two matrices [17].

$$\mathbf{J} = \mathbf{A}^{-1} \cdot \mathbf{B} \tag{8}$$

where **A** and **B** are called the parallel matrix and the serial matrix, respectively.

Now, the dexterity of the SPM can be calculated as follow [18]:

$$\text{dext}(\mathbf{J}) = \frac{1}{cond(\mathbf{J})} \tag{9}$$

With $cond(\mathbf{J})$ is a function equal to: $\|\mathbf{J}\| \cdot \|\mathbf{J}\|^{-1}$.

Figure 5a depicts the dexterity distribution over the whole workspace of the SPM and for a given value of the self-rotation $\phi = 130°$. The singularity zone crosses the WS and originates from a parallel singularity type that is more closely related to the behavior of matrix A. The determination of the matrix $det(\mathbf{A})$ over the entire WS is provided in Fig. 5b.

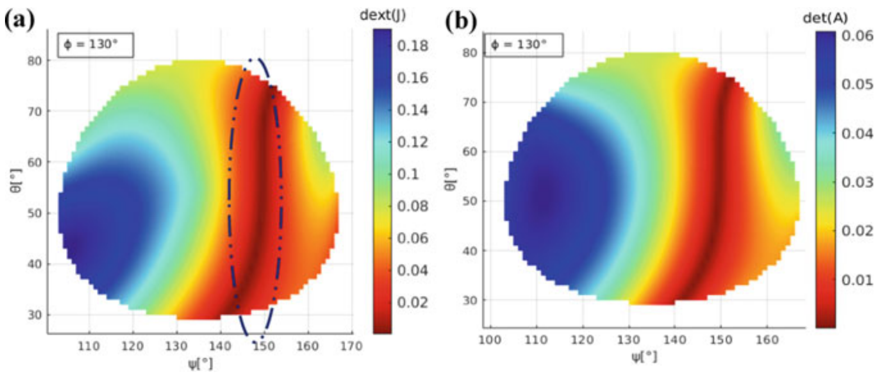

Fig. 5 With $\phi = 130°$, **a** dexterity distribution inside the SPM WS; **b** the values of the determinant of the matrix A

To address the issue arising from the parallel singularity, we have implemented a solution in our SPM architecture that utilizes actuator redundancy. The next section will provide further details on this approach.

3 Redundant SPM and Working Modes Evaluation

3.1 Redundant SPM

To address the issue of the parallel singularity, we have added a fourth motor on the passive joint near the mobile platform on leg B (refer to Fig. 6). It is important to note that selection of leg B is arbitrary, as all legs are identical. This modification enables an unlimited range of torque distribution and significantly improves the overall dexterity of SPM.

The kinematic model of the redundant SPM can be experienced as follows:

$$\mathbf{A} \cdot \boldsymbol{\omega} = \mathbf{B} \cdot \dot{\theta} \tag{10}$$

where $\boldsymbol{\omega}$ and $\dot{\theta}$ are the instantaneous angular velocity of the moving platform and the required speeds of the active joints, respectively.

With,

$$\mathbf{A} = [\mathbf{Z}_{2A} \cdot \mathbf{Z}_{3A}, \mathbf{Z}_{2B} \cdot \mathbf{Z}_{3B}, \mathbf{Z}_{2C} \cdot \mathbf{Z}_{3C}, \mathbf{Z}_{1B} \cdot \mathbf{Z}_{2B}]^T \tag{11}$$

$$\mathbf{B} = diag\begin{bmatrix} \mathbf{Z}_{1A}(\mathbf{Z}_{2A} \cdot \mathbf{Z}_{3A}), \mathbf{Z}_{1B}(\mathbf{Z}_{2B} \cdot \mathbf{Z}_{3B}) \\ , \mathbf{Z}_{1C}(\mathbf{Z}_{2C} \cdot \mathbf{Z}_{3C}), \mathbf{Z}_{3B}(\mathbf{Z}_{1B} \cdot \mathbf{Z}_{2B}) \end{bmatrix} \tag{12}$$

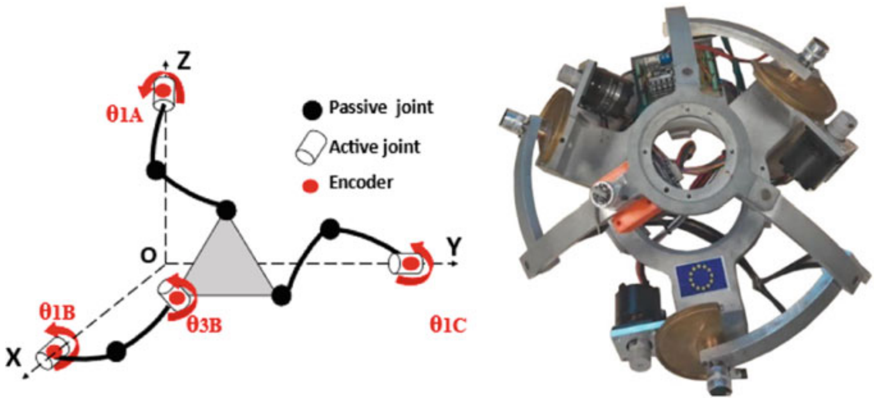

Fig. 6 The redundant SPM

The Jacobian matrix is expressed as a rectangular matrix, $\mathbf{J} = \mathbf{A}^{+} \cdot \mathbf{B}$ with $\mathbf{A}^{+} = \mathbf{A}^{T}\left(\mathbf{A}\mathbf{A}^{T}\right)^{-1}$. The matrix A is a non-square matrix and its inverse is computed Moore–Penrose pseudo-inverse [19].

The Jacobian is used to compute the joint torques for a given external force:

$$\boldsymbol{\tau} = \mathbf{J}^{\mathrm{T}} \cdot \mathbf{F}_{\mathbf{ext}} \tag{13}$$

The next step is to choose the most suitable working modes of the SPM, based on the evaluation of the maximum joint torque value, as detailed below.

3.2 Working Modes Comparison

Torque distribution is a critical criterion to consider. In some configurations, we may encounter the issue of one or more actuators reaching their torque limits, which is 0.8 Nm, risking damage to the motor or, in the same case, injure the user. Therefore, ensuring a safe distribution will guarantee safe control. To achieve this, we runed simulations for all 8 modes by applying an external force, $\mathbf{F}_{ext}$. Afterward, we determined the maximum torque value among the four motors and compared it to the predefined limit (refer to Fig. 7). It must be clarified that we have taken the absolute values of all torques. The torque comparison algorithm is outlined as follows:

1. Running different configurations (ψ, θ) in the workspace for each working mode, all while applying an external force $\mathbf{F}_{ext}$.
2. Solving the IKM for each configuration (ψ, θ) and computing the active joints $\boldsymbol{\theta}$.
3. Computing the Jacobian matrix $\mathbf{J}$.
4. Computing the joint torques $\boldsymbol{\tau}$ for the 4 motors.

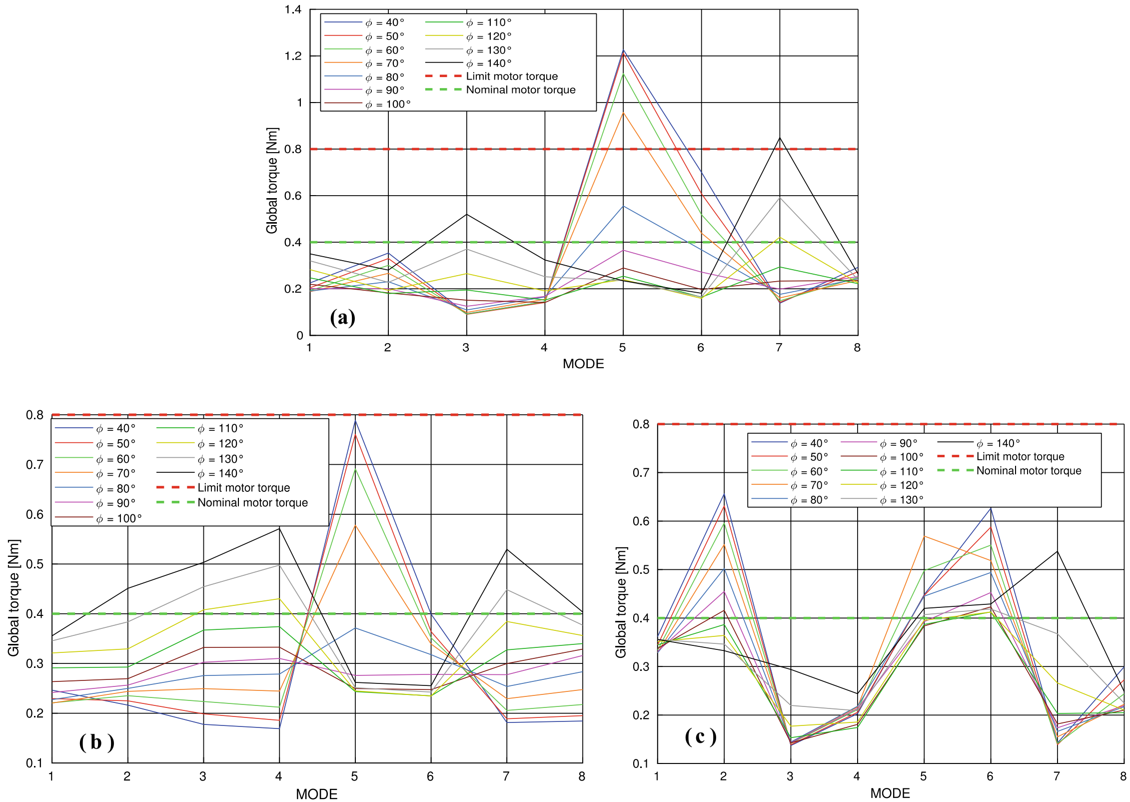

Fig. 7 Maximum torque values for all working mode: **a** for $\mathbf{F}_{ext} = [100]^{\mathrm{T}}$; **b** for $\mathbf{F}_{ext} = [010]^{\mathrm{T}}$; **c** for $\mathbf{F}_{ext} = [001]^{\mathrm{T}}$

5. Determining the global maximum torque for each mode.

After a comparative study of the torque distribution under various external forces, it is evident that modes 5 and 7 are unsuitable for our manipulator, exceeding the motor's torque limit and posing potential damage to both the motor and the user. Conversely, the remaining six modes (1, 2, 3, 4, 6, and 8) consistently operate within the prescribed motor torque limits across all configurations within the workspace. With a slight advantage for modes: 1 and 8. As they ensure that torque levels remain below the nominal value (0.4 Nm) of our simplex motor, across various proper rotation (ϕ).

4 Conclusion

In this article, we explored a 3DOF spherical parallel manipulator designed as a haptic interface for teleoperation tasks with force feedback. Initially, we presented its inverse kinematic model and outlined all possible working modes. Some configurations of the SPM faced an issue known as singularity, particularly parallel singularity inside the workspace. To address this, a redundant architecture was proposed, overcoming limitations observed in the original design and enhancing overall efficiency. Finally, a comparative study based on torque distribution was conducted on the different working modes under various external forces, revealing that modes 5 and 7 are not suitable, while approving all other work modes. Consequently, an additional comparative study based on the criteria of dexterity and proximity to singular configurations will be done to determine the most suitable mode.

References

1. Howe, R.D., Matsuoka, Y.: Robotics for surgery (1999). [Online]. Available: www.annualreviews.org
2. Jaffray, B.: Minimally invasive surgery. Arch. Dis. Child. **90**(5), 537–542 (2005). https://doi.org/10.1136/adc.2004.062760
3. El Rassi, I., El Rassi, J.M.: A review of haptic feedback in tele-operated robotic surgery. J. Med. Eng. Technol. **44**(5), 247–254 (2020). https://doi.org/10.1080/03091902.2020.1772391
4. Veziant, J., Bourdel, N., Slim, K.: Risks of viral contamination in healthcare professionals during laparoscopy in the Covid-19 pandemic. J. Visceral Surg. **157**(3), S59–S62 (2020). https://doi.org/10.1016/j.jviscsurg.2020.04.010
5. Alleblas, C.C.J., De Man, A.M., Van Den Haak, L., Vierhout, M.E., Jansen, F.W., Nieboer, T.E.: Prevalence of musculoskeletal disorders among surgeons performing minimally invasive surgery. Ann. Surg. **266**(6), 905–920 (2017). https://doi.org/10.1097/SLA.0000000000002223
6. Giri, G.S., Maddahi, Y., Zareinia, K.: An application-based review of haptics technology. Robotics **10**(1), 1–18 (2021). https://doi.org/10.3390/robotics10010029
7. Adams, R.J., Hannaford, B.: Control law design for haptic interfaces to virtual reality (2002)
8. Briot, S., Bonev, I.A.: Are parallel robots more accurate than serial robots? (2007) [Online]. Available: www.nrcresearchpress.com

9. Tanev, T.K.: Minimally-invasive-surgery parallel robot with non-identical limbs (2014). https://doi.org/10.1109/mesa.2014.6935558
10. Li, T., Payandeh, S.: Design of spherical parallel mechanisms for application to laparoscopic surgery. Robotica **20**(2), 133–138 (2002). https://doi.org/10.1017/S0263574701003873
11. Lee, J.H., Kim, H.W., Yi, B.-J, Suh, H.: Singularity-free algorithms and design scheme for a new 6-DOF parallel haptic device (2002)
12. Arsenault, M., Boudreau, R.: The synthesis of three-degree-of-freedom planar parallel mechanisms with revolute joints (3-RRR) for an optimal singularity-free workspace. J. Robot. Syst. **21**(5), 259–274 (2004). https://doi.org/10.1002/rob.20013
13. Bonev, I., Chablat, D., Wenger, P.: Working and assembly modes of the agile eye (2007) [Online]. Available: http://arxiv.org/abs/0708.3936
14. "Singularity Analysis of Closed-Loop Kinematic Chains"
15. Bai, S., Li, X., Angeles, J.: A review of spherical motion generation using either spherical parallel manipulators or spherical motors. Mech. Mach. Theory **140**, 377–388 (2019). https://doi.org/10.1016/j.mechmachtheory.2019.06.012
16. Chaker, A., Mlika, A., Laribi, M.A., Romdhane, L., Zeghloul, S.: Synthesis of spherical parallel manipulator for dexterous medical task. Front. Mech. Eng. **7**(2), 150–162 (2012). https://doi.org/10.1007/s11465-012-0325-4
17. Merlet, J.P.: Jacobian, manipulability, condition number, and accuracy of parallel robots. J. Mech. Des. **128**(1), 199–206 (2006). https://doi.org/10.1115/1.2121740
18. Wu, J., Wang, J.S., Wang, L.P., Li, T.M.: Dexterity and stiffness analysis of a three-degree-of-freedom planar parallel manipulator with actuation redundancy. Proc. Inst. Mech. Eng. C J. Mech. Eng. Sci. **221**(8), 961–969 (2007). https://doi.org/10.1243/09544062JMES456
19. Golub, G., Kahan, W.: Calculating the singular values and pseudo-inverse of a matrix. J. Soc. Ind. Appl. Math. Philadelphia **2**(2), 20 (1965). https://doi.org/10.1137/0702016

MEDROVER: Medical Assistant Robot for Patient Monitoring and Treatment Management

Roxana Rusu-Both and Balazs-Attila Molnar

Abstract This paper outlines the comprehensive design and implementation of MEDROVER, a semi-autonomous Medical Assistant Robot designed for patient monitoring and treatment management in healthcare. It offers user-controlled navigation via a mobile app and autonomous surveillance with real-time AI-driven fallen person detection. MEDROVER's ultrasonic sensors and mapping algorithm create a 2D environment map for precise navigation, accessible through the app. The robot's speaker facilitates humane communication via user-selected voice messages. The mobile app controls movement, video monitoring, voice messaging, server communication, map creation, and emergency notifications, enhancing healthcare services and supporting medical staff. Rigorous testing ensures reliable performance, making MEDROVER a promising medical assistant robot for the future of healthcare.

Keywords Medical assistant robot · Patient monitoring · Healthcare robotics

1 Introduction

In today's rapidly advancing world, healthcare faces new challenges, particularly in the context of contagious diseases like COVID-19. Recent years have witnessed significant progress in the field of robotics, particularly mobile robots, finding applications in various sectors, with healthcare standing out as a promising domain. The convergence of robotics and medicine offers innovative solutions to address these challenges. Mobile robots have been deployed for patient treatment and medication administration to improve precision and patient outcomes. Additionally, mobile robots enable real-time patient monitoring, like the RP-VITA, allowing remote assessments. In elderly care, robots like Jibo and Paro provide companionship, medication monitoring, and distress detection, enhancing well-being. This paper explores the transformative potential of healthcare robotics, emphasizing the development of a medical assistant robot equipped with advanced features for support in hazardous

R. Rusu-Both (✉) · B.-A. Molnar
Technical University of Cluj-Napoca, 400114 Cluj, Romania
e-mail: roxana.both@aut.utcluj.ro

D. Pisla et al. (eds.), *Advances in Service and Industrial Robotics*, Mechanisms and Machine Science 157, https://doi.org/10.1007/978-3-031-59257-7_23

and contagious environments. The remainder of the paper is structured as follows: Sect. 2 introduces briefly some robotic medical assistance systems. Section 3 introduces the prototype modeling while Sect. 4 presents the prototype implementation and testing procedures. Finally, Sect. 5 offers some conclusions.

2 Robotic Medical Assistance Systems

The field of medical assistant robots has seen notable advancements, driven by the fusion of cutting-edge technology with healthcare demands. These robots are now known for their versatility, adaptability, and enhanced user interfaces, ultimately enhancing patient care and healthcare workflows.

Scientific research has produced diverse examples of medical assistant robots with significant impact. Mobile medical assistant robots, exemplified by the RP-VITA, have shown promise in remote patient monitoring and consultations, particularly in emergency scenarios [1, 2]. Notable examples in the field include:

Moxi Robot by Diligent Robotics: Assists healthcare professionals with non-patient-facing tasks, enhancing operational efficiency. It uses advanced navigation and sensor technologies to operate autonomously [3].

TUG by Aethon: Deploys in hospitals for logistics and delivery tasks, streamlining internal operations and ensuring safe transport of medical supplies [4].

Robotic Exoskeletons for Rehabilitation: Wearable exoskeletons aid patients with mobility impairments in physical therapy, providing real-time feedback [5].

Socially Assistive Robots for Elderly Care: PARO therapeutic robot offers companionship and emotional support to the elderly, addressing social and psychological aspects of healthcare [6].

These examples showcase the dynamic nature of the field, spanning logistics, surgery, rehabilitation, and emotional support. Continued research and interdisciplinary collaboration will drive further advancements, offering new possibilities for healthcare efficiency and improved patient outcomes.

3 Modeling the Prototype

The first part of this section is focused on the functional analysis and the design requirements of the developed MEDROVER—medical assistant robot, while the second part will detail the conceptual design of the MEDROVER.

The MEDROVER robot is designed to execute fundamental nursing tasks, such as delivering medications and routine patient check-ups. It operates both semi-autonomously and autonomously. A key feature is environmental mapping, achieved through ultrasonic sensors and a mapping algorithm for precise navigation. The robot connects to a database to retain the map and position data between sessions. Additional functionalities include voice message transmission to patients, real-time

Table 1 Functional analysis of the MEDROVER

	What to do	How to do
MEDROVER	Transport medicine	Automatic/semi-automatic mode
MEDROVER	Detect a fallen patient	Surveillance mode—camera
MEDROVER	Map the environment	Ultrasonic sensors—database
MEDROVER	Voice messaging	Built in speaker
MEDROVER	Real-time video monitoring	Camera

image transmission for patient supervision, and a user-friendly mobile application for seamless interaction.

The functional analysis of the MEDROVER is presented in Table 1, detailing the main requirements to be achieved.

The developed mobile application allows the user, the medical staff to:

- View and control the robot's movement by specifying destination coordinates on the map.
- Access real-time video monitoring.
- Send voice messages to patients for providing directions, instructions, or offering comfort in a more human-like manner.

In terms of size, the prototype was intentionally designed with a compact form factor to facilitate maneuverability within narrow spaces, while still adhering to established requirements and functionalities. Specifically, the prototype was tailored to accommodate three ultrasonic sensors at the front, one on each side, and two at the rear of the robot. Ensuring adequate space for each hardware component, the prototype's dimensions are targeted to be approximately 30 cm in length, 15 cm in width, and about 24 cm in height. The body's shape was meticulously crafted to meet specified criteria, including provisions for the storage of medicines.

To guarantee optimal system performance, the design emphasized robustness for fast and accurate execution of functions in diverse situations. Efficient utilization and optimization of data structures and algorithms were pivotal elements in achieving this objective. Notably, the system must comply with the constraints posed by available hardware, software resources, and by technological and budgetary limitations. Thus, the testing, validation of functionalities, and performance checks were critical steps in the developmental phase of the prototype.

3.1 Software Architecture

This sub-section introduces the MedRover medical assistant robot's software architecture, ensuring smooth hardware and mobile application interaction. The system use-case diagram and software architecture, presented in Fig. 1 illustrates its functions, necessitating meticulous analysis requirement identification.

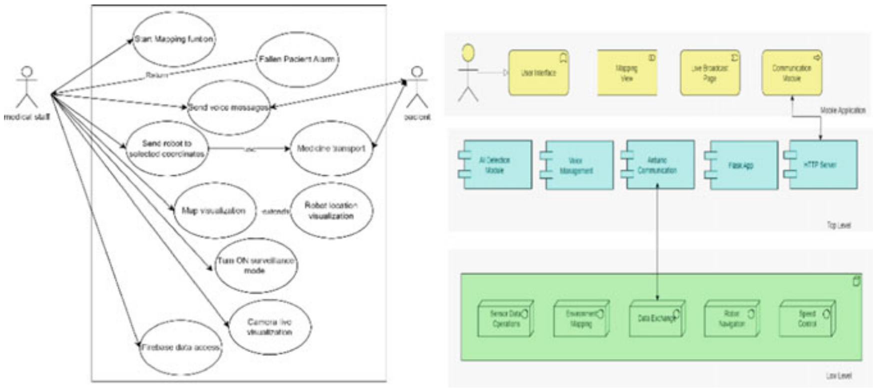

Fig. 1 System use case diagram and software architecture

Top Level: A Raspberry Pi development board for coordination and communication with the user interface using Python programming language. Threads enable concurrent process execution. One thread handles Arduino communication, while another manages the mobile app through an HTTP server. Additionally, image processing combined with AI models for detecting fallen patients, database initialization, Flask app control, and voice message management functions are integrated.

Low Level: Software functions for the Arduino development board involve sensor data retrieval and control signal transmission. The Arduino language, based on C/C++, is used for procedural programming. Functions include data exchange with Raspberry Pi, environment mapping, robot navigation, and encoder-based speed control. The code must also manage ultrasonic sensor data, gyroscopic readings, robot movement, and other functionalities.

Mobile Application: The app prioritizes user-friendly navigation. The app interacts with the MedRover robot via a Raspberry Pi-hosted HTTP server. Specific features include a live broadcast page, real-time mapping updates, and a user-friendly interface with buttons for robot control, map reset, and data storage. The mapping page employs components like Svg, Rectangle, and Circle to represent objects and the robot.

3.2 Hardware Architecture

In the context of hardware architecture, the development of a prototype involves the utilization of two distinct development boards: a Raspberry Pi 4B and an Arduino

Mega 2560. The Raspberry Pi To facilitate communication between these two development boards, the UART (Universal Asynchronous Receiver-Transmitter) communication protocol via USB was examined and used. The complete hardware components list is presented in Table 2. These components were carefully chosen to strike a balance between cost-effectiveness and meeting the performance and functionality requirements essential for the robot to execute its designated tasks.

Figure 2 illustrates the Arduino-based robot's perception and propulsion system. This hardware setup includes the Arduino Mega board with the L293D shield driver for power and motor (M1—M4) connections. Seven ultrasonic sensors (US1—US7) are linked to digital pins, and a MPU6050 gyroscope-accelerometer (MPU) connects via I2C pins. These components collaborate to control the MedRover robot effectively, ensuring seamless hardware-software communication. To link the Arduino and Raspberry Pi, a bidirectional USB Type-A to Type-B cable is used. A sound card connects to the Raspberry Pi via USB, and an audio amplifier facilitates speaker connection. Power for the audio system comes from two 18650 3.7 V batteries. The camera integrates with the Raspberry Pi through a dedicated port using a flexible cable for image capture and transmission.

Table 2 MEDROVER hardware components list

	Components	Function
MEDROVER	Raspberry Pi 4B development board	Automatic/semi-automatic mode
	Arduino Mega 2560 Development Board	Perception and propulsion system
	DC motors with 1:48 reducer	Propulsion system
	L293D driver shield motor for motor control	Propulsion system
	HC-SR04 ultrasonic sensors	Perception system—object detection
	Accelerometer and gyroscope module MPU6050	Environmental mapping
	Infrared speed sensors	Propulsion system—speed control
	Stereo audio amplifier TDA2822	Sound system
	FY2 5 W, 4Ω speaker	Sound system
	Raspberry Pi V2 Camera Module	Video surveillance
	Mecanum omnidirectional wheels	Propulsion system
	Batteries 18650 Li-Ion 3,7 V	Power system

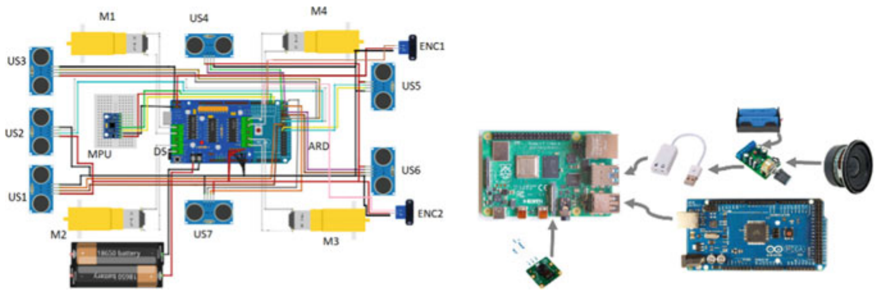

Fig. 2 Components diagram for the MEDROVER perception and propulsion system

3.3 3D Modeling

The robot's design strikes a balance between accommodating components and maneuverability. Autodesk's Fusion 360 was used in 3D modeling for subsequent 3D printing.

The lower platform of the MedRover robot's chassis, measures approximately 30 cm × 15 cm × 5 mm. It features specially designed pins for component stability, motor holders, and Raspberry Pi power supply support. The upper platform, measuring 55 mm in height, was designed to protect and conceal components while precisely positioning 7 ultrasonic sensors for accurate object detection. Spacer nuts and bolts secure the platforms. An additional 15 cm × 12 cm × 35 mm storage component for medicines connects to the upper deck using bolts. The final MedRover robot design incorporates all components, joining the lower and upper platforms, camera holder, and storage space, as seen in Fig. 3. A 13 cm bracket secures the camera to the upper platform using four screws.

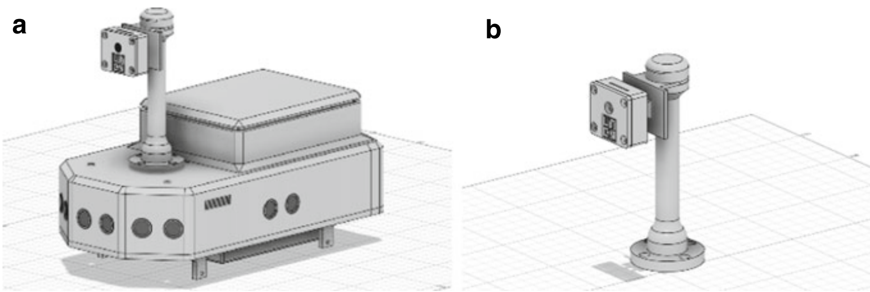

Fig. 3 MedRover's robot: **a** complete chassis assembly; **b** camera holder

Fig. 4 MEDROVER robot assembled prototype

4 Prototype Implementation and Testing

4.1 3D Printing and Assembly

During the prototype design phase, we used 3D printing technology to create a comprehensive chassis model from polylactic acid (PLA). Individual components were 3D printed separately and joined securely with screws. Assembly was accomplished using 8 M3 bolts (3 mm diameter) and 4 spacer nuts (55 mm length) to attach the lower and upper platforms. These bolts went from the bottom of the lower platform to the top of the upper platform. Additionally, 4 M3 bolts and nuts secured the upper platform to the storage space, while another 4 M4 bolts and nuts connected the upper platform to the camera holder. This process resulted in the fully assembled robot chassis, as seen in Fig. 4.

4.2 Fall Detection System

During the implementation of AI-based fallen person recognition, an artificial intelligence model was trained for this purpose, involving data preparation, model training, and integration into the application.

A diverse dataset of approximately 2000 images, representing various scenarios and conditions, was collected. Manual annotations were added using the LabelImg program, with 500 images reserved for validation. Google Colab and the Model Maker library were utilized for model training, with parameters such as training epochs (20) and batch size (4) configured. Fine-tuning was applied to enhance accuracy.

The model was exported in TensorFlow Lite format with quantization to reduce its size while maintaining accuracy. It was integrated into the application as the AIProcessing class, operating in a separate thread. This class initializes the camera and detection model, continuously capturing and processing images. If a fallen person

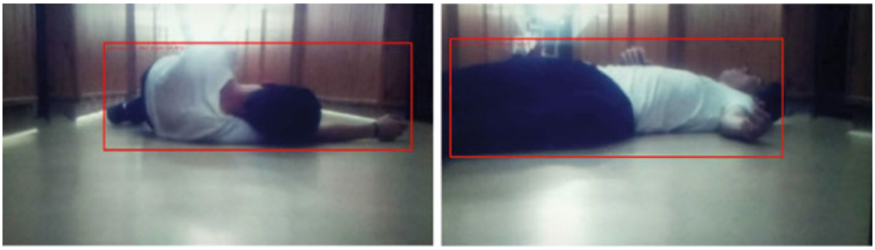

Fig. 5 Detection example of fallen persons on MedRover prototype

is detected, a signal is sent to the Arduino to stop the motors, and an alert sound is played.

The system achieves real-time fallen person detection with a processing speed of approximately 0.25 s per frame, enabling rapid response by medical staff.

Validation results on the real prototype showed a recognition rate of 94.31%, demonstrating the model's suitability for real-time detection of fallen individuals, Fig. 5.

4.3 Real Time Camera View

To achieve real-time camera visualization and patient communication, a Flask application and a dedicated HTML page were created. The Flask application manages functionalities, server operations, and user requests, while the HTML page displays the live camera feed and enables voice-based patient interaction. CSS styles format various page elements, including the navigation bar, camera background, buttons, and text fields for user input.

The Flask application was developed with imported modules: Flask, render_template, Response, request, send_from_directory, jsonify, and pyttsx3 for voice synthesis. Finally, the camera object was initialized, the pyttsx3 voice synthesis engine was configured, and a Flask instance was created with the app name.

Tests were conducted on the prototype to validate the real-time camera view and patient communication. These tests confirmed successful connection with the HTML page, real-time camera access, and proper interaction with dropdown menus and textboxes, Fig. 6. User-selected options and entered text resulted in immediate voice playback of messages, demonstrating the functionality's accuracy and responsiveness.

Fig. 6 HTML application for MedRover prototype video camera display and communication

4.4 Environment Mapping System

A two-dimensional representation of the surroundings can be generated using sensors for distance measurement, with ultrasonic sensors being the cost-effective choice for this project. To implement the environmental mapping system, the SLAM (Simultaneous Localization and Mapping) algorithm was integrated, allowing the robot to determine its position while constructing a detailed map of the environment [7]. In each loop iteration, sensor data, including distance measurements from sensors on both sides of the robot, is collected, processed, and transmitted to the Raspberry Pi for map creation and navigation.

To test the accuracy of the environmental mapping function and SLAM algorithm in calculating the position of the robot, the robot was moved with respect to known objects, such as walls, while the algorithm updated the robot's coordinates and map. As it can be seen in Fig. 7, the coordinates of the objects remain constant, while the coordinates of the robot (blue dot on the map) change accordingly.

The robot has two travel modes: user-dependent and autonomous surveillance. In the user-dependent mode, the robot moves to user-specified coordinates using ultrasonic sensors and gyroscope-accelerometer for orientation. The robot's coordinates are sent to the mobile application through the HTTP server. In autonomous surveillance mode, the robot detects and avoids obstacles, such as fallen patients.

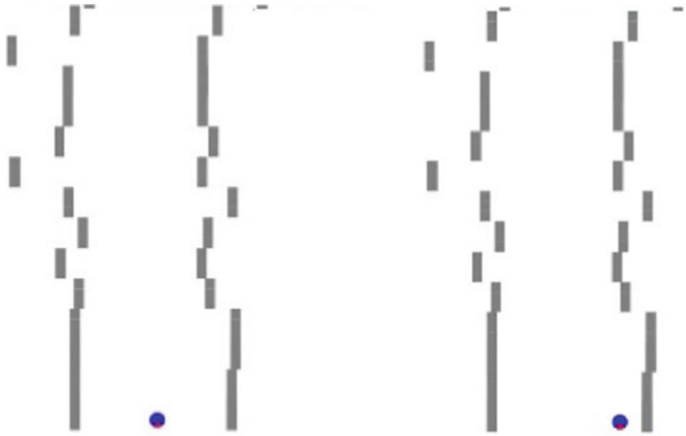

Fig. 7 MedRover prototype mapping algorithm test results

For precise distance estimation, a wheel speed control system was designed, consisting of four PI controllers (one for each wheel) tuned for desired closed-loop performance using Guillemin-Truxal [8]. The controllers were tested in simulation and implemented on the microcontroller for the prototype.

4.5 Mobile App Development Using React Native

The React Native framework was utilized for the mobile application, employing tabbed navigation with a bottom-TabNavigator for user-friendly access to various sections [9]. The application comprises four main components: HomePage, MapPage, LivePage, and AboutPage (Fig. 8).

The HomePage acts as the initial landing page, featuring an input field for the robot's ID code and providing access to other app pages upon code validation.

The MapPage provides comprehensive environmental mapping and robot movement details. It continuously updates the robot's position on the map during movement and offers controls to start or stop the robot, reset the environment map, and save it to the database. Users can also initiate surveillance mode, and an alert message appears if the robot detects a fallen person.

The LivePage displays real-time camera images from the Raspberry Pi's HTML application, enabling user interaction with patients. Users can halt automatic detection and view the camera upon opening the page.

The AboutPage serves as an informational resource, detailing the MedRover robot's chassis, functionalities, and components.

Following development, the application was exported via the Expo Go environment, creating an apk file compatible with Android and IOS.

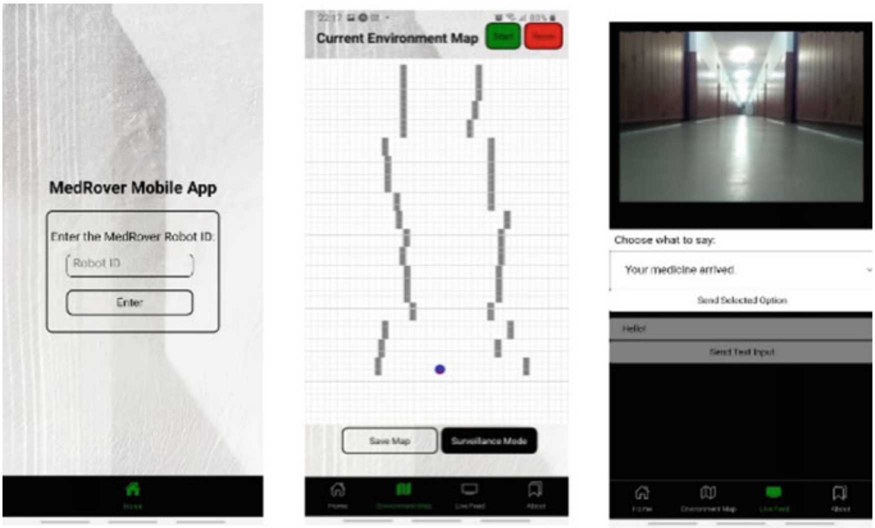

Fig. 8 MedRover Mobile application Home page, Map page, Live page

5 Conclusions

The work presented in this paper has delivered a functional robot prototype that aligns with predefined objectives. The thorough analysis and design phase successfully integrated crucial hardware components, enabling the robot's effective operation. Advanced image processing algorithms ensure prompt and accurate patient fall detection, even in critical situations. The environmental mapping system enhances navigational capabilities by collecting detailed environmental data and constructing precise maps. Additionally, the robot can transport medication, improving operational efficiency. A voice communication system facilitates seamless interactions with patients, while wheel speed control ensures consistent movement and reliability. Database connectivity stores environmental maps, location, and orientation data. A user-friendly mobile application empowers medical staff to oversee and direct the robot efficiently. Each functionality was tested individually but system tests were also performed under real conditions proving good results as detailed in Sect. 4.

In summary, this study affirms the functionality and efficiency of the developed system. The final prototype consistently and effectively performs its tasks, offering valuable support to medical staff in healthcare settings. These findings highlight the potential benefits of medical assistant robots for improving patient care and operational efficiency in medical environments.

Acknowledgements This research was supported by the project New frontiers in adaptive modular robotics for patient-centered medical rehabilitation—ASKLEPIOS, funded by European Union—NextGenerationEU and Romanian Government, under National Recovery and Resilience Plan for Romania, contract no. 760071/23.05.2023, code CF 121/15.11.2022, with Romanian Ministry of

Research, Innovation and Digitalization, within Component 9, investment I8 and by the project LymphMED-AI: Lymph nodes metastasis 283 evaluation and monitoring system based on ultrasound image analysis artificial intelligence algo-284 rithms, funded by EIT Health, under EIT Health RIS 2023 INNOVATION CALL, contract no. 285 15768/22.05.2023.

References

1. Chen, J., et al.: Application of da Vinci surgical robotic system in hepatobiliary surgery. Int. J. Surg. Med. (2017)
2. Wang, R., et al.: A medical assistive robot for telehealth care during the COVID-19 pandemic: development and usability study in an isolation ward. JMIR Hum. Factors (2023)
3. Diligent Robotics Homepage. https://www.diligentrobots.com/moxi. Accessed 20 Dec 2023
4. Aethon Hompage. https://aethon.com/mobile-robots-for-healthcare/. Accessed 20 Dec 2023
5. Lee, Y.-H., et al.: Therapeutic effects of robotic-exoskeleton-assisted gait rehabilitation and predictive factors of significant improvements in stroke patients: a randomized controlled trial. Bioengineering **10**, 585 (2023)
6. Bevilacqua, R., et al.: Social robotics to support older people with dementia: a study protocol with Paro seal robot in an Italian Alzheimer's day center. Front. Public Health. (2023)
7. Barak, N., Gaba, N., Aggarwal, S., Barak, N.: Two dimensional mapping by using single ultrasonic sensor. Int. J. Adv. Res. Comput. Sci. (2016)
8. Ogata, K.: Modern Control Engineering, 5th edn. Pearson Prentice H, New Jersey (2009)
9. Ward, D.: React Native Cookbook, 2nd edn. Packt Publishing (2019)

Mixed-Reality-Guided Teleoperation of a Collaborative Robot for Surgical Procedures

Gabriela Rus, Nadim Al Hajjar, Paul Tucan, Andra Ciocan, Calin Vaida, Corina Radu, Damien Chablat, and Doina Pisla

Abstract The development of advanced surgical systems embedding the Master–Slave control strategy introduced the possibility of remote interaction between the surgeon and the patient, also known as teleoperation. The present paper aims to integrate innovative technologies into the teleoperation process to enhance workflow during surgeries. The proposed system incorporates a collaborative robot, Kuka IIWA LBR, and Hololens 2 (an augmented reality device), allowing the user to control the robot in an expansive environment that integrates actual (real data) with additional digital information imported via Hololens 2. Experimental data demonstrate the user's ability to control the Kuka IIWA using various gestures to position it with respect to real or digital objects. Thus, this system offers a novel solution to manipulate robots used in surgeries in a more intuitive manner, contributing to the reduction of the learning curve for surgeons. Calibration and testing in multiple scenarios demonstrate the efficiency of the system in providing seamless movements.

Keywords Collaborative robot · Teleoperation · Laparoscopic holder · Mixed reality

G. Rus (✉) · P. Tucan · C. Vaida · D. Chablat · D. Pisla
CESTER, Technical University of Cluj-Napoca, 400114 Cluj-Napoca, Romania
e-mail: gabriela.rus@mep.utcluj.ro

D. Pisla
Technical Sciences Academy of Romania, 26 Dacia Blvd, 030167 Bucharest, Romania

N. Al Hajjar · A. Ciocan
Department of Surgery, "Iuliu Hatieganu" University of Medicine and Pharmacy, 400347 Cluj-Napoca, Romania

C. Radu
Department of Internal Medicine, "Iuliu Hatieganu" University of Medicine and Pharmacy, 400347 Cluj-Napoca, Romania

D. Chablat
École Centrale Nantes, Nantes Université, CNRS, LS2N, UMR 6004, F-44000, Nantes, France

D. Pisla et al. (eds.), *Advances in Service and Industrial Robotics*, Mechanisms and Machine Science 157, https://doi.org/10.1007/978-3-031-59257-7_24

1 Introduction

The concept of teleoperation in surgery marks a significant advancement in medical technology, allowing surgeons to manipulate instruments from a remote location with precision. This innovative approach enables the execution of intricate surgical procedures through robotic systems [1], enhancing the capabilities of medical professionals, especially for master–slave systems [2, 3].

According to this, it is important to underline how critical are the aspects related to precision and guidance. Surgeons need high precision to achieve goals while guidance offers real-time information for informed decisions. As medical professionals continually seek innovative solutions to improve patient outcomes, the integration of cutting-edge technologies becomes primary [4–7]. A significant component in this effort is the existent collaborative robotics systems.

The advantages of using collaborative robots in surgical procedure include (1) safety futures-force and torque sensors, vision systems, and software algorithms that allow them to detect the presence of humans and respond by slowing down or stopping; (2) adaptability and flexibility—due to their configuration can be easily reconfigured for various surgical procedures; (3) human–robot collaboration—these system being designed to interact with humans. Considering the presented aspects these systems showed their potential to be used in various complex surgery procedures such as Esophagectomy (esophageal resection), Pancreatectomy (pancreatic resection) and Hepatectomy (liver resection), which share a common issue, referring to the location of the tumors in the proximity of critical internal structures imposing highly accurate resection techniques.

The use of collaborative robots in surgery was discussed in many articles [8–11]. For example, the authors from [10] used the UR5 robot to hold and move the surgical instruments and the camera during surgeries. The authors of [11] used KUKA LWR 4+ robot to develop a collaborative control framework for teleoperations in Minimally Invasive Surgery (MIS).

Another innovative technology increasingly used in recent years, demonstrating real advantages in surgery is related to the augmented reality (AR) and virtual reality (VR) devices. These devices have the potential to improve surgeries in many aspects such as: surgical planning and visualization, training and simulation, enhanced navigation, remote assistance, reduced radiation exposure and postoperative monitoring and rehabilitation [12, 13].

The paper aims to analyze the potential of utilizing collaborative robots and an AR device (Hololens 2) to enhance teleoperation. The proposed system is designed to enable the manipulation of surgical robots without the need for additional joysticks such as 3D space-mouses or haptic devices, offering an intuitive interface. Simultaneously, it provides the capability for multi-user operation of the robot, allowing multiple users with HoloLens devices to use the system. Considering these aspects, the system can be used in intraoperative phase, having the potential to reduce learning curves and enhance the overall surgical process for surgeons.

Succeeding the introduction section, the paper is structured as follows: Section 2 describes the methodology for development of the proposed system including calibration and the protocol for testing. Section 3 describes the results, and Section 4 presents the discussions and the conclusions of the study.

2 Methodology

The teleoperation setup proposed for this study is composed of a collaborative robot, a laparoscopic camera attached to the robot through a customized flange, and the augmented reality device, HoloLens 2, as can be seen in Fig. 1. The transfer of data between systems is based on TCP/IP (Transmission Control Protocol/Internet Protocol) communication.

2.1 Materials

The chosen collaborative robot was **KUKA IIWA** (Intelligent Industrial Work Assistant) [14]. The configuration of the system (seven joints) includes integrated force torque sensors for safe and efficient operation, which enables suitable control of movement. Its collaborative features not only ensure safety but also make it easy for tasks which demand precise manipulation. A laparoscopic camera is connected to a specially tailored flange, this assembly being fixed to the end effector of the robot.

HoloLens 2, a Microsoft augmented reality device, introduces a hands-free advantage to the described setup. The HoloLens 2 hands free control makes it easier to perform precise movements based on hand movement, as part of teleoperation set-up.

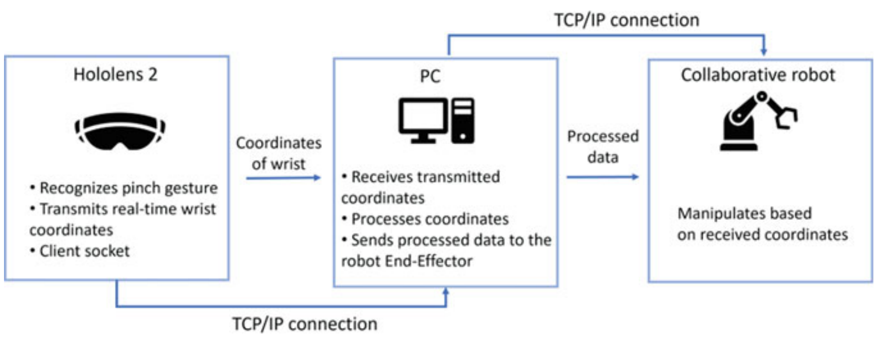

Fig. 1 Schematic representation of the proposed system

2.2 Communication

As can be seen in Fig. 2 the communication is based on TCP/IP connection, assuring real-time transfer of data.

In the described teleoperation framework, the HoloLens device hosts a standalone application that provides several functions including a client socket. This application is designed to transmit real-time wrist coordinates when a certain gesture (the pinching) is recognized, these coordinates being then directed to a server socket, created in Python. Thus, upon initiating the application, it verifies the connection with the Python server, and the application proceeds only when the connection between the client and server is established. The same prerequisite applies to the connection between Python and the robot. If the connection is successfully established among all participants, the pinch gesture from HoloLens is verified, and the data transfer is initiated upon the recognition of the gesture. The coordinates are further processed and sent to the end effector of the KUKA robot after being received by the Python server, enabling real-time control and manipulation. After the pinch gesture is finished, HoloLens does not transmit any more coordinates until the gesture is performed again, which stops unintentional robot movements. In order to assure the transfer of all of required data for a movement, a validation of the movement is

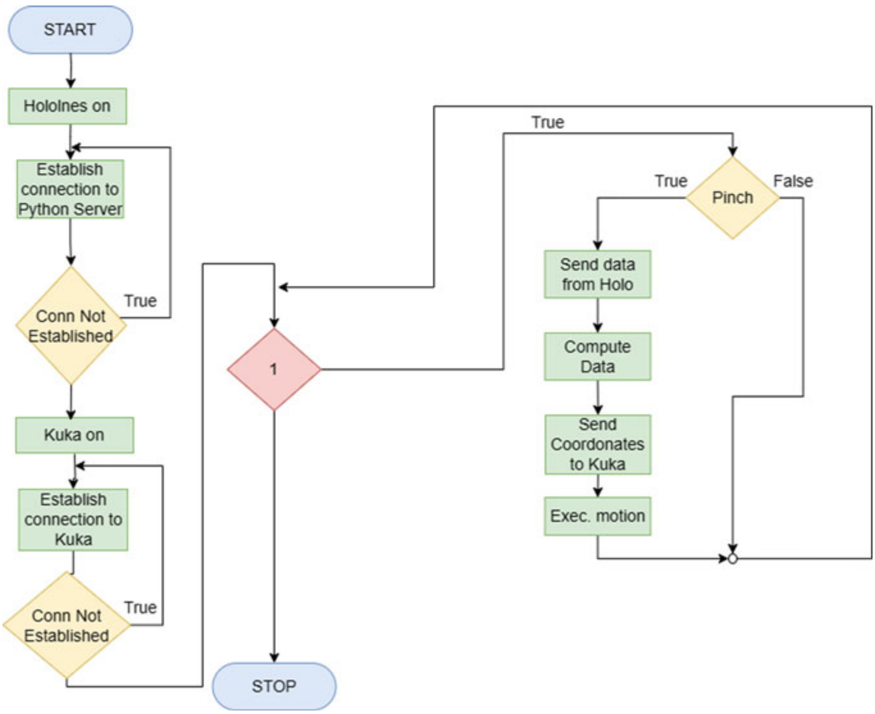

Fig. 2 Schematic representation of the data transfer between Hololens and Kuka

implemented in the user interface, thus the user will validate if the movement was executed by the robot or not.

2.3 Calibration

Hololens has been configured to consider the KUKA coordinate system throughout the calibration process, ensuring seamless integration and accurate interpretation of coordinates between the augmented reality device and the collaborative robot.

To address the unit disparity between the KUKA system, which operates in millimeters, and the Hololens, which uses meters, a normalization step was implemented.

Additionally, as coordinates are transmitted to the end effector of the KUKA collaborative robot, the calibration process incorporates the utilization of inverse kinematics.

For this procedure, the coordinates from the End-Effector are required. The origin of the coordinate system is positioned in the characteristic point of the End-Effector, and the axes aligned with the robot native ones enabling a fast computation with respect to the base of the robot. The integration of robot singularities and trajectory planning has been realized using the Kuka Sunrise Toolbox.

As part of the calibration process, the robot was moved to a known point in space. The coordinates of the tip of the laparoscopic camera were then registered for comparison using specific markers with locations defined accurately with respect to the fixed coordinates system of the robot. A similar process was carried out for the cursor from HoloLens.

Ultimately, the robot is positioned in a specific configuration, serving as the starting point for task execution. This strategic stance facilitates the seamless initiation of various tasks.

2.4 Protocol for Testing

The protocol for testing and ensuring the functionality of the collaborative robot, integrated with the Hololens, involves several key steps presented in Table 1. In the initial setup, the correct configuration and connection of the robot, as well as verifying the proper functioning of the Hololens is performed. Basic movement tests are then conducted in an open space to guarantee accurate motion. Calibration between the robot and Hololens is tested, and the recognition of pinch gestures with different hand orientations, is verified. Subsequently, specific movement tests are executed, with emphasis on the insertion of the laparoscopic camera through the trocar. The laparoscopic camera has 3 degrees of freedom (DOF) and can perform 2 rotational movements around the X-axis, and respectively around the Y-axis, as well as translation along the Z-axis (Fig. 3a).

Table 1 Testing protocol

Steps of protocol	Description
Initial setup	• Ensure proper installation and connection of the collaborative robot • Ensure Hololens functionality
Basic movements tests	• Perform basic movement tests in open space to ensure the robotic moves smoothly and accurately • Test the calibration between the robot and Hololens • Test the recognition of the gesture—with pinch gesture, without pinch gesture, with different orientation of the hand
Task 1	**Move laparoscopic camera on plane** (The movements are performed on a 2D plane). **Task description**: A paper where diverse geometrical figures are drawn, is placed in front of Kuka. The robot, based on the hand's movement, should be able to move to a certain point of a figure or to execute movements throughout the figures from the paper
Task 2	**Move laparoscopic camera on 3D space**. (The movement is performed on the 3D space). **Task description**: In proximity of the robot are placed both physical objects (a phantom torso) and holograms (projected from Hololens) The robot should be able to gentle touch these holograms, respectively to introduce the laparoscopic camera in torso
Task 3	**Following a trajectory**. **Task description**: The robot should be able to move based on certain trajectory drawn by the hand in order to enhance maneuverability and accuracy

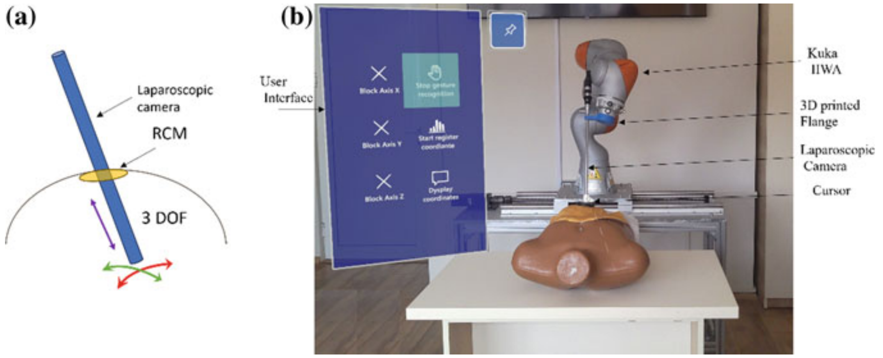

Fig. 3 **a** Motions of camera; **b execution of task 2**. Inserting the laparoscopic camera in the phantom torso (image from Hololens)

3 Results

Considering that the main purpose of this paper is to test the feasibility of a system composed from an AR device and a collaborative robot, in teleoperation surgery, aspects such as accuracy, delays and time to complete a task are critical metrics. The accuracy was calculated taking into account the coordinates of the cursor from

Hololens and the coordinate of the tip of laparoscopic camera (coordinates of the End-Effector + the offset caused by the length of the camera—30 cm). The average positional error was measured at 0.7 mm during the execution of movement 1, presented in protocol. The positional errors registered for the next step in protocol (movement 2), were 0.8 mm when the user had to touch the holograms with the laparoscopic camera and 1.1 mm when the task was the introduction of laparoscopic camera in torso (Fig. 3b).

For the final test the positions of the end effector and the positions of the hand have been registered to analyze the trajectories. As can be seen in Fig. 4, the collaborative robot has been able to follow closely the trajectory of the hand.

Considering the protocol for data transmission, the average delay registered between the hand and the robot was almost 0.1 ms. It has been observed that sudden movements tend to create an additional delay caused by the large amount of data that should be processed.

The average time to complete the tasks was 1 min and 45 s for the first one, 2 min and 15 s for touching all holograms, 1 min and 52 s for introducing the camera in the torso, and 40 s for task 3. These tasks were completed by three users with different levels of experience with the Hololens device.

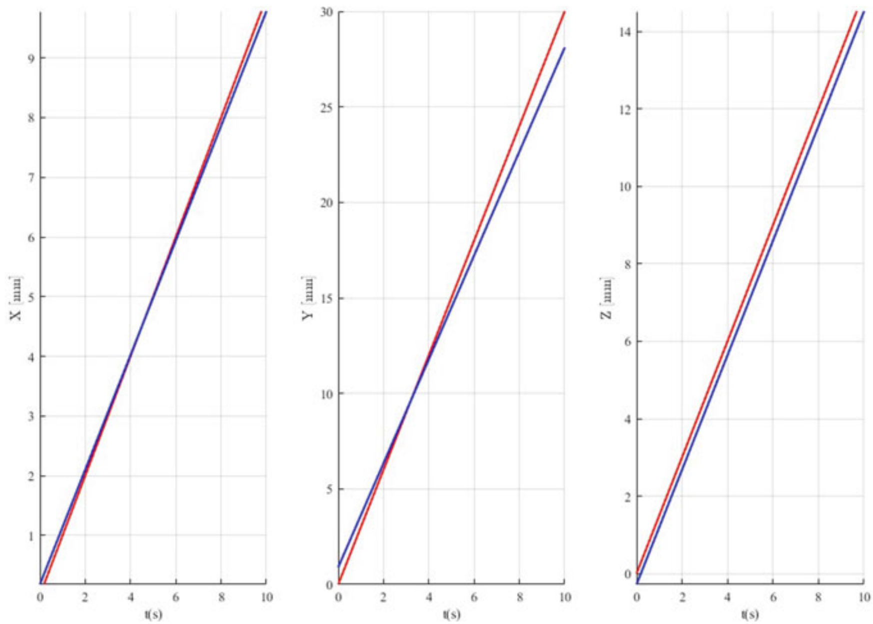

Fig. 4 Graphical representation of the trajectory registered from the wrist of the hand (red line) and end-effector trajectory (blue line)

4 Discussion and Conclusion

Based on the tests performed with the proposed system, Kuka collaborative robot demonstrated the capability to effectuate accurate movements based on real time commands from Hololens, for all proposed tasks. However, tasks of varying complexity showed proportional errors, as can be seen between Task 1 and Task 2, reflecting the demand for increased dexterity. Data transmission was executed with a small delay, which indicates the potential of this system to be used in real-time applications such as surgery.

The proposed system is feasible for teleoperation, bringing in addition the advantage of allowing multi-user manipulation if there are more Hololens devices, facilitating collaborative decision-making and enhancing overall surgical efficiency. This real-time, intuitive control system has the potential to optimize surgical procedures, reduce learning curves, and improve outcomes for the surgical team.

Another advantage is given by its collaborative design, thanks to which potential collisions do not lead to damage. Additionally, the robot provides the option to restrict each joint within a virtual plane, ensuring that the robot stays within predefined spatial boundaries.

To respond to the specific task of holder for laparoscopic camera, there are other aspects that should be also taken into consideration. First of all, in order to avoid unwanted behavior, the robot executes a linear displacement to the insertion point. Before the insertion, the camera is aligned with the insertion point. Following this alignment, the insertion is carried out incrementally, with minimal increment and minimal velocity (both the velocity and the increment are selected by the user from the interface). Another important factor is the scaling between the movement of the human operator and the robot. This component is also implemented in the user interface and allows the user to scale the movement, in accordance with his needs.

In conclusion, the teleoperation setup combining Kuka IIWA and HoloLens 2 can bring a significant advancement in surgical technology. The collaborative system, together with HoloLens device, used in intraoperative phase holds promise for improving surgical precision, safety, and overall outcomes.

This system, built around the collaboratives robot and the augmented reality device HoloLens 2, can be easily integrated into diverse collaborative systems.

Acknowledgements This work was supported by the project New smart and adaptive robotics solutions for personalized minimally invasive surgery in cancer treatment—ATHENA, funded by European Union—NextGenerationEU and Romanian Government, under National Recovery and Resilience Plan for Romania, contract no. 760072/23.05.2023, code CF 116/15.11.2022, through the Romanian Ministry of Research, Innovation and Digitalization, within Component 9, investment I8 and by a grant of the Ministry of Research, Innovation and Digitization, CNCS/CCCDI—UEFISCDI, project number PN-III-P2-2.1-PED-2021-2790 694PED—Enhance, within PNCDI III.

References

1. Pisla, D., Plitea, N., Gherman, B., Pisla, A., Vaida, C.: Kinematical analysis and design of a new surgical parallel robot. In: Proceedings of the 5th International Workshop on Computational Kinematics, Duisburg, Germany, pp. 273–282 (2009)
2. Luo, J., He, W.Y, Chenguang: Combined perception, control, and learning for teleoperation: key technologies, applications, and challenges. Cognitive Comput. Syst. **2**(2), 33–43 (2020). Title of a proceedings paper. In: Editor, F., Editor, S. (eds.) Conference 2016, LNCS, vol. 9999, pp. 1–13. Springer, Heidelberg (2016)
3. Vaida, C., Pisla, D., Plitea, N., Gherman, B., Gyurka, B., Stancel, E., Hesselbach, J., Raatz, A., Vlad, L., Graur, F.: Development of a control system for a parallel robot used in minimally invasive surgery. IFMBE Proc. **26**, 171–176 (2009)
4. Kazanzides, P., Vagvolgyi, B.P., Pryor, W., Deguet, A., Leonard, S., Whitcomb, L.L.: Teleoperation and visualization interfaces for remote intervention in space. Front. Robot. AI **8**, 747917 (2021)
5. Gerup, J., Soerensen, C.B., Dieckmann, P.: Augmented reality and mixed reality for healthcare education beyond surgery: an integrative review. Int. J. Med. Educ. **18**(11), 1–18 (2020)
6. Pisla, D., Birlescu, I., Vaida, C., Tucan, P., Pisla, A., Gherman, B., Crisan, N., Plitea, N.: Algebraic modeling of kinematics and singularities for a prostate biopsy parallel robot. Proc. Rom. Acad. Ser. A **19**, 489–497 (2019)
7. Vaida, C., Crisan, N., Birlescu, I., Andras, I., Pisla D.: Preliminary assessment of artificial intelligence agents for a SILS robotic system. In: 2021 International Conference on e-Health and Bioengineering (EHB), Iasi, Romania, pp. 1–6 (2021). https://doi.org/10.1109/EHB52898.2021.9657717
8. Tucan, P., Vaida, C., Horvath, D., Caprariu, A., Burz, A., Gherman, B., Iakab, S., Pisla, D.: Design and experimental setup of a robotic medical instrument for brachytherapy in non-resectable liver tumors. Cancers **14**, 5841 (2022)
9. Man, L., Meghan, M., Dhir, P., Aravindh, N., Edwards, P.A.: Telemedicine, telementoring, and telesurgery for surgical practices. Curr. Probl. Surg. (2021)
10. Schwaner, K., Iturrate, I., Holm, J.K.,Rosendahl Dam, C., Jensen, P., Rajeeth Savarimuthu, T.: MOPS: a modular and open platform for surgical robotics research. In: 2021 International Symposium on Medical Robotics (ISMR), Atlanta, GA, USA, pp. 1–8 (2021)
11. Su, H., Sandoval, J., Vieyres, P., et al.: Safety-enhanced collaborative framework for teleoperated minimally invasive surgery using a 7-DoF torque-controlled robot. Int. J. Control. Autom. Syst. **16**, 2915–2923 (2018)
12. Abdullah, T., Wiro, J.N., Eppo, B.W., Theo, W.: Evaluation of marker tracking using mono and stereo vision in Microsoft HoloLens for surgical navigation. In: Proceedings SPIE 12034, Medical Imaging 2022: Image-Guided Procedures, Robotic Interventions, and Modeling, pp. 1203415 (2022)
13. Birlo, M., Edwards, P.J.E., Clarkson, M., Stoyanov, D.: Utility of optical see-through head mounted displays in augmented reality-assisted surgery: a systematic review. Med. Image Anal. **77**, 102361 (2022). https://doi.org/10.1016/j.media.2022.102361
14. https://www.kuka.com/en-us/products/robotics-systems/industrial-robots/lbr-iiwa. Accessed in 15 Jan 2024

Task Oriented Collaborative Robots: Intervention in Repetitive Task for Worker Well-Being

Ashita Ashok, Jovan Šumarac, Aleksandar Rodić, and Karsten Berns

Abstract This study investigates the role of Task-Oriented Collaborative Robots in repetitive tasks, specifically focusing on enhancing worker well-being. A comprehensive dataset capturing key human ergonomic factors of fatigue, mood, and motivation across 150 builds of a furniture assembly task was developed. Utilising the precision of ZED2 RGB-D camera, three hours of visual data per 6 participants enabled monitoring of upper body movements. Each build sample is complemented by self-reported questionnaires on psychological states of mental fatigue (MF), mood, and motivation. The key findings reveal significant variations in fatigue levels, mood, and motivation and their correlation with task performance, measured by average task completion time. Notably, gender-based disparities in reporting MF and total completion time were observed. A key proposal to integrate verbal alerts with collaborative robots (cobots) such as UR5 emerges from this study. These findings underscore the potential of cobots in mitigating worker fatigue and improving task efficiency to revolutionize worker well-being and productivity in repetitive industrial tasks.

Keywords Collaborative robotics · Human robot collaboration · Repetitive task assistance

A. Ashok (✉) · K. Berns
Robotics Research Laboratory, University of Kaiserslautern-Landau, 67663 Kaiserslautern, Germany
e-mail: ashita.ashok@cs.rptu.de

K. Berns
e-mail: karsten.berns@cs.rptu.de

J. Šumarac · A. Rodić
Institute Mihajlo Pupin, University of Belgrade, Belgrade, Serbia
e-mail: jovan.sumarac@pupin.rs

A. Rodić
e-mail: aleksandar.rodic@pupin.rs

D. Pisla et al. (eds.), *Advances in Service and Industrial Robotics*, Mechanisms and Machine Science 157, https://doi.org/10.1007/978-3-031-59257-7_25

1 Introduction

In contemporary industrial contexts there is an increasing prevalence of repetitive tasks of manufacturing component and its assembly. Despite contributing significantly to mass assembly of identical or similar items on a significant scale, exposes the workforce to considerable challenges of well-being and productivity. It also increasing the risk of errors [4]. The workforce engaged in repetitive tasks find themselves conducting identical motions for long durations which leads to bodily strains known as musculoskeletal disorders (MSDs), as well as mental strains, such as mental fatigue (MF) and lower motivation. Furthermore, the physical demands, coupled with the monotony of the tasks, adversely impact the workers' mood. In order to address issues pertaining to the workforce, a collaborative approach towards repetitive manufacturing task with collaborative robots (cobots) can be considered for human-robot collaboration (HRC). In particular, the supportive HRC [3] scenario in which the robot assists the worker on the same task simultaneously within collaborative work-cell, emerges as a favorable approach. Cobots, equipped with sophisticated noncontact sensors and machine learning algorithms, aid human workers in optimal task execution. They enable real-time monitoring of physiological indicators and intervention during human detrimental factors.

Cobot intervention strategies in supportive HRC can be divided into two parts: One, where the cobot provides verbal alerts, and, another where the robot assists in the completion of the task. After the advent of the UR5[1] cobot in 2008 by Universal Robotics, cobot usage in industrial applications expanded rapidly. Collaborative robotics further highlights a potential avenue for enhancing worker well-being and repetitive task efficiency.

Existing research revolving in HRC includes human perception of action and intent recognition, learning from demonstration and reinforcement. It is recognized that posture related muscle fatigue during repetitive tasks can be assessed through factors such as intensity and duration. Despite the potential applications of HRC, there exists a research gap in the development of possible intervention strategies for cobots to assist human workers during a repetitive task, such as, assembling a drawer unit. There is additionally a lack of comprehensive datasets with labels of human detrimental factors such as MF, motivation, and mood, also known as microergonomics [9]. Acknowledgment of developing MF risks for assembly-line industrial workers, asks for further research to establish strategies to reduce this risk via cobot intervention and gain more insights on worker performance and well-being.

The presented study emphasizes human-centered cobot intervention strategies for assembly line industrial HRC with implementation focus on improving worker ergonomics. It highlights the development of a robust dataset and tailored intervention strategies. The main purpose of this work was to generate a dataset with human-annotated features of self-reported MF, mood, and motivation during assembly line task involving the continuous building of drawer units. This research underscores the measurement and thereafter modelling of human psychophysical data to increase task

[1] https://www.universal-robots.com/about-universal-robots/our-history/.

productivity and develop a cobot-supported algorithm for real-time identification of MF, offering intuitive feedback to human workers which also falls into the category of human-robot interaction (HRI).

The study's findings reveal that the collected dataset effectively illustrates worker fatigue induced during task execution. This dataset shows scope in developing cobot interventions to provide a supportive HRC scenario through audio alerts with the goal to maintain worker well-being. The current research builds on existing findings, aiming to provide an insight of naturally occurring fatigue and cobot interventions suitable for industrial environments.

2 Related Works

Mental fatigue (MF) is known to negatively influence the task performance of human workers, impacting situation awareness, accident rates, task difficulty and motivational levels [12]. This section discusses relevant studies on human-robot collaboration (HRC) in repetitive tasks, particularly focusing on workforce experiences with MF and cobot adaptation.

The concept of situational awareness in HRC involved examining the effects of gender and fatigue states on different levels of cobot assistance [6]. The study employed a UR10 robot in a 10-session, in-person HRC environment, engaging 16 participants in a metal surface polishing task. The task was carried out using a joystick control of the cobot in 4 conditions (fatigue/no fatigue; low/high). Fatigue was induced through a computer-based cognitive task (2-back test), with performance and situational awareness assessed using Likert scale, situation awareness rating technique (SART), and NASA task load index questionnaires, and heart rate variability (HRV) measurements. The principal finding of this study is that participants experienced higher levels of fatigue with low robotic assistance and less situational aware with high assistance. Furthermore, the research identified a significant interaction between MF and sex; notably, females reported greater fatigue than males under similar conditions.

A recent study explored the interaction between MF and performance in a repetitive dual-task setting [5]. A participant pool of 11 (N = 5 males, N = 6 females) performed both physical (repetitive lifting-lowering of a box) and cognitive (subtraction task) tasks both with and without an exoskeleton support (Exo versus NoExo). The study assessed task performance, workload, MF, and boredom using NASA-TLX, M-VAS, and B-VAS questionnaires. Post-task interventions included a 60-Minute Intervention (Stroop task) or Control Activity (watching documentary). The results indicated no significant interaction between MF and performance accuracy, or movement duration; increase in boredom after the Stroop task where as decrease after watching documentary. Further findings indicated job rotations with breaks to counter MF among industrial workers.

Another pivotal study by Shah et al. [12] focused on a UR16e cobot's adaption to assist fatigued human workers during the surface polishing task [12]. This study involved 16 participants, balanced by gender, using a joystick-controlled cobot following an S-shaped trajectory (same task as in [6]) modelled using discrete markov decision process. The cobot's intervention strategy was based on observed worker fatigue, with performance evaluated under various assistance conditions. The results concluded that robot adaptation policies during tasks were affective in reducing worker MF and improving task performance.

The critical distinction between these studies and the current research lies in the approach to fatigue induction. While previous studies induced fatigue externally through experimental tasks as the stressor, this study observes fatigue as it occurs intrinsically during task completion. This approach mirrors the real-world experience of industrial workers more closely, offering insights into natural fatigue occurrences in repetitive tasks.

3 Method

The primary objective of this study was to develop a dataset capturing human ergonomics, specifically to detect worker fatigue, mood and motivation during repetitive furniture assembly task. This dataset would subsequently facilitate the development of robot interventions to mitigate human errors, thereby increasing productivity and improving worker well-being.

3.1 HRC Setup

The experiment was conducted in the Robotics Laboratory of Institute Mihajlo Pupin, Serbia for the period of 1 week. A workspace was set up featuring a bi-manual Universal UR5 robot torso (as shown in Fig. 1) with StereoLabs ZED2 sensor mounted atop. RBG-D sensor positioned 1.25 m from the human worker, this setup included a task of assembling two drawer units in a repetitive manner, to simulate a continuous workflow. The next assembled drawer unit was disassembled behind the workspace by an experimenter and placed to the right of the worker. The ZED2 sensor monitored the participants, correlating physical activity with self-reported psychological states.

3.2 Participants

A participant sample of N = 6 (3 females; 3 males) were recruited. They provided written consent for the use of their video recordings and experimental data, and confirmed they were free from cognitive or muscular ailments. All participants were right handed with mean age of 27 years (range 22–35 years).

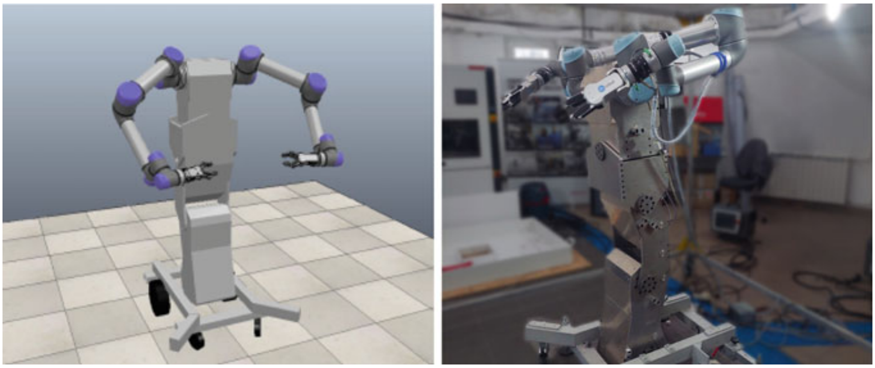

Fig. 1 The bi-manual Universal UR5 robot torso used in this study [11]

3.3 Experimental Design

Each session began with a task briefing by the experimenter along with the building instruction sheet. Participants were tasked with assembling a small and medium-sized drawer units, completing a total of 150 builds as shown in Fig. 2.[2] The task was structured into cycles: assembling a drawer unit, questionnaire completion, and then assembling the next drawer unit while the previous one was reset by an experimenter. The first cycle continued for one hour, followed by a 10 min break, second cycle, 1 h lunch break, third cycle, 10 min break, finally the fourth cycle ended the participant session. 2 males and 1 female participant finished their builds by the third cycle. The total mean completion time was 3 h 17 min. The following scenario provided to participants was: *In this scenario, imagine yourself as a beginner worker in the furniture industry, AEKI. Please answer the below listed questions that are related to the task you just finished. Make sure you answer as quickly as you can and only select one option per question.* After each assembly, they completed questionnaires on their motivation [8, 13], mood [2], and fatigue [7].

Among the 8 motivation assessment set, three task-specific questions were analyzed: I think that this task is interesting (M1); I feel good when doing this task (M4); I feel a great sense of personal satisfaction when I do it (M7). SAM ratings for mood covered Pleasant-Pleased-Neutral-Unsatisfied-Unpleasant (valence), Calm-Dull-Neutral-Wideawake-Excited (arousal), and Dependent-Power-lessness-Neutral-Powerful-Independent (dominance). For mental fatigue four task-specific questions out of 9 were analyzed: The task brings on fatigue (F2); Fatigue interferes with my physical functioning (F4); Fatigue interferes with carrying out certain duties and responsibilities (F7); Fatigue interferes with my work, family, or social life (F9).

[2] Note: Consent for image use obtained from participant.

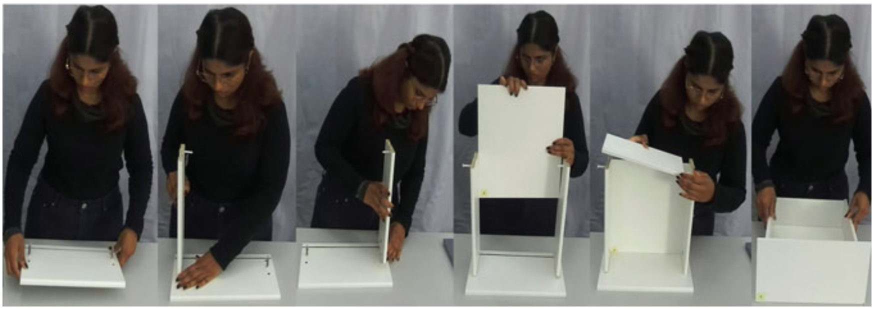

Fig. 2 A participant building a drawer unit during the 6-step experimental task

4 Dataset Analysis

The dataset collected for this study can be requested via email to the author.

4.1 Human Upper Body Tracking

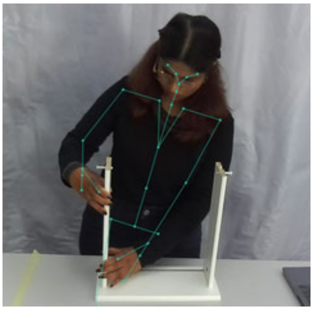

Fig. 3 A participant with 34-point skeletal model from ZED2

The analysis utilised approximately three hours of visual data per participant, with focus on spatiotemporal aspects of human upper body movements during the assembly task. The StereoLabs ZED2 RGB-D camera, chosen for its advanced human tracking algorithms, provides a 34-point skeletal model,[3] rendering a 2D visualization of the participant. For motion tracking, 20 key points (e.g. LEFT_WRIST(7), RIGHT_CLAVICLE(11), NOSE(27), etc.) were extracted as shown in Fig. 3. The

[3] https://www.stereolabs.com/docs/body-tracking.

adoption of external camera sensor, with its state-of-the-art skeleton tracking model is suitable for diverse user groups from industrial and laboratory settings.

4.2 Worker Fatigue, Mood, and Motivation

Human factors like mental fatigue (MF) influence human trust in the robot [12], therefore detecting worker fatigue, mood, and motivation is crucial for optimal human-robot collaboration (HRC). The study acknowledges and indicates gender-based disparities in total completion time and builds per hour, as illustrated in Table 1. Analyzing the Table 2 the following interpretations of worker states can be observed. Average MF ratings ranged from moderate (F2: 2.55–6.45) to significant (F4: 2.91–6.08, F7: 2.68–5.93, F9: 2.72–6.02), indicating varying levels of fatigue and its impact on physical functioning and daily responsibilities. Notably, participant P03 exhibited the highest fatigue levels (F2, F4, F7), with P01 scoring highest on F9, whereas P06 reported the lowest levels, underscoring individual differences. Emotional states were generally neutral, with valence averaging between 2.78 and 3.31, and arousal between 3.08 and 3.59, indicating a tendency towards feeling ’Wideawake’ rather than ’Dull’. Motivation ratings varied moderately (M1: 1.97–4.62, M4: 1.85–4.21, M7: 1.85–4.48), with P01 reporting the highest and P02 the lowest levels.

Table 1 Participant demographics

PId	Sex	Total(h:m)	Builds (per h)
P01	F	3:54	26 + 40 + 44 + 40
P02	M	3:36	29 + 46 + 36 + 39
P03	F	3:17	28 + 44 + 57 + 21
P04	F	3:02	44 + 53 + 53
P05	M	3:06	44 + 52+ 54
P06	M	2:51	50 + 58+ 42

5 Conclusion

This research aims to highlight the importance of integrating collaborative robots (cobots) in repetitive tasks to enhance worker well-being. Findings reveal significant variations in worker fatigue, mood, and motivation, with notable gender-based differences. Data from ZED2 camera for tracking and analyzing human upper body movements established a correlation between physical activity with psychological states. In light of these findings, the study advocates the next phase of research should

Table 2 Means fatigue, mood, and motivation levels of participants

PId*	F2	F4	F7	F9
P1	4.37	4.98	5.07	6.02
P2	3.96	3.94	3.82	3.48
P3	6.45	6.08	5.93	3.31
P4	6.01	5.14	4.27	4.00
P5	4.46	4.39	4.38	4.44
P6	2.55	2.91	2.68	2.72
PId‡	Val	Aro	Dom	
P1	2.78	3.08	3.30	
P2	3.10	3.32	3.2	
P3	2.06	2.62	4.19	
P4	3.27	3.32	2.8	
P5	3.86	3.59	3.48	
P6	3.43	3.43	3.00	
PId†	M1	M4	M7	
P1	4.62	4.21	4.48	
P2	1.97	1.96	1.85	
P3	2.35	2.39	2.19	
P4	3.99	4.02	3.68	
P5	3.04	2.98	3.08	
P6	3.16	3.81	3.47	

*Fatigue
‡Mood
† Motivation

refine cobot intervention strategies to address individual fatigue patterns across a larger, more diverse sample and various repetitive tasks. The study proposes the introduction of verbal interventions in cobots, as supported by prior research in verbal human-robot interaction (HRI) [1, 10]. Suggested adaptations include audio alerts [12] such as "Please take a break" in response to detected low fatigue levels, aiming to enhance worker well-being and trust in cobots. Future research directions include exploring personalized cobot responses. Additionally, investigating the long-term impacts of cobot assistance on worker productivity and mental health will provide deeper insights into supportive human-robot collaborative industrial settings.

Acknowledgements This study was supported by German Academic Exchange Service (DAAD) on a collaborative project titled Task Oriented Collaborative Robotics with Affect (TCRA) funded from 2022 to 2024.

References

1. Ashok, A., Pawlak, J., Paplu, S., Zafar, Z., Berns, K.: Paralinguistic cues in speech to adapt robot behavior in human-robot interaction. In: 2022 9th IEEE RAS/EMBS International Conference for Biomedical Robotics and Biomechatronics (BioRob), pp. 01–06. IEEE (2022)
2. Bradley, M.M., Lang, P.J.: Measuring emotion: the self-assessment manikin and the semantic differential. J. Behav. Ther. Exp. Psychiatry **25**(1), 49–59 (1994)
3. Cesta, A., Orlandini, A., Bernardi, G., Umbrico, A.: Towards a planning-based framework for symbiotic human-robot collaboration. In: 2016 IEEE 21st International Conference on Emerging Technologies and Factory Automation (ETFA), pp. 1–8. IEEE (2016)
4. Colim, A., Faria, C., Cunha, J., Oliveira, J., Sousa, N., Rocha, L.A.: Physical ergonomic improvement and safe design of an assembly workstation through collaborative robotics. Safety **7**(1), 14 (2021)
5. Govaerts, R., De Bock, S., Stas, L., El Makrini, I., Habay, J., Van Cutsem, J., Roelands, B., Vanderborght, B., Meeusen, R., De Pauw, K.: Work performance in industry: the impact of mental fatigue and a passive back exoskeleton on work efficiency. Appl. Ergon. **110**, 104026 (2023)
6. Hopko, S., Wang, J., Mehta, R.: Human factors considerations and metrics in shared space human-robot collaboration: a systematic review. Front. Robot. AI **9**, 799522 (2022)
7. Krupp, L.B., LaRocca, N.G., Muir-Nash, J., Steinberg, A.D.: The fatigue severity scale: application to patients with multiple sclerosis and systemic lupus erythematosus. Arch. Neurol. **46**(10), 1121–1123 (1989)
8. Lawler, E.E., Hall, D.T.: Relationship of job characteristics to job involvement, satisfaction, and intrinsic motivation. J. Appl. Psychol. **54**(4), 305 (1970)
9. Lorenzini, M., Lagomarsino, M., Fortini, L., Gholami, S., Ajoudani, A.: Ergonomic human-robot collaboration in industry: a review. Front. Robot. AI **9**, 262 (2023)
10. Paplu, S.H., Arif, M.N.I., Berns, K.: Adapting behaviour of socially interactive robot based on text sentiment. In: International Conference on Robotics in Alpe-Adria Danube Region, pp. 221–228. Springer (2021)
11. Rodić, A., Šumarac, J., Stevanović, I., Jovanović, M.: Cloud-enabled bi-manual collaborative robot with enhanced versatility for customized production. In: International Conference on Robotics in Alpe-Adria Danube Region, pp. 240–249. Springer (2021)
12. Shah, J.K., Yadav, A., Hopko, S.K., Mehta, R.K., Pagilla, P.R.: Robot adaptation under operator cognitive fatigue using reinforcement learning. In: 2023 32nd IEEE International Conference on Robot and Human Interactive Communication (RO-MAN), pp. 1467–1474. IEEE (2023)
13. Tremblay, M.A., Blanchard, C.M., Taylor, S., Pelletier, L.G., Villeneuve, M.: Work extrinsic and intrinsic motivation scale: its value for organizational psychology research. Can. J. Behav. Sci./Revue canadienne des sciences du comportement **41**(4), 213 (2009)

Part III
Industrial Robots and Education

Industry Needs in Robotics Education

Francesco Aggogeri, Nicola Pellegrini, and Riccardo Adamini

Abstract This paper presents the outcomes of the investigation conducted in a specific Italian region on the robotics usage and integration within the manufacturing sector. The adoption of robotic solutions has been examined selecting representative users and providing a technical survey. Data collection is based on homogeneous population of about 2500 companies, that 655 have been directly interviewed in 2021–2023 period. The used types of robots, their main applications, the corporate dimension, the issues experienced, are the information collected to build the needs derivate predominantly from the lack of competences. The results of the investigation highlight a presence of articulated robots. Large companies demonstrate a superior ability to adapt to robotic cells and the definite hiring strategy where the M.Sc. degree in Automation Engineering is the preferred figure. The mapped robotic competences gaps are the significant input to fine tuning the educational proposal from University at Engineering profile to react at industrial needs. Finally, companies of all sizes confirmed the vision on approval of the installed robots and indicated the intention to progress the implementation in the 2023–2026 period.

Keywords Industrial robotics · Robotics education · Robotics impacts

1 Introduction

As demonstrated in recent investigations [1, 2], the robotics installations are expected to increase by 10% in the next years, following the positive trend of the last decade. At the same time, production facilities are transforming into extremely flexible factories [3–7], allowing manufacturers to respond to customer demand for a greater variety of products [8], and maintaining high productivity indicators [9, 10]. Additionally, factory equipment is becoming increasingly digitalized [11–16]. These elements have contributed to the growth of new needs from Industry. New skills, abilities and

F. Aggogeri · N. Pellegrini (✉) · R. Adamini
Department of Mechanical and Industrial Engineering, Università degli Studi di Brescia, Brescia, Italy
e-mail: nicola.pellegrini@unibs.it

D. Pisla et al. (eds.), *Advances in Service and Industrial Robotics*, Mechanisms and Machine Science 157, https://doi.org/10.1007/978-3-031-59257-7_26

expertise are required to workers to facilitate the integration and management of these technologies. In this way, educational institutions and centers have the responsibility to map and analyze these requirements, to evaluate and promote new activities and courses, focused on covering possible knowledge gap [17–19]. This study aims to present the results of a structured investigation developed by BRIXIA Robotics and Industrial Automation monitoring center (https://osservatoriorobotica.unibs.it/) on the industrial robotics effects, involving a sample of + 600 companies, using both surveys and Italian company databases of statistical and financial analyses. The research has been developed in the Province of Brescia, a large industrial area in the north of Italy, characterized by 4890 manufacturing companies (large, medium and small enterprises) with a production value of + 48 billion Euro. A specific part of the study is devoted to collect data and information directly from robot end-users to assess the required expertise of companies' personnel to use robotics effectively.

2 Research Methodology

Italy is the sixth largest global market of industrial robots with an installation increase (year over year) by 6.5% in 2022. The Province of Brescia is one of the first areas in Europe for the number of installed robots and the density of robots per employee. The research focuses on exploring the mechanical industry that represents about 50% of the number of manufacturing companies and employees in the province of Brescia.

In the first part of the research a preliminary analysis of statistical company databases was performed to identify a heterogeneous sample of companies to be involved in the investigation. Then, a group of + 600 companies was selected based on several parameters (e.g., type of production systems, revenues, sales growth, number of employees, R&D investments, …) and classified in categories, as shown in Table 1.

The company survey was based on several topics: *state of the art*—to map the current state of company robotics (e.g., type of robots, applications, level of maturity, level of satisfaction of robotics use, …), *impact*—to assess the effects of robotics on company's key performance indicators (e.g., productivity, quality, availability), *competences*—to analysis the current workers' skills and the new required expertise and *future vision*—to evaluate the potential opportunities of robotics in the next years (2023–2026).

Table 1 Company clusters definition

Company cluster	No. employees	Revenues (Mln)—Euro	Total balance (Mln)—Euro
Large	> 250	> 50	> 43
Medium	< 250	< 50	< 43
Small	< 50	< 10	< 10
Micro	< 10	< 2	< 2

Table 2 The main issues experienced in industrial robotics applications

Robotics application issues	Large (%)	Medium (%)	Small (%)
Specialized personnel presence during production	31	29	11
Challenges in programming and managing the robot	9	24	40
Issues caused by sensors	22	14	18
Unexpected maintenances	17	17	22
Assistance	17	10	10
Malfunctioning of accessories	17	5	22
Frequent human intervention	17	5	0
Frequent production interruptions due to robot issues	9	2	0

2.1 *Overall Results of the Survey Investigation*

The main results of the investigation show an intense presence of robots (+10,000 units) in the involved companies with a high density of robots per employee (1 robot per 10 employees), although their implementation is still limited and fragmented in certain specific companies. The constraint is notable for small and medium-sized enterprises (SMEs), where investments of this type of technology have traditionally been expensive and inaccessible. The main installed model is the anthropomorphic robot that is used in machine tending and handling activities (100% large companies, 92% medium companies, and 77% small companies). There are several cases of SCARA and artesian robot applications. Unexpectedly, COBOTS, despite their considerable potential and adaptability to various business contexts, remain largely unknown or underutilized, in small and medium-sized enterprises. A significant group of companies (75%) are satisfied from the installation of robotics, while only 15% is not fully satisfied, identifying several criticalities and issues in robotics management.

Table 2 lists the main criticalities due to the use of robotics. For instance, small companies highlight the lack of employee expertise in programming and management the robots, while the robots installed in large companies' plants require an intense presence of specialized personnel during the production. Other issues are identified in using sensors and accessories. A significant part of these issues is directly linked to expertise and skills of the workers involved in the manufacturing processes.

2.2 *The Required Competencies for Industrial Robotics*

The outcome of the analysis shows the technological advancements that the companies are facing in the field of robotics, in terms of automation and abilities. To map the industry needs in robotics managing, the survey focused on a set of questions regarding the state of art of workers' expertise. It is noted that 18% of large companies declare partial skills of employees to use robots, while 38% of small companies highlights the lack of competencies of the internal personnel. This element represents a critical constraint to invest and install new technologies.

Nevertheless, a set of activities may be developed to compensate the lack of skills, as hiring new personnel with high expertise or training employees in life-long learning approach.

Table 3 states the implemented actions stratified by company size group.

The results underline the different approach in overcoming the robotics issues by type of companies. The large and medium-sized group focuses on hiring new personnel and strengthening the expertise of existing employees, while the small and micro-sized companies evaluate to use training or outsource the activities that are not able to solve using internal workers.

Table 4 shows the main competencies that companies evaluate for employees to use robots effectively.

The results confirm that large companies focus on robot simulations and virtual commissioning, digital twin and artificial intelligence to optimize the existing and new robotics systems.

In contrast, small and micro-sized companies prefer to increase the basic knowledge of robotics, selecting technical figures for robot programming and vision system integration. Finally, the investigation highlights an industrial demand by each type of companies related to the robot safety standards and mechanical maintenance for manufacturing companies.

In the light of these considerations, the main professional figures to be hired in the next future are listed in Table 5 by different type of companies.

The Master's degree in Automation Engineering is preferred by 54% of large companies that are looking for a multidisciplinary profile able to develop and implement hardware and software components. The industrial technician with a more direct and practical background, based on previous experience is the preferred figure for 56% small-micro companies also considering the general limited attitude to innovations.

The same action is recognized by 32% of large companies. Medium-sized companies have a more heterogeneous distribution of their preferences. The industrial technician and the M.Sc. Automation Engineer are the preferred figures for the half of medium-sized companies.

Industrial and Mechanical Engineer represent the alternative figures in robotic context, in particular in large companies with minor relevance, close to 25% and 14%, correspondingly.

Table 3 Actions to compensate for lack of skills

Types of actions	Large (%)	Medium (%)	Small (%)
New personnel hiring	26	20	5
Training for employees	90	90	58
No actions	0	0	42

Table 4 Actions to compensate for lack of competencies

Assets of competencies	Large (%)	Medium (%)	Small (%)
Robot simulation and virtual commissioning	84	62	12
Robot programming	72	75	81
Sensors installation and integration	62	45	34
Trajectory planning and definition	71	61	23
Mechanical maintenance	78	51	92
Programming for welding application	71	66	87
Integration of vision system	35	43	82
Digital Twin and MES communication	78	63	23
Artificial Intelligence (e.g., anomaly detection, perception and decision-support)	85	31	13
Layouts optimization procedures	82	42	28
Robotics cells design (basic knowledge of mechanics, electrics, and informatics)	88	65	32
Time and methods analysis	62	64	61
Robot safety standards	80	74	88
End-effector and gripper design	45	35	34
Basics of new robotics solutions (e.g. COBOT)	79	55	25
Knowledge to integrate robots with other devices (e.g. program languages)	85	65	43
Mechanical design of customized robots	48	34	25
Business cases for robot integration	39	48	54

Table 5 Actions to compensate for lack of skills

Hiring profile	Large (%)	Medium (%)	Small (%)
Industrial technician	32	49	56
Automation engineer (Bachelor's degree)	46	11	5
Automation engineer (Master's degree)	54	34	28
Industrial engineer (Master's degree)	25	16	13
Mechanical engineer (Master's degree)	14	9	4
Other engineer (Master's degree)	8	1	3

2.3 The Future Vision of Robotics in Local Area

In this section, authors present the collected robotic installations intentions for the period 2023–2026 in Brescia area. A significant correlation is noted related to the adoption of robotics and the hiring of specialized profiles in Automation Engineering among different size companies, Fig. 1. Three regions have been defined: (i) green coloured as grow business context with high potentials and the request of experienced human capital and advanced technologies, (ii) orange coloured region characterized by uncertainties and stationary business and (iii) grey coloured region as conservative and low risk business.

Large companies confirm to be leading in terms of adoption of advanced technologies, 98% of interviews expressed their intention to install robots in the next three years. Moreover, 61% of large companies intend to hire a M.Sc. Automation Engineer in the same time period. Then, the 57% of medium-sized companies expect to install robotics and 21% of them plan to hire an M.Sc. Automation Engineer.

Finally, SME companies declare a promising development, 78% is planning to adopt robotic solutions. However, the correlation with high human capital investment is not confirmed, 11% of SME plan to hire a M.Sc. Automation Engineer. Data shows that SMEs recognize the robotic trend and benefits although the awareness in competences is a substantial weakness topic.

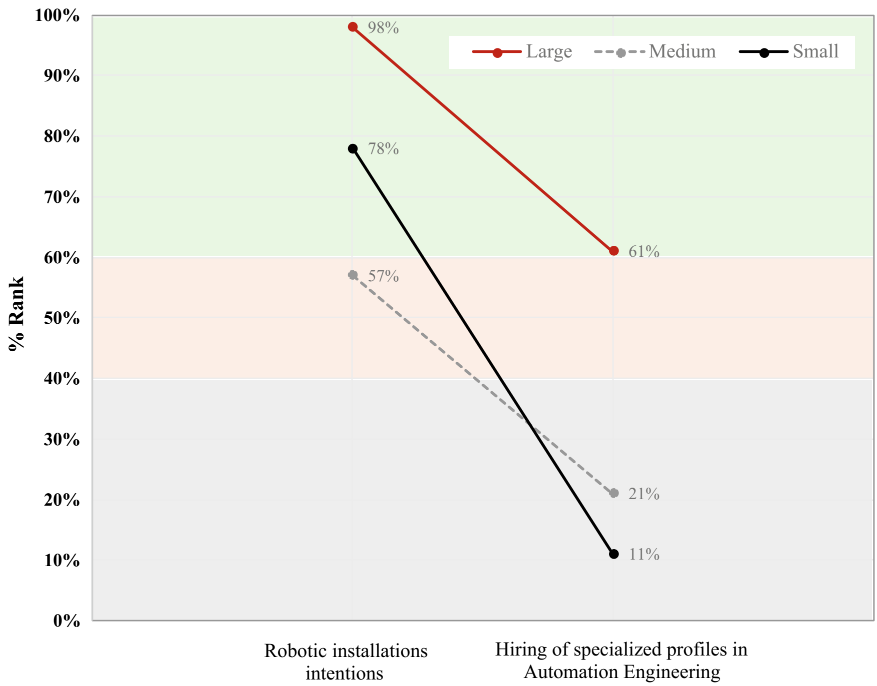

Fig. 1 Vision of robotics in Brescia area 2023–2026 period

3 Discussion and Conclusions

This study highlights the main opportunities that may be obtained from industrial robotics. The analysis of the collected data shows that the Province of Brescia is a significant area in Europe based quantitative parameters as: i) the number of installed robots, and ii) the density of robots per employee (1 robot per 10 employees). Nevertheless, local companies, in particular SME companies, exhibit constraints towards the integration of robotic cells due to a low awareness.

Education in robotics may enable the appropriate competence to enhance human resources in installation of robot, managing and optimization of robot adoption in industrial context.

The survey provides direct feedback of companies that considers the robot installation as a success story, and their intention in the continuous technological development. SME and micro sized companies recognize their boundaries in knowledge, for that reason the expert hiring and/or qualified training is a daily need.

Nowadays, the University of Brescia provides in various engineering curricula different courses that includes the main topics and aspects mapped in the survey to cover the identified knowledge gap in Automation and Robotics.

In particular, the Bachelor's degree of Automation Engineering the course "Functional design laboratory of automation systems"—75 h duration, in the Bachelor's degree of Product and process industrial techniques the course "Automation systems laboratory"—180 h duration, and in Master's degree the "Robotic cells and automation systems" course—90 h duration.

The active synergy demonstrated by the University and the local companies facilitates their technological transformation, sustaining and promoting initiatives to overcome the challenging needs, with respect to the demands of the industrial requirements.

Acknowledgements The authors sincerely thank all the companies that have participated to this investigation.

References

1. Fernandez-Macias, E., Klenert, D., Anton, J.I.: Not so disruptive yet? Characteristics, distribution and determinants of robots in Europe. Struct. Change Econ. Dyn. **58**, 76–89 (2021)
2. IFR 2022: IFR World Robotics 2022 Edition. International Federation of Robotics, Frankfurt am Main (2022)
3. Harold, L.S., Michael, Z., Justin Ryan, R.: The robotics revolution. Bost. Consult. Gr. **1**(1), 28 (2015)
4. Rigby, M.: Future-Proofing UK Manufacturing Current Investment Trends and Future Opportunities in Robotic Automation (2015)
5. Russmann, M., et al.: Industry 4.0: the future of productivity and growth in manufacturing industries. Bost. Consult. Gr. 1–20 (2015)
6. OECD: The Future of Productivity, vol. 1, no. 1 (2015)

7. Manyijka, J., Chui, M., Bughin, J., George, K., Willmott, P., Dewhurst, M.: A Future That Woks: Automation, Employment, and Productivity, pp. 1–28. McKinsey Global Institute (2017)
8. Gons, E., Ketzner, L., Carson, B., Peddicord, T., Mallory, G.: How AI and Robotics will disrupt the defence industry. Bost. Consult. Gr. (2018) [Online]. Available: http://k1.caict.ac.cn/yjts/qqzkgz/zksl/201804/P020180426375927121069.pdf
9. European Commission: The Changing Nature of Work and Skills in the Digital Age. Publications Office of the EU (2019)
10. Bollier, D.: The Future of Work: What It Means for Individuals, Businesses, Markets and Governments (2011)
11. Acemoglu, D., Restrepo, P.: Automation and new tasks: how technology displaces and reinstates labor. J. Econ. Perspect. **30**(2), 3–30 (2019)
12. Delponte, L.: European Artificial Intelligence (AI) Leadership, the Path for an Integrated Vision. Policy Department for Economic, Scientific and Quality of Life Policies, Directorate-General for Internal Policies (2018)
13. Elbestawi, M., Centea, D., Singh, I., Wanyama, T.: SEPT learning factory for industry 4.0 education and applied research. Procedia Manuf. **23**, 249–254 (2018)
14. Cedefop: Europe's Uneven Return to Job Growth, Forecasts up to 2025 Point to Major Differences in Skills Supply and Demand across Member States, p. 4 (2015)
15. Lanz, M., Koskinen, K.T.: Collaborative Systems and environments for future working life: towards the integration of workers, systems and manufacturing environments. In: The Impact of Digitalization in the Workplace, pp. 25–38. Springer (2018)
16. Lin, H.I.: Design of an intelligent robotic precise assembly system for rapid teaching and admittance control. Robot. Comput. Integr. Manuf. **64**, 101946 (2020)
17. Floroiu, D., Patic, P.C., Duta, L.: Trends in educational robotics. In: Aspragathos, N., Koustoumpardis, P., Moulianitis, V. (eds) Advances in Service and Industrial Robotics. RAAD 2018. Mechanisms and Machine Science, vol. 67. Springer, Cham (2019)
18. Merkel, L., Atug, J., Merhar, L., Schultz, C., Braunreuther, S., Reinhart, G.: Teaching smart production: an insight into the learning factory for cyber-physical production systems (LVP). Procedia Manuf. **9**, 269–274 (2017)
19. Lanz, M., Lobov, A., Katajisto, K., Makela P.: A concept and local implementation for industry-academy collaboration and life-long learning. In: Mourtzis, D., Chryssolouris, G. (eds.) Advanced Engineering Education & Training for Manufacturing Innovation, 8th CIRP Sponsored Conference on Learning Factories (CLF 2018). Procedia Manufacturing, vol. 23 (2018)

Unimate and Beyond: Exploring the Genesis of Industrial Robotics

Ovidiu-Aurelian Detesan and Iuliana Fabiola Moholea

Abstract This paper delves into the detailed historical advancement of robotics, tracing the trajectory of technological development that led to automation across various fields. The historical overview extends from ancient times to the mid-1960s, with a specific focus on the core of industrial robotics. Significant achievements that have profoundly influenced the contemporary industrial landscape are highlighted, unraveling the story from the early origins of robotics to the introduction of the first industrial robot, Unimate. Within the industrial context, pivotal innovations from the early stages of industry are unveiled, emphasizing their far-reaching impact on automation. Adopting a panoramic historical research approach and incorporating a multi-perspective view, this paper provides a comprehensive account of the evolutionary history of robotics. Beyond documenting technological advancements, it addresses broader issues, including challenges, implications, and ethical considerations associated with robotics. By lifting the veil on the evolutionary path of innovation and automation, this paper throws light on the first impact of robotics on industry.

Keywords Industrial robotics · History · Evolution

1 Introduction

The evolution of robotics is an incredible story filled with events that have shaped the course of human history and revolutionized it through technological developments and paradigm shifts. Robotic history can be traced from old ages where automatons and mechanical gadgets depicted humanity's first attempts to create automated systems.

O.-A. Detesan (✉) · I. F. Moholea
Technical University of Cluj-Napoca, Memorandumului 28, 400114 Cluj-Napoca, Romania
e-mail: ovidiu.detesan@mep.utcluj.ro

I. F. Moholea
e-mail: iuliana.moholea@mep.utcluj.ro

D. Pisla et al. (eds.), *Advances in Service and Industrial Robotics*, Mechanisms and Machine Science 157, https://doi.org/10.1007/978-3-031-59257-7_27

Present Day Landscape. The robotics of the moment is a wide area that encompasses different applications like autonomous vehicles, drones and humanoids. This has been made possible through increased Artificial Intelligence and Machine Learning as well as sensing technologies, which have advanced robotics into unfamiliar territories and redefined the way industries, health care services, education systems and normal life operate.

The history of robotics can be seen as a continuous process of innovation dating back to ancient automata leading to contemporary complex robots. On exploring the historical scenery of robotics it is clear that every epoch influenced these machines' development in one way or another hence changing their use in various sectors serving mankind.

The following *research question* can be formulated: how has the historical evolution of robotics, spanning from ancient times to the mid-1960s, influenced the development and integration of industrial robotics, with a specific focus on the emergence of the first industrial robot, Unimate?

To the previous question, the following *hypothesis* can be issued: the historical evolution of robotics has played a pivotal role in shaping the landscape of industrial automation. The progression from ancient automata to the mid-1960s, marked by key technological advancements, has laid the foundation for the integration of industrial robotics. Specifically, the introduction of Unimate, as the first industrial robot, represents a transformative milestone, catalyzing advancements in automation technologies and influencing societal perspectives on the role of robotics in industrial settings.

2 Ancient Automatons (Ancient Times to Seventeenth Century)

Ancient automata, spanning from ancient times to the seventeenth century, represent some of the earliest attempts to create self-moving and programmable machines. These early automata laid the foundation for the development of more sophisticated robots in later centuries. While the term *robotics* is a modern concept, the principles and ideas behind these ancient devices laid the framework for the development of automated and programmable machines. The following key examples show their significance in the context of the history of robots.

The Antikythera Mechanism (circa 150–100 BC). Often referred to as the world's first analog computer, the Antikythera Mechanism [1] was used for astronomical calculations. It consisted in advanced gear mechanisms and demonstrated the concept of a mechanical device performing complex calculations.

Hero of Alexandria's Automata. Hero of Alexandria **(circa 10–70 AD)**, a Greek engineer and mathematician, made some notable contributions to the field of automata [2, 3]. His work laid the foundation for the mechanical principles that would later influence the development of robotics. His work demonstrated principles of pneumatics, hydraulics, and mechanical engineering, materializing early programmable motion. Some of his creations include:

- *Theater of Automata*: Hero's most famous work is the "Theater of Automata", a collection of devices that used a system of ropes, pulleys, and simple machines to create moving figures and special effects. These devices were often used for entertainment in theaters and temples.
- *Automaton Puppets*: Hero designed mechanical puppets that could perform simple actions, such as pouring wine or playing a musical instrument. These automata were operated using a system of levers and pneumatics, demonstrating early forms of programmed motion.
- Aeolipile: While not an automaton, Hero's Aeolipile is another notable invention. It was a simple steam engine that displayed the transformative power of steam. Although not widely applied in his time, this invention laid the basis for future developments in steam-powered machinery.

Byzantine Emperor's Throne (Ninth Century). The throne was an automated seat that could move on its own [4]. It was reportedly created for the Byzantine Emperor by a group of engineers. This early example of an automated seat demonstrated the integration of mechanics for comfort and novelty.

Al-Jazari's Automata (Twelfth Century). Ismail Al-Jazari, a Muslim polymath [3], considered by some authors [5] The Father of Robotics, created various automata, including a peacock that could spread its tail and a waitress serving drinks. His work demonstrated the integration of engineering and artistic elements, illustrating the potential for automatons in entertainment.

3 Renaissance and Mechanical Designs (Fifteenth to Seventeenth Century)

During the fifteenth to seventeenth centuries, inventors and polymaths, including Leonardo da Vinci but not limited to him, explored various mechanical designs and concepts that laid the groundwork for advancements in engineering and automation. Some key aspects of their mechanical designs and concepts are presented as follows.

Johannes Müller von Königsberg, known as Regiomontanus (1436–1476). Regiomontanus made improvements to the *astrolabe*, an astronomical instrument used for solving problems related to time and the position of celestial objects [6]. His works explored the application of *automata in astronomy*, demonstrating a connection between mechanical devices and scientific calculations [3]. While not the inventor, his improvements to the astrolabe enhanced its precision and usability in navigation, astronomy, and surveying.

Leonardo da Vinci (1452–1519). Da Vinci's detailed *anatomical studies* influenced his mechanical designs, incorporating an understanding of human anatomy into his machines. He sketched designs for *humanoid automata*, including a knight and a mechanical lion, proving his fascination with mimicking life-like movements [7]. Da Vinci designed a machine that mimicked bird flight, known as the *ornithopter* [8]. While not built in his time, it featured wings that flapped like a bird's. Another of his designs was the *aerial screw*, an early concept resembling a helicopter with a rotating screw for vertical lift [3].

Jerónimo de Ayanz y Beaumont (1553–1613). Ayanz designed various *steam-powered devices*, including a steam engine for water pumping [9]. He worked on mechanical inventions to improve *mining operations*, demonstrating practical applications of his engineering concepts. Ayanz's steam engine design, though not fully realized during his time, laid the foundation for future developments in steam power.

Blaise Pascal (1623–1662). Pascal invented the *Pascaline*, an early mechanical calculator, to assist his father in financial calculations [10]. The Pascaline was a mechanical device with gears and dials that could perform addition and subtraction, representing an early form of automated calculation. He also contributed to the development of the hydraulic press, proving his understanding of fluid mechanics.

Johannes Kepler (1571–1630). Kepler formulated *the laws of planetary motion*, providing a theoretical framework for understanding the motion of celestial bodies [11]. He also designed various astronomical instruments for observing and studying celestial phenomena. As a contribution to the mechanical design, he introduced *Kepler's Pentagram.* While not a mechanical device, his design of a pentagram inscribed in a circle was later used in mechanical linkages, demonstrating mathematical precision in mechanical concepts.

These inventors contributed to the development of mechanical concepts during the fifteenth to seventeenth centuries, ranging from anatomically inspired designs to practical applications in astronomy, mining and calculation. While some of their ideas were not fully realized in their lifetimes, their work laid the foundation for subsequent advancements in engineering and automation.

4 Industrial Revolution and Early Automation (Eighteenth to Nineteenth Century)

The Industrial Revolution, spanning the Eighteenth to the nineteenth century, had a deep impact on early automation and the mechanization of labor. This transformative period marked a shift from agrarian and handcrafted economies to industrial and machine-based production. Notable inventions and technologies during this era laid the groundwork for the development of robotics by introducing mechanized processes and automated systems. Some key aspects of the impact of the Industrial Revolution on early automation are the following:

Textile Industry. The innovations in the textile industry marked a shift from manual labor to machine-based production, laying the foundation for automated manufacturing processes [12]. Some of the notable inventions count:

- *Spinning Jenny* (1764—James Hargreaves): The Spinning Jenny allowed one operator to spin multiple spools of thread simultaneously, significantly increasing textile production.
- *Water Frame* (1769—Richard Arkwright): The Water Frame used water power to mechanize spinning, improving efficiency and scale.
- *Power Loom* (1784—Edmund Cartwright): The Power Loom automated the weaving process, reducing the reliance on manual labor.

Steam Power and Factories. Steam power enabled the establishment of factories, centralizing production and facilitating the mechanization of various industries. Factories became hubs of automation, utilizing steam engines to power machinery and streamline production processes [13]. Among the notable inventions, the following contributions can be outlined:

- *Steam Engine* (1712—Thomas Newcomen, improved by James Watt): The steam engine revolutionized industry by providing a powerful and consistent source of energy.
- *Cotton Gin* (1793—Eli Whitney): While not directly related to steam power, the Cotton Gin automated the separation of cotton fibers from seeds, revolutionizing cotton processing.

Transportation and Communication. Improved transportation and communication networks enabled more efficient supply chains and coordination, contributing to the overall automation of industrial processes [14]. The following inventions are worthy to be mentioned here:

- *Steam Locomotive* (1804—Richard Trevithick, improved by George Stephenson): The steam locomotive transformed transportation, facilitating the movement of goods and people.
- *Telegraph* (1837—Samuel Morse): The telegraph revolutionized communication over long distances.

Machine Tools and Precision Engineering. Machine tools and precision engineering played a crucial role in the standardization of parts, enabling the mass production of interchangeable components [14]. Some of the notable inventions are:

- *Metal Cutting Lathe* (1775—Henry Maudslay): The metal cutting lathe allowed for the production of standardized and interchangeable parts.
- *Babbage's Analytical Engine* (1837—Charles Babbage): Although never completed, Babbage's design laid the theoretical foundation for modern computing and programmable machines.

Assembly Line and Mass Production. The assembly line concept, with its focus on repetitive tasks and standardized processes, set the stage for the development of modern robotics in manufacturing [14]. The most significant invention is:

- *Assembly Line* (1913—Henry Ford): While slightly beyond the nineteenth century, Henry Ford's implementation of the assembly line in automobile manufacturing stands for mass production and increased efficiency.

Impact on Labor. The Industrial Revolution brought about significant changes in the nature of work. While it led to increased productivity, it also raised concerns about working conditions and the displacement of traditional craftspeople.

The inventions and technologies of the Industrial Revolution laid the groundwork for the development of robotics by introducing automation, mechanization, and the concept of standardized, interchangeable parts. These advancements not only transformed industries but also set the stage for the evolution of automated systems and, eventually, the field of robotics in the twentieth century.

5 Early Twentieth Century and the Term "Robot" (1900–1939)

The term *robot* was first introduced by Czech playwright Karel Čapek (1890–1938) in his science fiction play titled "R.U.R." ("Rossum's Universal Robots"), written in 1920 [15]. The word *robot* in the play comes from the Czech word *robota*, which translates to *forced labor* or *drudgery*—in Romanian *robotă*, very similar to the original term. In R.U.R., robots are artificial beings created through biological and mechanical means to serve humans. The play explores themes of industrialization, automation, and the consequences of creating artificial life.

The key aspects of the achievements in the analyzed period are the following:

1. *Electrification of Factories*. The widespread adoption of electricity in factories replaced manual and steam-driven power systems. Electric motors allowed for more precise control in manufacturing processes, enhancing the potential for automation.
2. *Automated Machine Tools*. The development of automated machine tools, such as milling machines and lathes, contributed to the mechanization of various manufacturing processes. Numerical control systems and early forms of automation reduced the reliance on manual labor.
3. *Introduction of Conveyor Belts*. The implementation of conveyor belts in industrial processes facilitated the movement of materials along a continuous path, streamlining production and reducing manual handling.
4. *Introduction of Pneumatic and Hydraulic Systems*. Pneumatic and hydraulic systems were integrated into industrial machinery, providing controlled and efficient power transmission for automation.

The period from 1900 to 1939 witnessed a transformative shift in labor and manufacturing through the automation and mechanization of processes. Innovations in assembly line techniques, electrification, automated machine tools laid the groundwork for the development of robotics. These achievements not only increased efficiency in manufacturing but also set the stage for the evolution of robotics in the subsequent decades.

6 Post-World War II and the Rise of Industrial Robotics (1940s to 1960s)

World War II stimulated significant advancements in technology, driven by the demands of military conflict. Research and development efforts focused on radar, computing, and other technologies with military applications. It also accelerated the development of electronic computers, such as the ENIAC (Electronic Numerical Integrator and Computer). These early computers laid the foundation for computational advancements in the post-war era.

The aerospace industry saw substantial progress during the war, leading to the development of jet engines, guided missiles, and other aerospace technologies. The war promoted international scientific collaboration, bringing together researchers from various fields. This collaborative spirit continued after the war, fostering knowledge exchange and technological progress.

The emergence of industrial robotics is strictly connected to the introduction of automation in manufacturing through automated assembly lines. The concept of automation, inspired by wartime efforts, became increasingly relevant in streamlining production processes.

These circumstances made the appearance of the first industrial robot favorable. George Devol (1912–2011), an inventor, and Joseph Engelberger (1925–2015), an entrepreneur, collaborated to develop the first industrial robot called Unimate. Unimate was introduced in the early 1960s and was designed for use in industrial environments [16]. It was an electromechanical robot with a hydraulic arm, capable of performing a range of tasks, including material handling and spot welding on an assembly line.

Unimate revolutionized manufacturing by introducing automation to tasks that were traditionally performed by human workers [17]. Its applications in the automotive industry, particularly in tasks like welding, showcased the potential for robots to improve efficiency and precision.

Unimate became commercially successful, with the first unit installed at General Motors in 1961. Its success marked the beginning of the widespread adoption of industrial robotics in manufacturing. The development of Unimate by Devol and Engelberger paved the way for the industrial robotics industry. Engelberger, often referred to as the "Father of Robotics", played a crucial role in advocating for the use of robots in industrial settings.

As a conclusion, the post-World War II era witnessed a rapid transition from wartime technological advancements to civilian applications. The emergence of industrial robotics, exemplified by the development of Unimate, transformed manufacturing processes, laying the foundation for the modern era of automation and robotics in various industries.

7 Results and Conclusion

In conclusion, the historical journey of robotics reveals a fascinating evolution, from ancient automata to the pivotal moment with Unimate. This progression not only transformed industries but also influenced societal perspectives on automation. As we reflect on this history, it becomes evident that the roots of modern robotics extend deep into the past [18], shaping our present and pointing towards a future where automation continues to play a crucial role in various aspects of human life [19].

Through a multidisciplinary lens, incorporating perspectives from engineering, history, and sociology, this paper has uncovered key milestones and transformations that have shaped the landscape of industrial automation. It summarizes the key findings and connections made throughout this study, reinforcing the significance of the historical evolution of robotics [20] and its implications for contemporary society.

References

1. Freeth, T., Bitsakis, Y., Moussas, X., Seiradakis, J.H., Tselikas, A., Mangou, H., Zafeiropoulou, M., Hadland, R., et al.: Decoding the ancient Greek astronomical calculator known as the Antikythera mechanism. Nature **444**(7119), 587–591 (2006)
2. McKinnon, J.W.: Hero of Alexandria and Hydraulis. In: Sadie, S., Tyrrell, J. (eds.) The New Grove Dictionary of Music and Musicians (2nd ed.). Macmillan Publishers, London (2001)
3. Gasparetto, A.: Robots in history: legends and prototypes from ancient times to the industrial revolution. In: López-Cajún, C., Ceccarelli, M. (eds.) Explorations in the History of Machines and Mechanisms. History of Mechanism and Machine Science, vol. 32. Springer, Cham (2016)
4. Brett, G.: The automata in the Byzantine "Throne of Solomon." Speculum **29**(3), 477–487 (1954)
5. The Father of Robotics: Al-Jazari. https://www.baytalfann.com/post/the-father-of-robotics-al-jazari. Last accessed 15 Jan 2024
6. Johann Müller Regiomontanus. https://mathshistory.st-andrews.ac.uk/Biographies/Regiomontanus/. Last accessed 15 Jan 2024
7. Stephens, E., Heffernan, T.: We have always been robots: the history of robots and art. In: Herath, D., Kroos, C., Stelarc (eds.) Robots and Art. Cognitive Science and Technology, pp. 29–45. Springer, Singapore (2016)
8. Yates, D.R., Vaessen, C., Roupret, M.: From Leonardo to da Vinci: the history of robot-assisted surgery in urology. BJU Int. **108**(11), 1708–1713 (2011)
9. Howes, A.: Age of Invention: The Spanish Engine. https://www.ageofinvention.xyz/p/age-of-invention-the-spanish-engine. Last accessed 15 Jan 2024
10. Chapman, S.: Blaise Pascal (1623–1662) Tercentenary of the calculating machine. Nature **150**, 508–509 (1942)
11. Coullet, P., San Martin, J., Tirapegui, E.: Kepler in search of the Anaclastic. Chaos, Solitons & Fractals, **164** (2022)
12. Landes, D.S.: The Unbound Prometheus: Technological Change and Industrial Development in Western Europe from 1750 to the Present. Cambridge University Press (1969)
13. Hudson, J.: The history and development of robots. In: Robot Revolution: Understanding the Social and Economic Impact, pp. 19–32. Edward Elgar Publishing, Cheltenham (2019)
14. Lopez-Cajún, C., Ceccarelli, M. (eds.): Explorations in the History of Machines and Mechanisms, History of Mechanism and Machine Science, vol. 32. Springer, Cham (2016)

15. Čapek, K.: R.U.R. (Rossum's Universal Robots). The University of Adelaide Library, Adelaide (2014)
16. Gasparetto, A., Scalera, L.: From the unimate to the delta robot: the early decades of industrial robotics. In: Zhang, B., Ceccarelli, M. (eds.) Explorations in the History and Heritage of Machines and Mechanisms. History of Mechanism and Machine Science, vol. 37, pp. 284–295. Springer, Cham (2019)
17. Bell, G.: Making life: a brief history of human-robot interaction. In: Consumption Markets & Culture, vol. 21, issue 1, pp. 22–41. Taylor & Francis, Oxfordshire (2018)
18. Oh, C.G., Park, J.: From mechanical metamorphosis to empathic interaction: a historical overview of robotic creatures. J. Hum. Robot Interact. **3**(1), 4–19 (2014)
19. Zielinska, T.T.: History of service robots and new trends. In: Zhang, D., Wei, B. (eds.) Novel Design and Applications of Robotics Technologies, pp. 158–187. IGI Global, Hershey (2019)
20. Penaloza, C., Lucho, C., Cuellar, F.: Towards the design of robots inspired in ancient cultures as educational tools. In: Koh, J., Dunstan, B., Silvera-Tawil, D., Velonaki, M. (eds.) Cultural Robotics. CR 2015. Lecture Notes in Computer Science, vol. 9549. Springer, Cham (2016)

Beyond the Horizon: Anticipating Future Challenges in the Field of Robotics

Ovidiu-Aurelian Detesan and Iuliana Fabiola Moholea

Abstract This paper navigates the evolving landscape of robotics, examining current advancements, historical evolution, and anticipated challenges. Delving into technological and ethical dimensions, it provides a general overview. The current state reveals a dynamic robotics spectrum, from collaborative robots to AI-driven systems, transforming industries and daily life. Tracing the historical perspective, pivotal milestones are explored, and ongoing trends, like miniaturization and AI, shaping the future are identified. Anticipated challenges include AI integration complexities, sensing advancements, and ethical considerations in human–robot interaction. Ethical and social challenges encompass job displacement, ethical AI decision-making, and privacy concerns. Future applications show robotics in healthcare, transportation, manufacturing, space exploration, and daily life. The conclusion emphasizes the need for responsible innovation, interdisciplinary collaboration, and adaptive regulations to shape a future where robotics enriches human lives responsibly and sustainably.

Keywords Robotics · Evolution · Future challenges

1 Introduction

In the not-so-distant past, the realm of robotics was largely confined to controlled environments and specialized tasks. However, the persistent march of technological progress has propelled robotics into a new era, where machines are not only tools but integral parts of our daily lives. Standing at the threshold of a new technological frontier, it becomes imperative for individuals to explore the trajectory of robotics, discern its current state, and direct their attention towards the challenges

O.-A. Detesan (✉) · I. F. Moholea
Technical University of Cluj-Napoca, Memorandumului 28, 400114 Cluj-Napoca, Romania
e-mail: ovidiu.detesan@mep.utcluj.ro

I. F. Moholea
e-mail: iuliana.moholea@mep.utcluj.ro

D. Pisla et al. (eds.), *Advances in Service and Industrial Robotics*, Mechanisms and Machine Science 157, https://doi.org/10.1007/978-3-031-59257-7_28

that lie beyond the horizon. The purpose of this paper is to examine the evolving landscape of robotics, analyzing its current state, charting its historical evolution, and, more importantly, anticipating the challenges that will shape its future. Through a meticulous examination of current advancements and trends, the goal is to offer a comprehensive understanding of the factors shaping the trajectory of robotics. This endeavor aims to highlight the potential challenges that researchers, developers, and policymakers may encounter in the forthcoming years.

The scope of this paper encompasses an exploration of technological and ethical challenges that are anticipated to confront the field of robotics. From incorporating artificial intelligence to exploring the ethical implications of human–robot interaction the objective is to present a comprehensive picture. Recognizing the significance of these challenges is crucial not only for professionals in the field but also for policymakers, ethicists, and the general public who will be significantly impacted by the increasing use of robotics in various aspects of life.

2 Current State of Robotics

2.1 Overview of Current Robotics Technologies

Robotics has undergone a transformative evolution in recent years, marked by advancements in both hardware and software. Current robotic technologies span a wide spectrum, from traditional industrial robots to highly sophisticated, AI-driven systems. The convergence of robotics with technologies like computer vision, natural language processing, and advanced sensors has empowered robots to perform complex tasks with increased autonomy.

Traditional Industrial Robots: The traditional industrial robots have been instrumental in automating repetitive, high-precision tasks in manufacturing environments for decades [1]. These robots are typically large, stationary machines equipped with robotic arms and specialized end-effectors for tasks such as welding, assembly, painting, and material handling. Examples include industrial robots from manufacturers like Fanuc, ABB, and Yaskawa have been widely deployed in automotive, electronics, and other manufacturing sectors [2].

Collaborative Robots (Cobots): They are designed to work alongside human operators in shared workspaces, facilitating close collaboration and interaction between humans and robots. These robots are often equipped with advanced sensors [3] and safety features to ensure safe interaction with humans [4–6], enabling tasks such as assembly, pick-and-place operations, and quality inspection. Examples illustrate cobots from companies like Universal Robots, Rethink Robotics (now part of HAHN Group), and KUKA are increasingly being adopted in industries such as automotive, electronics, and consumer goods manufacturing [7].

AI-Driven Robotic Systems: They leverage artificial intelligence (AI) and machine learning (ML) algorithms to perceive, reason, and act autonomously in dynamic and unstructured environments [8]. These systems can learn from data, adapt to changing conditions, and make decisions in real-time without explicit programming, enabling tasks such as autonomous navigation, object recognition, and natural language processing. Examples: AI-driven robots include autonomous vehicles, humanoid robots, and service robots deployed in healthcare, retail, and hospitality sectors.

Specialized Robotics Platforms: Specialized robotics platforms are designed for specific applications and industries, offering tailored solutions to address unique challenges and requirements. These platforms may incorporate specialized hardware, software, and sensing technologies optimized for tasks such as medical surgery [9, 10], underwater exploration, space missions [11], and agricultural automation. Examples include surgical robots like the da Vinci Surgical System, underwater robots like the Remotely Operated Vehicles (ROVs) used in offshore oil and gas exploration, and agricultural robots for tasks such as harvesting and crop monitoring [12].

Emerging Robotics Technologies: They represent the frontier of innovation, exploring new paradigms such as soft robotics [13], bio-inspired robotics, swarm robotics, and nanorobotics. These technologies seek to emulate and integrate principles from nature, biology, and complex systems to develop robots with novel capabilities, adaptability, and resilience.

By highlighting the diverse spectrum of robotics technologies, ranging from traditional industrial robots to cutting-edge AI-driven systems and emerging innovations, it becomes evident that robotics is a rapidly evolving field with vast potential to transform industries, enhance productivity, and improve quality of life.

2.2 Recent Advancements in Robotics

Recent years have witnessed remarkable advancements in robotics, pushing the boundaries of what was once believed possible. The development of agile and dexterous robots capable of navigating unstructured environments has expanded their applications beyond factory floors. Progresses in machine learning have endowed robots with the ability to adapt and learn from their experiences, supporting a new era of intelligent automation. In the medical field, surgical robots offer unprecedented precision, while in logistics, autonomous drones and robots are reshaping supply chains.

2.3 Applications in Various Industries

Robotics has transcended its traditional industrial roots to penetrate diverse sectors. In manufacturing, robots make production processes more dynamic, enhancing efficiency and precision. The healthcare industry benefits from robotic-assisted surgeries [9], rehabilitation aids [14], and telepresence robots facilitating remote medical consultations. Autonomous vehicles, guided by robotic systems, are revolutionizing transportation, and service robots [15] are finding roles in tasks as varied as cleaning, hospitality, and customer service. The broadening spectrum of applications underscores the versatility and adaptability of contemporary robotic technologies.

The current state of robotics reflects a dynamic landscape, characterized by technological innovation and the integration of robots into various facets of our daily lives.

3 The Evolution of Robotics

3.1 Historical Perspective

The historical perspective of robotics traces back to ancient civilizations, where automata and mechanical devices were crafted for entertainment and practical purposes. Innovations continued through the medieval and Renaissance periods, with inventors like Hero of Alexandria [16] and Leonardo da Vinci creating clockwork automata and early mechanical devices. The Industrial Revolution marked a significant turning point, stimulating advancements in automation and laying the groundwork for modern robotics. Key milestones include the invention of the first industrial robot (Unimate) in 1954 by George Devol and Joseph Engelberger, leading to the widespread adoption of robots in manufacturing during the mid-twentieth century [17, 18]. Over time, robotics has evolved through advancements in control systems, sensing technologies, and artificial intelligence, shaping its trajectory towards greater autonomy, adaptability, and integration into various aspects of human life [19].

3.2 Trends Shaping the Future of Robotics

The evolution of robotics is shaped by trends that continue to redefine the capabilities of robotic systems. They include miniaturization and mobility, driven by advancements in materials science and microelectronics. Machine learning algorithms and artificial intelligence [8] enable robots to learn, adapt, and make decisions independently. Soft robotics [13] and bio-inspired design draw inspiration from natural organisms to enhance adaptability and resilience. Ethical and social implications such as job displacement [20, 21] and ethical AI decision-making require responsible innovation and regulation [22, 23]. The integration of robotics into diverse industries promises transformative impacts, from healthcare and transportation to manufacturing and space exploration. Human–robot collaboration and intuitive human–robot interaction are key focus areas for future development [24]. Robotics stands at the edge of transforming numerous sectors, elevating efficiency, productivity, and quality of life, all while approaching societal needs and challenges.

3.3 Emerging Technologies and Innovations

The evolution of robotics is propelled by ongoing research and development in emerging technologies. Emerging technologies and innovations in robotics encompass a wide range of cutting-edge developments. Soft robotics, inspired by natural organisms, utilizes flexible materials and compliant structures for enhanced adaptability [13]. Swarm robotics draws inspiration from collective behaviors observed in social insects, enabling collaboration among multiple robots to achieve complex tasks [25]. Advances in materials science enable the development of novel materials with unique properties for robotics applications. Nanorobotics explores the manipulation of matter at the nanoscale for precise control and manipulation. In the near-future world, nanorobots could be used for targeted drug delivery and medical interventions. Quantum robotics [25, 26] investigates the potential of quantum computing and quantum mechanics to revolutionize robotic systems. Cognitive robotics integrates cognitive science and artificial intelligence to create robots with human-like cognitive abilities [27]. These emerging technologies hold promise for enhancing the capabilities, versatility, and efficiency of robotic systems across various domains, paving the way for innovative applications and solutions to complex challenges.

4 Anticipated Challenges in Robotics

4.1 Technological Challenges

In the ever-evolving landscape of robotics, several technological challenges shape the horizon, demanding innovative solutions to propel the field forward.

Artificial Intelligence and Machine Learning Integration. As robots become more autonomous and adaptive, the integration of artificial intelligence (AI) and machine learning (ML) presents both opportunities and challenges. While AI enhances decision-making capabilities, the interpretability of complex algorithms remains a challenge. Ensuring transparency and ethical use of AI in robotics is critical to build trust and diminish unintended consequences [28].

Sensing and Perception. Robotic systems heavily rely on accurate sensing and perception for effective interaction with their environment. Challenges persist in developing sensors that can mimic the robustness and versatility of human senses [3, 18]. From handling varied lighting conditions to interpreting ambiguous sensory inputs, advancements in sensor technology are crucial to enhance the situational awareness of robots.

Human–Robot Interaction. As robots increasingly coexist with humans in various settings, ensuring smooth and intuitive human–robot interaction (HRI) becomes paramount [29, 30]. Challenges include developing natural language processing capabilities, understanding non-verbal indications, and creating robots that can adapt to diverse social contexts [31]. Ethical considerations in HRI, such as privacy and consent, also add complexity to the design and deployment of socially interactive robots [19].

4.2 Ethical and Social Challenges

The integration of robotics into our daily lives brings forth a myriad of ethical and social challenges, necessitating a careful examination of the potential impact on individuals and society.

Job Displacement and Economic Impact. The widespread adoption of robotic automation raises concerns about job displacement and economic ramifications. As machines take over routine and manual tasks, there is a need to address the potential loss of employment opportunities [20, 21]. Mitigating these challenges involves a proactive approach in retraining and up skilling the workforce to adapt to the evolving job market.

Ethical Considerations in Autonomous Systems. As autonomous systems become more prevalent, ethical considerations become paramount. Ensuring that robots make ethically sound decisions in complex situations is challenging. Ethical frameworks need to be integrated into the design and programming of robots to align their actions with societal values and norms [23].

Privacy and Security Concerns. The increasing presence of robots in private and public spaces raises concerns about privacy and security. Robots equipped with sensors and cameras may inattentively collect sensitive information. Addressing these concerns involves implementing robust privacy protection mechanisms and cybersecurity measures [22] to safeguard against unauthorized access and data breaches.

Navigating these ethical and social challenges requires a collaborative effort involving technologists, ethicists, policymakers, and the broader community to ensure that the integration of robotics aligns with societal values and contributes positively to the well-being of individuals and communities.

5 Future Applications and Opportunities

The future of healthcare is intertwined with robotics, moving forward in a new era of innovation and precision. This section explores the applications of robotics in health-care, from revolutionizing surgical procedures to extending medical care through telepresence and enhancing physical therapy with advanced rehabilitation robots. Table 1 shows the development of robotics applications in healthcare, highlighting diverse categories that promise transformative impacts on medical practices.

In the domain of transportation, the integration of robotics holds the potential to redefine how individuals move and navigate the world. This segment (Table 2) delves into the development of self-driving cars, autonomous delivery systems, and

Table 1 Future of robotics in healthcare

Application category	Examples
Surgical robotics for minimally invasive procedures	• Advancements in robotic-assisted surgery are revolutionizing healthcare, offering increased precision and less invasive procedures. Surgical robots enable surgeons to perform complex operations with enhanced dexterity and control
Telepresence robots for remote patient monitoring	• Telepresence robots provide a virtual presence for healthcare professionals, allowing remote patient consultations, monitoring, and check-ups. They can extend medical care to remote areas
Rehabilitation robots for physical therapy	• Robotics is playing a crucial role in physical therapy and rehabilitation. Exoskeletons and robotic prosthetics assist individuals with mobility deficiency, providing enhanced support for rehabilitation exercises and activities of daily living

intelligent transportation systems for smart cities, highlighting the potential for safer, more efficient, and interconnected modes of transportation.

Manufacturing and industry stand at the edge of a robotic revolution. This section sheds some light on the impact of collaborative robots (cobots), advanced automation in precision manufacturing, and the utilization of robots in hazardous environments. The advancements showcased in Table 3 depict a future where robotics enhances efficiency, quality, and safety in industrial processes.

As humanity extends its reach into the cosmos, the role of robotics in exploration and space missions becomes essential. Table 4 explores the challenges and innovations in planetary exploration, autonomous space probes and rovers, and robotics for

Table 2 Future of robotics in transportation

Application category	Examples
Development of self-driving cars and drones	• The development of autonomous vehicles, including self-driving cars and drones, holds the promise of safer and more efficient transportation. These technologies have the potential to reduce accidents, traffic congestion, and transportation costs
Autonomous delivery systems for logistics	• Companies are exploring the use of robots and drones for last-mile delivery of goods. Autonomous delivery vehicles can navigate urban environments, delivering packages with speed and precision
Intelligent transportation systems for smart cities	• Robotics and AI are integral to the concept of smart cities, where interconnected systems optimize traffic flow, reduce emissions, and enhance overall transportation efficiency

Table 3 Future of robotics in manufacturing and industry

Application category	Examples
Collaborative robots (cobots) working alongside human workers	• Cobots are designed to work alongside human workers in manufacturing settings, enhancing productivity and safety. They can handle repetitive tasks, allowing human workers to focus on more complex and strategic aspects of production
Advanced automation for precision manufacturing	• Robotics is contributing to advanced manufacturing processes, including 3D printing, precision machining, and assembly. This leads to improved product quality, reduced waste, and increased efficiency
Robotics for hazardous or difficult-to-reach environments	• Robots are increasingly employed in environments considered hazardous for humans, such as nuclear plants, underwater exploration, or space missions. These robots can perform tasks in conditions that are challenging or dangerous to human workers

satellite servicing and maintenance, reflecting on the top of scientific discovery and technological advancement.

The landscape of robotic assistants and companions is evolving rapidly, introducing a range of applications designed to enhance various aspects of human life. This section (Table 5) examines social robots for companionship, personal service robots for household tasks, and robotic caregiving for the elderly and individuals with disabilities. These developments underscore the potential of robotics to augment daily life and address diverse societal needs.

Table 4 Future challenge in exploration and space robotics

Application category	Examples
Robotic missions for planetary exploration	• Robotic missions to planets and celestial bodies, such as Mars rovers and lunar exploration missions, contribute to our understanding of the universe. These robots are equipped with advanced sensors and tools to conduct scientific experiments and gather data
Autonomous space probes and rovers	• Autonomous space probes and rovers are designed to operate independently in space, conducting experiments, collecting samples, and transmitting data back to Earth
Robotics for satellite servicing and maintenance	• Robotics plays a crucial role in servicing and maintaining satellites in orbit. Robotic arms and tools are employed to extend the operational life of satellites and perform repairs

Table 5 Future challenge in robotic assistants and companions

Application category	Examples
Social robots for companionship and assistance	• Social robots are designed to interact with humans in social and emotional capacities. They can provide companionship, assistance, and support, particularly for the elderly or individuals with disabilities
Personal service robots for household tasks	• Personal service robots are being developed to assist with household jobs, such as cleaning, cooking, and organizing. These robots aim to enhance the quality of life by reducing the burden of routine tasks
Robotic caregiving for the elderly and people with disabilities	• Robotics is entering the realm of caregiving, where robots can assist healthcare providers and family members in looking after individuals who require support. This includes monitoring vital signs, dispensing medication, and providing company

These future applications and opportunities in robotics show the diverse and transformative impact of robotics across various industries, from healthcare and transportation to manufacturing, space exploration, and everyday life. As technology progresses, these applications have the potential to redefine the way people live, work, and engage with the surrounding world.

6 Results and Conclusions

This paper has traversed the dynamic landscape of robotics, encompassing both its current state and evolutionary journey. From its humble beginnings to its current status as a transformative force, robotics has undergone remarkable advancements that have reshaped industries and daily life. By examining the historical evolution and current advancements, we have gained insights into the diverse spectrum of robotics technologies and their applications across various sectors.

In concluding this exploration into the future of robotics, the analysis positions individuals at the juncture of innovation and responsibility. The challenges and opportunities that unfold foretell a future where the integration of robotics into daily life is an unavoidable reality. In these concluding reflections, there is an invitation to contemplate the profound implications and potential trajectories that will mold the landscape of robotics. In this contemplation, there is a call to embrace the forthcoming era of robotics with a collective sense of responsibility, curiosity, and a profound understanding of the repercussions our decisions may impose on future generations. The canvas upon which the future is painted is expansive, and the combined strokes of innovation and ethical considerations will craft a portrait of a future where the potential of robotics is realized in ways that enhance the human experience.

References

1. Gasparetto, A., Scalera, L.: From the unimate to the delta robot: the early decades of industrial robotics. In: Zhang, B., Ceccarelli, M. (eds.) Explorations in the History and Heritage of Machines and Mechanisms. History of Mechanism and Machine Science, vol. 37, pp. 284–295. Springer, Cham (2019)
2. Karabegović, I., Turmanidze, R., Dašić, P.: Global trend of implementation of industrial robots relating to industry 4.0. In: Ivanov, V., Trojanowska, J., Pavlenko, I., Zajac, J., Peraković, D. (eds.) Advances in Design, Simulation and Manufacturing III. DSMIE 2020. Lecture Notes in Mechanical Engineering, pp. 147–155. Springer, Cham (2020)
3. Albustanji, R.N., Elmanaseer, S., Alkhatib, A.A.A.: Robotics: five senses plus one-an overview. Robotics **12**(3), 68 (2023)
4. Guanghong, Z.: Human-machine cooperation and path planning for complex road conditions. Sci. Program. **2021**, 7262281 (2021)
5. Selvam, A., Aggarwal, T., Mukherjee, M., Verma, Y.K.: Humans and robots: friends of the future? A bird's eye view of biomanufacturing industry 5.0. Biotechnol. Adv. 108237 (2023)
6. Shu, B., Solvang, B.: Architecture for task-dependent human-robot collaboration. In: 2021 IEEE/SICE International Symposium on System Integration (SII), pp. 207–212. Iwaki, Fukushima, Japan (2021)
7. Lee, J., Park, G., Ahn, S.: A performance evaluation of the collaborative robot system. In: 2021 21st International Conference on Control, Automation and Systems (ICCAS), pp. 1643–1648. Jeju, Republic of Korea (2021)
8. Russell, S.J., Norvig, P.: Artificial Intelligence: A Modern Approach. Prentice Hall, Upper Saddle River (2010)
9. Pisla, D., Al Hajjar, N., Gherman, B., Radu, C., Antal, T., Tucan, P., Literat, R., Vaida, C.: Development of a 6-DOF parallel robot for potential single-incision laparoscopic surgery application. Machines **11**(10), 978 (2023)
10. Amarillo, A., Sanchez, E., Caceres, J., et al.: Collaborative human-robot interaction interface: development for a spinal surgery robotic assistant. Int. J. Soc. Robot. **13**, 1473–1484 (2021)
11. Marvi, H.: Opportunities and challenges in space robotics. Adv. Intell. Syst. **5**(3), 2200277 (2023)
12. Lai, Y.L., Chen, P.L., Su, T.C., Hwang, W.Y., Chen, S.F., Yen, P.L.: A collaborative robot for tea harvesting with adjustable autonomy. Cybern. Syst. **53**(1), 4–22 (2022)
13. Polygerinos, P., Correll, N., et al.: Soft robotics: review of fluid-driven intrinsically soft devices; manufacturing, sensing, control, and applications in human–robot interaction: review of fluid-driven intrinsically soft robots. Adv. Eng. Mater. **19**(5) (2017)
14. Nadas, I., Tucan, P., Gherman, B., Banica, A., Rednic, V., Carbone, G., Pisla, D.: On the design and validation of a parallel robot for lower limb rehabilitation. Romanian J. Tech. Sci. **67**(2) (2022).
15. Zielinska, T.T.: History of service robots and new trends. In: Zhang, D., Wei, B. (eds.) Novel Design and Applications of Robotics Technologies, pp. 158–187. IGI Global, Hershey (2019)
16. McKinnon, J.W.: Hero of Alexandria and Hydraulis. In: Sadie, S., Tyrrell, J. (eds.) The New Grove Dictionary of Music and Musicians, 2nd edn. Macmillan Publishers, London (2001)
17. Ding, J.X., Guo, Z., Ren, Z., Deng, P.: State-of-the-art in perception technologies for collaborative robots. IEEE Sens. J. **22**(18), 17635–17645 (2022)
18. Klimaszewski, J., Gruszka, Ł., Możaryn, J.: Test framework for collaborative robot graphene-based electronic skin. In: Biele, C., Kacprzyk, J., Kopeć, W., Owsiński, J.W., Romanowski, A.,

Sikorski, M. (eds.) Digital Interaction and Machine Intelligence. MIDI 2021. Lecture Notes in Networks and Systems, vol. 440. Springer, Cham (2022)

19. Fong, T., Nourbakhsh, I., Dautenhahn, K.: A survey of socially interactive robots. Robot. Auton. Syst. **42**(3–4), 143–166 (2003)
20. Arntz, M., Gregory, T., Zierahn, U.: The risk of automation for jobs in OECD countries: a comparative analysis. In: OECD Social, Employment and Migration Working Papers, No. 189. OECD Publishing, Paris (2016)
21. Zhao, Y., Said, R., Ismail, N.W., Hamzah, H.Z.: Effect of industrial robots on employment in China: an industry level analysis. Comput. Intell. Neurosci. **2022**, 13 (2022). Article ID 2267237
22. Rostama, G., Bekhradi, A., Yannou, B.: From privacy by design to design for privacy. In: International Conference on Engineering Design (ICED), Vancouver (2017)
23. Lin, P., et al.: Robot ethics: mapping the issues for a mechanized world. Artif. Intell. **175**(5–6), 942–949 (2011)
24. Gusan, V., Tîtu, M.A., Oprean, C.: Industrial robots versus collaborative robots—the place and role in nonconventional technologies. Acta Tech. Napocensis Ser. Appl. Math. Mech. Eng. **65**(1), 101–110 (2022)
25. Mannone, M., Seidita, V., Chella, A.: Modeling and designing a robotic swarm: a quantum computing approach. Swarm Evol. Comput. **79**, 101297 (2023)
26. Petschnigg, C., Brandstötter, M., Pichler, H., Hofbaur, M., Dieber, B.: Quantum computation in robotic science and applications. In: 2019 International Conference on Robotics and Automation (ICRA), pp. 803–810. Montreal, QC, Canada (2019)
27. Cruz, F., Solis, M.A., Navarro-Guerrero, N.: Editorial: Cognitive inspired aspects of robot learning. Front. Neurorobot.urorobot. **17**, 1256788 (2023)
28. Bengio, Y., et al.: The Malicious Use of Artificial Intelligence: Forecasting, Prevention, and Mitigation. https://arxiv.org/pdf/1802.07228.pdf (2018). Last accessed 15 Jan 2024
29. Franklin, C.S., Dominguez, E.G., Fryman, J.D., Lewandowski, M.L.: Collaborative robotics: new era of human–robot cooperation in the workplace. J. Saf. Res. **74**, 153–160 (2020)
30. Liu, S., Wang, L., Wang, V.X.: Multimodal data-driven robot control for human–robot collaborative assembly. ASME J. Manuf. Sci. Eng. **144**(5), 051012 (2022).
31. Mazumder, A., Sahed, M.F., Tasneem, Z., Das, P., Badal, F.R., Ali, M.F., Islam, M.R.: Towards next generation digital twin in robotics: trends, scopes, challenges, and future. Heliyon (2023)

A Short Overview on Terrestrial Hybrid Locomotion Mobile Robots

Cosmin Straticiuc, Ioan Doroftei, and Cristina-Magda Cazacu

Abstract Hybrid locomotion mobile robots represent a state-of-the-art combination of different forms of locomotion that seamlessly combine multiple locomotion methods to improve adaptability and efficiency in different environments. Unlike traditional mobile robots, which are limited to a single movement, terrestrial hybrid locomotion mobile robots are using a combination of wheels, legs or tracks to navigate different terrains and overcome obstacles. These robots will be able to traverse complex landscapes, a challenge for traditional wheeled or legged robots. Hybrid locomotion mobile robots can be used in various applications, such as search and rescue missions, exploration of hostile and different environments, and military operation. In this paper a short overview of on terrestrial hybrid locomotion mobile robots is presented.

Keywords Terrestrial · Hybrid locomotion · Mobile robot

1 Introduction

Robot mobility is one of the most studied topics in locomotion robotics research and deals with the design, mapping, navigation, localization, motion planning and control of robots. A mobile robot with hybrid locomotion will be defined by its capacity to move from one location to another with the ability to use one or more modes of locomotion. These hybrid locomotion structures include mechanical, electrical, electromagnetic, pneumatic and hydraulic architectures that allow the robot to move in various environments.

The global market for service robots has grown significantly in recent years and has surpassed the industrial robotics market. In particular, ground mobile robots

C. Straticiuc · I. Doroftei (✉) · C.-M. Cazacu
"Gheorghe Asachi" Technical University of Iasi, 43 D. Mangeron Blvd, 700050 Iasi, Romania
e-mail: idorofte@mail.tuiasi.ro

I. Doroftei
Technical Sciences Academy of Romania, 26 Dacia Blvd, 030167 Bucharest, Romania

D. Pisla et al. (eds.), *Advances in Service and Industrial Robotics*, Mechanisms and Machine Science 157, https://doi.org/10.1007/978-3-031-59257-7_29

with hybrid locomotion system can become the most widespread category of service robots, with application fields such as agriculture, planetary exploration, homeland security, military, surveillance and intervention in case of terroristic attacks or in the presence of radioactive or chemical contamination areas.

There are a number of factors that can affect the success of the design, implementation or functionality of a mobile robotic platform. Many numerous studies emphasized the difficulty of creating a mobile robot that can work effectively in multiple scenarios and for different purposes. In general, mobile robots are designed to perform certain tasks in specific environmental conditions. One of the factors that influence the design of a mobile robot is the size, where bigger robots have the advantage of larger storage space and the drawback of a heavier weight, hence more energy required to perform the tasks. However, the bigger the system is, the easier it will become for the mobile robot to overcome obstacles. Smaller mobile robots will have a light weight, but also less sensors and less tasks that they could achieve.

Another factor when designing a mobile robot, and may be the most important one, is choosing the appropriate locomotion mechanism. In general, locomotion mechanisms for mobile robots can be divided into three categories: aerial, aquatic and terrestrial locomotion. Furthermore by combining two or more modes of locomotion a hybrid locomotion system is obtained.

Terrestrial locomotion can be further divided into wheeled mechanisms, tracked and legged mechanisms. Several criteria can be considered when comparing the advantages of different locomotion modes for terrestrial locomotion robots [1]. When considering energy efficiency as a primary criterion for locomotion mechanisms, wheels typically emerge as the most efficient option. The wheels provide low friction, which allows robots to move quickly and cover long distances with minimal energy consumption. Legs, on the other hand, are generally less energy efficient due to their complex articulation and the need to lift and reposition the robot's weight with each step. Tracks fall somewhere in between, providing effective traction on rough terrain, but use more energy than wheels on flat surfaces due to greater friction. When comparing locomotion mechanisms based on stability and load handling capability, each type offers unique advantages suited to different terrains and tasks. Wheels offer excellent stability and performance under moderate to heavy loads on flat and level surfaces due to their even weight distribution and constant contact. Legs, on the other hand, have excellent stability on different terrains. Their articulated design and ability to adjust the center of gravity make them suitable for transporting heavy loads over obstacles and difficult terrain. In addition, the legs provide stability and balance, enabling precise control and handling of loads. Tracks provide stability by distributing weight over a larger area, so they are well-suited for navigating on rough terrain, gravel or mud. Ultimately, the choice of locomotion mechanism depends on the specific load requirements of the task and the environmental conditions in which the robot operates.

To combine the advantages of these categories of locomotion multiple terrestrial hybrid locomotion mobile robots have been designed. In the following paragraphs some of these mechanisms are discussed.

2 Terrestrial Hybrid Locomotion Mobile Robots

The classification of terrestrial hybrid mobile robots expresses how these devices combine mobility strategies [2]. These robots are classified into different types based on their primary mode of locomotion and the coordination between them, as presented in Fig. 1. The classification of hybrid locomotion mobile robots reflects innovative advances in robotics and shows creativity in combining different locomotion methods to meet a wide range of challenges. As technology advances, these classifications are likely to evolve, pushing the limits of adaptability, efficiency, and problem-solving capabilities of hybrid locomotion mobile robots.

2.1 Wheel-Legged Mobile Robots

Wheeled-legged mobile robots represent a harmonious combination of two different modes of locomotion, wheels and legs, providing a versatile solution for navigating various terrains. This hybrid locomotion design offers the advantages of both systems, combining the speed and efficiency of the wheels on flat surfaces and the adaptability and stability of the legs on rough or uneven terrain.

The first wheeled-legged mobile robot presented in Fig. 2a is named ASGUARD and it was designed to work in harsh environments, with missions regarding search and rescue, patrolling, surveillance and so on. The robot is driven by four legs, directly actuated, each possessing a single rotational degree of freedom. The compliant legs of the robot are arranged around a central shaft allowing the robot to adjust the locomotion according to the environment. This type of mobile robot is programmed using an adaptive control based on Central Pattern Generator and it showed great results when tested climbing different types of stairs [3, 4].

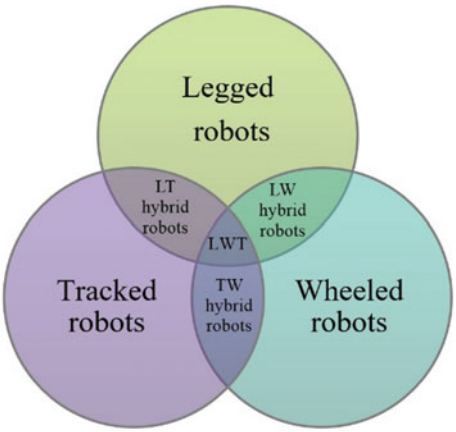

Fig. 1 Classification of terrestrial hybrid locomotion mobile robots [2]

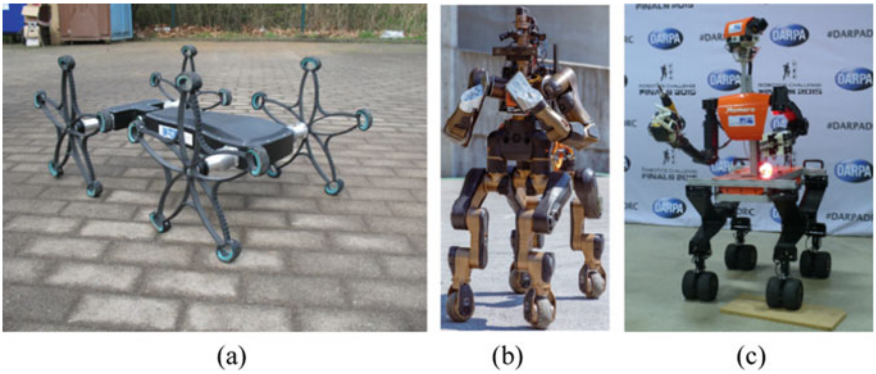

Fig. 2 Wheeled-legged robots: **a** ASGUARD [3, 4]; **b** CENTAURO [5]; **c** Momaro [6]

CENTAURO (Fig. 2b) is a mobile robot with humanoid architecture for the upper body configurations, designed to perform manipulation tasks. Each arm of the robot has seven degrees of freedom, allowing the robot to perform required movements with large dexterity. The legs are aimed at enabling both omni-directional wheeled motion and articulated legged locomotion. These legs have five degrees of freedom, which enables precise positioning and direction of the wheeled leg. The robot has the strength, durability and mechanical robustness needed to perform practical tasks in real-world scenarios, especially for large payloads and demanding physical interactions. This includes potential disaster situations and challenging collaborative tasks in an industrial environment [5].

Another mobile robot with humanoid architecture is Momaro, presented in Fig. 2c. In order to execute a diverse array of manipulation tasks, this robot is equipped with an anthropomorphic upper body with two 7 degrees of freedom manipulators, each ending with dexterous grippers [6]. The robot also incorporates an innovative locomotion design characterized by four legs, each ending in a steerable pair of wheels. With this configuration, the robot can achieve omnidirectional movements on fairly flat terrain, navigate over obstacles by stepping on them, and overcome variations in height by climbing.

Mobile robots with terrestrial hybrid locomotion can be used also for planetary exploration. The planetary rover Sherpa (Fig. 3a) has four wheeled-legs, each one of them offering six degrees of freedom [7]. The active suspension design allows different driving modes for the rover. The addition of self-locking gears to the suspension system allows body height to be maintained without active actuators. This function facilitates energy-efficient movement on wheels and at the same time ensures great flexibility in adapting to the ground and handling obstacles, as well as a considerable load capacity. Additionally, the rover will be equipped with a specially designed manipulator arm intended for locomotion support.

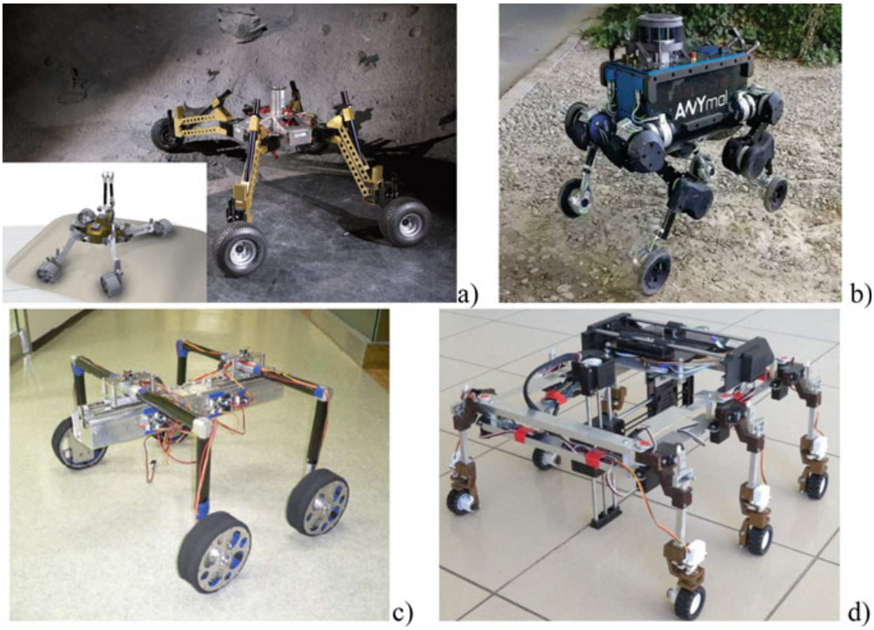

Fig. 3 Wheeled-legged robots: **a** Sherpa [7]; **b** ANYmal [8]; **c** Leg-wheel locomotion mobile robot [9]; **d** Hybrid locomotion mobile robot for agricultural application [10–13]

ANYmal (Fig. 3b) is a quadrupedal mobile robot equipped with non-steerable wheels integrated into its legs. This version of the robot demonstrates hybrid locomotion, executing a diverse range of gait sequences specifically tailored for challenging and uneven terrain completely torque-controlled system featuring four legs, each fitted with non-steerable wheels [8]. Its main goal is to assist humans through navigation and searches on rough terrain.

Many hybrid locomotion vehicles alternate between wheel-mode and leg-mode for their operation. The leg-wheel locomotion robot presented in Fig. 3c aims to overcome higher obstacles with a flow where wheel and leg movement is continuously executed [9]. In this case the management of load distribution is achieved through the torque applied to the twisting joint at the center of the body, together with a forward/backward shift of the body. At the experimentation phase the robot overrun big obstacles with a good continuous movement.

A hybrid locomotion mobile robot for agricultural application is presented in Fig. 3d. The locomotion system utilizes a Scotch Yoke mechanism as the leg, with a driving/steering wheel positioned at the end of this leg. The incorporation of hybrid locomotion enables this mobile manipulator to achieve higher speeds on flat terrain and swiftly change direction when functioning as a mobile platform (equipped with either 4 or 6 wheels). It can also navigate obstacles and adapt to uneven terrain when operating as a robot with legs. Additionally, the legs serve the dual purpose of functioning as an active suspension system [10–13].

As technology advances, the design and capabilities of wheeled-legged mobile robots continue to evolve, showing a promising direction in robotics where adaptability and efficiency are combined to resolve world's challenges.

2.2 Independent Leg and Wheel Mechanisms

Independent leg and wheel mechanisms allow the mobile robot to achieve remarkable mobility. On smooth surfaces, the wheels facilitate fast and energy-efficient movement like traditional wheeled robots. When the robot encounters uneven terrain or obstacles, it smoothly transitions to legged locomotion, taking advantage of the stability and flexibility of the leg-based movement.

The RT-Mover robot presented in Fig. 4a offers a simple mechanism and sufficient mobility to maintain a stable posture in various target environments. The robot can function in indoor settings with steps and uneven ground surfaces, in natural terrains and in artificial outdoor environments that present uneven ground. It has four drivable wheels and two leg-like axles, that achieve the minimum necessary leg function. The stability of the robot is increased and the final goal is that the robot will become a personal mobility vehicle for patients [14].

The Wheeleg robot (Fig. 4b) is a hybrid wheeled-legged robot that uses independent mechanisms in order to navigate challenging terrains. The two wheels and two legs of this robot are collaborating in order to facilitate locomotion. The front legs are pneumatically actuated while the two rear wheels are driven independently by separate DC motors [15]. In order to sustain the weight of the robot the locomotion will be effectuated via wheels, while the front legs are deployed only to enhance traction. This configuration allows the robot to skillfully climb and overcome obstacles. As a result, the grip of the robot on uneven terrain has improved compared to the four-wheeled solution. At the same time, it is faster, more stable and easier to control than the four-legged alternative.

In Fig. 4c is presented the HyTRO-I robot that possesses a four-wheel suspension system for fast movement on flat terrain, and a four-legged walking system for irregular terrain [16]. This robot is composed from three parts: the suspension torso, the wheeled vehicle and the four modular leg mechanism. The wheeled vehicle (that is connected to the torso) has two passive omni-directional wheels and two active driving wheels. The independently actuated wheels are positioned on the right and left sides, with two non-driven wheels located on the front and back. The legs, each with 3 degrees of freedom, are also connected to the torso. This configuration allows an increased versatility of the robot.

The terrestrial hybrid locomotion mobile robot presented in Fig. 4d is composed of a chassis with two legs and two wheels. The legs have two degrees of freedom each and passive wheels at the end, functioning as feet. The wheels are positioned at the read and they can be either actuated or passive, this is facilitated by electromagnetic clutches that connect these wheels at the shafts of their motors. What distinguishes this robot by similar ones is the operation mode, it can operate in three distinct

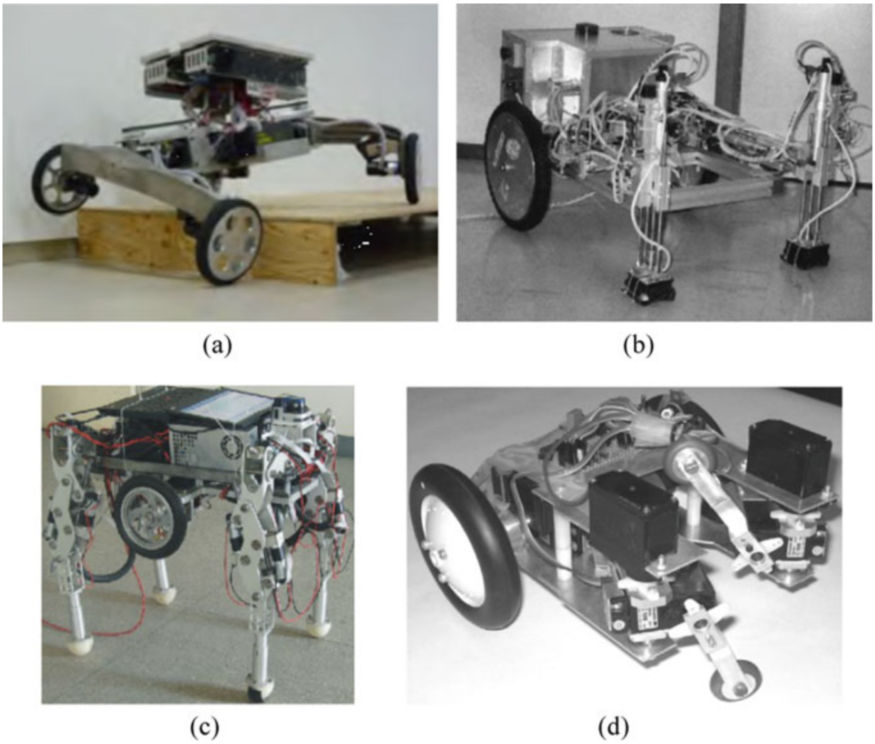

Fig. 4 Independent leg and wheel mechanisms: **a** RT-Mover [14]; **b** Wheeleg [15]; **c** HyTRo-I [16]; **d** Hybrid locomotion mobile robot [17]

locomotion modes: wheel mode (where the feet are passive and the two large wheels at the rear are actuated); first hybrid mode where the legs are active and the rear wheels are passive; second hybrid locomotion mode when both the legs and rear wheels are active [17].

The versatility of the independent leg and wheel mechanisms highlights the potential of these robots to transform the way complex tasks are performed in various environments, demonstrating the power of integrated, adaptive robotic systems.

2.3 Mobile Robots with Reconfigurable or Transformable Wheel

Reconfigurable or transformable wheeled mobile robots represent a significant innovation in robotics, demonstrating adaptability and versatility. These robots have a structure that allows their wheels to transform into alternate configurations, allowing them to navigate different terrains and overcome diverse challenges.

(a) (b) (c)

Fig. 5 Reconfigurable wheel: **a** Quattroped [18]; **b** Wheel transformer [19]; **c** Mobile robot with transformable wheel [20]

The design principle of the leg-wheel hybrid locomotion platform presented in Fig. 5a revolves around incorporating a "transformation mechanism" that can deform a specific section of the body to function either as a wheel or a leg. The transition from a full-circle rim (wheel mode) to two half-circle rims (leg mode) is controlled by a micro-RC servo motor located inside the spoke [18]. One semicircular rim is installed directly in the spoke, while the other is connected to the rotating horn atop the servo. Rotating the RC servo 180° causes the half-circle rim to either swing next to the other half-circle rim (leg mode) or move away from it (wheel mode). This allows changing the morphology of the platform from four wheels into four legs with 2 degrees of freedom.

The robot presented in Fig. 5b combines the advantages of circular and legged wheels. It maintains stability and energy efficiency while traveling on a flat surface when it uses the circular configuration. When the wheel encounters an obstacle, it smoothly transforms into a three-legged wheel. This transition from a circular leg structure is realized using only the frictional force between the wheel and the obstacle, so that no additional actuators are required. This legged wheel allows the robot to climb obstacles greater than the wheel radius [19].

Another transformable wheeled mobile robot, presented in Fig. 5c, is great for overcoming obstacles and navigating dynamic surfaces, while keeping a fast movement on flat terrain. The wheel of the robot consists of five spokes or legs, with four actively driven by a motor with the help of a slider-crank mechanism [20]. The fifth spoke is designed to be passive significantly reducing the actuation force needed for the transformation mechanism. Transformation is facilitated by two motors located at the front and back of the main body while two motors inside the robot's body move it forward. This innovative wheel allows a quick transition, depending of the terrain.

The most important feature of these mobile robots is their ability to dynamically change the wheel settings according to different scenarios. For example, they can switch from a conventional constant-speed wheel configuration to a leg-shaped configuration to improve stability and maneuverability on rough or uneven terrain.

This reconfiguration allows robots to handle a wide variety of environments and tasks, making them especially valuable in situations where adaptability is critical.

2.4 Mobile Robots with Wheels-Legs-Tracks

Mobile robots using wheels-legs-tracks as locomotion system represent a versatile category of robotic systems designed to seamlessly integrate three distinct modes of locomotion. This hybrid approach allows these robots to navigate various environments, combining the speed and efficiency of wheels on flat surfaces with the stability and adaptability of legs and tracks on rough terrain.

The mobile manipulator with hybrid locomotion from Fig. 6a presents a new design where the mobile platform and the manipulator arm are integrated into a single entity [21]. This means that the mobile platform can function as a manipulator arm, and conversely, the manipulator arm can serve as the mobile platform. The robot has an improved mobility because it's able to flip over when encountering an obstacle and then continue operating. The arm of the robot is used for manipulation but also for flipping the robot or aiding it when encountering an obstacle.

The mechanical structure of the WheTLHLoc robot (Fig. 6b) is designed to combine the advantages of tracked locomotion on soft terrain with the advantages of wheel locomotion on flat and compact surfaces. The transition between these two modes is achieved through two actuated wheels that are place at the end of rotating arms [22]. This allows the robot to move efficiently on stairs and by coordinating the movement of legs, wheels and tracks in a suitable combination.

In Fig. 6c is presented the hybrid locomotion robot AZIMUT that is composed of four autonomous articulations. Each segment integrates a leg, a track and a wheel, providing three degrees of freedom [23]. The leg can offer a 360-degree rotation around its attachment point. The system is designed to maintain its position once that required position is achieved, without consuming energy. To change the direction of movement the robot can use differential steering or it can adjust the orientation of its articulations. The platform can navigate into tight spaces with easy, behaving like an omnidirectional platform.

Chaos (Fig. 6d) is a compact unmanned ground vehicle that can ensure exceptional mobility. The modular running gear (four dual-drive receptacles) allows a quick attach of different modules like tracks, wheels, legs and so one, allowing a quick change in the method of locomotion [24]. Employing walking articulated tracks, the vehicle enables precise control over track beam speed and position. Each track operates independently, giving flexibility in coordinating track beam movements to achieve various vehicle gaits. With this configuration, it is possible to combine the benefits of tracks, wheels and legs into a single running equipment.

The versatility of mobile robots with wheels-legs-tracks rob makes them promising candidates for various applications, such as search and rescue missions, searching in remote or dangerous places, and tasks that require dynamic adaptation to different environments.

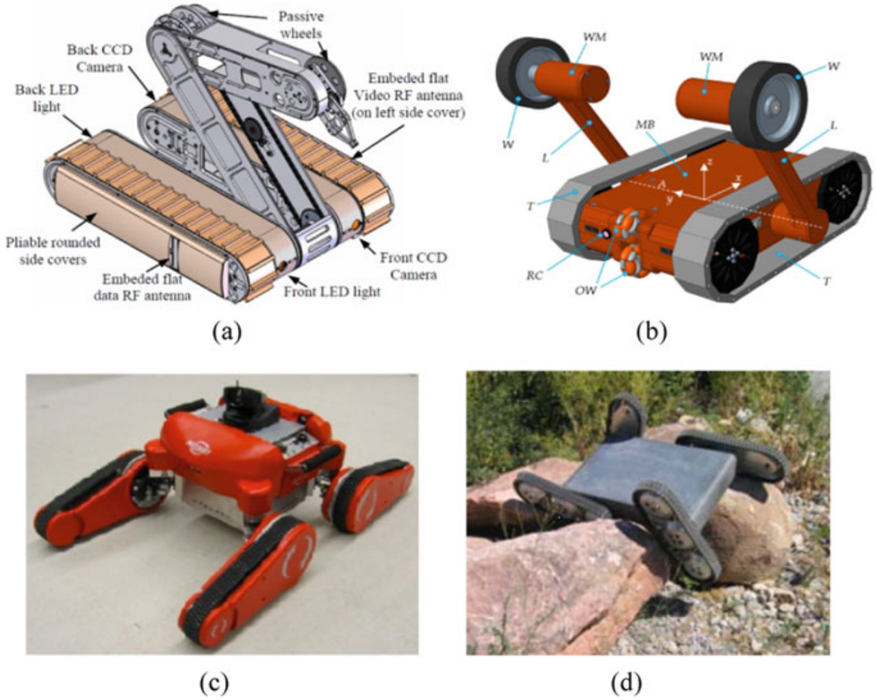

Fig. 6 Wheels-legs-tracks robots: **a** Mobile manipulator with hybrid locomotion [21]; **b** WheTLHLoc [22]; **c** AZIMUT [23]; **d** Chaos [24]

3 Conclusions

The field of robot mobility, particularly in the context of hybrid locomotion, has witnessed significant advancements and innovation. The increasing demand for service robots, exceeding industrial robotics, points out the growing importance of versatile mobile robots with hybrid locomotion. These mobile robots find applications in diverse fields such as agriculture, planetary exploration, homeland security, military, surveillance, and intervention in hazardous scenarios.

This article classifies terrestrial hybrid locomotion robots, based on combinations of different locomotion methods that address a wide range of challenges. By investigating various combinations of locomotion mechanisms such as wheels, legs, and tracks, this study highlights the potential to enhance robot mobility across different terrains and scenarios, laying the foundation for future research in this domain. Through the presented classification and case studies of terrestrial hybrid locomotion robots, the article underscores the versatility and adaptability of these robotic systems in real-world applications, ranging from agriculture to planetary exploration and disaster response. The observations provided advance the understanding of how different locomotion mechanisms can be combined to improve robot mobility.

Overall, the insights gained from this study have the potential to drive advancements in hybrid locomotion robotics and to contribute to the design and creation of more versatile and adaptable robots for diverse applications, thus highlighting the promising trajectory of robotics in addressing real-world challenges.

References

1. Lim, S.H., Teo, J.: Recent advances on locomotion mechanisms of hybrid mobile robots. WSEAS Trans. Syst. **14**, 11–25 (2015)
2. Zhu, Y., Fei, Y., Xu, H.: Stability analysis of a wheel-track-leg hybrid mobile robot. J. Intell. Rob. Syst. **91**, 515–528 (2018)
3. Eich, M., Grimminger, F., Kirchner, F.: Adaptive stair-climbing behaviour with a hybrid legged-wheeled robot. Adv. Mob. Robot. 768–775 (2008)
4. Eich, M., Grimminger, F., Kirchner, F.: Proprioceptive control of a hybrid legged-wheeled robot. In: 2008 IEEE International Conference on Robotics and Biomimetics, pp. 774–779 (2009)
5. Kashiri, N., Baccelliere, L., Muratore, L., Laurenzi, A., Ren, Z., Hoffman, E.M., Kamedula, M., Rigano, G.F., Malzahn, J., Cordasco, S., Guria, P.: Centauro: a hybrid locomotion and high power resilient manipulation platform. IEEE Robot. Autom. Lett. **4**(2), 1595–1602 (2019)
6. Schwarz, M., Rodehutskors, T., Schreiber, M., Behnke, S.: Hybrid driving-stepping locomotion with the wheeled-legged robot Momaro. In: 2016 IEEE International Conference on Robotics and Automation (ICRA), pp. 5589–5595. IEEE (2016)
7. Cordes, F., Dettmann, A., Kirchner, F.: Locomotion modes for a hybrid wheeled-leg planetary rover. In 2011 IEEE International Conference on Robotics and Biomimetics, pp. 2586–2592 (2011)
8. Bjelonic, M., Sankar, P.K., Bellicoso, C.D., Vallery, H., Hutter, M.: Rolling in the deep–hybrid locomotion for wheeled-legged robots using online trajectory optimization. IEEE Robot. Autom. Lett. **5**(2), 3626–3633 (2020)
9. Takahashi, M., Yoneda, K., Hirose, S.: Rough terrain locomotion of a leg-wheel hybrid quadruped robot. In: Proceedings 2006 IEEE International Conference on Robotics and Automation ICRA 2006, pp. 1090–1095. IEEE (2006)
10. Doroftei, I., Morar, C.A., Alaci, S., Hagan, M.G.: Kinematic design of a hybrid locomotion mobile manipulator for agricultural applications. Acta Tech. Napocensis—Ser.: Appl. Math. Mech. Eng. **65**(2S) (2022)
11. Conduraru (Slatineanu), A., Doroftei, I., Conduraru, I., Luca, D.: Hexapod locomotion of a leg-wheel hybrid mobile robot. Appl. Mech. Mater. **658**, 581–586 (2014)
12. Conduraru (Slatineanu), A., Doroftei, I., Conduraru, I.: Design and kinematic aspects of a hybrid locomotion robot. Adv. Mater. Res. **1036**, 764–769 (2014)
13. Doroftei, I., Morar, C.A., Hangan, M.G: Design and kinematic modeling of a mobile manipulator with hybrid locomotion for agricultural applications. J. Eng. Sci. Innov. **8**(4), 347–362 (2023)
14. Nakajima, S.: Mobile platform with leg-wheel mechanism for practical use. Mobile Robots—Current Trends (2011)
15. Lacagnina, M., Muscato, G., Sinatra, R.: Kinematics, dynamics and control of a hybrid robot wheeleg. Robot. Auton. Syst. **45**(3–4), 161–180 (2003)
16. Lu, D., Dong, E., Liu, C., Xu, M., Yang, J.: Design and development of a leg-wheel hybrid robot "HyTRo-I". In: 2013 IEEE/RSJ International Conference on Intelligent Robots and Systems, pp. 6031–6036. IEEE (2013)
17. Doroftei, I., Ion, I.: Design and locomotion modes of a small wheel-legged robot. Nature-Inspired Mob. Robot. 609–616 (2013)

18. Shen, S.Y., Li, C.H., Cheng, C.C., Lu, J.C., Wang, S.F., Lin, P.C.: Design of a leg-wheel hybrid mobile platform. In: 2009 IEEE/RSJ International Conference on Intelligent Robots and Systems, pp. 4682–4687. IEEE (2009)
19. Kim, Y.S., Jung, G.P., Kim, H., Cho, K.J., Chu, C.N.: Wheel transformer: a wheel-leg hybrid robot with passive transformable wheels. IEEE Trans. Rob. **30**(6), 1487–1498 (2014)
20. She, Y., Hurd, C.J., Su, H.J.: A transformable wheel robot with a passive leg. In: 2015 IEEE/RSJ International Conference on Intelligent Robots and Systems (IROS), pp. 4165–4170 (2015)
21. Ben-Tzvi, P., Goldenberg, A.A., Zu, J.W.: Design, simulations and optimization of a tracked mobile robot manipulator with hybrid locomotion and manipulation capabilities. In 2008 IEEE International Conference on Robotics and Automation, pp. 2307–2312. IEEE (2008)
22. Bruzzone, L., Baggetta, M., Nodehi, S.E., Bilancia, P., Fanghella, P.: Functional design of a hybrid leg-wheel-track ground mobile robot. Machines **9**(1), 10 (2021)
23. Lauria, M., Nadeau, I., Lepage, P., Morin, Y., Giguère, P., Gagnon, F., Létourneau, D., Michaud, F.: Design and control of a four steered wheeled mobile robot. In: IECON 2006–32nd Annual Conference on IEEE Industrial Electronics, pp. 4020–4025. IEEE (2006)
24. Lewis, P.J., Flann, N., Torrie, M.R., Poulson, E.A., Petroff, T., Witus, G.: Chaos, an intelligent ultra-mobile SUGV: combining the mobility of wheels, tracks, and legs. In: Unmanned Ground Vehicle Technology VII, vol. 5804, pp. 427–438. SPIE (2005)

Augmented Reality Guided 3D Printed Robotic Arm Assembly: A Comprehensive Framework for Interactive Learning

Radu Comes, Zsolt Levente Buna, Raul Silviu Rozsos, and Grigore Marian Pop

Abstract Augmented reality (AR) has emerged as a powerful tool for enhancing learning experiences, particularly in STEM fields like mechanical engineering. The study involves the development of an AR-enriched learning material that complemented a traditional project guide for designing a 5-degree-of-freedom robotic arm. The AR framework application employs Vuforia, a powerful tracking system, to seamlessly overlay virtual 3D models onto physical 3D printed parts. This enables students to visualize and interact with their designs in a realistic and engaging manner, enhancing their understanding of the design process and the physical properties of their creations. The integration of AR real-time tracking into the assembly of 3D-printed robotic arms has demonstrated its potential to enhance the learning experience for students in mechanical engineering. The ability to visualize and interact with 3D models in real-time can significantly improve their understanding of the design and assembly process, leading to improved learning outcomes.

Keywords Augmented reality · Interactive learning · 3D printing · Computer-aided design · STEM education

1 Introduction

In the past when students didn't have access to portable mobile devices (laptops, tablets, or smartphones) lectures were the primary method of teaching in engineering universities. As modern portable devices have become widely available and affordable, they are disrupting traditional learning paradigms, paving the way for personalized and interactive learning experiences [1].

R. Comes (✉) · Z. L. Buna · R. S. Rozsos · G. M. Pop
Department of Design Engineering and Robotics, Technical University of Cluj-Napoca, 400641 Cluj-Napoca, Romania
e-mail: comesradu@gmail.com

D. Pisla et al. (eds.), *Advances in Service and Industrial Robotics*, Mechanisms and Machine Science 157, https://doi.org/10.1007/978-3-031-59257-7_30

For practical applications, the students would use the equipment available within the laboratory classes, however the state-of-the art equipment wasn't widely available for all students to experience hands-on learning. University lectures often lacked the interactivity and engagement that are necessary for effective learning. Students were often passive participants in lectures, and they often struggled to retain the information that they were presented with. Traditional methods of teaching, such as lectures and PowerPoint presentations, have become less common in engineering universities in recent years [2]. This is due to several factors, including the increasing use of technology in education, the need for more active learning, and the desire to provide students with a more personalized learning experience [3].

Traditional learning methodologies should be re-evaluated to equip future engineers with the diverse skills and competencies required to thrive in the ever-evolving landscape of modern society. Augmented reality (AR), a technology that seamlessly overlays computer-generated elements like graphics, images, videos, and 3D objects onto the user's real-world environment, provides a compelling solution to enhance motivation and engagement in the educational process [4].

Augmented reality (AR) has the potential to revolutionize engineering education by providing students with immersive and interactive learning experiences. This can significantly enhance their understanding of complex engineering concepts and processes. AR and VR applications can bring abstract concepts to life, allowing students to interact with 3D models, simulations, and virtual worlds in a hands-on manner. This immersive learning experience can significantly enhance comprehension and retention of complex topics [5].

The paper aims to evaluate the effectiveness of an AR-enriched learning material in enhancing student understanding and engagement in mechanical engineering design projects, particularly in the context of a 5-axis robotic arm design project.

After the introduction, Sect. 2 presents Related Works regarding the use of AR technology paired with other technologies used within STEM education. Section 3 presents Materials and Methods and the proposed framework providing details regarding each component. Section 4 presents the results of the proposed case study AR application used for assembly instruction. Section 5 discusses the Conclusions and the Future Works.

2 Related Works

3D printing technologies have bridged the gap between ideas and creations in STEM and robotics education, empowering students with custom parts, rapid prototyping, and cost-effective solutions, a recently published survey [6] has highlighted the current challenges, trends and future directions.

Numerous studies have explored the integration of AR technology into STEM education, demonstrating its potential to enhance learning outcomes [7]. These studies have employed various AR approaches, including marker-based [8], marker less [4], and mixed reality (MR) [9]. As AR technology continues to evolve, its applications in STEM education are expanding, offering students more immersive, interactive, and engaging learning experiences.

Other researchers have also proposed a similar approach [10] to use AR technology to enhance distance learning in robotics to overcome limitations of online robotics lessons.

In a previous work, we explored the potential of augmented reality (AR) to enhance the learning experience for mechanical engineering students. We developed an AR-enriched learning material that complemented a traditional project guide for designing a 5-degree-of-freedom robotic arm. The AR application displayed 3D models of the robotic arm components directly on top of the project guide, providing students with an immersive and interactive learning experience [11].

A previous study demonstrated that using a combination of 3D printing and augmented reality (AR) enhanced student learning outcomes in a mechanical engineering design course. The study found that students who used the combined 3D printing and AR approach had better understanding of the design process, showed enhanced capacity to understand and interpret 3D representations and higher levels of engagement in the course material [12].

Researchers Scaravetti and François made use of the DIOTA software to integrate directly Catia CAD models within AR scenarios and implemented the final build on both head-mounted display with gesture recognition as well as handheld AR devices (tablets). They have created a wide range of training scenarios for multiple assemblies and have identified several functionalities that can support the needs of perception in regards to mechanical engineering learning [13].

Aliev et al. [14] have proposed the development of an AR software solution that makes use of 3D models of cutting tools, measuring tools as well as special equipment to address various aspects associated with mechanical engineering education.

Other researchers have developed a framework for implementing AR-based maintenance systems in the context of Industry 4.0 and made use of the popular Vuforia Engine paired to Unity software solution to enhance real-time instruction, guidance and remote assistance [15].

As presented by Takrouri et al. [7], AR enhances engineering education by providing interactive simulations, visualizations, and remote collaboration, but cost, standardization, and expertise hinder widespread adoption.

3 Materials and Methods

The project curriculum idea, which has started to be implemented since 2019, is intended for students pursuing Robotics at Technical University, offering both Romanian and English language studying options. The computer-Assisted Graphics discipline is a second year, first-semester discipline. For this discipline, students have both lectures, laboratory sessions, and a project. The project consists of seven sessions of two hours each. Within the practical project sessions, each student designs the robotic arm from scratch within SolidWorks.

In response to the global pandemic that began in 2019 when educators were compelled to adapt their teaching methods to an online environment. This shift necessitated the digitization of teaching materials, allowing for their dissemination via the internet to students. While this digital transformation presented new opportunities, it also introduced challenges.

We have gradually enhanced the project in 2020 with an AR application capable of adding the 3D models directly over the project book as well as video links that present step by step video guides for the design of each component [11].

Within this paper we propose the use of an advanced AR application that can track the 3D printed robotic arm assembly in real time. This will enable students to better understand the assembly procedure of the robotic arm components, stepper motors as well as the intended cable management of the robotic arm so that all cables are managed through the robotic arm assembly, and they are hidden using plastic covers.

The proposed framework that can enable real-time tracking using augmented reality starting with CAD models is presented in Fig. 1.

3.1 Computer Aided-Design

The robotic arm components were designed using SolidWorks—Part Design software, ensuring precision and accuracy in their geometry and dimensions. The components were then meticulously assembled within SolidWorks, creating a comprehensive 3D model of the entire arm structure. To facilitate the functionality of the robotic arm, CAD STEP file models of the servo motors were imported into the assembly. These models accurately represent the real-world servo motors, including their dimensions and mounting points.

The project guide introduces students to the fundamentals of SolidWorks software through the creation of a 3D-printable robotic arm [16]. The project guide covers key concepts like 3D modeling, assembly, and technical drawing drafting. It also incorporates interactive multimedia elements for an engaging learning experience (3D Pdf file that integrates CAD models).

For the robotic arm we made use of SolidWorks Composer to create various step-by-step assembly videos between each component and their associated stepper motors. To create the visualization element, we made use of the "digger tool" from SolidWorks Composer to showcase the stepper motor meticulously assembled and feature animated components to obtain animation's clarity and visual appeal.

In our pursuit of enhancing student understanding and engagement in mechanical engineering design projects, we have opted for SolidWorks as our primary CAD software. This decision is primarily driven by the availability of academic licenses within our faculty, enabling students to freely access and utilize this industry-standard tool. Moreover, SolidWorks holds substantial popularity among mechanical engineering companies in our region, ensuring that students are acquiring skills that are directly relevant to the professional world. Open-source parametric 3D modeling solutions such as FreeCAD can also be used for this endeavor as the output models can be

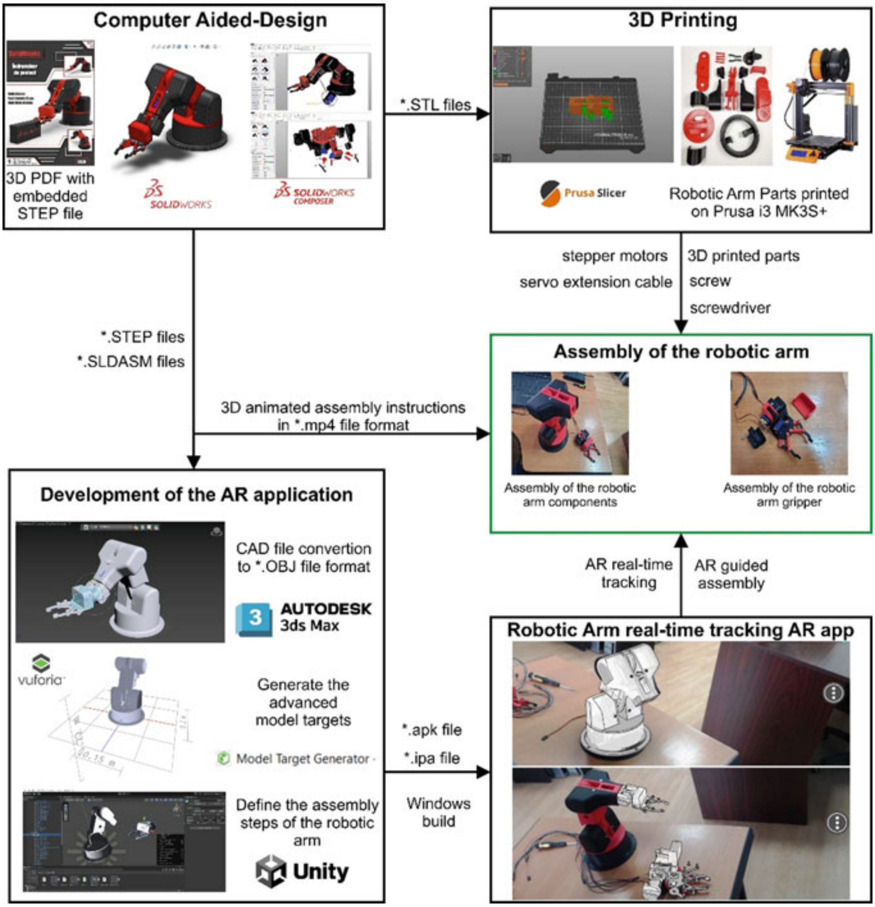

Fig. 1 Proposed framework used to develop the real-time tracking AR guided assembly

integrated within the framework using STEP file format which is used to exchange 3D product data between different CAD solutions.

3.2 3D Printing

To manufacture the 3D printed robotic arm, we made the Prusa I3 MK3S 3D printer, alongside the open-source Prusa slicer software. The Prusa I3 MK3S is renowned for its precision, reliability, and ease of use, making it an ideal choice for crafting intricate mechanical components. The Prusa slicer, an open-source application, further streamlined the manufacturing process by enabling us to seamlessly convert 3D models into printable files.

To manufacture the 3D printed robotic arm, we used the commonly available and budget-friendly PLA (Polylactic Acid) material as this has low shrinkage and wrapping issues making it ideal for intricate mechanical components. The final design of the 3D printed robotic arm comprises two distinct colors: red for the robotic arms' exterior and black for the plastic covers that conceal the servo motors and their associated cables.

3.3 Development of the AR Application

The augmented reality (AR) application we developed is built using the popular Unity software platform (version 2022.3.8f1), which offers robust cross-platform capabilities. This means that the application can run on a wide range of devices, including laptops, PCs paired with webcams, and smartphones or tablets. This cross-platform compatibility allows students to use the application and visualize the interactive real-time tracking assembly steps directly on the 3D printed parts of the robotic arm, regardless of their preferred device.

While within our case study the CAD model of the robotic arm was converted to an *.OBJ file format which is compatible with Unity and Vuforia using 3ds Max software, open-source solutions like Blender can also be used. However, this alternative approach requires utilizing a paid add-on to enable STEP file import within Blender or in some cases the STL file format can be used instead of STEP files for this conversion.

Within the proposed framework we made use of Vuforia Model Target Generator version 10.19.3 [17] to convert the 3D model of the robotic arm into a tracking dataset. This dataset enabled us to create a 3D model target that could be recognized by the Vuforia engine, allowing us to overlay virtual content onto the physical robotic arm.

To enhance the recognition accuracy and range of the model target, we opted to train our dataset using Vuforia's deep learning framework. This advanced training procedure allowed for automatic recognition of the robotic arm, without the need for Guide Views, and extended the recognition range up to 360°.

To define the assembly steps of the robotic arm we made use of 3ds Max and Unity to showcase the placement of the six servo motors within the robotic arm assembly. Each of these individual animations were exported from 3ds Max as FBX files, were integrated into the Unity environment to provide users with a comprehensive understanding of the robotic arm's intricate structure.

4 Results

The case study application regarding the assembly of the robotic arm gripper has been well-received by the students, indicating that the AR application makes it easier to perceive the location and assembly steps of each component compared to traditional documentation. Within Fig. 2 we have presented both the traditional documentation (PDF project guide, video animations as well as the proposed AR application). While no formal user experience analysis has been conducted, these initial impressions indicate that the AR application has the potential to enhance STEM education.

Our findings reveal that students have enthusiastically embraced the AR application used to visualize interactive assemblies' instruction onto real 3D printed parts. Even though they have already meticulously designed the robotic arm within SolidWorks and possess a comprehensive understanding of how each 3d printed part and each servo motor is assembled and fastened using screws, the proposed augmented reality experience provides an engaging and interactive layer of learning that has captivated students.

The case study augmented reality application made use of the cross-platform compatibility available in Unity which enabled the final build to be used by our students regardless of their preferred AR compatible device and their operating system. The application is compatible even with older devices, the minimum requirement for Android supported version is Android 8.0 (Oreo) which was released in 2017.

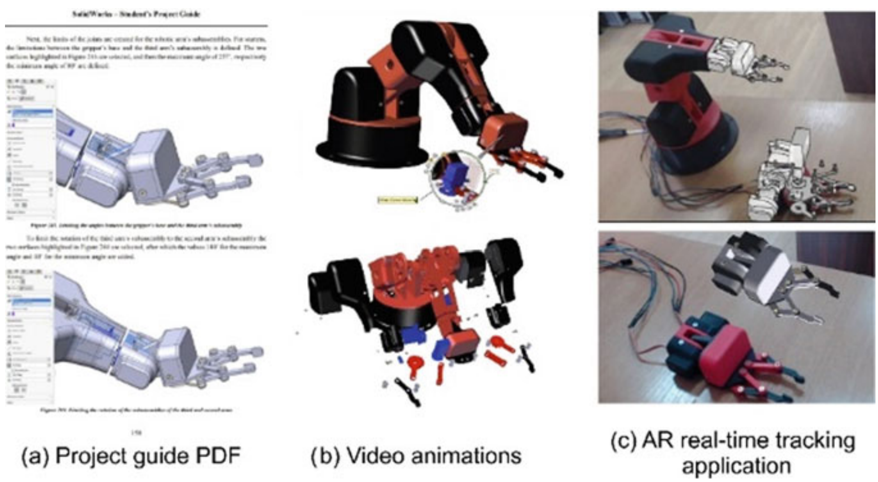

Fig. 2 **a** A page from the SolidWorks student's project guide regarding the assembly of the robotic arm. **b** Two screen captures from the animation created with SolidWorks composer. **c** The proposed AR application with the case study of the robotic gripper

5 Conclusions and Future Works

The developed AR application's interactive empowers students to manipulate the 3D printed components and observe real-time tracking assembly instructions for these. This hands-on engagement fosters active learning and encourages students to explore and experiment with the robotic arm's design.

One of our main goals was to make our application accessible across multiple platforms to facilitate the augmented reality-enhanced STEM education, enabling students to engage in hands-on and interactive learning about robotic arm assembly and engineering principles.

Building upon the proposed AR framework application for the robotic arm assembly, we envision the creation of a comprehensive suite of augmented and mixed reality experiences tailored to enhance STEM education within our university. The proposed framework, encompassing a versatile and easily adaptable platform, which has the potential to seamlessly integrate with a diverse range of STEM disciplines, including 3D computer-aided design (CAD), industrial design, and robotics.

While we haven't yet conducted a System Usability Scale system for the proposed AR application, we plan to do so in future work. This will allow us to gather insights from users and identify areas where the application can be improved.

References

1. Palkova, Z.: Mobile web 2.0 tools and applications in online training and tutoring. Handb. Mob. Teach. Learn. Second Ed. 609–634 (2019)
2. Arulanand, N., Ramesh Babu, A., Rajesh, P.K.: Enriched learning experience using augmented reality framework in engineering education. Procedia Comput. Sci. **172**, 937–942 (2020)
3. Solari, M., Vizquerra, M.I., Engel, A.: Students' interests for personalized learning: an analysis guide. Eur. J. Psychol. Educ. **38**, 1073–1109 (2023)
4. Boboc, R.G., Chiriac, R.L., Antonya, C.: How augmented reality could improve the student's attraction to learn mechanisms. Electronics **10**, 1–24 (2021)
5. Al-Ansi, A.M., Jaboob, M., Garad, A., Al-Ansi, A.: Analyzing augmented reality (AR) and virtual reality (VR) recent development in education. Soc. Sci. Hum. Open **8**(1), 1–10 (2023)
6. Abdullahi, A.Y., Hamza, M.F., Isa, A.I.: A survey on the contributions of 3D printing to robotics education—a decade review. Lect. Notes Electr. Eng. **730**, 289–302 (2022)
7. Takrouri, K., Causton, E., Simpson, B.: AR Technologies in Engineering Education: Applications, Potential, and Limitations in Digital, vol. 2, pp. 171–190 (2022)
8. Grodotzki, J., Müller, B.T., Tekkaya, A.E.: Introducing a general-purpose augmented reality platform for the use in engineering education. In: Advances in Industrial and Manufacturing Engineering, pp. 1–18 (2023)
9. Gattullo, M., Laviola, E., Boccaccio, A., Evangelista, A., Fiorention, M., Manghisi, V.M., Uva, A.E.: Design of a mixed reality application for stem distance education laboratories. Computers **11**, 1–24 (2022)
10. Pasalidou, C., Fachantidis, N.: Distance learning in the era of COVID-19: supporting educational robotics with augmented reality. In: International Conference on Educational Robotics in the Maker Era, EDUROBOTICS 2020, pp. 39–51 (2021)

11. Comes, R., Neamtu, C., Buna, Z.L.: Work-in-progress-augmented reality enriched project guide for mechanical engineering students. In: Proceedings 2021 7th International Conference on Immersive Learning Research Network, iLRN (2021)
12. Buna, Z.L., Rozsos, R.S., Comes, R., Bodi, S.: Enhaned learning material for mechanical engineering students. Acta Tech. Napocensis Ser.: Appl. Math. Mech. Eng. **65**, 39–44 (2022)
13. Scaravetti, D., François, R.: Implementation of augmented reality in a mechanical engineering training context. Computers **10**, 1–15 (2021)
14. Aliev, Y., Kozov, V., Ivanova, G., Ivanov, A.: 3D augmented reality software solution for mechanical engineering education. In: ACM Proceedings of the 18$^{\text{th}}$ International Conference on Computer Systems and Technologies, pp. 318–325 (2017)
15. Simon, J., Gogolák, L., Sárosi, J., Fürstner, I.: Augmented reality based distant maintenance approach. Actuators **12**, 302, 1–15 (2023)
16. Comes, R., Buna, Z.L., Rozsos, R.S.: SolidWorks—Indrumator de proiect. UTPress, Cluj-Napoca (2020)
17. Vuforia SDK Engine Developer Portal. https://developer.vuforia.com/downloads/sdk. Last accessed 20 Dec 2023

Part IV
Kinematics and Dynamics

Geometric Robot Calibration Using a Calibration Plate

Bernhard Rameder, Hubert Gattringer, and Andreas Müller

Abstract In this paper a new method for geometric robot calibration is introduced, which uses a calibration plate with precisely known distances between its measuring points. The relative measurement between two points on the calibration plate is used to determine predefined error parameters of the system. In comparison to conventional measurement methods, like laser tracker or motion capture systems, the calibration plate provides a more mechanically robust and cheaper alternative, which is furthermore easier to transport due to its small size. The calibration method, the plate design, the mathematical description of the error system as well as the identification of the parameters are described in detail. For identifying the error parameters, the least squares method and a constrained optimization problem are used. The functionality of this method was demonstrated in experiments that led to promising results, correlated with one of a laser tracker calibration. The modeling and identification of the error parameters is done for a gantry machine, but is not restricted to that type of robot.

Keywords Geometric calibration · Calibration plate · Measuring points · Gantry machine · Experimental calibration results

---

This work has been supported by the "LCM - K2 Center for Symbiotic Mechatronics" within the framework of the Austrian COMET-K2 program.

B. Rameder (✉) · H. Gattringer · A. Müller
Institute of Robotics, Johannes Kepler University Linz, Altenberger Straße 69, 4040 Linz, Austria
e-mail: bernhard.rameder@jku.at

H. Gattringer
e-mail: hubert.gattringer@jku.at

A. Müller
e-mail: a.mueller@jku.at

D. Pisla et al. (eds.), *Advances in Service and Industrial Robotics*, Mechanisms and Machine Science 157, https://doi.org/10.1007/978-3-031-59257-7_31

1 Introduction

As well as in industries as in scientific fields, it is crucial to have robotic systems with high accuracy to be able to fulfill tasks, that depends on a precise positioning of their end point, called end effector. In real systems deviations occur caused by mounting or manufacturing inaccuracies. Not only industrial robots benefit from a well known system description, but also gantry machines like milling machines, 3D printers and laser or water cutters are able to produce more precise products if calibrated. Therefore, the kinematics has to be expanded by error parameters, which are afterwards identified using a big set of measurements. This paper deals with a method for calibrating gantry machines with the use of a calibration plate with known geometry. Although the method is described for a gantry device, it can be expanded for industrial robots as well. In contrast to standard approaches, where usually the absolute position of the end effector is measured [1, 2], here we take use of the precisely known distance between two points on the calibration plate and its measured relative position. In the following, the calibration concept, the design of the calibration plate, the expanded kinematics and the novel identification process will be handled. At the end experimental results will confirm the functionality of this method.

2 Calibration Concept

The idea of using a calibration plate instead of an absolute measurement system such as a laser tracker to geometrically calibrate a system is based on a comparison between a measured relative distance and a known reference (1). The plate with defined relative distances ${}_M\mathbf{d}_{ik}$ between its measuring points, which capture the planar deviation of an energetic beam from their center, is placed somewhere within the work area of the machine. As proposed in [3, 4], a laser beam is used to position the device in the center of these points. In this case the orientation γ_M and the absolute position ${}_I\mathbf{r}_{0i}$ in the inertial frame is not known due to geometrical deviations from the ideal modeling. The actual position ${}_I\mathbf{r}_{0i}(\mathbf{q}, \mathbf{p}_e)$ deviates from the calculated forward kinematics ${}_I\mathbf{r}_{0i}(\mathbf{q})$, which uses the measured values of the axes $\mathbf{q}$, because of the geometrical errors $\mathbf{p}_e$, for instance axis misalignments (demonstrated by p_{e1}, p_{e2} and p_{e3}), as can be seen in Fig. 1. The alignment, described by γ_M for each pose j, depends on how the plate is positioned on the work area by the user. Hence, the error parameters $\mathbf{p}_e$ and the calibration plate orientations $\gamma_{M,j}$ have to be known to determine the exact pose of the plate in the inertial frame I. Furthermore, the forward kinematics has to be extended by the length of the laser beam L to close the kinematic loop to the point of impact P_I on the sensor surface [4], as shown in Fig. 1. All beam lengths of one pose are summarized in a vector $\mathbf{L}$. As the known distances

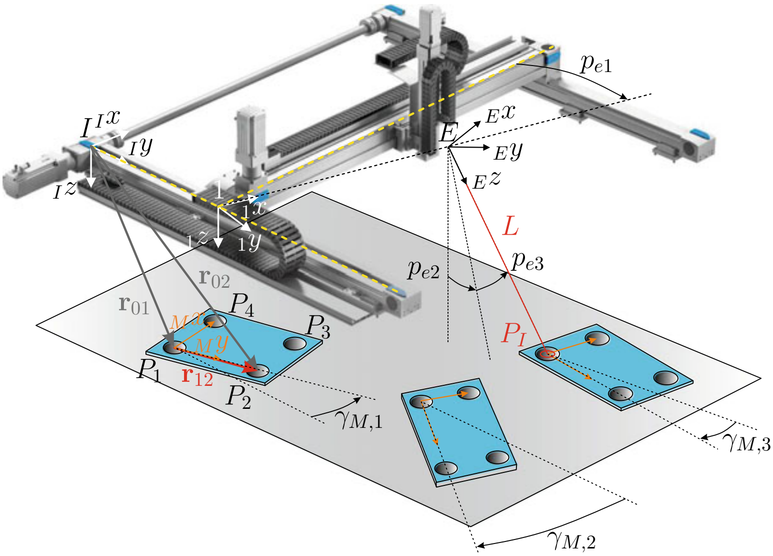

Fig. 1 Geometric calibration concept using a calibration plate (gantry figure [5])

$_M\mathbf{d}_{ik}$ between the measuring points i and k with $i \neq k$ are stated in the coordinate system of the calibration plate M, it is advisable to calculate the difference between the position vectors $_M\mathbf{r}_{ik}(\mathbf{q}, \mathbf{p}_e, \mathbf{L}, \gamma_M)$

$$_M\mathbf{r}_{0k} - {_M\mathbf{r}_{0i}} = {_M\mathbf{r}_{ik}} \stackrel{!}{=} {_M\mathbf{d}_{ik}} \tag{1}$$

in this frame too, whereas $_M\mathbf{d}_{ik}$ is the reference. The varying positioning of the calibration plate within the work area of the machine leads to a set of $j = 1, \ldots, m$ measuring poses. In this approach the first point for calculating the position error remained the same ($i = 1$), while the second one was iterated from two to the number of sensors on the calibration plate $k = 2, \ldots, n$. This results in a set of $3(n-1)$ equations when only the position is considered.

3 Calibration Plate

For the geometric error parameter identification it is necessary to have a reference measurement, which is used to form the position error vector $\Delta\mathbf{r}(\mathbf{q}, \mathbf{p}_e, \mathbf{L}, \gamma_M)$. As already mentioned, usually absolute measurements of the machine position are made. However, in this case the distances between two points on a calibration plate $_M\mathbf{d}_{ik}$ are used as reference values. Therefore, the geometry of this tool has to be known very accurately, which is realized by a measurement with a highly precise system in

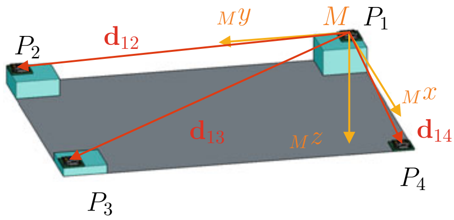

Fig. 2 Calibration plate setup with four measuring points

advance [6]. These measurements are stated in the body fixed frame M of the plate. The possible accuracy of the calibration process is thus depending on the accuracy of the reference distances ${}_M\mathbf{d}_{ik}$. Four-quadrant diodes are used as measuring points in order to be able to approach the defined reference targets. A laser pointer, mounted on the end effector E, allows the positioning of the machine in the center of the diodes. Encoder positions $\mathbf{q}$ of the single axis are saved on each measuring point for calculating the forward kinematics ${}_I\mathbf{r}_{0i}(\mathbf{q}, \mathbf{p}_e, L_i)$. Depending on the modeled system, certain error parameters require the calibration tool to have different sensor heights to be identifiable. An exemplary calibration plate setup is shown in Fig. 2.

4 Forward Kinematics and Position Error

To calculate the needed position error vector $\Delta\mathbf{r}(\mathbf{q}, \mathbf{p}_e, \mathbf{L}, \gamma_M)$, first the forward kinematics of the system including the error parameters has to be set up. Therefore, the kinematics has to be modeled to the point of impact P_I on the sensors by considering the laser length L, which is demonstrated in Fig. 1 for the third pose. The position vector to the end effector E is hereby extended by the length of the laser beam L_i between exit point and sensor surface [4], which leads to

$$ {}_I\mathbf{r}_{0i}(\mathbf{q}, \mathbf{p}_e, L_i) = {}_I\mathbf{r}_{0E}(\mathbf{q}, \mathbf{p}_e) + \mathbf{R}_{IE}(\mathbf{q}, \mathbf{p}_e) \begin{pmatrix} 0 & 0 & L_i \end{pmatrix}^T . \tag{2} $$

The difference between two position vectors heading to sensor surfaces results then in

$$ {}_I\mathbf{r}_{ik}(\mathbf{q}, \mathbf{p}_e, \mathbf{L}) = {}_I\mathbf{r}_{0k}(\mathbf{q}, \mathbf{p}_e, L_k) - {}_I\mathbf{r}_{0i}(\mathbf{q}, \mathbf{p}_e, L_i), \tag{3} $$

which is shown for the measuring points P_1 and P_2 of the first pose in Fig. 1. As there is no possibility to measure the length of the laser beam, one way to eliminate the parameters L_i and L_k is to transform (3) into the end effector frame E and eliminate the term which includes the lengths using a selection matrix

$$ \mathbf{S}_{xy} = \begin{pmatrix} 1 & 0 & 0 \\ 0 & 1 & 0 \end{pmatrix} . \tag{4} $$

Since L_i and L_k are defined in frame E in z direction, this provides the equation

$$
{}_E\mathbf{r}_{ik,xy}(\mathbf{q},\mathbf{p}_e) = \mathbf{S}_{xy}(\mathbf{R}_{EI}(\mathbf{q},\mathbf{p}_e)({}_I\mathbf{r}_{0E_k}(\mathbf{q},\mathbf{p}_e) - {}_I\mathbf{r}_{0E_i}(\mathbf{q},\mathbf{p}_e)) + \begin{pmatrix} 0 \\ 0 \\ L_k \end{pmatrix} - \begin{pmatrix} 0 \\ 0 \\ L_i \end{pmatrix}). \tag{5}
$$

After transforming the sensor distances into the end effector frame with the rotation matrix $\mathbf{R}_{MI}(\gamma_M)$ of the j^{th} pose, these distance ${}_E\mathbf{d}_{ik,xy} = \mathbf{S}_{xy}\mathbf{R}_{EI}\mathbf{R}_{IM\,M}\mathbf{d}_{ik}$ can be used to calculate the position error vector

$$
\Delta\mathbf{r}(\mathbf{q},\mathbf{p}_e,\gamma_M) = {}_E\mathbf{r}_{ik,xy}(\mathbf{q},\mathbf{p}_e) - {}_E\mathbf{d}_{ik,xy}(\mathbf{q},\mathbf{p}_e,\gamma_M) = 0. \tag{6}
$$

Despite the non measurable laser lengths are eliminated, after the selection some information is lost by cutting off an equation.

However, depending on the modeling of the system, which considers the error parameters, this is not heading to a result for certain choices of the modeled errors, for instance, when the modeling leads to an orientation of frame E_i in (5) that does not match with those of E_k. If this parameters are not negligible, the position error vector can be built in the body fixed calibration plate frame M. Hereby, the laser lengths can not be eliminated anymore and have to be changed into a part of the parameters that have to be identified. Nevertheless, one more equation is available per measuring point for the identification process. The changed working frame leads to the new position error vector

$$
{}_M\mathbf{r}_{ik}(\mathbf{q},\mathbf{p}_e,\mathbf{L},\gamma_M) = \mathbf{R}_{MI}(\gamma_M)\,{}_I\mathbf{r}_{ik}(\mathbf{q},\mathbf{p}_e,\mathbf{L}) \tag{7}
$$

$$
\Delta\mathbf{r}(\mathbf{q},\mathbf{p}_e,\mathbf{L},\gamma_M) = {}_M\mathbf{r}_{ik}(\mathbf{q},\mathbf{p}_e,\mathbf{L},\gamma_M) - {}_M\mathbf{d}_{ik} = 0 \tag{8}
$$

of pose j, which is finally used to identify the error parameter set.

5 Solution of the Calibration Problem

Once the position error vector is calculated, the modeled error parameters can be identified. In this paper two different approaches are used to estimate them.

5.1 Error Parameter Identification Using the Least Squares Method

On one hand $\Delta\mathbf{r}(\mathbf{q},\mathbf{p}_{id})$, where $\mathbf{p}_{id}^T = \begin{pmatrix}\mathbf{p}_e^T & \mathbf{L}^T & \gamma_M\end{pmatrix}$ now stands for all the parameters that have to be identified, can be linearized using Taylor series

$$\Delta\mathbf{r}(\mathbf{q},\mathbf{p}_{id}) = \underbrace{\Delta\mathbf{r}(\mathbf{q},\mathbf{p}_{id}^{(0)})}_{\overline{\mathbf{Q}}} + \underbrace{\left.\frac{\partial\Delta\mathbf{r}}{\partial\mathbf{p}_{id}}\right|_{\mathbf{p}_{id}^{(0)}}}_{\overline{\Theta}} \Delta\mathbf{p}_{id} + \mathcal{O}(\Delta\mathbf{p}_{id}^2) = 0\,, \tag{9}$$

neglecting the terms of higher order [7]. The parameters can be evaluated with the least squares method after filling the matrices $\overline{\mathbf{Q}}$ and $\overline{\Theta}$ with measurement values of the corresponding m calibration poses like

$$\underbrace{\begin{pmatrix}\overline{\mathbf{Q}}^1\\ \overline{\mathbf{Q}}^2\\ \vdots\\ \overline{\mathbf{Q}}^m\end{pmatrix}}_{\mathbf{Q}} = \underbrace{\begin{bmatrix}\overline{\Theta}^1_{int} & \overline{\Theta}^1_{ext} & 0 & 0\\ \overline{\Theta}^2_{int} & 0 & \overline{\Theta}^2_{ext} & 0\\ \vdots & \vdots & \ddots & \vdots\\ \overline{\Theta}^m_{int} & \dots & \dots & \overline{\Theta}^m_{ext}\end{bmatrix}}_{\Theta} \underbrace{\Delta\left(\mathbf{p}_e^T\ \mathbf{L}_1^T\ \gamma_{M,1}\ \mathbf{L}_2^T\ \gamma_{M,2}\ \dots\ \mathbf{L}_m^T\ \gamma_{M,m}\right)^T}_{\Delta\mathbf{p}_{id}^T} = 0. \tag{10}$$

The special depiction of Θ results from a separation of the intrinsic (int) and extrinsic (ext) parameters, as it is usual in camera calibration approaches [8]. Intrinsic parameters are the ones which belong to the system itself and does not change through the different measurement poses, whereas the extrinsic parameters belong to each pose. So each further pose generates a new set of laser lengths depending on the number of sensors on the calibration plate as well as a new plate orientation. The least squares estimation

$$\Delta\mathbf{p}_{id} = -[\Theta^T\Theta]^{-1}\Theta^T\mathbf{Q} \tag{11}$$

$$\mathbf{p}_{id}^{(1)} = \mathbf{p}_{id}^{(0)} + \Delta\mathbf{p}_{id} \tag{12}$$

is then repeated for some iterations

$$\mathbf{p}_{id}^{(n+1)} = \mathbf{p}_{id}^{(n)} - [\Theta^T\Theta]^{-1}\Theta^T\mathbf{Q} \tag{13}$$

until the change in parameters is below a given border [9]. As stated in (9) with $\mathbf{p}_{id}^{(0)}$ an initial error parameter set has to be chosen for the first iteration. Assuming the expected error parameter values to be very small, they are set to $\mathbf{p}_e^{(0)} = \mathbf{0}$ initially. Depending on the modeled parameters, some of them must be deviating from zero by a small random value, which is in the order of magnitude of the expected errors. The laser length $L_i^{(0)}$ can be initialized with the distance between exit point of the laser and the point of impact on the sensor surface using the uncalibrated kinematics. The initial calibration plate orientation $\gamma_{M,j}^{(0)}$ is estimated roughly due to its orientation on the work area. This leads to

$$\mathbf{p}_{id,j}^{T(0)} = \left(\mathbf{p}_e^{T(0)}\ \mathbf{L}_j^{T(0)}\ \gamma_{M,j}^{(0)}\right) \tag{14}$$

for the j^{th} measuring pose.

5.2 Error Parameter Identification Solving a Nonlinear Optimization Problem with Constraints

The fact that the equations for estimating the laser lengths $\mathbf{L}_j$ and the plate orientation $\gamma_{M,j}$ is restricted to the number of measurements per pose, as can be seen on $\overline{\Theta}^j_{ext}$ in (10), makes them difficult to identify. Due to this, a second approach for identifying the parameters $\mathbf{p}_{id}$ using a restricted optimization problem is introduced. The biggest advantage compared to the least squares method is the possibility to define constraints to specify realistic parameter limits. An appropriate choice may be a limitation of the error parameters in size of the maximum expected deviations. If the plate orientation is not varied randomly, but in a certain angular range, this can be taken as constraint for the plate alignment. Lastly, the laser lengths can be restricted to a predefined range, which is dependent on the geometry of the used machine. Nevertheless, the constraints have to be chosen in a plausible range, because possible solutions out of the restrictions are not taken into consideration. For optimization the nonlinear objective function

$$f(\mathbf{q}, \mathbf{p}_{id}) = \frac{\Delta\mathbf{r}^T(\mathbf{q}, \mathbf{p}_{id})\, \Delta\mathbf{r}(\mathbf{q}, \mathbf{p}_{id})}{2} \tag{15}$$

is introduced with the usage of $\Delta\mathbf{r}(\mathbf{q}, \mathbf{p}_{id})$ from (8). After filling the nonlinear position error vector with measurements

$$\Delta\mathbf{r}^T(\mathbf{q}, \mathbf{p}_{id}) = \left(\Delta\mathbf{r}_1^T(\mathbf{q}_1, \mathbf{p}_{id})\ \Delta\mathbf{r}_2^T(\mathbf{q}_2, \mathbf{p}_{id})\ \ldots\ \Delta\mathbf{r}_m^T(\mathbf{q}_m, \mathbf{p}_{id})\right) \tag{16}$$

of all m poses with each $3(n-1)$ equations, the optimization problem is defined as

$$\begin{aligned} &\min_{\mathbf{p}_{id}\in\mathbb{R}} f(\mathbf{q}, \mathbf{p}_{id}) \\ &\text{s.t. } \ \mathbf{p}_{min} \le \mathbf{p}_{id} \le \mathbf{p}_{max}\ , \end{aligned} \tag{17}$$

where $\mathbf{p}_{min}$ and $\mathbf{p}_{max}$ states the lower and upper bounds as described before. The computation is realized with *CasADI* [10] using the solver *IPOPT*. As an initial guess, the same parameters $\mathbf{p}^{(0)}_{id}$ as described for the least squares method can be used.

6 Experimental Results

For testing the procedure a three axis laser cutting machine with integrated laser beam was used. After centering the laser beam into the four-quadrant diodes, measurements of each axis encoder were saved. Furthermore, a raster laser tracker measurement ${}_I\mathbf{r}_{0E,ref}$ all over the work space was made additionally for validation using a *LEICA AT930 Absolute* system [11]. Although both described identification methods led to

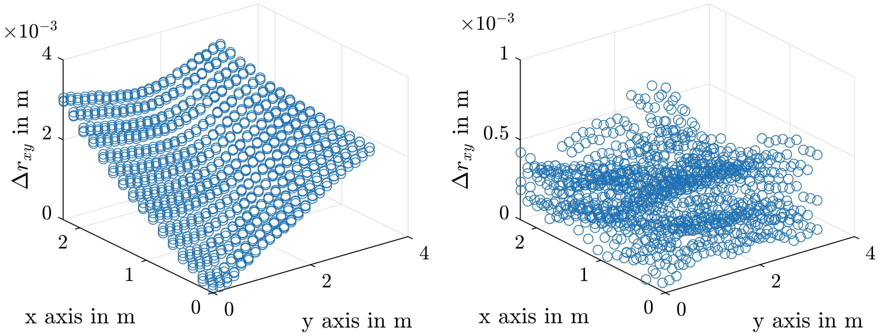

(a) Δr_{xy} of uncalibrated system (b) Δr_{xy} of calibrated system

Fig. 3 Absolute error between reference measurement and forward kinematics

Table 1 End effector accuracy of the different calibration methods

	$\Delta r_{max,xy}$ in mm	$\Delta r_{mean,xy}$ in mm
Uncalibrated robot	3.27	1.87
Laser tracker calibration	0.54	0.11
Calibration plate (proposed method)	0.81	0.26

approximately the same results, the constrained optimization was preferred and used here because the constraints prevent the estimated values from exceeding the assumed realistic range. Since the error parameters related with the z direction are difficult to identify in this case because of the given machine and calibration plate geometry, the error was only evaluated in the x and y direction, what is important for laser cutting machines anyway. Figure 3a shows the deviation of the uncalibrated forward kinematics of the system ${}_I\mathbf{r}_{0E}(\mathbf{q})$ in respect to the laser tracker measurement ${}_I\mathbf{r}_{0E,ref}$. Absolute errors up to some millimeters can be seen. The corresponding values of the maximum $\Delta r_{max,xy}$ and the mean error $\Delta r_{mean,xy}$ are given in Table 1. Figure 3b, on the other hand, shows the deviation of the reference measurement ${}_I\mathbf{r}_{0E,ref}$ from the kinematics corrected for the identified error parameters ${}_I\mathbf{r}_{0E}(\mathbf{q}, \mathbf{p}_e)$. The mean error could be reduced by about 86%. The deviations were evaluated and plotted on the measurement points of the reference raster using the saved encoder values and the identified error parameters.

7 Conclusion

The presented approach showed that it is possible to achieve good results using a calibration plate as a reference for geometric calibration instead of a laser tracker measurement for instance. Clear advantages compared to usual reference devices are the less sensible mechanical architecture of such calibration plates, their respectively small size, which makes them easy to handle for transport and above all the low manufacturing costs of the plate itself. Therefore, this method is ideal for the initial calibration of gantry machines and recalibration after any crashes is also a straightforward process. Further research in this area would be the extension of the method for industrial robots including their orientation.

References

1. Nubiola, A., Bonev, I.A.: Absolute calibration of an ABB IRB 1600 robot using a laser tracker. Robot. Comput.-Integr. Manuf. **29**(1), 236–245 (2013)
2. Nubiola, A., Slamani, M., Joubair, A., Bonev, I.A.: Comparison of two calibration methods for a small industrial robot based on an optical CMM and a laser tracker. Robotica **32**(3), 447–466 (2014)
3. Gatla, C.S., Lumia, R., Wood, J., Starr, G.: An automated method to calibrate industrial robots using a virtual closed kinematic chain. IEEE Trans. Robot. **23**(6), 1105–1116 (2007)
4. Gattringer, H., Neubauer, M., Kaserer, D., Müller, A.: A novel method for geometric robot calibration using laser pointer and cameras. In: Advances in Service and Industrial Robotics: Proceedings of the 26th International Conference on Robotics in Alpe-Adria-Danube Region, RAAD 2017, pp. 200–207. Springer, Berlin (2018)
5. Three-Dimensional Gantry YXCR: https://www.festo.com/gb/en/p/three-dimensional-gantry-id_YXCR. Accessed 14 Dec 2023
6. Usamentiaga, R., Garcia, D.: Multi-camera calibration for accurate geometric measurements in industrial environments. Measurement **134**, 345–358 (2019)
7. Siciliano, B., Khatib, O. (eds.): Springer Handbook of Robotics. Springer, Berlin (2008)
8. Heikkila, J.: Geometric camera calibration using circular control points. IEEE Trans. Pattern Anal. Mach. Intell. **22**(10), 1066–1077 (2000)
9. Smyth, G.K.: Nonlinear regression. Encyclop. Environ. **3**, 1405–1411 (2002)
10. Andersson, J.A.E., Gillis, J., Horn, G., Rawlings, J.B., Diehl, M.: CasADi—a software framework for nonlinear optimization and optimal control. In: Mathematical Programming Computation (2018)
11. Leica Absolute Tracker AT930: https://hexagon.com/products/leica-absolute-tracker-at930. Accessed 19 Dec 2023

Algorithm for Obtaining Balanced Specific Sliding Coefficients at the Points Where the Meshing Stars and Ends for External Spur Gears

T. A. Antal

Abstract The paper investigates the numerical possibility of obtaining equalized specific sliding coefficients for external involute spur gears based on new kinematical method that was developed in the general case of spatial gears and was customized for planar gears. The specific sliding coefficients at the points where the meshing begins (A) and ends (E) are evaluated to check if equalization is possible, then a proper numerical method is chosen and an algorithm is conceived to obtain the geometrical dimensions of the gears with optimized meshing characteristics by balanced sliding coefficients to provide longer lifetime.

Keywords Addendum modification · Algorithm · Balanced · Profile shifting coefficients · Spur gears · Specific sliding coefficients

1 Introduction

Friction and repeated contact between the teeth during operation will produce wear [1]. Abrasive wear produced by sliding gradually removes material from the teeth flanks and as it changes the tooth profile it will reduce the lifespan and the efficiency, leading, in time, to the failure of the gear. Several methods can be used to design the gears with profile shifting coefficients. Balancing the relative velocities [2] or the power lost by friction [3, 4] or the efficiency [5, 6] at the points where the meshing starts and ends, allows preventing premature wear and keeping the initial gearing conditions for a longer time [7]. In robotics, spur gears transfer rotational motion between two parallel axes. The motion of spur gears is accurate allowing precise positioning, and when this is combined with a higher working time various gear combinations can be developed for the actuation of the robotic systems, as illustrated in [8] for a surgical robot, in [9] for a robotic system for brachial monoparesis rehabilitation tasks or in gear boxes for industrial robotic solutions [10].

T. A. Antal (✉)
Technical University of Cluj-Napoca, Cluj-Napoca, Romania
e-mail: Tiberiu.Alexandru.Antal@mep.utcluj.ro

D. Pisla et al. (eds.), *Advances in Service and Industrial Robotics*, Mechanisms and Machine Science 157, https://doi.org/10.1007/978-3-031-59257-7_32

1.1 Specific Sliding Coefficients for External Spur Gears

Cylindrical gears with straight teeth fixed on parallel shafts are known as spur gears. When the teeth of the gears come into contact the rotational motion from one gear is transferred to the other. The contact is made on a line (called line of action) along witch the contact force produces a torque that is transferred from one gear to the other. In the general design case of gears, the profile shifting coefficient is used to adjust the tooth profile of gears. The profile shifting coefficient (also called addendum modification or correction, denoted as x_1, x_2 further on) defines a change in the gear's tooth height which affects the gear's overall size and the meshing process with effects on various gear parameters like the gear's center distance, tooth thickness, and contact ratio. While meshing the contact between the gears is with rolling with sliding. The sliding coefficient is a dimensionless parameter that indicates the degree of sliding between gear teeth during meshing. In most cases engineers aim to minimize the sliding coefficient (denoted as ζ further on) by the gear design or to balance the effects of the sliding to obtain better operating condition. From [11] the sliding coefficients between two, surfaces 1 and 2, in contact at point P, with rolling and sliding can be calculated with:

$$\zeta_{12} = \frac{\vec{V}_{12} \bullet \vec{V}_{12}}{\vec{V}_1 \bullet \vec{V}_{12}} \tag{1}$$

$$\zeta_{21} = \frac{\vec{V}_{21} \bullet \vec{V}_{21}}{\vec{V}_2 \bullet \vec{V}_{21}} \tag{2}$$

where $\vec{V}_1$ is the velocity of the surface 1 at point P; $\vec{V}_2$ is the velocity of the surface 2 at point P; $\vec{V}_{12}$ the relative velocity of surface 1 with respect of surface 2 at point P; $\vec{V}_{21}$ the relative velocity of surface 2 with respect surface 1 at point P. The following formulae were determined for the specific sliding coefficients [11] at points A and E, where the meshing starts and ends, in the case of the external spur gears.

$$\zeta_{12A} = (1 + u_{12}) \frac{1 - \Psi_{\mathrm{A}}}{1 + u_{12}(1 - \Psi_A)} \tag{3}$$

$$\zeta_{12E} = (1 + u_{12}) \frac{\Psi_{\mathrm{E}} - 1}{u_{12}\Psi_E} \tag{4}$$

$$\zeta_{21A} = (1 + u_{12}) \frac{\Psi_{\mathrm{A}} - 1}{\Psi_A} \tag{5}$$

$$\zeta_{21E} = (1 + u_{12}) \frac{\Psi_{\mathrm{E}} - 1}{\Psi_E - (1 + u_{12})} \tag{6}$$

where $u_{12} = \omega_1/\omega_2$ is the ratio of the angular velocities; ω_1 the angular velocity of the driving wheel, ω_2 the angular velocity of the driven wheel $\Psi_A = \frac{\tan(\alpha_A)}{\tan(\alpha_w)}$; $\Psi_E =$

$\frac{\tan(\alpha_E)}{\tan(\alpha_w)}$; α_A initial meshing angle at start; α_E final meshing angle at end; α_w the working meshing angle.

1.2 Computation of the Specific Sliding Coefficients for External Spur Gears

The following known formulae are specific to the geometry of the external spur gears [11, 12] and provide computation of the fundamental parameters to ensure proper meshing:

$$\cos(\alpha_A) = \frac{r_2}{r_{a2}}\cos(\alpha_0) \tag{7}$$

$$\cos(\alpha_E) = \frac{r_1}{r_{a1}}\cos(\alpha_0) \tag{8}$$

$$r_1 = \frac{mz_1}{2} \tag{9}$$

$$r_2 = \frac{mz_2}{2} \tag{10}$$

$$r_{a1} = \frac{m}{2}\left(z_1 + h_a^* + 2x_1 - 2k\right) \tag{11}$$

$$r_{a2} = \frac{m}{2}\left(z_2 + h_a^* + 2x_2 - 2k\right) \tag{12}$$

$$k = x_1 + x_2 - y \tag{13}$$

$$y = \frac{z_1 + z_2}{2}\left(\frac{\cos(\alpha_0)}{\cos(\alpha_w)} - 1\right) \tag{14}$$

where α_w is computed from the following equation, with $\alpha_0 = 20^\circ$:

$$x_1 + x_2 = [\tan(\alpha_w) - \alpha_w - (\tan(\alpha_0) - \alpha_0)]\frac{(z_1 + z_2)}{2\tan(\alpha_0)} \tag{15}$$

Before solving the equalization of the specific sliding coefficients at points A and E, where the meshing starts and ends, there is the problem of checking if this is possible. For this purpose, the surfaces from the Eqs. (3) and (6) will be graphically represented and it will be checked if there is an intersection between. The existence of intersection means that balance specific sliding can be found as balancing is the equalization from the following condition:

$$\zeta_{12A} = \zeta_{21E} \tag{16}$$

The x_1 and x_2 values are in range [0, 1] and the z_1 and z_2 values are given in the surface representations from Fig. 1. The Matlab code for obtaining the data from Table 1 is:

Table 1 $\zeta_{12A}(x_1,x_2)$ and $\zeta_{21E}(x_1,x_2)$ values, without equalization for $z_1 = 19$ and $z_2 = 19$

i	x_1	x_2	ζ_{12A}	ζ_{21E}	α_w [^{0}]	$\zeta_{12A}-\zeta_{21E}$
1	*0.00*	*0.00*	*−4.695*	*−4.695*	*20.000*	*0.000*
2	0.00	0.25	−3.983	−2.316	21.872	−1.666
3	0.00	0.50	−3.597	−1.381	23.446	−2.216
4	0.00	0.75	−3.357	−0.865	24.812	−2.491
5	0.00	1.00	−3.194	−0.531	26.027	−2.662
6	0.25	0.00	−2.316	−3.983	21.872	1.666
7	*0.25*	*0.25*	*−2.244*	*−2.244*	*23.446*	*0.000*
8	0.25	0.50	−2.199	−1.424	24.812	−0.775
9	0.25	0.75	−2.172	−0.937	26.027	−1.234
10	0.25	1.00	−2.155	−0.609	27.123	−1.545
11	0.50	0.00	−1.381	−3.597	23.446	2.216
12	0.50	0.25	−1.424	−2.199	24.812	0.775
13	*0.50*	*0.50*	*−1.462*	*−1.462*	*26.027*	*0.000*
14	0.50	0.75	−1.496	−0.999	27.123	−0.496
15	0.50	1.00	−1.526	−0.677	28.125	−0.848
16	0.75	0.00	−0.865	−3.357	24.812	2.491
17	0.75	0.25	−0.937	−2.172	26.027	1.234
18	0.75	0.50	−0.999	−1.496	27.123	0.496
19	*0.75*	*0.75*	*−1.053*	*−1.053*	*28.125*	*0.000*
20	0.75	1.00	−1.101	−0.738	29.049	−0.363
21	1.00	0.00	−0.531	−3.194	26.027	2.662
22	1.00	0.25	−0.609	−2.155	27.123	1.545
23	1.00	0.50	−0.677	−1.526	28.125	0.848
24	1.00	0.75	−0.738	−1.101	29.049	0.363
25	*1.00*	*1.00*	*−0.792*	*−0.792*	*29.907*	*0.000*

```
z1=19; z2=19; a0=deg2rad(20);
x1min=0;x1max=1.0;nx1=41;pasx1=(x1max-x1min)/(nx1-1);
x2min=0;x2max=1.0;nx2=nx1;pasx2=(x2max-x2min)/(nx2-1);
Z12a = zeros(nx1,nx2);Z21e = zeros(nx1,nx2);
for i=1:nx1
  x1=x1min+(i-1)*pasx1;VX1(i)=x1;
  for j=1:nx2
   x2=x2min+(j-1)*pasx2;VX2(j)=x2;
   aw=faw(x1,x2,z1,z2,a0); % (15)
   z12a=zetaa(x1,x2,z1,z2,a0,aw); % (3)
   z21e=zetae(x1,x2,z1,z2,a0,aw); % (6)
   Za(i,j)=z12a;%in red
   Ze(i,j)=z21e;%in yellow
   fprintf('%5.2f … %10.5f\n',x1,x2,z12a,z21e,rad2deg(aw),za-ze);
  end
end
```

We can observe in Table 1, if $z_1 = z_2$, and $x_1 = x_2$ we have equalization (see the italicized lines). The situation should also be found in the case of a general algorithm for solving the equalization and for any numbers of teeth. At the same time, we must take into account that in the calculation of sliding coefficients in Table 1 and the graphical representation from Fig. 1 the interferences that may appear between the teeth flaks were not considered. In order to avoid the tooth undercut and sharpening [11] additional restrictions apply to the results and the number of equalization solutions will decrease.

In Table 1, in the 25 rows of given pairs of profile shifting coefficients pairs, for 5 rows we have equal specific sliding coefficients, for 10 rows we have higher sliding at A point, and for 10 rows we have higher sliding at B point.

Fig. 1 Representation of $\zeta_{12A}(x_1,x_2)$—in red, and $\zeta_{21E}(x_1,x_2)$—in yellow, surfaces for $z_1 = 19$ and $z_2 = 19$

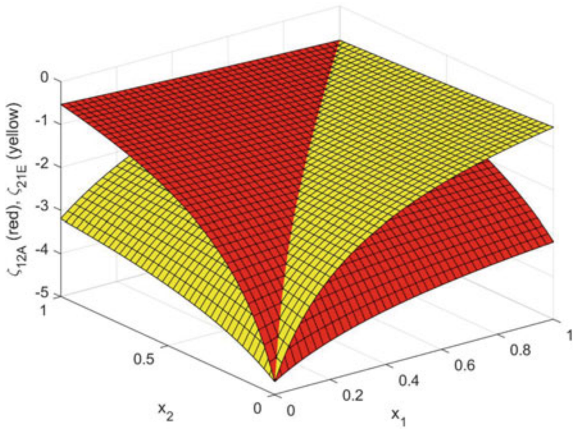

2 Algorithm for Equalizing the Specific Sliding Coefficients at the Points Where the Meshing Stars and Ends for External Spur Gears

Based on Eq. (16) the following Matlab function can be written.

```
function [ f ] = f_zeta(aw,x2,z1,z2,a0)
 x1=(inv_f(aw)-inv_f(a0))*(z1+z2)/2./tan(a0)-x2; % (15)
 f1=zeta12a(x1,x2,z1,z2,a0,aw); % (3)
 f2=zeta21e(x1,x2,z1,z2,a0,aw); % (6)
 f =f2-f1;
end
```

Where the ζ_{12A} is computed with the following Matlab function.

```
function [ zetaa ] = zeta12a(x1,x2,z1,z2,a0,aw)
     ha=1;
     u12=z2/z1;
     y=(z1+z2)*(cos(a0)/cos(aw)-1)/2.; % (14)
     k=x1+x2-y; % (13)
     r2pera2=z2/(z2+2*ha+2*x2-2*k); % (12)
     aa=acos(r2pera2*cos(a0)); % (7)
     psia = tan(aa)/tan(aw);
     zeta12a= (1+u12)*(1-psia)/(1+u12-u12*psia); % (3)
end
```

and the ζ_{21E} is computed with the following Matlab function:

```
function [ zetae ] = zeta21e(x1,x2,z1,z2,a0,aw)
    u12=z2/z1;
    y=(z1+z2)*(cos(a0)/cos(aw)-1)/2.; % (14)
    k=x1+x2-y; % (13)
    r1pera1=z1/(z1+2*ha+2*x1-2*k); % (11)
    ae=acos(r1pera1*cos(a0)); % (8)
    psie = tan(ae)/tan(aw);
    zeta21e= (1+u12)*(1-psie)/(1+u12-psie); % (6)
end
```

The following algorithm traverses the `[x2in, x2fin]` interval with a constant `step` in `n` equidistant points. The (16) in the `f_zeta` function will return an `aw` value for which the `f_zeta` is null in the [14^0, 32^0] interval for the `aw` angle. The solution is found using the bisection method. Bisection will always find a solution if the margins of the interval are correctly determined and it only needs the sign of the function [13] for that. The `find_interval` function seeks the left (`ast`) and the right (`aend`) interval margins where the solution is found. If the nonlinear equation solver from the `bisection` function will return real values the `x 1`, `zeta12a` and `zeta21e` values are computed. After the α_w angle, the tooth undercut and the sharpening limitations are checked the remaining values are printed and plotted.

```
ha=1;z1=19;z2=30;a0=deg2rad(20);
x2in=-1.0;x2fin=1.0; n=61; step=(x2fin-x2in)/(n-1);
plotcrt1x1=[];plotcrt1x2=[];

for i=1:n
 x2=x2in+(i-1)*step;
 [ast, aend] = find_interval(f_zeta(alfa,x2,z1,z2,a0);
 [aw, converging ] = bisection(@f_zeta,ast,aend,x2,z1,z2,ha,a0);
 if converging && (aw in [14^0, 32^0])
  x1=(inv_f(aw)-inv_f(a0))*(z1+z2)/2./tan(a0)-x2;
  za=zeta12a(x1,x2,z1,z2,a0,aw);
  ze=zeta21e(x1,x2,z1,z2,a0,aw);
..chechfor(tooth_undercut, tooth_sharpenig);
   if (not tooth_undercut && not tooth_sharpenig)
   fprintf('%9.5f .. \n',i, x1, x2, rad2deg(a_w),za,ze);
   plotcrt1x1=[plotcrt1x1 ; x1];
   plotcrt1x2=[plotcrt1x2 ; x2];
 end
end
```

3 Conclusions

Values of the specific profile shifting coefficients x_1 and x_2 can be determined using this algorithm to provide uniform wearing of teeth flanks at the points where the meshing ends and begins. For small and close values of the z_1 and z_2 number of teeth the equalization has fewer solutions (Table 2 has fewer values than Table 3). High equalized specific sliding coefficients, in absolute value, are obtained for negative values of the profile shifting coefficients. Low equalized specific sliding coefficients, in absolute value, are obtained for the positive values of the profile shifting coefficients. For no lubrication conditions the low values are preferred, while in the presence of lubrication the higher values can be used as hydrodynamic lubrication between gear teeth can be this way enhanced, leading to reduced friction, wear, and better gear performance. When the specific profile shifting coefficients, obtained from the equalized specific sliding coefficients, are used at the design of the gears the balanced wearing will increase the lifetime of the gears and provide a lower operating temperature.

Table 2 Profile shifting coefficients for equalized sliding coefficients for $z_1 = 19$ and $z_2 = 19$

i	x_1	x_2	ζ_{12A}	ζ_{21E}	α_w [^{0}]
10	−0.10000	−0.10000	−8.8245361	−8.8245361	18.16802
11	−0.00000	0.00000	−4.6957606	−4.6957606	20.00000
12	0.10000	0.10000	−3.2551503	−3.2551503	21.52617
13	0.20000	0.20000	−2.5031547	−2.5031547	22.84552
14	0.30000	0.30000	−2.0325107	−2.0325107	24.01401
15	0.40000	0.40000	−1.7055391	−1.7055391	25.06675
16	0.50000	0.50000	−1.4624285	−1.4624285	26.02736
17	0.60000	0.60000	−1.2728622	−1.2728622	26.91259
18	0.70000	0.70000	−1.1197626	−1.1197626	27.73481
19	0.80000	0.80000	−0.9927392	−0.9927392	28.50343
20	0.90000	0.90000	−0.8850853	−0.8850853	29.22580
21	1.00000	1.00000	−0.7922664	−0.7922664	29.90779

Table 3 Profile shifting coefficients for equalized sliding coefficients for $z_1 = 19$ and $z_2 = 57$

i	x_1	x_2	ζ_{12A}	ζ_{21E}	α_w [^{0}]
1	0.24933	−1.00000	−2.9145005	−2.9145005	16.15289
2	0.25666	−0.90000	−2.6251058	−2.6251058	16.82501
3	0.26593	−0.80000	−2.3900838	−2.3900838	17.45541
4	0.27697	−0.70000	−2.1943919	−2.1943919	18.04981
5	0.28960	−0.60000	−2.0281496	−2.0281496	18.61281
6	0.30370	−0.50000	−1.8845884	−1.8845884	19.14814
7	0.31917	−0.40000	−1.7589089	−1.7589089	19.65888
8	0.33591	−0.30000	−1.6476084	−1.6476084	20.14759
9	0.35386	−0.20000	−1.5480670	−1.5480670	20.61647
10	0.37295	−0.10000	−1.4582835	−1.4582835	21.06735
11	0.39311	0.00000	−1.3767011	−1.3767011	21.50185
12	0.41431	0.10000	−1.3020892	−1.3020892	21.92133
13	0.43650	0.20000	−1.2334607	−1.2334607	22.32701
14	0.45964	0.30000	−1.1700146	−1.1700146	22.71995
15	0.48369	0.40000	−1.1110925	−1.1110925	23.10109
16	0.50864	0.50000	−1.0561486	−1.0561486	23.47126
17	0.53445	0.60000	−1.0047255	−1.0047255	23.83120
18	0.56109	0.70000	−0.9564372	−0.9564372	24.18159
19	0.58855	0.80000	−0.9109551	−0.9109551	24.52301
20	0.61680	0.90000	−0.8679975	−0.8679975	24.85603
21	0.64583	1.00000	−0.8273216	−0.8273216	25.18111

Acknowledgements This work was supported by a grant from the Romanian Ministry of Research and In-novation, project number PN-III-P2-2.1-PED-2021-3430/608PED/2022 (Hope2Walk) within PNCDI III.

References

1. Chen, Z., et al.: Meshing frictional characteristics of spur gears under dry friction and heavy loads: effects of the preset pitting-like micro-textures array. Tribol. Int. **180**, 108296 (2023)
2. Antal, T.A., Antal, A.: Geometrical dimensions of helical gears with equalized relative velocities at the beginning and the ending of the meshing. In: Kecskemethy, A., Muller, A. (Eds) Computational Kinematics, pp. 385–392. Springer (2009)
3. Antal, T.A.: Addendum modification of cylindrical spur gears with equalized powers lost by friction between the teeth flanks at the points where the meshing stars and ends. Acta Technica Napocensis, Ser.: Appl. Mathem. Mech. Eng. **57**(3), 329–334 (2014)
4. Antal, T.A.: The power lost by friction, between the teeth flanks, for cylindrical spur gears, at the points where the meshing stars and ends. Acta Technica Napocensis, Ser.: Appl. Mathem. Mech. Eng. **57**(1), 7–10 (2015)
5. Diez-Ibarbia, A., del Rincon, A.F., Iglesias, M., et al.: Efficiency analysis of spur gears with a shifting profile. Meccanica **51**, 707–723 (2016)
6. Antal, T.A.: Addendum modification of spur gears with equalized efficiency at the points where the meshing stars and ends. MECHANIKA **6**, 480–485 (2015)
7. Eng, J., Karuppanan, S., Patil, S.: Frictional stress analysis of spur gear with misalignments. J. Mech. Eng. Sci. **12**(2), 3566–3580 (2018)
8. Vaida, C., Pisla, D., Plitea, N., Gherman, B., Gyurka, B., Stancel, E., Hesselbach, J., Raatz, A., Vlad, L., Graur, F.: Development of a control system for a parallel robot used in minimally invasive surgery. IFMBE Proc. **26**, 171–176 (2009)
9. Pisla, D., Tarnita, D., Tucan, P., Tohanean, N., Vaida, C., Geonea, I.D., Bogdan, G., Abrudan, C., Carbone, G., Plitea, N.: A parallel robot with torque monitoring for brachial Monoparesis rehabilitation tasks. Appl. Sci. **11**, 9932 (2021). https://doi.org/10.3390/app11219932
10. Okorn, I., Nagode, M., Klemenc, J.: Operating performance of external non-involute spur and helical gears: a review. J. Mech. Eng. **67**(5), 256–271 (2021)
11. Antal, T.A.: Profile shifting coefficients of spur gears with balanced specific sliding coefficients at the points where the meshing stars and ends. In: Pisla, D., Corves, B., Vaida, C. (Eds) New Trends in Mechanism and Machine Science. EuCoMeS 2020. Mechanisms and Machine, vol. 89, pp. 272–278. Springer (2020)
12. Sheng, W., Li, Z., Zhang, H., Zhu, R.: Geometry and design of spur gear drive associated with low sliding ratio. Adv. Mech. Eng. **13**(4), (2021)
13. Antal, T.A.: A review of the PHP server-side scripting language compared to C, C++ and Java for numerical engineering applications. Acta Technica Napocensis, Ser.: Appl. Mathem. Mech. Eng. **60**(1), 15–24 (2023)

A Novel Approach Exploiting Contact Points on Robot Structures for Enhanced End-Effector Accuracy

Jan Šifrer and Tadej Petrič

Abstract In this paper, we propose a novel approach that leverages contact points on the robot's structure to significantly enhance the precision of robotic mechanisms. This method involves a detailed analysis of how strategic contact utilization can lead to improved accuracy in robotic operations. Through experimental validation and comparative studies, we demonstrate the efficacy of this technique in refining the performance of robotic systems. Our findings highlight the potential of this approach in optimizing robotic functionality, opening new avenues for advanced robotic applications in various fields.

Keywords Robotic mechanisms · Accuracy · Jacobian matrix · Inverse kinematics

1 Introduction

In this paper, we address a pivotal challenge in collaborative robotic systems (Cobots), where precision is often compromised despite the integration of advanced sensors for human detection and collision avoidance. Our approach is to enhance Cobot accuracy by adopting human-like precision techniques. A typical human strategy involves stabilizing one's arms by resting them on a surface for tasks requiring fine motor skills, such as writing. We aim to apply this 'leaning' method to improve robotic accuracy. While previous research [1–3] has investigated various control strategies for robotics, our method uniquely combines force and position control across different robot segments, thereby refining task precision and enhancing Cobots' effectiveness and safety in human-robot collaborative settings.

This work was supported by Slovenian Research Agency grant N2-0269.

J. Šifrer (✉) · T. Petrič
Department of Automatics, Biocybernetics and Robotics, Jozef Stefan Institute, Jamova cesta 39, 1000 Ljubljana, Slovenia
e-mail: tadej.petric@ijs.si

Jozef Stefan International Postgraduate School, Jamova cesta 39, 1000 Ljubljana, Slovenia
e-mail: jan.sifrer@ijs.si

D. Pisla et al. (eds.), *Advances in Service and Industrial Robotics*, Mechanisms and Machine Science 157, https://doi.org/10.1007/978-3-031-59257-7_33

Significant strides have been made in the robotics field, particularly in multitasking and obstacle avoidance [4–6], with key developments including second-order inverse kinematics [7] and the augmented Jacobian method [8]. Our research integrates these established methodologies with our innovative 'leaning' concept, aiming to enhance task accuracy in critical human-robot interactions.

Furthermore, we extend our focus to the physical whole-body interactions of Cobots, particularly those with a moving base, as they represent a greater degree of autonomy and complexity in unstructured environments. Unlike traditional industrial robotics where the base is fixed and interactions are limited [9, 10], Cobots require advanced control mechanisms to manage contacts and physical interactions safely [11]. This capability is essential for operating in everyday environments, where making and breaking contacts, both intentional and unintentional, support dynamic movements.

The study of physical whole-body interactions, especially in humanoid Cobots, is crucial for enhancing positional accuracy, payload capacity, repeatability, and speed, while ensuring safety [12, 13]. Proper whole-body coordination and the ability to utilize whole-body contacts are imperative for the effective functioning of these robots. Our research aims to contribute to this field by proposing a novel approach to improve the precision of Cobots through a combination of advanced control strategies and human-inspired techniques.

In this paper, we introduce an approach aimed at improving the precision of collaborative robots (Cobots). By synergistically combining established robotic control methods with innovative techniques inspired by human behavior, our research addresses the challenges associated with whole-body interactions in dynamic and unstructured environments. This strategy is designed to extend the capabilities of Cobots beyond their current limitations. Our work makes a technical contributions to the field of robotics, enhancing the precision and functionality of Cobots. Moreover, it lays the groundwork for fostering more intuitive, safe, and effective interactions between humans and robots across a diverse range of applications.

2 Control Framework

Our aim is to refine the precision of the robotic mechanism through a unique strategy: enabling one of its body parts to lean against an object. Utilizing a redundant robotic system, we effectively split this concept into two distinct tasks. The first task involves the robotic mechanism leaning on the object with a predetermined force F, as depicted in Fig. 1. Concurrently, the second task requires the robot to execute an action using its end effector, while maintaining the initial contact and force F. From a robotics perspective, this approach can be described as prioritizing the leaning action as the primary task, with the movement of the end effector serving as a secondary yet integral task. This dual-task methodology is key to enhancing the precision and functionality of the robot in complex environments.

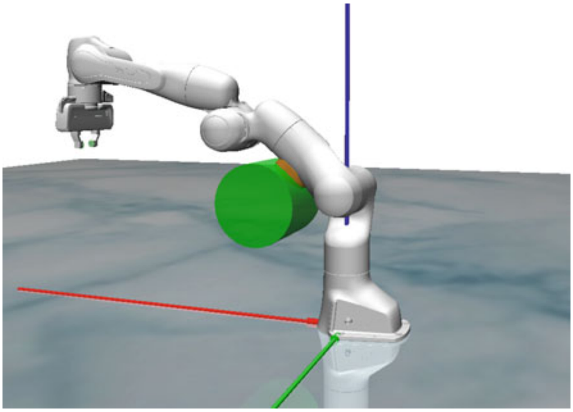

Fig. 1 Display of the robot leaning on the object

Movement within the robotic system can be described in two distinct ways. Firstly, it can be expressed through the joint space, which is represented by $\mathbf{q} = [q_0,\ q_1,\ \ldots,\ q_{N-1}]$. This notation details the configuration of the robot's mechanism, comprising $N-1$ joints, with N being 7 on our scenario. Secondly, movement can be articulated in the task space, symbolized by $\mathbf{x} = [x_1,\ x_2,\ \ldots,\ x_M]$. Here, M signifies the number of degrees of freedom assigned to each specific task. The intricate connection between these two representations is governed by the direct kinematic equation. This relationship is comprehensively elaborated in [14] and is expressed as follows:

$$\mathbf{x} = \mathbf{p}(\mathbf{q}), \tag{1}$$

where $\mathbf{p}$ is a nonlinear function. Moreover, by applying differentiation to the direct kinematic equation, we are able to formulate the first-order differential kinematic equation. This derivation offers a deeper understanding of the robot's movement dynamics, and is expressed as follows:

$$\dot{\mathbf{x}} = \mathbf{J}\dot{\mathbf{q}}, \tag{2}$$

where $\mathbf{J} = \frac{d\mathbf{p}(\mathbf{q})}{d\mathbf{q}}$ is the Jacobian matrix, which is dependent on the configuration $\mathbf{q}$. This equation shows how the end effector's position changes with slight configuration adjustments. Its ease of inversion allows for calculating configuration changes based on end effector position changes, expressed mathematically as:

$$\dot{\mathbf{q}} = \mathbf{J}^{+}\dot{\mathbf{x}}. \tag{3}$$

It's important to note that the Jacobian matrix $\mathbf{J}$ for redundant robotic systems is non-invertible. For these systems, we use the Moore-Penrose pseudo-inverse, denoted as $\mathbf{J}^{+}$.

When prioritizing certain joints in a robotic system, a weighted pseudo-inverse can be utilized, where weights are adjusted according to the significance of each joint. Both the Moore-Penrose pseudo-inverse and the weighted pseudo-inverse offer a parametric solution. Specifically, the Moore-Penrose inverse selects the solution with the smallest second norm. Conversely, the weighted pseudo-inverse enables control over the contribution of each joint to the final solution by adjusting their respective weights.

For both the Moore-Penrose and weighted pseudo-inverses, additional solutions are attainable by incorporating a vector that is multiplied by the kernel of the Jacobian matrix **J**. This approach facilitates the assignment of multiple tasks to the robot. The mathematical expression for this is:

$$\dot{\mathbf{q}} = \mathbf{J}^{+}\dot{\mathbf{x}} + \mathbf{N}\dot{\mathbf{q}}_0, \tag{4}$$

where **N** represents the null space or kernel of the matrix **J**, and $\mathbf{q}_0$ corresponds to our secondary task.

To address our challenge, we will apply Eq. (4). In this setup, the robot's primary task is to lean on the object, while its secondary task will be the controlled movement of the end effector.

To elucidate our primary task, we aim to have our robotic mechanism exert force on an object using a component positioned between the second and third joints. Consequently, this task exclusively pertains to the control of the first and second joints, with the associated Jacobian matrix taking the following form:

$$\mathbf{J}_f = \begin{bmatrix} 1 & 0 & 0 & 0 & 0 & 0 & 0 \\ 0 & 1 & 0 & 0 & 0 & 0 & 0 \end{bmatrix}. \tag{5}$$

It's crucial to emphasize that the Jacobian matrix under consideration is non-invertible. To address this, we will utilize the Moore-Penrose pseudo-inverse, yielding the following outcome:

$$\mathbf{J}_f^{+} = \begin{bmatrix} 1 & 0 & 0 & 0 & 0 & 0 & 0 \\ 0 & 1 & 0 & 0 & 0 & 0 & 0 \end{bmatrix}^T. \tag{6}$$

Please take note that the resulting pseudo-inverse, represented as $\mathbf{J}_f^{+}$, is essentially the transpose of the original Jacobian matrix $\mathbf{J}_f$. This stems from the fact that the task is defined in the joint space.

The subsequent phase entails establishing the desired contact force, denoted as F, which signifies the robotic pressure exerted on the object. In order to optimize the utilization of degrees of freedom for this specific task, our primary focus centers on the magnitude of the force. Assuming our target force magnitude is represented as F_d, we can compute the necessary adjustment required to achieve our objective, expressed as $e_f' = F_d - F$. Based on the experimental setup, illustrated in Fig. 1, and taking into account the robot's kinematics, it becomes evident that joint 1 lacks the capability to generate the vertical force required. However, in light of this limitation, we can simplify our approach by setting the first component of the vector $\mathbf{e}_f$ to zero, without compromising generality. Given the significant impact of the second joint on the leaning force, we can effectively represent $\mathbf{e}_f = [0,\ e'_f]^T$.

Finally, the resulting controller used was defined by

$$\dot{\mathbf{q}}_d = \mathbf{J}_f^{+}\mathbf{K}_f\mathbf{e}_f + \mathbf{N}_f\mathbf{J}_x^{+}\mathbf{K}_x\mathbf{e}_x, \tag{7}$$

where $\mathbf{N}_f$ represents the null-space projection of $\mathbf{J}_f$. Additionally, $\mathbf{K}_f$ and $\mathbf{K}_x$ denote the proportional gains for the force-feedback and the Cartesian controller, respectively. Furthermore $\mathbf{J}_x$ s defined as the weighted inverse of the end effector's Jacobian matrix, which is calculated as:

$$\mathbf{J}_x^{+} = \mathbf{N}_f^{-1}\mathbf{J}_x^{T}(\mathbf{J}_x\mathbf{N}_f^{-1}\mathbf{J}_x^{T} + \mu\mathbf{I})^{-1}. \tag{8}$$

Here, μ is a small scalar number and $\mathbf{I}$ is the identity matrix.

3 Method Evaluation

To effectively compare the precision of the end effector, we established a predefined curve for the end effector to follow. The deviation from this path was measured to assess the error during its movement.

In this paper, we explore the movement of the end effector along a curve that shapes into an infinity symbol (∞) with a specific radius r. To facilitate movement beyond a plane, we parameterized the curve to include a continuously varying third coordinate. The parametric representation of this curve, for any $t \in \mathbb{R}$, is expressed by

$$\left[\mathbf{x}_d\right] = \begin{bmatrix} r \cdot \sin(t) \cdot \cos(t) + 0.65 \\ r \cdot \cos(t) \\ r \cdot \sin(t) \cdot \cos^2(t) + 0.4 \end{bmatrix}. \tag{9}$$

To evaluate the efficacy of our proposed method, where the robot supports its structure, we compare it to the traditional approach where the robot operates without making contact. The tests are designed to highlight the performance differences between these two methodologies. In both scenarios, the robot is programmed to show increased flexibility in its initial two joints, intentionally demonstrating its precision capabilities, or lack thereof, in relatively straightforward tasks. This feature is especially pivotal in our new method. Here, unlike the traditional approach, the robot is not only tasked with movement but also with exerting a constant, controlled force. This dual functionality tests the robot's ability to maintain stability and accuracy under varying operational conditions. It also allows us to observe how the additional requirement of force application influences the robot's overall performance, particularly in terms of precision. By comparing these two methodologies, we aim to assess

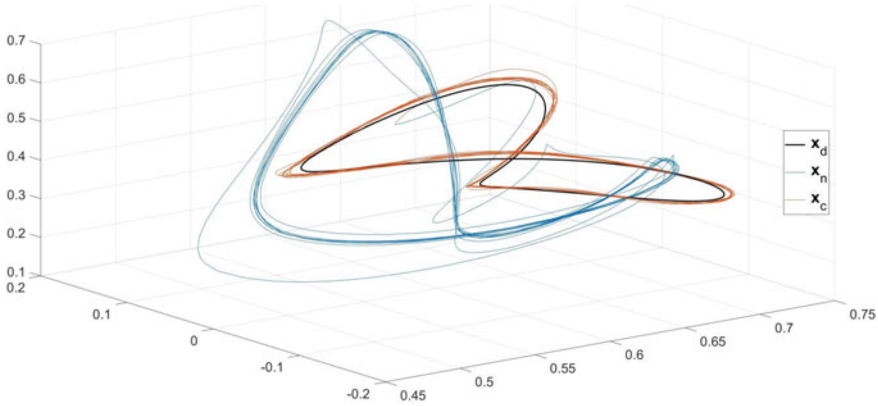

Fig. 2 Comparison of the end effector accuracy. Here, $\mathbf{x}_d$ indicates the designated trajectory, $\mathbf{x}_n$ represents the trajectory followed by the robot when it is not in contact, and $\mathbf{x}_c$ shows the trajectory when the robot is performing in contact with an object using the proposed approach

not just the functional capabilities of the robotic system, but also its adaptability and reliability in different operational contexts.

In Fig. 2, we present a detailed comparison of the mechanism's end effector accuracy between the basic and the new method. The graphical representation in this figure provides a clear visual interpretation of the discrepancies in performance metrics under each method. It is noteworthy that the enhanced flexibility in the robot's first two joints, a feature common to both methods, is designed to accentuate the effects of precision under different operational conditions.

Furthermore, the experiment includes a critical examination of how the additional task of maintaining a constant force $F = 10N$ in the new method impacts the overall precision of the end effector. This is in contrast to the basic method, where the robot operates without this additional force requirement. The comparative analysis is rooted in the quantification of accuracy using the error estimator e_r, which is given by

$$e_r = \|(x - x_x)\|_2 + \|(y - y_x)\|_2 + \|(z - z_x)\|_2. \tag{10}$$

We can observe that the robotic mechanism controlled by the basic method (represented by the blue curve) exhibits significantly lower accuracy compared to the one controlled by our new method (indicated by the red curve). This disparity in performance is quantitatively substantiated by the values obtained from our error estimator. For the basic method, the $e_r = 37.3$ is higher than the $e_r = 9.1$ recorded for the proposed method.

An analysis of Fig. 3 offers a detailed understanding of the variations in the position of the mechanism's end effector across different coordinates. It becomes evident that under the new method, the coordinate values of the end effector are significantly more congruent with the theoretical values when compared to those achieved with the

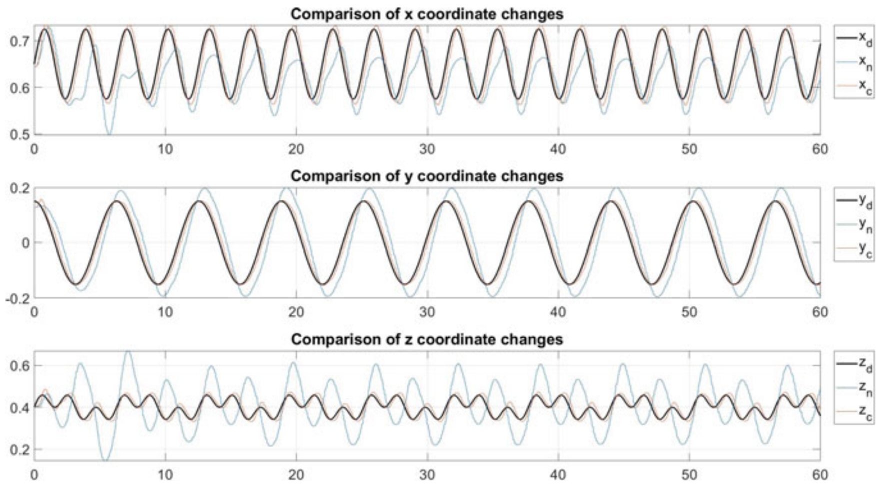

Fig. 3 Comparison of the accuracy of the mechanism's end effector by coordinates

basic method of robotic control. This comparison clearly demonstrates the superior accuracy and alignment of the new method with the intended trajectory, highlighting its effectiveness in precise robotic movements.

Analysis reveals that the largest discrepancy in the basic method is observed in the z coordinate. This is attributed to the robot's compliance in the first two joints coupled with its specific configuration. As depicted in Fig. 1, the robot's stance is such that the second joint bears most of the robot's weight. Coupled with the robot's relatively rapid movements and the inherent compliance of this second joint, the precision of motion is significantly compromised. This results in notable oscillations, particularly evident in the z coordinate as shown in Fig. 3.

Furthermore, due to the compliance in the first joint, deviations are also pronounced in the x and y coordinates. This multi-dimensional imprecision leads to an overall reduction in the accuracy of the robotic mechanism, as comprehensively demonstrated in Fig. 2. This analysis underlines the critical impact of joint compliance and robot configuration on the precision of end effector movements, particularly in multi-coordinate tasks.

4 Conclusion

In this paper, we unveiled an innovative approach that markedly enhances the precision of robotic mechanisms in specific scenarios by leveraging body contacts. Our study demonstrated a clear improvement in accuracy with this proposed method compared to the conventional approach, where the robot operates without contact. Our focus was particularly on the accuracy of the end effector, as evidenced by its ability to accurately trace a parameterized curve. The results from this comparison highlighted a considerable increase in precision with the use of our proposed method.

These findings not only affirm the efficacy of our approach but also illuminate the wider impact of such advancements in the field of robotic control. They suggest a promising path forward for robotic systems, emphasizing adaptability and physical interaction with their environments as key factors in achieving superior performance. This research paves the way for future developments in robotics, where integration with the surrounding environment becomes a critical component of advanced robotic functionality.

References

1. uz Zaman, U.K., Siadat, A., Baqai, A.A., Naveed, K., Kumar, A.A.: Handbook of Manufacturing Systems and Design: An Industry 4.0 Perspective. CRC Press (2023)
2. Pérez, R., Gutiérrez, S.C., Zotovic, R. (2018). A study on robot arm machining: advance and future challenges. Annal. DAAAM & Proc. **29** (2018)
3. Perez-Ubeda, R., Gutierrez, S., Zotovic, R., Lluch-Cerezo, J.: Study of the application of a collaborative robot for machining tasks. Procedia Manuf. **41**, 867–874 (2019). 8th Manufacturing Engineering Society International Conference, MESIC 2019, 19–21 June 2019, Madrid, Spain
4. Petrič, T., Žlajpah, L.: Smooth continuous transition between tasks on a kinematic control level: obstacle avoidance as a control problem. Robot. Autonom. Syst. **61**(9), 948–959 (2013)
5. Liegeois, A., et al.: Automatic supervisory control of the configuration and behavior of multibody mechanisms. IEEE Trans. Syst. Man Cybern. **7**(12), 868–871 (1977)
6. Zlajpah, L., Nemec, B.: Kinematic control algorithms for on-line obstacle avoidance for redundant manipulators. In: IEEE/RSJ International Conference on Intelligent Robots and Systems, vol. 2, pp. 1898–1903. IEEE (2002)
7. Khatib, O.: A unified approach for motion and force control of robot manipulators: the operational space formulation. IEEE J. Robot. Autom. **3**(1), 43–53 (1987)
8. Egeland, O.: Task-space tracking with redundant manipulators. IEEE J. Robot. Autom. **3**(5), 471–475 (1987)
9. Argall, B.D., Billard, A.G.: A survey of Tactile Human-Robot interactions. Robot. Autonom. Syst. **58**, 1159–1176 (2010)
10. Peternel, L., Petrič, T., Babič, J.: Robotic assembly solution by human-in-the-loop teaching method based on real-time stiffness modulation. Autonom. Robot. **42**, 1–17 (2018). Jan
11. Padois, V., Ivaldi, S., Babič, J., Mistry, M., Peters, J., Nori, F.: Whole-body multi-contact motion in humans and humanoids: advances of the codyco european project. Robot. Autonom. Syst. **90**, 97–117 (2017)
12. Kim, W., Peternel, L., Lorenzini, M., Babič, J., Ajoudani, A.: A human-robot collaboration framework for improving ergonomics during dexterous operation of power tools. Robot. Comput.-Integr. Manuf. **68**, 102084 (2021)
13. Kheddar, A., Caron, S., Gergondet, P., Comport, A., Tanguy, A., Ott, C., Henze, B., Mesesan, G., Englsberger, J., Roa, M.A., Wieber, P., Chaumette, F., Spindler, F., Oriolo, G., Lanari, L., Escande, A., Chappellet, K., Kanehiro, F., Rabaté, P.: Humanoid robots in aircraft manufacturing: the airbus use cases. IEEE Robot. Autom. Mag. **26**(4), 30–45 (2019)
14. Chiaverini, S., Oriolo, G., Walker, I.D.: Kinematically Redundant Manipulators, pp. 245–268. Springer, Berlin (2008)

Multi-axis Additive Manufacturing: Development of Slicer and Toolpath for 2.5D/3D/5D Printing

Gidugu Lakshmi Srinivas, Marius Laux, Vishnu Parameswaran Nair, and Mathias Brandstötter

Abstract In 3D printing, components are created incrementally along the normal direction through the sequential deposition of material. This methodology streamlines the manufacturing process and kinematics of 3D printers. However, due to the staircase effect, the conventional printing process has drawbacks such as additional material for supporting structures, more processing time, poor structural strength, and surface finish. Multi-axis 3D printing is the solution to overcome the stated problems. Nevertheless, a fully developed slicer is inaccessible. This paper describes the development of a slicer and toolpath for different printing strategies like 2.5D, 3D, 5D, and demonstrates its surface finish and structural strength. The HAGE1750L 5-axis machine is used to demonstrate the proposed methodology. The machine has three prismatic joints followed by tilting and rotating print bed. Initially, inverse kinematic equations of the machine are calculated, which will help give the joint parameters to the motors. The conformal slicer and toolpath are developed using the Rhino and Grasshopper software. Users can import or create the model into the Rhino, and slicer automatically creates the toolpath and G-code in Grasshopper for printing. The slicer generates isocurves of the geometry and divides the layers into points. It spiralizes the layers for continuous printing and calculates the flow rate of the extrusion material using the height of the nonlinear planes. It facilitates various parameters such as nozzle size, layer height, and thickness. Three tubes are designed, and compression test is conducted to validate the proposed methodology. Together,

WWW home page: http://www.admire.center.

G. L. Srinivas (✉) · M. Laux · V. P. Nair · M. Brandstötter
ADMiRE Research Center, Carinthia University of Applied Sciences, Europastraße 4, Villach, Austria
e-mail: l.gidugu@cuas.at

M. Laux
e-mail: m.laux@cuas.at

V. P. Nair
e-mail: v.nair@cuas.at

M. Brandstötter
e-mail: m.brandstoetter@cuas.at

D. Pisla et al. (eds.), *Advances in Service and Industrial Robotics*, Mechanisms and Machine Science 157, https://doi.org/10.1007/978-3-031-59257-7_34

the system delivers the design of the geometries, simulates the toolpath, generates the G-code, and prints models.

Keywords Inverse kinematics · Additive manufacturing · Conformal slicing · 3D/5D printing · Structural strength · Toolpath planning

1 Introduction

The significance of 3D printing in additive manufacturing (AM) is rapidly increasing, driven by its applications in prototyping, manufacturing processes, and customization across various industrial fields [4]. 3D printing can be done in different forms but fused filament fabrication (FFF) is most popular because of high availability and low cost [7]. However, 3D printing requires support material for overhangs, which causes material waste and additional post-processing. The multi-axis printing is the alternative to overcome these problems and it also improves the structural strength of the printed parts. However, a fully developed slicer is not available for multi-axis printer due to its complex structure and it requires the orientation of the nozzle to generate the G-code [3, 12].

AM exhibits certain limitations, including requirement for support material, surface finish, and anisotropy. Later, researchers are focused multi-axis printing using CNC machine or robotic arm to overcome the stated problems. In 1998, the first 5-DOF additive manufacturing machine was developed, using a high-powered laser as the energy source [11]. R. Fry et al. undertook quantitative experiments to examine the impact of printing at various orientations relative to gravity, as well as the effects of dynamically altering the build orientation concerning the build tray when fabricating overhanging features [2]. Lim et al. present an alternative approach known as curved layer printing, which involves generating a curved toolpath. This innovative curved layer printing method has found applications in diverse fields, including large-scale construction [10] and prosthetics [1, 6]. Nevertheless, multi-axis printers often encounter issues related to the collision of the nozzle or extruder head with the printed parts. Wu et al. proposed collision avoidance algorithm that estimates constraints on order of edges [16]. The use of parametric curves, such as Bézier curves, allows for the creation of complex part contours in FFF. However, aspects like contour manipulation, overlapping, and slicing strategies in the process remain relatively unexplored. 5-axis printers encounter time challenges in toolpath optimization and slicing, especially in non-supporting material printing. Improving slicing algorithms and harmonizing multi-axial printers can enhance control over material deposition, improving mechanical characteristics [14]. Material extrusion along multiple axes alters layering locally, distinguishing it from traditional 3D printing [9, 13]. In a study by Kaill et al., 5-axis printed samples demonstrated predicted mechanical behavior, outperforming 3D printed samples in compression loading tests [8]. Gunpinar et al. introduced Helical5AM, a technique employing helical print-paths for five-axis AM. Non-planar slicing enables material deposition in various directions, enhancing mechanical characteristics. This method accelerates collision-free tool orientation planning and is compatible with curved print-paths [5].

The main objective of this paper is to develop a slicer for multi-axis printing such as 2.5D, 3D, and 5D. The HAGE 1750L machine is used to demonstrate the proposed methodology. Initially, the forward and inverse kinematic equations of the machine are derived to find the joint values $\mathbf{q}$ of the machine. The slicer can easily adopt to the other multi-axis 3D printers by modifying its inverse kinematic equations. The toolpath generation in the slicer can help to visualize the traces of nozzle based on the given layer height. Users can change the slicer parameters based on the requirements and visualize the toolpath automatically. The advantageous of the multi-axis manufacturing is demonstrated in terms of structural strength and surface finish by printing the various tubes with three printing strategies. Before printing with the machine, the NCnetic V2.0 tool is used to check the G-code. It helps to simulate the path and collision detection among the nozzle, machine parts, and printed material.

2 Methodology

2.1 2.5D, 3D and 5D Printing

In this paper, three different printing strategies are used such as 2.5D, 3D, and 5D. In 2.5D and 3D printing, the nozzle follows the linear layers and iso curves respectively and advances in perpendicularly upward direction. Whereas in 5D printing, nozzle follows the iso curves and it is always normal to the curvature. The advantages and disadvantages of the different printing strategies as well as types of 5-axis CNC machine are provided in Fig. 1.

2.2 Forward Kinematics of the HAGE Xyzbc-Trt Machine with Rotary Axis Offset

This section derives the forward and inverse kinematic equations for the HAGE 1750L machine, which has a serial RRPPP structure. It is a multi-axis CNC machine used for printing filament or pellet material. It has a print volume of $1.2 \times 1.2 \times 1\ \mathrm{m}^3$ and $0.5 \times 0.5 \times 0.4\ \mathrm{m}^3$ for 3D and 5D printing, respectively. The machine has three prismatic joints (xyz-axes), and a printing bed that rotates about z-axis (c-rotation) mounted on tilting table that rotates about y-axis (b-rotation). The machine has rotary axis offset in the z-direction (f_z). The coordinate systems of the HAGE 1750L are shown in Fig. 2. In short, the machine's configuration is named xyzbc-trt (table rotation/tilting) with rotary offset. The forward kinematics of the machine is calculated by describing a relation between the printing bed (B) coordinate system and nozzle

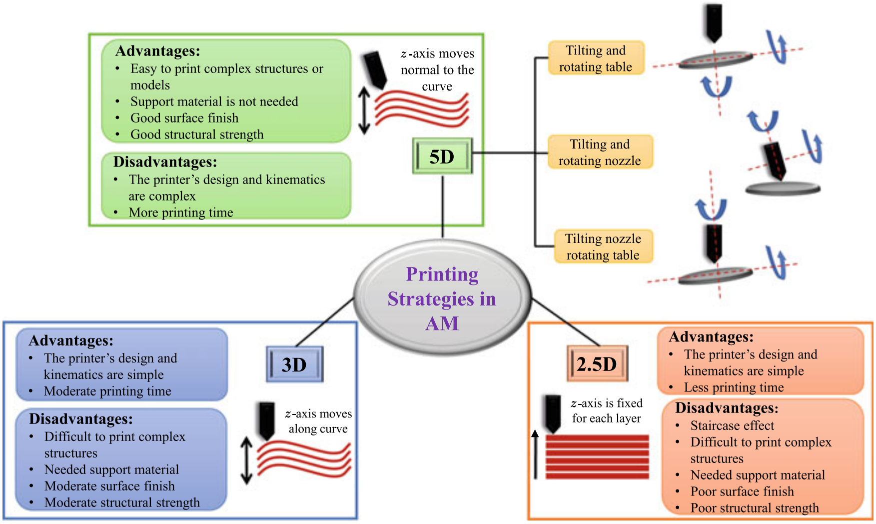

Fig. 1 Advantages and disadvantages of 2.5D, 3D, and 5D (types of 5-axis machine)

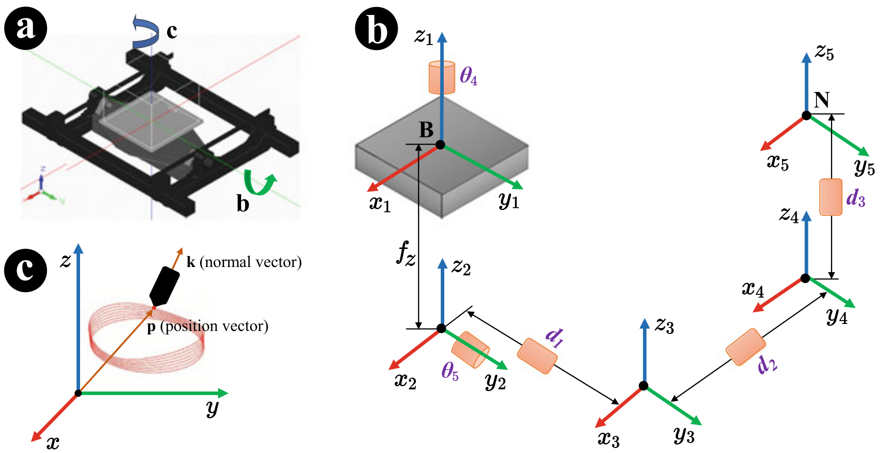

Fig. 2 **a** The printing bed (c-rotation) and tilting table (b-rotation) of HAGE 1750L. **b** Assignment of coordinate systems of the machine from print bed (B) to nozzle (N) with prismatic and revolute joints. **c** Location of the nozzle and its normal and position vector

or extruder (N) coordinate system. This can be defined by a homogenous transformation matrix BNT by succeeding transformation between the coordinate systems, as shown in (1). The homogenous transformation matrix of each structural element, such as c rotation of the bed, offset in z-direction, b-rotation of the tilting table and linear movements in three directions are shown in (2). The matrix multiplication gives the forward transformation matrix of the HAGE 1750L, as shown in (3). The first 3×3 matrix and last column vector represents the orientation and position of the nozzle, respectively. The last column of (3) is the position vector $\mathbf{p}$, and it can be written in the matrix form for calculation of inverse form, as shown in (4). In the following equations, $s_i = \sin(\theta_i)$ and $c_i = \cos(\theta_i)$ hold for $i = 4, 5$.

$$ {}^{B}_{N}\mathbf{T} = {}^{B}_{c}\mathbf{T} \cdot {}^{c}_{F}\mathbf{T} \cdot {}^{F}_{b}\mathbf{T} \cdot {}^{b}_{N}\mathbf{T} \tag{1} $$

$$ {}^{B}_{N}\mathbf{T} = \begin{bmatrix} c_4 & -s_4 & 0 & 0 \\ s_4 & c_4 & 0 & 0 \\ 0 & 0 & 1 & 0 \\ 0 & 0 & 0 & 1 \end{bmatrix} \cdot \begin{bmatrix} 1 & 0 & 0 & 0 \\ 0 & 1 & 0 & 0 \\ 0 & 0 & 1 & F_z \\ 0 & 0 & 0 & 1 \end{bmatrix} \cdot \begin{bmatrix} c_5 & 0 & s_5 & 0 \\ 0 & 1 & 0 & 0 \\ -s_5 & 0 & c_5 & 0 \\ 0 & 0 & 0 & 1 \end{bmatrix} \cdot \begin{bmatrix} 1 & 0 & 0 & d_1 \\ 0 & 1 & 0 & d_2 \\ 0 & 0 & 1 & d_3 - f_z \\ 0 & 0 & 0 & 1 \end{bmatrix} \tag{2} $$

$$ {}^{B}_{N}\mathbf{T} = \begin{bmatrix} c_4c_5 & -s_4 & c_4s_5 & c_4c_5d_1 - s_4d_2 + c_4s_5d_3 - c_4s_5f_z \\ s_4c_5 & c_4 & s_4s_5 & s_4c_5d_1 + c_4d_2 + s_4s_5d_3 - s_4s_5f_z \\ -s_5 & 0 & c_5 & -s_5d_1 + c_5d_3 - c_5f_z + f_z \\ 0 & 0 & 0 & 1 \end{bmatrix} \tag{3} $$

$$ \begin{bmatrix} x \\ y \\ z \\ 1 \end{bmatrix} = \begin{bmatrix} c_4c_5 & -s_4 & c_4s_5 & c_4s_5f_z \\ s_4c_5 & c_4 & s_4s_5 & -s_4s_5f_z \\ -s_5 & 0 & c_5 & -c_5f_z + f_z \\ 0 & 0 & 0 & 1 \end{bmatrix} \cdot \begin{bmatrix} d_1 \\ d_2 \\ d_3 \\ 1 \end{bmatrix} = \mathbf{D} \cdot \begin{bmatrix} d_1 \\ d_2 \\ d_3 \\ 1 \end{bmatrix} \tag{4} $$

2.3 *Inverse Kinematics of the Machines*

To compute the values of the prismatic joints $d_1, \ldots, d_3$, we are using (4) and the inverse of $\mathbf{D}$. The final prismatic joint angles of the motors are given in (5), these are used to reach the target position by the nozzle tip.

$$ d_1 = c_4c_5x + s_4c_5y - s_5z + s_5f_z \tag{5} $$

$$ d_2 = -s_4x + c_4y \tag{6} $$

$$ d_3 = c_4s_5x + s_4s_5y + c_5z - c_5f_z + f_z \tag{7} $$

The orientation of the extruder is computed using the normal vector $\mathbf{k}$ of the curve at divided points as shown in Fig. 2c. The information of the normal vector can be obtained from the perpendicular frames in Grasshopper. It is equivalent to the first column of (3), and the rotation angles θ_4 and θ_5 are provided below.

$$ \theta_4 = \mathrm{a}\tan 2(k_y, k_x) \tag{8} $$

$$ \theta_5 = \mathrm{a}\sin(-k_z) \tag{9} $$

3 Conformal Slicing Using Grasshopper

3.1 Slicer for Multi-axis Printing

The Grasshopper software is the visual scripting language used to develop the slicing algorithm for generating the G-code. Grasshopper is a plugin that runs within the Rhino CAD modeling software. Different printing strategies (2.5D, 3D, and 5D) are demonstrated using a non-linear surface tubes such as star, ellipse, and hexagonal, as shown in Fig. 3. In 2.5D and 3D printing, nozzle follows the linear layers, this creates the seam at the corner of the object. Whereas in 5D printing, a ramp is created to eliminate the seam and make the printing spiralize that results in uniform printing thickness and avoids the retraction of the material [15].

The tubes are designed in the Rhino CAD software, the base and height of the all geometries are approximately 50 and 100 mm, respectively. The base shape is created by selecting its respective polygon and control point curve is shaped to extrude the object using array curve in the software. The loft option is used to visualize the final geometry by selecting the curves in the sequence of bottom to top. Later, the iso curve functional block is used to create the nonlinear curves to mimic the geometry curvature.

3.2 G-Code Generation

The slicer automatically generates the toolpath for imported geometry into Rhino and the user can select the slicing parameters such as layer height, layer thickness, nozzle size, etc. Initially, each layer of iso curves are divided into the required number of points in the slicer and nozzle should follows the cartesian coordinates (xyz) and

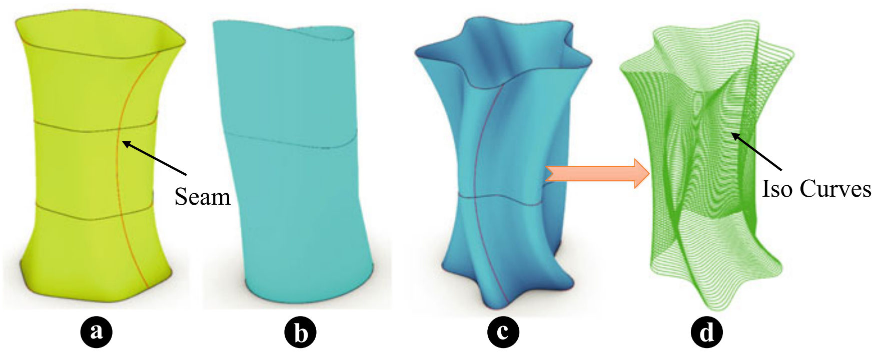

Fig. 3 Different non-linear surface tubes such as **a** hexagonal, **b** ellipse, **c** star, and **d** iso curves of the star

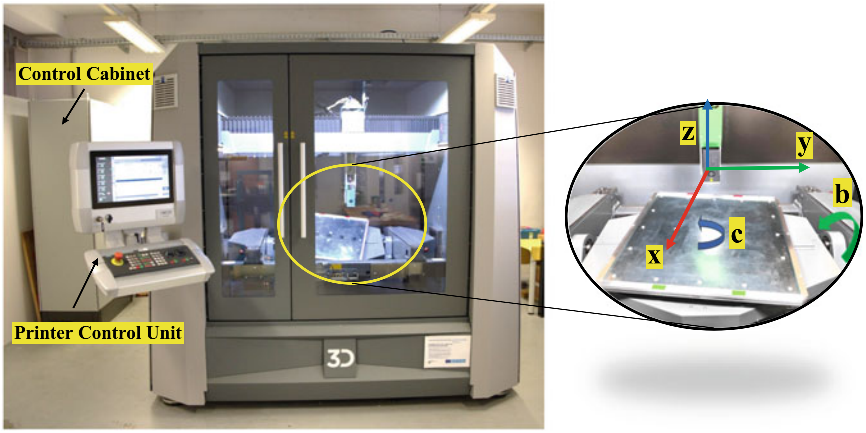

Fig. 4 The HAGE 1750L machine with control unit and its coordinate systems

normal vector **k**. Using inverse kinematic equations as detailed in the Sect. 2, joint parameter are derived as shown in (5) and (6). The flow rate is calculated in the grasshopper based on the distance between the layers and the line segments [15]. Finally, the printer commands know as G-code is generated from the output of inverse kinematics equations and flowrate. The code is saved as an MPF file and sent to the HAGE 1750L machine for printing the models using tough PLA material from the filament manufacturer Form Futura.

3.3 Experimental Setup

The structural strength of the models is examined using a Zwick Roell Z020 testing machine. The experiment involves positioning the model between compression plates, applying force using a movable crosshead connected to a 20 kN load cell. The force is exerted until it decreases to 80% of its maximum value. A force versus displacement graph is generated and compared among different printed models.

4 Results and Discussion

As detailed in the above section, the G-code generated from the slicer is imported to the HAGE machine using external drive. The setup of the machine and its coordinate system is shown in Fig. 4. The printer is controlled by the Siemens Sinumerik 840D sl with positioning accuracy and print speed as 0.05 mm and 150 mm/s, respectively.

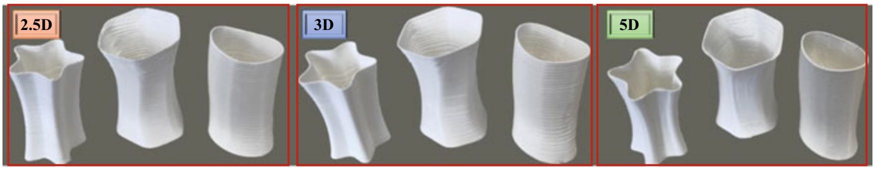

Fig. 5 Printed components (star, hexagonal, and ellipse) of 2.5D, 3D, and 5D

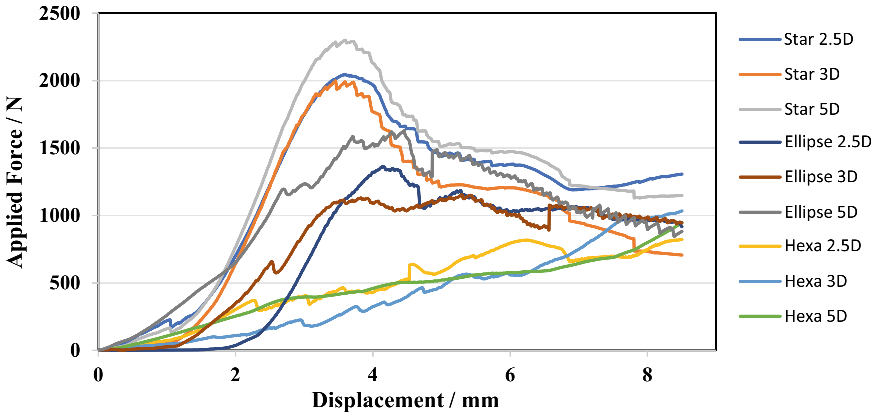

Fig. 6 Printed components (star, hexagonal, and ellipse) of 2.5D, 3D, and 5D

The 2.5D models exhibit inferior geometrical features, characterized by a staircase effect, in contrast to 3D and 5D printing, as shown in Fig. 5. Each three samples are printed for compression tests that involves star, ellipse, and hexagonal samples in 2.5D, 3D, and 5D printing aim to assess their respective structural strengths.

Structural strength: The compression test is conducted to find the structural strength of the printed components using an universal testing machine (UTM). The average applied force vs displacement graph is plotted for all test sample, as shown in Fig. 6. The best maximum of average forces is recorded as 2292.2, 1033.9, and 1627.8 N for Star 5D, Hexagonal 3D, and Ellipse 5D, respectively. The hexagonal models yield unexpected findings, experiencing buckling during testing. The maximum value for Hexa 3D is obtained post-component failure. Overall, the 5D printed components shown good surface finish and structural strength compared to the 2.5D and 3D.

5 Conclusions

Traditional 3D printing builds parts layer-by-layer along the z-axis, resulting in weak structures, longer printing times, and the need for support structures. Multi-axis 3D printing addresses these issues, allowing diverse filament deposition for improved mechanical characteristics, especially with anisotropic polymers. This paper proposed conformal slicer and toolpath for the multi-axis printer using Rhino CAD and

Grasshopper software. Initially, forward and inverse kinematics of the HAGE 1750L machine are derived. The iso curves are generated for nonlinear printing to mimic the geometric features and extrusion values are calculated using functional blocks in the Grasshopper. Users can select the different printing strategies, slicer parameters such as 2.5D, 3D, 5D, nozzle size, layer thickness, layer height etc. The slicer automatically generates the toolpath and G-code for printing. Three different objects are designed and printed to validate the proposed methodology. The compression test is conducted to find the structural strength of the components using UTM. The average force vs displacement graphs are plotted for all test samples. The 5D printing results for star and ellipse are recorded 11.2 and 19.3% more compared to other printing strategies. However, the results for ellipse 5D printing is not expected because it is subjected to more buckling during the test. Overall, the proposed slicer is helpful for multi-axis printing, and it is easy adoptable for other printers by changing its kinematic equations.

Acknowledgements This research work was supported by the Federal Ministry for Digital and Economic Affairs (BMDW) within the framework of "COIN Aufbau", 8th call of the Austrian Research Promotion Agency (FFG), iLEAD—project number 884136.

References

1. Anas, S., Khan, M.Y., Rafey, M., Faheem, K.: Concept of 5d printing technology and its applicability in the healthcare industry. Mater. Today: Proc. **56**, 1726–1732 (2022)
2. Fry, N.R., Richardson, R.C., Boyle, J.H.: Robotic additive manufacturing system for dynamic build orientations. Rapid Prototyp. J. **26**(4), 659–667 (2020)
3. Gardner, J., Nethercott-Garabet, T., Kaill, N., Campbell, R., Bingham, G.A., Engstrøm, D., Balc, N.: Aligning material extrusion direction with mechanical stress via 5-axis tool paths. In: 2018 International Solid Freeform Fabrication Symposium. University of Texas at Austin (2018)
4. Gul, J.Z., Sajid, M., Rehman, M.M., Siddiqui, G.U., Shah, I., Kim, K.H., Lee, J.W., Choi, K.H.: 3D printing for soft robotics–a review. Sci. Technol. Adv. Mater. **19**(1), 243–262 (2018)
5. Gunpinar, E., Armanfar, A.: Helical5am: Five-axis parametrized helical additive manufacturing. Journal of Materials Processing Technology **304**, 117565 (2022)
6. Haleem, A., Javaid, M., Vaishya, R.: 5d printing and its expected applications in orthopaedics. J. Clin. Orthopaed. Trauma **10**(4), 809–810 (2019)
7. Kafle, A., Luis, E., Silwal, R., Pan, H.M., Shrestha, P.L., Bastola, A.K.: 3D/4D printing of polymers: fused deposition modelling (FDM), selective laser sintering (SLS), and stereolithography (SLA). Polymers **13**(18), 3101 (2021)
8. Kaill, N., Campbell, R.I., Pradel, P., Bingham, G.: A comparative study between 3-axis and 5-axis additively manufactured samples and their ability to resist compressive loading. In: 2019 International Solid Freeform Fabrication Symposium. University of Texas at Austin (2019)
9. Kubalak, J.R., Wicks, A.L., Williams, C.B.: Exploring multi-axis material extrusion additive manufacturing for improving mechanical properties of printed parts. Rapid Prototyp. J. **25**(2), 356–362 (2018)
10. Lim, S., Buswell, R.A., Valentine, P.J., Piker, D., Austin, S.A., De Kestelier, X.: Modelling curved-layered printing paths for fabricating large-scale construction components. Addit. Manuf. **12**, 216–230 (2016)

11. Milewski, J.O., Lewis, G.K., Thoma, D., Keel, G., Nemec, R.B., Reinert, R.: Directed light fabrication of a solid metal hemisphere using 5-axis powder deposition. J. Mater. Process. Technol. **75**(1–3), 165–172 (1998)
12. Mishra, S.B., Khan, M.S., Banerjee, D., Kumar, M.A.: Journey from 2d to 5d printing: a brief review. Adv. Mechan. Ind. Eng. 95–101 (2022)
13. Ramos, B., Pinho, D., Martins, D., Vaz, A., Vicente, L.: Optimal 3d printing of complex objects in a 5–axis printer. Optim. Eng. 1–32 (2022)
14. Shembekar, A.V., Yoon, Y.J., Kanyuck, A., Gupta, S.K.: Trajectory planning for conformal 3D printing using non-planar layers. In: International Design Engineering Technical Conferences and Computers and Information in Engineering Conference, vol. 51722. American Society of Mechanical Engineers (2018)
15. Srinivas, G.L., Pawel, M., Marius, L., Faller, L.M., et al.: Supportless 5-axis 3d-printing and conformal slicing: a simulation-based approach. In: 2023 24th International Conference on Thermal, Mechanical and Multi-Physics Simulation and Experiments in Microelectronics and Microsystems (EuroSimE), pp. 1–7. IEEE (2023)
16. Wu, R., Peng, H., Guimbretière, F., Marschner, S.: Printing arbitrary meshes with a 5DOF wireframe printer. ACM Trans. Gr. (TOG) **35**(4), 1–9 (2016)

Comparative Study of the Kinematic Performance Indices for the 3-U(RPRGR)RU and the 3-URU Parallel Robots

Alexandru Oarcea, Elida-Gabriela Tulcan, Robert Kristof, and Erwin-Christian Lovasz

Abstract The research focuses on a novel three-degree-of-freedom parallel robot structure that is powered by using linear actuators, driving geared linkages. The main advantage of this design is the ability to avoid singular positions of first and second type as well as the large angular positions imposed on the links of the URU (U—Universal joint; R—Revolute joint) kinematic chains. The purpose of this article is to compare the kinematic performance of the 3-URU parallel robot with that of the robotic structure presented in this paper, the 3-U(RPRGR)RU parallel robot (P—Actuated prismatic joint; G—Geared transmission joint). To assess various configurations and compute the performance indices of the two given structures, and to compare them, MathWorks MATLAB was utilized. Analytical and numerical methods were used for determining the performance indices distributions. The obtained results show that the use of the actuating linkage improves the kinematic performance of the structure in the lower regions of the workspace.

Keywords Parallel robot · 3-U(RPRGR)RU parallel robot · 3-URU parallel robot · Kinematic performance analysis · Geared linkage · Performance indices

A. Oarcea (✉) · E.-G. Tulcan · R. Kristof · E.-C. Lovasz
Polytechnic University of Timisoara, 300006 Timisoara, Romania
e-mail: alexandru.oarcea@student.upt.ro

E.-G. Tulcan
e-mail: elida.tulcan@student.upt.ro

R. Kristof
e-mail: robert.kristof@upt.ro

E.-C. Lovasz
e-mail: erwin.lovasz@upt.ro

D. Pisla et al. (eds.), *Advances in Service and Industrial Robotics*, Mechanisms and Machine Science 157, https://doi.org/10.1007/978-3-031-59257-7_35

1 Introduction

Over the last few decades, robotics has developed dramatically, transforming industries, and expanding the possibilities of humankind. One type of robot that has shown a lot of promise as a solution for applications requiring high rigidity, speed, and precision is the parallel robot. Despite their excellent performance, classic parallel robots sometimes lack the flexibility to adapt to changing circumstances or compensate for unforeseen failures [1].

The initial purpose of parallel robots, developed in the 1970s and 1980s, was assembly and production. Most of these early parallel robots were used in environments for research and development [2]. Typically, they were enormous and costly. A growing number of jobs, including assembly, packing, manufacturing, and inspection, are being performed by parallel robots. Technology breakthroughs, such as the development of more powerful and trustworthy motors, have made parallel robots more competitive and reliable than before.

The 3-U$\underline{\text{R}}$U parallel robot is composed of one fixed platform, one mobile platform and three URU kinematic chains, connecting the two previously mentioned platforms. The arrangement of the universal joints from each end of the URU kinematic chains on the fixed and moving platform is made in such manner so that the rotation among the axis defined by the centers of the universal joint and the connected revolute joint of the URU kinematic chain is suppressed. In this configuration, the robot behaves like a 3-U$\underline{\text{P}}$U parallel robot [3], thus imposing purely translational movement for the mobile platform. For the actuation of the robotic structure, three R$\underline{\text{P}}$RGR (Revolute—Prismatic—Revolute—Geared transmission—Revolute joints) linkages were used, configuration in which the output revolute joint of the linkage is shared with the revolute joint of the URU kinematic chain, thus resulting a sufficient actuation for each kinematic chain so that the robotic structure is kinematically defined [2].

The kinematic performance indices are metrics that embody performance criteria like dexterity, manipulability, and ability to change direction of motion, that are expressed as dimensionless values, thus being a reliable method for comparing two or more robotic structures [4].

2 Description of the 3-U(R$\underline{\text{P}}$RGR)RU Parallel Robot

The structures studied in this paper are three-degrees-of-freedom (3DOF) spatial parallel robots, having three URU kinematic chains, a fixed platform, and a moving platform (Fig. 1).

The URU kinematic chain is the main kinematic unit the defines both robotic structures. In the case of 3-U(RPRGR)RU parallel robot, each chain's revolute joint is actuated by an RPRGR linkage [2].

For the U(R$\underline{\text{P}}$RGR)RU kinematic chain, the following notations were introduced to the joints and links for the purpose of analyzing the kinematic performance of the

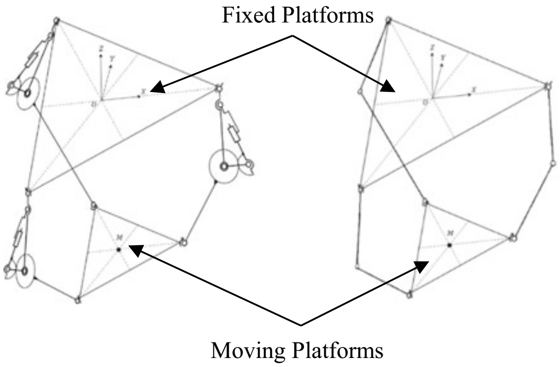

Fig. 1 Representation of the 3-U(R$\underline{\text{P}}$RGR)RU (left) and the 3-U$\underline{\text{R}}$U parallel robots (right)

two robots (Fig. 2): A_i—fixed universal joints; B_i—revolute joints; C_i—actuated prismatic joints; D_i—revolute joints; E_i—revolute joints; F_i—universal joints; 0—fixed platform; R—radius of the fixed platform; $\overline{1_i \ldots 5_i}$—moving links; $l_{\overline{1_i \ldots 5_i}}$—length of the moving links; 6—moving platform; r—radius of the moving platform [5].

In the case of the 3-U$\underline{\text{R}}$U parallel robot, the same notations were used since the main difference between the kinematic structures of the robots is the presence of the RPRGR linkage.

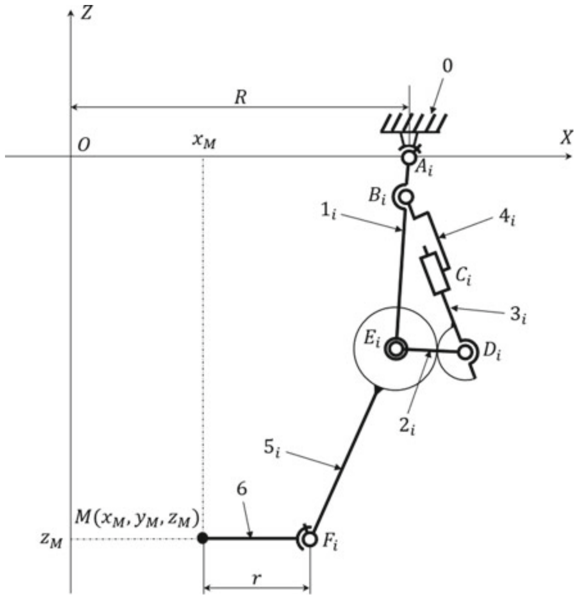

Fig. 2 Representation of U(R$\underline{\text{P}}$RGR)RU kinematic chain

3 Kinematic Performance Analysis

Determining the analytical Jacobian matrices that specify the kinematic behavior of the robotic structures is necessary to ascertain the kinematic performance of both structures [5]. Finding each robotic structure's transfer function will yield the Jacobian matrices. The behavior of the URU kinematic chain and the analytical connection that produces the driven angular position of the revolute joint are analyzed to derive the transfer functions of the robotic structures.

The transfer function of the 3-U(R$\underline{\text{P}}$RGR)RU parallel robot is [6]:

$$F_i(X, Q) = \left(x_{F_i} - x_{A_i}\right)^2 + \left(y_{F_i} - y_{A_i}\right)^2 + \left(z_{F_i} - z_{A_1}\right)^2 - l_{A_iF_i}^2 = 0,\ i = \overline{1\ldots3}. \tag{1}$$

where $X = \begin{bmatrix} x_M & y_M & z_M \end{bmatrix}$ are the coordinates of the moving platform, $Q = \begin{bmatrix} s_1 & s_2 & s_3 \end{bmatrix}$ are the generalized coordinates of the robot, particularly, the strokes of the linear actuators and where:

- x_{A_i}, y_{A_i} and z_{A_i}—coordinates of the centers of the universal joints A_i
- x_{F_i}, y_{F_i} and z_{F_i}—coordinates of the centers of the universal joints F_i.

Furthermore, the distance between the centers of the universal joints $l_{A_iF_i}$, $i = \overline{1\ldots3}$, can be expressed as:

$$l_{A_iF_i} = \sqrt{l_{1_i}^2 + l_{5_i}^2 - 2l_{1_i}l_{5_i}\cos\chi_i(\mathrm{s}_i)} \tag{2}$$

where the angular values imposed by the RPRGR linkage to the links of the URU kinematic chains, χ_i, is:

$$\chi_i(\mathrm{s}_i) = (1 - \rho)\cdot\psi_i(\mathrm{s}_i) + \rho\cdot\phi_i(\mathrm{s}_i) + \Delta\chi_i \tag{3}$$

where:

$$\psi_i(\mathrm{s}_i) = \mathrm{acos}\left(\frac{\mathrm{s}_i^2 - \mathrm{l}_{1_i}^2 - \mathrm{l}_{2_i}^2}{2\mathrm{l}_{1_i}\mathrm{l}_{2_i}}\right);\ \phi_i(\mathrm{s}_i) = \mathrm{acos}\left(\frac{\mathrm{l}_{2_i}^2 - \mathrm{l}_{1_i}^2 - \mathrm{s}_i^2}{2\mathrm{l}_{1_i}\mathrm{s}_i}\right);\ \rho = \pm\frac{r_3}{r_5} \tag{4}$$

- r_3 and r_5—radiuses of drive and driven gears.
- $\Delta\chi_i$—initial angular value between links 1_i and 5_i.

In the case of the 3-URU parallel robot, the transfer function is:

$$G_i(X, Q) = \left(x_{F_i} - x_{A_i}\right)^2 + \left(y_{F_i} - y_{A_i}\right)^2 + \left(z_{F_i} - z_{A_1}\right)^2 - l_{A_iF_i}^2 = 0 \tag{5}$$

where $X = \begin{bmatrix} x_M & y_M & z_M \end{bmatrix}$ are the coordinates of the moving platform, $Q = \begin{bmatrix} \chi_1 & \chi_2 & \chi_3 \end{bmatrix}$ are the generalized coordinates of the robot, particularly, the angular position of the links of each URU kinematic chain and where:

$$l_{A_i F_i} = \sqrt{l_{1_i}^2 + l_{5_i}^2 - 2 l_{1_i} l_{5_i} \cos \chi_i} \tag{6}$$

Kinematic performance indices are measurements that show the robot's kinematic performance, whereas performance indices are metrics that indicate the measurement and quantification of numerous performance traits [4].

The performance indices analyzed for the 3-U(R$\underline{\text{P}}$RGR)RU and 3-U$\underline{\text{R}}$U parallel robots are:

- Manipulability Index (μ)
- Condition Number (k)
- Local Conditioning Index (LCI)
- Minimum Singular Value (MSV)

To evaluate the previously presented indices of the robotic system, it is imposed to determine the Jacobian matrices since all the previously presented indices are computed based on them. The two partial Jacobian matrices for each robotic system are:

$$J_{q1} = \begin{bmatrix} \frac{\partial F_1(X,Q)}{\partial s_1} & \frac{\partial F_1(X,Q)}{\partial s_2} & \frac{\partial F_1(X,Q)}{\partial s_3} \\ \frac{\partial F_2(X,Q)}{\partial s_1} & \frac{\partial F_2(X,Q)}{\partial s_2} & \frac{\partial F_2(X,Q)}{\partial s_3} \\ \frac{\partial F_3(X,Q)}{\partial s_1} & \frac{\partial F_3(X,Q)}{\partial s_2} & \frac{\partial F_3(X,Q)}{\partial s_3} \end{bmatrix}$$
$$J_{q2} = \begin{bmatrix} \frac{\partial G_1(X,Q)}{\partial \chi_1} & \frac{\partial G_1(X,Q)}{\partial \chi_2} & \frac{\partial G_1(X,Q)}{\partial \chi_3} \\ \frac{\partial G_2(X,Q)}{\partial \chi_1} & \frac{\partial G_2(X,Q)}{\partial \chi_2} & \frac{\partial G_2(X,Q)}{\partial \chi_3} \\ \frac{\partial G_3(X,Q)}{\partial \chi_1} & \frac{\partial G_3(X,Q)}{\partial \chi_2} & \frac{\partial G_3(X,Q)}{\partial \chi_3} \end{bmatrix} \tag{7}$$

$$J_{x1} = \begin{bmatrix} \frac{\partial F_1(X,Q)}{\partial x_M} & \frac{\partial F_1(X,Q)}{\partial y_M} & \frac{\partial F_1(X,Q)}{\partial z_M} \\ \frac{\partial F_2(X,Q)}{\partial x_M} & \frac{\partial F_2(X,Q)}{\partial y_M} & \frac{\partial F_2(X,Q)}{\partial z_M} \\ \frac{\partial F_3(X,Q)}{\partial x_M} & \frac{\partial F_3(X,Q)}{\partial y_M} & \frac{\partial F_3(X,Q)}{\partial z_M} \end{bmatrix}$$
$$J_{x2} = \begin{bmatrix} \frac{\partial G_1(X,Q)}{\partial x_M} & \frac{\partial G_1(X,Q)}{\partial y_M} & \frac{\partial G_1(X,Q)}{\partial z_M} \\ \frac{\partial G_2(X,Q)}{\partial x_M} & \frac{\partial G_2(X,Q)}{\partial y_M} & \frac{\partial G_2(X,Q)}{\partial z_M} \\ \frac{\partial G_3(X,Q)}{\partial x_M} & \frac{\partial G_3(X,Q)}{\partial y_M} & \frac{\partial G_3(X,Q)}{\partial z_M} \end{bmatrix} \tag{8}$$

The Jacobian matrix is computed as $J = J_{x1}^{-1} \cdot J_{q1}$ for the 3-U(R$\underline{\text{P}}$RGR)RU parallel robot and $J = J_{x2}^{-1} \cdot J_{q2}$ for the 3-URU parallel robot.

Yoshikawa established a performance measure called the Manipulability Index (μ), which is determined as follows [7].

$$\mu = |det(J)| \tag{9}$$

To compute the Condition Number (k) it is required to compute the value of the matrix product $J \cdot J^T$ and their respective eigenvectors. Additionally, the Jacobian matrix's Condition Number is defined as the ratio of its maximum to minimal singular values, and it may be represented as follows [7]:

$$k = \sqrt{\frac{\lambda_{\max}}{\lambda_{\min}}} \tag{10}$$

Finding the condition number's reciprocal value yields the Local Conditioning Index (LCI) [8]:

$$LCI = \frac{1}{k} \tag{11}$$

Based on the unit length movement for every joint in the robotic structure, the Minimum Singular Value (MSV) shows the smallest change in the end-effector's speed that is feasible [9].

$$MSV = \min(\sigma_i) \tag{12}$$

4 Results

The performance indices of the 3-U(RPRGR)RU and 3-URU parallel robots were computed using MathWorks MATLAB, based on enforced building parameters and the calculated Jacobian matrix, to assess the kinematic performance indices. The performance indicators were evaluated using the following constructive parameters (Table 1).

- **Manipulability Index (μ)**

It is observed from Fig. 3 that both robotic structures have increased manipulability near the center of the workspace that gradually is reduced by the borders.

Table 1 Constructive parameters of the 3-U(R$\underline{\text{P}}$RGR)RU and 3-URU parallel robots

Parameter name	Symbol	Value	Unit
Fixed platform radius	R	250	mm
Moving platform radius	r	150	mm
Upper link length	l_{1_i}	100	mm
Lower link length	l_{5_i}	230	mm
Carrier link	l_{2_i}	100	mm
Stoke of the actuators	s_i	0–200	mm
Gear ratio	ρ	2	–

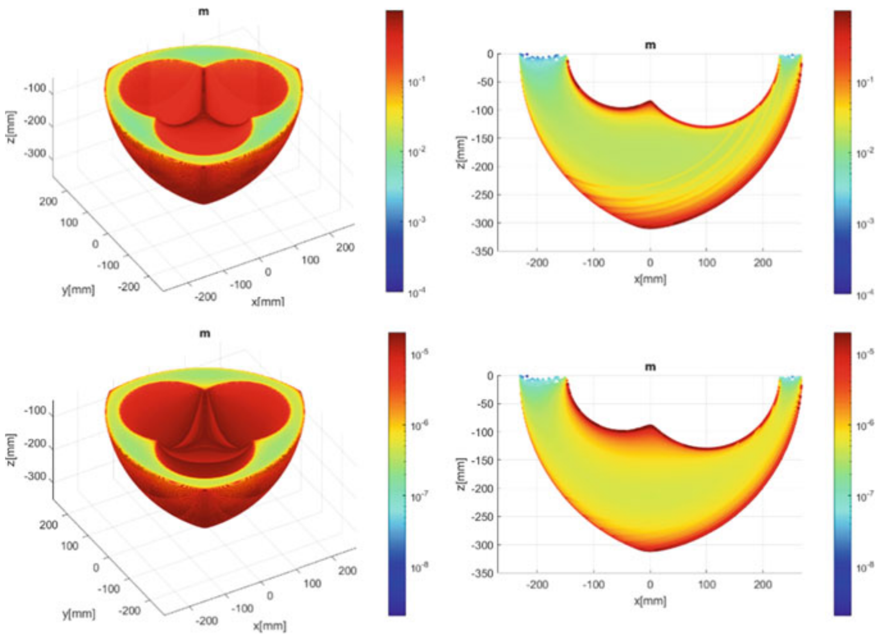

Fig. 3 Manipulability index (3-U(RPRGR)RU isometric view—top left, XZ section plane—top right, 3-URU isometric view—bottom left, XZ section plane—bottom right)

Furthermore, it is observed that the 3-U(RPRGR)RU robot has increased manipulability towards lower regions of the reachable workspace while the 3-URU robot has increased manipulability towards higher regions of the reachable workspace.

- **Condition Number (k)**

It is observed from Fig. 4 that both robotic structures are dexterous inside the reachable workspace. Furthermore, it is observed that the 3-U(RPRGR)RU parallel robot has increased dexterity towards the lateral regions of the reachable workspace.

- **Local Conditioning Index (LCI)**

It is observed from Fig. 5 that both robotic structures are well conditioned inside all the reachable workspace. Furthermore, it is observed that the 3-U(RPRGR)RU parallel robot is better conditioned towards the higher reachable regions of the workspace, while the 3-URU parallel robot is better conditioned towards the lower and lateral reachable regions of the workspace.

- **Minimal Singular Value (MSV)**

It is observed from Fig. 6 that both robotic structures have increased abilities of changing the direction of motion in the central regions of the workspace that is gradually reduced by approaching the side borders of the workspace. Furthermore,

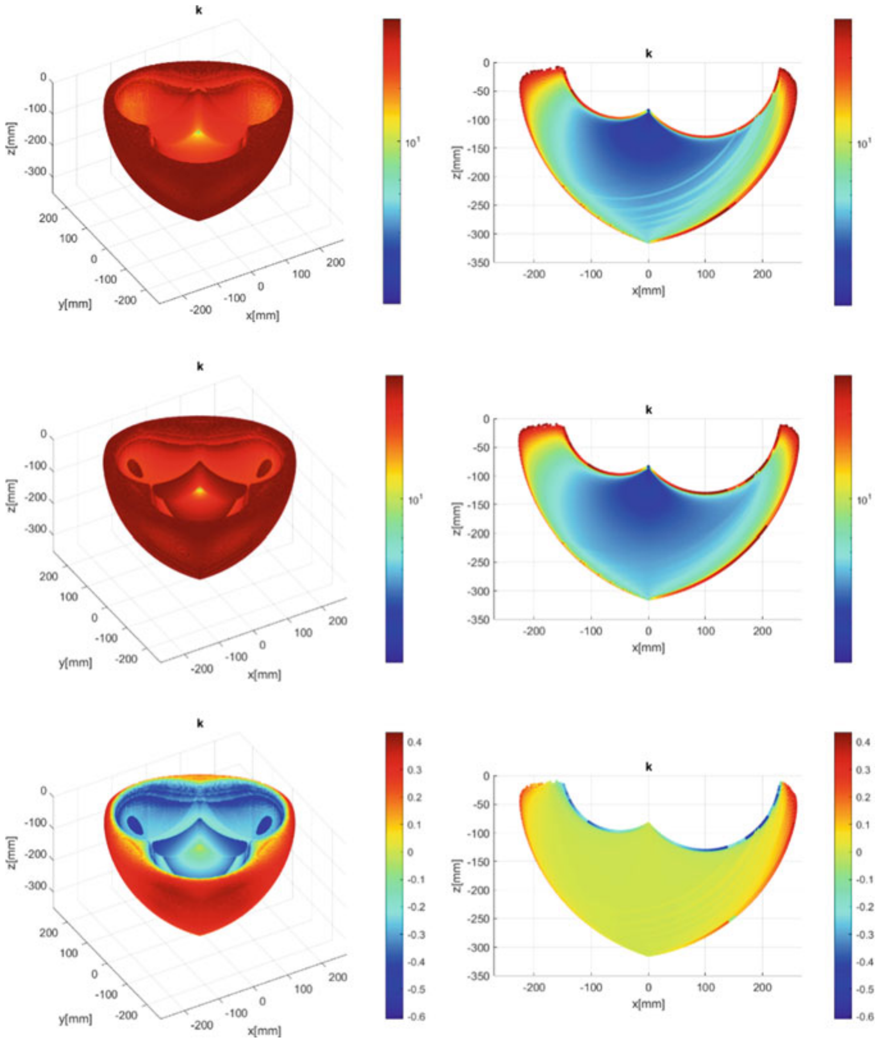

Fig. 4 Condition Number (3-U(R$\underline{\text{P}}$RGR)RU isometric view—top left, XZ section plane—top right, 3-U$\underline{\text{R}}$U isometric view—middle left, XZ section plane—middle right, delta isometric view –bottom left, XZ section plane—bottom right)

it is observed that the 3-U(R$\underline{\text{P}}$RGR)RU parallel robot has increased potential of changing direction in the lower regions of the reachable workspace, while the 3-U$\underline{\text{R}}$U parallel robot has increased potential of changing direction in the higher regions of the reachable workspace.

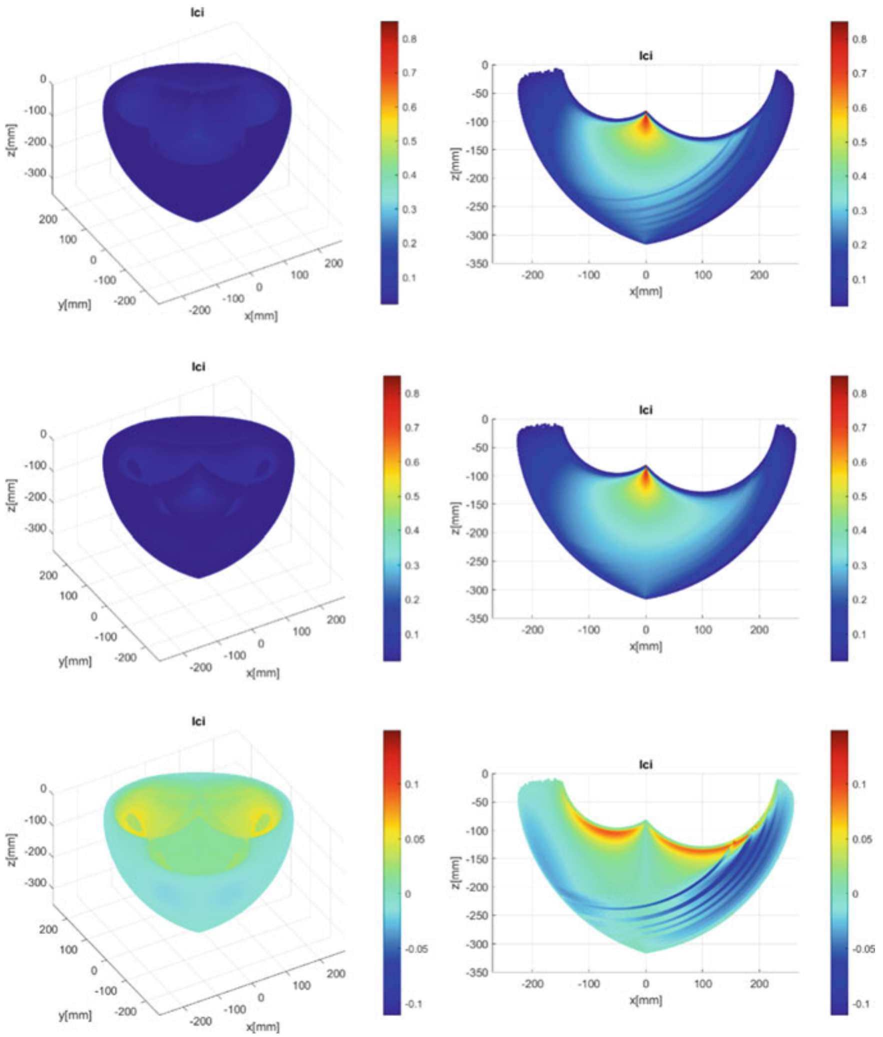

Fig. 5 Local Conditioning Index (3-U(RPRGR)RU isometric view—top left, XZ section plane—top right, 3-URU isometric view—middle left, XZ section plane—middle right, delta isometric view –bottom left, XZ section plane—bottom right)

5 Conclusions

In this paper, kinematic performance of the 3-U(RPRGR)RU and 3-URU parallel robots was analyzed and compared, based on the transfer functions of the 3-U(RPRGR)RU and 3-URU parallel robots, and the Jacobian matrices. MathWorks MATLAB was used to determine the numerical values of the performance indices inside the reachable workspace and compare the result of the two structures.

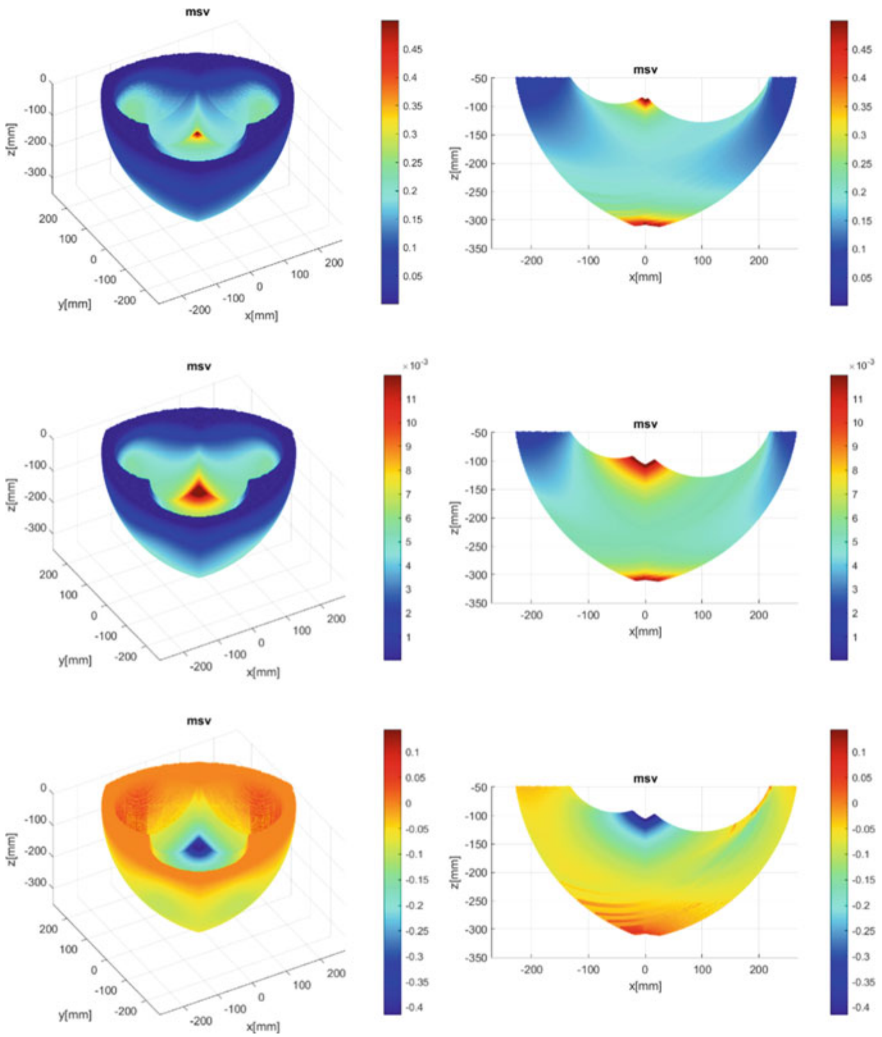

Fig. 6 Minimal Singular Value (3-U(RPRGR)RU isometric view—top left, XZ section plane—top right, 3-URU isometric view—middle left, XZ section plane—middle right, delta isometric view –bottom left, XZ section plane—bottom right)

From the presented results, it is concluded that the use of RPRGR linkage for the actuation of the revolute joint of each URU kinematic chain, improves the kinematic performance of the robotic structures in the lower regions of the reachable workspace, thus making such structures behave better in real case applications, like manipulations, assembly, etc.

Further research is proposed to compare the dynamic performance measures of the two presented structures and investigate performance-cost metrics for the physical implementation of the two presented structures.

References

1. Liu, X., Wan, B., Liu, Y., Chen, R., Yao, J., Zhao, Y.: Kinematic performance analysis and dimensional optimization of new symmetric parallel mechanism 6RPS with multi-redundant actuations. J. Mech. Robot. (2024). https://doi.org/10.1115/1.4063873
2. Oarcea, A., Tulcan, E.G., Lovasz, E.C.: Kinematic analysis of the 3-U(RPRGR)RU parallel robot. In: Laribi, M.A., Nelson, C.A., Ceccarelli, M., Zeghloul, S. (eds.) New Advances in Mechanisms, Transmissions and Applications. MeTrApp 2023. Mechanisms and Machine Science, vol. 124. Springer, Cham (2023). https://doi.org/10.1007/978-3-031-29815-8_19
3. Hu, B., Yao, Y., Wu, P., Lu, Y.: A comparison study of two 3-UPU translational parallel manipulators. Int. J. Adv. Rob. Syst. **10**(4), 190 (2013). https://doi.org/10.5772/53394
4. Patel, S., Sobh, T.: Manipulator performance measures—a comprehensive literature survey. J. Intell. Robot. Syst. **77**, 1–24 (2014). https://doi.org/10.1007/s10846-014-0024-y
5. Lovasz, E.-C., Modler, K.-H., Pop, C., Pop, F., Mărgineanu, D.T., Maniu, I.: Type synthesis and analysis of geared linkages with linear actuation. Mechanika **24**(1), 108–114 (2018)
6. Demjen, T., Lovasz, E.-C., Ceccarelli, M., Sticlaru, C., Lupuţi, A.-M.-F., Oarcea, A., Silaghi-Perju, D.-C.: Design of the five-bar linkage with singularity-free workspace. Robotica **41**(11), 3361–3379 (2023). https://doi.org/10.1017/S0263574723001042
7. Tondu, B.: A zonotope-based approach for manipulability study of redundant robot limbs. Int. J. Humanoid Robot. **10**, 1350023 (2013). https://doi.org/10.1142/s0219843613500230
8. Gosselin, C., Angeles, J.: A global performance index for the kinematic optimization of robotic manipulators. ASME. J. Mech. Des. **113**(3), 220–226 (1991). https://doi.org/10.1115/1.2912772
9. Angeles, J., López-Cajún, C.: Kinematic isotropy and the conditioning index of serial robotic manipulators. Int. J. Robot. Res. IJRR **11**, 560–571 (1992). https://doi.org/10.1177/027836499201100605

Kinematic Analysis of the Seven-Bar Linkage 7-PR(RRRR)RP Used for Medical Disinfection Robot

Elida-Gabriela Tulcan, Carmen Sticlaru, Alexandru Oarcea, Melania Olivia Sandu, and Erwin-Christian Lovasz

Abstract The paper presents the type synthesis and analysis of a seven-bar linkage. The type synthesis equations lead to the computation of the symmetrical seven-bar linkage with both prismatic and revolute joints. The analysis of the mechanism shows the high variation of both its stroke and its height from the minimum to the maximum configuration. Since current disinfection robots cannot operate in multiple configurations and only disinfect large areas, the purpose of the paper is to demonstrate how folding mechanisms structures are more useful for the design of medical disinfection robots. Considering their structure allows multiple configurations, they can be used to disinfect different types of areas from the medical environment.

Keywords Seven-bar linkages · Folding mechanisms · Kinematic analysis · Medical robots · Disinfection robots

1 Introduction

The study of the seven-bar linkages has been only briefly conducted, even if they find applicability in a wide range of applications, from industrial applications to medical applications. For instance, examples include a seven-bar mechanical press with

E.-G. Tulcan (✉) · C. Sticlaru · A. Oarcea · M. O. Sandu · E.-C. Lovasz
Politehnica University of Timişoara, 300006 Timişoara, Romania
e-mail: elida.tulcan@student.upt.ro

C. Sticlaru
e-mail: carmen.sticlaru@upt.ro

A. Oarcea
e-mail: alexandru.oarcea@student.upt.ro

M. O. Sandu
e-mail: melania.sandu@upt.ro

E.-C. Lovasz
e-mail: erwin.lovasz@upt.ro

D. Pisla et al. (eds.), *Advances in Service and Industrial Robotics*, Mechanisms and Machine Science 157, https://doi.org/10.1007/978-3-031-59257-7_36

hybrid-driven mechanism for deep drawing [1, 2], a geometric and kinematic analysis of a seven-bar three-fixed-pivoted-compound-joint mechanism [3], an analytical method to synthesize a seven-bar slider mechanism with variable topology for motion between two dead-center positions [4] and last but not least, a novel approach to design a seven-bar linkage for pure-rolling cutting by optimizing centrodes [5].

The considered seven-bar linkage is intended to be further used in the development of a reconfigurable medical disinfection robot for the hard-to-reach areas of the medical environment, while the paper itself is part of a series of papers [6, 7] where multiple types of mechanisms are analyzed in order to establish the optimal folding mechanism structure for a disinfection robot. The current medical disinfection robots cannot operate in different configurations, thus being difficult to perform an effective disinfection process in the areas where the space is limited.

The paper is structured in 5 sections: Sect. 1—Introduction, Sect. 2—Type synthesis of the seven-bar linkage, where the symmetrical 7-PR(RRRR)RP linkage was selected, Sect. 3—Kinematic analysis of the symmetrical seven-bar linkage, where the transmission equation was computed and the y_M coordinate of the characteristic point M and the strokes were determined as solution of the forward and inverse kinematics, Sect. 4—Numerical example, where the results of the kinematic analysis are characterized in order to better exemplify the usability of the design and Sect. 5—Conclusions, where all the obtained results and future work are highlighted.

2 Type Synthesis of the Seven-Bar Linkage

The type synthesis, also known as the determination of all mechanism structures from the kinematic point of view, was shown detailed in [8, 9] and particularly in [10].

By imposing the mechanism degree of freedom (DOF) (M = 2), the number of kinematic loops (N = 2) and the number of the kinematic pairs with DOF = 2 ($e_4 = 0$, where e_4—number of kinematic pairs with DOF = 4), it results, from the condition to have a constrain motion of a mechanism, the correlation between the number of elements n and the number of kinematic pairs e_1 with DOF = 1:

$$e_1 = \frac{3 \cdot n - 5}{2} \in \mathrm{N} \tag{1}$$

The second convenable solution of the Eq. (1) is:

$$n = 7 \rightarrow e_1 = 8 \tag{2}$$

which is relevant for our study of the seven-bar linkage.

The number of elements of different ranks follow from the Diophantine equation system:

$$\begin{cases} 7 = n_2 + n_3 \\ 16 = 2 \cdot n_2 + 3 \cdot n_3 \end{cases} \tag{3}$$

with the solution:

$$n_2 = 5(\text{binary elements}), n_3 = 2(\text{ternary elements}) \tag{4}$$

By applying the Franz Reuleaux method for the kinematic chain of the seven-bar linkage using 6 revolute joints and 2 prismatic joints, we obtain the linkage structures presented in Fig. 1. This method consists in successively considering an element as frame, two elements (jointed in frame) as drive elements and one element as driven element or one joint as characteristic point. The proposed notation for this type of linkage chain is 7-PR(RRRR)RP, where R—revolute joint and P—prismatic joint, while in the brackets is indicated the parallel connected kinematic chain.

Additionally, the developed linkages also contain in-between the brackets the considered frame element (ex. (e)) and underlined the drive joints, which in this case are the prismatic joints (ex. PR(RRRR)RP(a)). The similar structures were removed in the development.

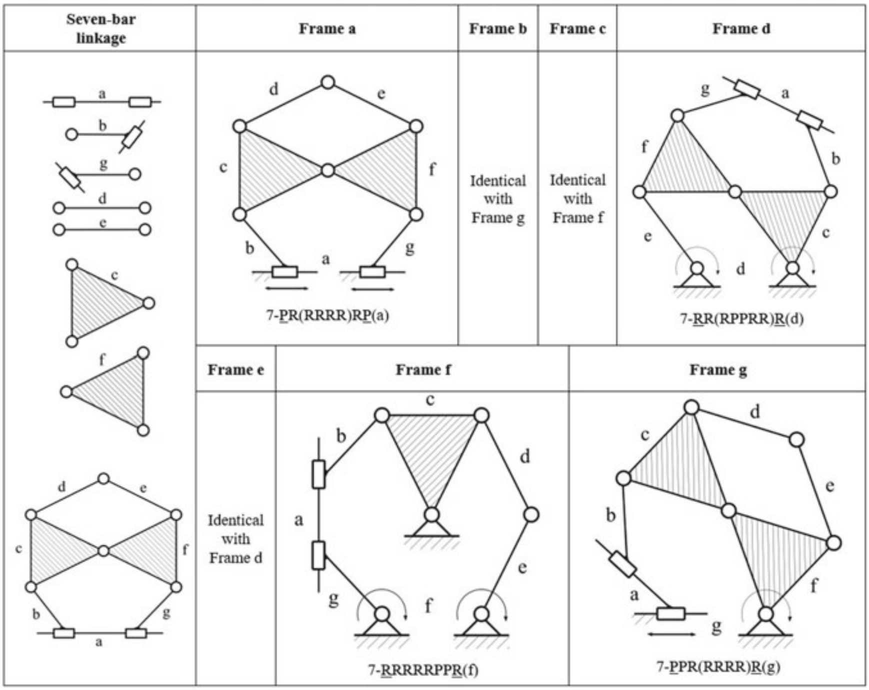

Fig. 1 Development by Reuleaux method of the seven-bar linkage

3 Kinematic Analysis of the Symmetrical Seven-Bar Linkage

The analyzed seven-bar linkage 7-$\underline{\mathrm{P}}$R(RRRR)R$\underline{\mathrm{P}}$(a), which is presented in Fig. 2, was chosen from the developed type synthesis because of its symmetrical design to the y axes.

Besides that, due to functional requirements, the lengths of the drive elements l_3 ($l_{31} + l_{32}$) and l_6 ($l_{61} + l_{62}$), as well as the lengths of the driven elements l_4 and l_5 were chosen to be equal ($l_{31} = l_{32} = l_{61} = l_{62},\ l_4 = l_5$).

The positional angles φ_3 (equal to φ_6) and φ_4 (equal to φ_5) can be written as a dependency to strokes using the following equations:

$$\varphi_3(s) = \arccos\left(\frac{s}{l_{31} + l_{32}}\right) \tag{5}$$

$$\varphi_4(s) = \arccos\frac{l_{32} \cdot s}{l_4 \cdot (l_{31} + l_{32})} \tag{6}$$

The vectorial loop equation from the frame joints A_0 and H_0 to the characteristic point M is:

$$-s + l_{31} \cdot e^{i \cdot \varphi_3} + l_4 \cdot e^{i \cdot \varphi_4} = i \cdot y_M \tag{7}$$

The following transmission equation was obtained by separating the terms which contain the angle φ_3 from the terms which contain the angle φ_4 in Eq. (7), writing

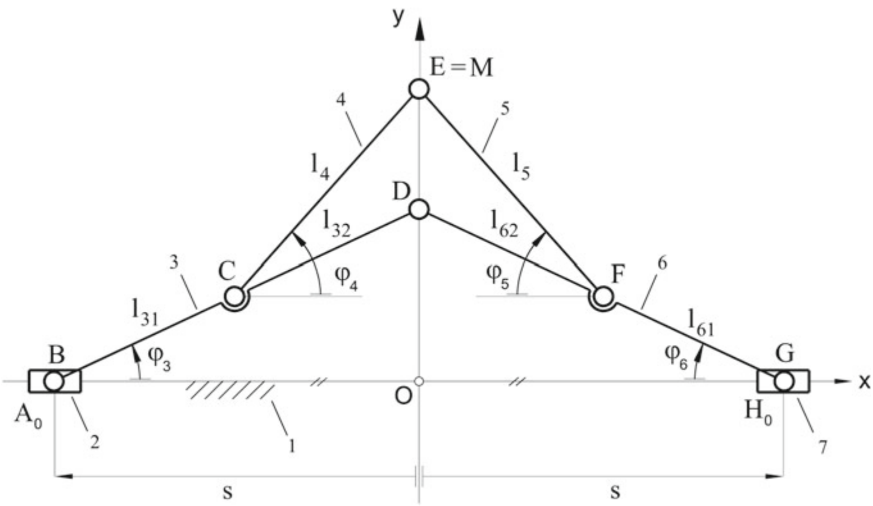

Fig. 2 Kinematic scheme of the symmetrical seven-bar linkage 7-$\underline{\mathrm{P}}$R(RRRR)R$\underline{\mathrm{P}}$

its complex conjugate equation and multiplying them accordingly:

$$F(s, y_M) : 0 = 2 \cdot \mathrm{s} \cdot l_{31} \cdot cos\varphi_3 + 2 \cdot y_{\mathrm{M}} \cdot l_{31} \cdot sin\varphi_3 \\ - l_{31}^2 - s^2 - y_{\mathrm{M}}^2 + l_4^2 \tag{8}$$

3.1 Forward Kinematics

The forward kinematics considers the length of the elements and the stroke s as known parameters, while the coordinates of the characteristic point M must be computed.

By writing Eq. (8) with y_M being the unknown, it results the following form:

$$F(s, y_M) : 0 = y_M^2 + A_1(s) \cdot y_M + B_1(s) \tag{9}$$

where the coefficients are:

$$A_1(s) = -2 \cdot l_{31} \cdot sin\varphi_3 = -2 \cdot l_{31} \cdot \sqrt{1 - \left(\frac{s}{l_{31} + l_{32}}\right)^2}$$
$$B_1(s) = s^2 + l_{31}^2 - l_4^2 - 2 \cdot \mathrm{s} \cdot l_{31} \cdot cos\varphi_3 \\ = s^2 + l_{31}^2 - l_4^2 - 2 \cdot \mathrm{s} \cdot l_{31} \cdot \left(\frac{s}{l_{31} + l_{32}}\right) \tag{10}$$

The solution of the forward kinematics is:

$$y_M = -\sqrt{(l_4 \cdot l_{31} + l_4 \cdot l_{32} + l_{32} \cdot \mathrm{s}) \cdot (l_4 \cdot l_{31} + l_4 \cdot l_{32} - l_{32} \cdot \mathrm{s})} \\ + l_{31}^2 \cdot \sqrt{1 - \left(\frac{s}{l_{31} + l_{32}}\right)^2} + \frac{l_{31} \cdot l_{32} \cdot \sqrt{1 - \left(\frac{s}{l_{31}+l_{32}}\right)^2}}{l_{31} + l_{32}} \tag{11}$$

3.2 Inverse Kinematics

The inverse kinematics considers the lengths of the elements and the coordinates of the characteristic point M known, while the strokes must be determined.

By writing Eq. (8) with s being the unknown, it results the following form:

$$F(s, y_M) : 0 = \mathrm{s}^2 + A_2(y_M) \cdot \mathrm{s} + B_2(y_M) \tag{12}$$

where the coefficients are:

$$A_2(y_M) = -2 \cdot l_{31} \cdot cos\varphi_3 = -2 \cdot l_{31} \cdot \left(\frac{s}{l_{31}+l_{32}}\right)$$
$$B_2(y_M) = y_M^2 + l_{31}^2 - l_4^2 - 2 \cdot y_M \cdot l_{31} \cdot sin\varphi_3$$
$$= y_M^2 + l_{31}^2 - l_4^2 - 2 \cdot y_M \cdot l_{31} \cdot \sqrt{1-\left(\frac{s}{l_{31}+l_{32}}\right)^2} \tag{13}$$

The solution of the inverse kinematics is:

$$s = \frac{\sqrt{\begin{array}{c} l_{31}^4 - l_{31}^2 \cdot y_{\mathrm{M}}^2 - l_{32}^2 \cdot y_{\mathrm{M}}^2 - l_4^2 \cdot l_{31}^2 + l_4^2 \cdot l_{32}^2 - l_{31}^2 \cdot l_{32}^2 + \\ +2 \cdot l_{31} \cdot y_M \cdot \sqrt{l_4^2 \cdot l_{31}^2 - l_4^2 \cdot l_{32}^2 - l_{31}^2 \cdot l_{32}^2 + l_{32}^4 + l_{32}^2 \cdot y_{\mathrm{M}}^2} \end{array}}}{l_{31}-l_{32}} \tag{14}$$

In order to avoid the type I and type II singularities, it is mandatory that both partial derivatives of the transmission function $\mathrm{F}(\mathrm{s}, \mathrm{y_M})$ to be non-zero values.

$$\frac{\partial F(s, y_M)}{\partial s} = 2 \cdot \mathrm{s} - \frac{4 \cdot \mathrm{s} \cdot l_{31}}{l_{31}+l_{32}} + \frac{2 \cdot l_{31} s \cdot y_{\mathrm{M}}}{\sqrt{1-\left(\frac{s}{l_{31}+l_{32}}\right)^2} \cdot (l_{31}+l_{32})^2} \neq 0 \tag{15}$$

$$\frac{\partial F(s, y_M)}{\partial y_M} = 2 \cdot y_M - 2 \cdot l_{31} \cdot \sqrt{1-\left(\frac{s}{l_{31}+l_{32}}\right)^2} \neq 0 \tag{16}$$

4 Numerical Example

Due to functional requirements, the strokes was chosen to range between 50 mm and ($l_{31} + l_{32}$—10) mm, while the lengths of the elements were chosen to be $l_{31} = l_{32} = l_{61} = l_{62} = 120$ mm and $l_4 = l_5 = 170$ mm. Considering these values, the characteristic point M has the coordinates (0, 159) in the minimum configuration and the coordinates (0, 285) in the maximum configuration.

By solving Eq. (5) we obtain positional angle φ_3 range between 16.5° in the minimum configuration and 77.9° in the maximum configuration. Figure 3 presents the dependency between the positional angle φ_3 and the strokes. As it can be observed, it is a linear dependency, with the positional angle φ_3 increasing together with the strokes.

By solving Eq. (6) we obtain positional angle φ_4 range between 47.4° in the minimum configuration and 81.5° in the maximum configuration. Figure 4 presents the dependency between the positional angle φ_4 and the strokes. As it can be observed, this is also a linear dependency, with the positional angle φ_4 increasing together with the strokes.

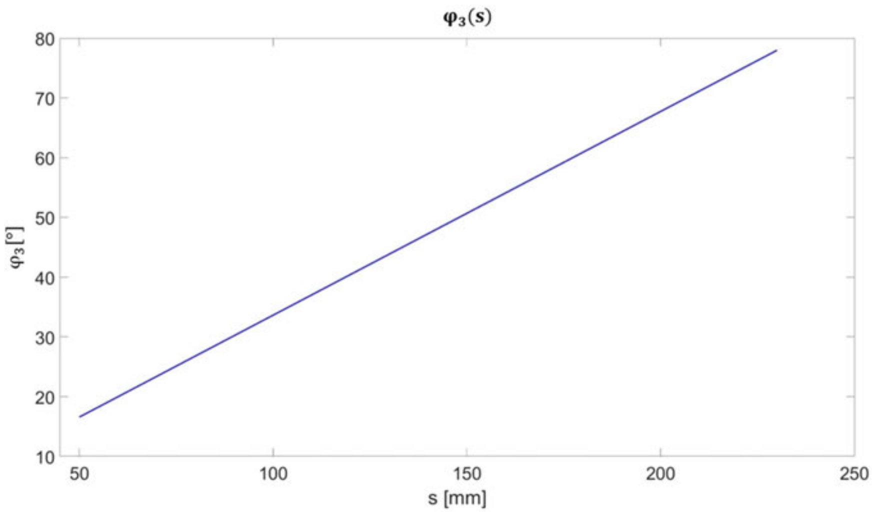

Fig. 3 Positional angle φ_3 as a dependency of strokes

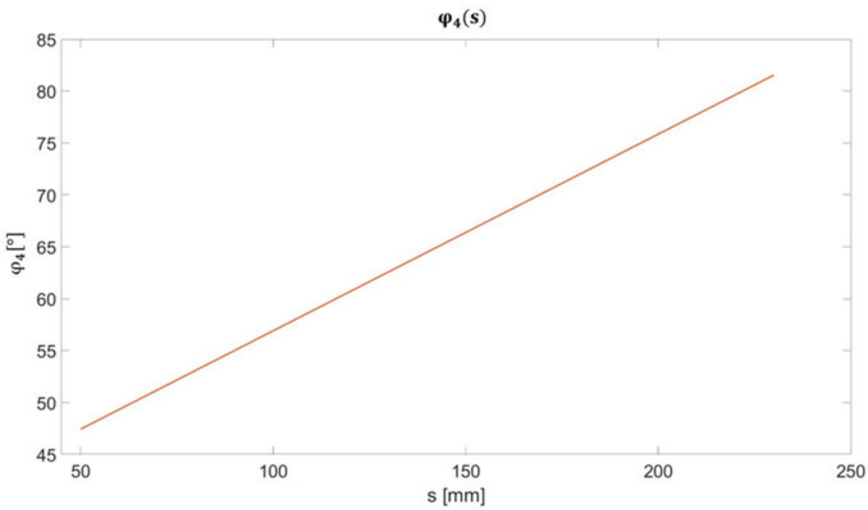

Fig. 4 Positional angle φ_4 as a dependency of strokes

Numerical values related to the minimum configuration of the mechanism are presented in Table 1, while numerical values related to the maximum configuration of the mechanism are presented in Table 2.

Figure 5 presents the symmetrical seven-bar linkage in its minimum and maximum configuration. As it can be observed, all configurations inside the workspace can be reached without having collinearity between the neighboring elements.

Table 1 Design values of the main parameters in the minimum configuration

Parameter	Value
s_{max}	50 mm
$\varphi_{3min} = \varphi_{6min}$	16.5°
$\varphi_{4min} = \varphi_{5min}$	47.4°
x_{min}	0 mm
y_{min}	159 mm

Table 2 Design values of the main parameters in the maximum configuration

Parameter	Value
s_{min}	230 mm
$\varphi_{3max} = \varphi_{6max}$	77.9°
$\varphi_{4max} = \varphi_{5max}$	81.5°
x_{max}	0 mm
y_{max}	285 mm

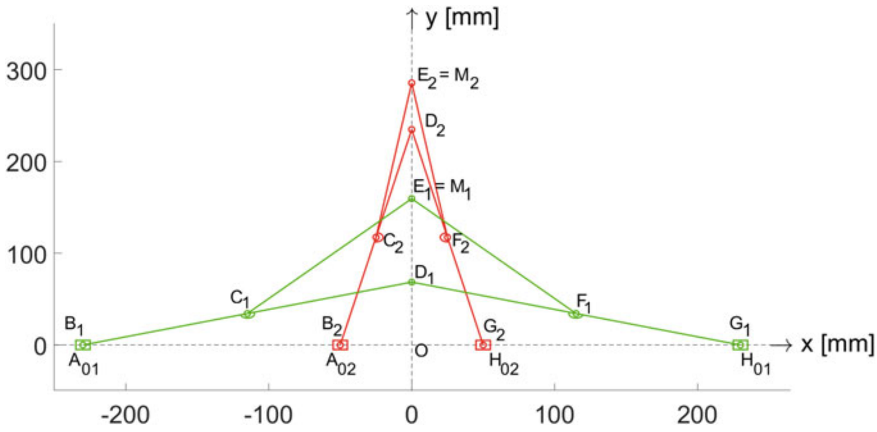

Fig. 5 The seven-bar linkage in its minimum (green) and maximum (red) configuration

5 Conclusions

The paper presented the type synthesis, kinematic analysis and numerical example of a symmetrical seven-bar linkage with revolute and prismatic joints. The numerical example chapter presented the two extreme configurations of the mechanism, concluding that all configurations inside the workspace can be reached without having singularities in the total workspace.

The presented structure is further intended to be used to design a medical disinfection robot with a folding mechanism. The main reason behind considering this type of mechanism, as also highlighted in the numerical example section, is because it allows a large height and stroke variation between its extreme configurations, therefore being a good choice for disinfecting both the hard-to-reach areas and the accessible areas from the medical environment and other facilities.

Further studies will focus on other feasible mechanism structures for a medical disinfection robot with folding mechanism, such as four-bar linkages, five-bar linkages, six-bar linkages and other seven-bar linkages, as well as on comparing them in order to establish which one is more appropriate. Moreover, a prototype of the medical disinfection robot will also be developed in order to perform experimental tests.

References

1. Li, H., Zhang, Y.: Seven-bar mechanical press with hybrid-driven mechanism for deep drawing; Part 1: kinematics analysis and optimum design. J. Mech. Sci. Technol. **24**, 2153–2160 (2010)
2. Li, H., Zhang, Y.: Seven-bar mechanical press with hybrid-driven mechanism for deep drawing; part 2: dynamic modeling and simulation. J. Mech. Sci. Technol. **24**, 2161–2167 (2010)
3. Wei, G., Dai, J.S.: Geometric and kinematic analysis of a seven-bar three-fixed-pivoted compound-joint mechanism. Mech. Mach. Theory **45**, 170–184 (2010)
4. Daivagna, U.M., Balli, S.S.: Synthesis of a seven-bar slider mechanism with variable topology for motion between two dead-center positions. In: Proceedings of the World Congress on Engineering 2010, pp. 1454–1459, U.K. (2010)
5. Liu, B., Ma, Y., Wang, D., Bai, S., Li, Y., Li, K.: Kinematic design of a seven-bar linkage with optimized centrodes for pure-rolling cutting. Mathematic. Probl. Eng. 1–11 (2017)
6. Tulcan, E.-G., Oarcea, A., Lovasz, E.-C.: Analytical synthesis of the seven-bar linkage 7-RR(RRRR)RR used for medical disinfection robot. In: Petuya, V., Quaglia, G., Parikyan, T., Carbone, G. (eds.) Proceedings of I4SDG Workshop 2023. I4SDG 2023. Mechanisms and Machine Science, vol 134. Springer, Cham (2023)
7. Tulcan, E.-G., Sticlaru, C., Lovasz, E.-C.: Design of a medical robot with folding mechanism used for disinfection in the hard-to-reach areas. In: Tarnita, D., Dumitru, N., Pisla, D., Carbone, G., Geonea, I. (eds.) New Trends in Medical and Service Robotics. MESROB 2023. Mechanisms and Machine Science, vol 133. Springer, Cham (2023)
8. Freudenstein, F., Dobrjanskyj, L.: On a theory for the type synthesis of mechanisms. In: Görtler, H. (eds.) Proceedings of the 11th International Congress of Applied Mechanics, Applied Mechanis, pp. 420–428. Springer, Germany (1966)
9. Luck, K., Modler, K.-H.: Getriebetechnik. Analyse—Synthese—Optimierung, Akademie-Verlag, Berlin (1990)
10. Demjen, T., Lovasz, E.-C., Ceccarelli, M., Sticlaru, C., Lupuți, A.-M.-F.: Analytical synthesis of five-bar linkage used for 3D printer structure. In: Niola, V., Gasparetto, A., Quaglia, G., Carbone, G. (eds.) The International Conference of IFToMM ITALY, Mechanisms and Machine Science, vol. 112, pp. 105–113. Springer, Italy (2022)

Experimental Evaluation of a Collision Avoidance Control for Redundant Manipulators

Giacomo Palmieri, Luca Carbonari, Daniele Costa, Matteo Forlini, Federico Neri, and Cecilia Scoccia

Abstract This paper presents the implementation and testing of an obstacle avoidance algorithm for redundant kinematics manipulators, focusing on its experimental implementation on the KUKA LBR iiwa robot. The algorithm, previously validated in simulations, is based on the null space method and a closed-loop inverse kinematics control law, enabling real-time updates of the robot's motion to avoid collisions with dynamic obstacles. The document outlines the hardware/software architecture of the robotic system, featuring an external controller implemented on a standard PC communicating with the robot controller via TCP/IP protocol. The control execution rate ensures a smooth system control. A test case is presented to assess the method's applicability to a real system and discuss key implementation parameters.

Keywords Collaborative robotics · Collision avoidance · Human–robot collaboration · Redundant manipulators

1 Introduction

In collaborative robotic cells, when an operator enters the robot's workspace, the manipulator often needs to decrease its speed and halt immediately upon direct contact. This precautionary measure, while necessary for safety, can result in a slowdown in production. Even if reduced speed is mandatory, obstacle avoidance strategies can be a way to avoid the stop of the robot when the risk of collision verifies, thus mitigating the loss of production of collaborative robotic cells. Numerous papers in the literature discuss obstacle avoidance for mobile robots, a widely encountered challenge. A more intricate issue involves collision avoidance for industrial manipulators, which face workspace constraints and singularities. Here, redundant manipulators provide increased dexterity compared to conventional 6-degree-of-freedom (DOF) robots. This enhances the potential for developing task-specific control strategies

G. Palmieri · L. Carbonari · D. Costa · M. Forlini · F. Neri (✉) · C. Scoccia
Department of Industrial Engineering and Mathematical Sciences, Polytechnic University of Marche, Ancona, Italy
e-mail: federico.neri@pm.univpm.it

D. Pisla et al. (eds.), *Advances in Service and Industrial Robotics*, Mechanisms and Machine Science 157, https://doi.org/10.1007/978-3-031-59257-7_37

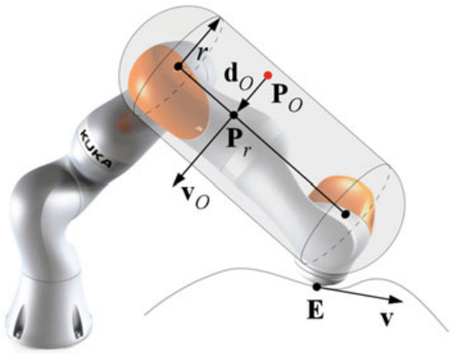

Fig. 1 Linear velocity of the end-effector **E** and of the control point $\mathbf{P}_r$ closest to the obstacle $\mathbf{P}_O$

that leverage the extra degrees of freedom. [1]. A proficient control strategy should enable real-time updates of the robot's motion to compensate for moving obstacles or new obstacles entering the workspace. Simultaneously, it should incorporate a redundancy control strategy to leverage the manipulator's dexterity for avoiding collisions with internal points of its kinematic chain. Additionally, it should integrate a robust technique for avoiding singular configurations during motion. Several examples of such kind of control laws can be found in literature, mainly based on the generation of a repulsive velocity to be assigned to the point of the kinematic chain of he manipulator which is closest to an obstacle [5, 9]. Such an approach is typically applied to redundant manipulators [7, 11], where additional tasks can be assigned maintaining the trajectory of the end-effector. For example, a collision between an obstacle and the robot's elbow can be avoided without changing the motion of the end-effector selecting between the infinite inverse kinematics solutions available for each pose of the end-effector. Moreover, the magnitude of the repulsive velocity can be conceptualized as a function of various parameters beyond just the positions of obstacles and the robot. For instance, it may consider factors such as the relative speed [8] or other energetic criteria [12]. The authors studied this kind of approach in [10] for a simplified planar case, and then developed it to be implemented to the KUKA LBR iiwa manipulator [6], which is the 7-DOF serial collaborative robot represented in Fig. 1. A strategy employing the least-square damped method is utilized to invert the Jacobian matrices, ensuring avoidance of passages through points that are dangerously close to singular configurations.

2 Control Strategy

Basic principles of the control strategy are outlined in this section; for a more detailed discussion, please refer to the original publication[6]. The velocity kinematics of a generic redundant manipulator can be written as $\dot{\mathbf{x}} = \mathbf{J}\dot{\mathbf{q}}$, being $\dot{\mathbf{q}}$ the vector of joint velocities and $\mathbf{J}$ the $6 \times n$ Jacobian (with n number of the joints of the manipulator,

$n \geq 6$). The vector of joint positions is $\mathbf{q} = \left[q_1 \ldots q_n\right]^T$ where $q_1 \ldots q_n$ are the n joints variables of the kinematic chain. The inverse of the Jacobian $\mathbf{J}$ of the redundant system can be obtained as a damped inverse:

$$\mathbf{J}^* = \mathbf{J}^T (\mathbf{J}\mathbf{J}^T + \lambda^2 \mathbf{I})^{-1} \tag{1}$$

where λ is the damping factor, defined as a function of the smallest singular value of the Jacobian matrix [2, 6]. Due to redundancy, the inverse kinematics problem is not uniquely defined. Using a Closed-Loop Inverse Kinematics (CLIK) control law and given a trajectory planned in terms of Cartesian-space velocity $\dot{\mathbf{x}}$, the inverse kinematics problem can be solved as:

$$\dot{\mathbf{q}} = \mathbf{J}^* (\dot{\mathbf{x}} + \mathbf{K}\mathbf{e}) + \mathbf{N}\dot{\mathbf{q}}_0 \tag{2}$$

The terms of Eq. (2) are defined as follows: $\dot{\mathbf{q}}_0$ is the joint null space velocity, whose effect is to generate internal motions leaving the pose of end-effector unchanged; $\mathbf{N} = \mathbf{I} - \mathbf{J}^*\mathbf{J}$ is the orthogonal projection into the null space of $\mathbf{J}$; $\mathbf{K}$ is a gain matrix (usually diagonal) to be tuned on the application; and $\mathbf{e}$ is a vector of orientation and position errors ($\mathbf{e}_r$ and $\mathbf{e}_p$), defined as:

$$\mathbf{e} = \begin{bmatrix} \mathbf{e}_r \\ \mathbf{e}_p \end{bmatrix} = \begin{bmatrix} \frac{1}{2} (\mathbf{i} \times \mathbf{i}_d + \mathbf{j} \times \mathbf{j}_d + \mathbf{k} \times \mathbf{k}_d) \\ \mathbf{P} - \mathbf{P}_d \end{bmatrix} \tag{3}$$

In (3) the subscript d stands for desired planned variable, $\mathbf{P}$ is the position of the end-effector, while $\mathbf{i}$, $\mathbf{j}$ and $\mathbf{k}$ are the unit vectors of the end-effector reference frame. The collision avoidance strategy is subsequently integrated as an additional velocity component aimed at separating the end-effector and other components of the robot from nearby obstacles. This contribution is determined by the distance between the obstacle and each body of the robotic system. Consequently, it is necessary to compute the distance of each obstacle from every link to identify the obstacle–link pair with the shortest distance. The calculation of the distance between an obstacle $\mathbf{P}_O$ and a link [3] follows the procedures outlined in Fig. 2. Here, $\mathbf{d}_l$ represents the vector connecting the proximal to the distal extremity of the link; $\mathbf{d}_p$ and $\mathbf{d}_d$ denote

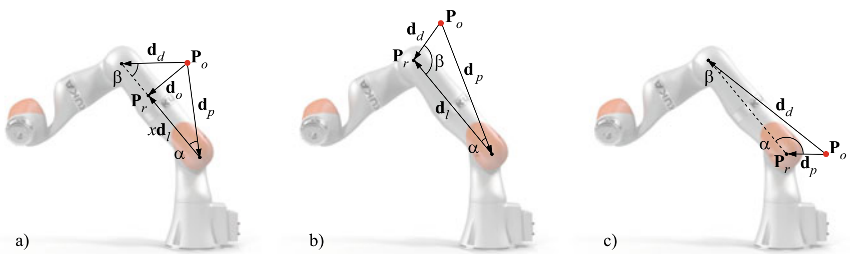

Fig. 2 Obstacle to robot body distance in the three considered cases

the distances between the obstacle and the proximal and distal extremities of the link, respectively; $\mathbf{P}_r$ is the point on the link closest to the obstacle. Specifically:

(a) If $cos\alpha \geq 0$ and $\cos\beta \geq 0$, then the distance $\mathbf{d}_O = \mathbf{P}_r - \mathbf{P}_O$ is orthogonal to the link, and the position of $\mathbf{P}_r$ is defined by the scalar parameter x:

$$d_O = \frac{|\mathbf{d}_l \times \mathbf{d}_p|}{d_l} \qquad x = \frac{d_p \cos\alpha}{d_l}, \quad 0 < x < 1 \tag{4}$$

(b) If $\cos\beta < 0$, $\mathbf{P}_r$ is coincident with the distal extremity of the link, thus:

$$\mathbf{d}_O = \mathbf{d}_d \qquad x = 1 \tag{5}$$

(c) If $\cos\alpha < 0$, $\mathbf{P}_r$ is coincident with the proximal extremity of the link, thus:

$$\mathbf{d}_O = \mathbf{d}_p \qquad x = 0 \tag{6}$$

Once $\mathbf{P}_r$ and $\mathbf{d}_O$ are determined by the previous procedure it is possible to impose the repulsive velocity $\mathbf{v}_O$ in addition to the task velocity $\mathbf{v}$ of the end-effector (Fig. 1). In terms of equations, the following expressions (7) must be imposed in order to assign the two velocity tasks above described:

$$\mathbf{J}\dot{\mathbf{q}} = \dot{\mathbf{x}} \qquad \mathbf{J}_{0p}\dot{\mathbf{q}} = \mathbf{v}_O \tag{7}$$

where $\mathbf{J}_{0p}$ represents the $(3 \times n)$ upper part of the Jacobian matrix $\mathbf{J}_0$ associated to the velocity of the point $\mathbf{P}_r$. Thus, Eq. (2) can be modified in [4]:

$$\dot{\mathbf{q}} = \mathbf{J}^* \left(\dot{\mathbf{x}} + \mathbf{K}\mathbf{e}\right) + (\mathbf{J}_{0p}\mathbf{N})^*(\mathbf{v}_O - \mathbf{J}_{0p}\mathbf{J}^*\dot{\mathbf{x}}) \tag{8}$$

The first term in Eq. (8) aims to generate the velocity of the end effector with the minimum joint velocity, thereby minimizing the motor effort. The second term directs the motion of the point $\mathbf{P}_r$ of the robot, ensuring the additional task of collision avoidance. A critical aspect of the algorithm lies in planning the repulsive speed $\mathbf{v}_O$. Here, a nominal repulsive velocity v_{rep} is adjusted by an activation term a_v, which smoothly varies with the distance d_o. The direction of this velocity aligns with the distance vector $\mathbf{d}_O$: $\mathbf{v}_O = a_v v_{rep}\hat{\mathbf{d}}_O$. A second activation term a_h is used to smoothly activate the second term of Eq. (8) in order to avoid control discontinuities [6]. The final form becomes:

$$\dot{\mathbf{q}} = \mathbf{J}^* \left(\dot{\mathbf{x}} + \mathbf{K}\mathbf{e}\right) + a_h(\mathbf{J}_{0p}\mathbf{N})^*(a_v v_{rep}\hat{\mathbf{d}}_O - \mathbf{J}_{0p}\mathbf{J}^*\dot{\mathbf{x}}) \tag{9}$$

In case an obstacle is going to interfere with the end-effect of the robot an additional term of velocity is added to Eq. (9):

$$\dot{\mathbf{q}} = \mathbf{J}^* \left(\dot{\mathbf{x}} + \mathbf{K}\mathbf{e}\right) + a_h(\mathbf{J}_{0p}\mathbf{N})^*(a_v v_{rep}\hat{\mathbf{d}}_O - \mathbf{J}_{0p}\mathbf{J}^*\dot{\mathbf{x}}) + \mathbf{J}_p^* a_{ee} v_{rep}\hat{\mathbf{d}}_{ee} \tag{10}$$

where $\mathbf{J}_p$ is the translation part of the Jacobian, a_e an additional activation parameter and $\hat{\mathbf{d}}_{ee}$ is the direction of the distance between the obstacle and the end-effector. The control algorithm underwent verification via simulations to determine appropriate values for control parameters, including the corrective proportional gain $\mathbf{K}$, the radius r defining the safety region around the robot's links, and the magnitude of the repulsive velocity v_{rep}. However, it's important to note that these parameter values may vary considerably when the algorithm is deployed on a real system.

3 Experimental Tests

The robot KUKA KMR iiwa was used to test the transferability of the control algorithm from simulation to a real system. The robot consists of a mobile platform (kept stationary during tests) on which the LBR robotic arm is installed. The robotic arm is equipped by a collaborative gripper to replicate the encumbrance of a generic tool. The control architecture of the system consists of a PC-based external controller used for motion planning, which generates a real-time reference signal in terms of joint velocity that is sent to the robot controller via TCP. The same communication protocol allows the actual positions to be read from the robot's encoders to close the external control loop at a frequency above 200 Hz in all cases tested, which proved sufficient to ensure smooth control of the system. The position of obstacles in the workspace was imposed via software, then communicated directly to the controller without any kind of measurement. At the same time, physical obstacles were placed in those a priori defined positions to generate a realistic scenario. The only effect of this kind of test setup is to exclude any kind of error due to the measurement system that would be used to acquire the position of the obstacles in real time. In fact, the purpose of the study is to specifically test the accuracy and efficiency of control algorithms, regardless of the type of obstacle perception sensors. A simple linear motion in the horizontal direction was used as the reference trajectory for the tests. A sequence of frames for this motion is shown in Fig. 3. The orientation of the tool is kept fixed, in the typical attitude for a pick and place application. Figure 4 gives the plots of joint positions and rates, which correspond to a standard motion planning

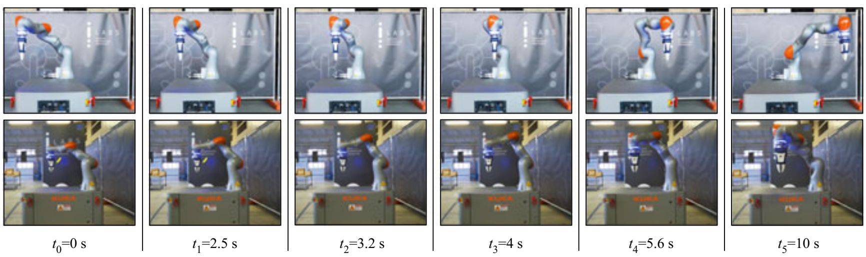

Fig. 3 Sequence of the free motion of the robot

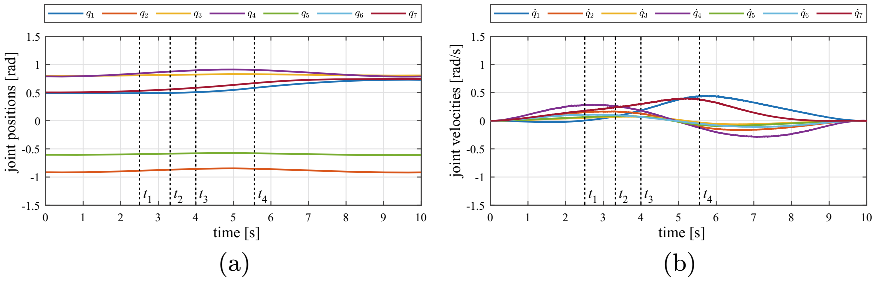

Fig. 4 Joint positions (**a**) and rates (**b**) for the free motion of the robot

with a 5th order polynomial time law. Two obstacles were then introduced in the scene with a different scope. The first obstacle, physically represented by the red and white ball in Fig. 5, is positioned right along the planned trajectory, so it interferes with the robot's gripper; in this case, the only way to avoid the collision is to move away from the planned trajectory, and then recover the original path by taking advantage of the CLIK approach. The second obstacle, i.e. the green ball, is outside the planned trajectory but interferes with the robot's elbow; in this case, the algorithm tries to take advantage of kinematic redundancy to change the internal configuration of the arm without changing the motion of the end-effector. The frames in Fig. 5 were selected by identifying the time steps at which the presence of the obstacles affects the robot's motion. At $t_1 = 2, 5$ s the end-effector enters the area of influence of the first obstacle and the control begins to react by changing its speed. Subsequently, the trajectory of the end-effector modifies, as sketched by the yellow curve in Fig. 5. At $t_2 = 3.2$ s the elbow approaches the area of influence of the second obstacle and a rearrangement of the internal configuration of the kinematic chain begins till the configuration of $t_3 = 4$ s is reached, which allows to overcome the obstacle without a collision while the end effector recovers the drift from the original path. At $t_5 = 5.6$ s the distance between the forearm of the robot and the obstacle is newly decreasing reaching the activation threshold; thus, there is a second rearrangement of the arm, while the end-effector is perfectly able to execute the planned linear motion which ends in 10 s. The same time-steps have been reported in Fig. 6 to identify the most relevant phases of the motion over the plots of joint positions and velocities. A way to better evaluate the effort of the control is to make a quantitative comparison between the reference motion and the motion resulting from the collision avoidance correction. Figure 7 plots the difference between the two cases and a first consideration can be done on the peaks of joint velocities due to the control reaction: such peaks are below the limit of $\pi/2$ rad/s, which is a threshold identified as acceptable based on an empirical evaluation. Nevertheless, the average Cartesian velocity was kept lower than approximately 0.1 m/s, which may represent a value that can be too low for some applications. By the way, the algorithms allows to cut the joint rates at imposed limits when Cartesian velocities are higher or when sudden corrections may verify. As a consequence, a drift from the path is expected, but this effect may not represent

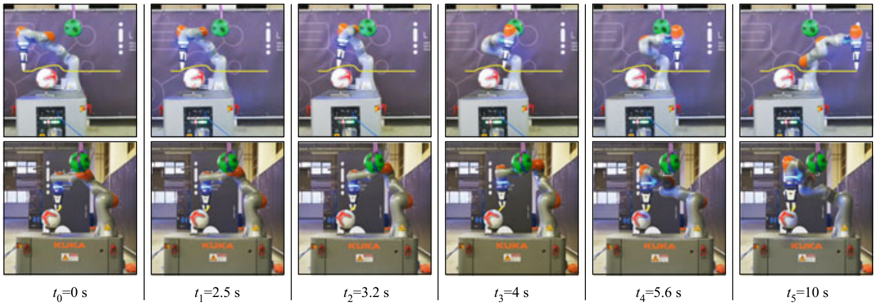

Fig. 5 Sequence of the collision avoidance test

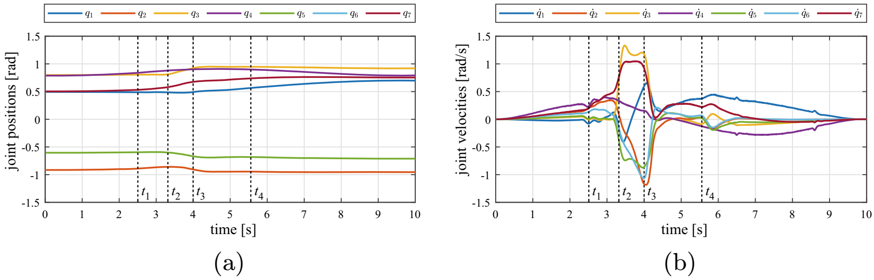

Fig. 6 Joint positions (**a**) and rates (**b**) for the collision avoidance test

a problem thanks to the CLIK approach. Thus, the effect of a joint speed saturation would be analogous to the disturbance due to an obstacle placed along the path, that forces the end-effector to deviate and recover after the obstacle is overcame. A second consideration can be done on how the redundancy of the kinematic chain is exploited: looking at the control effort relative to position (left of Fig. 7) it results that the difference between reference and actual motion doesn't decrease to zero after the effect of the obstacles. This means that, even if the planned pose of the end-effector is reached, a different internal kinematic configuration is assumed. Thus, it is not properly correct to represent the effort of the control as the difference between joint variables, because in the present application different configurations are admitted. Nevertheless, in some cases it could be necessary to recover the planned joint configuration besides the Cartesian pose. This could be done by adding to the control law (9) an additional corrective term:

$$\dot{\mathbf{q}} = \mathbf{J}^* \left(\dot{\mathbf{x}} + \mathbf{K}\mathbf{e}\right) + a_h (\mathbf{J}_{0p}\mathbf{N})^* (a_v v_{rep} \hat{\mathbf{d}}_O - \mathbf{J}_{0p}\mathbf{J}^* \dot{\mathbf{x}}) + \mathbf{K}_q \boldsymbol{\delta}_q \tag{11}$$

where $\mathbf{K}_q$ is a diagonal gain matrix and $\mathbf{e}_q$ is the difference between actual and planned joint position: $\boldsymbol{\delta}_q = \mathbf{q} - \mathbf{q}_{pl}$.

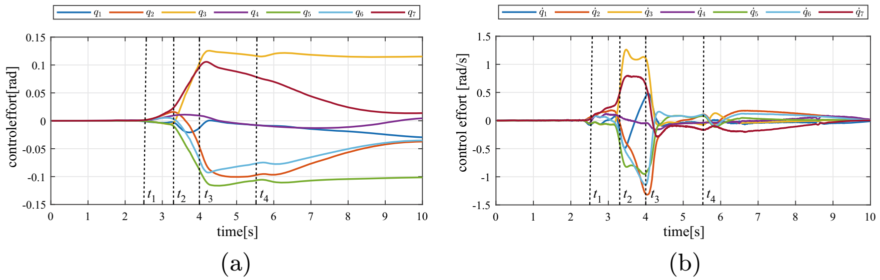

Fig. 7 Control effort in terms of joint positions (**a**) and joint rates (**b**)

4 Conclusions

An experimental validation of a collision avoidance control framework for redundant manipulators was presented. The algorithm, previously verified by simulations, was shown to be transferable to a real system with a cycle rate higher than 200 Hz; the control was able to update the robot's trajectory in real time to avoid two obstacles, the first interfering with the end-effector, the second with the arm elbow. In the latter case, the algorithm was able to optimally exploit the redundancy of the kinematic chain: the obstacle was overcome without changing the trajectory of the end-effector, but rather by changing the internal configuration of the manipulator. The efficiency and accuracy of the algorithm were demonstrated by excluding from the analysis the effect of any measurement system to be used to detect obstacles. Obviously, in a real system where collision avoidance control is to be implemented, the actual accuracy and robustness should be evaluated by also considering the integration of the sensor system, which will be object of future works.

References

1. Bottin, M., Rosati, G.: Trajectory optimization of a redundant serial robot using cartesian via points and kinematic decoupling. Robotics **8**(4) (2019)
2. Chiriatti, G., Palmieri, G., Scoccia, C., Palpacelli, M.C., Callegari, M.: Adaptive obstacle avoidance for a class of collaborative robots. Machines **9**(6), 113 (2021)
3. Khatib, O.: Real-time obstacle avoidance for manipulators and mobile robots. Int. J. Robot. Res. **5**, 90–98 (1986)
4. Lee, K.K., Buss, M.: Obstacle avoidance for redundant robots using jacobian transpose method. In: 2007 IEEE/RSJ International Conference on Intelligent Robots and Systems, pp. 3509–3514. IEEE (2007)
5. Maciejewski, A.A., Klein, C.A.: Obstacle avoidance for kinematically redundant manipulators in dynamically varying environments. Int. J. Robot. Res. **4**(3), 109–117 (1985)
6. Palmieri, G., Scoccia, C.: Motion planning and control of redundant manipulators for dynamical obstacle avoidance. Machines **9**(6) (2021)
7. Safeea, M., Béarée, R., Neto, P.: Collision avoidance of redundant robotic manipulators using newton's method. J. Intell. Robot. Syst. **99**(3), 673–681 (2020)

8. Safeea, M., Neto, P., Bearee, R.: On-line collision avoidance for collaborative robot manipulators by adjusting off-line generated paths: an industrial use case. Robot. Autonom. Syst. **119**, 278–288 (2019)
9. Scimmi, L.S., Melchiorre, M., Troise, M., Mauro, S., Pastorelli, S.: A practical and effective layout for a safe human-robot collaborative assembly task. Appl. Sci. **11**(4), 1763 (2021)
10. Scoccia, C., Palmieri, G., Palpacelli, M.C., Callegari, M.: A collision avoidance strategy for redundant manipulators in dynamically variable environments: On-line perturbations of off-line generated trajectories. Machines **9**(2) (2021)
11. Simas, H., Di Gregorio, R.: Collision avoidance for redundant 7-dof robots using a critically damped dynamic approach. Robotics **11**(5) (2022)
12. Zhang, H., Jin, H., Liu, Z., Liu, Y., Zhu, Y., Zhao, J.: Real-time kinematic control for redundant manipulators in a time-varying environment: multiple-dynamic obstacle avoidance and fast tracking of a moving object. IEEE Trans. Ind. Inf. **16**(1), 28–41 (2019)

Automatic Differentiation of Serial Manipulator Jacobians Using Multidual Algebra

Daniel Condurache, Mihail Cojocari, Iosif Birlescu, and Bogdan Gherman

Abstract Nowadays, the usage of robots is continuously growing and aims to replace human work in different areas as much as possible. Some places, like medicine or nanotechnology, require high-precision multilink robot end-effector control. Regarding accurate trajectory tracking, conventional computation methods for high-order derivatives of multi-Doff manipulators are highly time-consuming and offer only approximative results. Inaccurate results, in the end, reduce the performance of multi-Doff manipulators and re-strict utilization in the areas where high precision and response time are necessary. It is essential to employ an advanced technique for computing higher-order Jacobian matrix derivatives to achieve precise control. This paper explores a novel approach for deriving the Jacobian matrix of a multilink robot using multi-dual algebra. With multidual algebra and its automatic differentiation proprieties, obtaining an exact value for higher-order acceleration is possible. Combining multidual algebra and automatic differentiation enhances our ability to compute derivatives efficiently and accurately, improving performance and reliability in various applications. This method is applicable everywhere, for any lower-pair serial kinematic chain and any order of higher-order acceleration.

Keywords Multidual algebra · Automatic differentiation · Serial manipulator Jacobians · Higher-order acceleration · Jacobian differentiation

D. Condurache (✉) · M. Cojocari
Technical University of Iasi, D. Mangeron 59, 700050 Iasi, Romania
e-mail: daniel.condurache@tuiasi.ro

D. Condurache
Technical Sciences Academy of Romania, 26 Dacia Blvd, 030167 Bucharest, Romania

I. Birlescu · B. Gherman
Technical University of Cluj-Napoca, Memorandumului 28, 400114 Cluj-Napoca, Romania

D. Pisla et al. (eds.), *Advances in Service and Industrial Robotics*, Mechanisms and Machine Science 157, https://doi.org/10.1007/978-3-031-59257-7_38

1 Introduction

Higher-order derivatives of the Jacobian have an essential role in robotic device design, kinematics, and real-time control [1]. This paper presents an applicative simultaneous method for nth-order vector field derivation based on multidual algebra. A hypercomplex trigonometric function is given to understand better automatic differentiation using multidual algebra. In the last section, a didactic example calculates the first, second, and third-order derivatives for robots Jacobian simultaneously using multidual algebra and multidual transform.

2 Multidual Algebra and Automatic Derivation

2.1 Multidual Numbers

Multidual algebra is based on multidual numbers and their proprieties. A set of multidual numbers is introduced as follows $\hat{\mathbb{R}} = \mathbb{R} + \varepsilon\mathbb{R} + \ldots + \varepsilon^n\mathbb{R}$; $\varepsilon \neq 0$, $\varepsilon^{n+1} = 0$, where $\mathbb{R}$ are the set of real numbers and $n \in \mathbb{N}$ represent a natural number [2, 3].

Two generic multidual elements $\hat{x}, \hat{y} \in \hat{\mathbb{R}}$ that have the form [4]:

$$\hat{x} = x + x_1\varepsilon + \ldots + x_n\varepsilon^n;\ x, x_k \in \mathbb{R}, k = \overline{1, n} \tag{1}$$

$$\hat{y} = y + y_1\varepsilon + \ldots + y_n\varepsilon^n;\ y, y_k \in \mathbb{R}, k = \overline{1, n}. \tag{2}$$

Next by $x = Re\hat{x}$ and $Mu\hat{x} = \sum_{k=1}^{n} x_k\varepsilon^k$ will be denoted the real parts and respectively, multidual parts of the multidual number $\hat{x}$. Also, we will denote by $x_k = \frac{d\hat{x}}{d\varepsilon^k}$; $k = \overline{1, n}$, the k order multidual component of the multidual number $\hat{x}$. Addition and, respectively, multiplication operation of two multidual number from [3, 4] are listed below by

$$\hat{x} + \hat{y} = \sum_{k=0}^{n} (x_k + y_k)\varepsilon^k, \tag{3}$$

$$\hat{x}\hat{y} = \sum_{k=0}^{n} \left(\sum_{p=0}^{k} x_p y_{k-p} \right) \varepsilon^k \tag{4}$$

In Eqs. (3–4), is denoted by $x_0 = x$, $y_0 = y$ and $\varepsilon^0 = 1$.

2.2 Multidual Functions

Let be $f : \mathbb{I} \subseteq \mathbb{R} \to \mathbb{R}$, $f = f(x)$ a nth differentiable real function. Below is defined the multidual function $\hat{f}$ of multidual variable $\hat{x}$ by equation [3, 4]:

$$f(\hat{x}) = f(x) + \sum_{k=1}^{n} \frac{\Delta(x)^k}{k!} f^{(k)}(x) \tag{5}$$

where: $\Delta(x) = \hat{x} - x = \sum_{k=1}^{n} x_k \varepsilon^k$.

Using Eq. (5), next multidual functions was defined [3, 4]:

$$\sin \hat{x} = \sin x + \sum_{k=1}^{n} \frac{\Delta(x)^k}{k!} \sin\left(x + k\frac{\pi}{2}\right), \tag{6}$$

$$\cos \hat{x} = \cos x + \sum_{k=1}^{n} \frac{\Delta(x)^k}{k!} \cos\left(x + k\frac{\pi}{2}\right). \tag{7}$$

2.3 Multidual Differential Transform

If we have a real function of real time variable, nth differentiable, $n \in \mathbb{N}$ $f : \mathbb{I} \subseteq \mathbb{R} \to \mathbb{R}$, $f = f(t)$. To this function, it associated the multidual function of real variable $\breve{f}$ given by the next equation [3, 4]:

$$\breve{f} = f + \varepsilon \dot{f} + \ldots + \frac{\varepsilon^n}{n!} f^{(n)} = e^{\varepsilon \mathrm{D}} f, \tag{8}$$

where $e^{\varepsilon \mathrm{D}} = 1 + \varepsilon \mathrm{D} + \ldots + \frac{\varepsilon^n}{n!} \mathrm{D}^n$ with $\mathrm{D} = \frac{d}{dt}$ was denoted the derivative operator with respect to time [3, 4].

The proprieties of multidual differential transform are defined by next theorem.

Theorem 1 *Being f and g two real function of class $C^n(\mathbb{I})$. The following properties take place* [3, 4]:

$$\overbrace{f + g} = \breve{f} + \breve{g}, \tag{9}$$

$$\breve{fg} = \breve{f}\,\breve{g}, \tag{10}$$

$$\breve{\lambda f} = \lambda \breve{f}, \forall \lambda \in \mathbb{R}, \tag{11}$$

$$\underset{\smile}{f}(\alpha) = f\left(\underset{\smile}{\alpha}\right), \alpha \in C^n(\mathbb{I}), \tag{12}$$

$$\dot{\underset{\smile}{f}} = \underset{\smile}{\dot{f}}. \tag{13}$$

3 Higher-Order Kinematics of Lower-Pair Chains

Let be a lower-pair chain described by kinematic mapping [5]:

$$\mathrm{g} = f_m(\mathrm{q}) = \exp\left(\mathbf{Y}_1\mathrm{q}_1\right)\exp\left(\mathbf{Y}_2\mathrm{q}_2\right)\ldots\exp\left(\mathbf{Y}_m\mathrm{q}_m\right), m \in \mathbb{N} \tag{14}$$

known also as Brockett formula.

In Eq. (14), $\mathbf{Y}_k, k = \overline{1, m}$ denotes the screw coordinate vectors and $\mathrm{q}_k, k = \overline{1, m}$ denotes the joint variable [5].

Theorem 2 *The Jacobian on end effector of kinematic chain given by the kinematic mapping* (14) *it results from matrix:*

$$\mathbf{J} = [\mathbf{S}_1, \mathbf{S}_2, \ldots, \mathbf{S}_m] \tag{15}$$

where $\mathbf{S}_1 = \mathbf{Y}_1$*, and:*

$$\mathbf{S}_k = \mathrm{Ad}_{f_{k-1}}\mathbf{Y}_k, k = \overline{2, m} \tag{16}$$

is instantaneous joint screw coordinate of joint k and $\mathrm{q}_k, k = \overline{1, m}$*, is time variable.*

Proof Let:

$$g = \exp\left(\mathbf{Y}_1\mathrm{q}_1\right)\exp\left(\mathbf{Y}_2\mathrm{q}_2\right)\ldots\exp\left(\mathbf{Y}_m\mathrm{q}_m\right) \tag{17}$$

Also, from (17) it follows:

$$g^{-1} = \exp\left(-\mathbf{Y}_m\mathrm{q}_m\right)\ldots\exp\left(-\mathbf{Y}_2\mathrm{q}_2\right)\exp\left(-\mathbf{Y}_1\mathrm{q}_1\right) \tag{18}$$

Considering that the spatial twist $\mathbf{T} = [\boldsymbol{\omega}_m, \mathbf{v}_m]^T$ of end-effector of serial spatial kinematic chain given by Eq. (14); $\mathbf{T}$ is defined by equation:

$$\tilde{\mathbf{T}} = \dot{g}g^{-1} \tag{19}$$

In Eq. (19), $\tilde{\mathbf{T}} = \begin{bmatrix} \tilde{\boldsymbol{\omega}}_m & \mathbf{v}_m \\ \mathbf{0} & 0 \end{bmatrix}$, $\tilde{\omega}_m$ is a skew-symmetric tensor corresponding to vector $\boldsymbol{\omega}_m$.With Eqs. (17) and (19), result:

$$\mathbf{T} = \boldsymbol{J}\dot{\mathbf{q}}, \tag{20}$$

where $\mathbf{q} = \left[\mathrm{q}_1, \mathrm{q}_2, \ldots, \mathrm{q}_m\right]^T$, is joints variable n-time differentiable.

The higher-order vector field of the end-effector is given by the n-time derivative of spatial twist $\mathbf{T}$, which is equivalent to calculating the n-time derivative of Jacobian $\boldsymbol{J}$.

Using multidual differential transform (see Sect. 2.3) by Eq. (15) result:

$$\breve{\boldsymbol{J}} = \left[\breve{\boldsymbol{S}}_1, \breve{\boldsymbol{S}}_2, \ \ldots, \breve{\boldsymbol{S}}_m\right] \tag{21}$$

In previous equation $\mathbf{S}_k = \mathbf{S}_k\left(\mathrm{q}_1, \mathrm{q}_2, \ldots, \mathrm{q}_k\right), , k = \overline{1, m}$. By results of the **Theorem 1**:

$$\breve{\boldsymbol{S}}_k = \mathbf{S}_k\left(\breve{q}_1, \ \breve{q}_2, \ \ldots, \breve{q}_k\right) \tag{22}$$

By Eqs. (21), (22) and **Theorem 1** result:

$$\breve{\boldsymbol{J}} = \boldsymbol{J} + \varepsilon\dot{\boldsymbol{J}} + \ldots + \frac{\varepsilon^n}{n!}\boldsymbol{J}^{(n)} \tag{23}$$

4 Automatic Differentiation of Sine and Cosine Functions with Multidual Algebra

An example of directly finding the 3rd derivative, $\varepsilon^4 = 0$, for the sine function using the method described above using the results of Sect. 2 is described below.

In the first step parameter $\Delta(x) = \hat{x} - x$ is defined

$$\Delta(x) = x_1\varepsilon + x_2\varepsilon^2 + x_3\varepsilon^3. \tag{24}$$

Then using Eq. (14) and $\Delta(x)$, after some algebra, will have the next form:

$$\sin[\hat{x}] = \sin[x] + x_1\cos[\mathrm{x}]\varepsilon + \left\{x_2\cos[x] - \frac{1}{2}x_1^2\sin[x]\right\}\varepsilon^2 \\ + \left\{(x_3 - \frac{1}{6}x_1^3)\cos[x] - x_1x_2\sin[x]\right\}\varepsilon^3 \tag{25}$$

In next step x is substituted with α, x_1 is substituted with $\frac{\dot{\alpha}}{1!}$, x_2 is substituted with $\frac{\ddot{\alpha}}{2!}$, x_3 is substituted with $\frac{\dddot{\alpha}}{3!}$, and we obtain:

$$\sin\left[\breve{\alpha}\right] = \sin[\alpha] + \dot{\alpha}\cos[\alpha]\varepsilon + \frac{\left(\ddot{\alpha}\cos[\alpha] - \dot{\alpha}^2\sin[\alpha]\right)\varepsilon^2}{2} + \frac{\left(\dddot{\alpha}\cos[\alpha] - \dot{\alpha}^3\cos[\alpha] - 3\dot{\alpha}\ddot{\alpha}\sin[\alpha]\right)\varepsilon^3}{6} \tag{26}$$

In the same way, on result:

$$\cos\left[\breve{\alpha}\right] = \cos[\alpha] - \dot{\alpha}\sin[\alpha]\varepsilon - \frac{\left(\ddot{\alpha}\sin[\alpha] + \dot{\alpha}^2\cos[\alpha]\right)\varepsilon^2}{2} - \frac{\left(\dddot{\alpha}\sin[\alpha] - \dot{\alpha}^3\sin[\alpha] + 3\dot{\alpha}\ddot{\alpha}\cos[\alpha]\right)\varepsilon^3}{6} \tag{27}$$

5 Application

Exact multilink robot end effector control is required in modern robotics to have precise control. Serial manipulator kinematics establish the crucial link between joint variables in joint-space coordinates and the end effector configuration in task-space coordinates. When we directly differentiate the forward kinematics function, we obtain a Jacobian matrix. The Jacobian matrix, denoted as $\boldsymbol{J}$, encodes the sensitivity of the end effector's motion with respect to changes in joint variables, it allows us to determine how changes in joint velocities affect the end effector's motion. To achieve accurate trajectory tracking, it is essential to compute higher-order Jacobian matrix derivatives. In this section are calculated first, second, and third derivatives of Jacobian in Maple software using multidual algebra.

Let be the next Jacobian of 2-link robot (Fig. 1):

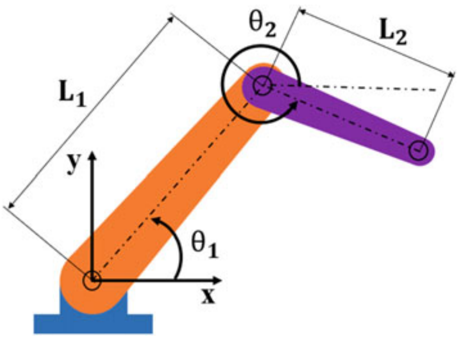

Fig. 1 Schematic representation of 2-link robot

$$\boldsymbol{J} = \begin{pmatrix} -L_2 \sin[\theta_1 + \theta_2] - L_1 \sin[\theta_1] & -L_2 \sin[\theta_1 + \theta_2] \\ L_2 \cos[\theta_1 + \theta_2] - L_1 \cos[\theta_1] & L_2 \cos[\theta_1 + \theta_2] \end{pmatrix} \tag{28}$$

In same way as in previous section angle $[\theta_1]$ and $[\theta_1 + \theta_2]$ from Jacobian expression are substituted in multidual function of sine and cosine.

$$\begin{aligned} \sin[\overbrace{\theta_1 + \theta_2}] = {} & \sin[\theta_1 + \theta_2] + \left\{\left(\dot{\theta}_1 + \dot{\theta}_2\right)\cos[\theta_1 + \theta_2]\right\}\varepsilon \\ & + \tfrac{1}{2}\left\{\left(\ddot{\theta}_1 + \ddot{\theta}_2\right)\cos[\theta_1 + \theta_2] - \left(\dot{\theta}_1 + \dot{\theta}_2\right)^2 \sin[\theta_1 + \theta_2]\right\}\ \varepsilon^2 \\ & + \tfrac{1}{6}\left\{\left(\dddot{\theta}_1 + \dddot{\theta}_2\right)\cos[\theta_1 + \theta_2] - 3\left(\dot{\theta}_1\ddot{\theta}_1 + \dot{\theta}_1\ddot{\theta}_2 + \ddot{\theta}_1\dot{\theta}_2 + \dot{\theta}_2\ddot{\theta}_2\right)\sin[\theta_1 + \theta_2] \right. \\ & \left. - \left(\dot{\theta}_1 + \dot{\theta}_2\right)^3 \cos[\theta_1 + \theta_2]\right\}\ \varepsilon^3 \end{aligned} \tag{29}$$

$$\begin{aligned} \sin\left[\breve{\theta}_1\right] = {} & \sin[\theta_1] + \left\{\dot{\theta}_1 \cos[\theta_1]\right\}\varepsilon \\ & + \frac{1}{2}\left\{(\ddot{\theta}_1 \cos[\theta_1] - \dot{\theta}_1^2 \sin[\theta_1])\right\}\varepsilon^2 \\ & + \frac{1}{6}\left\{\dddot{\theta}_1 \cos[\theta_1] - 3\dot{\theta}_1\ddot{\theta}_1 \sin[\theta_1] - \dot{\theta}_1^3 \cos[\theta_1]\right\}\varepsilon^3 \end{aligned} \tag{30}$$

$$\begin{aligned} \cos[\overbrace{\theta_1 + \theta_2}] = {} & \cos[\theta_1 + \theta_2] - \left\{\left(\dot{\theta}_1 + \dot{\theta}_2\right)\sin[\theta_1 + \theta_2]\right\}\varepsilon \\ & - \tfrac{1}{2}\left\{\left(\ddot{\theta}_1 + \ddot{\theta}_2\right)\sin[\theta_1 + \theta_2] + \left(\dot{\theta}_1 + \dot{\theta}_2\right)^2 \cos[\theta_1 + \theta_2]\right\}\ \varepsilon^2 \\ & - \tfrac{1}{6}\left\{\left(\dddot{\theta}_1 + \dddot{\theta}_2\right)\sin[\theta_1 + \theta_2] + 3\left(\dot{\theta}_1\ddot{\theta}_1 + \dot{\theta}_1\ddot{\theta}_2 + \ddot{\theta}_1\dot{\theta}_2 + \dot{\theta}_2\ddot{\theta}_2\right)\cos[\theta_1 + \theta_2] \right. \\ & \left. - \left(\dot{\theta}_1 + \dot{\theta}_2\right)^3 \sin[\theta_1 + \theta_2]\right\}\ \varepsilon^3 \end{aligned} \tag{31}$$

$$\begin{aligned} \cos\left[\breve{\theta}_1\right] = {} & \cos\theta_1 - \left\{\dot{\theta}_1 \sin[\theta_1]\right\}\varepsilon \\ & - \frac{1}{2}\left\{\ddot{\theta}_1 \sin[\theta_1] + \dot{\theta}_1^2 \cos[\theta_1]\ \right\}\ \varepsilon^2 \\ & - \frac{1}{6}\left\{\dddot{\theta}_1 \sin[\theta_1] + 3\dot{\theta}_1\ddot{\theta}_1 \cos[\theta_1] - \dot{\theta}_1^3 \sin[\theta_1]\right\}\varepsilon^3 \end{aligned} \tag{32}$$

Using sine and cosine function Eqs. (29–32) and expression rearrangements by ε order, the multidual representation of Jacobian matrix is obtained. The multidual form allows us to express not only the first-order derivatives (velocity) but also higher-order derivatives (acceleration, jerk, etc.), Eqs. (33–37) capture the higher-order derivatives of the Jacobian, providing a comprehensive understanding of the robot's kinematics.

$$\breve{\boldsymbol{J}} = \begin{pmatrix} \breve{j}_{11} & \breve{j}_{12} \\ \breve{j}_{21} & \breve{j}_{22} \end{pmatrix} \tag{33}$$

$$\begin{aligned}
\breve{j}_{11} &= -L_2 \sin[\theta_1 + \theta_2] - L_1 \sin[\theta_1] \\
&\quad - \left\{L_2\left(\dot{\theta}_1 + \dot{\theta}_2\right) \cos[\theta_1 + \theta_2] + L_1 \dot{\theta}_1 \cos[\theta_1]\right\}\varepsilon \\
&\quad - \frac{1}{2}\left\{L_2\left[\left(\ddot{\theta}_1 + \ddot{\theta}_2\right) \cos[\theta_1 + \theta_2] - \left(\dot{\theta}_1 + \dot{\theta}_2\right)^2 \sin[\theta_1 + \theta_2]\right]\right. \\
&\quad \left. + \ L_1\left[\ddot{\theta}_1 \cos[\theta_1] - \dot{\theta}_1^2 \sin[\theta_1]\right]\right\} \varepsilon^2 \\
&\quad - \frac{1}{6}\left\{L_2\left[\left(\dddot{\theta}_1 + \dddot{\theta}_2\right) \cos[\theta_1 + \theta_2] \ - 3\left(\dot{\theta}_1 \ddot{\theta}_1 + \dot{\theta}_1 \ddot{\theta}_2 + \ddot{\theta}_1 \dot{\theta}_2 + \dot{\theta}_2 \ddot{\theta}_2\right) \sin[\theta_1 + \theta_2]\right.\right. \\
&\quad \left. - \left(\dot{\theta}_1 + \dot{\theta}_2\right)^3 \cos[\theta_1 + \theta_2]\right] \\
&\quad \left. + L_1\left[\dddot{\theta}_1 \cos[\theta_1] - 3\dot{\theta}_1 \ddot{\theta}_1 \sin[\theta_1] - \dot{\theta}_1^3 \cos[\theta_1]\right]\right\}\varepsilon^3
\end{aligned} \tag{34}$$

$$\begin{aligned}
\breve{j}_{12} &= -L_2 \sin[\theta_1 + \theta_2] - L_2\left(\dot{\theta}_1 + \dot{\theta}_2\right) \cos[\theta_1 + \theta_2]\varepsilon \\
&\quad - \frac{1}{2}L_2\left[\left(\ddot{\theta}_1 + \ddot{\theta}_2\right) \cos[\theta_1 + \theta_2] - \left(\dot{\theta}_1 + \dot{\theta}_2\right)^2 \sin[\theta_1 + \theta_2]\right] \varepsilon^2 \\
&\quad - \frac{1}{6}L_2\left[\left(\dddot{\theta}_1 + \dddot{\theta}_2\right) \cos[\theta_1 + \theta_2] \ - 3\left(\dot{\theta}_1 \ddot{\theta}_1 + \dot{\theta}_1 \ddot{\theta}_2 + \ddot{\theta}_1 \dot{\theta}_2 + \dot{\theta}_2 \ddot{\theta}_2\right) \sin[\theta_1 + \theta_2]\right. \\
&\quad \left. - \left[\left(\dot{\theta}_1 + \dot{\theta}_2\right)^3 \cos[\theta_1 + \theta_2]\right]\right]\varepsilon^3
\end{aligned} \tag{35}$$

$$\begin{aligned}
\breve{j}_{21} &= L_2 \cos[\theta_1 + \theta_2] - L_1 \cos[\theta_1] + \left[L_1 \dot{\theta}_1 \sin[\theta_1] - L_2\left(\dot{\theta}_1 + \dot{\theta}_2\right) \sin[\theta_1 + \theta_2]\right]\varepsilon \\
&\quad - \frac{1}{2}\left\{L_2\left[\left(\ddot{\theta}_1 + \ddot{\theta}_2\right) \sin[\theta_1 + \theta_2] + \left(\dot{\theta}_1 + \dot{\theta}_2\right)^2 \cos[\theta_1 + \theta_2]\right]\right. \\
&\quad \left. - L_1\left[\ddot{\theta}_1 \sin[\theta_1] + \dot{\theta}_1^2 \cos[\theta_1]\right]\right\} \varepsilon^2 \\
&\quad - \frac{1}{6}\left\{L_2\left[\left(\dddot{\theta}_1 + \dddot{\theta}_2\right) \sin[\theta_1 + \theta_2] + 3\left(\dot{\theta}_1 \ddot{\theta}_1 + \dot{\theta}_1 \ddot{\theta}_2 + \ddot{\theta}_1 \dot{\theta}_2 + \dot{\theta}_2 \ddot{\theta}_2\right) \cos[\theta_1 + \theta_2]\right.\right. \\
&\quad \left. - \left(\dot{\theta}_1 + \dot{\theta}_2\right)^3 \sin[\theta_1 + \theta_2]\right] \\
&\quad \left. + L_1\left(\dddot{\theta}_1 \sin[\theta_1] + 3\dot{\theta}_1 \ddot{\theta}_1 \cos[\theta_1] - \dot{\theta}_1^3 \sin[\theta_1]\right)\right\} \varepsilon^3
\end{aligned} \tag{36}$$

$$\begin{aligned}
\breve{j}_{22} &= L_2 \cos[\theta_1 + \theta_2] - L_2\left(\dot{\theta}_1 + \dot{\theta}_2\right) \sin[\theta_1 + \theta_2]\varepsilon \\
&\quad - \frac{1}{2}L_2\left[\left(\ddot{\theta}_1 + \ddot{\theta}_2\right) \sin[\theta_1 + \theta_2] + \left(\dot{\theta}_1 + \dot{\theta}_2\right)^2 \cos[\theta_1 + \theta_2]\right] \varepsilon^2 \\
&\quad - \frac{1}{6}L_2\left\{\left(\dddot{\theta}_1 + \dddot{\theta}_2\right) \sin[\theta_1 + \theta_2] + 3\left(\dot{\theta}_1 \ddot{\theta}_1 + \dot{\theta}_1 \ddot{\theta}_2 + \ddot{\theta}_1 \dot{\theta}_2 + \dot{\theta}_2 \ddot{\theta}_2\right) \cos[\theta_1 + \theta_2]\right. \\
&\quad \left. - \left(\dot{\theta}_1 + \dot{\theta}_2\right)^3 \sin[\theta_1 + \theta_2]\right\} \varepsilon^3
\end{aligned} \tag{37}$$

By Eq. (23), we obtain the exact value of:

- **Jacobian** (*all terms without* ε):

$$\boldsymbol{J} = \begin{pmatrix} -L_2 \sin[\theta_1 + \theta_2] - L_1 \sin[\theta_1] & -L_2 \sin[\theta_1 + \theta_2] \\ L_2 \cos[\theta_1 + \theta_2] - L_1 \cos[\theta_1] & L_2 \cos[\theta_1 + \theta_2] \end{pmatrix} \tag{38}$$

- **Jacobian first derivative** (*all terms with* ε):

$$\dot{\boldsymbol{J}} = \begin{pmatrix} -L_2(\dot{\theta}_1 + \dot{\theta}_2)\cos[\theta_1+\theta_2] - L_1\dot{\theta}_1\cos[\theta_1] & -L_2(\dot{\theta}_1 + \dot{\theta}_2)\cos[\theta_1+\theta_2] \\ -L_2(\dot{\theta}_1 + \dot{\theta}_2)\sin[\theta_1+\theta_2] + L_1\dot{\theta}_1\sin[\theta_1] & -L_2(\dot{\theta}_1 + \dot{\theta}_2)\sin[\theta_1+\theta_2] \end{pmatrix} \tag{39}$$

- **Jacobian second derivative** (*all terms with* ε^2):

$$\ddot{\boldsymbol{J}} = \begin{pmatrix} \ddot{J}_{11} & \ddot{J}_{12} \\ \ddot{J}_{21} & \ddot{J}_{22} \end{pmatrix} \tag{40}$$

$$\begin{aligned}\ddot{J}_{11} = {} & L_2(\dot{\theta}_1 + \dot{\theta}_2)^2\sin[\theta_1+\theta_2] - L_2(\ddot{\theta}_1 + \ddot{\theta}_2)\cos[\theta_1+\theta_2] \\ & - L_1(\ddot{\theta}_1\cos[\theta_1] - \dot{\theta}_1^2\sin[\theta_1])\end{aligned} \tag{41}$$

$$\ddot{J}_{12} = L_2(\dot{\theta}_1 + \dot{\theta}_2)^2\sin[\theta_1+\theta_2] - L_2(\ddot{\theta}_1 + \ddot{\theta}_2)\cos[\theta_1+\theta_2] \tag{42}$$

$$\begin{aligned}\ddot{J}_{21} = {} & -L_2(\dot{\theta}_1 + \dot{\theta}_2)^2\cos[\theta_1+\theta_2] - L_2(\ddot{\theta}_1 + \ddot{\theta}_2)\sin[\theta_1+\theta_2] \\ & + L_1(\ddot{\theta}_1\sin[\theta_1] + \dot{\theta}_1^2\cos[\theta_1])\end{aligned} \tag{43}$$

$$\ddot{J}_{22} = -L_2(\dot{\theta}_1 + \dot{\theta}_2)^2\cos[\theta_1+\theta_2] - L_2(\ddot{\theta}_1 + \ddot{\theta}_2)\sin[\theta_1+\theta_2] \tag{44}$$

- **Jacobian third derivative** (*all terms with* ε^3)

$$\dddot{\boldsymbol{J}} = \begin{pmatrix} \dddot{J}_{11} & \dddot{J}_{12} \\ \dddot{J}_{21} & \dddot{J}_{22} \end{pmatrix} \tag{45}$$

$$\begin{aligned}\dddot{J}_{11} = {} & \{L_1(\dot{\theta}_1^3 - \dddot{\theta}_1) + L_2(\dot{\theta}_1^3 + 3\dot{\theta}_1^2\dot{\theta}_2 + 3\dot{\theta}_1\dot{\theta}_2^2 + \dot{\theta}_2^3 - \dddot{\theta}_1 - \dddot{\theta}_2)\cos[\theta_2] \\ & + 3L_2(\dot{\theta}_1\ddot{\theta}_1 + \dot{\theta}_1\ddot{\theta}_2 + \ddot{\theta}_1\dot{\theta}_2 + \dot{\theta}_2\ddot{\theta}_2)\sin[\theta_2]\}\cos[\theta_1] \\ & + \{3L_1\dot{\theta}_1\ddot{\theta}_1 - L_2(\dot{\theta}_1^3 + 3\dot{\theta}_1^2\dot{\theta}_2 + 3\dot{\theta}_1\dot{\theta}_2^2 + \dot{\theta}_2^3 - \dddot{\theta}_1 - \dddot{\theta}_2)\sin[\theta_2] \\ & + 3L_2(\dot{\theta}_1\ddot{\theta}_1 + \dot{\theta}_1\ddot{\theta}_2 + \ddot{\theta}_1\dot{\theta}_2 + \dot{\theta}_2\ddot{\theta}_2)\cos[\theta_2]\}\sin[\theta_1]\end{aligned} \tag{46}$$

$$\begin{aligned}\dddot{J}_{12} = {} & L_2\left(\dot{\theta}_1^3 + 3\dot{\theta}_1^2\dot{\theta}_2 + 3\dot{\theta}_1\dot{\theta}_2^2 + \dot{\theta}_2^3 - \dddot{\theta}_1 - \dddot{\theta}_2\right)\cos[\theta_1+\theta_2] \\ & + 3L_2(\dot{\theta}_1\ddot{\theta}_1 + \dot{\theta}_1\ddot{\theta}_2 + \ddot{\theta}_1\dot{\theta}_2 + \dot{\theta}_2\ddot{\theta}_2)\sin[\theta_1+\theta_2]\end{aligned} \tag{47}$$

$$\begin{aligned}\dddot{J}_{21} = {} & \left\{L_1\left(-\dot{\theta}_1^3 + \dddot{\theta}_1\right) + L_2\left(\dot{\theta}_1^3 + 3\dot{\theta}_1^2\dot{\theta}_2 + 3\dot{\theta}_1\dot{\theta}_2^2 + \dot{\theta}_2^3 - \dddot{\theta}_1 - \dddot{\theta}_2\right)\cos[\theta_2] \right. \\ & \left. + 3L_2(\dot{\theta}_1\ddot{\theta}_1 + \dot{\theta}_1\ddot{\theta}_2 + \ddot{\theta}_1\dot{\theta}_2 + \dot{\theta}_2\ddot{\theta}_2)\sin[\theta_2]\right\}\sin[\theta_1] \\ & + \left\{3L_1\dot{\theta}_1\ddot{\theta}_1 + L_2\left(\dot{\theta}_1^3 + 3\dot{\theta}_1^2\dot{\theta}_2 + 3\dot{\theta}_1\dot{\theta}_2^2 + \dot{\theta}_2^3 - \dddot{\theta}_1 - \dddot{\theta}_2\right)\sin[\theta_2] \right. \\ & \left. - 3L_2(\dot{\theta}_1\ddot{\theta}_1 + \dot{\theta}_1\ddot{\theta}_2 + \ddot{\theta}_1\dot{\theta}_2 + \dot{\theta}_2\ddot{\theta}_2)\cos[\theta_2]\right\}\cos[\theta_1]\end{aligned} \tag{48}$$

$$\begin{aligned}\dddot{J}_{22} &= L_2\left(\dot{\theta}_1^3 + 3\dot{\theta}_1^2\dot{\theta}_2 + 3\dot{\theta}_1\dot{\theta}_2^2 + \dot{\theta}_2^3 - \dddot{\theta}_1 - \dddot{\theta}_2\right)\sin[\theta_1 + \theta_2] \\ &\quad - 3L_2\left(\dot{\theta}_1\ddot{\theta}_1 + \dot{\theta}_1\ddot{\theta}_2 + \ddot{\theta}_1\dot{\theta}_2 + \dot{\theta}_2\ddot{\theta}_2\right)\cos[\theta_1 + \theta_2]\end{aligned} \tag{49}$$

6 Conclusion

Precise higher-order derivatives are essential across scientific research, engineering, and mathematical modelling. This paper's velocity, acceleration, jerk, and jounce vector fields are extracted simultaneously from Jacobian's multidual expression. This method has universal applicability, spanning various fields and disciplines. Whether in robotics, physics, or optimization algorithms, accurate derivatives play a fundamental role in understanding complex systems and achieving optimal outcomes. With multidual algebra, precise higher-order derivatives can be extracted quickly with less resource consumption. The calculation was done in Maple software and can be adapted for any link, number of joints, and higher-order accelerations.

Acknowledgements This work was supported by the project New smart and adaptive robotics solutions for personalized minimally invasive surgery in cancer treatment—ATHENA, funded by European Union—NextGenerationEU and Romanian Government, under National Recovery and Resilience Plan for Romania, contract no. 760072/23.05.2023, code CF 116/15.11.2022, through the Romanian Ministry of Research, Innovation and Digitalization, within Component 9, investment I8.

References

1. Zhongtao, F., Spyrakos-Papastavridis, E., Lin, Y., Dai, J.S.: Analytical expressions of serial manipulator Jacobians and their high-order derivatives based on lie theory. In: 2020 IEEE Int. Conf. on Robotics and Automation (ICRA), pp. 7095–7100. (2020)
2. Messelmi, F.: Analysis of dual functions, annual review of chaos theory, bifurcations and dynamical systems, vol. 4, pp. 37–54. (2013). ISSN 2253-0371
3. Condurache, D.: "Higher-order kinematics of lower-pair chains with hyper-multidual algebra" IDETC/CIE 2022, St. Louis, Missouri. August 14–17 (2022)
4. Condurache, D., Cojocari, M., Popa, I.: Hypercomplex dual lie nilpotent algebras and higher-order kinematics of rigid body. In: Mechanisms and Machine Science, vol 127. Springer, Cham, (2022)
5. Müller, A.: An overview of formulae for the higher-order kinematics of lower-pair chains with applications in robotics and mechanism theory. Mech. Mach. Theory **142**, 103594 (2019)

Mathematical and Mechanical Model of a Tamping Rammer for Making Rammed Earth Walls

Radu Mircea Morariu-Gligor

Abstract The paper presents a mechanization/automation model for the process of making rammed earth walls. Since all the parameters of the production system depend on the compaction process, the paper proposes a mechanical and mathematical model of a tamping rammer used for the construction of rammer earth walls. Based on this mathematical model, a series of studies can be carried out on the influence of the various components of the compactor on both the compaction process and the entire robot.

Keywords Rammed earth wall · Tamping rammer · Mathematical model

1 Introduction

Earth is one of the oldest and most widely used natural building materials, having been used for thousands of years on all continents, from the ancient Great Wall of China 4000 years ago to the residential buildings in present. Rammed earth has been seen as an easy and cheap way to build fortifications and houses quickly. It is estimated that more than a third of the human population still lives in earthen houses.

For many years, the use of rammed earth was abandoned and neglected, especially after the industrial revolution, due to the availability of other construction materials. Recent concerns about global warming and the depletion of natural resources are prompting the search for materials and technologies that will reduce the impact on the environment, CO_2 emissions and energy consumption.

Rammed earth involves mixing dry earth with water and possibly an addition of fibers to improve its mechanical strength. Rammed earth that uses only clay as a binder is called unstabilized rammed earth (URE), and rammed earth that uses other binders (lime, cement) in addition to clay is called stabilized rammed earth (SRE).

The amount of cement added is small (3–10%), depending on the quality of the soil, but it gives the mixture increased strength and durability. The ideal soil for

R. M. Morariu-Gligor (✉)
Technical University of Cluj-Napoca, 103-105 Muncii Blvd, Cluj-Napoca, Romania
e-mail: rmogli70@yahoo.com

D. Pisla et al. (eds.), *Advances in Service and Industrial Robotics*, Mechanisms and Machine Science 157, https://doi.org/10.1007/978-3-031-59257-7_39

rammed earth construction consists of a good mixture of clay (about 10–40%), silt (about 10–40%), sand (about 35–65%) and even very fine gravel [1–3].

The advantages of using rammed earth are: it requires little water or additives to improve its properties, it is easy to work with and can be recycled, it has good thermal and sound insulation properties, does not emit harmful emissions and it doesn't burn.

The manufacturing of rammed earth walls requires an additive manufacturing technology through which the structures are made by adding and compacting successive layers of earth, between two vertical walls that define the width of the wall.

The traditional technology involves repeatedly hammering the end of a wooden post into the soil mixture to compress it [4]. Figure 1 shows the technology for making rammed earth walls [2], the stages being the following:

1. Building the wall foundation: The size of the foundation is chosen depending on the type of supported structure and the bearing capacity of the soil under the foundation. The depth of the foundation must ensure the avoidance of frost below, and the land adjacent to the base of a rammed earth wall must be well drained.
2. Fitting the formwork: The formwork used in the construction of earth walls is made of wood or steel. They must be sufficiently strong, rigid and stable to withstand the pressures to which they are subjected during the pouring of the soil mixture and the compaction process.
3. Adding a layer of soil: The soil mixture is poured into the formwork, creating a uniform level approximately 15 cm thick.
4. Mechanical ramming of the soil layer: By compaction, the soil layer is compressed to about 8–10 cm thick. The appearance of the wall will depend on the soil and aggregate used, being made up of horizontal layers that may differ in terms of color and texture.

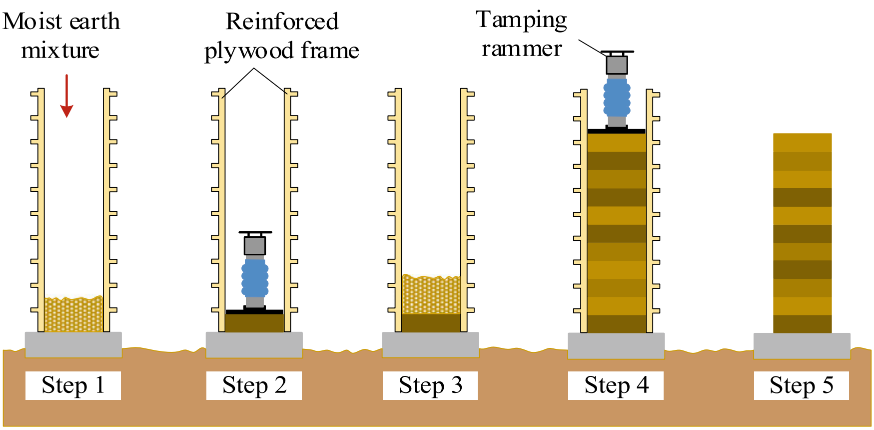

Fig. 1 The compaction process for rammed earth wall [4]

5. Removing the formwork and reassembling it in the direction of the wall elevation.

Steps 2–5 are repeated successively until the desired height of the wall is obtained.

As it can be seen, the soil ramming process is labor-intensive and energy-intensive.

The technology of building with rammed earth has involved the replacement of hand tools with electric and/or fuel-powered tools to improve efficiency, productivity, and quality.

2 Description of the Robot for Making Walls from Rammed Earth

The construction of rammed earth walls involves compacting the soil, in layers, between two vertical formworks which are then moved higher up to ensure the deposition and compaction of a new layer of soil.

The aim is to eliminate the use of the human operator and to automate ramming operations, earthworks and formwork handling. Automated processes result in higher structural strength, better construction quality, increased productivity and reduced material consumption, all with minimal human intervention.

In the last 10 years, there has been a growing interest in the mechanization of earth construction, in particular in advanced manufacturing of earth construction [5]. There are also studies exploring the possibility of using digital manufacturing technologies such as 3D printing [6] or robotic manufacturing in construction [7]. Studies on achieving optimal blends, development and realization of improved, automated manufacturing technologies are essential.

In paper [1], two automated systems for manufacturing rammed earth walls are presented. In 2020, the company Form Earth© (Australia) was preselling a prototype of an automated earth wall manufacturing system called FreeForm (see Fig. 2) [8]. The system consists of a frame, a material hopper, a compaction tool and a slip formwork system. The material is fed along the entire length of the formwork, thus ensuring an even layer of soil. The compaction tool climbs vertically with the formwork and moves inside the formwork to achieve compaction. A sensor system ensures that the optimum compaction level is achieved. When one layer is completed, the whole system moves upwards to compact the next layer.

An automated system for making walls from rammed earth should consist of the following subsystems (see Fig. 3): formwork handling system (1), tamping rammer (2), tamping rammer positioning and vertical movement system (3), tamping rammer positioning and horizontal movement system (4), frame (5). In addition, there must be a material supply system.

The frame must ensure the support and the assembly of the other subsystems, must be rigid enough but not too heavy to be easily handled. The formwork handling system must ensure that the formwork can be moved vertically, fixed to the frame and must withstand the pressures of the ground layer. The tamping rammers can

Fig. 2 The form earth system for making compacted earth walls [8]

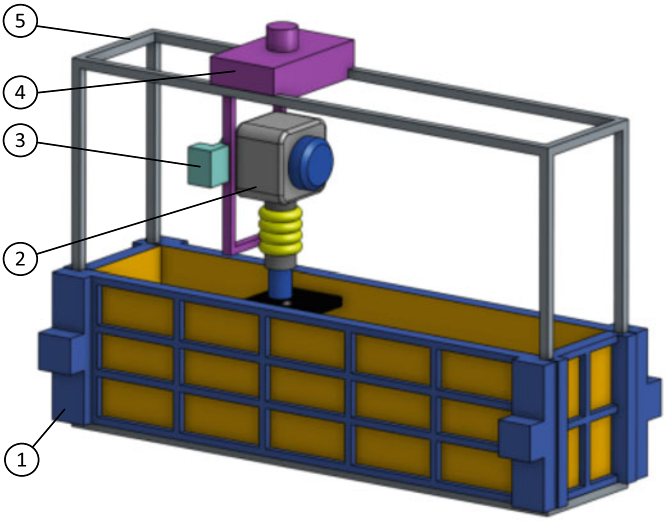

Fig. 3 Automated system for making walls from rammed earth

be driven by electric or gasoline engines and contain a slider-crank mechanism that drives the tamping rammer's sole via a helical spring-damper assembly [9, 10].

The positioning and vertical movement system must ensure that the tamping rammer is placed on the mix layer and is allowed to move vertically during compaction.

The system for positioning and moving horizontally must ensure that the tamping rammer is positioned at the end of the formwork and that it can move in both directions along the mix layer (along the frame). The horizontal movement must have an adjustable advance according to the desired degree of compaction.

3 Mechanical and Mathematical Model of the Tamping Rammer

The operation of the tamping rammer is influenced by a number of parameters which can be: kinematical (determined by the characteristics of the drive motor), geometrical (determined by the dimensions of the components) and mechanical (determined by the mass of the machine or the forces developed in the helical springs).

Weight is an important factor, as excessive weight requires higher energy consumption without improving compaction characteristics. The height from which the ram strikes is also very important. The sole may be achieved either by means of a slider-crank system in conjunction with a spring-damping system or by means of a vibration generator with one or two eccentric masses.

It is very important to determine: the moment and power required (at the drive motor), the masses of the component parts, the dimensions of the component parts and the distances between them, the elastic and damping elements [10]. It is also necessary to know the forces and pressures with which the earth acts on the formwork during the compaction process in order to design the frame and the formwork drive system. With the help of the mathematical model, the parameters of the compaction process can be analyzed, leading to an increase in machine efficiency.

The slider-crank mechanism acts via helical springs on the crank plate. The sole executes an oscillatory movement with a certain frequency and amplitude. The damping effect is provided by an oil-filled bellows cylinder.

In the mechanical model shown in Fig. 4, the soil is modelled using the Kelvin-Voigt model consisting of a helical spring and a damper mounted in parallel. The values of the elastic and damping constants are a function of the nature of the compacted mixture as well as its degree of compaction.

The following simplifying assumptions were used in the mathematical model: movement is only in the vertical direction, the moment of inertia **I** and the driving moment **M** are constant, the elastic and damping constants are linear.

The notations used to develop the mathematical model are as follows: $\mathbf{z_1}$ and $\mathbf{z_2}$—parameters defining motor and sole position; **M**—driving moment; $\boldsymbol{\omega}$—crank angular speed; $\boldsymbol{\varphi}$—angle between crank handle and vertical axis; $\boldsymbol{\psi}$—angle between connecting rod and vertical axis; $\mathbf{m_1}$—mass of the motor frame, together with the motor; $\mathbf{m_2}$—mass of the slider-crank mechanism together with the springs; $\mathbf{m_3}$—mass of the sole; **r**—crank length; **b**—connecting rod length; **h**—length of springs in the assembled state; $\mathbf{k_1}$—the elasticity constant of the helical springs [N/m]; $\mathbf{c_1}$—the damping coefficient of the viscous damper [Ns/m]; $\mathbf{k_2}$—the elasticity constant of the soil [N/m]; $\mathbf{c_2}$—the damping coefficient of the soil [Ns/m];

The mechanical system has two degrees of freedom, the parameters that define its position at a given moment are: $\mathbf{z_1}$—the displacement of the motor frame, and $\mathbf{z_2}$—the displacement of the sole. The crank, on which acts the constant driving moment **M**, performs a rotational movement with constant angular velocity, in the counterclockwise direction. This generates a force, $\mathbf{T_0}$, which is applied to the rod at its end.

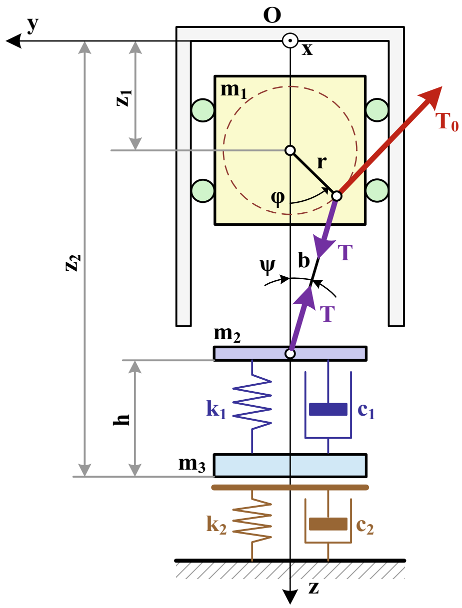

Fig. 4 Mathematical model of the tamping rammer

Applying Newton's laws, we obtain the differential equations that define the motion of the three masses m_1, m_2, and m_3, respectively:

$$m_1\ddot{z}_1 = m_1 g - T_0 \sin\varphi + T\cos\psi \tag{1}$$

$$m_2\frac{d^2}{dt^2}(z_1 + r\cos\varphi + b\cos\psi) = m_2 g - T\cos\psi +$$

$$+k_1(z_2 - z_1 - h - r\cos\varphi - b\cos\psi) + c_1\left(\dot{z}_2 - \dot{z}_1 + r\omega\sin\varphi + b\dot{\psi}\sin\psi\right) \tag{2}$$

$$\begin{aligned} m_3\ddot{z}_2 = {} & m_3 g - k_1(z_2 - z_1 - h - r\cos\varphi - b\cos\psi) \\ & - c_1\left(\dot{z}_2 - \dot{z}_1 + r\omega\sin\varphi + b\dot{\psi}\sin\psi\right) \\ & - \begin{cases} 0 & z_2 \le r + b + h \\ [k_2(z_2 - r - b - h) + c_2\dot{z}_2] & z_2 > r + b + h \end{cases} \end{aligned} \tag{3}$$

In Eq. (3) the mass m_3 is considered not to be in permanent contact with the surface to be compacted. The derivative is calculated:

$$\begin{aligned} & \frac{d^2}{dt^2}(z_1 + r\cdot\cos\varphi + b\cdot\cos\psi) \\ & = \frac{d}{dt}\left(\dot{z}_1 - \omega r\sin\varphi - b\dot{\psi}\sin\psi\right) \end{aligned}$$

$$= \ddot{z}_1 - \omega^2 r \cos\varphi - b\ddot{\psi}\sin\psi - b\dot{\psi}^2\cos\psi \tag{4}$$

Equation (2) becomes:

$$\begin{aligned} & m_2\ddot{z}_1 - m_2 \cdot \omega^2 \cdot r \cdot \cos\varphi - m_2 \cdot b \cdot \ddot{\psi} \cdot \sin\psi - m_2 \cdot b \cdot \dot{\psi}^2 \cdot \cos\psi \\ & = m_2 \cdot g - T \cdot \cos\psi + k_1 \cdot (z_2 - z_1 - h - r \cdot \cos\varphi - b \cdot \cos\psi) \\ & \quad + c_1 \cdot \left(\dot{z}_2 - \dot{z}_1 + r \cdot \omega \cdot \sin\varphi + b \cdot \dot{\psi} \cdot \sin\psi\right) \end{aligned} \tag{5}$$

From Eq. (1) the expression for the force T is derived and substituted into the last equation, obtaining:

$$\begin{aligned} (m_1 + m_2)\ddot{z}_1 &= (m_1 + m_2)g - T_0 \sin\varphi \\ & \quad + k_1(z_2 - z_1 - h - r\cos\varphi - b\cos\psi) \\ & \quad + c_1\left(\dot{z}_2 - \dot{z}_1 + r\omega\sin\varphi + b\dot{\psi}\sin\psi\right) \\ & \quad + m_2\left(\omega^2 r\cos\varphi + b\ddot{\psi}\sin\psi + b\dot{\psi}^2\cos\psi\right) \end{aligned} \tag{6}$$

The system of differential equations describing the motion of the motor frame and the sole is composed of two differential equations as follows:

$$\begin{aligned} & (m_1 + m_2)\ddot{z}_1 = (m_1 + m_2)g \\ & \quad - T_0\sin\varphi + k_1(z_2 - z_1 - h - r\cos\varphi - b\cos\psi) \\ & \quad + c_1\left(\dot{z}_2 - \dot{z}_1 + r\omega\sin\varphi + b\dot{\psi}\sin\psi\right) \\ & \quad + m_2\left(\omega^2 r\cos\varphi + b\ddot{\psi}\sin\psi + b\dot{\psi}^2\cos\psi\right) \\ & m_3\ddot{z}_2 = m_3 g - k_1(z_2 - z_1 - h - r\cos\varphi - b\cos\psi) \\ & \quad - c_1\left(\dot{z}_2 - \dot{z}_1 + r\omega\sin\varphi + b\dot{\psi}\sin\psi\right) \\ & \quad - \begin{cases} 0 & z_2 \le r + b + h \\ [k_2(z_2 - r - b - h) + c_2\dot{z}_2] & z_2 > r + b + h \end{cases} \end{aligned} \tag{7}$$

With the help of this mathematical model, the behavior of the tamping rammer component of the robot for the manufacturing rammed earth walls can be analyzed.

To solve this system of differential equations, a program in the C language was written, using the 4th order Runge–Kutta method.

In Table 1 are presented the input data for 4 different variants of tamping rammers, and Figs. 5 and 6 illustrate the variations in frame and foot displacements considering each variant separately.

The values of the damping constant (k_2) and of the damping coefficient (c_2) used in soil modeling are: $k_2 = 800{,}000$ [N/m] and $c_2 = 3500$ [Ns/m] respectively.

Table 1 The input data for the four variants of tamping rammers

Input data	Symbol	Var. 1	Var. 2	Var. 3	Var. 4
Driving moment [Nm]	M	16	18	23	27
Crank's rotation speed [rpm]	n	650	700	600	650
Mass of the motor frame [kg]	m_1	36	45	50	65
Mass of the slider-crank mechanism [kg]	m_2	4.5	6	7.5	8
Mass of the sole [kg]	m_3	12	16	20	24
Crank length [m]	r	0.025	0.0275	0.030	0.030
Connecting rod length [m]	b	0.210	0.215	0.200	0.225
Length of springs in the assembled state [m]	h	0.120	0.125	0.130	0.135
The elasticity constant of the helical springs [N/m]	k_1	65,000	68,000	70,000	72,000
The damping coefficient [Ns/m]	c_1	310	290	300	310

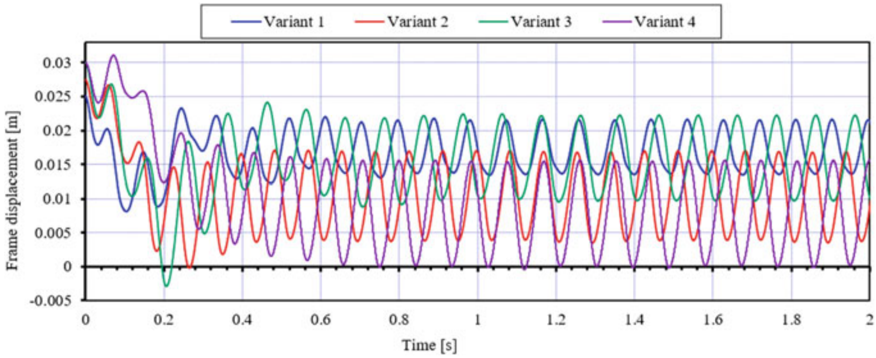

Fig. 5 The displacements of the frame

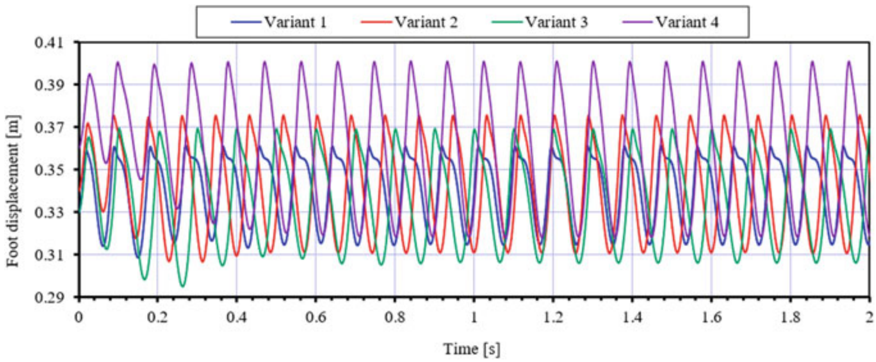

Fig. 6 The displacements of the compacting plate

4 Conclusions

Using the previously presented mathematical model, a series of parameters that define the behavior of the tamping rammer can be determined, such as:

- The vertical displacement of the motor frame and the sole of the tamping rammer;
- The pressure force on the soil, generated by the sole of the tamping rammer;
- The influence of the mass values and the geometric dimensions of the components;
- The influence of the engine rotation speed and its power on the tamping rammer;
- The influence of the elastic and damping characteristics;
- The choice of appropriate technical solutions and the appropriate dimensioning of the formwork lifting system and the horizontal and vertical displacement systems.

The current paper presents a variant of a robot for building rammed earth walls, which uses a tamping rammer. The analysis of the operation of the tamping rammer and the influence it has on the entire robot is essential. Therefore, the mechanical and mathematical modeling of the tamping rammer was considered necessary, thus offering a useful tool to those who want to approach this field.

Based on it, computation programs can be designed to analyze the influences of all the parameters that determine the operation of the tamping rammer. From the analysis of these parameters, the complexity of the operation of such a robot is observed and a series of possible themes for further research can be highlighted, regarding both the method of choosing a construction variant and the dimensioning of the robot's component elements.

References

1. Gomaa, M., Schade, S., Bao, D.W., Xie, Y.M.: Automation in rammed earth construction for industry 4.0: precedent work, current progress and future prospect. J. Cleaner Prod. **398** (2023). ISSN 0959-6526. https://doi.org/10.1016/j.jclepro.2023.136569
2. Niroumand, H., Akbari, R., Khanlari, K., Gültekin, A.B., Barcelo, J.A.: A systematic literature review of rammed earth walls. Soil Mech. Found. Eng. **58**(4) (2021). https://doi.org/10.1007/s11204-021-09742-y
3. Totla, P., Sadwilkar, M., More, S., Kallada, B., Deshmukh, B., Puranik, A.: Sustainable rammed earth structure: a structurally integral, cost-effective and eco-friendly alternative to conventional construction material. Int. J. Innov. Technol. Explor. Eng. (IJITEE) **8**(11S), (2019). ISSN: 2278-3075. https://doi.org/10.35940/ijitee.K1077.09811S19
4. Minke, G.: In: Earth Construction Handbook: The Building Material Earth in Morden Architecture. WIT Press, Southampton, UK (2000)
5. Giuffrida, G., Caponett, R., Cuom, M.: An overview on contemporary rammed earth buildings: technological advances in production, construction and material characterization. In: IOP Conference Series: Earth and Environmental Science, Milan, Italy, vol. 296 (2019). https://doi.org/10.1088/1755-1315/296/1/012018
6. Gomaa, M., Jabi, W., Soebarto, V., Xie, Y.M.: Digital manufacturing for earth construction: a critical review. J. Cleaner Prod. **338** (2022). ISSN 0959-6526. https://doi.org/10.1016/j.jclepro.2022.130630

7. Guanqi Z.: Automatic robotic construction for customizable rammed earth walls. In: Proceedings of the 28th International Conference of the Association for Computer-Aided Architectural Design Research in Asia (CAADRIA), Hong Kong, vol. 2, pp. 109–118. (2023). https://doi.org/10.52842/conf.caadria.2023.2.109;
8. FormEarth.: Free form rammed earth (2022). https://formearth.com
9. Crişan, A.V., Morariu-Gligor, R.M.: A study on the impact force in case of tamping rammers. RJAV **16**(1) (2019). ISSN 1584-7284
10. Morariu-Gligor, R.M.: The study of the dynamic behavior for a tamping rammer. Symmetry **14**, 980 (2022). https://doi.org/10.3390/sym14050980

Establishing of Dynamic Control Functions for a Hybrid Robot Based on Analytical Mechanics Principles

Claudiu Schonstein

Abstract The use of complex mechanical systems in different tasks assumes the controlling of each motor from the kinematic joints known as dynamic control equations. The moving differential equations for any mechanical system can be expressed very efficiently based on principles from Analytical Mechanics, among which the method developed by Lagrange—Euler provides explicit equations of motion. The Lagrange—Euler second kind formalism is an analytical approach extremely useful in modelling of multibody systems which uses an important notion in dynamics—kinetic energy. These equations can be used to analyze and devise advanced control strategies by mathematical modeling based on mathematical algorithms. In this paper, for two robot structures (serial and mobile), considering that are working independently, will be established the dynamic control functions, using a generalized algorithm, consisting in geometrical, kinematical and dynamical modeling.

Keywords Robots · Dynamic control functions · Kinetic energy · Algorithm

1 Introduction

The use of a robot for a task assumes the control of motions, by dedicated mathematical algorithms. A complete modelling of a robot consists in geometrical, kinematical, and dynamic behavior for the mechanical structure, based on dedicated algorithms [1]. The dynamic equations of motion, important for mechanical design, control, and simulation, provide the relationships between actuation and forces acting on robot mechanisms, and the kinematic parameters and motion trajectories that result [2].

The specialized principles of kinematics and dynamics employed for robotic systems fall within the broader study of multibody dynamics. Multibody dynamics is the study of the dynamics of mechanical systems that are comprised of several interconnected bodies [3]. The approach, presented further in the paper, regarding the control of robotic systems is a popular starting point for mechanical and control

C. Schonstein (✉)
Technical University of Cluj-Napoca, Cluj-Napoca, Romania
e-mail: Claudiu.Schonstein@mep.utcluj.ro

D. Pisla et al. (eds.), *Advances in Service and Industrial Robotics*, Mechanisms and Machine Science 157, https://doi.org/10.1007/978-3-031-59257-7_40

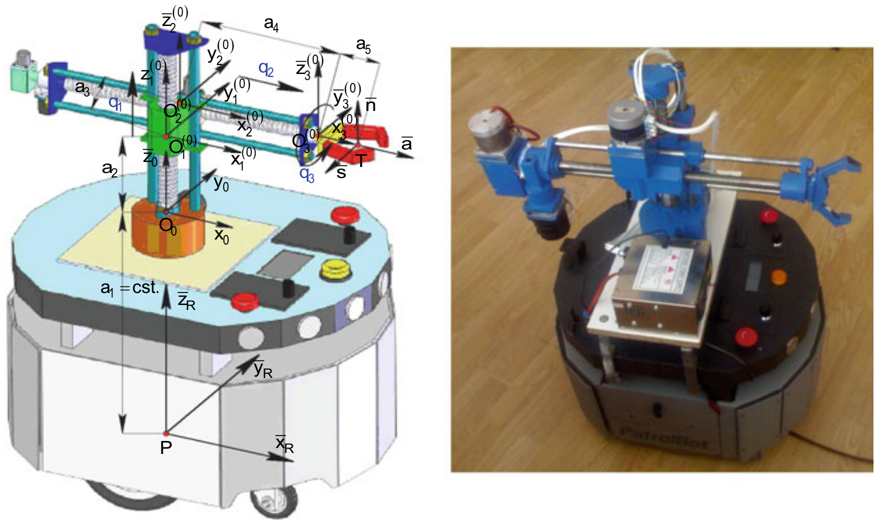

Fig. 1 The hybrid structure (2TR + PatrolBot)

design. The methodology is applicable to a reasonably large collection of mechanical systems and can also be used to motivate and understand alternative control schemes [4].

In this paper is presented a concept of complex robot structure (see Fig. 1) consisting in a serial structure 2TR type, and a mobile robot PatrolBot [5], which can be used in different tasks of handling, sorting, or moving different work pieces from point to point.

For this structure the driving moments, known as dynamic control functions, will be presented based on concepts from advanced mechanics of complex systems as [6, 7], considering the geometrical characteristics, and mass properties of structure. As an important remark, the dynamic control functions are established separately for each robot, because the structures are working independently.

Section 2 presents, based on algorithms for geometry (Sect. 2.1) and kinematics (Sect. 2.2) the dynamic control functions (Sect. 2.3) for the 2TR serial robot, taking into account the dimensional characteristics of the structure. The dynamic model is established on the basis of Lagrange-Euler second kind equations, formalism specific to non-conservative mechanical systems and with holonomous links.

In Sect. 3 are presented, based on kinematical restrictions (Sect. 2.1), the kinematic model (Sect. 2.2), and the dynamic control functions (Sect. 2.3) for the mobile robot. As in Sect. 2, there is used the same Lagrange-Euler second kind formalism, but specific to mechanical systems and with nonholonomous links.

2 Dynamics Control Functions for the 2TR Serial Structure

As it can be observed from Fig. 1, the serial structure has three degrees of freedom ($i = 1 \to 3$), considered generalized coordinates $q_i,\ i = 1 \to 3$ consisting in two translations (q_1 along O_{z_0} and q_2 along O_{x_0} axis), and q_3 representing a rotation of the end effector around O_{x_0} axis.

2.1 Geometry Equations for Serial Structure

According to [6] to establish the control functions, first must be known the Direct Geometry Equations. Applying the Locating Matrix Algorithm, it is determined the following column vector of generalized coordinates [8]:

$$
{}^{0}\overline{X}(\overline{\theta}) = \begin{bmatrix} \left(p_x\ p_y\ p_z\right)^T \\ \cdots\cdots\cdots\cdots\cdots \\ \left(\alpha_z\ \beta_y\ \gamma_z\right)^T \end{bmatrix} = \left\{ \begin{bmatrix} a_4 + a_5 + q_2 \\ a_3 = cst. \\ a_2 + q_1 \end{bmatrix} \left[\pi/2\ \pi/2\ \pi + q_3\right]^T \right\}^T, \tag{1}
$$

representing the direct geometry equations, where $\overline{\theta} = [q_i,\ i = 1 \to 3]^T$ is a column vector of generalized coordinates from each driving joint of the robot.

2.2 Kinematics Equations for Serial Structure

To obtain the kinematics equations, is used the Algorithm of Matrix Exponential in kinematics, and the time derivative of Jacobian matrix [9]. According to [8], the direct kinematics equations for the serial type structure are:

$$
\begin{gathered}
{}^{0}\dot{\overline{X}} \equiv \begin{bmatrix} {}^{0}\overline{v}_3 \\ --- \\ {}^{0}\overline{\omega}_3 \end{bmatrix} = {}^{0}J\left(\overline{\theta}\right) \cdot \dot{\overline{\theta}} = \begin{bmatrix} \left(\dot{q}_2\ 0\ \dot{q}_1\right)^T \\ \left(\dot{q}_3\ 0\ 0\right)^T \end{bmatrix}, \\
{}^{0}\ddot{\overline{X}} \equiv \begin{bmatrix} {}^{0}\dot{\overline{v}}_3 \\ --- \\ {}^{0}\dot{\overline{\omega}}_3 \end{bmatrix} = {}^{0}J\left(\overline{\theta}\right) \cdot \ddot{\overline{\theta}} = \begin{bmatrix} \left(\ddot{q}_2\ 0\ \ddot{q}_1\right)^T \\ \left(\ddot{q}_3\ 0\ 0\right)^T \end{bmatrix}
\end{gathered} \tag{2}
$$

The expressions contained in Eq. (2) where ${}^{0}J\left(\overline{\theta}\right)$ is the Jacobian matrix characterize the motion of the final effector of the 2TR robot in the Cartesian space, and:

$$
{}^{0}J(\overline{\theta}) = \left[{}^{0}J_1 \; {}^{0}J_2 \; {}^{0}J_3 \right], \quad \begin{array}{l} {}^{0}J_1 = \left[0\;0\;1\;0\;0\;0 \right]^T \\ {}^{0}J_2 = \left[1\;0\;0\;0\;0\;0 \right]^T \\ {}^{0}J_3 = \left[0\;0\;0\;1\;0\;0 \right]^T \end{array} \tag{3}
$$

2.3 Dynamics Equations for the 2TR Serial Structure

A complete dynamic modelling, according to the specialized literature [6, 10] comprises the control motion expressions of the driving motors belonging to the robot being studied, as well as the dynamic behavior of the transmission structure of the movement [11]. The differential equations of motion are determined based on Lagrange-Euler second kind equations, because the formalism is specific to non-conservative mechanical systems and with holonomous links. Hence, the equations of motion of the mechanical structure of the 2TR type serial robot will be determined considering the expression [12]:

$$
Q^i_{\mathfrak{F}} + Q^i_g + Q^i_{SU} = Q^i_m\left(\overline{\theta}; \dot{\overline{\theta}}; \ddot{\overline{\theta}}\right), \; i = 1 \rightarrow 3 \tag{4}
$$

where $Q^i_{\mathcal{F}}$; Q^i_g; Q^i_{SU} are generalized inertia forces, generalized gravitational forces, and generalized handling forces, described in [6]. The expressions for generalized inertia forces, is presented as:

$$
Q^i_{\mathfrak{F}} = \frac{d}{dt}\left[\frac{\partial \, E_k\left(\overline{\theta}; \dot{\overline{\theta}}\right)}{\partial \, \dot{q}_i}\right] - \frac{\partial E_k\left(\overline{\theta}; \dot{\overline{\theta}}\right)}{\partial q_i} \tag{5}
$$

Based on König's theorem, the expression for kinetic energy is:

$$
E^j_k = (-1)^{\Delta_M} \cdot \frac{1 - \Delta_M}{1 + 3 \cdot \Delta_M} \cdot \left\{ \frac{1}{2} \cdot M_j \cdot {}^{j}\overline{v}^T_{C_j} \cdot {}^{j}\overline{v}_{C_j} \right\} + \Delta^2_M \cdot \frac{1}{2} \cdot {}^{j}\overline{\omega}^T_j \cdot {}^{j}I^*_j \cdot {}^{j}\overline{\omega}_j \tag{6}
$$

where: $\Delta_M = \{\{-1; \mathit{general\,motion}\}; \{0; \mathit{translation}\}; \{1; \text{ rotation}\}\}$, ${}^{j}\overline{v}_{C_j}$ and ${}^{j}\overline{\omega}_j$ representing the linear and angular velocity of the mass center for each element, ${}^{j}I^*_j$ is the inertial axial-centrifugal tensor of element (j), according to the frame applied in the mass center. Considering [8], the kinetic energy for the 2TR structure, is:

$$
\begin{aligned}
E_k\left(\overline{\theta},\ \dot{\overline{\theta}}\right) &= \sum_{j=1}^{3}\left\{\frac{1}{2}\cdot M_j\cdot {}^j\overline{v}_{Cj}^T\cdot {}^j\overline{v}_{Cj}+\frac{1}{2}\cdot {}^j\overline{\omega}_j^T\cdot {}^jI_j^*\cdot {}^j\overline{\omega}_j\right\}\\
&=\sum_{j=1}^{3}\left\{\frac{1}{2}\cdot M_j\cdot {}^j\overline{v}_{Cj}^T\cdot {}^j\overline{v}_{Cj}\right\}+\frac{1}{2}\cdot {}^3\overline{\omega}_3^T\cdot {}^3I_3^*\cdot {}^3\overline{\omega}_3\\
&=3.731\cdot \dot{q}_1^2+1.814\cdot \dot{q}_2^2+760.45\cdot 10^{-6}\cdot \dot{q}_3^2\\
&\quad+\dot{q}_1\cdot \dot{q}_3\cdot \left(5.2\cdot 10^{-3}\cdot \cos q_3+1.97\cdot 10^{-3}\cdot \sin q_3\right);
\end{aligned}
\tag{7}
$$

According to the expression (5), the generalized force of inertia is determined by:

$$
\begin{aligned}
Q_{\mathfrak{F}}^1\left(\overline{\theta}\right) &= \left(1.972\cdot 10^{-3}\cdot \cos q_3-5.209\cdot 10^{-3}\cdot \sin q_3\right)\cdot \dot{q}_3^2\\
&\quad+7.463\cdot \ddot{q}_1+\left(5.209\cdot 10^{-3}\cdot \cos q_3+1.972\cdot 10^{-3}\cdot \sin q_3\right)\cdot \ddot{q}_3
\end{aligned}
\tag{8}
$$

$$
Q_{\mathfrak{F}}^2\left(\overline{\theta}\right)=\frac{d}{dt}\left[\frac{\partial E_k}{\partial \dot{q}_2}\right]-\frac{\partial E_k}{\partial q_2}=3.6286\cdot \ddot{q}_2 \tag{9}
$$

$$
\begin{aligned}
Q_{\mathfrak{F}}^3\left(\overline{\theta}\right) &= \frac{d}{dt}\left[\frac{\partial E_k}{\partial \dot{q}_3}\right]-\frac{\partial E_k}{\partial q_3}\\
&=\left(5.209\cdot 10^{-3}\cdot \cos q_3+1.97\cdot 10^{-3}\cdot \sin q_3\right)\cdot \ddot{q}_1\\
&\quad+1.52\cdot 10^{-3}\cdot \ddot{q}_3
\end{aligned}
\tag{10}
$$

The generalized gravitational forces are defined as:

$$
Q_g^i\left(\overline{\theta}\right)={}^0J_i\left(\overline{\theta}\right)^T\ \cdot\ {}^0F_{x_i}\left(\overline{\theta}\right), \tag{11}
$$

where ${}^0J_i\left(\overline{\theta}\right)^T$ is the line (i) of the transposed of Jacobian matrix defined in expression (3), and ${}^0F_{x_i}\left(\overline{\theta}\right)$ is the resultant force-moment vector of gravitational loads in the range $[i \rightarrow 3]$, whose expression for the 2TR structure of is presented in [8].

According to Eq. (11), the generalized gravitational forces for the 2TR structure is [6]:

$$
\begin{aligned}
Q_g^1\left(\overline{\theta}\right)=73.186; \qquad Q_g^2\left(\overline{\theta}\right)=0\\
Q_g^3\left(\overline{\theta}\right)=51.081\cdot 10^{-3}\cdot \cos q_3+19.339\cdot 10^{-3}\cdot \sin q_3
\end{aligned}
\tag{12}
$$

The generalized handling forces are expressed [6]:

$$
Q_{SU}^i(\theta)={}^0J_i^T(\theta)\cdot {}^0F_{iX}(\theta),\quad i=1\rightarrow 3 \tag{13}
$$

where ${}^0F_{iX}(\theta)$, $i = 1 \rightarrow 3$ is, the vector of the resultant force-load handling moment. For the 2TR robot, according to expression (13), there is obtained according to [8]:

$$Q_{SU}^{1}\left(\overline{\theta}\right) = 9.806 \cdot m_{SU}; \quad Q_{SU}^{2}\left(\overline{\theta}\right) = Q_{SU}^{3}\left(\overline{\theta}\right) = 0 \tag{14}$$

where m_{SU} represents the handling load.

Considering the constructive form and dimensions of the robot, based on the characteristic frictions existing in the mechanical system of motion transmission, according to expressions (12–14) substituted in Eq. (4), conducts to the driving moments of motors as [8]:

$$\begin{aligned} Q_m^1 = {} & 7.47 \cdot \ddot{q}_1 + \left(28.7 \cdot 10^{-9} - 11.6 \cdot 10^{-7} \cdot \cos q_3 - 43.95 \cdot 10^{-8} \cdot \sin q_3\right) \cdot \ddot{q}_2 \\ & + \left(-26.55 \cdot 10^{-9} + 52.09 \cdot 10^{-4} \cdot \cos q_3 + 19.72 \cdot 10^{-4} \cdot \sin q_3\right) \cdot \ddot{q}_3 \\ & + \left(90.71 \cdot 10^{-9} + 19.72 \cdot 10^{-4} \cdot \cos q_3 - 52.09 \cdot 10^{-4} \cdot \sin q_3\right) \cdot \dot{q}_3^2 \\ & + \left(9.806 - 20.76 \cdot 10^{-5} \cdot \cos q_3\right) \cdot m_{SU} + 73.186 \end{aligned} \tag{15}$$

$$Q_m^2 = 48.21 \cdot 10^{-3} \cdot \ddot{q}_2 + 39.03 \cdot 10^{-9} \tag{16}$$

$$\begin{aligned} Q_m^3 = {} & \left(5.2 \cdot 10^{-3} \cdot \cos q_3 + 1.97 \cdot 10^{-3} \cdot \sin q_3\right) \cdot \ddot{q}_1 + 1.52 \cdot 10^{-3} \cdot \ddot{q}_3 \\ & + 51.08 \cdot 10^{-3} \cdot \cos q_3 + 19.34 \cdot 10^{-3} \cdot \sin q_3 \\ & + 824.67 \cdot 10^{-6} \cdot \left\{\left[\dot{q}_3^2\left(1.97 \cdot 10^{-3} \cdot \cos q_3 - 5.2 \cdot 10^{-3} \cdot \sin q_3\right) + 1.3 \cdot \ddot{q}_1 \right.\right. \\ & \left. + \left(5.2 \cdot 10^{-3} \cdot \cos q_3 + 1.97 \cdot 10^{-3} \cdot \sin q_3\right) \cdot \ddot{q}_3 + 9.806 \cdot m_{SU} + 12.8\right]^2 \\ & + \left[\left(5.2 \cdot 10^{-3} \cdot \cos q_3 + 1.97 \cdot 10^{-3} \cdot \sin q_3\right) \cdot \dot{q}_3^2 \right. \\ & \left.\left. + \left(5.2 \cdot 10^{-3} \cdot \sin q_3 - 1.97 \cdot 10^{-3} \cdot \cos q_3\right) \cdot \ddot{q}_3\right]^2\right\}^{1/2}, \end{aligned} \tag{17}$$

3 Dynamics Control Functions for the Mobile Structure

In the Fig. 2, is considered a mobile robot called PatrolBot [5]. The mechanical structure of the robot, has two driving wheels, which are rolling around O_1, O_2 and two driven wheels which according to the same Fig. 2, are rotating around O_3 and O_4 respectively around vertical $\overline{z}$ axis.

According to above statements, where $(PC = x_C)$, in finite displacement the robot has the independent parameters, presented as follows [1]:

$$\overline{X}(t) = \left[q_i^*(t); \quad i = 1 \to 9\ \right]^T \tag{18}$$

In keeping with Fig. 2 and [15], according to differential principles from analytical mechanics presented in [6], the kinematical constrains for the mobile robot are [8]:

Fig. 2 The independent parameters of mobile robot PatrolBot (bottom view)

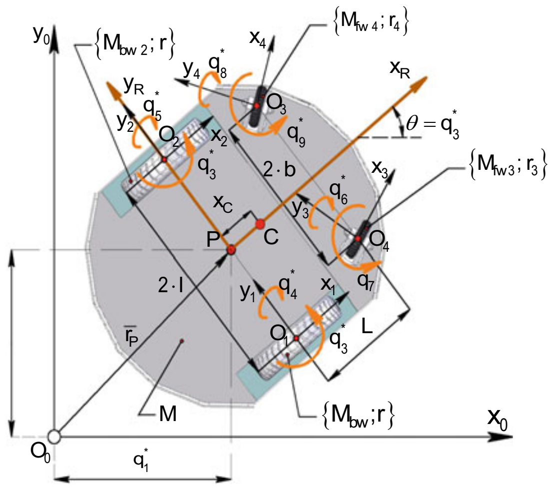

$$
\begin{gathered}
-sq_3^* \cdot \dot{q}_1^* + cq_3^* \cdot \dot{q}_2^* = 0 \\
cq_3^* \cdot \dot{q}_1^* + sq_3^* \cdot \dot{q}_2^* + l \cdot \dot{q}_3^* - r \cdot \dot{q}_4^* = 0, \quad cq_3^* \cdot \dot{q}_1^* + sq_3^* \cdot \dot{q}_2^* - l \cdot \dot{q}_3^* - r \cdot \dot{q}_5^* = 0 \\
-s(q_3^* + q_7^*) \cdot \dot{q}_1^* + c(q_3^* + q_7^*) \cdot \dot{q}_2^* + (L \cdot cq_7^* + b \cdot sq_7^*) \cdot \dot{q}_3^* = 0 \\
-s(q_3^* + q_9^*) \cdot \dot{q}_1^* + c(q_3^* + q_7^*) \cdot \dot{q}_2^* + (L \cdot cq_9^* + b \cdot sq_9^*) \cdot \dot{q}_3^* = 0 \\
c(q_3^* + q_7^*) \cdot \dot{q}_1^* + s(q_3^* + q_7^*) \cdot \dot{q}_2^* + (L \cdot sq_7^* - b \cdot cq_7^*) \cdot \dot{q}_3^* - r_3 \cdot \dot{q}_6^* = 0 \\
c(q_3^* + q_9^*) \cdot \dot{q}_1^* + s(q_3^* + q_9^*) \cdot \dot{q}_2^* + (L \cdot sq_9^* - b \cdot cq_9^*) \cdot \dot{q}_3^* - r_4 \cdot \dot{q}_8^* = 0
\end{gathered}
\tag{19}
$$

where $cq_i = \cos q_i, \ \ and \ \ sq_i = \sin q_i$, and $r_3 = r_4$.

In Eq. (19), the kinematical restrictions are referring to side displacement, the rolling of back wheels without slipping, side displacement and rolling without slipping of front wheels.

3.1 Kinematic Equations for the Mobile Robot PatrolBot

The motion of the robot is due to the wheels $M_{bw\,1}$, $M_{bw\,2}$ where $q_4^*(t) \neq q_5^*(t)$ are the rotation angles from the two driving wheels. In keeping the fact that is forbidden the robot's spinning around wheels axes, the expression of the operational velocities is [8, 14]:

$$\dot{\overline{X}} = \begin{bmatrix} \dot{q}_1^* \\ \dot{q}_2^* \\ \omega = \dot{q}_3^* \end{bmatrix} = \begin{bmatrix} cq_3^* & 0 \\ sq_3^* & 0 \\ 0 & 1 \end{bmatrix} \cdot \begin{bmatrix} \frac{r}{2} \cdot \left(\dot{q}_4^* + \dot{q}_5^*\right) \\ \frac{r}{2 \cdot l} \cdot \left(\dot{q}_4^* - \dot{q}_5^*\right) \end{bmatrix} \tag{20}$$

3.2 Dynamic Equations for the Mobile Robot PatrolBot

To establish the dynamics equations there is used the kinetic energy, included in the Lagrange–Euler second kind equations, according to [6, 16] written as:

$$\frac{d}{dt}\left(\frac{\partial E_k}{\partial \dot{q}_i}\right) - \frac{\partial E_k}{\partial q_i} = Q_m^i + \sum_{i=1}^{7} \lambda_j \cdot a_{ji} \ ; \tag{21}$$

where E_k represents the total kinetic energy of the mechanical system and Q_m^i are the driving forces. In the same equations $\lambda_j,\ j = 1 \rightarrow 7$ represents undetermined Lagrange parameters, while a_{ji} are considered the coefficients of the elementary displacements $q_i^* = q_i^*(t),\ i = 1 \rightarrow 9$ from Eq. (19). The kinetic energy of the mobile robot, is:

$$\begin{aligned} E_k\left(q_i^*;\ \dot{q}_i^*;\ \ i = 1 \rightarrow 9\right) &= E_k^A\left(q_i^*;\ \dot{q}_i^*;\ i = 1 \rightarrow 3\right) \\ &+ \sum_{j=1}^{4} E_k^j\left(q_i^*;\ \dot{q}_i^*;\ i = 4 \rightarrow 9\right), \end{aligned} \tag{22}$$

where E_k^A is the kinetic energy of the robot without wheels, and E_k^j represents kinetic energy of the wheels. The total kinetic energy for the robot is [6, 14]:

$$\begin{aligned} E_k = {} & \frac{1}{2} \cdot M \cdot \left[\left(\dot{q}_1^*\right)^2 + \left(\dot{q}_2^*\right)^2\right] - M_A \cdot x_C \cdot \dot{q}_3^* \cdot \left(\dot{q}_1^* \cdot sq_3^* - \dot{q}_2^* \cdot cq_3^*\right) \\ & + \frac{1}{2} \cdot I_R \cdot \left(\dot{q}_3^*\right)^2 + \frac{M_b \cdot r^2}{4} \cdot \left[\left(\dot{q}_4^*\right)^2 + \left(\dot{q}_5^*\right)^2\right] \\ & + M_f \cdot \left(\dot{q}_3^*\right)^2 \cdot \left(b^2 + L^2\right) - 2 \cdot M_f \cdot \dot{q}_3^* \cdot L \cdot \left[\left(\dot{q}_1^*\right)^2 \cdot sq_3^* - \left(\dot{q}_2^*\right)^2 \cdot cq_3^*\right] \\ & + \frac{M_f \cdot r_4^2}{4} \cdot \left[\left(\dot{q}_6^*\right)^2 + \left(\dot{q}_8^*\right)^2 + \frac{1}{2} \cdot \left[\left(\dot{q}_7^*\right)^2 + \left(\dot{q}_9^*\right)^2\right]\right] \end{aligned} \tag{23}$$

where: $M = M_A + 2 \cdot M_{bw} + 2 \cdot M_{fw}$ and M_A-the mass of the robot without wheels; $M_b = M_{bw\,1} = M_{bw\,2}$-the mass of a back wheel; $M_f = M_{fw\,1} = M_{fw\,2}$- the mass of a front wheel; $I_R = I_\Delta + \frac{M_b \cdot r^2}{2} + 2 \cdot M_b \cdot l^2$, and I_Δ the inertia moment of the structure. As a remark, in calculus there will be replaced M_A, M_b, M_f, I_Δ, l, L with corresponding values.

In keeping with Eqs. (23) and (21) there are obtained the differential equations [8]:

$$Q_m^4 = Q_m^5 = \frac{r}{2} \cdot \left[M \cdot \left(\ddot{q}_1^* \cdot cq_3^* + \ddot{q}_2^* \cdot sq_3\right) + \varepsilon \cdot \left(M_f \cdot r_3 + M_b \cdot r\right) + \mu \cdot M \cdot g\right] \tag{24}$$

$$Q_m^4 = -Q_m^5 = \left[\frac{I_\Delta + 2 \cdot M_f \cdot \left(b^2 + L^2\right)}{2 \cdot l} + M_f \cdot \frac{L^2 + b^2}{2 \cdot l} + M_b \cdot \frac{l}{2}\right] \cdot r \cdot \ddot{q}_3^* + \frac{\mu \cdot M \cdot g \cdot r}{2 \cdot [\mu \cdot (r_3 - r) + L]} \cdot \left[(x_C - \mu \cdot r) \cdot \frac{\sqrt{L^2 + b^2}}{l} + (L - x_C + \mu \cdot r_3)\right] \tag{25}$$

Equations (24) and (25) are representing the torks of the driving wheels from the mobile robot PatrolBot, in case of translation and orientation known as dynamic control functions.

4 Conclusions

The main task of a robot is to describe motion trajectories, based on control functions, which is to displace from a point to a programmed position. Hence, the dynamic modelling of robots is fundamental for accomplishing these types of tasks. In the paper presented above were determined the dynamic control functions for a concept of hybrid robot system, based on the geometric and kinematic behavior. For both considered structures, there have been established the dynamic control functions, on the basis of Lagrange-Euler second kind formalism, using kinetic energy as central function from the Analytical Mechanics of the rigid body. In addition to the need for computational efficiency, the control functions are expressed as a compact set of equations for ease of development and implementation. The algorithms are used for geometric and kinematic modelling are in general form and are applicable to robot mechanisms with general connectivity, geometry, and joint types.

As an important remark, the generalised variables contained in Eqs. (15–17) and ((24)–(25)) should be replaced with time polynomial functions according to the working process where is included the hybrid structure composed by the serial 2TR type and mobile robot.

Future research efforts will be focused mainly on the control applications and improvement of the developed model. Significant tasks include development of torques control because position control is only suitable when a robot is following a spatial trajectory.

References

1. Tucan, P., Vaida, C., Horvath, D., Caprariu, A., Burz, A., Gherman, B., Iakab, S., Pisla, D.: Design and experimental setup of a robotic medical instrument for brachytherapy in non-resectable liver tumors (2022). https://doi.org/10.3390/cancers14235841
2. Spong, M.W.: Robot motion control. In: Baillieul, J., Samad, T. (Eds) Encyclopedia of Systems and Control. Springer, Cham (2021). https://doi.org/10.1007/978-3-030-44184-5_168
3. Featherstone, R., Orin, D.E.: Dynamics. In: Siciliano, B., Khatib, O. (Eds) Springer Handbook of Robotics. Springer, Berlin, Heidelberg (2008). https://doi.org/10.1007/978-3-540-30301-5_3
4. Pisla, D., Vaida, C., Birlescu, I., Hajjar, N.A., Gherman, B., Radu, C., Plitea, N.: Risk management for the reliability of robotic assisted treatment of non-resectable liver tumors. Appl. Sci. **10**, 52 (2020). https://doi.org/10.3390/app10010052
5. https://www.fit.vutbr.cz/~plascencia/patrolbot/Research_PatrolBot_3rd_gen_User_Guide_RevA.pdf. Last Accessed 21 Jan 2024
6. Negrean, I., Duca, A., Negrean, D.C., Kacso, K.: Mecanică avansată în robotică. UT Press, Cluj-Napoca (2008). ISBN 978-973-662-420-9
7. Pisla, D., Birlescu, I., Crisan, N., Pusca, A., Andras, I., Tucan, P., Radu, C., Gherman, B., Vaida, C.: Singularity analysis and geometric optimization of a 6-DOF parallel robot for SILS. Machines **10**, 764 (2022). https://doi.org/10.3390/machines10090764
8. Schonstein, C.: Contribuții în dezvoltarea unei structuri robotizate hibride, PhD Thesis, PhD Thesis, TUCN, Cluj-Napoca (2011)
9. Negrean, I., Schonstein C.: Advanced studies on matrix exponentials in robotics, Published in the Acta Technica Napocensis. Series: Appl. Mathem. Mech. Cluj-Napoca, Romania **53**(I), 13–18 (2010)
10. Ardema, M.D.: In: Analytical Dynamics Theory and Applications, pp. 225–243. Springer US (2006). ISBN 978-0-306-48681-4
11. Covaciu, F.: Actuation and control of a serial robotic arm with four degrees of freedom, Acta Technica Napocensis—Series: Appl. Mathem. Mech. Eng. **61**(3), 347–356. (2019). ISSN: 1221-5872
12. Negrean, I., Schonstein C.: Formulations in robotics based on variational principles. In: Proceedings of AQTR 2010 IEEE-TTTC, International Conference on Automation, Quality and Testing, Robotics, Cluj-Napoca, Romania, pp. 281–286. (2010). ISBN 978-1-4244-6722-8
13. Solea, R., Filipescu, A., Stamatescu, G.: Sliding-mode real-time mobile platform control in the presence of uncertainties. In: Proceedings of the IEEE Conference on Decision and Control, pp. 7747–7752. (2010). https://doi.org/10.1109/CDC.2009.5399667
14. Kalman, K.: Contribuţii privind modelarea şi simularea roboţilor mobili şi roboţilor cu structură serială, PhD Thesis, TUCN, Cluj-Napoca (2011)
15. Negrean, I., Schonstein, C., Kacso, K., Negrean C., Duca, A.: Formulations about dynamics of mobile robots. In: The 5-th International Conference, Robotics 2010, Cluj-Napoca, Romania, Published in the Robotics and Automation Systems, vols. 166–167 of Solid State Phenomena, pp. 309–314. (2010). ISSN 1012-0394
16. Park, F.C.: Computational aspects of the product-of-exponentials formula for robot kinematics. IEEE Trans. Autom. Control **39**(3) (1994)

Part V
Motion Planning and Control

Time-Optimal Transport of Loosely Placed Liquid Filled Cups Along Prescribed Paths

Klaus Zauner, Hubert Gattringer, and Andreas Müller

Abstract Handling loosely placed objects with robotic manipulators is a difficult task from the point of view of trajectory planning and control. This becomes even more challenging when the object to be handled is a container filled with liquid. This paper addresses the task of transporting a liquid-filled cup placed on a tray along a prescribed path in shortest time. The objective is to minimize swapping, thus avoiding spillage of the fluid. To this end, the sloshing dynamics is incorporated into the dynamic model used within the optimal control problem formulation. The optimization problem is solved using a direct multiple shooting approach.

Keywords Time-optimal path following · Waiter motion problem · Sloshing

1 Introduction

Within modern industrial robotics, a pivotal focus lies on movements that are optimized in terms of time. For some applications the movement is to trace a predefined geometric path, parameterized through a designated path parameter. This pursuit of determining the time evolution of the path parameter is commonly known as time-optimized path following [6]. In tandem with the inherent limitations imposed by the robotic system, the optimization process must also navigate through constraints linked to the specific task intended during the movement. The scope of this paper is dedicated to the intricate domain of task constraints, with a particular emphasis on resolving the "waiter motion problem" [4, 5]. This problem entails the intricate task of transporting a loosely positioned, liquid-filled cup on a tray affixed to the

K. Zauner (✉) · H. Gattringer · A. Müller
Institute of Robotics, Johannes Kepler University Linz, Altenberger Strasse, 69 4040 Linz, Austria
e-mail: klaus.zauner@jku.at

H. Gattringer
e-mail: hubert.gattringer@jku.at

A. Müller
e-mail: a.mueller@jku.at

D. Pisla et al. (eds.), *Advances in Service and Industrial Robotics*, Mechanisms and Machine Science 157, https://doi.org/10.1007/978-3-031-59257-7_41

end-effector of a robotic manipulator [2, 3, 9]. The paper commences with the formulation of the general path following problem, expressed in terms of a joint space representation of the path. Subsequently, the formulation systematically extends to encompass task constraints. Initially, constraints are devised to stabilize the position of a general rigid body on the tray, thwarting undesirable movements such as lifting, sliding, and tilting during the motion. These constraints are intricately defined based on the constraining forces exerted on the body. Moving forward, the study advances to consider the fluid dynamics associated with a liquid-filled cup, modeled simplistically through a spherical pendulum [7]. This inclusion of internal dynamics introduces an additional layer of complexity to the optimization problem. The final optimal control problem is solved using a direct multiple shooting method, implemented in the CasADi framework.

2 Problem Formulation

2.1 Time-Optimal Path Following

Let $\mathcal{Z} \subset \mathbb{R}^6$ denote the task space of a n joint serial robotic manipulator with the end effector position and orientation ${}_I\mathbf{z}_E^T = ({}_I\mathbf{r}_E, {}_I\boldsymbol{\varphi}_E)$, resolved in the inertial frame $\mathcal{F}_I$, and joint coordinates $q_i \in \mathbb{R},\ i \in \{x, y, z, A, B, C\}$. The robot under consideration is basically a three axes linear robot that has been extended by a three axes rotation unit at its end effector. The coupling point is denoted as H. This point should be routed along a parameterized path ${}_I\mathbf{r}_H(\sigma) : \sigma \in [0, 1] \to \mathbb{R}^3$. The time-optimal path following problem consists in finding the time evolution $\sigma(t),\ t \in [0, t_E]$ such that the w_t-weighted end time t_E and the w_u-weighted input are minimized and necessary constraints are satisfied. The coupling point H only depends on the coordinates q_z, q_x and q_y. Therefore we partition the vector $\mathbf{q} = (\mathbf{q}_L^T(\sigma), \mathbf{q}_R^T)^T$ into two parts $\mathbf{q}_L(\sigma) = (q_z(\sigma), q_x(\sigma), q_y(\sigma))^T$ and $\mathbf{q}_R = (q_B, q_C, q_A)^T$. With lower $\underline{(\cdot)}$ and upper $\bar{(\cdot)}$ bounds on the joint velocities $\dot{\mathbf{q}}_L \in \mathbb{R}^3$ and accelerations $\ddot{\mathbf{q}}_L \in \mathbb{R}^3$ the resulting optimization problem is

$$
\begin{aligned}
&\min_{t_E,\mathbf{u}} \int_0^{t_E} \left(w_t + w_u \mathbf{u}^T \mathbf{u}\right) \mathrm{d}t \\
\text{s.t.}\quad &\underline{\mathbf{q}}_L \le \mathbf{q}_L \le \bar{\mathbf{q}}_L \\
&\underline{\dot{\mathbf{q}}}_L \le \dot{\mathbf{q}}_L \le \bar{\dot{\mathbf{q}}}_L \\
&\underline{\ddot{\mathbf{q}}}_L \le \ddot{\mathbf{q}}_L \le \bar{\ddot{\mathbf{q}}}_L
\end{aligned}
\tag{1}
$$

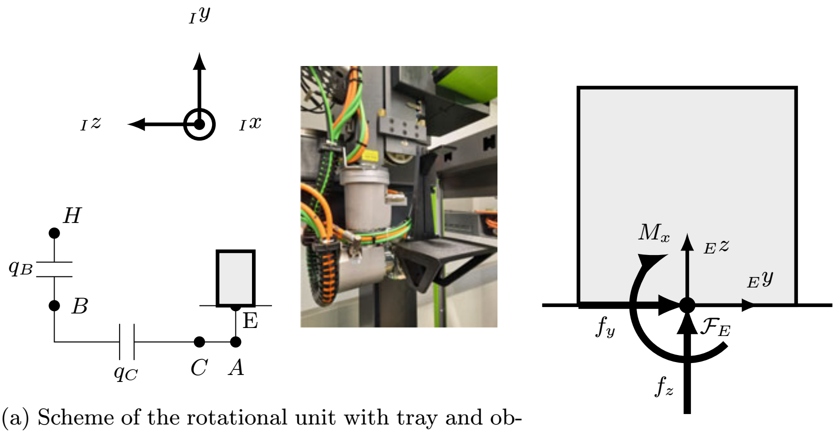

(a) Scheme of the rotational unit with tray and object

(b) Object on tray, $y - z$ view

Fig. 1 Robot scheme (**a**) and rigid object loosely placed on a tray, mounted on the end effector (**b**)

2.2 Dynamics Model

The optimization problem (1) does not account for any dynamics. A dynamic robot model

$$\mathbf{M}(\mathbf{q})\ddot{\mathbf{q}} + \mathbf{G}(\mathbf{q}, \dot{\mathbf{q}})\dot{\mathbf{q}} + \mathbf{g}(\mathbf{q}) = \mathbf{Q}_{\mathrm{M}}, \tag{2}$$

with the generalized mass matrix $\mathbf{M}(\mathbf{q})$, the vector of generalized Coriolis and centrifugal forces $\mathbf{G}(\mathbf{q}, \dot{\mathbf{q}})\dot{\mathbf{q}}$, gravitational forces $\mathbf{g}(\mathbf{q})$ and the vector of motor torques $\mathbf{Q}_{\mathrm{M}}$, allows to bound the latter ones within the robots capabilities. Taking into account the fact that the first three axes are linear axes and that the rotational degrees of freedom do not have significant arm lengths, the limitation of the motor torques is dispensed and the accelerations are limited instead. As we want to realize the transport of a loosely placed, rigid object along a prescribed path, we need to model the related dynamics. Considering the body, as shown in Fig. 1b, as a subsystem with the describing velocity $\dot{\mathbf{y}}_{\mathrm{obj}} = ({}_E\mathbf{v}_E^T, {}_E\boldsymbol{\omega}_E^T)^T$ of the contact point with the tray, the equation of motion results in

$$\mathbf{M}_{\mathrm{obj}}\ddot{\mathbf{y}}_{\mathrm{obj}} + \mathbf{G}_{\mathrm{obj}}\dot{\mathbf{y}}_{\mathrm{obj}} - \mathbf{Q}_{\mathrm{obj}} = \mathbf{Q}^z_{\mathrm{obj}}. \tag{3}$$

$\mathbf{Q}^z_{\mathrm{obj}} = \left(\mathbf{f}^{zT}, \mathbf{M}^{zT}\right)^T$ denotes the contact wrench with the constraint force $\mathbf{f}^z = (f_x, f_y, f_z)^T$ and torque $\mathbf{M}^z = (M_x, M_y, M_z)^T$. The contact wrench allows to state the task constraints for the transport, as shown in the following subsection.

2.3 Task Constraints: Loosely Placed Object

To ensure successful transportation of the object, it must be prevented from lifting, sliding or tipping over. With the elements of the contact wrench, the related conditions can be formulated as derived in [4].

– *Non-lifting condition:* The condition for preventing the loss of contact between object and tray is
$$f_z \geq 0. \tag{4}$$

– *Non-slipping condition:* The slipping of the body is only counteracted by the static friction between the body and the tray. Therefore the dynamic reaction force $||f_T|| = \sqrt{f_x^2 + f_y^2}$ tangential to the contact plane must be lower than the friction force, or
$$||f_T|| \leq \mu_0 f_z. \tag{5}$$

  The static friction coefficientμ_0 relates to the angle ρ under which sliding start as $\tan(\rho) = \mu_0$. It can therefore be determined via a simple experiment.

– *Non-tipping-over condition:* The torques M_x and M_y or actually the resulting torque would tip the cup around a point on its footprint unless the condition
$$\sqrt{M_x^2 + M_y^2} \leq r_o f_z, \tag{6}$$
  with r_o the radius of the cup, is met.

2.4 Task Constraints: Liquid Filled Cup

Assuming that the rigid body of Sect. 2.2 is a liquid filled cup, the fluids dynamics need to be modeled and taken into account during the optimization in order to prevent sloshing. A viable approach is to model the liquid as a spherical pendulum, see Fig. 2, of length L with the fluid representing lumped mass m, based on the procedure shown in [7]. The pendulum is modeled as subsystem in the frame $\mathcal{F}_P$ which is aligned with the end effector frame $\mathcal{F}_E$. The describing velocities are $\dot{\mathbf{y}}_{\text{pend}} = ({}_P\mathbf{v}_P^T, {}_P\boldsymbol{\omega}_P^T, \dot{\varphi}, \dot{\vartheta})^T$. The liquids surface is assumed to stay normal to the pendulum for any pendulum angles $\mathbf{q}_F = (\varphi, \vartheta)^T$, which are identified as angles of a rotation around the ${}_Px$ axis and the resulting ${}'_Py$ axis subsequently. The friction of the wall and the fluids inner damping are modeled with viscous damping d. The EOMs are of the form (2) without the input in form of generalized motor torques. The derivation can be done by using *Lagrangian Equations of the Second Type*. It yields the pendulums dynamics in the general form
$$\ddot{\mathbf{q}}_F = \mathbf{f}_F(\mathbf{q}, \dot{\mathbf{q}}, \ddot{\mathbf{q}}, \mathbf{q}_F, \dot{\mathbf{q}}_F). \tag{7}$$

Fig. 2 Scheme of the tray with a liquid filled cup, y-z view

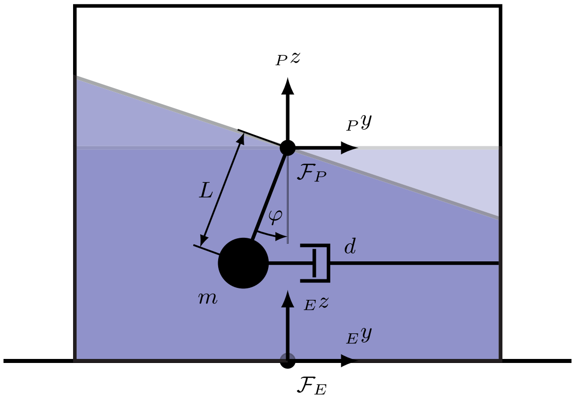

The most evident condition is that the liquid must not reach the edge of the cup. Again, a state vector $\mathbf{x}_F = (\mathbf{q}_F, \dot{\mathbf{q}}_F)^T$ is introduced, which allows to state the constraints as

$$\underline{\mathbf{x}}_F \leq \mathbf{x}_F \leq \bar{\mathbf{x}}_F. \tag{8}$$

3 Solution of the Optimal Control Problem

The path following for the point H in combination with the liquid transport requires the movement of all six axes of the robot. The movement of the three linear axes is parameterized via the path parameter. In order to obtain continuous accelerations and thus also torques, the jerk is assumed to be piecewise constant as input. Solving the optimal control problem means the determination of the time evolution of the path parameter $\sigma(t),\ t \in [0, t_E]$ and the required trajectories for the rotational degrees of freedom $\mathbf{q}_R$. Therefore a dynamical system

$$\dot{\mathbf{x}} = \mathbf{f}(\mathbf{x}, \mathbf{u}) \tag{9}$$

is formulated where $\mathbf{x} = (\sigma, \dot{\sigma}, \ddot{\sigma}, \mathbf{x}_R^T, \mathbf{x}_F^T)^T$ denotes the state and $u = (\sigma^{(3)}, \mathbf{q}_R^{(3)})$ the input. The corresponding state vectors be $\mathbf{x}_L = (\mathbf{q}_L^T(\sigma), \dot{\mathbf{q}}_L^T(\dot{\sigma}), \ddot{\mathbf{q}}_L^T(\dot{\sigma}, \ddot{\sigma}))^T$ and $\mathbf{x}_R = (\mathbf{q}_R^T, \dot{\mathbf{q}}_R^T, \ddot{\mathbf{q}}_R^T)^T$. For the path parameter and the rotatory degrees of freedom, this is a simple integrator chain whereas the dynamics of the state $\mathbf{x}_F$ is given by (7). The optimal control problem (OCP) now states to

Table 1 Numerical values of the kinematic parameters, the parameters for the cup transport constraints (4), (5) and (6) and the fluid pendulum model

Kinematics		Cup		Fluid	
$r_{AE,x}$ in m	0.07	μ_0 in 1	0.35	L in m	0.027
$r_{AE,y}$ in m	0	r_o in m	0.05	m in kg	0.55
$r_{AE,z}$ in m	0.055			d in $\frac{\text{kg}}{\text{s}}$	0.2
				$\bar{\mathbf{q}}_F$ in rad	$\frac{\pi}{18}$
				$\bar{\dot{\mathbf{q}}}_F$ in $\frac{\text{rad}}{\text{s}}$	$\frac{5\pi}{9}$

$$
\begin{array}{llr}
 & \min\limits_{t_e,\mathbf{u}} \int\limits_0^{t_e} \left(w_t + w_u \mathbf{u}^T \mathbf{u}\right) \mathrm{d}t & \\
\text{s.t.} & \underline{\mathbf{q}} \le \mathbf{q} \le \bar{\mathbf{q}}, & -f_z \le 0 \\
 & \underline{\dot{\mathbf{q}}} \le \dot{\mathbf{q}} \le \bar{\dot{\mathbf{q}}}, & \sqrt{f_x^2 + f_y^2} - \mu f_z \le 0 \\
 & \underline{\ddot{\mathbf{q}}} \le \ddot{\mathbf{q}} \le \bar{\ddot{\mathbf{q}}}, & \sqrt{M_x^2 + M_y^2} - r_o f_z \le 0 \\
 & \underline{\mathbf{x}}_F \le \mathbf{x}_F \le \bar{\mathbf{x}}_F & \\
 & \dot{\mathbf{x}} = \mathbf{f}(\mathbf{x}, \mathbf{u}) &
\end{array} \tag{10}
$$

Out of the manifold techniques for solving the OCP (10) we choose the direct multiple shooting method implemented in the CasADi framework [1] using IPOPT [8]. The number of shooting intervals is set to $N = 400$ and the numerical integration of the cost function and the ODE (9) is performed by using a *Runge-Kutta* scheme of 4th order. The weighting factors are set to $w_t = 1$ and $w_u = 10^{-4}$.

4 Results

The following results are for a lemniscate-path in the horizontal plane (Table 1).

$$
{}_I\mathbf{r}_H^T(\sigma) = \left(\frac{a\sqrt{2}\cos(\sigma 2\pi)}{\sin(\sigma 2\pi)^2 + 1}, \frac{a\sqrt{2}\cos(\sigma 2\pi)\sin(\sigma 2\pi)}{\sin(\sigma 2\pi)^2 + 1}, 0 \right), \tag{11}
$$

of the point H, with $\sigma \in [0, 1]$.

As Fig. 3 depicts, the given task can be carried out without any violation of the velocity and acceleration constraints on the robot axes. Figures 3c–f show the joint velocities and accelerations normalized to their respective limits. In Fig. 4 the constraints (4), (5) and (6) are depicted in the form $(\cdot) \le 0$. In order to omit sloshing, the fluid pendulum's angles $\mathbf{q}_F$ and their respective velocities were constrained by (8). Figure 5 confirms the compliance of the optimization result. Based on the optimization results, it can be assumed that the liquid transport can be carried out as presented, provided that the assumed parameters are accurate and the liquid model is sufficiently precise.

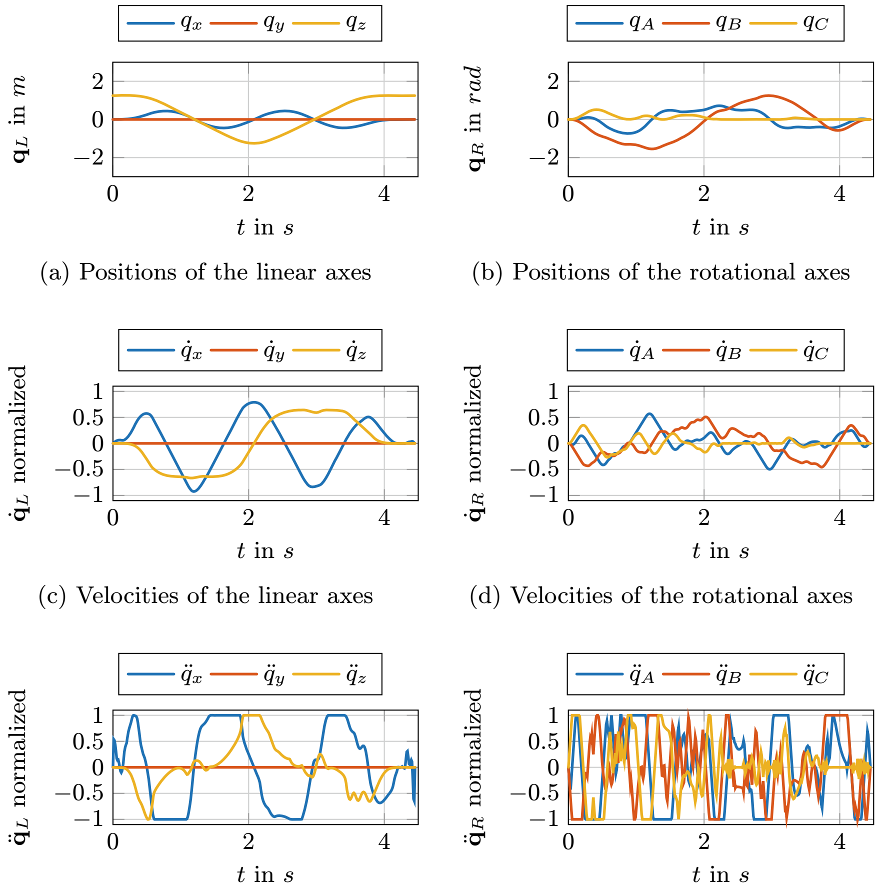

(a) Positions of the linear axes (b) Positions of the rotational axes

(c) Velocities of the linear axes (d) Velocities of the rotational axes

(e) Accelerations of the linear axes (f) Accelerations of the rotational axes

Fig. 3 Time evolution of the robot coordinates and their respective limits

Fig. 4 Constraints regarding the losely placed cup

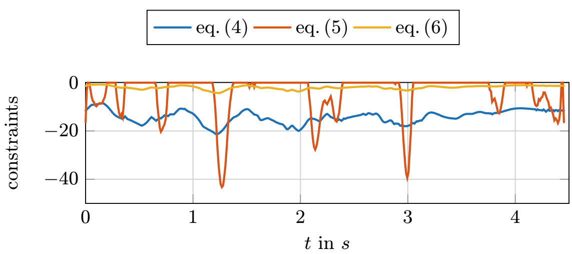

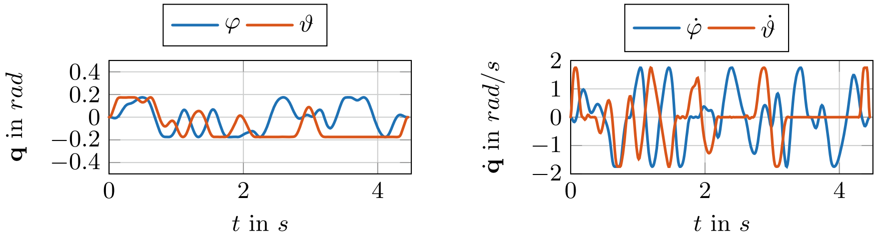

(a) Angles φ and ϑ (b) Angular velocities $\dot{\varphi}$ and $\dot{\vartheta}$

Fig. 5 Constraints regarding the liquid

5 Conclusion

This paper systematically addresses the challenge of time-optimal path following for an industrial robot, gradually incorporating the complex constraints associated with transporting a loosely positioned, liquid-filled cup. Commencing with the well-established problem of time-optimal path following, our approach involves calculating the constraining forces necessary to maintain the cup's stability during movement. Building upon these forces, we formulate constraints designed to prevent undesired cup behaviors as lifting, sliding, and tilting during the robot's motion. To account for the internal dynamics of the liquid-filled cup, a simplified pendulum model is employed to approximate fluid dynamics. This step aims in constraining the tilt of the liquid surface during the motion. The optimal control problem is solved through the direct multiple shooting method. The choosen target path for the end-effector point H is specified as a lemniscate within the horizontal plane of the workspace.

In addition, tests on real robots are planned to verify the procedure. In the future, the model of the liquid-filled cup is also to be extended in such a way that the shift in the center of gravity of the cup due to the movement of the liquid is taken into account when calculating the constraining forces.

Acknowledgements This work has been supported by the "LCM - K2 Center for Symbiotic Mechatronics" within the framework of the Austrian COMET-K2 program.

References

1. Andersson, J.A.E., Gillis, J., Horn, G., Rawlings, J.B., Diehl, M.: CasADi—A software framework for nonlinear optimization and optimal control. Mathem. Program. Comput. (2018)
2. Di Leva, R., Carricato, M., Gattringer, H., Müller, A.: Sloshing dynamics estimation for liquid-filled containers under 2-dimensional excitation. In: ECCOMAS Thematic Conference on Multibody Dynamics. pp. 80–89. (2021)
3. Di Leva, R., Carricato, M., Gattringer, H., Müller, A.: Sloshing dynamics estimation for liquid-filled containers performing 3-dimensional motions: modeling and experimental validation. Multibody Syst. Dyn. **56**(2), 153–171 (2022)

4. Gattringer, H., Müller, A., Oberherber, M., Kaserer, D.: Time-optimal robotic manipulation on a predefined path of loosely placed objects: modeling and experiment. Mechatronics **84**, 102753 (2022)
5. Geu Flores, F., Kecskeméthy, A.: Time-optimal path planning for the general waiter motion problem. In: Advances in Mechanisms, Robotics and Design Education and Research, pp. 189–203. Springer (2013)
6. Geu Flores, F., Kecskeméthy, A., Pöttker, A.: Time-optimal motion planning along specified paths for multibody systems including dry friction and power constraints. In: 13th World Congress in Mechanism and Machine Science (2011)
7. Reinhold, J., Amersdorfer, M., Meurer, T.: A dynamic optimization approach for sloshing free transport of liquid filled containers using an industrial robot. In: 2019 IEEE/RSJ International Conference on Intelligent Robots and Systems (IROS), pp. 2336 – 2341. (2019)
8. Wächter, A., Biegler, L.: On the implementation of a primal-dual interior point filter line search algorithm for large-scale nonlinear programming. Mathemat. Program. **106**, 25–57 (2006)
9. Yano, K., Terashima, K.: Robust liquid container transfer control for complete sloshing suppression. IEEE Trans. Control. Syst. Technol. **9**, 483–493 (2001)

Constrained Online Motion Generation from Unfiltered User Commands

Thomas Kordik, Christian Zauner, Hubert Gattringer, and Andreas Müller

Abstract In manually operated robotic applications, where operators use a joystick as input device, it is more intuitive to command the velocity rather than the position. Existing algorithms, however, that admit following an arbitrary desired velocity in order to generate smooth trajectories, do not take into account the dynamic limits of velocity and position. In this paper a method is introduced for the smooth online path-parameter generation from unfiltered operator input that respects bounds on position, velocity, acceleration, and jerk. It builds upon a time discrete second-order smoothing filter. $\mathcal{C}^3$ continuous trajectories are computed that achieve a motion between defined start and terminal positions in minimal time. A geometric path description based on B-spline interpolation connecting multiple points in task space is presented. The velocity signal deduced from this description is used as a time scaling parameter. Specific parametrization of the B-spline curve allows for generating motions where the tangential velocity is nearly proportional to the joystick modulation.

Keywords Online trajectory generation · Nonlinear filter · B-spline interpolation · Industrial robotics · Unfiltered operator command

1 Introduction

In industrial robot applications, it is often required to manually move a robot, which is often referred to as 'jogging mode'. Different means of inputs can be used to this end

T. Kordik (✉) · C. Zauner · H. Gattringer · A. Müller
Institute of Robotics, Johannes Kepler University Linz, Altenberger Straße 69, 4040 Linz, Austria
e-mail: thomas.kordik@jku.at

C. Zauner
e-mail: christian.zauner@jku.at

H. Gattringer
e-mail: hubert.gattringer@jku.at

A. Müller
e-mail: a.mueller@jku.at

D. Pisla et al. (eds.), *Advances in Service and Industrial Robotics*, Mechanisms and Machine Science 157, https://doi.org/10.1007/978-3-031-59257-7_42

and robot jogging can either be realized in single- or multi-axis movements in both, joint and task space coordinates. Applications include the recovering of the robot position, after an error, traversing a robot through a narrow and crowded environment or checking a planned path for collisions. This jogging mode is usually executed with constant velocity. However, this often appears counter-intuitive for robot operators that use a joystick to jog along a specified geometric path, similar to the concept presented in [8]. Therefore, smoothing of the user input to generate a smooth path parameter online is needed, as otherwise the discontinuities of the user input would directly affect the planned trajectory. In previous works, Kroeger et. al [6, 7] have proposed several types of online smooth trajectory generators using defined velocity or acceleration profiles, for the time-optimal trajectory planning between operating points. A different approach, relying on nonlinear smoothing filters instead of predefined trajectory profiles, is presented in [2–4, 11]. Here, time continous as well as discrete filters with a cascade structure and various smoothing characteristics for the tracking of a reference signal are investigated. Originally intended to generate feedforward control actions, it was also applied to time-parametrize a path planning problem similar to the problem setting of this contribution in [10]. What both of these methods for smooth trajectory generation have in common, is that only dynamic limits on the first and second derivatives of the reference signal without overshooting can be considered. For jogging with variable velocity along a prescribed path, these developed algorithms are not directly applicable since bounds on position and velocity level cannot be guaranteed. Thus, this paper addresses a method for the online generation of a smooth path-parameter with a desired initial value σ_0 and terminal value σ_E where the path-parameter's velocity follows an arbitrary desired velocity, e.g. a joystick modulation input and constraints for position, velocity, acceleration and jerk can be taken into account. Furthermore, a path planning algorithm based on B-splines connecting various waypoints $\mathbf{P}_j$ in task space favorable for jogging is provided. The desired geometric path $\mathbf{r}(\sigma)$ is split into straight lines between given waypoints and a predefined smoothing radius is defined around each waypoint. A B-spline of degree $p = 6$ is constructed where the knot vector and control points are chosen in a way that the B-spline acts similar to a piecewise geometric curve consisting of Bézier curves. Connecting Bézier curves with $\mathcal{C}^3$ continuity, in general, their degree must be $p = 7$. The same can be achieved with a Bézier curve degree of $p = 6$ when using symmetric placement of control points and knots. The paper is structured as follows. In Sect. 2 the method of generating a smooth path-parameter is described. The discrete time control law C_3 as shown in [11] serves as the foundation and is revised in Sect. 2.1. Necessary adaptations and extensions to allow the generation of a path-parameter $\sigma_n = \sigma(nT)$ with initial and terminal values σ_0 and σ_E with varying velocity $\dot{\sigma}_n = \dot{\sigma}(nT)$ are described in Sect. 2.2 and 2.3 and final results for an exemplary operator input are presented in Sect. 2.4. Section 3 covers the definition of a geometric path suitable for jogging using B-splines and in Sect. 4 the paper is summarized and an outlook on future work is presented.

2 Smooth Path-Parameter Generation

2.1 Discrete Time Second Order Nonlinear Smoothing Filter

Looking at its future application, the trajectory smoother is designed to run on an industrial PC with a finite sampling time T. Thus, the time discrete control law C_3 is used where its output tracks a reference signal r_n. The filter structure is shown in Fig. 1. Here, indicated by blue borders, the structure of the second-order trajectory smoother by Zanasi et al. [11] is depicted.
The nonlinear control law is given by

$$C_3 : \begin{cases} \dddot{\sigma}_n = -\dddot{\sigma}_{\mathrm{M}}\, \mathrm{sat}(\lambda_n)\, \frac{1+\mathrm{sgn}(\ddot{\sigma}_n \mathrm{sgn}(\lambda_n)+\dot{\sigma}_{\mathrm{M}} - T\dddot{\sigma}_{\mathrm{M}})}{2} \\ \lambda_n = \dot{z}_n + \frac{z_n}{m} + \frac{(m-1)}{2}\mathrm{sgn}(z_n) \\ m = \mathrm{floor}\left(\frac{1+\sqrt{1+8|z_n|}}{2}\right) \\ z_n = \frac{1}{T\dddot{\sigma}_{\mathrm{M}}}\left(\frac{y_n}{T} + \frac{\dot{y}_n}{2}\right) \\ \dot{z}_n = \frac{\dot{y}_n}{T\dddot{\sigma}_{\mathrm{M}}}. \end{cases} \tag{1}$$

Let the time discrete reference signal r_n be a desired velocity input $r_n = \dot{\sigma}_{n,\mathrm{d}}$, the filter output is then a bounded signal $\dddot{\sigma}_n$ where integrating it twice over time yields a trapezoidal signal in $\ddot{\sigma}_n$ which follows its reference $r_n = \dot{\sigma}_{n,\mathrm{d}}$ in minimal time without overshooting. Limits for the first and second time derivative are described by $\ddot{\sigma}_{\mathrm{M}}$ as well as $\dddot{\sigma}_{\mathrm{M}}$. The tracking error is respectively defined as $y_n = r_n - \dot{\sigma}_n$ and the velocity error as $\dot{y}_n = \dot{r}_n - \ddot{\sigma}_n$. The filter state in state-space is represented by $\mathbf{z} = [z_n, \dot{z}_n]^T$. The time-derivative of the filter input r_n can be calculated with

$$\dot{r}_n = \frac{1}{T}(r_n - r_{n-1}). \tag{2}$$

The used saturation function is defined as

$$\mathrm{sat}(\lambda_n) = \begin{cases} \lambda_n & \text{if } |\lambda_n| \le 1 \\ \mathrm{sgn}(\lambda_n) & \text{else.} \end{cases} \tag{3}$$

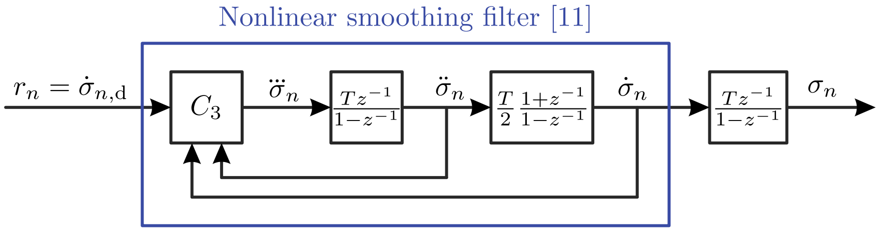

Fig. 1 Extended filter structure of the second-order smoothing filter

For a smooth reference signal the filter limits are satisfied at all times. In case of discontinous reference signals, i.e. input steps, limits cannot directly be guaranteed but are only violated minimally. This issue can, however, be easily bypassed by lowering the limits by a small safety region. Another benefit, not considered here but theoretically possible, is the adaptation of limits while the filter is used. For proof of the mentioned properties, we refer to the provided literature.

2.2 Second-Order Filter Extension

Choosing the reference signal $r = \dot{\sigma}_{\mathrm{d}}$ to be the arbitrary desired velocity input of a joystick $\dot{\sigma}_{\mathrm{d}}$ and further integrating $\dot{\sigma}$ naturally, achieves the generation of a smooth path-parameter σ with the desired controlled velocity $\dot{\sigma}$. The complete and extended filter structure is depicted in Fig. 1. Applying the trajectory smoother in this way only enables to directly consider velocity $\dot{\sigma}_{\mathrm{M}}$, acceleration $\ddot{\sigma}_{\mathrm{M}}$ and jerk $\dddot{\sigma}_{\mathrm{M}}$ limits. In general, there are additional limits for the path-parameter position σ_n itself, namely the initial and terminal values σ_0 and σ_{E}. For continous-time setups, it would be sufficient to integrate the instantaneous filter value $\dddot{\sigma}_n$ thrice over time and calculate the latest possible point of time, where safe deceleration without violating dynamic limits is guaranteed. Then, a symmetrical trapezoidal profile for the acceleration with maximum jerk is applied to come to a standstill at σ_{E} in minimal time.

2.3 Challenges for Discrete-Time Implementation

On the other hand, for discrete-time formulations, there are several issues that need to be addressed. Discrete-time integration of $\dot{\sigma}_n$ leads to a time delay that equals three times the sample time T. Therefore, the latest three values $\dot{\sigma}_{n-1}, \dot{\sigma}_{n-2}, \dot{\sigma}_{n-3}$ have to be saved and used to calculate the latest possible moment for safe deceleration. Furthermore, due to the finite sample time the maximal achievable accuracy is $|\sigma_{\mathrm{E}} - \sigma_n| \leq \frac{\dddot{\sigma}_{\mathrm{M}} T^3}{6}$, as only either $\dddot{\sigma}_n = \pm\dddot{\sigma}_{\mathrm{M}}$ or $\dddot{\sigma}_n = 0$ are applied during ramp-down. This is particularly problematic since this might lead to significant jerks at the defined ends of a prescribed geometric path, where σ_n is used as the path-parameter. To overcome this issue, instead of integrating the maximum jerk until standstill, a ramp-down trajectory proposed in [5] is applied. Here, an optimal control problem for an unsymmetrical trapezoidal acceleration trajectory, also taking into account dynamic limits, is solved for the necessary jerk to exactly reach the desired terminal value $\sigma_n = \sigma_{\mathrm{E}}$.

2.4 Exemplary Velocity Input and Results

To show the functionality of the proposed method, an exemplary velocity input representing the modulation of a joystick is used as input in a simulation implemented

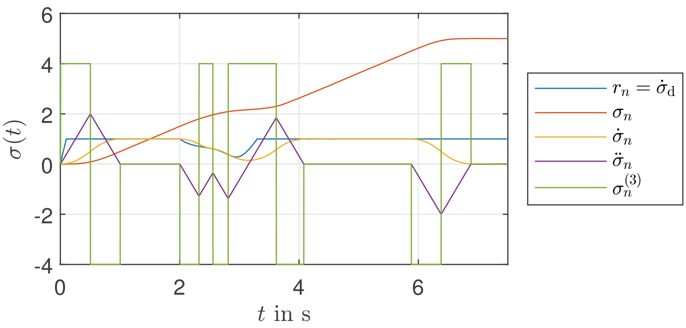

Fig. 2 Exemplary velocity input signal and resulting smooth trajectory

in *MATLAB 2019b*. To account for measurement noise and shaking hands and to avoid constantly applying acceleration and deceleration, the joystick input is minimally preprocessed. Small dead-zones in form of fine discretization of the reference signal $r_n = \dot{\sigma}_{n,\mathrm{d}}$ is applied. Both the joystick input as well as the resulting smoothed signal with its derivatives is depicted in Fig. 2, where the output velocity $\dot{\sigma}_n$ tracks the reference $r_n = \dot{\sigma}_{n,\mathrm{d}}$ in minimal time while respecting all dynamic limits.

3 Jogging in Task Space

Jogging in task space can be either moving directly along the axes of an inertial fixed Cartesian coordinate frame or moving along a prescribed path. For the latter, most often it is required to follow a geometric path that can be described by waypoints $\mathbf{P}_j, \quad j = 0, \ldots, N$ where smoothing radii around the intermediate points $\mathbf{P}_1, \ldots, \mathbf{P}_{N-1}$ are allowed. A well-established tool addressing this issue is B-spline interpolation [9]. A B-spline curve $\mathbf{C}(u)$ of degree p is defined by

$$\mathbf{C}(u) = \sum_{i=0}^{m} N_{i,p}\mathbf{p}_i, \quad u_0 \leq u \leq u_{\mathrm{E}} \tag{4}$$

with the B-spline basis functions

$$N_{i,0}(u) = \begin{cases} 1 & \text{if } u_i \leq u \leq u_{i+1} \\ 0 & \text{else,} \end{cases} \tag{5}$$

$$N_{i,p}(u) = \frac{u - u_i}{u_{i+p} - u_i} N_{i,p-1}(u) + \frac{u_{i+p+1} - u}{u_{i+p+1} - u_{i+1}} N_{i+1,p-1}(u). \tag{6}$$

Control points are described by $\mathbf{p}_i$ and with u_i we denote the knots summarized in a knot vector U. Although possible for any dimension, this contribution focuses on

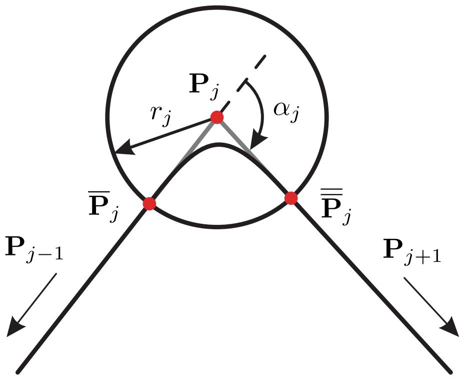

Fig. 3 Construction of intersection points $\overline{\mathbf{P}}_j, \overline{\overline{\mathbf{P}}}_j$

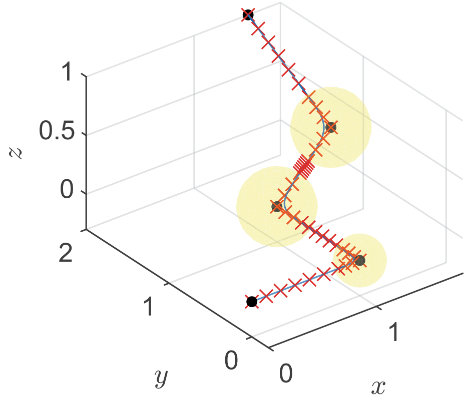

Fig. 4 Constructed geometric path connecting waypoints $\mathbf{P}_0 \ldots \mathbf{P}_4$

a 3D-path planning setup. Initially, all waypoints are connected by straight lines. Afterwards, spheres with the smoothing radii $r_j, \quad j = 1, \ldots, N-1$ are introduced and intersection points $\overline{\mathbf{P}}_j, \overline{\overline{\mathbf{P}}}_j$ are calculated. This procedure is indicated in Fig. 3. Ultimately, a single B-Spline curve is constructed, that runs through the starting point $\mathbf{P}_0$, all intersection points $\overline{\mathbf{P}}_j, \overline{\overline{\mathbf{P}}}_j, \quad j = 1, \ldots, N-1$ and the terminal point $\mathbf{P}_N$. In order to define the B-spline curve, some parameter choices have to be made since the desired geometric path should be of $\mathcal{C}^3$ continuity. Firstly, an arc length-like parametrization of u is used where instead of the arc length itself u_E is calculated by the sum of all connecting straights lengths and $u_0 = 0$ is chosen. Therefore, the path-parameter is defined on $u \in [0, u_\mathrm{E}]$ and the knot vector is constructed as

$$U = \{\underbrace{u_0, \ldots, u_0}_{p+1}, \underbrace{\overline{u}_1, \ldots, \overline{u}_1}_{p}, \ldots, \underbrace{\overline{\overline{u}}_{N-1}, \ldots, \overline{\overline{u}}_{N-1}}_{p}, \underbrace{u_N, \ldots, u_N}_{p+1}\}. \tag{7}$$

The outer knots $u_0 = 0$, $u_N = u_\mathrm{E}$ are of multiplicity $p+1$ and the inner knots of multiplicity p. The inner knot values $\overline{u}_j$ and $\overline{\overline{u}}_j$ are the cumulative sum of the initial straights at the transition points $\overline{\mathbf{P}}_j$ and $\overline{\overline{\mathbf{P}}}_j$. With this specific choice, the B-spline acts like a piecewise geometric curve consisting of Bézier curves [1]. In general, to fulfill $\mathcal{C}^3$ continuity at the transitions, 7th-degree Bézier curves would need to be used. Considering symmetry in the definition of the knots and control points, the same can be achieved with Bézier curves of degree $p = 6$. Consequently, seven conditions can be formulated specifying the position of the control points. This leads to the formulation of the system of equations

$$\mathbf{C}(\overline{u}_j) = \overline{\mathbf{P}}_j \qquad \mathbf{C}(\overline{\overline{u}}_j) = \overline{\overline{\mathbf{P}}}_j \tag{8}$$

$$\mathbf{C}'(\overline{u}_j) = \frac{\mathbf{P}_j - \overline{\mathbf{P}}_j}{|\mathbf{P}_j - \overline{\mathbf{P}}_j|} \qquad \mathbf{C}'(\overline{\overline{u}}_j) = \frac{\overline{\overline{\mathbf{P}}}_j - \mathbf{P}_j}{|\overline{\overline{\mathbf{P}}}_j - \mathbf{P}_j|} \tag{9}$$

$$\mathbf{C}''(\overline{u}_j) = 0 \qquad \mathbf{C}''(\overline{\overline{u}}_j) = 0 \tag{10}$$

$$\mathbf{C}'''(\overline{\overline{u}}_j) = 0 \tag{11}$$

that is solved for the control points $\mathbf{p}_i$ subsequently guaranteeing $\mathcal{C}^3$ smoothness. The straights at the starting and terminal points are approached analogously. Continuity on position level is guaranteed by (8), (9) forces continuity for the first derivative and additionally requires the first derivative to equal $|\mathbf{C}'(u)| = \left|\frac{\mathrm{d}\mathbf{C}(\mathrm{u})}{\mathrm{d}u}\right| = 1$. Analogously, continuitiy for the second derivative is ensured by (10). The combination of (11) and symmetric smoothing radii in form of spheres further guarantees $\mathcal{C}^3$. The result is an equidistant placement of the control points, both on the connecting straights and on the initial straights inside the smoothing spheres. In Fig. 4, this is depicted for the interpolation of exemplary points in 3D space. This specific parametrization additionally yields properties that favor jogging, which are shown in Fig. 5. First and foremost, both the connecting straights as well as the smoothing arcs can be calculated with the same setup. Since for a straight the entry and exit tangents are collinear, $|\mathbf{C}'(u)| = 1$ holds for the whole straight. In constrast, the first derivative $|\mathbf{C}'(u)|$ buckles during a smoothing arc. The buckling depends on the pitch angle α_j shown in Fig. 3. It reaches its maximum at the arc apex and can be described by

$$|\mathbf{C}'|_{\min} = \sqrt{\frac{1 + \cos(\alpha)}{2}} \tag{12}$$

resulting from evaluating $|\mathbf{C}'(u)|$ at its apex $u = \frac{\overline{u}_j + \overline{\overline{u}}_j}{2}$. Using now a smooth path-parameter output of Sect. 2 for time-parametrization $u = \sigma(t)$ the trajectory in task space $\mathbf{r}(t)$, can then be described by

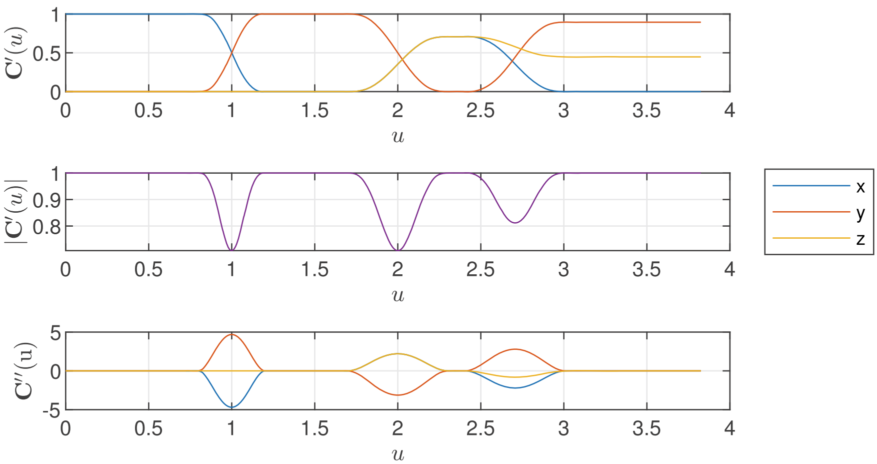

Fig. 5 Derivatives of the B-spline curve $\mathbf{C}(u)$

$$\mathbf{r}(t) = \mathbf{C}(\sigma(t)) \tag{13}$$
$$\dot{\mathbf{r}}(t) = \mathbf{C}'(\sigma(t))\dot{\sigma}(t) \tag{14}$$
$$\ddot{\mathbf{r}}(t) = \mathbf{C}''(\sigma(t))\dot{\sigma}^2(t) + \mathbf{C}'(\sigma(t))\ddot{\sigma}(t) \tag{15}$$
$$\dddot{\mathbf{r}}(t) = \mathbf{C}'''(\sigma(t))\dot{\sigma}^3(t) + 3\mathbf{C}''(\sigma(t))\dot{\sigma}(t)\ddot{\sigma}(t) + \mathbf{C}'(\sigma(t))\dddot{\sigma}(t). \tag{16}$$

The increase of intuitivity of the proposed methods then becomes clear. On the connecting straights the tangential velocity directly relates to the operator input due to conditions (9). The pitch angle dependent buckling of $\mathbf{r}'(t)$ further acts beneficial in narrow curves as it prevents excessive accelerations and jerks.

4 Conclusion and Outlook

In industrial applications, joysticks are a popular interface between a robot and its operator. Here, it is more intuitive to command a velocity rather than a position by modulating the joystick when it comes to robot jogging. To this end, a method for the generation of a smooth path-parameter following an arbitrary desired velocity corresponding to the modulation of the joystick is introduced. The reference signal is processed and integrated while all relevant dynamic limits are satisfied. The functionality was further tested on an industrial PC *X20 CP1586* of *B&R Industrial Automation GmbH* where no notable differences to the simulation were apparent. Moreover, a B-spline based path-planning algorithm suited for jogging in task space was implemented. This idea is also directly applicable for single-axis jogging in joint space. The solution of Sect. 2 is equatable with the joint coordinate trajectory $q_n = \sigma_n$. Beneficially, the joint limits then also match with those of the path-parameter and are guaranteed to be satisfied. As for now, in the generation of a smooth path-parameter only its own limits can be incorporated. While for single-axis jogging in joint space both are the same, this is not the case during jogging in task space. Here, the relation between the path-parameter and joint coordinate limits is system dependent and nonlinear. In conclusion, developing a way to address joint limits directly during the path-parametrization for jogging in task space will be of interest. Additionally, as the geometric path-planning only addressed position, future work will regard finding a smooth parametrization for the orientation of a robot, too.

Acknowledgements Supported by the "LCM K2 Center for Symbiotic Mechatronics" within the framework of the Austrian COMET-K2 program.

References

1. Bézier, P.: Numerical control : mathematics and applications (1972)
2. Biagiotti, L., Melchiorri, C.: Trajectory planning for automatic machines and robots. Springer Science & Business Media (2008)
3. Biagiotti, L., Melchiorri, C.: Zero-phase velocity tracking of vibratory systems with actuation constraints. Control Eng. Pract. **87**, 1–16 (2019). Jun
4. Biagiotti, L., Zanasi, R.: Time-optimal regulation of a chain of integrators with saturated input and internal variables: an application to trajectory planning. IFAC Proc. **43**(14), 1278–1283 (2010). Sep
5. Kaserer, D., Gattringer, H., Muller, A.: Online robot-object synchronization with geometric constraints and limits on velocity, acceleration, and jerk. IEEE Robot. Autom. Lett. **3**(4), 3169–3176 (2018)
6. Kroeger, T., Wahl, F.: Online trajectory generation: basic concepts for instantaneous reactions to unforeseen events. IEEE Trans. Robot. **26**(1), 94–111 (2010)
7. Kroeger, T.: On-Line Trajectory Generation in Robotic Systems Basic Concepts for Instantaneous Reactions to Unforeseen (Sensor) Events. Springer (2010)
8. Meiringer, M., Kugi, A., Kemmetmuller, W.: Semi-autonomous operation of a mobile concrete pump. Autom. Constr. **156**, 105079 (2023)
9. Piegl, L., Tiller, W.: The NURBS Book. Springer, Berlin Heidelberg (1995)
10. Winkler, A., Grabmair, G.: Design and implementation of a path planning for a high-dynamic handling system. In: Proceedings of the Austrian Robotics Workshop, vol. 2014, pp. 69–75 (2014)
11. Zanasi, R., Bianco, C.L., Tonielli, A.: Nonlinear filters for the generation of smooth trajectories. Automatica **36**(3), 439–448 (2000)

Orientation Trajectory Planning Based on Unit Quaternions for Spray Painting Robots

Andrea Vegnaduzzo, Lorenzo Scalera, Daniele Pillan, and Alessandro Gasparetto

Abstract In this paper, we present an approach for the orientation trajectory planning based on cubic B-splines with cumulative basis functions and unit quaternions for spray painting robots. The orientation representation based on unit quaternions avoids potential issues due to the representation singularity of Euler angles. Experimental results on an industrial spray painting robot demonstrate the feasibility of the proposed approach in obtaining a good approximation of the input orientations. Furthermore, continuity in velocity and acceleration is achieved, as well as limited values of the tangential velocity of the robot end-effector, as required in spray painting.

Keywords Robotics · Trajectory planning · Spray painting · B-spline curve · Unit quaternion

1 Introduction

Robotic spray painting is a complex and challenging operation that leverages the precision and efficiency of robots to apply paint and coatings in various manufacturing industries. The automation of spray painting offers advantages such as consistent and high-quality finishes, reduced waste, and enhanced safety [1, 2].

The process of defining the tool trajectory for the spray operation, which includes specifying the sequence of positions and orientations for the robot during the task, can be carried out using a variety of methods, ranging from entirely manual, where

A. Vegnaduzzo · L. Scalera · A. Gasparetto (✉)
University of Udine, 33100 Udine, Italy
e-mail: alessandro.gasparetto@uniud.it

A. Vegnaduzzo
e-mail: vegnaduzzo.andrea@spes.uniud.it

L. Scalera
e-mail: lorenzo.scalera@uniud.it

D. Pillan
CMA Robotics, 33050 Pavia di Udine, Italy
e-mail: pillan@cmarobot.it

D. Pisla et al. (eds.), *Advances in Service and Industrial Robotics*, Mechanisms and Machine Science 157, https://doi.org/10.1007/978-3-031-59257-7_43

every movement is controlled by human operators, to fully automated procedures. For instance, in [3] the authors propose a CAD-based optimization of path planning implementing the Chinese postman algorithm to define the best path for the robot tool. In [4], a path-constrained trajectory planning strategy for spray painting robots based on a look-ahead filtering operation is presented to ensure limited values of the tangential speed.

While the results regarding the planning of translation trajectories are more mature, the design of orientation trajectories for robotic systems, and particularly for spray painting robots, remains an ongoing field of investigation. Orientation trajectory in robotics refers to the planned sequence of rotations that the robot tool or end-effector must follow during a task. Orientations are often represented by means of Euler angles (ϕ, θ, ψ) using rotation matrices belonging to the special orthogonal group $\mathbb{SO}(3)$. However, Euler angles are affected by the representation singularity, i.e., no solution is available for $\theta = \pm\pi/2$ [5].

For this reason, an alternative representation of rigid body orientation based on quaternions can be adopted [6]. Several works can be found in the literature on the use of the quaternion representation for different applications, spanning from computer graphics to virtual reality. In [7], a general construction scheme for unit quaternion curves with simple high order derivatives is presented for computer graphics applications. The method can transform a curve in $\mathbb{R}^3$, defined as a weighted sum of basis functions, into its unit quaternion analogue in $\mathbb{SO}(3)$. Due to the generality of the approach, several well-known spline curves (such as Bézier, Hermite, and B-spline curves) are used to build unit quaternions that share many differential properties with their original curves. The method proposed in [7] is further developed in [8], where a generalization of the parameterization of B-spline curves is described to improve continuity and local controllability, and in [9], where cubic B-spline quaternion curves are combined with the SLERP method. Furthermore, a survey of higher order rigid body motion interpolation methods for continuous trajectory estimation is reported in [10]. However, to the best of the author's knowledge, no examples of orientation trajectory planning approaches based on cubic B-splines with cumulative basis functions and unit quaternion for robotic spray painting can be found in the present literature.

In this paper, we present an approach for the orientation trajectory planning based on cubic B-splines with cumulative basis functions and unit quaternions for spray painting robots. The orientation representation based on unit quaternions avoids potential issues due to the representation singularity of Euler angles. Experimental results on a GR 630R robot by CMA Robotics demonstrate the feasibility of the proposed approach in obtaining a good approximation of the input orientations, continuity in velocity and acceleration, as well as limited values of the tangential velocity of the robot end-effector.

The remainder of the paper is laid out as follows. First, the orientation trajectory planning algorithm is described in Sect. 2. Then, the experimental results are discussed in Sect. 3. Finally, Sect. 4 concludes the work.

2 The Orientation Trajectory Planning Algorithm

The proposed orientation trajectory planning algorithm is based on a parametric representation of the trajectory of the robot end-effector as the parametric vector function $r(u) = [x, y, z, s, v_0, v_1, v_2]^T$, in which every component is dependent on the motion law $u(t)$, which is a function of the time t. $[x, y, z]^T$ represents the position of the robot end-effector, whereas s and $[v_0, v_1, v_2]^T$ are the scalar and vector components of the quaternion $q = [s, v] = [s, v_0, v_1, v_2]^T$ used to describe the orientation of the robot end-effector. In this work, a unit quaternion representation is used, i.e., we consider quaternions with $\|q\| = 1$.

In this work we will focus on the orientation trajectory planning using cubic B-splines to obtain a smooth curve with $\mathbb{C}^2$ continuity interpolating a given set of data points. The same motion law $u(t)$ is used for both position and orientation. A B-spline curve of degree p (or alternatively order $k = p + 1$) can be obtained as a linear combination of a proper number of basis functions $B_{i,k}$, and can be defined as follows [11]:

$$P(u) = \sum_{i=0}^{n} p_i B_{i,k}(u) \tag{1}$$

p_i is the sequence of the $n + 1$ control points that are multiplied by the basis functions $B_{i,k}$. The i-th B-spline basis function is defined, using the Cox-De Boor recursion formula [12, 13], as:

$$B_{i,1}(u) = \begin{cases} 1, & \text{if} \quad u_i < u < u_{i+1} \\ 0, & \text{otherwise} \end{cases} \tag{2}$$

$$B_{i,k}(u) = \frac{u - u_i}{u_{i+k-1} - u_i} B_{i,k-1}(u) + \frac{u_{i+k} - u}{u_{i+k} - u_{i+1}} B_{i+1,k-1}(u), \quad k > 0 \tag{3}$$

The motion law $u = u(t)$ is the independent variable and represents the curvilinear abscissa in the knot vector. However, to use the B-spline curve formulation with the quaternions we need to convert the basis form to the cumulative form with the following procedure.

Given a sequence of points $p_0, p_1, \cdots, p_n$, the curve $P(u)$ that interpolates each point p_i at $u = i$ can be defined as:

$$P(u) = p_0 + \alpha_1(u)\Delta p_1 + \alpha_2(u)\Delta p_2 + \cdots + \alpha_n(u)\Delta p_n = p_0 + \sum_{i=1}^{n} \alpha_i(u)\Delta p_i \tag{4}$$

where

$$\Delta p_i = p_i - p_{i-1}$$
$$\alpha_i(u) = \begin{cases} 0, & \text{if} \quad u < i \\ u - i, & \text{if} \quad i \le u < i + 1 \\ 1, & \text{if} \quad u \ge i + 1 \end{cases} \tag{5}$$

In the same manner, given a sequence of unit quaternions $q_n, q_{n-1}, \cdots, q_0 \in \mathbb{S}^3$, we can build a $\mathbb{C}^0$-continuous unit quaternion curve $q(u)$ lying on the unit hypersphere $\mathbb{S}^3 = \{(s, v_0, v_1, v_2) \in \mathbb{R}^4, \|s^2 + v_0^2 + v_1^2 + v_2^2\| = 1\}$, which interpolates each quaternion q_i at $u = i$, using the spherical interpolation for each couple of consecutive quaternions. The composition of a sequence of quaternions is performed by means of the non-commutative multiplication operation. If the sequence is evaluated in the global frame of reference, the spherical interpolation of a sequence of quaternions is given by the following equation:

$$q(u) = \exp(\omega_n \alpha_n(u)) \exp(\omega_{n-1}\alpha_{n-1}(u)) \ldots \exp(\omega_0 \alpha_0(u))\, q_0 = \Big(\prod_{i=n}^{1} \exp(\omega_i \alpha_i(u))\Big) q_0 \quad (6)$$

where $\omega_i = \log(q_i q_{i-1}^{-1})$ represents the angular velocity.

The expression in Eq. (6) is called cumulative form of $q(u)$ and it is obtained through the multiplication of the quaternions $q_i = \exp(\omega_i \alpha_i(u))$. If α_i is chosen to be a $\mathbb{C}^k$-continue basis function, it is then possible to define a quaternion curve with the same continuity degree.

The cumulative form of a B-spline in $\mathbb{R}^3$ can be written as:

$$P(u) = p_0 \tilde{B}_{0,k}(u) + \sum_{i=1}^{n} \Delta p_i \tilde{B}_{i,k}(u) \quad (7)$$

with $\Delta p_i = p_i - p_{i-1}$. The basis functions are defined as:

$$\tilde{B}_{i,k}(u) = \sum_{j=i}^{n} B_{j,k}(u) = \begin{cases} \sum_{j=i}^{i+k} B_{j,k}(u), & \text{if} \quad u_i < u < u_{i+k-1} \\ 1, & \text{if} \quad u \geq u_{i+k-1} \\ 0, & \text{if} \quad u \leq u_i \end{cases} \quad (8)$$

Recalling Eqs. (6), (7), (8) and substituting $P(u)$ with $q(u)$, p_0 with q_0, Δp_i with ω_i, and the sum with a product, we obtain:

$$q(u) = \Big(\prod_{i=n}^{1} \exp(\omega_i \tilde{B}_{i,k}(u))\Big) q_0^{\tilde{B}_{0,k}(u)} \quad (9)$$

The resulting curve $q(u)$ is $\mathbb{C}^{k-2}$-continue. Therefore, the continuity of the angular acceleration can be imposed by choosing $k = 4$, i.e. $B_{i,4}(u)$ base functions.

Compared to the previous basis functions of (1) that vary in the range $[u_i, u_{i+k}]$, the cumulative functions vary in the interval $[u_i, u_{i+k-1}]$, as shown in Fig. 1. The local controllability property is also maintained, given that the cumulative function is precisely the sum of the previous basis functions. From these properties, it follows that it is possible to rewrite Eq. (9) in a form such that it is possible to calculate it iteratively by considering a restricted number of control points at each loop. Therefore, the function $q(u)$ in the interval $u_l \leq u < u_{l+1}$ depends only on $q_l, \ldots, q_{l-k}, q_{l-k+1}$, and it can be rewritten as:

$$\begin{aligned} q(u) &= \Big(\prod_{i=n}^{l+1} \exp(\omega_i \cdot 0)\Big)\Big(\prod_{i=l}^{l-k+2} \exp(\omega_i \tilde{B}_{i,k}(u))\Big)\Big(\prod_{i=l-k+1}^{1} \exp(\omega_i \cdot 1)\Big) q_0 \\ &= \Big(\prod_{i=l}^{l-k+2} \exp(\omega_i \tilde{B}_{i,k}(u))\Big) q_{l-k+1} \end{aligned} \quad (10)$$

By varying the control point q_l, the curve will change in the interval $[u_l, u_{l+k}]$. Finally, the rotation angle $\theta(u)$ can be computed with the following equation:

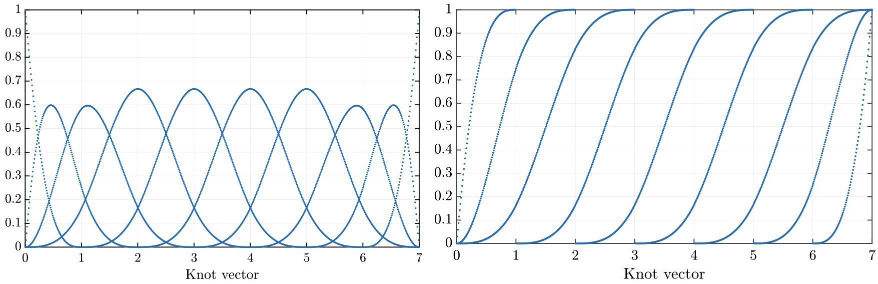

Fig. 1 Cubic basis functions (**a**); cumulative cubic basis functions (**b**)

$$\theta(u) = 2||\log(q(u))|| \tag{11}$$

The procedure for the definition of the B-spline curve (global interpolation) requires the definition of the control points, expressed as unit quaternions. This problem results in a system of nonlinear equations that requires solution via an iterative procedure, that is not reported here due to space constraints. However, the reader can refer to [7, 14, 15] for the complete formulation of the method.

The motion law $u(t)$ for the robot is planned using double-S speed profiles to obtain a smooth trajectory that limits the vibrations of the mechanical system. The planning of the motion law considers velocity, acceleration and jerk limits of the robot. The maximum tangential velocities of the B-spline curve are also taken into account to comply the requirements of spray painting. To satisfy these specifications, the look-ahead filtering approach described in [4, 16] is used to limit the end-effector tangential velocity and reduce joint acceleration values.

3 Experimental Results

The method is tested on a GR 630R robot by CMA Robotics with 6 °C of freedom and 3 kg of payload (Fig. 2a). This manipulator is designed for spraying operations, such as liquid painting or powder coating on surfaces of metal, wood, and plastic. To assess the validity of the generated trajectories, the three-dimensional model of a car bumper is chosen, since it features various curvatures at different heights that allow obtaining multiple orientation values for interpolation. The trajectory to be generated follows the path near the headlights, where a rapid change in curvature typically occurs. Figure 2b shows the off-line simulation with the selected bumper, the robot, and the path to be executed. The end-effector poses (highlighted in red) are sampled so as to maintain the paint gun orthogonal to the workpiece surface.

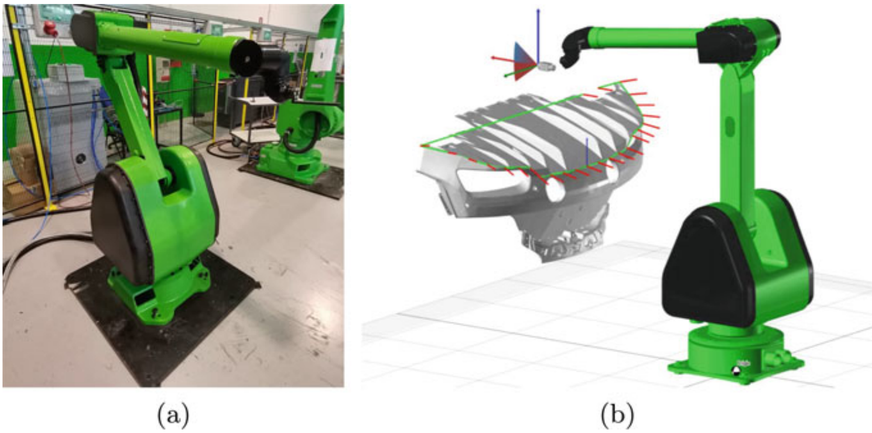

Fig. 2 GR 630R robot by CMA robotics (**a**); off-line simulator (**b**)

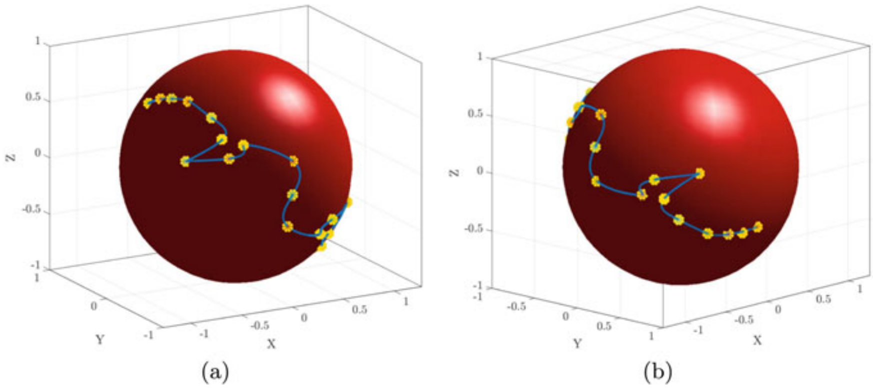

Fig. 3 Results of the interpolation of the input quaternions q_i on the unit hypersphere $\mathbb{S}^3$: front (**a**); and back (**b**)

Figure 3a, b show the results of the interpolation of the input quaternions q_i on the unit hypersphere $\mathbb{S}^3$. The blue curve represents the locus of the points of the unit hypersphere belonging to the curve $q(u)$, which interpolates the input values q_i provided (yellow markers). Furthermore, Fig. 4a shows the resulting rotation angle and the input angles: the curve results slightly translated with respect to the input data since the way points are calculated approximately with the iterative procedure described in [14]. In Fig. 4b, the tangential velocity profile of the robot end-effector is shown. The two ramps are almost symmetrical, with continuity between ramp and constant speed phase. The maximum variation compared to the desired speed (0.3 m/s) is below 4%.

The joint positions, velocities, accelerations and jerks obtained from the robot controller during the experimental test are reported in Fig. 4c–f. All the robot joint

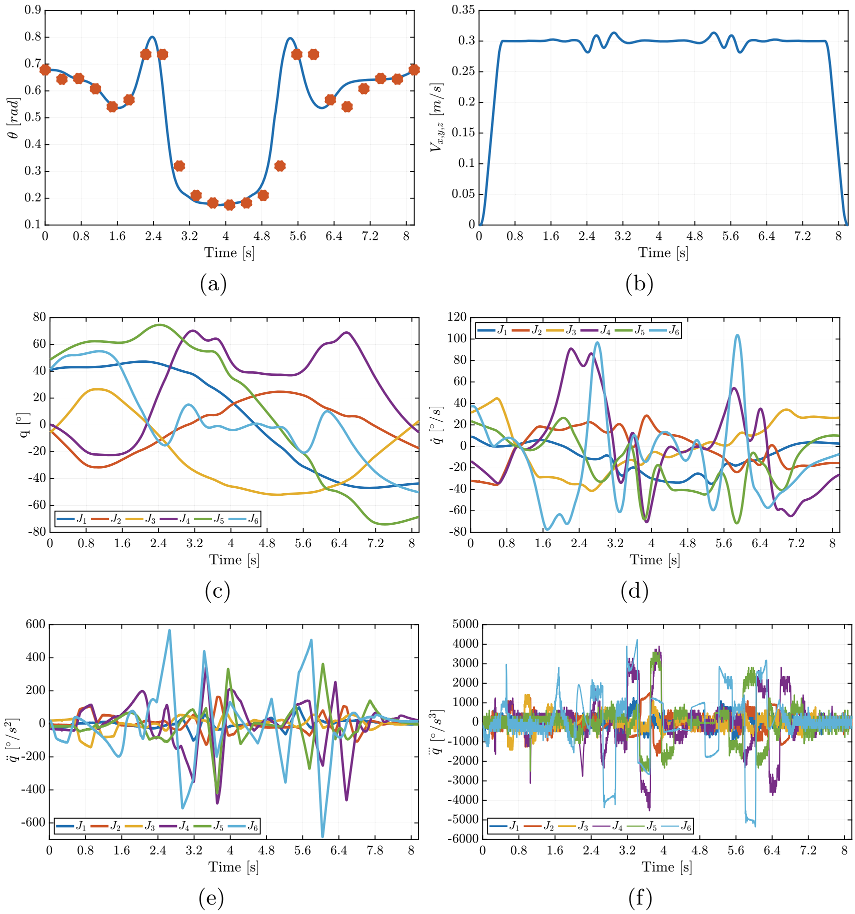

Fig. 4 Experimental results: resulting angle θ (blue curve) and input angles (red markers) (**a**); tangential velocity of the robot end-effector (**b**); joint positions (**c**); joint velocities (**d**); joint accelerations (**e**); joint jerks (**f**)

positions show a smooth behavior, respecting the joint ranges and the kinematic limits of the manipulator. The peaks in the velocity profile correspond to the maximum deviation of the tangential speed, and do not exceed the speed limit of the robot (120 °/s). Finally, joint accelerations show $\mathbb{C}^0$ continuity, and the maximum values of jerk are equal to 4000 °/s^3.

4 Conclusions

In this paper, an approach for the orientation trajectory planning based on cubic B-splines with cumulative basis functions and unit quaternions is applied for robotic spray painting, to avoid potential issues due to the representation singularity of Euler angles. Experimental results on a GR 630R industrial robot by CMA Robotics demonstrate the feasibility of the proposed approach in obtaining a good approximation of the input orientations. Continuity in velocity and acceleration is also achieved, as well as limited values of the tangential velocity.

References

1. Boscariol, P., Gasparetto, A., Scalera, L.: Path planning for special robotic operations. In: Robot Design: From Theory to Service Applications, pp. 69–95. Springer International Publishing, Cham (2023)
2. Scalera, L., Mazzon, E., Gallina, P., Gasparetto, A.: Airbrush robotic painting system: experimental validation of a colour spray model. In: 26th International conference on robotics in alpe-adria-danube region, pp. 549–556. Springer (2018)
3. Gasparetto, A., Vidoni, R., Saccavini, E., Pillan, D.: Optimal path planning for painting robots. In: Engineering Systems Design and Analysis, vol 49170, pp 601–608 (2010)
4. Trigatti, G., Boscariol, P., Scalera, L., Pillan, D., Gasparetto, A.: A new path-constrained trajectory planning strategy for spray painting robots. Int. J. Adv. Manuf. Tech. **98**, 2287–2296 (2018)
5. Sciavicco, L., Siciliano, B.: Modelling and Control of Robot Manipulators. Springer Science & Business Media, London (2001)
6. Dam, E.B., Koch, M., Lillholm, M.: Quaternions, Interpolation and Animation, vol. 2. Københavns Universitet, Copenhagen, Denmark, Datalogisk Institut (1998)
7. Kim, M.-J., Kim, M.-S., Shin, S.Y.: A general construction scheme for unit quaternion curves with simple high order derivatives. In: 22nd annual conference on computer graphics and interactive techniques, SIGGRAPH '95, pp 369–376, New York, NY, USA, 1995. Association for Computing Machinery
8. Xing, Y., Ren-zheng, X., Tan, J.-Q., Fan, W., Hong, L.: A class of generalized b-spline quaternion curves. Appl. Math. Comput. **271**, 288–300 (2015)
9. Niu, X., Wang, T.: C^2-continuous orientation trajectory planning for robot based on spline quaternion curve. Assembly Automat. **38**(3), 282–290 (2018)
10. Haarbach, A., Birdal, T., Ilic, S.: Survey of higher order rigid body motion interpolation methods for keyframe animation and continuous-time trajectory estimation. In: International Conference on 3D Vision, pp. 381–389. IEEE (2018)
11. Biagiotti, L., Melchiorri, C.: Trajectory Planning for Automatic Machines and Robots. Springer Science & Business Media, Heidelberg (2008)
12. Cox, M.G.: The numerical evaluation of B-splines. IMA J. Appl. Math. **10**(2), 134–149 (1972)
13. De Boor, C.: On calculating with B-splines. J. Approx. Theo. **6**(1), 50–62 (1972)
14. Kim, M.-J., Kim, M.-S., Shin, S.: A C^2-continous B-spline quaternion curve interpolating a given sequence of solid orientations, pp. 72–81 (1995)
15. Houdek, V., Verlinden, O., Hajžman, M.: Non-uniform quaternion spline interpolation in vehicle kinematics (2022)
16. Trigatti, G., Boscariol, P., Scalera, L., Pillan, D., Gasparetto, A.: A look-ahead trajectory planning algorithm for spray painting robots with non-spherical wrists. In: 4th IFToMM Symposium on Mechanism Design for Robotics, pp 235–242. Springer (2019)

RobotBlockSet (RBS)—A Comprehensive Robotics Framework

Leon Žlajpah and Tadej Petrič

Abstract In this paper, we present the comprehensive robotics framework **RBS**, which addresses the critical need for seamless integration between simulation and real-world execution in robotics. The proposed framework provides a unified solution for designing, testing, and executing robotic applications, bridging the gap between virtual and physical environments. By providing interfaces for various simulators and real robots, along with tools for robot modeling, motion planning, and execution, **RBS** streamlines the development process. It removes the complexity associated with the transition from simulation to real systems, shortens development times and enables fast and efficient design iterations. This innovative framework holds great promise for advancing robotics research and development. It enables researchers and engineers to realise the full potential of simulation and real-world testing in the development of state-of-the-art robotic systems.

Keywords Robot motion control · Robot simulation · Real-time robot systems

1 Introduction

Decades of research in robotic systems have underscored the indispensable role of appropriate software in their development. Despite the rapid advancement of computer capabilities, the creative input of human designers remains crucial throughout the development process. To enhance efficiency and facilitate quick and easy design—from trajectory planning to real robotic system implementation—providing designers with effective tools has proven a highly successful approach.

This work was supported by Slovenian Research Agency grant P2-0076 and N2-0269.

L. Žlajpah (✉) · T. Petrič
Department of Automatics, Biocybernetics and Robotics, Jožef Stefan Institute, Ljubljana, Slovenia
e-mail: leon.zlajpah@ijs.si

T. Petrič
e-mail: tadej.petric@ijs.si

D. Pisla et al. (eds.), *Advances in Service and Industrial Robotics*, Mechanisms and Machine Science 157, https://doi.org/10.1007/978-3-031-59257-7_44

Simulation has emerged as an indispensable tool in robotics, aiding in the design, exploration, and development of robotic applications [14]. It offers a thorough examination of robots' structure, characteristics, and behaviors at various levels, with each level demanding specific simulation tools [13]. As robotics systems grow in complexity, the role of simulation becomes more critical, particularly in advanced systems that require models covering diverse structural and functional aspects, utilizing various physics engines with unique advantages [4]. This approach is especially relevant in deep learning and fields like Reinforcement Learning, which need extensive data, as simulation can generate synthetic data and replicate experiments that would be challenging in real-world settings [2]. The primary aim of simulation is to facilitate the design process, allowing for the testing of algorithms before real-world implementation [1, 8, 12]. Despite the necessity of final validation on actual robot systems, simulation can significantly streamline the design process, reducing both effort and development time. The latest advancements involve integrating the entire design phase, from simulation to execution, into a single framework, a challenging yet crucial endeavor that requires different methods and tools for each planning step.

Numerous simulators are available for use in the field of robotics. CoppeliaSim [11] stands out as a comprehensive 3D robot simulation platform designed for modeling, simulating, and controlling orobotic systems, primarily in research and development. MuJoCo [7] serves as an efficient physics engine focusing on simulating and controlling the dynamics of robotic systems, especially in scenarios involving multiple joints and rich contact interactions. The Robotics Toolbox by Peter Corke [3], a MATLAB-based toolkit, and MathWorks Robotics System Toolbox [9], prove invaluable for researchers and engineers, providing essential functions for modeling, simulating, and controlling robotic systems, including capabilities for kinematics, dynamics, and trajectory planning. Gazebo, an open-source robot simulation environment, is a versatile platform supporting 3D simulations that aid in testing and developing robotic algorithms. Often utilized in conjunction with the Robot Operating System (ROS) [10], Gazebo [6] contributes to comprehensive robotic system development. RoboDK [5] serves as a user-friendly simulation and programming environment, particularly suited for industrial settings, enabling users to design, test, and generate programs for real robots. Simulators like ABB RobotStudio and Yaskawa's MotoSim are tailored specifically for industrial robots, functioning as simulation and programming tools. These tools allow users to simulate movements, optimize paths, and generate programs for real robot execution in industrial applications.

Each simulator listed possesses its unique set of advantages and drawbacks, and the choice among them depends on specific requirements. However, these systems' general complexity and versatility can pose challenges for the average user. Moreover, certain simulators are restricted to use only with robots from their respective companies, limiting their universality. In response, we aim to merge the broad applicability of universal software with the user-friendly nature of an integrated development environment. This approach is intended for users who want to interact with robots without delving into the specifics of each robot and its control. To facilitate the utilization of any simulator or real robot for planning purposes, we have developed a comprehensive robotics framework **RBS**. This framework seamlessly connects robot motion planning processes to various simulators or real robots, providing a versatile solution for planning and execution. A notable advantage is the seamless transition from simulation to a real robot, eliminating the need for additional coding.

In the following, we describe the **RBS**. Initially, we outline the concept of our framework. Subsequently, we elaborate on the interfaces for communication with various simulators and connections with real robots. Following that, we detail the tools for robot modeling, motion planning, and motion execution. Lastly, we provide examples illustrating the practical application of RBS.

2 Concept of RBS

A comprehensive robotics framework demands several key attributes to address to the diverse needs of users and applications. Openness is paramount, requiring easy access to the system, an open architecture, and seamless integration of modules. Reconfigurability is essential for swift modifications and the verification of effects. Ease of use is critical for a broad user base with varying expertise levels, enabling easy testing in simulation environments and on real robots while concealing intricate implementation details. A unified set of tools and environments enhances the overall usability.

The underlying concept involves the control of different robots employing varied interfaces, emphasizing adaptability to diverse robotic systems. It encompasses the integration of different sensor systems, such as vision and force sensors, fostering a holistic understanding of the robot's surroundings. Furthermore, the framework is designed to facilitate scenarios for complex robot tasks, providing tools to visualize robots and their environments (using simulators). Lastly, the framework can also support distributed computation across multiple computers, ensuring scalability and efficiency in handling computational tasks related to robotics.

The overall structure of the **RBS** framework could be divided into three parts (see Fig. 1):

- **RBS** : The main part is the **RBS** toolbox, which provides functions for robot programming, generation of trajectories and motion, and various tools for robot analysis. It also includes a communication interface for communicating with target robotic systems via an intermediate layer.
- **MW**: As some robots require special communication protocols or if special low-level robot control is required we use the intermediate layer between **RBS** and TP, where middleware software is used to provide the necessary functionality. In our implementations, we mainly use the open-source robot software middleware ROS or Simulink Real-Time applications.
- **TP**: This part represents the target platform (TP), which we want to control. As TP we can use a real robot including different sensors and other devices, or TP is a simulator where a robot system and its environment are simulated.

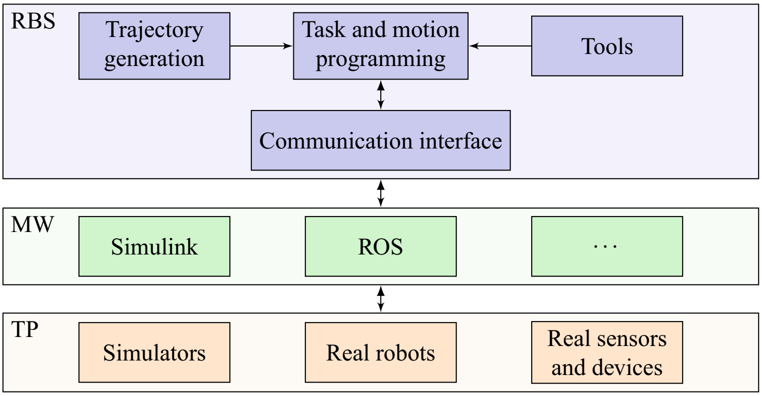

Fig. 1 Overall structure of RBS framework

Originally developed in MATLAB, the toolbox has been meticulously ported to Python, ensuring the seamless transition of its robotics-specific functionality to the Python ecosystem. This adaptation expands the accessibility of the toolbox, empowering users with the versatility of Python while retaining the rich set of features essential for robotics design and simulation.

3 Robot Classes

The toolbox uses an object-oriented approach to represent robots, sensors, and other devices as distinct classes, enabling a modular and flexible design paradigm. Hence, in the **RBS** Toolbox all objects are defined as classes, which have different properties and methods. The core functionality of the **RBS** lies in offering uniform control for various robots. This is achieved by introducing a robot superclass, denoted as **robot**. Serving as the parent class for specific implementation classes dedicated to individual robots, **robot** ensures a standardized approach to robot control across diverse systems.

The superclass **robot** serves as the overarching framework that establishes general properties and methods essential for controlling any robot, encompassing elements such as motion generation methods, kinematic controllers, transformations between different robot state representations, conversions across distinct spaces, utility functions, and more. Some of these methods are abstract and necessitate definition in the target or implementation class. Target subclasses are responsible for defining these abstract methods and incorporating all specific functionalities tailored to the target environment. These subclasses also include methods dedicated to communication with the target platform. On the other hand, implementation classes encompass all specific functionalities of individual robots and may need to redefine certain methods already defined in the superclass to adapt them to the particular requirements of each robot.

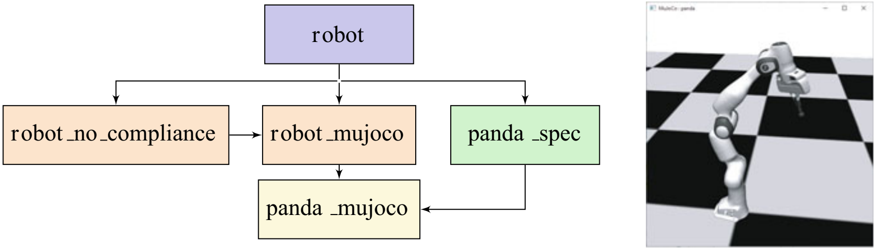

Fig. 2 Matlab definition of robot object (left) for a Franka Emika Panda robot simulated in MuJoCo simulator (right)

To prevent code duplication, the implementation employs subclasses, which group related properties and methods. These subclasses extend inherited methods, providing specialized functionality while reusing common aspects. Moreover, they have the flexibility to introduce new methods and properties. This hierarchical organization of classes streamlines the development process and ensures transparency, making the creation of robot objects more straightforward and comprehensible.

Figure 2 explains the structure of a robot class used to define a robot object — Panda robot object **panda_mujoco** for MuJoCo simulator target, which inherits basic **robot** class and several subclasses at several levels. First are the subclasses defining the parameters and methods for a specific target (**robot_mujoco**, related to the MuJoCo simulator) and **robot_no_compliance** to define dummy compliance-related methods, which MuJoCo does not support. The specific robot parameters and methods are defined in subclasses named **panda_spec**. The final robot object is defined as a subclass of all the classes mentioned above. The **panda_mujoco** is defined in Matlab as:

```
classdef panda_mujoco < robot_mujoco & panda_spec
  methods
    function robot=panda_mujoco(varargin)
      opt=set_options({},varargin);
      robot=robot@robot_mujoco('Panda',opt);
      robot.Specifications;
      robot.control_strategy='JointPosition';
      robot.Init;
    end
  end % methods
end % classdef
```

or in Python as:

```
class panda_mujoco(robot_mujoco,
    robot_no_compliance, panda):
  def __init__(self, robot_name="Panda",
     **kwargs):
     panda.__init__(self)
     kwargs.setdefault("host", "localhost
    ")
     robot_mujoco.__init__(self,
    robot_name, **kwargs)
     self.__dict__.update(kwargs)
     self.Init()
  def __del__(self):
     robot_mujoco.__del__(self)
     self.Message("Robot deleted", 2)
```

4 Interfaces

The main feature of **RBS**, distinguishing it from other programming environments, is that it allows the user to easily work with a real robot or a robot in a simulator. In principle, everything at the user level is independent of the selected robot and platform. The only thing that needs to be done is to choose the appropriate robot object. The appropriate communication interface and MW then ensure the communication between the **RBS** and the robot.

In our environment, simulators are only used to simulate the robot system as realistically as possible. We do not include any custom controller in the simulator like in [12] or other functionalities regarding the robot control. This means that the communication interface ensures only that the states of the robot and other devices are read via sensors and that the robot and other devices are controlled via the corresponding actuators. Consequently, the simulator used as a target platform must be able to simulate all the necessary sensors and actuators, which is not a problem with modern simulators such as MuJoCo, CoppeliaSIm or Gazebo. It is also desirable that the simulation takes place in real-time, so that the gap between the real and simulated system is as small as possible.

In case it is necessary to use a special control method on the robot, we realize these algorithms as a part of MW, and the same algorithms are used for the real and simulated robot.

The actual implementation of the interfaces depends on the target platform. If direct communication with the platform is not possible, such as with CoppeliaSim, then using the appropriate software at the MW level is necessary. When connecting **RBS** with robots and simulators, we mainly use ROS. Choosing ROS as middleware is a good choice, given its continuous development and widespread support among various real robots and simulation software. Typically, we use ROS subscribers to get the robot’s state and sensor data, publishers to send commands to the robot, and ROS services to change control strategies and other parameters.

When the target platform (robot or simulator) does not support ROS then we develop special real-time MW applications based on TCP/IP or UDP communication protocols. For example, to communicate with KUKA LWR arms with Fast Research Interface (FRI) we have developed Simulink Real-Time Target application which allows easy and reliable communication with the robot. To interact with MuJoCo we included in MuJoCo a TCP/IP server similar to MuJoCo/HAPTIX [7], which allows interaction with the model in MuJoCo simulator.

5 Tools

The **RBS** toolbox offers tools for describing 3D object positions and orientations using homogeneous matrices and quaternions. It includes a dedicated quaternion class for essential operations, transformation functions between representations, and features for motion generation, interpolation, and approximation. Additionally, it provides tools for constructing robot kinematic models and various utility functions, making it a versatile resource in robotics.

5.1 Robot Models

The effective and scalable management of various kinds of robot models is the base of **RBS**'s generality. To be able to control the motion of a robot we use in **RBS** kinematic models of robot manipulators. Kinematic models can be automatically generated using the Denavit-Hartenberg (DH), the Modified Denavit-Hartenberg (MDH) kinematic parameters, or the kinematic model is generated from the Unified Robot Description Format (URDF) file describing the robot. The **RBS** also provides functions to join serial kinematic chains into one kinematic chain. The obtained kinematic models are used in **RBS** controllers which support a variety of control strategies including also different redundancy resolution algorithms.

5.2 Motion Control and Trajectory Generation

An essential feature within robotic control framework involves the creation of paths and trajectories. The **RBS** Toolbox offers utilities for generating paths and trajectories in both joint and task space. For each type of motion **RBS** provides high-level motion methods, which include trajectory generation and low-level methods, which execute the motion. When a high-level motion method is executed (like `robot.CMove(x,2)`, first the trajectory for the desired movement is calculated (positions and velocities). Trajectory generation is done in two steps. First we do the interpolation. For interpolation in joint space we can use standard linear interpolation

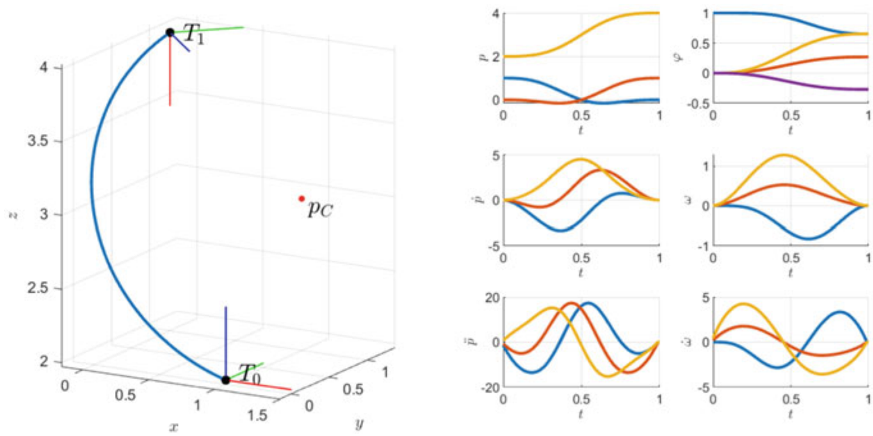

Fig. 3 Cartesian circular trajectorj using 5th order polynomial

functions. Also for interpolation of 3D positions in Cartesian task space, we can use standard linear interpolation. On the other hand, the interpolation of orientations is not so straightforward. In **RBS**Toolbox we use in most cases the linear spherical interpolation SLERP. So, interpolating between two spatial poses we combine linear interpolation for positions and SLERP interpolation for orientations. Then, we calculate the time evolution specifying the duration of movement from the initial to the final position and the velocity profile. For example, to move from initial position T_0 to final position T_1 along arc using 5th order polynomial we calculate the trajectory using command:

```
T0=rp2t(eye(3),[1 0 2]');
T1=rp2t(rot_y(pi/2)*rot_x(pi/4),[0 1 4]');
t=0:0.01:1;
pC=[1 1 3]';
[xt,vt]=carc(T0,T1,pC,t,@jpoly);
```

The generated trajectories shown in Fig. 3 are sent to robot controller using the low-level motion method (`robot.GoTo_T`) in a loop for each sample until the end of the trajectory is reached.

To generate a more complex motion, like continuous motion over or near many points, **RBS** provides sophisticated path generation methods. For example, using function `pathoverpoints` we can generate smooth trajectories from the initial point via or near intermediate points to the final point, and then command the robot to move along this path:

```
[xi,si]=pathoverpoints(pt,'Interp','spline','Plot',
    'on');
r.CPath(xi,12)  % do motion along path in 12 sec
```

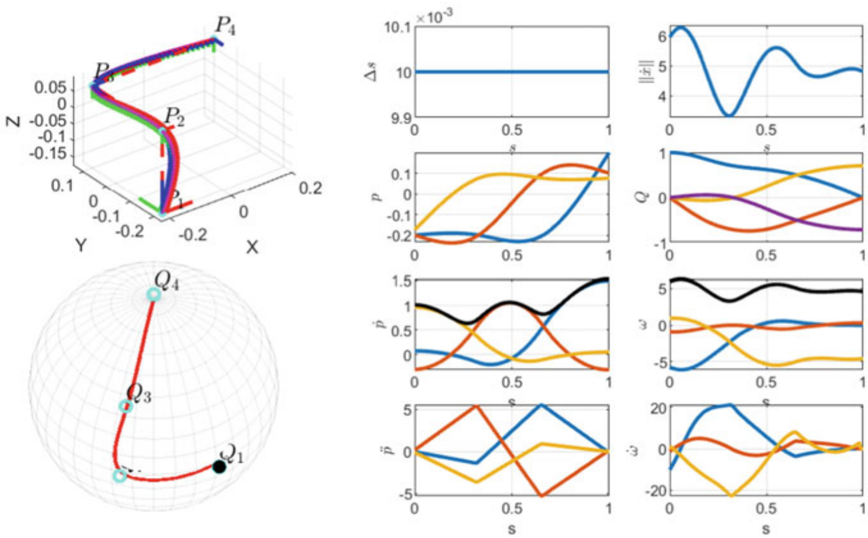

Fig. 4 Cartesian path over multiple points using spline and slerp interpolation

Figure 4 shows path generated using cubic spline interpolation over all points. Consequently, generated trajectories have smooth velocities but the accelerations are not smooth.

We can use RBF parametrization path generation over multiple points (see Fig. 5). Compared to spline interpolation, we can also define here the initial and final conditions for velocity and acceleration.

```
RBF=encodeRBF(sp,points,N,c,sig,ic,coff,sfac); %
   Encode path
r.CRBFPath(RBF,12) % go along path in 12 sec
r.CRBFPath(RBF,12,'Direction','Backward') % go back
   in 12 sec
```

6 Demonstration Experiment

A real use case best demonstrates the usefulness of **RBS**. We chose a robot cell for the final quality control of the ovens. In the process of planning the cell, **RBS** was intensively used both for selecting the robot and for planning and optimizing the inspection tasks. Finally, we implemented the developed application easily on a real robot Franka Emika Panda using ROS without changing the developed program.

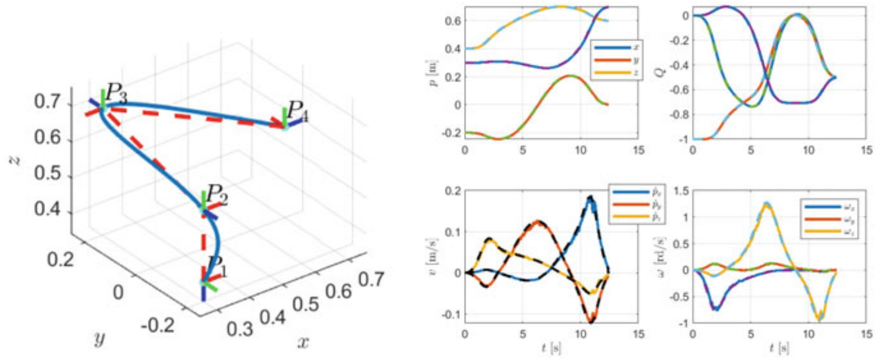

Fig. 5 Cartesian path over multiple points using RBF encoded path

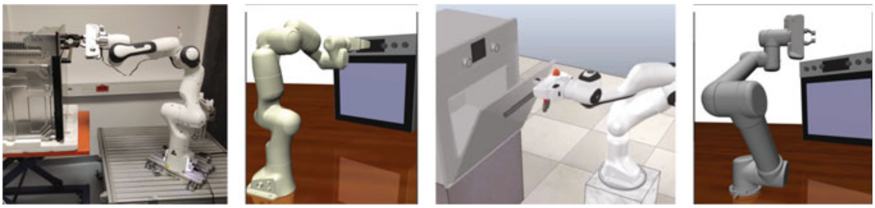

Panda in real cell | Panda in MuJoCo | Panda in CoppeliaSim | UR5 in MuJoCo

Fig. 6 Experiment using different target robot systems

Figure 6 shows the work-cell environment implemented using different TP: Real robot cell, simulation in MuJoCo and simulation in CoppeliaSim.

For example. the following code has been used to open the oven doors. Depending on the selected target robot system, we have only to change the definition of robot and gripper object. For the real robot we used **`panda_ros`**, and when the TP was a simulator, we have to use **`panda_mujoco`** or **`panda_coppelia`** for MuJoCo or Coppelia-Sim simulator, respectively. Additionally, when we want to use another robot, we just define the corresponding robot object, e.q. to use UR5 robot in MuJoCo (e.g. far-right image on Fig. 6) we define the robot object as **`ur5_mujoco`**—everything else in the code remains the same.

```
% Define robot and gripper object, set robot
   parameters
r=panda_ros;  % Real robot object using ROS
g=panda_gripper_ros;  % Robot gripper object using
   ROS
r.SetGripper(g);
r.SetTCP(T_Handle) % Set tool frame for door
   grasping
r.SetLoad('Mass',0.2,'COM',[0 0 0.05]','Inertia',
   zeros(3,3))
r.SetCollisionBehaviour(100,100,100)
r.SetObject(T_oven)  % Set object frame to oven
r.gripper.Open
r.SetJointSoft(0.5)  % Make robot compliant before
   grasping
% Move gripper behind door handle, Move in object
   frame
r.OApproach(O_Handle,[0.05 0 0.000]',5)
r.OApproach(O_Handle,[0.01 0 0.006]',1)
r.OMove(O_Handle,0.5)
% Open oven door by pulling handle
r.OMove(O_Handle_open,5)
% Release door handle
r.TMove([0 -0.017 0]',0.5)  % Move in tool frame
r.TMove([0 0 -0.1]',1)
```

7 Conclusion

The **RBS** Toolbox is a significant advancement in robotics, offering a comprehensive set of tools for designing, simulating, and testing robot manipulators with a unified syntax that simplifies operation across various systems. Its ability to transition seamlessly between simulated environments and actual robotic platforms enhances research and development efficiency, reducing time and resources needed. This toolbox democratizes access to robotic technologies, making it easier for newcomers and students to engage with sophisticated systems, and its adaptability across different platforms highlights its potential for widespread application in fields like manufacturing, healthcare, and disaster response. The **RBS** Toolbox not only streamlines robotic development but also expands the possibilities for broader adoption and innovation in robotics.

References

1. Choi, H.S., Crump, C., Duriez, C., Elmquist, A., Hager, G., Han, D., Hearl, F., Hodgins, J., Jain, A., Leve, F., Li, C., Meier, F., Negrut, D., Righetti, L., Rodriguez, A., Tan, J., Trinkle, J.: On the use of simulation in robotics: opportunities, challenges, and suggestions for moving forward. Proc. Natl. Acad. Sci. U. S. A. **118**(1), 1–9 (2021)
2. Collins, J., Howard, D., Leitner, J.: Quantifying the reality gap in robotic manipulation tasks. In: Proceedings—IEEE International Conference on Robotics and Automation, pp. 6706–6712 (2019)
3. Corke, P.: Robotics, Vision and Control. Springer (2017)
4. Erez, T., Tassa, Y., Todorov, E.: Simulation tools for model-based robotics: comparison of Bullet, Havok, MuJoCo, ODE and PhysX. In: Proceedings—IEEE International Conference on Robotics and Automation, pp. 4397–4404 (2015)
5. Garbev, A., Atanassov, A.: Comparative analysis of RoboDK and robot operating system for solving diagnostics tasks in off-line programming. In: 2020 International Conference Automatics and Informatics, ICAI 2020—Proceedings (2020)
6. Koenig, N., Howard, A.: Design and use paradigms for Gazebo, an open-source multi-robot simulator. In: 2004 IEEE/RSJ International Conference on Intelligent Robots and Systems (IROS), vol. 3, pp. 2149–2154 (2004)
7. Kumar, V., Todorov, E.: MuJoCo HAPTIX: a virtual reality system for hand manipulation. In: IEEE-RAS International Conference on Humanoid Robots, pp. 657–663 (2015)
8. Liu, C.K., Negrut, D.: The role of physics-based simulators in robotics. Annu. Rev. Control Robot. Autonom. Syst. **4**, 35–58 (2021)
9. MathWorks: Robotics System Toolbox [online]. https://www.mathworks.com/help/robotics/
10. Quigley, M., Gerkey, B., Conley, K., Faust, J., Foote, T., Leibs, J., Berger, E., Wheeler, R., Ng, A.: ROS: an open-source robot operating system. In: ICRA Workshop on Open Source Software. p. 5. IEEE, Kobe, Japan (2009)
11. Rohmer, E., Singh, S.P., Freese, M.: V-REP: a versatile and scalable robot simulation framework. In: IEEE International Conference on Intelligent Robots and Systems, pp. 1321–1326 (2013)
12. Singh, R.P., Gergondet, P., Kanehiro, F.: Mc-Mujoco: simulating articulated robots with FSM controllers in MuJoCo. In: 2023 IEEE/SICE International Symposium on System Integration, SII 2023 (Figure 1) (2023)
13. Žlajpah, L.: Integrated environment for modelling, simulation and control design for robotic manipulators. J. Intell. Robot. Syst.: Theory Appl. **32**(2), 219–234 (2001)
14. Žlajpah, L.: Simulation in robotics. Math. Comput. Simul. **79**(4), 879–897 (2008)

AI-Based Multi-criteria Path Planning of Cartesian Robot with Telescopic Arm for Tree Fruit Picking

Aleksandar Rodić, Uroš Ilić, and Ilija Stevanović

Abstract The paper presents a hybrid neuro-fuzzy applicative interface for path planning and multi-criteria motion optimization of an agriculture service robot with a telescopic arm designed for picking fruit from trees on the large orchards. The intelligent optimization system is based on application of artificial intelligence algorithms–neural networks and fuzzy inference system, which includes necessary knowledge about the kinematic and dynamic behavior of the robot in the operation task space, including data on the coordinates of places intended for disposal of the picked fruits from the tree. The intelligent system for path planning of the robot determines in real time the points in the working space that meet three set qualitative criteria for decision-making: (i) the shortest paths, (ii) the fastest paths, and (iii) the minimum energy consumption for catching, picking and carrying away the harvested fruits to the nearest place provided for the disposal of the fruits. The applied artificial neural network, described in the paper, is used for training, i.e. acquisition of the knowledge about the kinematic and dynamic behavior of the robot in the workspace in order to replace the process of numerically demanding calculation of the robot model in real time. Fuzzy classifier as a smart inference system has the role of choosing the best, optimal solution for the robot path that satisfies the set criteria functions.

Keywords Fruit picking robots · Knowledge-based path planning · Artificial intelligence · Artificial neural networks · Fuzzy inference system

1 Introduction

In the automated fruit picking tasks by robots, the main technical challenges are related to solving problems regard to the efficiency and reliability of machine vision (in a real-environment conditions of exploitation) as well as to optimizing the performing of work tasks in the limited workspace of the robot. It mainly boils down to optimizing the movement of the end-effector of the manipulator and minimizing

A. Rodić (✉) · U. Ilić · I. Stevanović
Institute Mihajlo Pupin, Belgrade, Serbia
e-mail: aleksandar.rodic@pupin.rs

D. Pisla et al. (eds.), *Advances in Service and Industrial Robotics*, Mechanisms and Machine Science 157, https://doi.org/10.1007/978-3-031-59257-7_45

Fig. 1 The fruit picking robot with cartesian coordinate mechanism for basic positioning and with the complementary telescopic arm equipped with a customized gripper. Extended arm position on the left and retracted position on the right side

energy consumption. Energy minimization is the primary problem with battery-powered devices, i.e. in self-propelled electric vehicles with robotic pickers. Technical problems related to machine (robot) vision are related to the presence of physical obstacles in the workspace of the robot task and limited access to fruits due to the presence of branches, leaves, parts of the tree, objects, etc., but also to the influence of shadows or excessive reflection due to direct exposure of camera to sunlight. These problems were discussed more in the paper [1]. At this point, the research focus is on the optimization of robot trajectories during the picking process. A fruit picking robot is expected to achieve human sensibility and dexterity, and manipulation speed. The length of the picking cycle varies depending on the external conditions, the size of the tree, the bigness of the fruits, the lighting of the space, etc. The paper [2] presents the technical details of a robot for picking fruit from trees shown in (Fig. 1).

2 State of the Art

Nowadays, four common path planning algorithms were frequently implemented in the research literature. These are: A-star, Probabilistic Road Map, Rapidly exploring Random Tree, and improved rapidly exploring Random Tree [3]. Aiming to realize the obstacle avoidance of the picking robot in dynamic and unstructured environments, an improved rapidly exploring random tree (RRT) algorithm was considered in [4, 5]. Aiming to realize the obstacle avoidance of the fruit tree pruning manipulator in unstructured complex natural environment, an improved bidirectional fast extended random tree (RRT-Connect) algorithm was presented in [6]. The paper [7] introduces a fast and robust collision-free path-planning method based on deep reinforcement learning. A recurrent neural network is first adopted to remember and exploit the past states observed by the robot, and then a deep deterministic policy gradient algorithm (DDPG) predicts a collision-free path from the states [7]. A Time-Optimal Rapidly-exploring Rrandom Tree (TO-RRT) algorithm is also proposed in

[8]. First, this algorithm controls the target offset probability of the random tree through the potential field and introduces a node-first search strategy to make the random tree quickly escape from the repulsive potential field. Second, an attractive step size and a "step-size dichotomy" are proposed to improve the directional search ability of the random tree outside the repulsive potential field and solve the problem of an excessively large step size in extreme cases. Finally, a regression superposition algorithm is used to enhance the ability of the random tree to explore unknown space in the repulsive potential field [8]. Optimal path planning refers to find the collision free, shortest and smooth route between start and goal positions. Rapidly-exploring Random Tree Star (RRT*) is a renowned sampling based planning approach [8, 9]. The Rapidly-exploring Random Tree (RRT) obstacle avoidance algorithm was used to establish a collision-free path to reach the target pruning points. The path smoothing and optimization algorithms were also used to reduce path length and calculate the optimize path [10]. Under limited environment, PRM (Probabilistic Roadmap Method) algorithm is used to plan initial path in mobile robot path planning, a path optimization algorithm is proposed based on the improved node method and geometric smooth strategy [11]. A method based on improved ant colony algorithm was explored in [12] to optimize the initial path. The Traveling Salesman Paradigm (TSP) is used to plan the sequence of sensing and harvesting tasks taking into account the costs of the sensing and harvesting actions and the traveling times [2, 13]. Accordingly, a hierarchical optimal path planning (HOPP) algorithm is designed to significantly reduce or minimize the time cost during robotic apple harvesting in a 3D environment [14]. We have conducted a more comprehensive comparative analysis, providing a deeper insight into how our hybrid neuro-fuzzy applicative interface surpasses existing state-of-the-art technologies. Our empirical results showcase significant advantages, such as faster computation time, improved obstacle avoidance capabilities, and enhanced energy efficiency, compared to conventional path planning algorithms. Moreover, we have illustrated the robustness and adaptability of our algorithm through diverse agricultural scenarios, highlighting its ability to dynamically adjust trajectory planning strategies to accommodate variations in environmental conditions. Furthermore, we have outlined potential future research directions, including the integration of machine learning techniques for adaptive decision-making and extending the applicability of our algorithm to other robotic harvesting tasks.

3 Problem Setting

Path planning, carrying out the task of picking fruit from trees in an automated way using robots in the presence of obstacles, disturbances and environmental uncertainties of different nature is a complex task and requires application of intelligent techniques and robust control algorithms. The intelligent path planner of the robot for picking fruit from trees is inspired by the human manner of reasoning and logic planning a strategy for carrying out such type of tasks based on skill and experience.

When picking fruit manually, the human picker usually approaches in the following way. First, the fruits that are at the lowest levels of the tree are picked in order, and then one goes to the higher parts so that the fruits from the lower branches are not torn off by maneuvering the body. At the same time, in this order, the least physical effort is made and the least physical strength is consumed. In the second case, when people work according to the norm, to harvest the largest amount of fruit in the shortest possible time, they direct their attention to the zones where the largest numbers of targets are grouped and where there are the fewest obstacles–branches, leaves, auxiliary objects, etc. This means that a person naturally takes care to satisfy two intuitive criteria: (i) minimum power consumption, and (ii) the shortest time to complete the task by crossing the shortest paths. The third criterion refers to the choice of a path (direction of movement) where there are no visible obstacles. This concept of robot motion planning is implemented in the work by applying intelligent learning techniques and fuzzy reasoning based on skill and experience.

The picking process takes place in the robot's workspace in several characteristic stages, which are illustrated in Fig. 2. Using machine vision algorithms (for color, pattern recognition, texture, depth identification, etc.) points $j = 1, \ldots, n$ were detected which are randomly distributed in the space and whose coordinates are known with a satisfactory precision. The movements of the robot can be classified into several characteristic phases: (i) approaching phase along points *a-b-c-d*, (ii) targeting, from point d to point $k + 1$, (iii) gripping i.e. picking at the point $k + 1$, which involves gripping the fruit from the branch on to which it was attached, (iv) carrying the harvested fruit through points *d-c* and depositing the fruit at the point b to the box or some storage. The starting point of the robot gripper is at point a, the movement cycle ends at point b. Points k and $k + 1$ are neighboring points in the task workspace that includes a cloud of $j = 1,\ldots,n$ points. The distance k to $k + 1$ point is the shortest distance between two adjacent points, while points k' and $k + 1$ form a vector that defines the shortest path of the center of mass of the robot gripper from the starting point to the goal (Fig. 2).

The research task in this paper boils down to finding the optimal movement between points in the work space of the task or order of points in this space so that the robot's gripper achieves the shortest path or the fastest trajectory between points and minimizes the power economy (energy required) to reach all points P_j, $j = 1, \ldots, n$.

4 Intelligent Path Planning

The intelligent path planner of the picking robot (Fig. 1) is shown in Fig. 3 with the corresponding block diagram. The smart path planner uses available data on the coordinates of points in the task workspace, received from the machine vision module and cameras that map the workspace and identify the coordinates of points representing fruits that are in the field of view and within reach of the telescopic robotic arm. Cameras and corresponding machine vision algorithms enable the detection of point clouds in the robot's random space. These points represent the particular targets

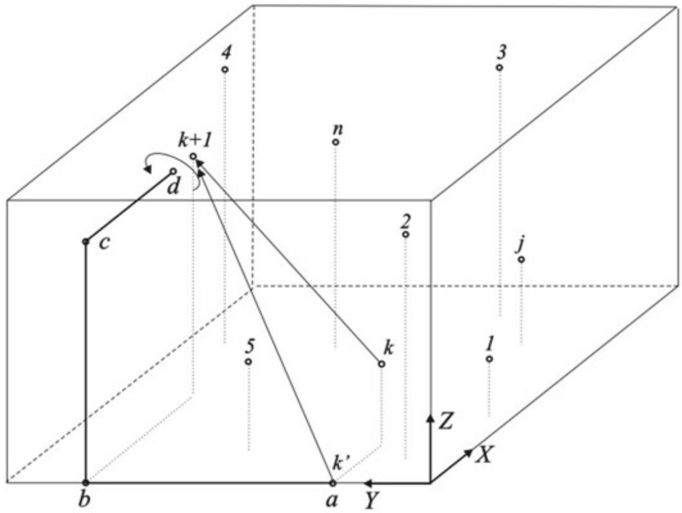

Fig. 2 Graphic representation of the picking robot phases in the operation space. Position of the target points in a workspace. Points of interest that define the phases of motion of the robot's end-effector

that the robot's gripper needs to reach and grab the fruit on the tree branch. The path planner, thanks to the structure of the artificial neural network (ANN) that has learned knowledge about the kinematics and dynamics of the manipulator, as well as thanks to the fuzzy reasoning system, determines the optimal sequence of execution of the robot's movements. It boils down to determining the sequence of points belonging to the robot's workspace that should be reached by the movable, extendable telescopic arm. The starting point of the robot is the one where the robot stopped in the previous random cycle (point "*a*", Fig. 2) where the harvested fruit was placed on the conveyor belt or in a buffer provided for that. Based on knowing the coordinates of these two points *k'* and $k + 1$, the mutual distance vector $D = \left[D_x \; D_y \; D_z\right]$ is calculated. Projections of the vector *D*, shown in Fig. 3, are used in the trajectory generator to determine the movement (position q, velocity $\dot{q}$ and acceleration $\ddot{q}$) in each individual joint of the robot picker. The process of determining the next target point takes place simultaneously while the robot executes the capture of the current target. This execution parallelism enables reliable real-time system management. Motion planning cycles are repeated until the last point in the target point cloud is reached. During the picking process, disturbances occur such that some points disappear from the field of visibility (for example, when the fruit falls from the branch or is obscured by a physical obstacle or its contours are lost due to the intensity of the lighting) before the robot reaches them. For this reason, the smart robot scheduler does continuous updating of the visible set of points or checking whether all points are available. In this way, the quality (maturity) and size of the fruits can also be checked, and thus their classification by quality can be carried out while the picking operation is in progress.

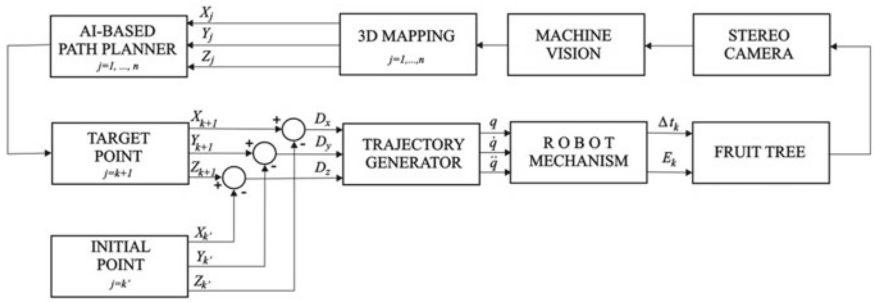

Fig. 3 Block-diagram of a robotic system for picking fruit from trees with blocks for optimal path planning based on application of artificial intelligence algorithms

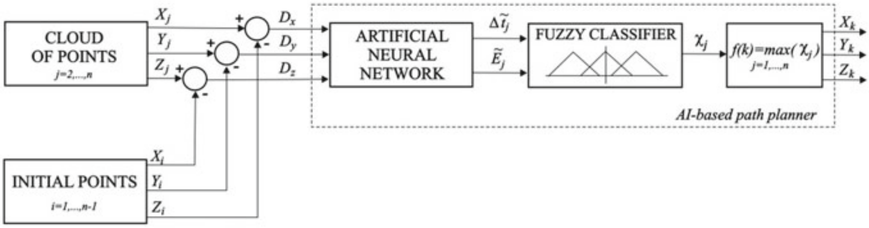

Fig. 4 Architecture of the hybrid neuro-fuzzy robot path planner based on machine learning and multi-criteria fuzzy inference system—fuzzy classifier

The intelligent path planner consists of two independent blocks (Fig. 4) that make up: (i) an artificial neural network, and (ii) a fuzzy classifier. The output from the fuzzy classifier is the performance index (χ_j) which is determined for each individual point $j = k$ from the robot's workspace. The optimal path is the one that brings the robot to the target point for which the maximum value of the performance index *f(j = k)* is determined.

5 Connectionist Structure of Model Identifier

Path planning and robot trajectory generation are numerically demanding processes. In addition to the possibility of parallel processing of task management in the robot controller, this task requires the rationalization of the processor calculation time and the optimization of the process parameters. Since it is necessary to know the kinematics and dynamics of the robot in the random space of the task to plan the path, their calculation in real time would be critical from the point of view of execution time. That would definitely slow down the robot and reduce its operational capabilities. Therefore, in this paper, it is proposed that instead of the classical calculation of the robot model, it should be substituted with a simpler approximate model obtained by

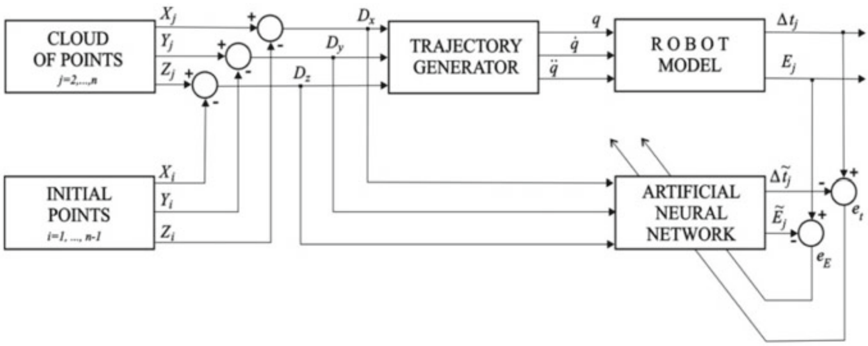

Fig. 5 Block diagram of a system for training a neural network intended for learning a kinematic and dynamic model of the fruit-picking robot shown in Fig. 1

training the network structure for learning i.e. ANN shown in Fig. 5. Three variables D_x, D_y, D_z representing the distance projections of points *k'* and $k + 1$ to the robot's absolute coordinate system are fed to the input of the artificial neural network (Fig. 4). This vector carries with it information about the possible movements of the robot in its workspace. Two variables $\Delta\tilde{t}_j$ and $\widetilde{E}_j$, $j = 1,\ldots,n$ are obtained at the output of the neural network. The process of training the neural network takes place in several epochs on the entire set of points from the task space, and the training ends when the deviation values e_t and e_E on the comparators fall below the set value of the error. The learning network can then be considered sufficiently trained to approximate the robot model with the desired accuracy. The number of mathematical operations performed in the approximate model is significantly less than the number of operations in the conventional differential equations based model of the robot. The fuzzy classifier within the intelligent robot path planner has the role of ranking the points according to the optimality of the choice or quantifies the performance index of the robot's movement to each target point in the operational task space (Fig. 6).

Two quantities previously generated by the neural network are fed to the input of the fuzzy classifier (Fig. 4). These are the path duration Δt_j and the energy consumption E_j for the movement of the robot from the starting point to the selected target point. The starting point is the place where the robot deposited the harvested fruit in the previous working cycle (e.g. point k', Fig. 2).

6 Examples

In the paper it was tested a knowledge-based algorithm (block diagram, Figs. 3 and 4) for robot path planning by use of the neural network as an identifier of the kinematics and dynamics of the robot mechanism and a fuzzy classifier to enable achieving optimality of motion. For this purpose, *n* points representing the positions of the fruits on the branches are randomly generated, as a model of the distribution of fruits on the

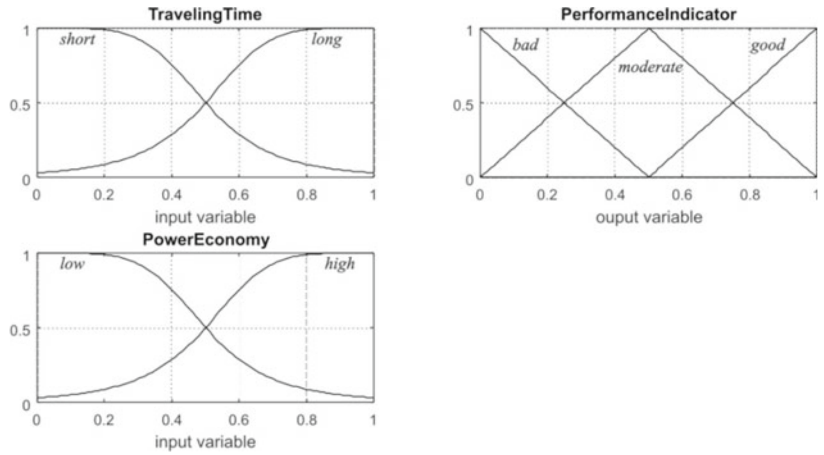

If *TravelingTime* is 'short' then *PerformaceIndicator* is 'good' (WF=1)
If *TravelingTime* is 'long' then *PerformaceIndicator* is 'bad' (WF=1)
If *PowerEconomy* is 'low' then *PerformaceIndicator* is 'good' (WF=1)
If *PowerEconomy* is 'high' then *PerformaceIndicator* is 'bad' (WF=1)
If *TravelingTime* is 'short' and *PowerEconomy* is 'high' then *PerformaceIndicator* is 'moderate' (WF=1)
If *TravelingTime* is 'long' and *PowerEconomy* is 'low' then *PerformaceIndicator* is 'moderate' (WF=1)

Fig. 6 Membership functions, fuzzy rules and weighting factors of the synthesized fuzzy classifier responsible for path optimization

tree in the robot workspace. A Cartesian robot with a telescopic arm has a working space that is limited by width $A = 1.50\ m$ (Y-direction, Fig. 2), height $B = 1.00\ m$ (Z-direction) and depth $C = 2.25\ m$ (X-direction). In the observed operation space, $n = 79$ points were identified (with their coordinates $X_j, Y_j, Z_j, j = 1, \ldots, 79$) in the reference coordinate system of the robot (Fig. 2). To determine the optimal movement of the robot in the operational space of the task, the block diagram shown in Figs. 4 and 5. The ANN (Fig. 5) was previously trained by use of a separate set of 1000 points. A three-layer neural network was used with *three* input variables, *two* output variables and $n_1 = 12$ and $n_2 = 9$ neurons in the hidden layers of the network. For network convergence, the Levenberg–Marquardt backpropagation convergence algorithm from Matlab, Neural Networks Toolbox was implemented.

The ANN (Fig. 5) was previously trained by use of a separate set of 1000 points. A three-layer neural network was used with *three* input variables, *two* output variables and $n_1 = 12$ and $n_2 = 9$ neurons in the hidden layers of the network. For network convergence, the Levenberg–Marquardt backpropagation convergence algorithm from Matlab, Neural Networks Toolbox was implemented.

In order to verify the effectiveness of the proposed path planning methodology, the following motion planning methods were considered: 1) selection of the closest point–neighbor (starting from the zero position of the robot), 2) multi-criteria knowledge-based path optimization proposed in this paper, 3) selection of points

Table 1 Overview of the quantitative indicators of path planning by use different methods

	T_{path}(sec)	E_{path}(Wh)	L_{path}(m)	χ
Method 1	575.69	23.32	178.16	0.2800
Method 2	535.57	21.43	178.16	0.3128
Method 3	551.44	23.62	209.30	0.2872
Method 4	582.08	23.26	178.45	0.2783

in order by species moving in the direction of the Y-axis and going down in the direction of the negative Z-axis, and 4) selecting the points in a re-sequence starting from the closest and moving to the farthest in the X-direction of the robot (Fig. 2). Quantitative indicators of the optimality of path selection are presented in Table 1.

By analysis results shown in Table 1, it can be seen that the indicators do not differ significantly between the selected examples of movement planning methods. It was confirmed that with the application of the Method 2, which is based on AI algorithms, the best results are achieved i.e. the shortest path time T_{path}, the shortest path of the robot gripper L_{path}, the smallest energy consumption E_{path} for the movement of the robot, and finally the highest average value of the performance index χ. If know that the tests for the verification of the path planning method of the robot gripper were done at a time interval of *500–600 s*, then it can be concluded that for 12 h of the continuous operation, the savings in time and energy can be evident.

We have acknowledged the limitations of our system in maneuvering around obstacles and harvesting crops in dense or obstructed areas. To mitigate these challenges, we have proposed enhancements to our algorithm, including advanced obstacle detection and avoidance strategies, as well as improved adaptability to dynamic environmental conditions. These improvements aim to make our solution more robust and versatile for real-world application. We have implemented statistical analysis techniques to quantify the performance of our AI system objectively. This includes measures such as mean absolute error, root mean square error, and correlation coefficients to assess the accuracy and reliability of our system's predictions and outputs. Additionally, we have incorporated error metrics to evaluate the discrepancies between predicted and actual outcomes, providing insights into the system's performance under various conditions. By analyzing these errors, we can identify potential sources of inaccuracies and refine our algorithm accordingly.

7 Conclusion

The paper presents a knowledge-based method of path planning of a robot for picking fruit from trees, using AI algorithms. A multi-layered ANN was used as an identifier of the robot model and a supplementary fuzzy classifier for determining the performance index of movement optimality, whose rules contain the evaluation criteria. Expectations were confirmed that the applied AI algorithms improve the efficiency of the robot picker in terms of achieving optimal paths in the operational task space. We have conducted a comprehensive analysis of potential limitations associated with our proposed AI system and its implementation in real-world agricultural environments. This includes considerations such as computational complexity, robustness to environmental variability and generalizability across different crop types and farming practices. Also, we have explored possible improvements and future research directions to overcome these limitations and enhance the effectiveness of our system. This involves discussing advancements in AI algorithms, sensor technologies, and robotics hardware that could be leveraged to improve the performance and adaptability of our system in diverse agricultural settings.

Acknowledgements This work is the result of research and development carried out as extension of the project “Development of a demonstration prototype of a manipulative robot for picking edible plums–proof of concept", contract no. 623-1-22, innovation voucher no. 1216 co-financed by the Innovation Fund of the Republic of Serbia, 2022.

References

1. Stevanović, I., Ilić, U., Rodić, A.: Prototyping of Robot Harvester for Plum Farmyards—Mechanical Design. Mechanisms and Machine Science, 2023. https://doi.org/10.1007/978-3-031-32606-6_55. EID: 2-s2.0–85163373564. ISSN: 22110992 22110984
2. Šumarac, J., Kljajić, J., Rodić, A.: Fruit Detection Algorithm for a Plum Harvesting Robot Based on Improved YOLOv7, Mechanisms and Machine Science, 2023. EID: 2-s2.0–85163280254, ISSN: 22110992 22110984. https://doi.org/10.1007/978-3-031-32606-6_52
3. Li, Y., Ma, S., Ding, Z., Li, L., Xin, Y., Su, C.: Path Planning of a Robotic Manipulator for Pruning Apple Trees based on RRT-Connect Algorithm. American Society of Agricultural and Biological Engineers (2022). https://doi.org/10.13031/aim.202200750
4. Cai, J., Wang, F., Lu, Q., Wang, J.: Real-time path planning for citrus picking robot based on SBL_PRM. Trans. Chin. Soc. Agric. Eng. **25**(6), 158–162 (2009)
5. Cao, X., Zou, X., Jia, C., Chen, M., Zeng, Z.: RRT-based path planning for an intelligent litchi-picking manipulator. Comput. Electron. Agric. **156**, 105–118 (2019). https://doi.org/10.1016/j.compag.2018.10.031
6. Chen, Y., Fu, Y., Zhang, B., Fu, W., Shen, C.: Path planning of the fruit tree pruning manipulator based on improved RRT-Connect algorithm. Int. J. Agric. Biol. Eng. **15**, 177–188 (2022)
7. Lin, G., Zhu, L., Li, J., Zou, X., Tang, Y.: Collision-free path planning for a guava-harvesting robot based on recurrent deep reinforcement learning. Comput. Electron. Agric. **188**, 106350 (2021). https://doi.org/10.1016/j.compag.2021.106350
8. Liu, C., Feng, Q., Tang, Z., Wang, X., Geng, J., Lijia, X.: Motion planning of the citrus-picking manipulator based on the TO-RRT algorithm. Agriculture **12**(5), 581 (2022). https://doi.org/10.3390/agriculture12050581
9. Noreen, I., Khan, A., Habib, Z.: Optimal path planning using RRT* based approaches: a survey and future directions. Int. J. Adv. Comput. Sci. Appl. **7**(11) (2016)
10. Zahid, A., He, L., Choi, D. D., Schupp, J., Heinemann, P.: Collision free path planning of a robotic manipulator for pruning apple trees. In: Paper presented at 2020 ASABE Annual International Meeting Virtual Online (2020). https://doi.org/10.13031/aim.202000439
11. Gang, L., Wang, J.: PRM path planning optimization algorithm research. WSEAS Trans. Syst. Control **11**, 81–86 (2016)

12. Ji, W., Li, J., Zhao, D.A., Jun, Y.: Obstacle avoidance path planning for harvesting robot manipulator based maklink graph and improved ant colony algorithm. Appl. Mech. Mater. **530**, 1063–1067 (2014). https://doi.org/10.4028/www.scientific.net/AMM.530-531.1063
13. Kurtser, P., Edan, Y.: Planning the sequence of tasks for harvesting robots. Robot. Auton. Syst. **131**, 103591 (2020). https://doi.org/10.1016/j.robot.2020.103591
14. Liu, D.W.: Hierarchial optimal path planning (HOPP) for robotic apple harvesting. Int. J. Health Sci. Res. (2022)

Design of a Data Collection System for Robot Digital Twins

Lenţoiu Ionuţ, Borangiu Theodor, and Răileanu Silviu

Abstract The paper presents a software architecture designed for data gathering in robot digital twins (DT). This system acquires information and data from the industrial robot, the automated process performed by the robot, and the devices linked to the robot (such as conveyor belt, ASRS, and smart meters). The data retrieval is facilitated by an edge processing framework that includes the robot controller and IoT gateways. The software system comprises a data acquisition agent that is directly linked to the edge processing hardware, a local database for storing the acquired information, and a user interface that offers various data display possibilities. The DT software is designed to collect robot data in two modes: continually from the robot controller and the IoT gateways using specialized software tools provided by the robot manufacturer, and discretely from special program instructions through messages. Experiments with the DT data collection system are conducted for ABB IRC5 industrial robot controllers.

Keywords Industrial robot · Digital twin · Data acquisition · Edge processing

L. Ionuţ · B. Theodor · R. Silviu (✉)
Department of Automation and Applied Informatics, University Politehnica of Bucharest, Bucureşti, Romania
e-mail: silviu.raileanu@upb.ro

L. Ionuţ
e-mail: ionut.lentoiu@upb.ro

B. Theodor
e-mail: theodor.borangiu@upb.ro

B. Theodor
Academy of Romanian Scientists, Bucureşti, Romania

D. Pisla et al. (eds.), *Advances in Service and Industrial Robotics*, Mechanisms and Machine Science 157, https://doi.org/10.1007/978-3-031-59257-7_46

1 Introduction

The Factory of the Future (FoF) initiative involves the integration of digital technology into manufacturing processes and the interconnectedness of shop floor devices, systems, and services through digital counterparts in Cyber Physical Systems (CPS) frameworks [1, 2]. This integration also extends vertically to the fully automated enterprise layers [3, 4]. Process and resource data collection for real-time processing are crucial in CPS. They involve acquiring data, aggregating information from various sources, storing and analyzing data in the cloud. These processes enable monitoring the status of the equipment, detecting unexpected events, predicting failures, customizing maintenance, optimizing operations scheduling, and assigning resources. They also facilitate process supervision and control, as well as simulation with preconfigured device layout during the design stage of industrial robots integrated in production structures. The monitoring, control, supervision, and design functions are carried out on a global scale, encompassing the aggregated context of devices, processes, and workplaces, with the assistance of digital twin technologies [5].

The general digital twin construct comprises three elements: (a) a physical device part of the material world; (b) a software entity existing in the virtual space; (c) a set of connections between the physical and virtual systems [6]. In the industrial domain, a digital twin (DT) is an electronic version of a specific production device (e.g., a robot or end-effector) or a group of devices (such as a team of robots). The DT can operate in various software environments to coordinate both virtual and real systems using sensor data. This coordination is achieved through the application of physics models, mathematical algorithms, and data transformations. From the perspective of reality modelling, two categories of decision trees are defined: (i) A *data-driven* digital twin is a type of DT that collects data from the robot and its partner devices, i.e., conveyor belt, other robots; it is synchronized with the physical twin which is the actual robot system; (ii) A *model-driven* digital twin is a type of DT that does not have a physical component. It is a virtual model of the robot and its controller (a software system) hat can be used for layout validation, application design, and parameter adaptation [7].

The utilization of the digital twin technology offers several benefits: (a) perceptibility: DTs provide information about the execution of operations by individual robots and interconnected members of robot teams, such as collaborative welding robots [8]; (b) prediction: using modelling techniques, DTs can forecast future states, behaviours or parameter evolutions, such as robot energy consumption; (c) interaction with the physical twin: DTs can be integrated in the robot control systems to track and correct motion, detect unexpected events, and make ad hoc protecting decisions [9–11]; (d) analysis: DTs activate triggering procedures to clarify and provide details about changes in states and performances of robots for health monitoring and maintenance.

The current paper is organized in the following manner: Sect. 2 outlines the structure of the robot DT. Section 3 details the DT data stream collection layer, which serves as a software system within the edge computing framework of the industrial robot. Section 4 presents the experimental results obtained from an ABB robot type using the proposed edge computing DT layer. The last section offers conclusions and defines future research directions.

2 Aggregated Digital Twin Architecture

The proposed robot monitoring architecture is composed of an aggregation of digital twin instances, each of them being associated with a component of the robot system. It is also possible to query information about robot teams shared by large production applications by aggregating these individual robot DT instances.

This section of the article details how data-driven DTs of industrial robots instances are organised, designed, implemented, and used for monitoring, preventive maintenance, supervision, and optimization of task allocation for manufacturing infrastructures containing industrial robots. These individual DT instances are scalable and can be software configured to meet production needs. They collect data from internal robot sensors and encoders, and specific robot operating systems to establish bidirectional connectivity between the physical resource and its informational counterpart. This process sustains intelligent decision making for: proper operating of the motion controller, authorizing execution of motions, optimized trajectory generation, stopping robot motions and reconfiguring work parameters (speed limitations, acceleration, arm configuration), gripper and tool change.

The aggregated data-driven digital model of an industrial robot is updated with information gathered from the physical and environmental space. To detect functional abnormalities, assign tasks and determine whether predictive maintenance is necessary, the DT saves data related to operating cost, performance, and status in the cloud.

As seen in Fig. 1, the data-driven DT architecture designed to monitor and control the energy consumption, and maintain proper operating of an industrial robot is organised on four layers that allow bidirectional data flows. Decision-making occurs at the informational layer and is applied to the physical layer.

Layer 1: Data collection, aggregation, and local processing employs smart power meters that use Wi-Fi to track energy consumption (EC). The collected data is first sent to a local database for logical alignment, time synchronisation and reduction and then to the cloud; data from smart sensors (e.g., housing vibrations, temperature, gripper contact effort) is added as working context information. Layer 1 also monitors the robot controller and operating system parameters and variables including supply voltages for hardware components, number of engine-level errors detected, joints values, executed instructions and speed profile data of trajectories.

Layer 2: Data transmission involves real-time data synchronization between the local database and cloud infrastructure on one side, and hardware devices, operating systems, and manufacturing services, on the other side, all of which are integral

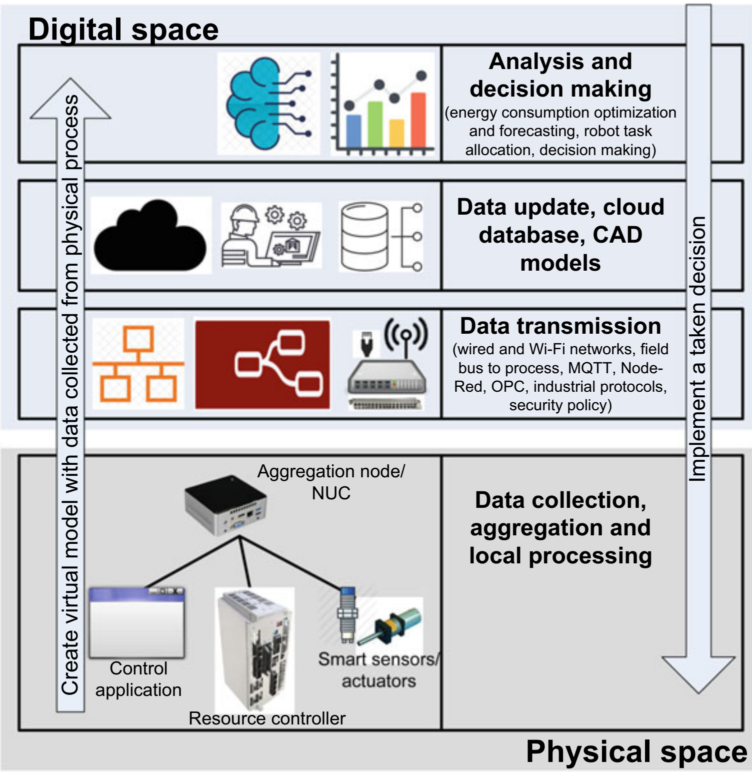

Fig. 1 The 4-layer aggregate data-driven robot digital twin architecture

components of the Internet of Things. Industrial protocols are used with a special focus on data security and low latency/high transmission speed.

Layer 3: Data Update, Cloud Database, CAD models: data aggregation from multiple physical sources, storage of information in structured text and 3D (Computer Aided Design) format.

Layer 4: Analysis and Decision Making use simulation and real-time emulation tools to execute application programs. These software tools are used for various purposes such as validating robot trajectories, tuning parameters, monitoring proper functioning, documenting, and contributing to support of optimized operation allocation on robots included in shop floors with shared resources. The robot- and process-data streams aligned and pre-processed on Layer 1 of the data-driven DT are gathered and combined in the models stored in the cloud database. These models are then used to extract knowledge and make predictions about the performances of the robot, changes in parameters, and the costs associated with their utilization. This knowledge is used to adjust motion parameters of individual robots and, by aggregation, to optimize the concurrent allocation of jobs to shared members of a robot team.

3 DT Software Architecture for Robot Data Collection

The software architecture for robot data collection on DT Layer 1 consists of a set of agents. Figure 2 shows this DT system architecture designed for an *n*-robot team.

These agents are uniquely associated with each robot, having the role of collecting information from two sources (resource controller and embedded systems to which sensors are connected). The information is synchronized (e.g., energy consumption data is aligned with joint movement, movement instructions, trajectories, and speed limits). Data is collected for all active robots in the team and EC models per type of operation/trajectory are created. Also, robot status and process data are collected (operation in execution/finished, operation result, robot working/idle/in stand-by). The data streams are collected in real time, aligned logically and in time (i.e., EC data for a completed operation) and sent to a local database the analysis of proper robot operating (health monitoring) and identification of significant deviations from the normal EC value range (ad-hoc robot protection actions are triggered, e.g., power disabling).

The insights extracted from the aligned and pre-processed robot and process data, minimized trough map-reduce techniques, is transferred to the cloud and combined with historical data to reduce energy consumption, forecast EC at global batch execution horizon, and optimize on demand task allocation to shared robot team members.

From the technical point of view, the communication solution with the cloud database (CDB) representing DT layer 2 can be implemented in two ways: (a) by remote procedures for database update and (b) using a communication protocol (TCP, MQTT, OPC) or flow-based tool (Node-Red) linked with a database updating agent [13].

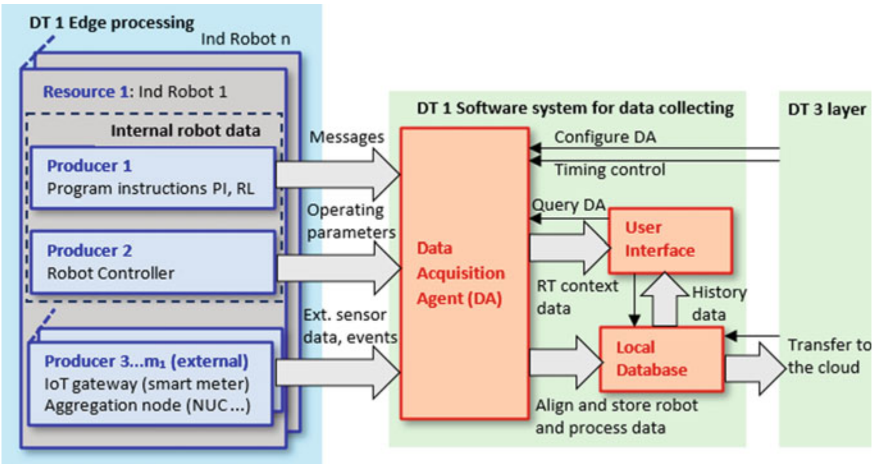

Fig. 2 The software system architecture for edge data collecting and processing in DT layer 1

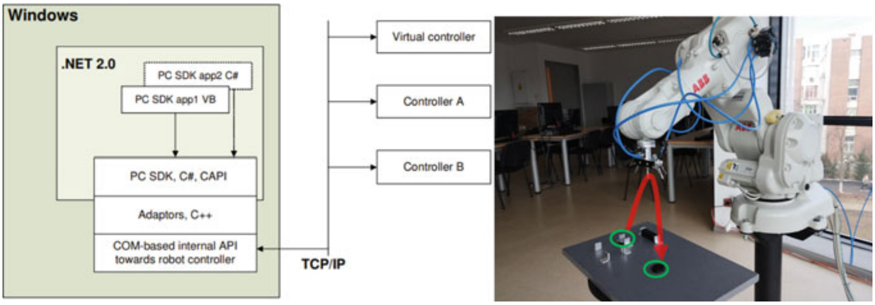

Fig. 3 Software architecture of the ABB PC SDK (ABB Robotics) and the physical system

In the reported research, robot data is directly collected from the IRB ABB industrial robot at time intervals of 0.2 s using the Software Development Kit ABB PC SDK [12]. PC SDK is a software tool that uses Microsoft.NET and Microsoft Visual Studio and allows developing custom user interfaces for IRC5 robot controllers. The advantage of using such a tool is the ability to access and monitor multiple robot systems from a single location A custom interface was realized as independent application that communicates with the *n* robot controllers of a robot team (Fig. 3).

The PC SDK communicates with the industrial robot controller by help of an own Controller API (CAPI) based on the COM technology. This API employs sockets and the local TCP/IP protocol stack to receive and interpret messages from real and virtual controllers. The classes by which the robot controller's functionality can be known constitute the CAPI organised in 11 domains, from which the following are used for robot health and EC monitoring by the digital twin layers DT 1 and DT 3: Controllers, EventLogDomain, IOSystemDomain, MotionDomain, RapidDomain and Messaging. Event log messages are used to extract knowledge about the controller status and the processes that are currently run, and the execution of RAPID programs. The DT can be used with any controller from ABB compatible with PC SDK without a limitation in the number of equipment monitored. To adapt this solution to other robot manufacturers the interface should be implemented.

Data sampling for continuous robot status monitoring has been established at 200 ms for two main reasons: (a) the PC CAPI is unable to ensure hard real-time demands because of the slower network communication rate via TCP/IP and of the robot controller's frequent higher priority tasks (e.g., trajectory generation); (b) the minimum response time for IRC5 robot controllers is in the range of 10–100 ms. Using the Controller API the following data can be collected on the DT 1 layer: status of input/output signals, coordinates of robot points, joint values, information on events, and error messages.

For situations in which this condition is not met, like in the case of IRC5 ABB robot controllers, a solution has been developed that allows simultaneously sending IP information to the data acquisition agent of DT 1 and performing the robot operation. This solution consists in redefining those PI of the robot programming language that are of interest for the DT to generate and send messages to the DA. The PIs redefined

Table 1 Robot motion instructions redefined for message transmission to the DA

Original instruction	New instruction	Description
MoveJ (point, parameters)	DT_MoveJ (point, parameters)	Linear movement in joint space
MoveL (point, parameters)	DT_MoveL (point, parameters)	Linear movement in Cartesian space
WaitTime (time)	DT_WaitTime (time)	Delay

in Table 1 first send information about the instruction type, prescribed parameters (e.g., desired joint values and estimated execution time, then execute the respective instruction, and send again information concerning the execution of the instruction at PI completion (joint displacements and execution time).

Other PIs of interest for DT Layer 1 concern visual inspection of the scene foreground, object recognition and locating, visual measurements and robot calibration.

4 Experimental Results

The software implementation for robot data collection on DT Layer 1 was tested on an ABB IRB 140 6-d.o.f. vertical articulated industrial robot. The test trajectory consists of a repetitive part handling for a 1D vertical stack as presented in Fig. 3.

Using functions of the CAPI PC SDK 5.13 class library motion domain objController.MotionSystem.ActiveMechanicalUnit.GetPosition(), the set of joint values are saved in a C# agent. The values are stored as JointTarget types, and they represent the working parameters of interest.

Using the software designed for the DT layer 1, the following data sets have been acquired and plotted on the same graph: instantaneous power (Fig. 4, orange series, measured in Watt), trajectories (Fig. 4, light blue and green zones representing handling sequences (HS) for five objects in the vertical stack), and joints values (Fig. 4, light green, dark green, purple, and three shades of blue series representing the 6 revolute joints of the articulated vertical robot–measured in degrees). Figure 4 exemplifies a handling sequence of five objects organized in a 1-dimensional vertical stack by repeated pick and place procedures).

This real-time variation of the six robot joint displacements characterizes the robot operation and can be related to its working parameters (programmed speed and acceleration, number of motion cycles, load, cumulated work time, release of the mechanical brake and activation of the motors), status (wear, time elapsed from the last effected maintenance), and environment. The DT stores the evolution of joint values tagged with these EC characteristics as a digital signature, compares it to past EC patterns to monitor the robot health, adjust motion parameters at EC increase, customize maintenance, stop the robot at EC peak or predict ECs of robot team members to weigh correspondingly their participation in batch processes for global EC optimization.

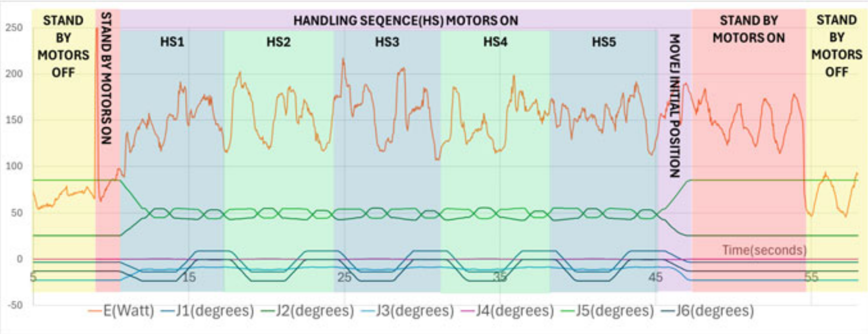

Fig. 4 Instantaneous power correlated with joint movements, instruction types and trajectories

5 Conclusions

A software solution for robot digital twin data collection is described in this paper. The designed system uses an edge processing platform that includes the robot controller and IoT gateways to access data from the robot, the served process and the working environment. A smart meter measures the energy consumed by the robot in different operations. The software system of the robot DT data acquisition layer is composed of a data acquisition agent directly coupled to the edge processing hardware, a local database, and a user interface with several data display options.

The DT data collection software monitors the robot and retrieves real-time data describing its operating mode, parameters, and performance. This data will be used in further developments to identify industrial robot operating patterns, and comparatively analyse them with historical data stored in the cloud to help optimize motion trajectories (avoid jerks and collisions, keep the imposed speed profile, minimize time and energy consumption) and production processes (reduce product operation cycles, optimize batch execution time).

Future research will focus on the usage of AI/ML to detect usage models and to predict energy consumption. The authors will focus on the monitoring and analysis of the pick and place process to optimize the energy consumption and robot movements. In addition, we plan to extend the data collection to several robots and long periods of time.

Acknowledgements This work was supported by a grant from the National Program for Research of the National Association of Technical Universities–GNAC ARUT 2023.

References

1. Peres, R.S., Rocha, A.D., Leitão, P., Barata, J.: IDARTS–towards intelligent data analysis and real-time supervision for industry 4.0. Comput. Ind. **101**, 138–146 (2018). https://doi.org/10.1016/j.compind.2018.07.004
2. Redelinghuys, A.J.H., Kruger, K., Basson, A.H.: A six-layer architecture for digital twins with aggregation. In: Proceedings SOHOMA'18, Studies in Computational Intelligence, Vol. 803. Chapter 32, pp. 412–423. Springer (2019)
3. Soldatos, J., Cavadini, F.A., Lazaro, O.: The digital shopfloor: industrial automation in the industry 4.0 era, river publishers series in automation, control and robotics, https://doi.org/10.13052/rp-9788770220408 (2020)
4. Kritzinger, W., Karner, M., Traar, G., Henjes, J., Sihn, W.: Digital twin in manufacturing: a categorical literature review and classification, IFAC-PapersOnLine. **51**(11), 1016–1022. Elsevier (2018). https://doi.org/10.1016/j.ifacol.2018.08.474
5. Negri, E., Fumagalli, L., Macchi, M.: A review of the roles of digital twin in CPS-based production systems, Procedia Manuf. **11**, 939–948. ScienceDirect (2017). https://doi.org/10.1016/j.promfg.2017.07.198
6. Grieves, M., Vickers, J.: Digital twin: mitigating unpredictable, undesirable emergent behavior in complex systems. In: Transdisciplinary Perspectives on Complex Systems, pp. 85–113. Springer (2017). https://doi.org/10.1007/978-3-319-38756-7_4
7. Stan, M., Borangiu, T., Răileanu, S., Data-and model-driven digital twins for design and logistics control of product distribution, In: Proceedings of 23rd International Conference on Control Systems and Computer Science (CSCS), pp. 33–40 (2021). IEEE Catalog no. CFP2172U-ART. https://doi.org/10.1109/CSCS52396.2021.00013
8. Melesse, T.Y., Di Pasquale, V., Riemma, S.: Digital twin models in industrial operations: a systematic literature review. Procedia Manuf. **42**, 267–272 (2020)
9. Da Cunha, C., Cardin, O., Gallot, G., Viaud, J.: Designing the digital twins of reconfigurable manufacturing systems: application on a smart factory. IFAC-PapersOnLine. **54**(1), 874–879 (2021). https://doi.org/10.1016/j.ifacol.2021.08.103
10. Gloria, A., Cercasa, F., Souto, N.: Design and implementation of an IoT gateway to create smart environments, In: Proceedings of the 8th International Conference on Ambient Systems, Networks and Technologies ANT'17 (2017). https://doi.org/10.1016/j.procs.2017.05.343
11. Anton, F., Borangiu, T., Răileanu, S., Anton, S.: Cloud-based digital twin for robot integration in intelligent manufacturing systems, advances in service and industrial robotics. In: Proceedngs of RAAD 2020, Mechanisms and Machine Science, vol. 84, pp. 565–573. Springer, Cham (2020). https://doi.org/10.1007/978-3-030-48989-2_60
12. ABB Robotics. Application manual PC SDK. RobotWare 5.14, ID: 3HAC036957–001. https://library.e.abb.com/public/124d6b59313ed85fc125793400410c5b/3HAC036957-en.pdf. ABB AB. Accessed 12 05 2023
13. Note-RED. Note-RED Documentation. https://nodered.org/docs/. (2023). Accessed 6 01 2024

Physical Interaction Interpretation in Industrial Robotics Using Dynamic Time Warping Principles

Zaviša Gordić and Kosta Jovanović

Abstract This paper presents an approach to interpretation of the context of physical interaction of a robot with its surroundings using principles of Dynamic Time Warping (DTW). Forces originating from physical interaction reflect their influence on robot joints through the measurements of robot joint currents, which deviate from their values without interaction. Contextual information is annotated to a representative example of deviations and used as reference value for the contact task-induced signal deviations. Context of ongoing task executions obtained by comparing recent measurements of deviations and comparing them with the most similar section of their reference values using modifications of the original DTW algorithm. The analysis is based on previously recorded experimental measurements of robot joint currents while performing different types of contact tasks including assembly and load manipulation tasks. Results are discussed in terms of their reliability, accuracy and additional signals or rules needed to interpret them correctly.

Keywords Industry 4.0 · Dynamic time warping · Context extraction and interpretation · Industrial robot

1 Introduction

The interconnected and event-driven environment of Industry 4.0 offers numerous advantages compared to traditional production environments, most notably in domain of resource use optimization, efficiency, agility, and related resilience to planned and unplanned changes. These advantages are achieved through interconnection of production entities with each other and with various sorts of production monitoring, planning and optimization software solutions. Industrial robots, as some of the most agile and universal hardware components in the production environment, are used for different types of manipulation, processing, assembly, and inspection tasks. They

Z. Gordić (✉) · K. Jovanović
School of Electrical Engineering, ETF Robotics Laboratory, University of Belgrade, 11000 Belgrade, Serbia
e-mail: zavisa@etf.rs

D. Pisla et al. (eds.), *Advances in Service and Industrial Robotics*, Mechanisms and Machine Science 157, https://doi.org/10.1007/978-3-031-59257-7_47

are, and will continue to be, the backbone of industrial automation in the foreseeable future, thanks not only to the sheer number of integrated units [1] but also to their performance and reliability. In general, synchronization and integration capabilities of industrial robots enable them to successfully exchange information with the remaining production entities, which was adequate for the needs of Industry 3.0 environments. However, there are two main preconditions for their full integration in Industry 4.0 environment.

The first, and most important aspect is safety in collaborative setting with human workers. This topic has been the subject of numerous research [2–10], in which many approaches have been proposed and elaborated. Without a doubt, regardless of the type or topology [3] of physical interaction with workers, the safety aspect deserves the attention it has, since the consequences for humans can be drastic [11, 12]. However, this paper will focus on the other, somewhat related, yet often overlooked aspect that limits their potential for complete integration, is the type and content of the provided information about the ongoing interaction with surroundings.

In an environment in which context of events dictates the behaviour of other production entities, and is responsible for their optimal use, industrial robots have to do their part. It is not difficult to implement some pre-determined exchange of information of the robot with other production resources for all envisioned scenarios. To some extent, the context of operation can be obtained from the coded actions/ functions that a robot uses during a its task, which is always very useful to know. However, observation and interpretation of interaction forces effects on the robot can provide more details about the properties and the quality of the action being performed. For example, the analysis of interaction forces can indicate whether a particular load has the expected weight distribution, was it successfully carried to its destination in its entirety, was the subject of interaction placed accurately on the predetermined position, whether there were some unexpected forces during the assembly which was presumed successful. All deviations outside tolerances from expected forces may indicate that additional action is needed, which is particularly useful in automated and unsupervised environments. In Industry 4.0 context, it can trigger predetermined event-driven actions to mitigate propagation of faults and erroneous states and/or enable informed human intervention.

Research in the field of interaction interpretation and context provision was mainly focused on the domain of human–robot interaction [13–16], particularly in service and medical robots. For production and industrial scenarios, most research is directed towards collision detection and physical human–robot interaction (pHRI). However, production environments featuring shared workspace and collaboration of humans and robots often only require presence and interaction with humans for certain phases or tasks. Hence, interactions with humans are only a fraction of all robot interactions during a production cycle, and although interpretation of pHRI is crucially important from the safety standpoint, interpretation of other robot interactions should not be overlooked.

This paper will present and discuss an approach to interaction forces interpretation based on modifications of Dynamic Time Warping (DTW) algorithm [9, 10]. The approach relies on the analysis of interaction-induced effects on joint current/torque measurements which are available on industrial robots without additional sensors, but the principles are also applicable to measurements from force/torque sensors.

The second section aims to explain the principle behind the presented interaction interpretation, the algorithms used and the requirements for implementation.

The third section presents application of the described principles on measurements experimentally obtained from an industrial robot performing different types of contact tasks along with their discussion and analysis of additional sources of information.

Conclusions are summarized in the fourth section, analysing advantages and disadvantages of the presented approach as well as possible directions of future research.

2 The Principle of Interaction Interpretation

The approach presented in this paper relies on the fact that a typical task assigned to an industrial robot is repetitive in nature, although it may not always repeat in identical cycles. The forces which occur during physical interaction of the robot with its surroundings while executing the observed contact tasks affect the current measurements or torque estimates within the robot joints. These influences manifest themselves as deviations of joint currents/torques from their respective values originating from the robot movement itself. A representative measurement of the force-induced deviation can therefore be recorded and used as a reference sequence to compare future deviations originating from the contact task itself, as presented in [9, 10].

To understand which phase of the contact task execution robot is currently performing, the approach presented in this paper relies on previously developed modifications of the original Dynamic Time Warping algorithm which enable flexible and optimal matching of time series sequences. The first modification [9], mDTW enables one signal to be compared to the most similar section of the second, reference signal, in real-time, which is applicable in cases when the robot task repeats in identical cycles. The KA-mDTW algorithm [10] considers the kinematic parameters of the robot to extend the field of application, enabling optimal matching with spatial joint positions and orientations different to the reference ones. The signal compared with the aforementioned reference sequence using previously mentioned algorithms is called measurement vector. Measurement vector consists of adequately chosen number of successive samples of measurements of each of the joint currents/torques with first-in-first-out logic. Comparing it using mDTW or KA-mDTW with the reference sequence results in the section of the reference sequence which is most similar to it.

One idea which can be used to interpret the operation is that each task consists of certain number of phases, and that each phase can be assigned a value or some other type of descriptor which would help interpret the task execution context, as illustrated on Fig. 1. In the context of implementation, each phase would correspond to certain

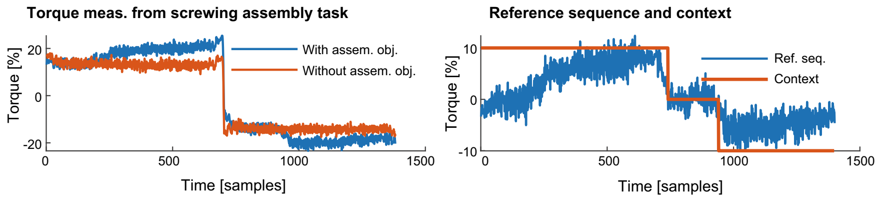

Fig. 1 Assembly by screwing task. (left) Joint torque measurements from the 6th axis with and without the assembly object. Difference between these two signals gives the contact task-induced deviation used as reference sequ. (right) Reference shown in blue and the associated context information representing task execution phase shown in red with $\times$ 10 scaled descriptor values belonging to screwing (descr. val. 1), pause (descr. val. 0) and unscrewing (descr. val. -1) phase

number of samples of deviation induced by the contact task external forces. Hence, each sample of the reference sequence can have not only a numerical measured current/torque deviation value, but also a descriptor indicating to which phase of the task execution it belongs. Depending on the task complexity and/or the level of detail required for optimal context interpretation, the granularity of the descriptors may vary.

During operation, the information about the current task execution context is extracted from the measurement vector received from the robot. As explained earlier, each of the samples from the matched section of the reference sequence has a descriptor assigned to it. The most recent value of the measurement vector is paired with the last sample of the matched section of reference sequence and hence the descriptor assigned to it should indicate the phase of task the robot is currently at. Once the descriptors are obtained, various rules and operations can be applied to the measurement vector values to further interpret them. For example. Depending on the execution phase, or values from the measurement vector, it is possible to check if the task is being properly executed by observing maximum or cumulative matching error peak values etc.

Rather than a complete solution, the presented principle should therefore be primarily observed as a tool which enables correct matching of signals and opens possibilities for their interpretation. Application examples with interpretation and possible implications to the operation of robot and/or other production entities will be discussed next.

3 Results and Discussion

This section presents examples which illustrate potential implementation of the proposed approach using experimentally obtained measurements. Measurements were performed in 2 cycles in which the robot performed identical movement. In the first cycle of measurements the movement was performed without the actual load or assembly object, and measurements from this cycle include all the dynamics of the robot, except for the dynamics of the contact task itself. The second cycle of measurements was performed with the actual load and the assembly object, and they include the dynamics of the contact task itself. The difference between these two cycles of measurement provides deviations which are caused by the forces originating from the contact task itself. For the simulation purposes, a representative deviation comprising all task phases is used as a reference sequence and is assigned context. Different, shorter portions of deviation are used as the measurement vector, and together with reference sequence are the inputs to the DTW algorithm modifications described previously. In real applications, deviations can be obtained as differences between model-predicted values of the system and the actual measurement or as measurements from force-torque sensors.

The first example to be analysed is related to assembly/disassembly by screwing/ unscrewing. Robot's 6th axis was used to perform the rotation movement needed to screw the nut onto a protruding bolt with preplaced helical spring washer and tighten it. The inverse action needed to perform the disassembly was performed after a brief pause.

Figure 1 on the left part shows 6th axis joint torque estimates recorded while these actions were performed with the presence of the actual assembly object, and without. The right part of the image shows the difference between the two cycles of measurement, which is the actual input to the mDTW algorithm. The measurement from the right graph reflects all phases of the screwing/unscrewing motion and is selected to be used as the reference sequence. The red line on the same graph represents the context information assigned to the reference sequence with descriptor values for the 3 main phases on the task: 1 for the assembly, 0 for the pause, and -1 for the disassembly phase.

Figure 2 shows the first example of mDTW used to perform the signals matching and context interpretation. The upper left section shows the signal from which the section, shown in red, was extracted and used as measurement vector for the purposes of the illustration. The upper middle part of the Fig. 2 shows how these signals were matched and the matching error. The upper right graph shows the reference sequence along with the assigned context information, and the section of the reference sequence correctly matched with the measurement vector, resulting in correct context identification.

Similar to graphs on the upper row of Fig. 2, results shown on the lower row show optimally matched measurement vector with most similar section of the reference sequence and correct interpretation of the current task phase. The identified section belongs to the unscrewing phase, and the last matched sample clearly aligns with the context value of -1. It is also possible to notice that some of the samples which belonged to the simulated measurement vector belonged to the pause phase, with context value 0, which was also correctly identified on the matched section of the reference sequence.

The second example of assembly task is the snap fit assembly. Similar to the screwing example, 2 cycles of measurements were performed with and without the actual assembly object. This particular assembly object had 2 levels of latches, which is indicated by the 2 prominent peaks on the left section of Fig. 3. The middle graph

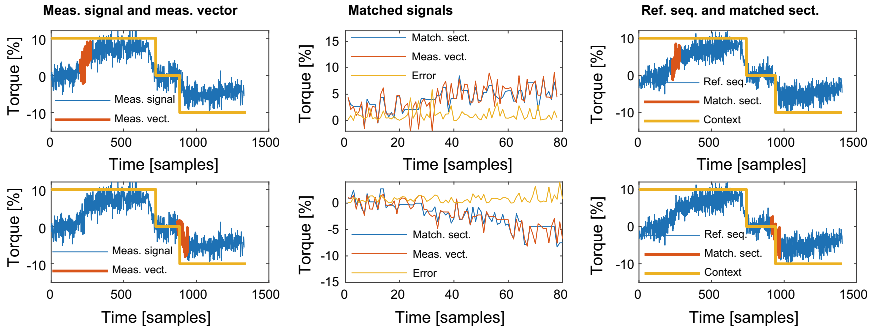

Fig. 2 Two examples of the screwing assembly task context interpretation. (upper row) Example 1. (lower row) Example 2. (left column) Segments of the recorded deviation signal, shown in red were used as the measurement vector and their associated context. (middle column) Matching of the meas. vect. with most similar section of the ref. seq. and the matching error. (right column) Correctly identified section of the meas. seq. indicating correctly interpreted context

of the same figure shows the reference, the deviation caused by the assembly task itself along with annotated context information—0 for the phases prior to and after the assembly phase, value 1 for the first latch and number 2 for the second latch activation. The right section illustrates how positioning inaccuracies of less than 2 mm cause slight deviations in peak values and shapes for both latches, important for the context interpretation.

Figure 4 on the upper left graph shows section of one of the deviation signals which was used as a measurement vector. The upper middle graph shows how it was matched with the most similar section of the reference sequence, and the sample-wise error signal without prominent peaks, indicating good match. The upper right section shows that the section was indeed correctly identified and that the resulting context information will also be correctly interpreted as belonging to the 2nd latch activation phase.

Figure 4 also shows another example from the same task, but from a different execution cycle, in which the assembly object was not placed accurately. As on the

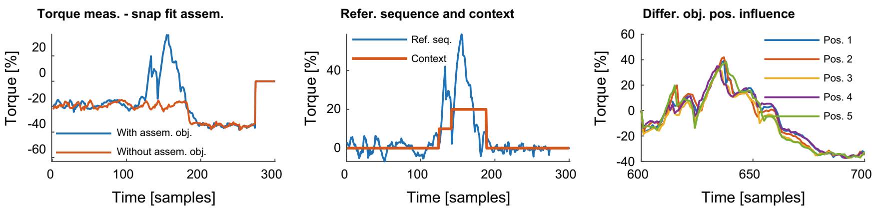

Fig. 3 Snap fit assembly task. (left) Joint torque measurements from the 2nd axis with and without the assembly object. (middle) Deviation induced by the task itself shown in blue and the scaled ($\times$ 10) associated context information representing task execution phase shown in red. (right) Small positioning inaccuracies lead to differences in peak values

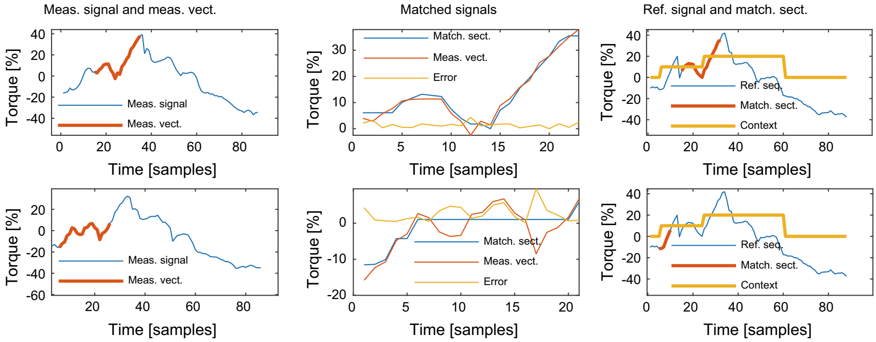

Fig. 4 Interpretation of phases of the snap fit assembly task in 2 examples. (upper row) Example 1 with correct interpretation. (lower row) Example 2 indicates that matching was not done properly. (left column) Segments of deviation signal, shown in red, used as the measurement vector and the associated context. (middle column) Matching of the meas. vect. with most similar section of the ref. seq. and the matching error. Upper graph shows correct matching and corresponding small sample-wise error. Lower row shows peak in the matching error, indicating a potential mismatch. (right column) Identified section of the meas. seq. indicating correctly interpreted context in the upper graph. Lower graph shows that the matched section of ref. seq. was not correctly interpreted, and the associated context was not correctly identified

upper row of the figure, the lower left graph shows which section of the deviation signal was used as a measurement vector. It is important to note that the last, most recent sample belongs to the 2nd latch activation phase, while most of the previous samples belong to the 1st latch activation phase. The sample-wise on the lower middle matching error signal shows a peak which indicates that, although the identified section is the one with the smallest matching error, i.e. most similar from the DTW perspective, there are some samples that do not match well. Results on the lower right part of Fig. 4 show which section was identified as the most similar. Comparison with the measurement vector on the upper graph clearly indicates that they do not represent the same span/interval, being wrongly identified as belonging to the very beginning of 1st latch activation phase.

This example shows that, although the mDTW algorithm did manage to find the optimal match from the perspective of error minimization, its direct application would point to a wrong execution phase. However, additional signals, logic and rules can be applied [17, 18] to monitor indicators and make correct context interpretation. There are different approaches to addressing this and similar situations. Depending on the consequences a misinterpretation can have for the particular process, the indicators such as peak or cumulative value of the matching error could be used to signal an unexpected event and react in some predetermined way including stopping the system, discarding the part after task completion, or alerting the human operator. If consequences are not of crucial importance, another response may be to continue with signal matching and observe causality of the matched samples. Leaving certain samples of the reference sequence unmatched by simply skipping them or matching the most recent sample of measurement vector to some of the previously matched samples of reference sequence could also be valid indicators of unexpected system behaviour which need additional interpretation. The implications of erroneous event identification depend on many factors, but can be useful in many scenarios, including quality control, detecting faults of the entity that identified the problem, or some other production entity etc.

In this particular case, the real reason for matching which did not correspond to the real situation was the inaccurate placement of the assembly object, causing smaller peak value of the deviation at the moment of 1st latch activation. A rule can be set that if the peak sample of the 1st latch activation was skipped, the system would indicate that the peak value of the 1st latch activation of current execution cycle was lower tan expected, which would be the correct context interpretation in this particular case.

Previous two examples relied on matching using the mDTW algorithm, which relies only on the values of joint currents or torques. The application of KA-mDTW algorithm, however, requires also joint angle measurements as inputs. Therefore, in case of its application, the reference sequence and measurement vector contain additional angle measurements. The additional information enables KM-mDTW algorithm to match samples in spatial robot joint configurations different to those during which the reference sequence was recorded, enabling matching during execution of similar movements, rather than identical. For context extraction, the angle measurements represent another source of information which can be used to enhance context interpretation.

The first example using KA-mDTW algorithm represents a load manipulation task. Load picking and placing deviations are shown on the upper left graph of Fig. 5. The blue section indicates the section of the deviation measurement, which was chosen as a reference sequence, whereas the red section was chosen to represent the measurement vector. The upper right graph shows the equivalent lever lengths for the observed joint corresponding to the joint current measurements on the upper left graph. These lever lengths are calculated using angle measurements and robot's kinematic model. The lower middle graph shows that with inclusion of equivalent lever length using KA-mDTW, signals become comparable. The lower right graph shows correct identification of the reference sequence section needed for task phase interpretation and context extraction, which was correctly identified to belong the load releasing phase. Same signals without equivalent lever length information would have been matched with relatively small error, but with wrong context, as shown in Fig. 5 lower left graph.

The final example shows another task with snap fit assembly, but with a single latching level. Figure 6 clearly shows the importance of additional information calculated using joint angles. Without it, the reference sequence would not be correctly matched with the measurement vector, and the entire cycle, which was properly executed, would have been interpreted as a fault, as shown on the second graph lower row.

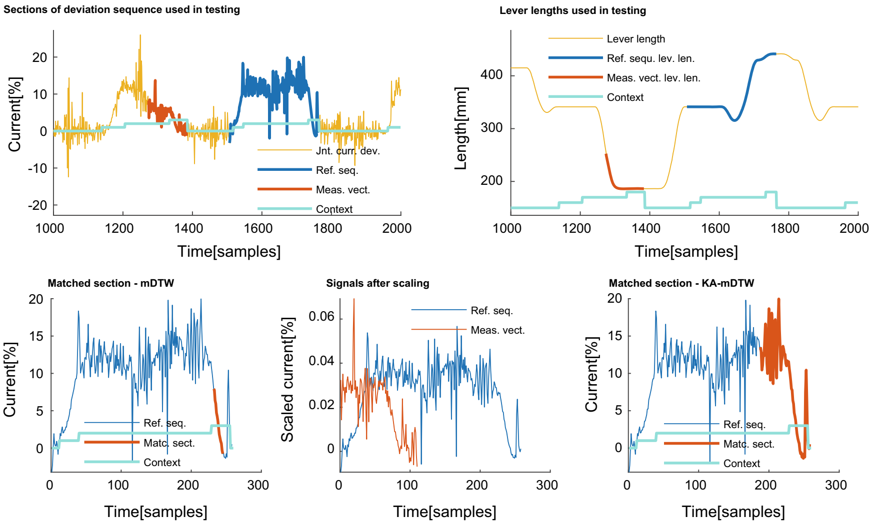

Fig. 5 Load manipulation task interpretation using KA-mDTW. (upper left) Deviation signal with marked sections used as refer. seq, and meas. vect. (upper right) Equivalent lever lengths corresponding to the deviation signal calculated using joint angles. (lower left) Signals matched using mDTW algorithm. (lower middle) Compared signals scaled with additional lever length information. (lower right) Correct KA-mDTW phase identification and context interpretation

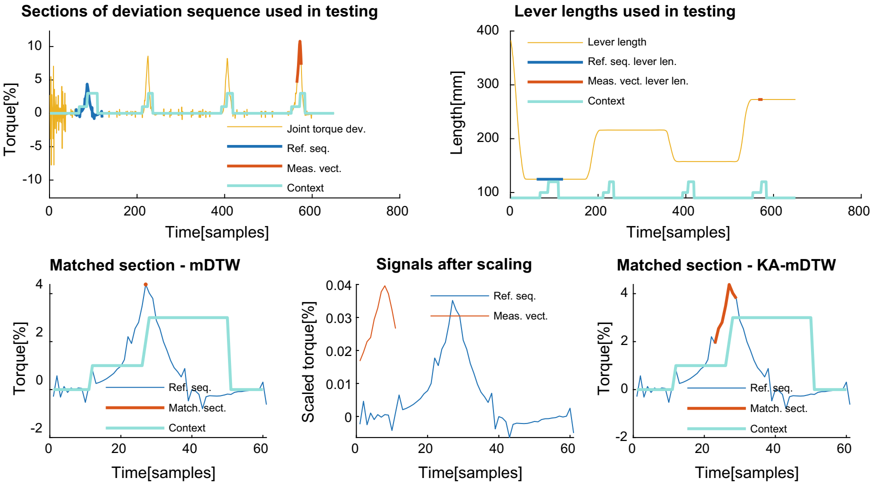

Fig. 6 Snap fit assembly task interpretation using KA-mDTW. (upper left) Deviation signal with marked sections used as refer. seq, and meas. vect. (upper right) Corresponding equiv. lever lengths of the deviation signal. (lower left) Misidentification of the task phase using mDTW without lever lengths as a source of context information. (lower middle) Signals scaled with equiv. lever length values. (lower right) Correct phase identification and context interpretation

4 Conclusion

The presented approach to context interpretation relies on the previously developed algorithms for elastic similarity measurement based on the real time application of Dynamic Time Warping principles. Using DTW modifications, measurement vector from the robot, containing information about the influence of contact forces would be matched with the most similar section of the reference sequence. Context information would be extracted from the section of the reference sequence which is most similar to the measurement vector. The approach was tested on several scenarios using measurements from an industrial robot performing different types of contact tasks. Matching using mDTW and KA-mDTW has shown that the context information can be correctly extracted from the reference sequence in most cases using a relatively simple approach.

The basic premise is that the appropriate similar section will be found, and correctly determined, which may not be the case, as shown in the examples. However, the presented cases are only the beginning of the context extraction since various operations and rules can be applied from the extracted information. Additional signals can be used as well to support correct interpretation and decision making, such as joint angles, different IO signals, or information from other production entities. However, arguably the biggest drawback of the presented approach is that it requires significant inputs about context provision in the setup phase of the reference sequence. Many aspects rely on heuristics, and in general case, expertise human needed for setup. Some level of context information can be extracted automatically from IO signals, or certain commands and annotated to the reference sequence, but this approach also requires certain expertise.

To reduce reliance on external inputs for context interpretation, future work will examine the possibility of application of additional signal matching algorithms, including EDIT distance and LCS (Longest Common Subsequence) in particular, running in parallel to the modifications DTW. Another possibility will be to work on real-time application of feature extraction using [19, 20]. To further facilitate interpretation of the context, Fuzzy logic rule application potential will also be examined, as boundaries between certain task execution phases can sometimes be blurry.

Acknowledgements This research was partially supported by the Science Fund of the Republic of Serbia, Modular and Versatile Collaborative Intelligent Waste Management Robotic System for Circular Economy—CircuBot, under Grant 6784.

References

1. International Federation of Robotics. World robotics 2021—industrial robots. International Federation of Robotics. Frankfurt, Germany (2021)
2. Pedrocchi, N., Vicentini, F., Matteo, M., Tosatti, L.M.: Safe human-robot cooperation in an industrial environment. Int. J. Adv. Robot. Syst. **10**, 27 (2013)

3. De Luca, F., Flacco: Integrated control for pHRI: collision avoidance, detection, reaction and collaboration, In: IEEE RAS and EMBS International Conference on Biomedical Robotics and Biomechatronics—BioRob, pp. 288–295. Roma, Italy (2012)
4. De Luca, A., Mattone, R.: Sensorless robot collision detection and hybrid force/motion control. In: IEEE International Conference on Robotics and Automation—ICRA, pp. 1011–1016. Edmonton, Alberta, Canada (2005)
5. Flacco, A., De Luca, A.: Safe physical human-robot collaboration. In: IEEE/RSJ International Conference on Intelligent Robots and Systems—IROS, p. 2072. Tokyo, Japan (2013)
6. Geravand, M., Flacco, F., De Luca, A.: Human-robot physical interaction and collaboration using an industrial robot with a closed control architecture. In: IEEE International Conference on Robotics and Automation—ICRA, pp. 4000–4007. Karlsruhe, Germany (2013)
7. Mariotti, E., Magrini, E., De Luca, A.: Admittance control for human-robot interaction using an industrial robot equipped with a F/T sensor. In: 2019 International Conference on Robotics and Automation (ICRA), pp. 6130–6136. Montreal, Quebec, Canada (2019)
8. Sharkawy, A.-N., Koustoumpardis, P.N.: Human-robot interaction: a review and analysis on variable admittance control, safety, and perspectives. Machines **10**(7), 591 (2022)
9. Gordić, Z., Jovanović, K.: Collision detection on industrial robots in repetitive tasks using modified dynamic time warping. Robotica, 1–20 (2019)
10. Gordić, Z., Jovanović, K.: A framework for inclusion of unmodelled contact tasks dynamics in industrial robotics. Sensors. **22** (2022)
11. Haddadin, S., Albu-Schäffer, A., Luca, A.D., Hirzinger, G.: Evaluation of collision detection and reaction for a human-friendly robot on biological tissues. In: Proceedings of the IARP International Workshop on Technical Challenges and for Dependable Robots in Human Environments, 18–19 May. Los Angeles, CA, USA (2008)
12. Haddadin, S., Albu-Schäffer, A., Hirzinger, G.: Safety evaluation of physical human-robot interaction via crash-testing. In: Robotics: Science and Systems, MIT Press, pp. 217–224. Cambridge, MA, USA (2007)
13. Zachary, W., Johnson, M., Hoffman, R., Thomas, T., Rosoff, A., Santarelli, T.: A context-based approach to robot-human interaction. Procedia Manuf. **3**, 1052–1059 (2015)
14. Menezes, P., Quintas, J., Dias, J.M.: The role of context information in human-robot interaction (2014)
15. Feng, Y., Perugia, G., Yu, S., et al.: Context-enhanced human-robot interaction: exploring the role of system interactivity and multimodal stimuli on the engagement of people with dementia. Int. J. Soc. Rob. **14**, 807–826 (2022)
16. Zachary, W., Johnson, M., Hoffman, R., Thomas, T., Rosoff, A., Santarelli, T.: A context-based approach to robot-human interaction. Procedia Manuf. **3**, 1052–1059 (2015). https://doi.org/10.1016/j.promfg.2015.07.171
17. Gordić, Z., Jovanović K.: Influence of unmodelled external forces on the quality of collision detection. In: Berns, K., Görges, D. Advances in Service and Industrial Robotics. RAAD 2019. Advances in Intelligent Systems and Computing, vol. 980. Springer, Cham (2020)
18. Gordić, Z., Jovanović, K.: Identifying unmodelled dynamics in contact tasks in industrial robotics, In: Proceedings of the 7th International Conference on Electrical, Electronic and Computing Engineering, IcETRAN 2020, pp. 695–700 Jun (2020)
19. Alaee, S., Kamgar, K., Keogh, E.: Matrix profile XXII: exact discovery of time series motifs under DTW. In: 2020 IEEE International Conference on Data Mining (ICDM), pp. 900–905). IEEE (2020, November)
20. Keogh, E.: Fast similarity search in the presence of longitudinal scaling in time series databases. In: Proceedings Ninth IEEE International Conference on Tools with Artificial Intelligence, pp. 578–584. Newport Beach, CA, USA (1997). https://doi.org/10.1109/TAI.1997.632306

Electromagnetic Simulation of Robotic Dynamic Scenes for Novel Sensor Developments

Vlaho-Josip Štironja, Luka Petrović, Dubravko Tomić, Zvonimir Šipuš, and Ivan Petrović

Abstract To ensure the safety and efficiency of human-robot collaboration, new sensor modalities are required that capture a robot's entire environment and provide a sense of touch. Robotic skins based on either pressure or capacitive sensors provide a sensing range of up to 20 cm and enable the robot to react to contact with its environment. A novel robotic skin with a sensor that utilizes the electromagnetic (EM) properties of flexible metasurfaces could have a sensing range of up to 1 m and enable predictive motion planning and safe robot control. The development of this sensor requires EM simulation of dynamic scenes, which cannot be performed directly with existing simulators. To overcome this challenge, we propose and implement a software bridge between a robotic and a full-wave EM simulator to facilitate the development of novel sensors. We experimentally validated our framework by simulating two dynamic scenes and determining the scattering parameters of skin-mounted antennas that correlate with the distance between the object and the sensor.

1 Introduction

The rapid advancement of robotics has led to an increased presence of robots in both human-centric and industrial environments, giving rise to new challenges related to system efficiency and human safety. To effectively interact with humans, robots require accurate real-time perception of their environment to minimize the risk of collision. Commonly used sensors (e.g., cameras and lidars) offer rich semantic information, but may fall short in completely capturing the surrounding environment due to a restricted field of view or occlusions, and they often operate at a limited frame rate. Consequently, tasks performed by robots are often too slow and too simple, posing an important obstacle to robot utilization in healthcare, agile manufacturing and many other fields. To address these challenges, one potential solution involves equipping robots with novel sensor modalities, such as a flexible sensing skin [1],

V.-J. Štironja · L. Petrović (✉) · D. Tomić · Z. Šipuš · I. Petrović
Faculty of Electrical Engineering and Computing, University of Zagreb, Unska 3, Zagreb, Croatia
e-mail: luka.petrovic@fer.hr

D. Pisla et al. (eds.), *Advances in Service and Industrial Robotics*, Mechanisms and Machine Science 157, https://doi.org/10.1007/978-3-031-59257-7_48

in addition to standard perception sensors. This integration would enhance the overall perception capabilities of robots, mitigating risks and enabling their effective deployment in diverse fields.

Existing stretchable e-skins of pressure sensors [2, 3] are based on piezoelectric, piezo-resistive, conductive and capacitive sensing, and some companies (e.g., Fogale Robotics, Bosch) offer commercial solutions [4]. Yet, pressure-based proximity skins require contact, while capacitive sensors have a sensing range of only up to 20 cm and suffer from low measurement accuracy in the nonlinear detection range. A new sensor modality could exploit the electromagnetic properties of flexible metasurfaces [5, 6] for near-field and far-field sensing based on surface waves and their possible transformation into leaky waves. The measurement of the correlation between transmitted and received signals at all pairs of ports on the skin can be used to monitor the effects of folding the flexible skin and provide measurements of position of objects in the surrounding environment. This topic is an active area of research and is investigated in the scope of the EU Pathfinder Open project *Flexible intelligent near-field sensing skins—FITNESS*.[1]

To develop this sensor and enable its utilization in collaborative robotics, first we need to be able to estimate positions of ports mounted on the skin for each robot configuration. Next, we need to simulate the possibly dynamic EM environment and analyze the obtained scattering parameters (S-parameters) to infer the positions of objects in the environment. This process requires both robotic and full-wave EM simulators. Widely available robotic simulators [7, 8] do not consider object EM properties (e.g., permittivity and permeability) and are not able to simulate EM phenomena. On the other hand, full-wave EM simulators only simulate static scenes and lack the ability to manipulate kinematic chains.

To address these issues, in this paper we propose a simulation framework that features a software bridge between a robotic and a full-wave EM simulator, enabling the EM simulation of dynamic scenes. Our framework relies on a robotics simulator for creating dynamic scenes and reasoning about robot kinematics, while full-wave EM simulator computes the desired S-parameters. The proposed software bridge discretizes the robotic dynamic scene and automatically conducts the EM simulation of the scene at each time instant. We experimentally validated our framework by simulating two dynamic scenes and determining the S-parameters of skin-mounted antennas that correlate with the distance between the object and the sensor. In addition to the novel e-skin development, the proposed simulation framework could be used to develop other novel sensors that are based on the EM phenomena.

2 The Proposed Simulation Framework

Consider a robot arm equipped with a smart skin that has a set of antennas. We want to simulate the S-parameter values for these antennas in order to infer the distance of

[1] https://fitness-pathfinder.eu.

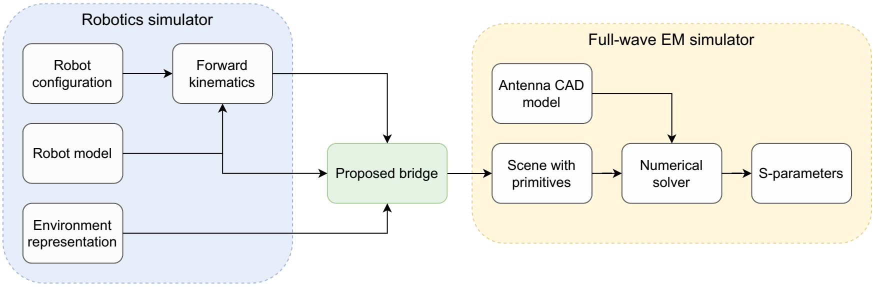

Fig. 1 The architecture of the proposed simulation framework

objects from the skin and, if possible, their position relative to the robot. We want to know the S-parameter values at each point during the robot arm motion. To this end, we propose a simulation framework that leverages existing robotic and full-wave EM simulators. The robotics simulator takes the robot configuration at each discrete time instant of the robot's trajectory and, given the robot model, computes forward kinematics. The proposed software bridge uses geometric primitives (e.g., spheres and cubes) to approximate the environment representation and the robot model at the calculated pose. This scene is passed to the full-wave EM simulator which uses a numerical solver and the antenna CAD model to compute the S-parameters. The architecture of the proposed simulation framework is shown in Fig. 1.

2.1 Robot and Environment Modeling

The robot configuration at a given time instant t_i is defined as a set of joint positions $\mathbf{q}_i$ in the configuration space $\mathbf{q}_i \in \mathcal{Q} \subset \mathbb{R}^n$ which comprises all feasible joint positions, where n is the number of degrees of freedom (DoF). Similarly, the robot's end-effector poses $\mathbf{x}$ form the task space $\mathbf{x} \in \mathcal{X} \subset \mathbb{R}^p$. The robot's forward kinematics function is defined as the following nonlinear mapping

$$\mathbf{f} : \mathcal{Q} \rightarrow \mathcal{X}. \tag{1}$$

The robot's body can be modeled as a set of arbitrary number of points, $\mathcal{B} \in \mathbb{R}^w$, $w \in \mathbb{N}$. Given a robot's configuration $\mathbf{q}_i$, the forward kinematics function can also provide the pose of a point $b \in \mathcal{B}$ of the robot body in Euclidean space.

In practical applications, the set of points $\mathcal{B}$ can be approximated with a set of geometric primitives (e.g., spheres, polyhedra, ellipsoids) that encompass the robot's body. In the proposed simulation framework, we deem the robot body as a set of spheres, which is a representation ubiquitously utilized in trajectory optimization methods [9]. In the case of a robotic arm, we manually generate a discrete set of spheres for each link. This is illustrated in Fig. 2, where for the Universal Robots

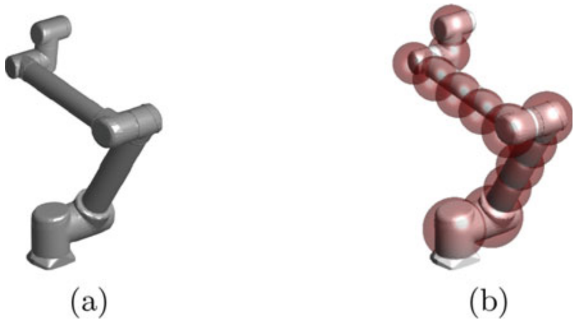

Fig. 2 An example of representing the Universal Robots UR10 robot with a mesh model (**a**) and with a set of spheres (**b**). The robot can be adequately represented by only 13 spheres, which allows particularly efficient collision checking

UR10 arm we show the mesh model that closely resembles the actual robot, both with and without the corresponding set of spheres overlayed. By using spheres as geometric primitives, the nearest distance from an obstacle to any point in the set $\mathcal{B}$ is simple to compute, which enables efficient collision checking that is crucial for achieving real-time algorithm execution on current hardware. While the set-of-spheres robot representation is not the most accurate way of modeling the robot's body, its simplicity facilitates the EM simulation of the robot arm in a dynamic environment. We choose this representation since EM simulation with a mesh model can become computationally complex, requiring days to simulate a complex dynamic scene. The mentioned simplicity also implies that a set-of-spheres model can easily be manually constructed by a human operator, enabling fast deployment in practical applications.

2.2 S-Parameters

The S-parameters describe how the electrical signal of a single frequency is scattered or transmitted within the network and compress very complicated networks into black-box models [10–13]. They are often used in radiofrequency (RF) and microwave engineering to characterize behavior of linear electrical networks (e.g., an RF amplifier or an antenna), both in free space or in the presence of some objects. The S-parameters provide the relation between power waves traveling in and out of the network, which is a more convenient representation at higher frequencies in comparison to voltage and current [14]. The waves traveling into the n-th port of the network are called incident waves and denoted with a_n, while the waves traveling out of the network are called reflected waves and denoted with b_n. Incident and reflected waves for a 2-port network are shown in Fig. 3.

The expression which relates the voltage U_n and current I_n at port n with the incident and reflected wave is

$$a_n = \frac{U_n + I_n Z_0}{2\sqrt{\mathrm{Re}(Z_0)}}, \quad b_n = \frac{U_n - I_n Z_0^*}{2\sqrt{\mathrm{Re}(Z_0)}}, \tag{2}$$

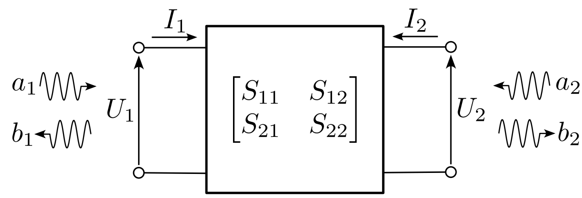

Fig. 3 An illustration of a general 2-port network with incident (a_1, a_2) and reflected power waves (b_1, b_2)

where Z_0 is an arbitrary reference impedance that may be represented with a complex number, but typically it is set to the characteristic impedance of the transmission lines in the system (e.g., $Z_0 = 50\,\Omega$). As noted before, the S-matrix gives the relation between all a_n and b_n, $n = 1, 2, ..., N$ for the N-port network

$$\mathbf{b} = \mathbf{S}\mathbf{a}, \tag{3}$$

where **a** and **b** are $(n \times 1)$ vectors, while **S** is an $(n \times n)$ matrix with elements (S_{ij}). From this equation then follows

$$S_{ij} = \left. \frac{b_i}{a_j} \right|_{a_n = 0, \forall n \neq j}. \tag{4}$$

The parameter S_{ij} can be interpreted as the ratio of a power wave leaving at port i, when there is only an incident power wave at port j. In case of $i = j$, the S_{ii} is the reflected power at the same port. For this reason the diagonal elements of **S** are called reflection coefficients, while the off-diagonal elements are called transmission coefficients. In general, S_{ij} is a complex number because the network affects both the magnitude and the phase. The S-parameters of a multi-port network mounted on the robotic skin are dependent on the electromagnetic properties of the environment, which could be leveraged to develop a new sensor that can accurately determine positions of objects relative to the skin.

2.3 Bridging Robotics and Full-Wave EM Simulation

In order to conduct the full-wave EM simulation of robotic dynamic scene, we rely on the robotics simulator to create a scene with the robot and environment model. Our robotics simulator of choice is Matlab Robotics Toolbox, which has many existing robot models and can be interfaced with the Robot Operating System (ROS) for communication with the real-world robot. For the full-wave EM simulation, we use the industry-standard CST Studio Suite software. The proposed software bridge enables communication between the two simulators by creating a local object linking and embedding (OLE) automation server using an OLE-compliant component object model (COM) server. COM is an object-oriented system designed for creating binary software components, allowing them to interact with a variety of programming languages. We compile our bridge in the Microsoft Windows system as the Matlab COM function is exclusively compatible with this platform. Using our bridge, we can create or load the simulated robotic dynamic environment in Matlab and pass the information to the CST simulator. Our implementation approximates the scene from a robotic simulator with geometric primitives and passes the scene description at each discrete time instant to the full-wave EM simulator, which then uses a numerical solver and the antenna CAD model to compute the ground-truth S-parameters. The results of the EM simulation, in our case the obtained S-parameters, are passed back for analysis and visualization.

3 Results

To evaluate the proposed simulation framework, we conducted two dynamic scene scenarios. The first scenario featured a single static antenna and a box object moving away from the port. We calculated the S-parameter of the antenna port through time and graphed its value against the increasing distance. In the second scenario, a Kuka Iiwa 14 robot was equipped with two antennas, resembling a simple e-skin. The robot executed a trajectory in close proximity to the large box obstacle resembling a wall in the environment. We computed the S-parameters of both antenna ports, which could subsequently be used to infer the distance of nearby objects. Both experiments were performed on a system with a 3.5-GHz Intel Core i7-7567U processor and 16 GB of RAM.

3.1 Moving Box Scenario

We conducted the first simulation in CST with a 26 GHz wave launcher object with 4.64×4.64 cm dimensions and a perfect electric conductor (PEC) box object with dimensions 0.5×0.5 cm. We used the proposed software bridge to control the movement of the PEC box in the CST simulator through Matlab. The distance in the z-axis between the launcher and the box was discretized at 1 mm intervals, resulting in 40 consecutive simulations, effectively simulating a dynamic environment, as illustrated in Fig. 4a. Given a discretization time of 0.1 s, the box moves with a translational velocity in the z-axis of 0.01 m/s. The simulation was executed using hexahedral mesh and the TD-C calculation type. Each simulation took approximately 10 min of computation time. The obtained S_{11} parameter magnitude increases with the distance along the z-axis of the port, as shown in Fig. 4, a result that may be used to determine the distance of a moving object relative to the port, facilitating new sensor developments. The distance at which we observe changes in the S-parameter can be increased with different object size and with a different antenna type. We leave this analysis for future work.

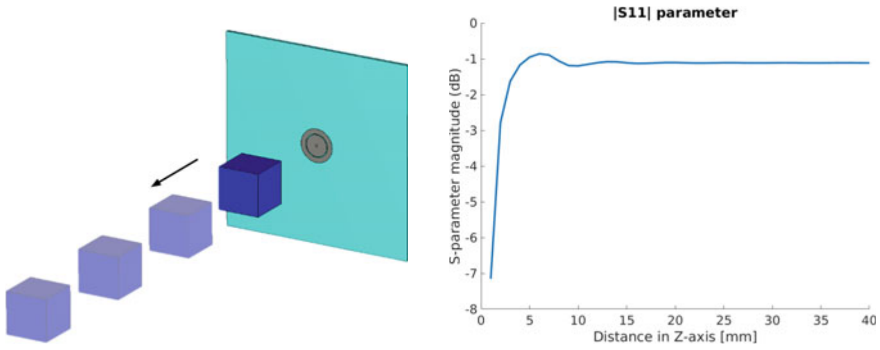

(a) Moving box scenario (b) S-parameter magnitude

Fig. 4 The experimental scenario featuring (**a**) EM simulation of a box moving along the z-axis of the sensor antenna and (**b**) the corresponding S-parameter depending on the distance between the moving box and the antenna

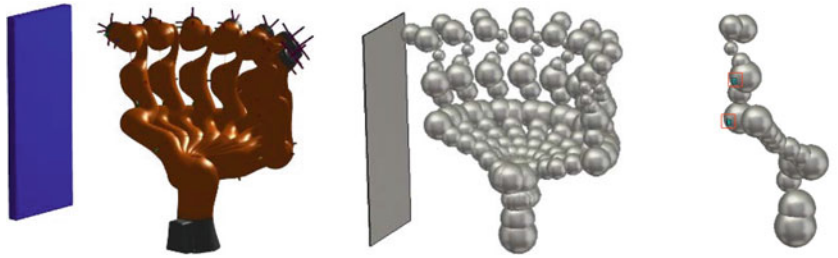

(a) Matlab scene (b) CST scene (c) Arm spheres

Fig. 5 Experimental scenario including Kuka Iiwa 14 and PEC wall in (**a**) robotics simulator, (**b**) EM simulator. The arm is approximated with a set of spheres and has two equipped antennas, visible inside red squares (**c**)

3.2 Robotic Arm Trajectory Scenario

For the second scenario, we used Matlab to simulate a robot arm trajectory execution near a wall in the environment. We used the proposed software bridge to discretize the robot trajectory with duration of 1 s, compute the forward kinematics at every time instant, and represent the scene using PEC box and spheres in the CST simulator. The visual representation of the environment through time in both Matlab and CST is shown in Fig. 5. Additionally, using our bridge we imported a preexisting discrete copper antenna model into CST and placed two instances of the antenna on different joints of the robot, as shown in Fig. 5c. The dimensions of antennas are 1.8×2.2 cm, and they operate at 10 GHz. We manually adjusted the cells-per-wavelength mesh parameter to optimize simulation runtime. Each simulation took approximately 90 min of computation time. While the obtained S-parameters mag-

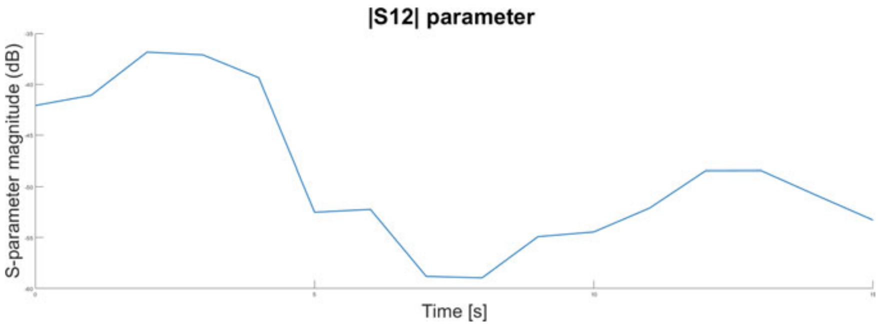

Fig. 6 S_{12} parameter magnitude in the robotic arm trajectory scenario

nitudes, which are shown in Fig. 6, cannot be directly correlated to distance, the proposed simulation framework can be utilized to verify analytical models or to collect large amounts of data for training deep models. In particular, the S_{12} parameter can be used to determine the relative position of sensors on the flexible skin.

4 Conclusion

In this paper, we presented a framework that enables the EM simulation of robotic dynamic scenes. We proposed a software bridge that first takes robot and environment representations from the robotic simulator and approximates the scene with geometric primitives. The scene information is then passed to the EM simulator in order to compute the S-parameters at the ports, enabling the development of sensors based on EM phenomena, e.g., a novel robotic skin. We experimentally validated our framework by simulating two dynamic scenes and determining the S-parameters of skin-mounted antennas that correlate with the distance between the object and the sensor. We believe that our framework can be leveraged for modeling novel sensors that are accurate and efficient, serving as a first step for evaluation and comparison with analytical models. In future work, we will analyze how different object and antenna properties affect the S-parameters. We will also investigate precision and repeatability in real-world conditions, a well as the effect of interferences.

Acknowledgements This work has been supported by the HORIZON EUROPE EIC Pathfinder Open programme under grant agreement No 101098996 “Flexible intelligent near-field sensing skins (FITNESS)”.

References

1. O'Neill, J., Lu, J., Dockter, R., Kowalewski, T.: Practical, stretchable smart skin sensors for contact-aware robots in safe and collaborative interactions. In: International Conference on Robotics and Automation (ICRA). pp. 624–629. IEEE (2015)
2. Xie, M., Hisano, K., Zhu, M., Toyoshi, T., Pan, M., Okada, S., Tsutsumi, O., Kawamura, S., Bowen, C.: Flexible multifunctional sensors for wearable and robotic applications. Adv. Mater. Technol. **4**(3), 1800626 (2019)
3. Schlegl, T., Kröger, T., Gaschler, A., Khatib, O., Zangl, H.: Virtual whiskers-highly responsive robot collision avoidance. In: 2013 IEEE/RSJ International Conference on Intelligent Robots and Systems. pp. 5373–5379. IEEE (2013)
4. M'Colo, K.E., Luong, B., Crosnier, A., Néel, C., Fraisse, P.: Obstacle avoidance using a capacitive skin for safe human-robot interaction. In: International Conference on Intelligent Robots and Systems (IROS). pp. 6742–6747. IEEE/RSJ (2019)
5. Quevedo-Teruel, O., Chen, H., Díaz-Rubio, A., Gok, G., Grbic, A., Minatti, G., Martini, E., Maci, S., Eleftheriades, G.V., Chen, M., et al.: Roadmap on metasurfaces. J. Opt. **21**(7), 073002 (2019)
6. Bodehou, M., Craeye, C., Martini, E., Huynen, I.: A quasi-direct method for the surface impedance design of modulated metasurface antennas. IEEE Trans. Antennas Propag. **67**(1), 24–36 (2018)
7. Koenig, N., Howard, A.: Design and use paradigms for gazebo, an open-source multi-robot simulator. In: International Conference on Intelligent Robots and Systems (IROS). vol. 3, pp. 2149–2154. IEEE/RSJ (2004)
8. Michel, O.: Cyberbotics ltd. webots™: professional mobile robot simulation. Int. J. Adv. Robot. Syst. **1**(1), 5 (2004)
9. Ratliff, N., Zucker, M., Bagnell, J.A., Srinivasa, S.: Chomp: Gradient optimization techniques for efficient motion planning. In: International Conference on Robotics and Automation. pp. 489–494. IEEE (2009)
10. Pozar, D.: Microwave Engineering, 4th edn. Wiley (2011). https://books.google.hr/books?id=JegbAAAAQBAJ
11. Matthaei, G.L., Young, L., Jones, E.M.: Microwave filters, impedance-matching networks, and coupling structures (1980)
12. He, J., Gui, L., Jiang, T., Zhou, C., Lv, L.: Analysis on scattering parameters for coupled microstrip lines with bend discontinuities. In: Sixth International Conference on Wireless Communications and Signal Processing (WCSP). pp. 1–4 (2014)
13. Tomić D., Žanić, D.: Analysis of scattering parameters of finite stealthy transmission line. In: 2023 International Symposium ELMAR. pp. 129–132 (2023)
14. Kurokawa, K.: Power waves and the scattering matrix. IEEE Trans. Microw. Theory Tech. **13**(2), 194–202 (1965)

Challenges in Polystyrene Mold Making for Clay Panels Using Robotic Hotwire Carving

Marko Jovanović, Andrej Čilag, Marko Vučić, Igor Babić, Mirko Raković, Vesna Stojaković, and Bojan Tepavčević

Abstract This paper examines a key challenge in mold-making for relief clay panels: the issue of heat-induced curling and surface damage caused by dripping molten plastic during the robotic hotwire cutting process. Our study specifically focuses on analyzing how the speed of the hotwire tool influences the look of the mold ridges. The emphasis is placed on the end-effector's velocity pertaining to transition and orientation between the toolpath targets. We hypothesize that the time taken for the tool to travel between two targets is a critical factor, potentially leading to excessive heat buildup in the mold's ridges. By conducting a toolpath evaluation, we aim to determine if the prolonged travel time, rather than just the cutting speed, contributes to the excessive heat that causes edge curling and surface damage on the ridges. This research contributes to the mold-making process for clay panels, as it seeks to identify the speed-related factors that can be adjusted to mitigate these issues. Our findings are expected to provide valuable insights into the quality and precision of molds used for imprinting clay.

Keywords Hotwire temperature · Orientation · End-effector velocity · Signal analyzer

1 Introduction

Over the past two decades, architectural fabrication has undergone a significant transformation, primarily driven by the integration of industrial robots. This evolution, pioneered by innovators such as Gramazio and Kohler with their work on the Facade Gantenbein Winery [1], and further explored in Bechthold's research [2], has revolutionized traditional construction techniques, merging them with advanced computational design. These developments have enabled more intricate and precise

M. Jovanović (✉) · A. Čilag · M. Vučić · I. Babić · M. Raković · V. Stojaković · B. Tepavčević
Faculty of Technical Sciences, University of Novi Sad, 21000 Novi Sad, Serbia
e-mail: markojovanovic@uns.ac.rs
URL: http://www.ftn.uns.ac.rs

D. Pisla et al. (eds.), *Advances in Service and Industrial Robotics*, Mechanisms and Machine Science 157, https://doi.org/10.1007/978-3-031-59257-7_49

architectural designs, utilizing the versatility of industrial robots, which is evident in the diversity of their end-effectors or tools [3].

In the specialized field of Digital Ceramics [4], this technological advancement has led to innovative approaches in fabricating clay panels, employing both mold-making and sculpting. Robotic hotwire cutting and milling are used to fabricate polystyrene molds for shaping clay elements [5–7], while computational methods by Tan and Dritsas [8] and Guo et al. [9] have shown potential in direct sculpting and carving of clay panels, albeit requiring extensive tool path optimization.

In this context, hotwire carving emerges as a suitable approach to combine the clay sculpting and hotwire cutting to fabricate intricate molds for clay imprinting (Fig. 1a). This technique, inspired by traditional clay sculpting but enhanced with robotic accuracy, addresses the malleability challenge effectively. Key considerations for robotic toolpath generation in hotwire cutting are temperature control and cutting speed, as these significantly impact mold quality (Fig. 1b). Various research methodologies address these parameters. Vučić et al. [10] relies on empirical data for fabricating porous structures, while other studies, like those of Brooks and Aitchison [11] and Gallina et al. [12] incorporate sensory feedback in the hotwire cutting process, optimizing it for expandable polystyrene foam. This necessitates comprehensive analysis and preparation, as shown by Park et al. [13] in their architectural foam cutting study.

This study seeks to enhance the understanding of mold-making in Digital Ceramics, focusing on the intricacies of using industrial hotwire cutting for creating molds. Our investigation centers on the problems of heat-induced curling (Fig. 1c) and surface damage caused by molten plastic dripping during the hotwire cutting process(Fig. 1d).

The aim is to analyze if the speed of the hotwire tool, specifically the velocity in terms of transition and orientation between targets, affects these issues. We hypothe-

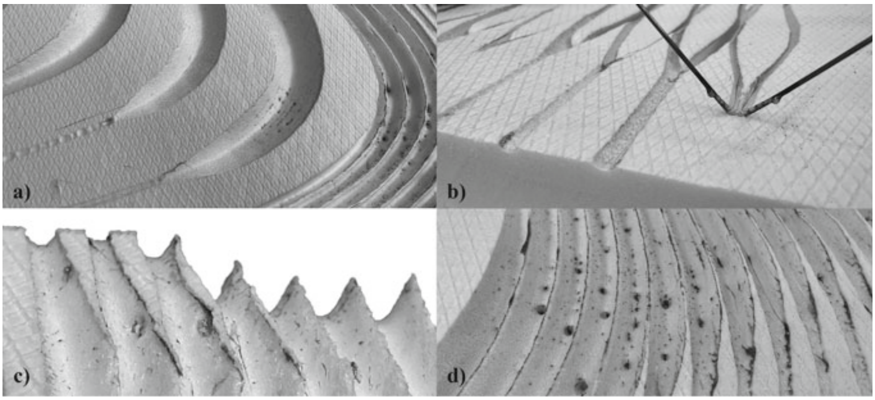

Fig. 1 Polystyrene mold for clay imprinting; **a** relief mold with ridges; **b** hotwire carving tool cutting out ridges; **c** heat-induced curling effect on the ridge sides; **d** surface damage caused by the molten plastic dripping

size that prolonged travel time between targets contributes significantly to excessive heat buildup, leading to curling of the mold's edges and damage to the surfaces. This research contributes to the field by identifying critical speed-related factors in the hotwire cutting process that can be adjusted to mitigate these challenges, ensuring the quality and precision of molds for clay panel imprinting. Our findings are expected to offer valuable insights into optimizing the mold-making process, aligning the technical precision of robotic fabrication with the aesthetic requirements of ceramic design.

2 Methodology

The methodology of this study is structured into two primary subsections - the design logic for the relief ridge mold and the fabrication approach using robotic hotwire carving. This dual-pronged approach offers a holistic view of the methodology, underlining the importance of both design and fabrication in creating effective polystyrene molds for Digital Ceramics.

2.1 Design Logic

The relief mold design hinges on the creation of specific ridge patterns. These ridges are formed by employing Boolean difference operations on a set of solid models, derived from swept polysurfaces. These polysurfaces are generated using closed planar profile curves and guideline curves (GC), which are then capped to complete the solid forms (Fig. 2).

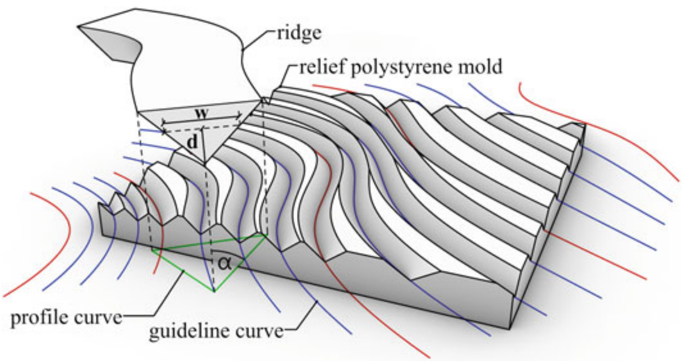

Fig. 2 Relief Ridge Mold—Utilizing a profile curve in conjunction with a guideline curve to generate a swept surface ridge, enabling the precise subtraction of material from the polystyrene block model for mold creation

Guideline Curves Guideline curves are pivotal as they dictate the path followed by the hotwire tool. The tool's profile, chosen to be an isosceles right triangle, is positioned perpendicularly to the tangent vectors at each GC's start. To form the ridges, the profile curve is swept along the GC, ensuring it extends beyond the block's borders for effective subtraction. The utilization of spline-based GCs offers fluidity and intricate tiling possibilities, enabling versatile interpretations of tectonics in the clay material. A critical aspect is the interrelation between ridge depth and width, governed by Eq. 1:

$$w = 2 * \tan(\alpha) * d. \tag{1}$$

Here, w represents the ridge width, α is the angle between the inclined profile edges and the vertical axis, and d signifies the desired depth. Appropriate values for depth and width are essential to ensure a balanced interaction between ridges and flat panel areas.

To streamline the creation of spline GCs, a primary GC is generated first (Fig. 2, shown in red), with subsequent curves interpolated over a designated span relative to the ridge width (Fig. 2, shown in blue). The number of interpolated curves is determined as the ceiling rounded quotient of the longest distance between main neighboring curves and the width w.

To address overlaps and ensure ridge uniformity, the profile shape is rotated around the vertical axis at each point along the GC by an angle "β", calculated as per Eq. 2:

$$\beta = \arccos \frac{w_1}{w}. \tag{2}$$

where w_1 is the shortest distance between the specific point and the neighboring curve. This process results in a swept surface with varying profile curves, culminating in the final relief mold design. With the design phase complete, the focus shifts to the fabrication process.

2.2 Fabrication

Unlike conventional 3D printing or CNC milling methods, our fabrication phase heavily relies on the precise orientation and position data of the tooling process. This approach is critical for the accurate execution of commands by the industrial robot, closely aligning with the pre-designed 3D model.

The critical aspect of the fabrication involves meticulously orienting the robot's end effector, equipped with the cutting tool. This precise orientation is essential for ensuring both dexterity and accuracy during the cutting process. The transition from digital design to physical fabrication requires the generation of "targets" that define the position and orientation of the robot arm's end effector, employing inverse kinematics for determining the robot's joint angles during transitions between targets.

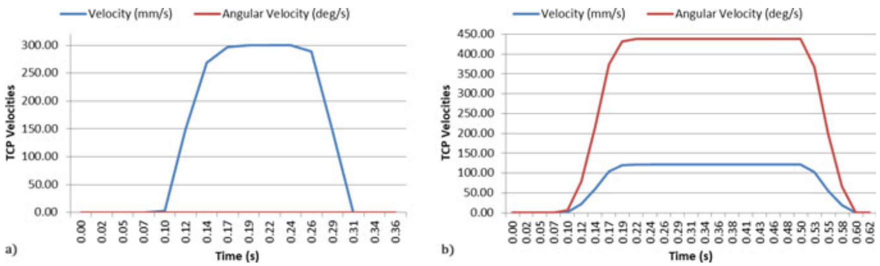

Fig. 3 Difference in TCP velocities between two targets with varying orientations. **a** Case I: identical orientations of targets; **b** Case II: the second target is rotated around the z-axis by 180°C, showcasing the effect on the robot's velocity

Additionally, the fabrication process integrates extra targets along existing toolpaths, enabling smooth entry and exit of the tool from the polystyrene block. Simulation tools play a pivotal role at this stage, covering aspects like target reachability, joint movement, and collision detection. These simulations are crucial to confirm that all targets fall within the robot's operational range, the joint angles remain within their limits, and no collision risks are present.

Our approach to address potential fabrication issues hinges on the analysis of the robot's Tool Center Point (TCP) movement over short distances, especially when significant orientation changes are involved. To analyze this, ABB Robot Studio [14] programming environment was used that allows signal analysis to monitor the velocity and other parameters of the robot itself. We posit that in such scenarios, the robot prioritizes angular velocity adjustments, leading to a recalibration or reduction in its velocity. This hypothesis was tested on two closely positioned targets with varying orientations—one with identical orientations and the other with a target rotated 180 °C around the z-axis. As illustrated in Fig. 3, in the first scenario, the robot maintains maximum velocity with negligible angular velocity, whereas in the second scenario, a dominant angular velocity necessitates a reduction in velocity.

3 Results and Discussion

Our study focused on the mold-making process using an industrial robot, which moves along a path of targets to form the desired mold profiles in a polystyrene block (Fig. 4a). The tool that is used is a 1.6 mm hotwire tool that is shaped as an isosceles trianlge with one side having parts feeding into the heating tool. The primary issue observed was the excessive melting of polystyrene, particularly in areas where mold profiles are narrower. We hypothesize that this problem is predominantly due to deviations from the constant velocity of the TCP during the cutting process. In this study, we examine a specific example of the off-line simulation process for fabricating relief ridge molds. Figure 4b shows a panel with targets in front of the

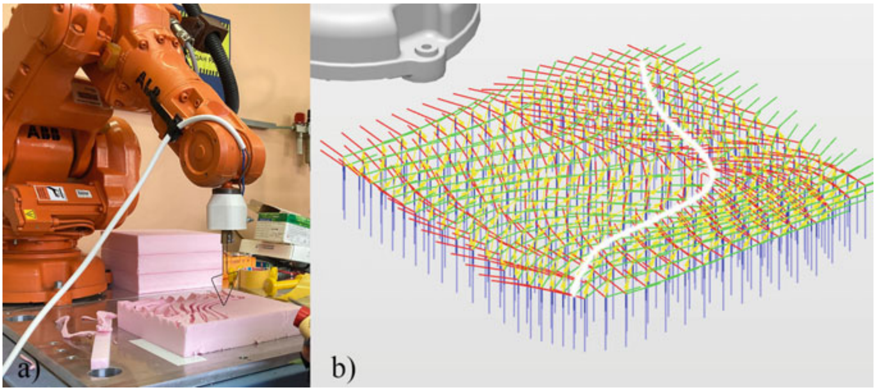

Fig. 4 Selected path for detailed analysis

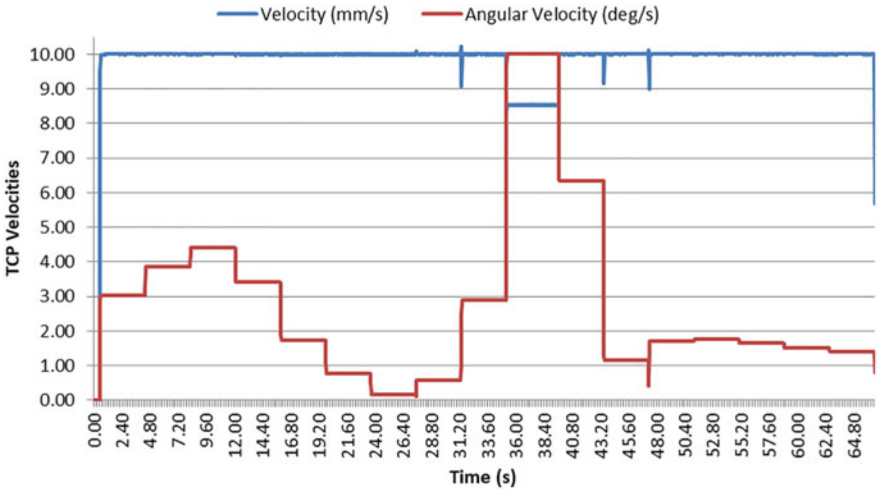

Fig. 5 TCP velocities (velocity and angular velocity) of the analyzed path, highlighting areas where problems occur

robot, with a specific trajectory highlighted in white, to investigate both velocity and angular velocity between neighboring targets.

In order to test this we focused on the system analyzer to check if the quuality depends significantly on maintaining a constant TCP velocity. When the robot's TCP transitions between targets that are closely spaced and have significant orientation changes, the angular velocity tends to increase, resulting in a corresponding decrease in velocity. This phenomenon was particularly noticeable in areas where the orientation change was substantial, leading to longer exposure of the mold to the hot wire and consequently higher temperatures than intended.

Figure 5 shows a critical part of the path where the problem is evident. Around 36 s into the path execution, a significant change in target orientation leads to a marked decrease in velocity and an increase in angular velocity. This reduction in velocity causes the tool to remain longer on the path, which is assumed to result in excessive melting of the mold material.

The robot's movements are instructed to achieve both linear movement and TCP reorientation simultaneously. However, when the distance between targets is too small to satisfy the orientation change at maximum velocity, the robot prioritizes angular velocity, and the velocity is recalculated and reduced. This issue is compounded by the robot's maximum velocity limits as defined in its movement instructions [15].

Our findings highlight a critical aspect of robotic mold fabrication: the importance of balancing TCP velocities to avoid excessive melting and deformation of the mold. Future work will involve testing this observation on a series of smaller tiles to compare results and further refine the fabrication process.

4 Conclusion

Our study identifies that the quality of polystyrene molds in clay panel fabrication is highly dependent on maintaining constant TCP velocities. Deviations from these velocities, particularly in scenarios with tight target spacing and significant orientation changes, lead to detrimental effects such as excessive melting and deformation of the mold. This research highlights the need for careful calculation and control of TCP velocities during the hotwire cutting process. Future work will focus on optimizing these velocity parameters to prevent issues like curling and excessive melting, thus improving the overall quality and precision of the mold-making process in Digital Ceramics.

References

1. Gramazio, F., Kohler, M.: Facade Gantenbein Winery. Urban. Flux **8**, 88–91 (2009)
2. Bechthold, M.: The return of the future—a second go at robotic construction. Architectural Des. **80**(4), 116–121 (2010)
3. Pigram, D., McGee, W.: Formation embedded design. In: Proceedings of the 31st Annual Conference of the Association for Computer Aided Design in Architecture (ACADIA), pp. 122–131 (2011)
4. Sabin, J.E.: Digital ceramics: crafts-based media for novel material expression and information Mediation at the architectural ccale. In: ACADIA 10: LIFE in: formation, on responsive information and variations in architecture. In: Proceedings of the 30th Annual Conference of the Association for Computer Aided Design in Architecture (ACADIA), pp. 174–182 (2010)
5. Ko, M., Shin, D., Ahn, H., Park, H.: InFormed ceramics: multi-axis clay 3D printing on freeform molds. In: Robotic Fabrication in Architecture, Art and Design 2018: Foreword by Sigrid Brell-

Çokcan and Johannes Braumann, Association for Robots in Architecture, pp. 297-308, Springer International Publishing (2019)
6. Rosenwasser, D., Mantell, S., and Sabin, J.: Clay non-wovens: robotic fabrication and digital ceramics. In: Proceedings of the 37th Annual Conference of the Association for Computer Aided Design in Architecture (ACADIA), Massachusetts Institute of Technology, School of Architecture+ Planning, Department of Architecture, Association for Computer Aided Design in Architecture, Cambridge, MA, USA, pp. 2-4 (2017)
7. Friedman, J., Kim, H., Mesa, O.: Experiments in additive clay depositions: woven clay. In: Robotic Fabrication in Architecture, Art and Design, vol. 2014, pp. 261–272 (2014)
8. Tan, R. and Stylianos, D.: Clay robotics: tool making and sculpting of clay with a six-axis robot. In Living systems and micro-utopias: towards continuous designing. In: Proceedings of the 21st International Conference on Computer-Aided Architectural Design Research in Asia (CAADRIA 2016), Melbourne 30 March-2 April 2016, pp. 579-588 (2016)
9. Guo, Z., Zhang, Z., Li, C.: Robotic Carving Craft, Research on the Application of Robotic Carving Technology in the Inheritance of Traditional Carving Craft. In: Proceedings of the 27th CAADRIA Conference, Sydney, 9-15 April 2022, pp. 747-756. https://doi.org/10.52842/conf.caadria.2022.1.747 (2022)
10. Vučić, M., Jovanović, M., Raković, M.: Fabricating porous structures using robotic hotwire cutting. Nexus Netw. J. **25**(4), 849–866 (2023)
11. Brooks, H.L., Aitchison, D.R.: Force feedback temperature control for hot-tool plastic foam cutting. Proc. Inst. Mech. Eng. Part B: J. Eng. Manuf. **224**(5), 709–719 (2010)
12. Gallina, P., Mosca, R., Pascutto, P.: Optimized hotwire cutting robotic system for expandable polystyrene foam. In: AMST'05 Advanced Manufacturing Systems and Technology: Proceedings of the Seventh International Conference, pp. 377-386, Springer Vienna (2005)
13. Park, S., Park, J.H., Jung, S., Ji, S.J.: Foam cutting for an architectural installation using industrial robot arm: calibration, error, and deviation analysis. Autom. Constr. **133**, 103986 (2022)
14. Holubek, R., Delgado Sobrino, D.R., Koštál, P., Ružarovský, R.: Offline programming of an ABB robot using imported CAD models in the RobotStudio software environment. Appl. Mech. Mater. **693**, 62–67 (2014)
15. ABB Robotics: Technical reference manual: RAPID Instructions, Functions and Data types, accessed January 25, 2024, available on https://library.e.abb.com/public/688894b98123f87bc1257cc50044e809/Technical%20reference%20manual_RAPID_3HAC16581-1_revJ_en.pdf

Robotic Platform for Position Control of a Ball

Simona-Daiana Sim, Attila Medgyesi, Zs. Lendek, Calin Vaida, Vlad Mihai Mihaly, Mircea Susca, Petru Dobra, and José Machado

Abstract The present paper proposes and describes an approach to stabilizing a ball on a rectangular surface using a three-armed robotic system. The system is based on advanced image detection for accurate ball and surface identification. The hardware includes three servo motors controlled by an Arduino board, and the camera used is a mobile phone connected to the computer. The control of the arm movements is achieved by a PD controller. The components were printed with a 3D printer. The technical details of the system, as well as the PD controller are presented in detail, highlighting the effective interaction between the theoretical and practical sides.

S.-D. Sim (✉) · A. Medgyesi · Zs. Lendek · V. M. Mihaly · M. Susca · P. Dobra
Department of Automation, Technical University of Cluj-Napoca, Memorandumului 28, 400114 Cluj-Napoca, Romania
e-mail: simona.sim@aut.utcluj.ro

A. Medgyesi
e-mail: medgyesi.is.attila@student.utcluj.ro

Zs. Lendek
e-mail: zsofia.lendek@aut.utcluj.ro

V. M. Mihaly
e-mail: vlad.mihaly@aut.utcluj.ro

M. Susca
e-mail: mircea.susca@aut.utcluj.ro

P. Dobra
e-mail: petru.dobra@aut.utcluj.ro

C. Vaida · J. Machado
CESTER Research Center, Technical University of Cluj-Napoca, Muncii Ave. 103-105, 400641 Cluj-Napoca, Romania
e-mail: calin.vaida@mep.utcluj.ro

J. Machado
e-mail: jmachado@dem.uminho.pt

J. Machado
Metrics Research Center, University of Minho, Campus of Azurém, 4800-058 Guimarães, Portugal

D. Pisla et al. (eds.), *Advances in Service and Industrial Robotics*, Mechanisms and Machine Science 157, https://doi.org/10.1007/978-3-031-59257-7_50

The development of this system offers an interdisciplinary perspective, combining knowledge from mechatronics, machine vision, and robotic control.

Keywords Robotic control · Image processing · Rehabilitation control

1 Introduction

In recent decades, the field of robotics [1–3] has seen significant advances, bringing with them new challenges and opportunities in the development of autonomous systems. One of these areas is real-time robotic control [4], where advanced technologies [5] are used to coordinate and regulate the movements of mechanical systems. In this context, the present article proposes an approach for stabilizing a ball in the center of a rectangular surface, using a complex system consisting of three robot arms controlled by servo motors.

The aim is to develop a control system capable of monitoring and adjusting the position of the ball on the given surface. This approach requires the use [6] of a closed control loop in which information from the environment is captured by a video camera. The system determines the necessary commands for the servo motors of the robot arms, thus keeping the ball in the center of the surface.

Works such as [7–10] have addressed similar position control problems using different technologies and algorithms. Relevant aspects of machine vision and image processing are discussed in [11]. These previous works serve as reference to our work. The development and implementation of the system in [12] integrates knowledge from mechatronics, control engineering, machine vision, and signal processing [13–15] served as inspiration to use small servo motors, and a low-cost development board to implement the described detection and control algorithm. A key issue is the robustness of control systems to disturbances and uncertainties given the dynamic environment and variable interactions with the ball and the surface. Robust control strategies are discussed in [16], motivating the choice of a PD controller. Also, the dynamic model is described as in [17].

The main goal is to present a multidisciplinary educational project with variations in the fields of mechanics, image processing and control. Similar systems have been developed and advanced control approaches used. For example, [9] presents an effective control based on neural networks. In this paper, we show that a simple PD controller can also stabilize the system. Also, such a project is one with low costs, the advantage being given by the development board used and the use of the phone's camera for image detection instead of a specialized camera.

The article presents the hardware design, the mathematical model, control strategies, and software applicability. It is intended as a first step to implement functional software in medical robots, which are currently having a great impact. The designed and developed platform is versatile and can be used effectively in ankle rehabilitation applications, such as [18].

The article is structured as follows: In Sect. 2 the hardware part is presented, including the development board, the servo motors and the 3D support; in Sect. 3 we describe the image processing and ball detection; Sect. 4 presents the mathematical model of the system and the controllers described; in Sect. 5 the results are presented, and Sect. 6 concludes the paper.

2 Hardware Design

For the hardware design of the system, we opted to use three servo motors to control the movements of the robotic arms and thus the position of the platform via an Arduino board. This system provides a flexible and efficient platform for implementing control algorithms. We chose SG90 micro servomotors [19] because of their precision and ability to control specific rotation angles. They allow precise adjustment of the angle of rotation, smooth and controlled movements, essential for keeping the ball on the rectangular surface. Parameters such as speed, torque, and angular position can be adjusted using the Arduino board for implementing the controller.

The Arduino Nano board (small, direct connection to computer) is the core of the control system, facilitating efficient communication between the computer and servo motors. Programs implemented on the Arduino receive information from the computer and generate the appropriate signals to control the arm movements. The board also offers the possibility to use a diverse set of software libraries and resources such as Servo and UART serial communication libraries [20, 21], simplifying the development and implementation of control algorithms.

Using a mobile phone as a camera has many advantages. Modern phones are equipped with high-performance cameras and image sensors, providing quality data for visual analysis. This is why we chose to use a mobile phone instead of more advanced camera system.

To design the structural components of the system, 3D modelling of the arms and other necessary elements (like support elements) was first realized. This process allowed an accurate and adaptable design to the geometric requirements of the system. The size of the platform is 140×140 mm. The elements were subsequently printed using a 3D printer. The PLA materials used for printing are selected for strength, durability, and weight to ensure optimal operation of the robotic arms. The 3D model and the resulting platform are shown in Fig. 1. The servo motors are located under the platform and control its inclination through the angle of rotation. The motors are located 61 mm from the center, every motor rotated with 120°. The camera is placed above the board to detect its entire area, including the position of the ball when it is placed. The spherical couplings are at a distance of 65 mm from the center of the platform. The distance of the platform from the table is chosen to ensure the largest and most efficient range of movement of the platform and is 58 mm. The arm between A and B is 36 mm long, between the engine and A the arm is 26 mm long.

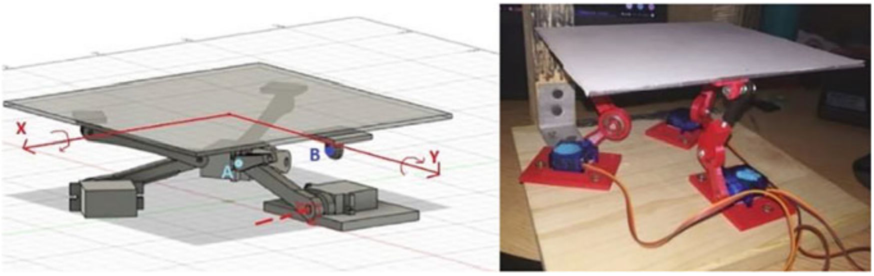

Fig. 1 D model and the actual system

3 Image Processing

Image detection is a crucial component in our system, and the use of the OpenCV library in the Python language has significantly facilitated this functionality.

For surface identification, we implemented *cv2.findContours* from *OpenCV*, a function that locates and highlights contours in an image. This allowed us to define and delineate the area we consider relevant for keeping the ball in the center of the rectangular surface. The algorithm dynamically adapts to changes in light and contrast, thus ensuring consistent and accurate detection of the area of interest. These image sensing techniques are integral to obtain the position of the ball and platform and to control the position of the ball.

For ball detection, we used the *cv2.HoughCircles* function from *OpenCV*, which is based on the Hough transform [22] to identify circles in images. This algorithm is used for accurately identifying the position of the ball on the platform. The parameters have been tuned based on the actual radius of the ball and experiments to ensure robust detection that is adaptable to operating environment variables. Figure 2 illustrates how the platform is delineated and how the ball is detected.

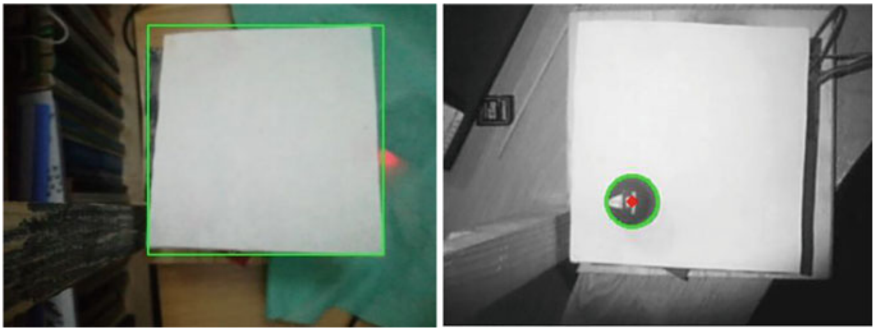

Fig. 2 Platform and ball detection

4 Geometric Model Calculation

Since the ball on the platform is unstable, precise ball stabilization involves controlling platform movements. To achieve this goal, the servo motors are used to change the platform angle in the x and $y-$ axis direction. Therefore the backward kinematics, i.e., the motor angles as a function of the controlled platform angles are computed.

Our system has three actuators (red in Fig. 1 under the white platform), providing three degrees of freedom when positioning the platform. These degrees of freedom are represented by the angles on the x and $y-$ axis and the distance of the platform from the table. The kinematic model of the system is based on [23]. The dynamic model [24] is obtained considering the angle rr as an input and the position as output. Point A is a rotary coupling, Point B is a spherical coupling. Given the height imposed by the system, we compute the coordinates of points A and B, as shown in Fig. 1, and we obtain a system of equations providing arithmetical connection between the angle of the motors and the $x - y$ angles of the platform.

5 Controller Design and Results

Under the assumption of two friction and stiction, the dynamic model [17] in the direction of the x-axis is:

$$\ddot{x} = g \cdot \sin(u) \tag{1}$$

where $g = 9.81\,\text{m/s}^2$ and similarly for the y-axis.

To control the system, both PID and PD controllers were considered. The controller provides a desired x, y angle for the platform, which is converted to servo motor angles determined based on the geometric model. Since our goal is to stabilize the ball at a desired position (x^{d}, y^{d}). The position error on the x axis is computed as $e_x = x - x^d$ and the desired velocity should be 0. So $e_{vx} = v_x$.

A stabilizing PD control law was determined as:

$$\text{Command}_x = e_x \cdot (-0.08) + e_{vx} \cdot (-0.018) \tag{2}$$

where the control gains were tuned to ensure fast error correction, and to reduce overshoot.

A comparison was also made between a PD and a PID regulator. A larger overshoot and a more pronounced oscillation can be observed in the case of the PID regulator, compared to the more calibrated response given by the PD regulator. The XX position of the ball using the PD and PID controllers in simulation is shown in Fig. 3.

Although the gains were initially experimentally chosen, the PD control provably stabilizes the ball at a desired point. One can, for instance, use the Lyapunov function:

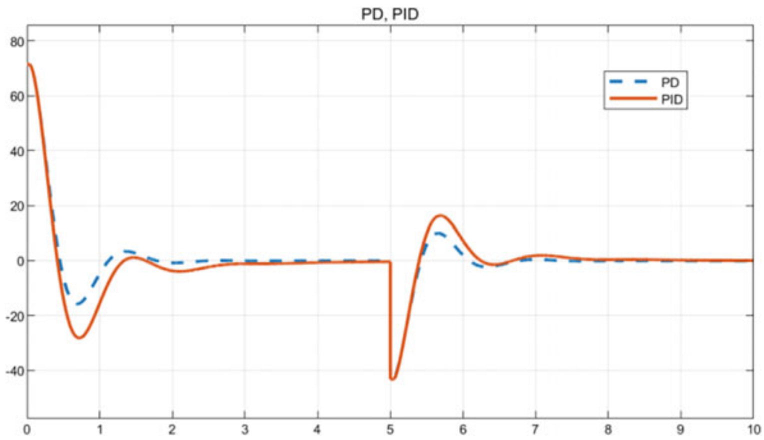

Fig. 3 Simulation results

$$V(e_x, e_{vx}) = 1.5 \cdot e_x^2 + 1.9 \cdot e_{vx}^2 + 0.15 \cdot e_x \cdot e_{vx} \quad (3)$$

which is positive definite and its derivative along the trajectories of the closed loop system is negative for initial points close enough to the desired point.

Therefore, for practical implementation the PD controller (2) was chosen. The controller was then implemented in Python and loaded on the board to control the servo motors in discrete time, with a sampling period of $Ts = 0.03$ sec. Implementation on the hardware allowed fine adjustments, such as taking into account a delay that occurs due to the video camera of the phone that captures the image and optimizations in real time.

The experimental results can be seen in Fig. 4. We have also tested the disturbance rejection capabilities at second 49 when a disturbance occurs, which is rejected.

A video of one of the experiments is available at https://www.lendek.net/files/videos/raad24.mp4

6 Conclusions

This paper describes a solution for stabilizing a ball on a rectangular surface. By using a three-arm servo-driven system with image-based control, the project demonstrates the potential of combining several domains (3D printing, image processing, robot and servo motor control). Stabilization and disturbance rejection was achieved using a PD controller.

Extending this perspective could have significant applications in the field of rehabilitation. Medical robots are used to assist in the medical rehabilitation of patients

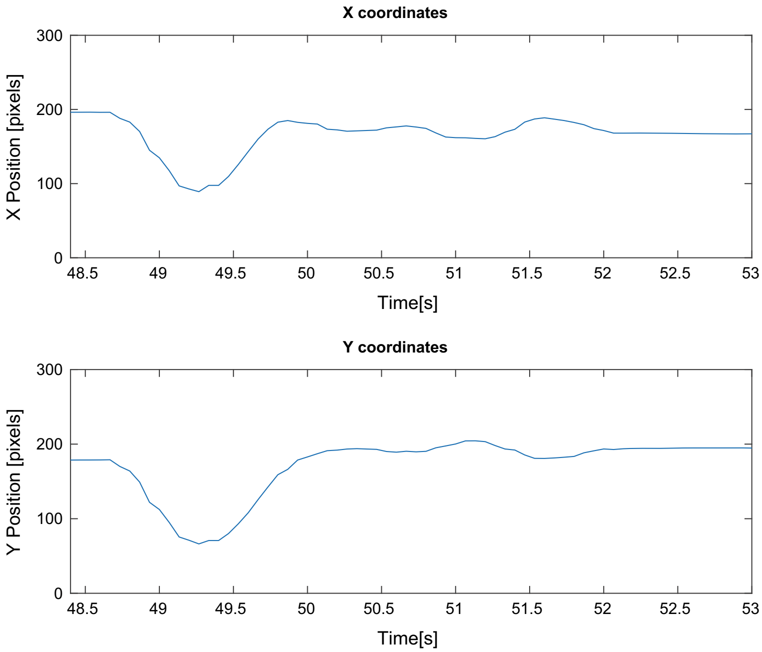

Fig. 4 Experimental results

with different neuromotor deficits, helping to improve mobility and motor function. Similarly to controlling the position of the ball, a PD controller is useful for developing advanced human–robot interactive activities.

By implementing an advanced detection system, without the need for additional markers, the platform allows ball tracking in this initial project. Similar approaches will be developed to detect the position of a limb, either upper or lower, by analyzing its relative movements to the joint in question. The images provide real-time data about the position and movement, thus contributing to the effective assessment and management a rehabilitation process. Several modes of human–machine interactions in which position control is necessary are described in [18]. By implementing a position control algorithm, this platform has the potential to become a useful tool to assist patients in executing correct and controlled movements [25]. The control algorithm is simple enough to be implemented in medical rehabilitation where active human–robot interaction, combined with other multimodal stimulation techniques has shown great potential based on multiple clinical trials with assistive, resistive and path guidance as elective control solutions for chronic patients [17]. A pilot study for this control solution on a lower limb rehabilitation device is scheduled for clinical trials this year.

Acknowledgements This research was supported by the project New frontiers in adaptive modular robotics for patient-centered medical rehabilitation–ASKLEPIOS, funded by European Union–NextGenerationEU and Romanian Government, under National Recovery and Resilience Plan for Romania, contract no. 760071/23.05.2023, code CF 121/15.11.2022, with Romanian Ministry of Research, Innovation and Digitalization, within Component 9, investment 18.

References

1. Ghosal, A.: Robotics: fundamental concepts and analysis. Oxford University Press (2006)
2. Lynch, K.M., Park, F.C.: Modern robotics. Cambridge Univesity Press (2017)
3. Raheja, J.L., Shyam, R., Kumar, U., Prasad, P.B.: Real-time robotic hand control using hand gestures. In: 2010 Second International Conference on Machine Learning and Computing. Bangalore, India (2010)
4. Niku, S.B.: Introduction to Robotics: Analysis, control. John Wiley & Sons, Applications (2020)
5. Padhy, P.K., Sasaki, T., Nakamura, S., Hashimoto, H.: Modeling and position control of mobile robot. In: 2010 11th IEEE International Workshop on Advanced Motion Control (AMC). Nagaoka, Japan (2010)
6. Karnopp, D.C., Margolis, D.L., Rosenberg, R.C.: System dynamics: modeling, simulation, and control of mechatronic systems. John Wiley & Sons Inc, (2012)
7. Proakis, J.G., Manolakis, D.G.: Digital signal processing, third edition ed. Prentice-Hall International INC (1996)
8. Rabiner, L.R., Gold, B.: Theory and application of digital signal processing. Prentice-Hall (1975)
9. Janschek, K.: Mechatronic systems design: methods, models, concepts. Springer (2012)
10. Yuen, H., Princen, J., Illingworth, J., Kittler, J.: Comparative study of hough transform methods for circle finding. Image Vis. Comput. **8**, 71–77 (1990)
11. Arduino Libraries (Online). Available: https://www.arduino.cc/reference/en/libraries/servo/
12. Arduino Functions. (Online). Available: https://www.arduino.cc/reference/en/language/functions/communication/serial/.
13. Lohmann, B.: Control systems, robotics and automation: system analysis and control. Classical Approaches-III, EOLSS (2009)
14. Fornarelli, L., Young, J., McKenna, T., Koya, E., Hedley, J.: Stastaball: design and control of a statically stable ball robot. Robotics **34**, 12 (2023)
15. Prakash, R., Behera, L., Mohan, S., Jagannathan, S.: Dynamic trajectory generation and a robust controller to intercept a moving ball in a game setting. IEEE Trans. Control Syst. Technol. **28**, 1418–1432 (2020)
16. Longhui, Q., Haijun, P., Xiaonan, H., Mingchao, L., Weicheng, H.: Modeling and simulation of dynamics in soft robotics: a review of numerical approaches. Curr. Robot. Rep., 1–13 (2023)
17. Pour, R.K., Khajvand, H., Moosavian, S.A.A.: Fuzzy logic trajectory tracking control of a 3-RRS ball and plate parallel manipulator. In International Conference on Robotics and Mechatronics. Tehran, Iran (2016)
18. Sheet, S.M.S.D.: EE.II.AC (Online). Available: http://www.ee.ic.ac.uk/pcheung/teaching/DE1_EE/stores/sg90_datasheet.pdf
19. Berghuis, H., Nijmeijer, H.: Global regulation of robots using only position measurements. Syst. Control Lett. **21**, 289–293 (1993)
20. Kuncan, M., Kaplan, K., Acar, F., Kundakci, M.I., Ertunc, M.H.: Fuzzy logic based ball on plate balancing system real time control by image. Int. J. Nat. Eng. Sci. **10**(3), 28–32 (2016)
21. Basteris, A., Nijenhuis, S.M., Stienen, A.H., Buurke, J.H., Prange, G.B.: Training modalities in robot-mediated upper limb rehabilitation in stroke: a framework for classification based on a systematic review. J. NeuroEngineering Rehabil. **11** (2014)

22. Mohammadi, A., Ryu, J-C.: Neural network-based PID compensation for nonlinear systems: ball-on-plate example. Int. J. Dyn. Control. **8** (2020)
23. Awtar, S., Bernard, C., Boklund, N., Master, A., Ueda, D., Craig, K.: Mechatronic design of a ball-on-plate balancing system. Mechatronics **12**(2), 217–228 (2002)
24. Tohanean, N., Tucan, P., Vanta, O.-M., Abrudan, C., Pintea, S., Gherman, B., Burz, A., Banica, A., Vaida, C., Neguran, D., Ordog, A., Tarnita, D., Pisla, D.: The efficacity of the neuroassist robotic system for motor rehabilitation of the upper limb—promising results from a pilot study. J. Clin. Med. **12**, 425 (2023)
25. Acosta, G., Núñez López, J., Jiménez-Builes, J.: Control of a ball-and-plate system using a State-feedback controller. Ingeniare **28**, 6–15 (2020)

Part VI
Service Robotics and Applications

Embracing the Gentle Touch: Design and Simulation of an Intelligent Soft Fingertip for Adaptive Agricultural Harvesting

Nader Al Khatib and Daniele Cafolla

Abstract The increasing needs of a swiftly growing global population have emphasized the limitations of conventional agricultural methods, especially in agricultural harvesting. Interestingly, the agricultural labour force is anticipated to decrease resulting in unharvested and a subsequent loss of products. This paper presents an intelligent robotic end-effector designed for transformative applications across diverse industries, particularly in manufacturing and agriculture. The innovative system integrates engineering advancements and simulation refinement to achieve adaptability, precision, and controlled release capabilities. Looking forward, the continuous refinement and optimization of this technology are deemed essential. The paper concludes by positioning this project as both a culmination of current achievements and a foundation for the evolving field of intelligent robotic manipulation.

Keywords Intelligent robotics · Agricultural robotics · Harvesting · Manipulation · Baromorph end-effector

1 Introduction

The escalating demands of a rapidly expanding global population heavily highlighted the inadequacies in traditional agricultural practices, particularly in the realm of agricultural harvesting. Forecasts suggest a 40% surge in human numbers by 2050, necessitating a doubling of fruit production on a correspondingly expanded agricultural area [1]. Paradoxically, the labour force in agriculture is predicted to halve, implicating a deficit of around 5 million harvesters and consequentially, products

N. Al Khatib (✉) · D. Cafolla
Faculty of Science and Engineering, Department of Computer Science, Swansea University, Swansea, UK
e-mail: nader.alkhatib@swansea.ac.uk

D. Cafolla
e-mail: daniele.cafolla@swansea.ac.uk

D. Pisla et al. (eds.), *Advances in Service and Industrial Robotics*, Mechanisms and Machine Science 157, https://doi.org/10.1007/978-3-031-59257-7_51

worth the annual consumption of the European Union go unpicked annually [2]. This presents an exigent issue where an estimated USD 30 billion is lost in sales, underlining the urgency for groundbreaking solutions [3].

In this light, the advent of intelligent robotics presents a compelling avenue, with the capacity to address labour deficits and reinforce the efficiency of harvesting operations [4]. Prior endeavours in automating harvesting operations have focused on emulating the dexterity and sensory perception of human hands, keenly observed in manual harvesting [5, 6]. The role of end-effectors has become a focal point of inquiry due to their direct relation to the integrity of the harvest and operational efficacy [5–7, 8]. Advanced methods of fabrication such as 3D printing, alongside computational tools like finite element analysis, are leveraged in the design cycle to enhance the performance of these end-effectors [7].

Pioneering end-effectors drawn inspiration from nature, the Festo's bionic "chameleon gripper", are inspired by nature's adaptability, mimicking the chameleon's tongue in dexterousness and sensitivity, and excelling in handling irregularly shaped objects [8]. This approach embodies a profound intelligence of biomimicry, crafting robotic solutions that are as ingenious as they are functional.

A variety of current research supports this new approach in the realm of robotic harvesting. For example, a study extends the comprehension of the interplay between robotic mechanism and agricultural efficiency, proposing a novel dual-arm robotic harvester optimized for a specific crop architecture [10]. These advancements, coupled with others from emerging research, such as the development of a robotic harvester adept at navigating the unpredictable terrain of an orchard floor [8], or the design of advanced machine learning algorithms for precise fruit detection and picking [11], highlight the dynamic progression of the sector.

Synthesizing these advancements with existing literature underscores a trend in agricultural robotics towards solutions that are finely tuned, targeted, and adaptive. The emerging path aims to bridge crucial gaps in labour and production, harmoniously aligning with the pressing sustainability and ecological goals of the modern era.

Profound innovation in harvesting technology and overall agricultural productivity hinges on the seamless integration of robotic systems that embody ingenuity, effectiveness, and adaptability to the unpredictable elements intrinsic to nature. Grounded in rigorous academic exploration and developmental work, these strides in technology have the potential to become the key in surmounting the dual challenges of a soaring global populace and a contraction in agricultural labour.

In this paper, the proposal introduces a distinct angle introducing embedded channels with a specific morphology for compressed air within the fingertips themselves in combination with rigid structures, allowing for fine-tuned control over grip stiffness in different scenarios. The proposed solution balances the malleable nature of existing grippers with the durability of traditional mechanisms, offering a transformative approach to grip modulation that can be adjusted in real-time. The fingertips can morphologically adapt their embedded shape and texture to enhance embracement and minimize damage, ensuring the integrity of a diverse range of harvested goods, from the robustness of root vegetables to the delicacy of vine-ripened tomatoes. The design and simulation of compliant soft modular fingertips is introduced, inspired by the nuanced movement and adaptability of human fingertips. Different morphologies have been tested and the one that endeavours to encapsulate the deft touch required to handle different ranges of agricultural products without compromising speed or convenience has been chosen.

The goal of the presented concept is to push the existing frontiers of agricultural robotics by seamlessly integrating advanced sensing and actuation techniques with principles derived from soft robotics. This integration aims to harmonize the traditionally conflicting demands of gentle handling and operational efficiency in the context of harvesting applications.

2 Device Operation Principle

The heart of the system lies in the cellular cushions distributed across the end-effector's gripping surface. These cushions, resembling cells, facilitate adaptability and precision in robotic handling. Figure 1 shows the conceptual scheme of the proposal.

What sets this system apart is the incorporation of precision valves or pumps, acting as gatekeepers for the inflation and deflation of cellular cushions. The valves, that will have a future development, receive instructions from the intelligent system, which conducts a prior analysis of the surface characteristics of the target object. This strategic analysis enables the system to determine optimal grip parameters, considering factors like texture, shape, and material composition. Additionally, the adaptability of cell dimensions adds another layer of sophistication to the system. The

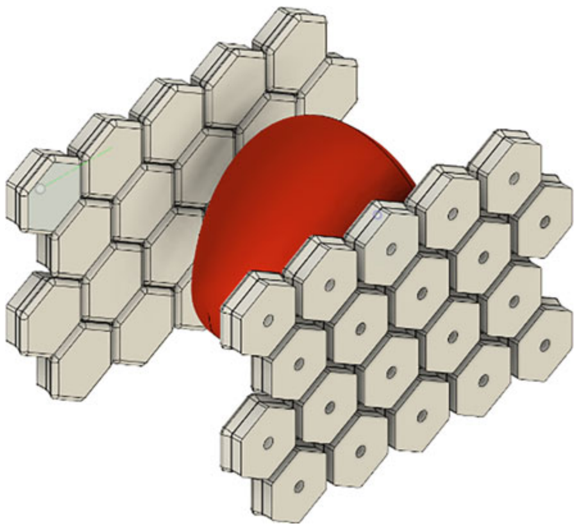

Fig. 1 Scenario of strawberry picking with double plates

cellular cushions, being the fundamental building blocks, can be tailored to specific needs and spatial constraints. In contrast to this, the before mentioned systems, while also incorporating adaptive features, lack the customization, that facilitates a fine-tuned adaptation to diverse objects. The proposed cellular cushions, akin to fundamental building blocks, offer a high degree of customization. Tailoring the dimensions of these cells becomes a strategic option, allowing the system to be fine-tuned to specific requirements and spatial constraints. This adaptability in cell dimensions represents a dynamic characteristic not explicitly mirrored in systems that primarily focus on geometric adaptability without the added dimension of regulating pressure.

The integration of cellular cushions, coupled with the future development of precision controls, positions our system as a comprehensive solution that excels not only in adaptability to object geometry but also in regulating the pressure exerted during the gripping process. This dual functionality distinguishes our system from others in the field, contributing to a more nuanced and precise approach to robotic handling.

3 Fingertip Module Simulation

To understand the capability of the proposed design a FEM analysis using the described conceptual design has been analysed using the material which characteristics are shown in Table 1. The fingertip inflation mechanism utilizes a specific air intake located at the back of each module, with its position determined by the application identified with the letter “C.” Furthermore, Fig. 2 shows the adaptability of the module’s shape (B), and dimensions (A) allows for customization, catering to the unique needs of gripping different products.

For this simulation, a module of A = 22.05 mm and B = 120.00° has been set.

The simulation centres around a simplified representation of a strawberry, acting as a model object enclosed by the inflating cushion array. In this regard, a targeted air pressure range of 0.00–1.00 bar was chosen as a benchmark for the specific example, providing a foundation for customizing deformation according to the component’s specifications.

Ensuring the attainment of the designated pressure within the gripping system is fundamental for optimizing its performance and adaptability across diverse gripping. This approach allows for the utilization of compressors or dedicated air pumps to

Table 1 FEM input parameters

Parameters	Value
Material:	Silicon, rubber
Density	1.25E-06 kg/mm^3
Poisson ratio	0.49
Young’s modulus	0.003 GPa

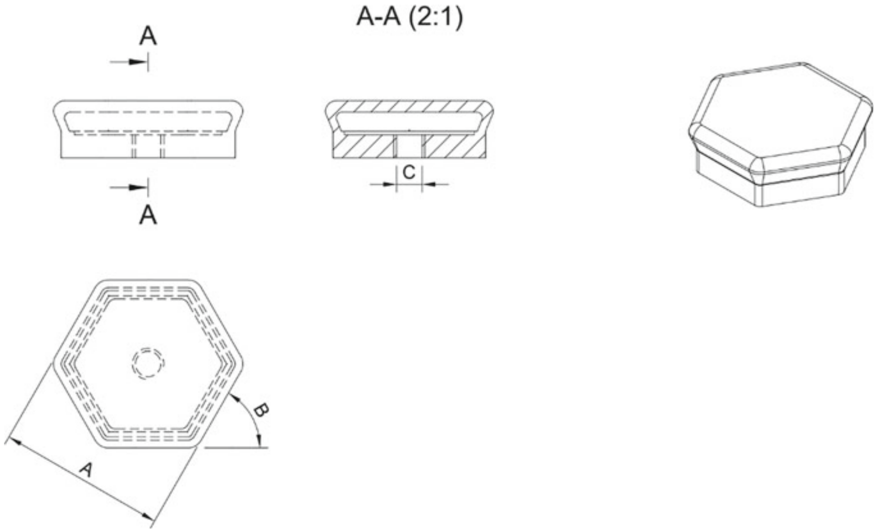

Fig. 2 Technical drawings of the specific module

deliver air to the cellular cushions distributed across the gripping surface of the end-effector. It is crucial to acknowledge that employing components with diverse shapes, thicknesses, and materials may necessitate adjustments in the pressure settings. This adaptability ensures that the system can dynamically accommodate variations in the characteristics of the components being gripped, underscoring its versatility across a spectrum of applications.

Specifically, the simulation addresses three key stages of inflation, each aligned with precise pressure levels: 0.00 bar, 0.50 bar, and 1 bar.

The observed displacement plays a consequential role as it gives rise to a distinct cavity, demarcated by the differential in displacement. The existence of this cavity is visually corroborated in the figures presented in Sections in Fig. 3 and in Fig. 4. Notably, during this process, the maximum displacement observed is 7.86 mm, that can be seen in the Fig. 5. These sections offer a visual narrative, illustrating how the cavity forms and functions as an enveloping structure for the product held within the grasp of the end-effector.

The results of this simulation quantify the system's performance through key parameters such as displacement and shows the dynamic process of cavity formation. This dual assessment contributes to a comprehensive understanding of how the proposed system effectively adapts to different pressure scenarios, offering a glimpse into its potential applications in real-world gripping and handling scenarios.

Furthermore, the simulation results align with anticipated behaviour, highlighting the system's adaptive capabilities and precision. One identified vulnerability in the proposed gripping system lies in the potential risk of puncturing and subsequent air loss from the surface. However, a strategic mitigation approach is envisioned to address this concern effectively. By incorporating an additional protective layer

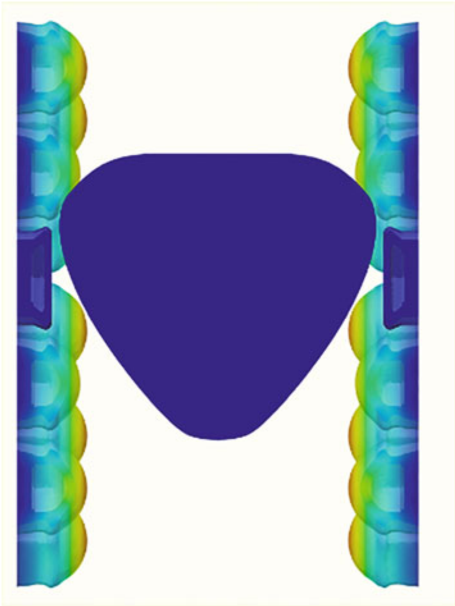

Fig. 3 Section view of the inflating areas

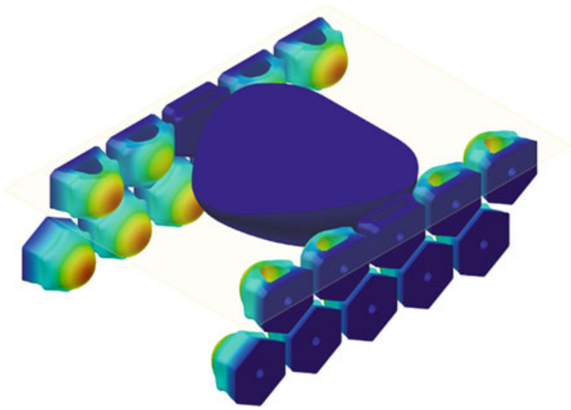

Fig. 4 Section view of the inflating areas in isometric view

or a soft isolating material, the system can bolster its resilience against puncturing objects.

This supplementary layer serves as a preventive barrier, acting as a shield between the external environment and the air chamber within the gripping surface. In the event of contact with sharp or puncturing objects, the protective layer absorbs or deflects potential threats, minimizing the risk of damage to the system's integrity. This proactive measure not only safeguards against air loss but also enhances the overall durability and longevity of the gripping mechanism. The significance of these findings lies in the system's ability to dynamically create a designated space,

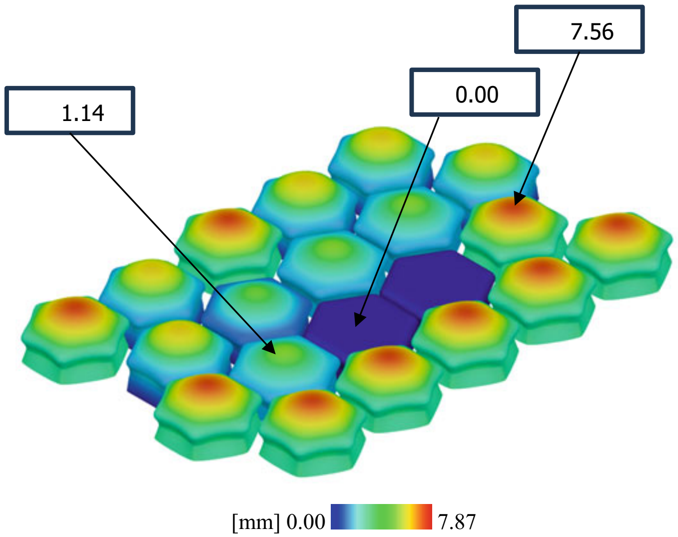

Fig. 5 Deformation scale

or cavity, for the grasped product at different pressure levels. This adaptive response, highlighted through the simulation stages, underscores the nuanced control and versatility embedded in the proposed gripping mechanism. As the pressure levels vary, the system adeptly adjusts, influencing the displacement and consequent formation of the enveloping structure, thereby ensuring optimal handling of diverse products.

Finally, the FEM results shed light on several crucial aspects of the system:

- Pressure Distribution: The simulation provided insights into how the cellular cushions distribute pressure across the gripping surface during inflation. This is paramount in understanding how the system adapts to different gripping scenarios and pressures.
- Deformation Patterns: By analysing deformation patterns under different conditions, the FEM offered a nuanced understanding of how the system responds to external forces and object geometries. This is crucial for ensuring controlled and precise gripping.
- Stress Analysis: The FEM highlighted stress concentrations within the system, guiding the identification of potential weak points. Addressing stress concentrations is essential for enhancing the overall structural integrity and reliability of the system.
- Dynamic Response: The FEM simulations delved into the dynamic response of the system during gripping and releasing actions. This provided valuable insights into the system's adaptability and responsiveness in real-world applications.

4 Conclusions

This project's integrated approach, encompassing engineering innovation, and simulation refinement, positions the intelligent robotic end-effector as a transformative solution in diverse industries. From manufacturing to agriculture, its adaptability, precision, and controlled release capabilities promise to redefine the landscape of robotic manipulation. A comprehensive FEM was conducted to scrutinize the structural behaviour of the proposed gripping system. The analysis encompassed diverse scenarios, evaluating the system's response to varying pressures, deformations, and potential stress points. The key objective was to ascertain the system's robustness and its ability to withstand operational challenges, including the identified weak point of potential puncturing and air loss.

Ongoing refinement and optimization of this technology will be essential. This project serves not only as a culmination of current achievements but as a foundation for the evolving field of intelligent robotic manipulation.

References

1. Godfray, H.C.J., Beddington, J.R., Crute, I.R., Haddad, L., Lawrence, D., Muir, J.F., Pretty, J., Robinson, S., Thomas, S.M., Toulmin, C.: Food security: the challenge of feeding 9 billion people. Science **327**(5967), 812–818 (2010)
2. Canning, P., Charles, A., Huang, S., Polenske, K.R., Waters, A.: Energy use in the U.S. food system. USDA Economic Research Report No. (ERR-94), p. 33 (2010)
3. Tilman, D., Balzer, C., Hill, J., Befort, B.L.: Global food demand and the sustainable intensification of agriculture. Proc. Natl. Acad. Sci. **108**(50), 20260–20264 (2011)
4. Kondo, N., Monta, M., Fujiura, T.: Robotic harvesting system for eggplants. Comput. Electron. Agric. **25**(1–2), 133–148 (2000)
5. Harrell, R.C., Adsit, P.D., Nadler, M.: Agricultural robotics. In: Shimon, Y. (ed.) Handbook of Industrial Robotics, 2nd edn., pp. 1195–1208. John Wiley & Sons, Inc. (1999)
6. Van Henten, E.J., van't Slot, D.A., Hol, C.W.J., van Willigenburg, L.G.: Optimal manipulation of plant stems in cut-tulip harvesting. Comput. Electron. Agric. **33**(1), 1–21 (2002)
7. Hughes, J., Culha, U., Giardina, F., Guenther, F., Rosendo, A., Iida, F.: Soft manipulators and grippers: a review. Front. Rob. AI **3**, 69 (2016)

Increasing the Energy Efficiency of Robotic Workplaces

Rostislav Wierbica, Jakub Krejčí, Václav Krys, and Tomáš Kot

Abstract Like other industrial sectors, the robotics industry is pressured to reduce energy consumption while maintaining production efficiency. In addition to the economic benefits, reducing consumption also reduces the carbon footprint of production. While reducing consumption by changing mechanical structures and restructuring production lines can be beneficial, it reduces the versatility of robotic workplaces and is time-consuming. Our proposed solution reduces the energy consumption of the robotic workstation based on the optimal placement of the work object in the robotic cell. In this case, the optimization process is simulated on an industrial robot software platform. The result of the optimization is the determination of the most energy-optimal position for the placement of the work object. In experiments, it was found that up to 71.8% of the energy consumption of the 6-DOF industrial robot can be saved by this approach. The correlation between the simulated and real workplace tasks was also verified.

Keywords Energy consumption · Industrial robot · Workplace layout · Simulation · Optimization · Industry 5.0

1 Introduction

The motivation for energy optimization of robotic workplaces is primarily to reduce the economic burden of these workplaces, to save costs in the industry and to reduce the carbon footprint of production, which is part of the Industrial Revolution 5.0 [1]. Numerous studies described in this survey [2] come up with several different approaches for reducing energy consumption. These include optimizing non-energy efficient components in the design, which, for example, includes appropriately selected powertrains for each robot axis. Optimization of mechanical structures that address the lightweighting of robot arms and reduction of inertial force. Regular maintenance of the robot system can also achieve energy savings, which will lead

R. Wierbica (✉) · J. Krejčí · V. Krys · T. Kot
Department of Robotics, VSB—Technical University of Ostrava, 708 00 Ostrava, Czech Republic
e-mail: rostislav.wierbica@vsb.cz

D. Pisla et al. (eds.), *Advances in Service and Industrial Robotics*, Mechanisms and Machine Science 157, https://doi.org/10.1007/978-3-031-59257-7_52

to higher component efficiency. In our study, we present an approach through the robot software that focuses on the proper setup of the operation itself. Unlike the [3] paper, where the measurement is performed using an external 3-phase power quality analyzer, our study uses only software tools to determine the optimal settings. When using RobotStudio software for the ABB family of robots, we assume that the dynamic model does not differ from the real robot model. With this assumption, we can simulate the robot's task in all possible settings and situations and determine the most suitable position for energy consumption. The paper also describes the software developed to filter out invalid robot positions so that only valid positions are included in the simulation. Similarly to paper [4], we examine various robot parameter settings, such as robot speed. Part of our work also focuses on the configuration of the robot's joints, which significantly impact energy consumption. The optimization process results in an energy map indicating the positions where the lowest energy consumption is expected. Implementing this methodology in production planning using industrial robots would lead, as already mentioned, to economic and environmental savings.

1.1 Inputs for the Optimization Process

The assumed inputs for the optimization process are models of the robot and its workplace, including all peripherals. Models should be as close to reality as possible but do not have to be exact replicas. In principle, the more accurate the models are, the more accurate the simulation results are expected to be. Anyway, we can use simplified models for peripherals that are relevant for the simulation only because of possible collisions with the robot when performing the task. As mentioned in the introduction, a prerequisite for relevant simulation results is a dynamic and kinematic robot model. For this reason, the ABB RobotStudio software, which is expected to fulfil this requirement, is used. If a similar simulation tool was not used, it would be necessary to follow a similar procedure as in the [5] article, which describes identifying a dynamic robot model. Another expected input for the simulation is the exact trajectory of the robot's TCP (Tool Center Point) that the industrial robot executes when performing a given task. For this reason, our proposed optimization procedure is particularly suitable for applications with a technologically fixed trajectory, such as robotic deburring, gluing, sealing, etc.

2 The Optimization Procedure

The goal of this research is not to find the optimal trajectory but to find the optimal location of the trajectory concerning the robot in the robot workspace and also to find the optimal robot joint configuration (pose) for a given trajectory. The search for trajectory positions in space is performed to compare the energy consumption at different locations in the robot's workspace. When designing a workspace, the robot may be placed in an energetically disadvantageous position. At the same time, there may be a position in which the robot performs the same task with less energy consumption. So, as a part of the optimization process, shown in the Fig. 1, the entire workspace of the robot in which the task can be performed is searched. After this, all valid positions found are compared regarding robot energy consumption. Because of the many possible entry positions, custom software is used to find all theoretically valid trajectory positions. Note that this software is unnecessary for this application, but its use will speed up the entire simulation process. The procedure for finding trajectory positions is described in Sect. 2.1. Two case studies were conducted to verify the simulations. For this purpose, two robotic workstations were chosen, each designed for a different technological operation. The results of the studies are presented in Sect. 2.3.

2.1 *Preparing the Grid of Work Object Placement Options*

The trajectories are always programmed from a reference WorkObject, a user-defined coordinate system. A custom simulation software is used to find the positions of these WorkObjects. In this software, the robot's kinematic parameters (Denavit-Hartenberg parameters, joint ranges) and collision volumes are defined. The software is used to find all possible positions of the WorkObjects in which the robot can perform the desired task. This is done in a discrete representation of the workspace—in a grid, so only positions a chosen distance apart (in our case—50 mm) are tried. This process is done to save simulation time in the following steps—it is not desirable to perform full dynamic simulation on tasks that the robot cannot fulfill for kinematic, dimensional or collision reasons. For the first case study in Fig. 2a, 66,873 positions were theoretically possible, but only 6726 valid positions remained after filtering out.

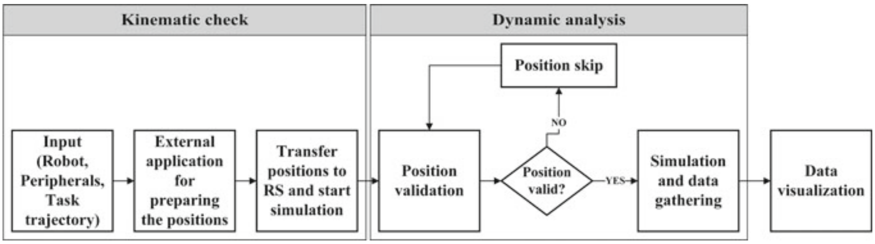

Fig. 1 Flowchart of the optimization procedure

Although the robot's kinematic parameters and collision volumes are defined in the custom software, it may happen that some positions of the filtered work objects will be invalid for the real robot. This is because our software does not know all the constraints of the real robot. These constraints will only occur during the simulation in RobotStudio. Therefore, modifying the simulation to check these positions beforehand is necessary. If a given position of a WorkObject is found to be invalid, the position is skipped. This will achieve as much automation of this process as possible.

2.2 Description of the Case Studies

Two case studies were conducted with two different trajectories and two different robots to evaluate the results. As a first case study in the Fig. 2a, a task that could simulate robotic deburring is chosen. An ABB IRB1600-10/1.2 robot is used, considering an end effector (payload) of 2.8 kg. The robot's TCP speed is 100 mm/s, and the cycle time is 12.4 s. The simulation model is created in RobotStudio. In this sim-

(a) ABB IRB 1600 (real workplace)

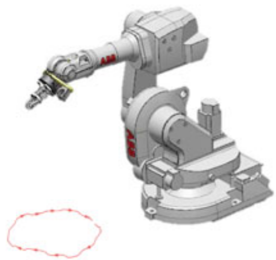

(b) ABB IRB 1600 (simulation)

(c) ABB IRB 140 (real workplace)

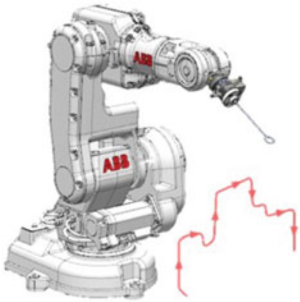

(d) ABB IRB 140 (simulation)

Fig. 2 Illustration of case studies

ulation scene, a virtual controller is created based on a backup of the real controller from the workstation. The experiment always considers the same circular trajectory, which is not flat – it changes in the z-axis with a radius of 350 mm. As a second case study in the Fig. 2c, a task that could simulate robotic sealing or the application of a sealing compound is chosen. An ABB IRB 140-6/0.81 robot is used, considering an end effector (payload) of 1 kg. The robot's TCP speed is 100 mm/s, and the cycle time is 18 s. The simulation model is created in RobotStudio as in the previous case. In the experiment, a variously shaped planar trajectory is considered.

2.3 Simulation Results

The results from the first case study show that the influence of the trajectory position and the robot configuration used is significant. In this case, two possible robot configurations were used to perform the task. Figure 3 presents the simulated energy consumption results. Shown are energy maps that show different robot configurations. The energy consumption is expressed as a color spectrum from green to red. The blue line shows the simplified kinematic structure of the robot. For configurations 1 and 2, significantly more energy-intensive locations can be found. Table 1 shows the lowest and highest energy consumption for each robot configuration and the percentage differences between the lowest and highest values. For this particular case, an energy saving of 65.5% can be achieved by performing the same task.

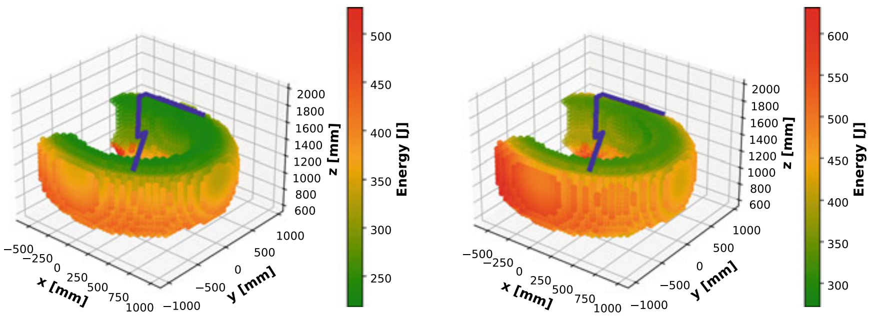

(a) Energy consumption conf 1 (b) Energy consumption conf 2

Fig. 3 Energy consumption of the robot IRB 1600

The results from the second case study with the ABB IRB 140 robot confirm the results from the previous study—the influence of the trajectory position and the robot configuration used on the energy consumption is also evident here. In this case, four possible robot configurations were used. For this task, the number of valid positions varies considerably between the different robot configurations. Figure 4

Table 1 Energy consumption of IRB 1600

Joint configuration	Lowest energy [J]	Highest energy [J]	Energy difference [%]	Maximum energy difference [%]
1	218	527	58.6	
2	272	631	56.9	65.5

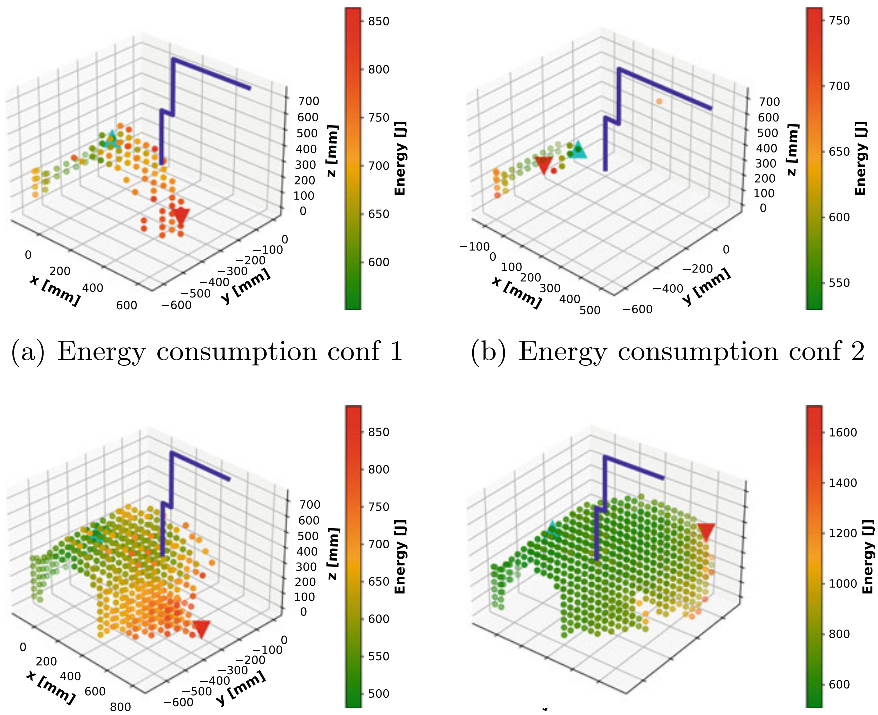

(a) Energy consumption conf 1 (b) Energy consumption conf 2

(c) Energy consumption conf 3 (d) Energy consumption conf 4

Fig. 4 Energy consumption of the robot IRB 140

presents the simulated energy consumption results, the same description applies here as in the previous case. Table 2 shows each robot configuration's most minor and most significant energy consumption. Also, the percentage differences between the smallest and largest values are shown. For this particular case, an energy saving of 71.8% can be achieved by performing the same task.

Table 2 Energy consumption of IRB 140

Joint configuration	Lowest energy [J]	Highest energy [J]	Energy difference [%]	Maximum energy difference [%]
1	551	864	36.2	
2	530	759	30.2	71.8
3	481	884	45.6	
4	507	1703	70.2	

2.4 Simulation Verification

Three comparative measurements were made to understand better how the energy consumed from the simulation model and the real workplace differ. The measurements were performed on an ABB IRB1600-10/1.2 robot with a robot endpoint speed of 100 mm/s and a cycle time of 12.4 s. A certain correlation can be seen in the Fig. 5 when comparing the results from the simulation model and the real measurements. The simulation's energy consumption waveforms match the real measurements' waveforms. However, they differ in the values—e.g. one cycle of the first comparison measurement has a consumption of 389 J in the simulation and 478 J in the real measurement, a difference of 18.6%. A similar difference was measured for the second measurement, which was 19.5%. The most significant difference of 27.2% was found in the third measurement. The differences between the simulations

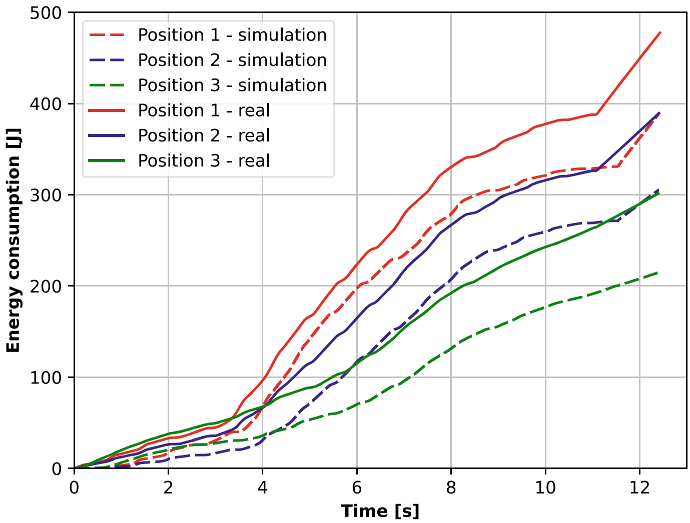

Fig. 5 Energy comparison of simulation and real measurement

and the real measurement are most likely due to the inaccurate dynamic model in RobotStudio, non-existent resistance, missing wiring, etc.

3 Conclusion and Future Work

Our paper describes a procedure to optimize the layout inside a robotic workplace to reduce energy consumption and execute a work cycle for selected process applications. It is worth noting that the approach in this research considers finding the relative position of trajectories between the robot and the robot workstation. Thus, it does not matter if it is looking for the location of the trajectory relative to the robot or the robot's location relative to the trajectory. In this article, we search for the location of trajectories relative to the robot. Applying the optimization to two case studies shows that up to 71.8% of the robot's energy consumption can be saved in this way. In our approach, we also use our software, which can significantly speed up the simulation in the case of more complex robot trajectories. For example, in the first case study, the trajectory consists of 116 points—with this number of points, the check in the custom software takes 0.43 s. In RobotStudio, this check would take approximately 1200 s, which is 3000 times longer. Significant time savings can be achieved when designing robot workstations frequently, working with more complex trajectories and working with multiple robots. The method was tested on two serial robots but we presume it is applicable to other kinematic structures as well.

Future work should primarily focus on the applicability of this solution to a broader spectrum of robots. The custom software to classify possible positions could also be used to efficiently use resources, e.g., to recommend a more energy-efficient robot. By positioning the robot or the trajectory appropriately in the workplace, it may be possible to find a robot that is, for example, smaller and lighter but with sufficient carrying capacity to perform the task. Furthermore, there is also an expectation to apply the optimization to multiple workstations to debug potential problems better. Finally, future simulations could implement modern AI technologies—for example, reinforcement learning.

Acknowledgements This article was co-funded by the European Union under the REFRESH—Research Excellence for Region Sustainability and High-tech Industries project number CZ.10.03.01/00/22_003/0000048 via the Operational Programme Just Transition and by specific research project SP2024/082, financed by the state budget of the Czech Republic.

References

1. Maddikunta, P.K.R., Pham, Q.-V., Deepa, P.B.N., Dev, K., Gadekallu, T.R., Ruby, R., Liyanage, M.: Industry 5.0: a survey on enabling technologies and potential applications. J. Ind. Inf. Integr. **26**, 100257 (2022)

2. Soori, M., Arezoo, B., Dastres, R.: Optimization of energy consumption in industrial robots, a review. Cogn. Robot. **3**, 142–157 (2023)
3. Rassõlkin, A., Hõimoja, H., Teemets, R.: Energy saving possibilities in the industrial robot irb 1600 control. In: 2011 7th International Conference-Workshop Compatibility and Power Electronics (CPE), pp. 226–229. IEEE (2011)
4. Paryanto, Brossog, M., Kohl, J., Merhof, J., Spreng, s., Franke, J.: Energy consumption and dynamic behavior analysis of a six-axis industrial robot in an assembly system. Procedia CIRP **23**, 131–136 (2014). 5th CATS 2014—CIRP Conference on Assembly Technologies and Systems
5. Ding, L., Wu, H., Yao, Y., Yang, Y.: Dynamic model identification for 6-dof industrial robots. J. Robot. **2015**, 9 (2015)

Design of an Under-Actuated Mechanism for Collecting and Cutting Crop Samples in Precision Agriculture

Giuseppe Quaglia, Luca Samperi, Lorenzo Baglieri, Giovanni Colucci, Luigi Tagliavini, and Andrea Botta

Abstract Automating the processes of sampling and harvesting in precision agriculture is essential to expand the range of potential application scenarios. In this regard, this paper presents the design and development of an under-actuated device for grapevine harvesting and sampling. The tool is intended to be part of a set of tools from which a rover for precision agriculture can choose to perform various tasks. The tool presented in this paper is designed specifically for the gripper of a 7 d.o.f. robotic arm equipped by the rover Agri.Q, a service robot designed for agriculture. However, the design of the tool can be adapted to work with other robotic arm grippers. In this research, the gripper output contact forces and the required cut forces are experimentally measured to clearly define the design requirements of the tool. Then, the functional design of the system is described and a kinematic model of the mechanism is presented. Finally, the tool prototype is presented and tested with green peduncles ranging from 2 mm to 6 mm in diameter.

Keywords SDG 12 · Autonomous harvesting · Under-actuated mechanism · Service robot · Precision agriculture

1 Introduction

In traditional agriculture, the inherent challenges of resource management, labor efficiency, and environmental impact have long posed significant impediments to sustainable and optimized crop production. Precision agriculture channels technological advancements to address these challenges by incorporating data-driven methodologies [1]. Consequently, the integration of robotics stands out as a promising path. Robots equipped with advanced sensing, actuation, and decision-making capabilities hold the potential to reform farming practices, offering targeted and efficient interventions at a level of precision that is unattainable through traditional means [3].

G. Quaglia (✉) · L. Samperi · L. Baglieri · G. Colucci · L. Tagliavini · A. Botta
DIMEAS Department of Mechanical and Aerospace Engineering, Politecnico di Torino, Corso Duca degli Abruzzi 24, 10129 Torino, Italy
e-mail: giuseppe.quaglia@polito.it

D. Pisla et al. (eds.), *Advances in Service and Industrial Robotics*, Mechanisms and Machine Science 157, https://doi.org/10.1007/978-3-031-59257-7_53

Performing tasks such as harvesting, pruning, or any activity involving the precise cutting and collection of plant parts poses a significant challenge for robots due to the complex nature of the environment [5, 8]. In response to these challenges, the authors have proposed Agri.Q, a mobile robotic platform designed for precision agriculture in vineyards, featuring a robotic arm (Kinova Jaco 2) tailored for interacting with crops [2, 4]. Agri.Q has an eight wheels locomotion system, similar to one previously designed for the small-size robot Epi.q-Mod [6]. While the robotic arm incorporates a two-finger gripper suitable for general grasping tasks, the need for a specialized tool for cutting and collecting plant samples arises. To address this requirement without altering the robotic arm's end-effector, and to enhance flexibility and modularity, this study presents the design of an innovative under-actuated tool previously explored in [7]. This tool is specifically devised to cut and collect samples, utilizing a general-purpose robotic gripper for grasping and actuation of the tool.

2 Design Requirements

The robotic arm gripper must autonomously grasp, hold, and control the tools needed. Moreover, the forces exerted by the gripper fingers should facilitate the tool actuation, initially securing a sample, then cutting its branch, and later storing the sample. Consequently, the designed mechanism should fit the robotic gripper and harness its grasping force to execute its tasks. Therefore, to achieve an optimal design, experimental data were collected for both the gripper grasping force and the required cutting force.

2.1 Gripping Force Evaluation

The design of the presented under-actuated tool for autonomous crop sampling envisions its easy adaptation on robotic grippers with different geometries and architectures. To develop an experimental case study, a tool has been designed and prototype has been built around the commercial Kinova Gen2 KG-2 model. This under-actuated two-finger gripper ensures the manipulation of cylindrical objects ranging from 55 to 100 mm in diameter. Even though different gripping modes are enabled by this gripper architecture, i.e. contact forces can be exchanged in different ways between the four phalanges and the target object, this work only considers a manipulation configuration where the proximal phalanges exert force on the grasping and cutting tool. This choice is based on the experimental characterization of the proximal and distal gripping forces of KG-2 as a function of its two degrees of freedom, which shows that the action of the proximal phalanges alone leads to the highest possible contact forces.

Figure 1a shows the experimental layout used to measure the gripper contact force F_c on the proximal phalange, where the robotic end-effector is kept fixed, and

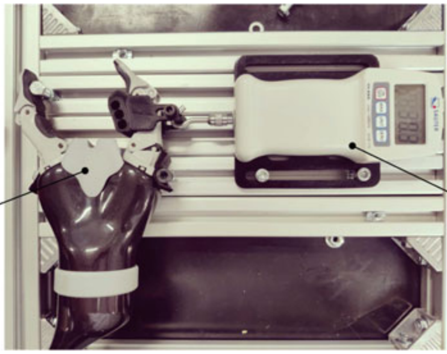

(a)

Test N°	F_c (max closure), N	F_c (min closure), N
1	29.9 ± 1.25	55.6 ± 1.25
2	30.1 ± 1.25	62.8 ± 1.25
3	30.3 ± 1.25	58.4 ± 1.25
4	29.3 ± 1.25	60.6 ± 1.25
5	28.9 ± 1.25	60.5 ± 1.25
6	29.2 ± 1.25	59.4 ± 1.25
7	30.0 ± 1.25	60.7 ± 1.25
8	27.5 ± 1.25	57.6 ± 1.25
9	28.4 ± 1.25	57.8 ± 1.25
10	29.4 ± 1.25	60.3 ± 1.25

(b)

Fig. 1 **a** Experimental setup to evaluate gripper contact force F_c on the proximal phalange in the maximum closure configuration. **b** Experimental results

a digital dynamometer evaluates the orthogonal contact force exchanged with the gripper over its whole range of motion. The contact force, measured as the average value of ten runs, is 59 N in the maximum opening configuration and 29 N in the maximum closure configuration (Fig. 1b).

2.2 Experimental Cutting Forces

To evaluate the force required to cut branches of various diameters, a dedicated experimental setup was devised (Fig. 2a). A blade is fixed to a load cell mounted on a linear guide whose displacement is measured by a potentiometer. A second blade is placed at the end of the linear guide stroke. Several grapevine branches with diameter ϕ ranging from 1.5 mm up to 5 mm and different dryness were tested. For each test, a branch was held above the fixed blade, while the moving blade was pushed down until the branch was cut. Both the cutting force and the blade displacement readings were measured.

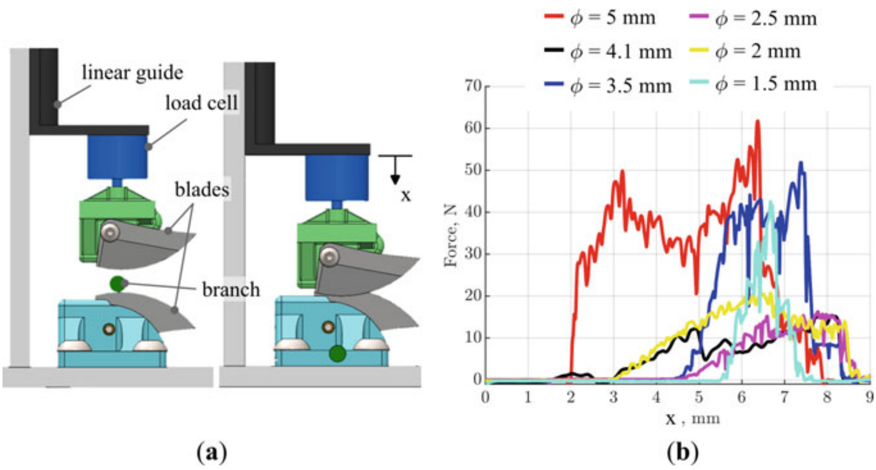

Fig. 2 **a** Experimental setup to evaluate branches cutting force. **b** Force required to cut branches of various diameters

Figure 2b illustrates the filtered experimental data. Each curve depicts the initial contact of the moving blade with the branch (indicated by the onset of force increase) and the moment when the branch is successfully cut (marked by a sudden force drop). Typically, larger branch diameters ϕ correspond to increased cutting forces. However, branch dryness also influences the outcomes. Nevertheless, the primary parameter essential for the design of the cutting tool is the maximum required force, which is 60.6 N.

3 Crop Sampling Tool Design

The under-actuated tool for autonomous crop sampling can be seen as a mechanical system in between the robotic gripper and the target crop. Thus, the gripper specifications and the cutting forces previously discussed constitute a set of requirements for the design procedure. Figure 3 depicts the functional architecture of the tool, namely an under-actuated linkage with four links and two compression springs acting, respectively, between links 1 and 2 and between links 3 and 4. The combined action of these springs and a mechanical end stop (cursor in E) maintains the tool wide open when not actuated, as described by Fig. 3a. For clarity purposes, link 1 is represented as fixed, as well as the two hinge joints in D and B. In this fashion, the input force F_{in} exerted by the robotic gripper is entirely applied in A. Furthermore, C and F are the two points at which the blades cut the branch (Fig. 3b, c).

It should be underlined that, in the actual device, none of the links of the mechanism is fixed to the distal link of the robotic arm. Link 1 and Link 2 have geometrical interfaces that match the geometry of the gripper fingers. One finger applies F_{in} to

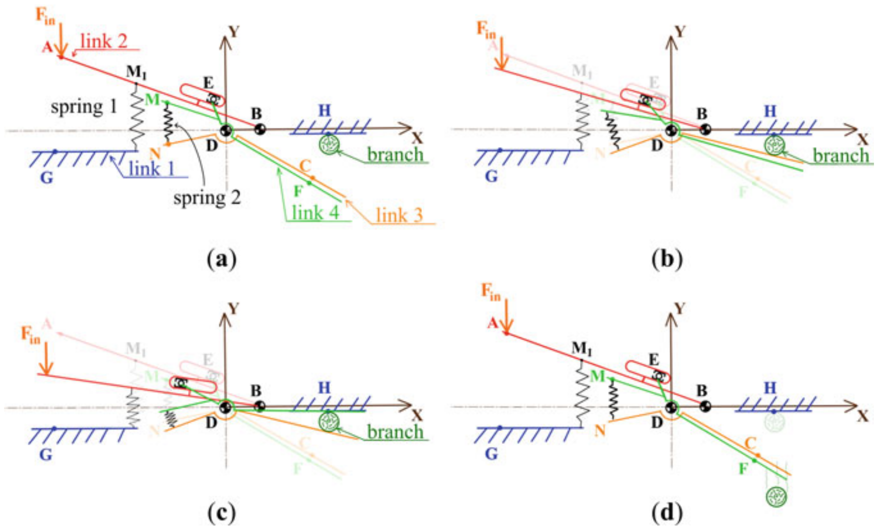

Fig. 3 Functional architecture of the under-actuated tool for autonomous crop sampling. **a** Rest configuration. **b** Grasping configuration (links 3 and 1). **c** Branch cutting (links 1 and 4) and subsequent holding (links 1 and 4). **d** Branch release

Link 2, as depicted in Fig. 4, and the other applies the same F_{in} to Link 1, symmetrically with respect to the X axis. Nevertheless, Link 1 is considered as fixed to simplify the quasi-static modelling of the mechanism (i.e., F_{in} applied to Link 1 is modelled as a reaction force).

Fig. 4 Sampling tool geometric parameters

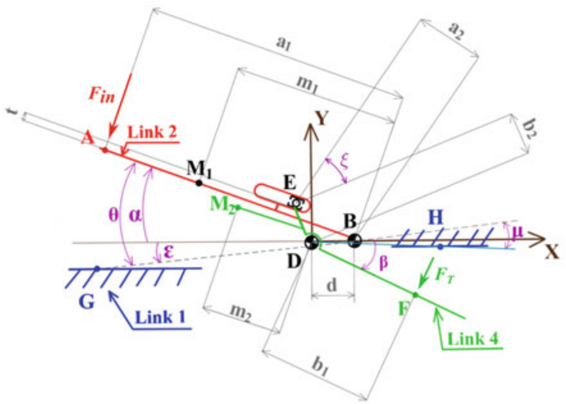

Table 1 Crop sampling tool final set of parameters

Name	Value
a_1	130 mm
a_2	28 mm
b_1	25 mm
b_2	21 mm
d	15 mm
t	5 mm
$m_1 = m_2$	35 mm
K_1	0.58 N/mm
K_2	0.68 N/mm

3.1 Kinematic Model

Figure 4 shows a simplified representation of the crop sampling tool (link 3 devoted to branch grasping is not reported) and the geometric parameters influencing system performance. As main design specifications, the tool must guarantee the proper cutting of a peduncle with a maximum diameter of 6 mm with the reach of a maximum cutting force F_T= 60 N (Fig. 2) with an input force F_{in}= 30 N, that is the minimum orthogonal force exerted by the gripper in correspondence of the proximal phalange, as discussed above.

The tool performance can be evaluated in terms of both output blade rotation and cutting forces. If, on one hand, a higher output blade rotation allows the sampling of crops with a higher peduncle diameter, it also leads to lower values of output cutting forces. To this aim, the linkage gain parameter can be defined as follows:

$$G_F = \frac{F_T}{F_{in}} \tag{1}$$

Hence, the final set of geometric parameters, which allows a maximum angle $\beta \approx$ 20 deg, a total encumbrance along x axis of 130 mm and a force gain factor $G_F \approx 2.5$, is reported in Table 1.

3.2 Executive Design and Prototyping

To test the functionality of the mechanism, a prototype was built mainly in additive manufacturing based on the previous considerations. Links 1 and 2 were shaped to accommodate the 2-finger gripper and facilitate an autonomous and secure grasping of the tool. By redesigning the geometry of these two links, it is possible to adapt the device to other two-finger grippers. The two blades have been slightly modified

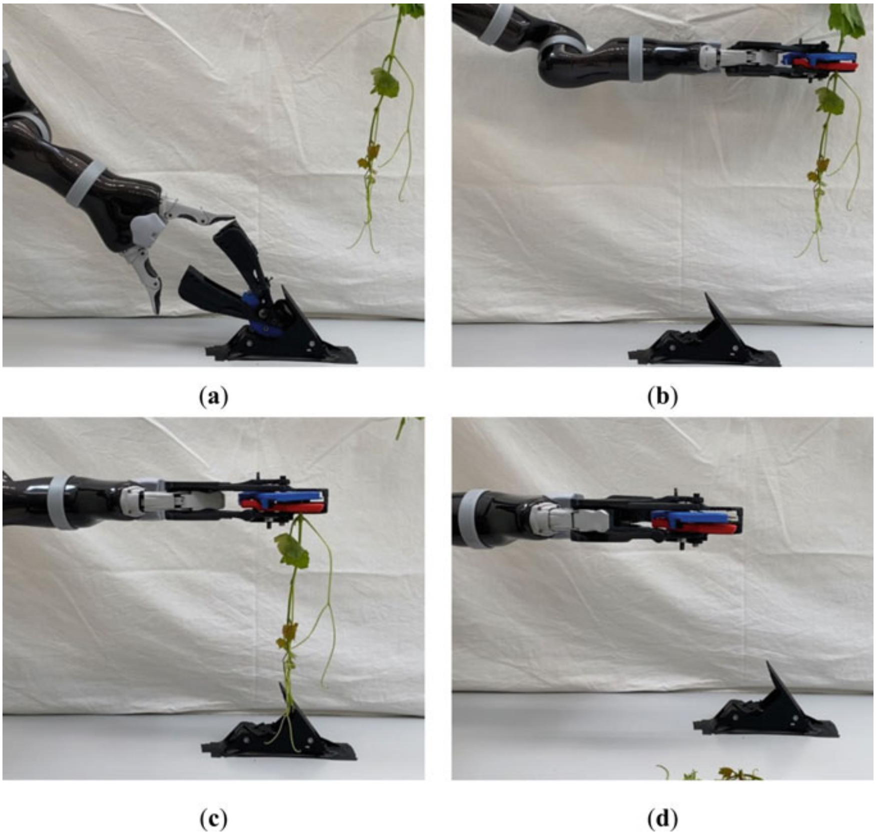

Fig. 5 Operation sequence for the grasping and cutting of a sample: **a** tool grasping, **b** peduncle grasped, **c** peduncle cut, **d** sample released

starting from commercial blades for manual pruning. A high friction layer was added to link 3 to securely hold branches. All springs present a preload regulation system to tune the under-actuated mechanism behavior.

The developed tool and its entire application process were experimentally validated. In Fig. 5, the steps of operations for a sampling task during the experimental trials are depicted. The functionality of the tool was validated with green peduncles ranging from 2 to 6 mm in diameter.

The test followed a predetermined automated procedure, leveraging prior knowledge of the peduncle's pose concerning the robotic arm. In the structured and controlled laboratory environment, the robot equipped with the tool performed a grapevine sample collection with a success rate of 100%.

4 Conclusions

This paper details the design, testing, and experimental validation of a crop sampling tool aimed at collaborative robotic arms, specifically those with two fingers grippers, for automated grapevine harvesting and sampling. This tool is conceived as part of a toolset from which a rover for precision agriculture can automatically choose. In particular, this research is part of the project Agri.Q that mounts a collaborative 7 d.o.f. robotic arm, the Kinova Jaco2. Leveraging the tool's under-actuated mechanism and passive interface compatible with commercial two-finger grippers, the device exploits a single input for both grasping and cutting procedures. Experimental tests were conducted to evaluate gripper grasping forces and required cutting forces and to drive the tool design. Secondly, the under-actuated mechanism is described and a kinematic model of the device is derived. Based on the required cutting forces and available gripper forces, the force gain of the device was selected as 2.5. The paper concludes with the executive design, prototype development, and successful experimental validation of the grasping and cutting tool. Although the experimental trials do not take into account all the uncertainties that would affect the real implementation of the concept in an agricultural environment, this preliminary study has demonstrated that the concept of interchangeable tools that can be autonomously grasped and used by the robot arm is worthy of further investigation. As further developments, sensors and control algorithms will be added to the system to measure the relative pose of the peduncle to be cut with respect to the robotic arm. When the process will be fully automated, the last stage will be to assess the effectiveness of the tool in terms of accuracy, repeatability, efficiency, and resolution, which are strictly dependent on the entire system performance.

References

1. Bechar, A., Vigneault, C.: Agricultural robots for field operations: concepts and components. Biosyst. Eng. **149**, 94–111 (2016). https://doi.org/10.1016/j.biosystemseng.2016.06.014
2. Botta, A., Cavallone, P.: Robotics applied to precision agriculture: the sustainable Agri.q rover case study. In: Proceedings of I4SDG Workshop 2021. Mechanisms and Machine Science, vol. 108, pp. 41–50. Springer International Publishing, Cham (2022). 10.1007/978-3-030-87383-7_5
3. Botta, A., Cavallone, P., Baglieri, L., Colucci, G., Tagliavini, L., Quaglia, G.: A review of robots, perception, and tasks in precision agriculture. Appl. Mech. **3**(3), 830–854 (2022). https://doi.org/10.3390/applmech3030049
4. Colucci, G., Tagliavini, L., Botta, A., Baglieri, L., Quaglia, G.: Decoupled motion planning of a mobile manipulator for precision agriculture. Robotica **41**(6), 1872–1887 (2023). https://doi.org/10.1017/S0263574723000243
5. Kang, H., Zhou, H., Chen, C.: Visual perception and modeling for autonomous apple harvesting. IEEE Access **8**, 62151–62163 (2020). https://doi.org/10.1109/ACCESS.2020.2984556
6. Quaglia, G., Butera, L.G., Chiapello, E., Bruzzone, L.: Ugv epi.q-mod. In: Ceccarelli, M., Glazunov, V.A. (eds.) Advances on Theory and Practice of Robots and Manipulators, pp. 331–339. Springer International Publishing, Cham (2014)

7. Quaglia, G., Tagliavini, L., Colucci, G., Vorfi, A., Botta, A., Baglieri, L.: Design and prototyping of an interchangeable and underactuated tool for automatic harvesting. Robotics **11**(6), 145 (2022). https://doi.org/10.3390/robotics11060145
8. Xiong, Y., Ge, Y., Grimstad, L., From, P.J.: An autonomous strawberry-harvesting robot: design, development, integration, and field evaluation. J. Field Robot. **37**(2), 202–224 (2020). https://doi.org/10.1002/rob.21889

An Exoskeleton for Overhead Work Support Equipped with Pneumatic Artificial Muscles: An Insight on Transmission Design

Maria Paterna, Carlo De Benedictis, and Carlo Ferraresi

Abstract Exoskeletons are wearable systems designed to assist human limb movement and reduce human muscle effort. Passive upper-limb exoskeletons are recently spreading in industrial environments to aid workers during long, repetitive overhead tasks. Generally, these devices engage spring systems to counterbalance the gravitational torque about the shoulder joint. This paper investigates and compares the effects of two different transmissions on the performance of a passive upper-limb exoskeleton based on pneumatic artificial muscles. Simulation results highlight that the different design solutions can either favor a wider range of motion or, alternatively, a better ergonomics and ease of assembling and wearing the device.

Keywords Passive exoskeleton · Upper limb exoskeleton · Pneumatic artificial muscles · Soft actuators · Wearable systems

1 Introduction

Exoskeletons are active or passive devices that, in general, mimic human kinematics to support limb motions and empower the user. Based on the aided human limbs, they can be classified into lower-limb and upper-limb exoskeletons. Generally, the latter must deliver less force and torque, but they are more complex from the kinematic point of view. The primary purpose of a lower-limb exoskeleton is to assist locomotion, to provide stability, and to support user weight. Therefore, the high torque demands usually require electric [1], pneumatic [2], or hydraulic actuators [3]. On the other hand, an upper-limb exoskeleton must ensure a wide range of motion to allow manipulation tasks. Active upper-limb exoskeletons have been employed in rehabilitation to control the movement of physically impaired patients. However, the high number of degrees of freedom (DOF) of the upper limb (9 DOF) and the complexity of actuating and actively controlling each DOF while avoiding the singularities increase

M. Paterna · C. De Benedictis (✉) · C. Ferraresi
Department of Mechanical and Aerospace Engineering, Politecnico Di Torino, Turin, Italy
e-mail: carlo.debenedictis@polito.it

D. Pisla et al. (eds.), *Advances in Service and Industrial Robotics*, Mechanisms and Machine Science 157, https://doi.org/10.1007/978-3-031-59257-7_54

the overall footprint, inertia, and power consumption. Therefore, these exoskeletons are typically mounted on a stationary platform [4, 5]. Although some examples of wearable active upper-limb exoskeletons designed to assist workers during overhead repetitive tasks are present in the literature [6–8], passive exoskeletons exploiting one or multiple springs and a transmission to transform elastic energy into an assistive action are generally preferred in the industrial environment [9–11], aimed at balancing the gravitational torque on the shoulder thus reducing workers' muscular effort. Springs are commonly employed because of their linear behavior. However, they have a relatively low energy density, and a preload system is required to regulate the exoskeleton's supporting action.

Alternatively to traditional spring systems, pneumatic artificial muscles (PAMs) might be employed as nonlinear gas springs because of their elastic properties [12, 13]. They have a high power-to-weight ratio and are simple to install, so they have no negative impact on the weight and total size of the device. Moreover, safe human-exoskeleton interaction is ensured by their softness and resemblance to human skeleton muscles. Furthermore, broad customization of the actuator's response to suit different working tasks is made possible by the availability of PAMs in various sizes as well as thanks to the ability to modify the action level by adjusting the supply pressure. Finally, PAMs may be used in industrial applications since they are low-cost, resistant to high temperatures, thermal gradients, dusty and dirty environments. Despite all these advantageous features, no passive upper-limb exoskeletons currently use PAM for gravity-balancing purposes.

This work is focused on a passive upper-limb industrial exoskeleton based on McKibben PAMs for assisting workers during prolonged overhead tasks. By design, the torque provided by the exoskeleton at the shoulder joint should be as close as possible to the gravitational one. Therefore, a transmission capable of matching PAM nonlinear characteristic to external demand is necessary. This paper focuses on identifying the transmission that optimizes the exoskeleton performance. Two design solutions are presented and discussed. The PAMs are positioned behind the user's back in both scenarios, and the traction force is transmitted by a cable that slides on a fixed shoulder pad of appropriate profile (configuration A) or wraps on a cam that rotates about the shoulder flexion axis (configuration B). Configuration A has been already presented in a previous work of the authors [13]. The results highlighted high support action (up to 74% of the gravitational torque is provided by the exoskeleton) but a limited range of motion (shoulder flexion between 90° and 120°). This paper tests a different PAM size and optimizes its characteristic parameters (i.e., supply pressure and initial contraction ratio) to expand the range of movement exploited by configuration A. The second solution (configuration B) is also studied and discussed. The numerical simulation results obtained with the two configurations are presented to compare the different performance.

2 Exoskeleton Transmission Design

A commercial PAM (DMSP-10-350N-RM-CM, FESTO, Germany), with an internal diameter of 10 mm and a nominal length of 350 mm, has been considered in this work, among other options. PAM maximum allowable contraction and pre-tensioning are 25% ($\approx$ 87 mm) and 3% ($\approx$ 10 mm) of the muscle nominal length, respectively.

Figure 1 illustrates the PAM static characteristic, which can be approximated by Eq. (1) [14]:

$$F = (0.01534p + 130.8)\,e^{-0.3972k} - 0.02605\,pk + 0.7911\,p - 127.1 \tag{1}$$

In Eq. (1), F is the PAM traction force, p is the supply pressure, and k is the contraction ratio.

The PAM force is transmitted by a Dyneema® wire (Braided climax–200daN, OCKERT, Germany), which is considered inextensible for transmission design purposes. In the following, the different transmission configurations are shown.

2.1 Configuration a: Fixed Pad-Based Transmission

Configuration A of the transmission is shown in Fig. 2.

Two PAMs (1), one for each arm, are on the back of the user, with the upper ends fastened to the structure and the lower ends joined to a wire (2) that wraps around a shoulder pad (3) and connects to the bracelet (4) that supports the arm of the user. Two revolute joints (5–6) ensure shoulder flexion (Fig. 2b) and abduction (Fig. 2c).

The shoulder pad profile is designed to approximate the gravitational torque at the shoulder by using the graphical method described in previous works of the authors [12, 13]. The result is shown in Fig. 3a, together with the PAM force lever arm

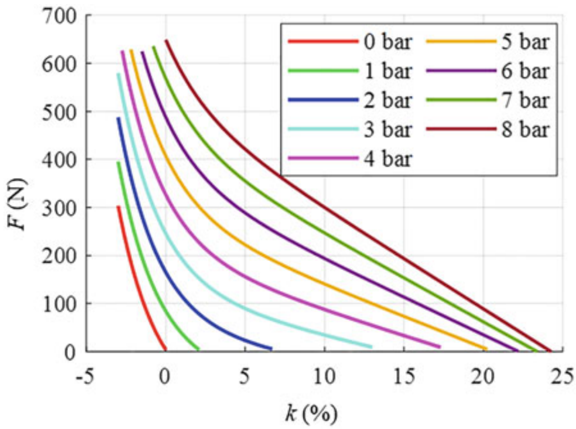

Fig. 1 PAM static characteristics

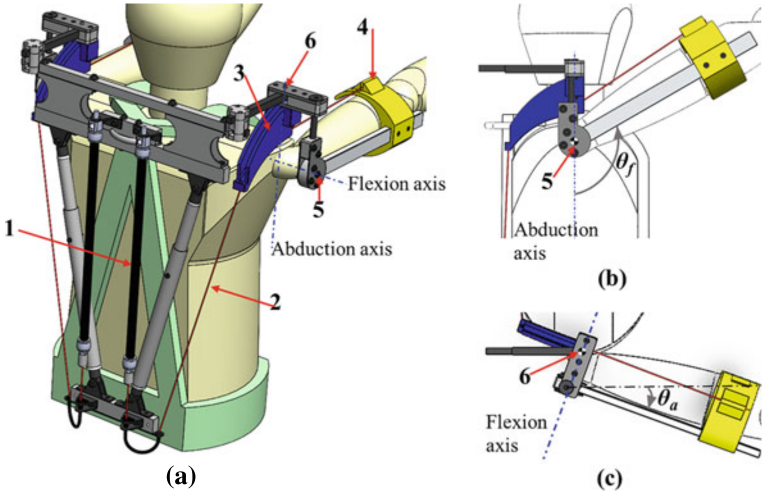

Fig. 2 Configuration A of the transmission implemented into the exoskeleton structure (**a**); the exoskeleton arm in flexed (**b**) and abducted (**c**) positions. θ_f and θ_a are the shoulder flexion and abduction angles, respectively

(Fig. 3b) and the muscle stretching with respect to the mounting length (i.e., the length of the muscle in operating conditions when the shoulder flexion angle is 90°, Fig. 3c).

It should be noted that the gravitational torque on the shoulder is maximum for a flexion angle of 90° and decreases both as this angle increases and decreases. On the other hand, the force provided by the PAM has an ever-increasing trend as its length increases. Therefore, the PAM behavior follows the trend of the gravitational torque above 90°, while they are in contrast for lower angles (Fig. 3c).

Since the reduction in gravitational torque above 90° does not accurately match the decrease in PAM force, the shoulder pad profile has been designed to guarantee an increase in the PAM force lever arm in that range. At the same time, a significant

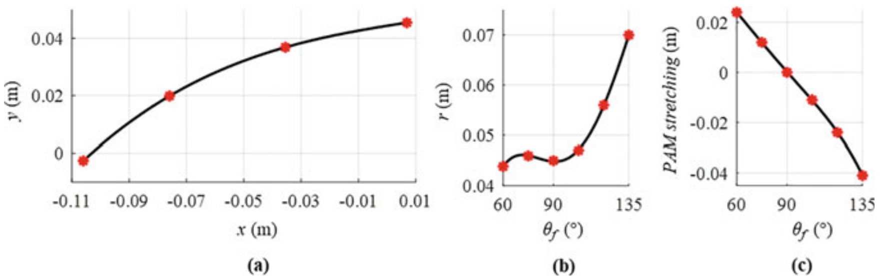

Fig. 3 Shoulder pad profile (**a**) along with the PAM force lever arm (**b**) and stretching (**c**) for shoulder flexion angles between 60° and 135°. The red dots are the data extrapolated from the CAD while the black line is the result of interpolation

reduction in the lever arm below 90° should be achieved. Unfortunately, this feature can't be granted by the shoulder pad. As a result, the user should make a considerable effort to move the arms below the horizontal, thus limiting the operating range of the exoskeleton only to flexion angles greater than 90°.

2.2 Configuration B: Rotating Cam-Based Transmission

In configuration B (Fig. 4), one end of the wire is still connected to the PAM lower end, and the other end runs inside a sheath fixed to the exoskeleton arm through a sheath clip (1) and then joins the cam (2). The latter, in turn, is integral with the strut (3) that sustains the bracelet (4). Therefore, the PAM contraction causes the cam rotation and, consequently, the elevation of the arm of the user.

The cam adoption aims to extend the exoskeleton working range. As shown in Fig. 4c, the cam profile and its ability to rotate around the shoulder flexion axis both contribute to a significant reduction in the PAM force lever arm. The cam profile that minimizes the mismatch between the gravitational and assistive torque is again identified through a graphical approach, starting from the PAM lever arm values at 45°, 90°, and 135°. Given a defined supply pressure ($p = 4$ bar) and initial contraction ratio ($k_{90} = 0\%$), the PAM force lever arm at 90° shoulder flexion is obtained from the static equilibrium of the system, resulting in a 30 mm value. Then, the lever arm at 135° is set to 50 mm to achieve the required assisting torque without obstructing the user's view. Finally, the PAM lever arm at 45° is selected equal to 10 mm to obtain forces and contraction values that fall within the static PAM characteristic shown in Fig. 1.

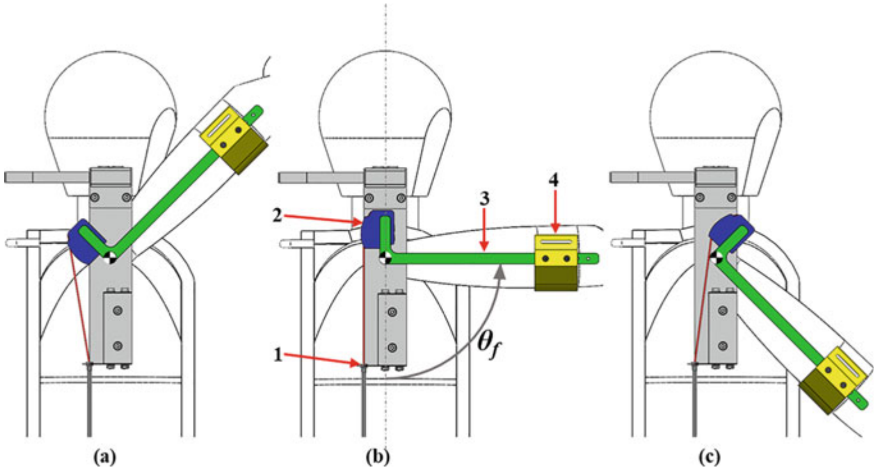

Fig. 4 Configuration B of the transmission shown for different shoulder flexion angles: (**a**) $\theta_f = 135°$; (**b**) $\theta_f = 90°$; (**c**) $\theta_f = 45°$

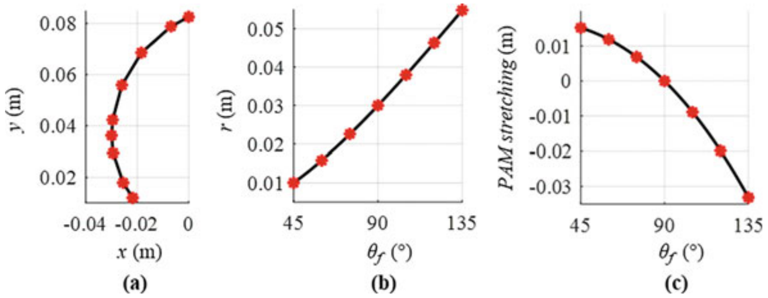

Fig. 5 Cam profile (**a**) along with the PAM force lever arm (**b**) and stretching (**c**) for shoulder flexion angles between 45° and 135°. The red dots are the data extrapolated from the CAD while the black line is the result of interpolation

The PAM stretching and lever arm are extrapolated from CAD design for six shoulder flexion angles (45°, 60°, 75°, 90°, 105°, 120°, 135°) and interpolated over the working range. The results of this method for the rotating cam are shown in Fig. 5.

3 Simulations and Results

Accurate tuning of p and k_{90} can improve the match between gravitational (M_g) and assistive (M_{PAM}) torques. Values of p and k_{90} are varied between 4 bar and 5 bar and between 0% and 2%, respectively. The pressure range has been identified to ensure that the PAM traction force magnitude is adequate for the application, given the lever arms shown in Figs. 3b and 5b. On the other hand, k_{90} greater than 2% is not considered to avoid excessive stroke reduction. Among the possible combinations of p and k_{90}, the one that minimizes the torque error expressed by Eq. (2) is chosen.

$$E = 100 \cdot \sqrt{\frac{1}{N} \sum_{i=\theta_m}^{135} \left(\frac{M_{PAM}(i) - M_g(i)}{M_g(i)} \right)^2} \tag{2}$$

θ_m is the minimum flexion angle achieved by the exoskeleton, and it is set to 90° and 45° for A and B configurations, respectively; N is the number of samples.

As shown in Fig. 6, the influence of the parameters on the torque error for each configuration is comparable. Regarding configuration B (Fig. 6b), the contraction ratio must be equal to 0.6% to minimize the torque error. Conversely, the error decreases as the contraction ratio increases in configuration A (Fig. 6a). The latter also requires a higher supply pressure.

The optimal (p, k_{90}) combination, one for each transmission solution, is then considered to evaluate the system performance in different conditions: unloaded

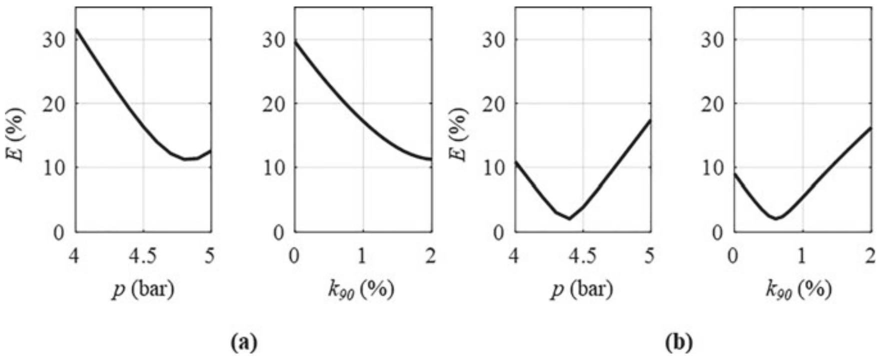

Fig. 6 Percentage error values between gravitational and assistive torque generated by configuration A (**a**) and B (**b**), obtained by varying optimization parameters

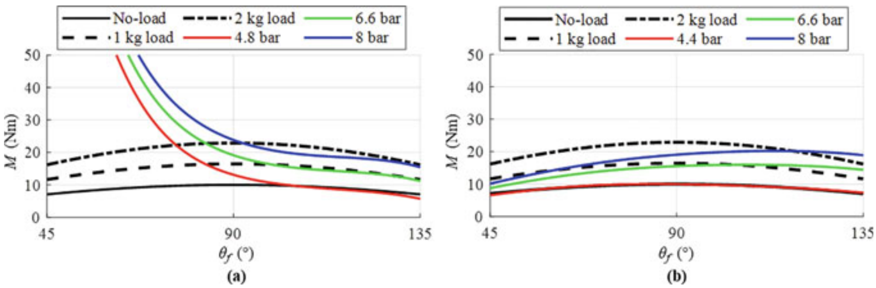

Fig. 7 Gravitational torque for different load conditions as well as the torque exerted by the exoskeleton at different supply pressures by employing A (**a**) and B (**b**) transmission design

condition, considering only the user's arm weight, and two loaded conditions, in which the user holds a tool of 1 or 2 kg in the hand (Fig. 7).

Figure 7a shows that configuration A does not allow to reach shoulder flexion angles lower than 80° with a feasible approach. Below this value, the assistive torque that needs to be counteracted by the user can exceed five times the gravitational torque.

On the contrary, configuration B (Fig. 7b) allows accurate tracking of the gravitational torque in the unloaded condition, although the exoskeleton performance worsens by increasing the load in the hand. The percentage error, in fact, raises from 2 to $13\% - 20\%$ of the gravitational torque when the load in the hand increases from 0 kg to $1 - 2$ kg. Nonetheless, the exoskeleton support action is always higher than 80%, and the residual torque is low enough to be easily compensated by the user's muscle action. It is likely that an appropriate regulation of supply pressure could further adapt the device behavior to different scenarios.

Regarding the mechanical strength of the system, some concerns are related to the fact that, for flexion angles lower than 60°, the maximum elongation of the PAM prescribed by the manufacturer (3%) is exceeded (3.7% if $\theta_f = 45°$). This would likely result in unsafe conditions for the system, affecting long-term stability and reliability. However, that could be tackled by optimizing the design of the transmission or by searching for different PAMs (commercial or custom-made) with more appropriate features.

4 Conclusion

This work compared two different transmissions for a passive exoskeleton energized by pneumatic artificial muscles. In both solutions, within the respective operating ranges, the assistive torque of the exoskeleton compensates for more than 80% of the gravitational torque.

The design solution based on a cam rotating around the shoulder flexion axis proves to be more convenient regarding the operating range compared to the solution based on a fixed pad. On the other hand, the cam-based solution shows less adaptability to the presence of a load in the operator's hand. Moreover, it requires placing the cam in a lateral position with respect to the shoulder, thus requiring the creation of a more complex and bulky structure and determining the arising of an abduction moment which is exerted on the user's shoulder. Therefore, a future activity will concern the in-depth analysis of this solution in order to identify a possible ergonomic and compact configuration.

Regardless of the transmission adopted, the exoskeleton-human interaction forces should be investigated in the future to guarantee user safety and to achieve ergonomic behavior that helps improving the acceptance of such devices by workers. That should be attained by ensuring structural strength without unnecessary increase of device's weight and bulkiness.

Finally, a prototype of both transmissions should be developed to test their performance in a real-world scenario. In particular, the model neglected friction phenomena, device's weight, pneumatic losses, and PAM hysteresis. However, all these aspects could affect the actual behavior of the system.

References

1. Harib, O., Hereid, A., Agrawal, A., Gurriet, T., Finet, S., Boeris, G., Duburcq, A., Mungai, M.E., Masselin, M., Ames, A.D., Sreenath, K., Grizzle, J.W.: Feedback control of an exoskeleton for paraplegics: toward robustly stable hands-free dynamic walking. IEEE Control. Syst. **38**, 61–87 (2018). https://doi.org/10.1109/MCS.2018.2866604
2. Galle, S., Malcolm, P., Collins, S.H., De Clercq, D.: Reducing the metabolic cost of walking with an ankle exoskeleton: interaction between actuation timing and power. J. NeuroEngineering Rehabil. **14**, 35 (2017). https://doi.org/10.1186/s12984-017-0235-0
3. Sun, M., Ouyang, X., Mattila, J., Yang, H., Hou, G.: One novel hydraulic actuating system for the lower-body exoskeleton. Chin. J. Mech. Eng. **34**, 31 (2021). https://doi.org/10.1186/s10033-021-00535-w

4. Ai, L., Zhou, T., Wu, L., Qian, W., Xiao, X., Guo, Z.: Design of a 6 DOF cable-driven upper limb exoskeleton. In: Liu, X.-J., Nie, Z., Yu, J., Xie, F., and Song, R. (eds.) Intelligent Robotics and Applications, pp. 728–736. Springer International Publishing, Cham (2021). https://doi.org/10.1007/978-3-030-89095-7_69
5. Trigili, E., Crea, S., Moise, M., Baldoni, A., Cempini, M., Ercolini, G., Marconi, D., Posteraro, F., Carrozza, M.C., Vitiello, N.: Design and experimental characterization of a shoulder-elbow exoskeleton with compliant joints for post-stroke rehabilitation. IEEE/ASME Trans. Mechatron. **24**, 1485–1496 (2019). https://doi.org/10.1109/TMECH.2019.2907465
6. Mauri, A., Lettori, J., Fusi, G., Fausti, D., Mor, M., Braghin, F., Legnani, G., Roveda, L.: Mechanical and control design of an industrial exoskeleton for advanced human empowering in heavy parts manipulation tasks. Robotics **8**, 65 (2019). https://doi.org/10.3390/robotics8030065
7. Bilancia, P., Berselli, G.: Conceptual design and virtual prototyping of a wearable upper limb exoskeleton for assisted operations. Int. J. Interact. Des. Manuf. **15**, 525–539 (2021). https://doi.org/10.1007/s12008-021-00779-9
8. Liu, C., Liang, H., Murata, Y., Li, P., Ueda, N., Matsuzawa, R., Zhu, C.: A wearable lightweight exoskeleton with full degrees of freedom for upper-limb power assistance. Adv. Rob. **35**, 413–424 (2021). https://doi.org/10.1080/01691864.2020.1854115
9. Hyun, D.J., Bae, K., Kim, K., Nam, S., Lee, D.: A light-weight passive upper arm assistive exoskeleton based on multi-linkage spring-energy dissipation mechanism for overhead tasks. Rob. Auton. Syst. **122**, 103309 (2019). https://doi.org/10.1016/j.robot.2019.103309
10. Maurice, P., Camernik, J., Gorjan, D., Schirrmeister, B., Bornmann, J., Tagliapietra, L., Latella, C., Pucci, D., Fritzsche, L., Ivaldi, S., Babic, J.: Objective and subjective effects of a passive exoskeleton on overhead work. IEEE Trans. Neural Syst. Rehabil. Eng. **28**, 152–164 (2020). https://doi.org/10.1109/TNSRE.2019.2945368
11. Yin, P., Yang, L., Qu, S., Wang, C.: Effects of a passive upper extremity exoskeleton for overhead tasks. J. Electromyogr. Kinesiol. **55**, 102478 (2020). https://doi.org/10.1016/j.jelekin.2020.102478
12. Magnetti Gisolo, S., Muscolo, G.G., Paterna, M., De Benedictis, C., Ferraresi, C.: Feasibility study of a passive pneumatic exoskeleton for upper limbs based on a McKibben artificial muscle. In: Zeghloul, S., Laribi, M.A., and Sandoval, J. (eds.) Advances in Service and Industrial Robotics, pp. 208–217. Springer International Publishing, Cham (2021). https://doi.org/10.1007/978-3-030-75259-0_23
13. Paterna, M., Magnetti Gisolo, S., De Benedictis, C., Muscolo, G.G., Ferraresi, C.: A passive upper-limb exoskeleton for industrial application based on pneumatic artificial muscles. Mech. Sci. **13**, 387–398 (2022). https://doi.org/10.5194/ms-13-387-2022
14. Piteľ, J., Tóthová, M.: Modelling of pneumatic muscle actuator using hill's model with different approximations of static characteristics of artificial muscle. MATEC Web Conference, Vol. 76, p. 02015 (2016). https://doi.org/10.1051/matecconf/20167602015

A Literature Review and Design Considerations Towards a Gripper for Tomato Harvesting

Dmitry Malyshev, Luigino Filice, Giovanni Mirabelli, Francesco Longo, Bruno Bernardi, Giuseppe Carbone, and Larisa Rybak

Abstract The paper reviews current commercial and research solutions in the field of grippers for automated tomato harvesting. The gripping devices are classified according to the method of harvesting tomatoes, namely individual fruits and branches. The requirements that the design of a gripping device for harvesting tomatoes must satisfy are formulated also based on preliminary laboratory tests. The requirements include the mechanical properties of the tomatoes and the required characteristics of the gripping device. A preliminary design concept is also proposed for harvesting tomatoes with a specific focus on the large-size tomato varieties.

Keywords Tomato harvesting · Gripper · Harvesting robots

1 Introduction

Tomato harvesting is a very important task requiring extensive manual work. Several companies, including Priva, Octiva, and Xihelm, are actively developing automation and robotics for tomato cultivation. Xihelm is focused on robotic solutions for tomato harvesting, but no implementation has been documented yet. Floating Company Robotics offers a commercial robot specifically designed for efficient cherry tomato harvesting. However, concerns arise regarding the careful placement

D. Malyshev (✉) · L. Filice · G. Mirabelli · F. Longo · G. Carbone
Department of Mechanical, Energy, and Management Engineering, Università Della Calabria, Rende, Italy
e-mail: dmitry.malyshev@unical.it

G. Carbone
e-mail: giuseppe.carbone@unical.it

D. Malyshev · L. Rybak
Belgorod State Technological University Named After V. G. Shukhov, Belgorod, Russia

B. Bernardi
Department of Agricultural Sciences, Università Mediterranea di Reggio Calabria, Reggio Calabria, Italy

D. Pisla et al. (eds.), *Advances in Service and Industrial Robotics*, Mechanisms and Machine Science 157, https://doi.org/10.1007/978-3-031-59257-7_55

of branches, potentially impacting fruit shelf life. Metomotion provides a commercial robot capable of harvesting various tomato varieties using scissor-shaped grippers. Inaho has developed a unique cherry tomato-picking robot with parallel modules resembling a soft conveyor belt, although multiple attempts may be needed for harvesting, posing potential fruit damage. Pioneering research in tomato harvesting emerged in Japan in the 1980s [1] with contributions from Tateshi Fujira and collaborations with Naoshi Kondo [2]. Some papers present only schematic designs without further development [3, 4]. A solar-powered robotic system using artificial balls for experiments is condered in [5]. However, it is still an open problem to provide an adaptable grasping solution for small productions of large size tomatoes.

2 Review of Existing Solutions

Literature review has been made as based on the procedure, which consisted of searching for sources dedicated to robotic tomato harvesting in Scopus, Researchgate and Google. An analysis was carried out of the source, as well as other sources on same topic found in connection with this source (citations, references, the same authors). Within the framework of the current paper, a filtered part of the found sources relating to the development of entire robotic systems or their gripping devices is cited.

Some of the earliest development of tomato grippers, along with other robotic components, began in Japan [6]. To date, researchers from around the world have developed several different gripping devices for harvesting tomatoes. They may have a different number of fingers and a different way of grasping and tearing off the fruit. Let's analyze existing solutions, grouping them by the type of object being grasped.

Mobile platform chassis for tomato harvesting robots were developed in [7–9], but these seem applicable to a broader range of fruits and vegetables. A post-harvest device on a mobile platform for safely moving tomatoes to a basket is developed in [9]. A system using a movable cart to control manual tomato harvesting is considered in [10]. Kinematics and workspace for manipulators considering the required harvesting area are considered in [11]. Manipulator for tomato harvesting, its simulation, checking design parameters, force-torque calculations, and developing a control system, excluding the gripping device aspect are considered in [12].

It is worth noting the competition for robotic tomato picking, which has been held in the city of Kitakyushu (Japan) annually since 2014 [13]. The competition takes place in a greenhouse at the Kitakyushu Research & Science Park. Its dimensions are 10×20 m. The greenhouse is equipped with IoT sensors that measure temperature, humidity, soil pH and light. The competition mainly involves teams from the city of Kitakyushu, but teams from other universities also participate. To pick tomatoes, robots need to adapt to lighting conditions, which brings the task closer to real-life conditions. The team from the HAYAHI-LAB laboratory won the competition the most times. Over the years of the competition, several scientific results were obtained, and published in papers [14, 15].

2.1 Gripping Devices for Individual Fruits

It is worth noting that as a result of the review, not a single commercial solution was identified that uses individual fruit harvesting. However, most of the research work is devoted specifically to individual fruit harvesting.

Some of the agricultural grips can be combined into a group of flexible grips, printed using a 3D printer using flexible materials. One of these grips, designed specifically for harvesting tomatoes, is discussed in [16]. A similar grip, but used for various objects, including tomatoes, is discussed in [17].

A three-finger gripper made of ABS + plastic with force sensors, based on a crank-slider mechanism, is proposed in [18]. The influence of gripper motor parameters such as input current and motor speed on the shrinking process and deformation of tomatoes was investigated in [19]. A recently popular AI tool Chat GPT, was used during the design development in [20]. The gripper design consists of two hemispheres, similar to the design proposed earlier in [21]. A device for harvesting tomatoes is proposed in [22], based on drawing tomatoes with air and cutting off the fruit. There are also many other grippers designed for tomatoes [23–33].

2.2 Gripping Devices for Branches with Fruit

All commercial solutions found for harvesting tomatoes use branch picking or other methods of group harvesting. Descriptions of commercial solutions are described in introduction. The number of research solutions for branch gripping is extremely limited [34, 35].

3 Requirements and Challenges

The advancement of robotic technologies for tomato picking necessitates thorough planning and execution of field experiments. They are based on the measurement of the response to mechanical stresses of controlled compression and penetration under controlled deformation conditions, i.e. the conditions to be monitored when harvesting operations are planned to be mechanized in order not to damage the product.

3.1 Tomatoes Properties

Table 1 shows the properties of tomatoes that should be taken into account when designing gripping devices.

Table 1 Tomatoes properties

Property	Min value	Max value	Comment
Weight	14 g (Grape)	454 g (Beefsteak and Heirloom)	Based on the size of tomatoes of different varieties
Size	10 mm (Cherry)	150 mm (Beefsteak and Heirloom)	Based on the size of the tomatoes of different varieties
Young's modulus	2.32	4.07	According to [18, 36–38]
Poisson's ratio	0.55	0.74	According to [18, 36–38]
Shape	Spherical	Ellipsoid/irregular	According to [23, 39, 40]
Stiffness	3 N/mm (mature)	30 N/mm (green)	According to [23, 39, 40]
Grasping plane	Horizontal	$\pm$ 15° from horizontal	According to [23, 39, 40]
Surface	Smooth and dry	Dusty and wed	According to [23, 39, 40]
Pose altitude	300 mm	1500 mm	According to [23, 39, 40]
Stalk orientation	Vertical	$\pm$ 3° from vertical	According to [23, 39, 40]

3.2 Compression and Penetration Tests

To assess the firmness of the tomatoes, a series of compression and penetration tests were carried out on different tomato varieties. The aim was to establish action thresholds for the gripper so as not to damage the fruit. The tests were carried out at room temperature using a TA-TX Plus texture analyzer (Fig. 1). The different cultivars of tomatoes chosen were: Piccadilly tomatoes, Cherry Tomatoes, Rib Tomatoes, Oxheart Tomatoes, and Grape Tomatoes. Three ripening indices were considered: unripe tomato, medium ripe tomato, and fully ripe tomato. Compression tests involved loading the sample between two plates, applying a force and recording the deformation. The cycle included compression, decompression and a second compression, revealing changes in the structure of the sample. This assessed material behavior under compressive pressures, plastic flow and ductile fracture limits. Penetration tests used cone penetrometers to measure stress–strain properties by inserting a metal cone into the specimen at a constant speed and force. The probes were applied in triplicate with a 100 mm dish and 5 mm tip, a test speed of 2 mm/sec and a trigger force of 5 g. Compression indices varied for different samples (10 mm for Piccadilly, 20 mm for others), while penetration tests maintained a 10 mm index. The thresholds found during the tests (Figs. 2 and 3) ranged from 9.29 to 28.13 N for penetration (on fully ripe grape tomatoes and unripe cherry tomatoes respectively), while for compression these values were 30.16–302.89 N (on medium ripe Piccadilly tomatoes and unripe cherry tomatoes respectively).

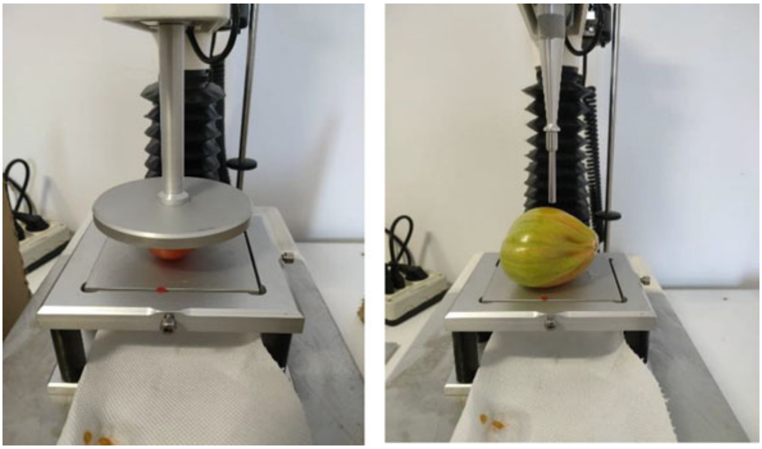

Fig. 1 TA-TX plus texture analyzer during tests

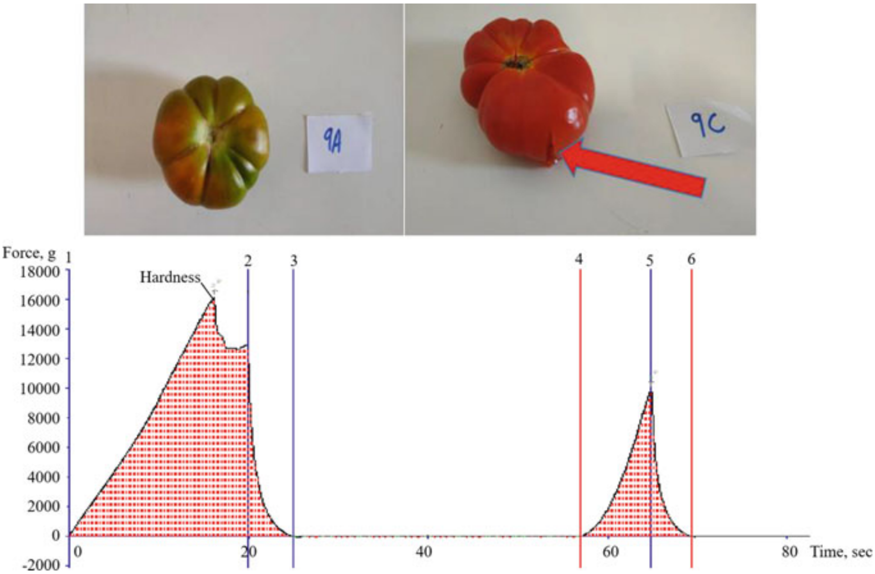

Fig. 2 Example of compressed tomato and its damage (showed by arrow) and maximum peaks obtained during trials

3.3 Regulatory Considerations

Based on the analysis performed and the sizes of tomatoes of various varieties, requirements have been drawn up that must be met by a tomato gripping device (Table 2).

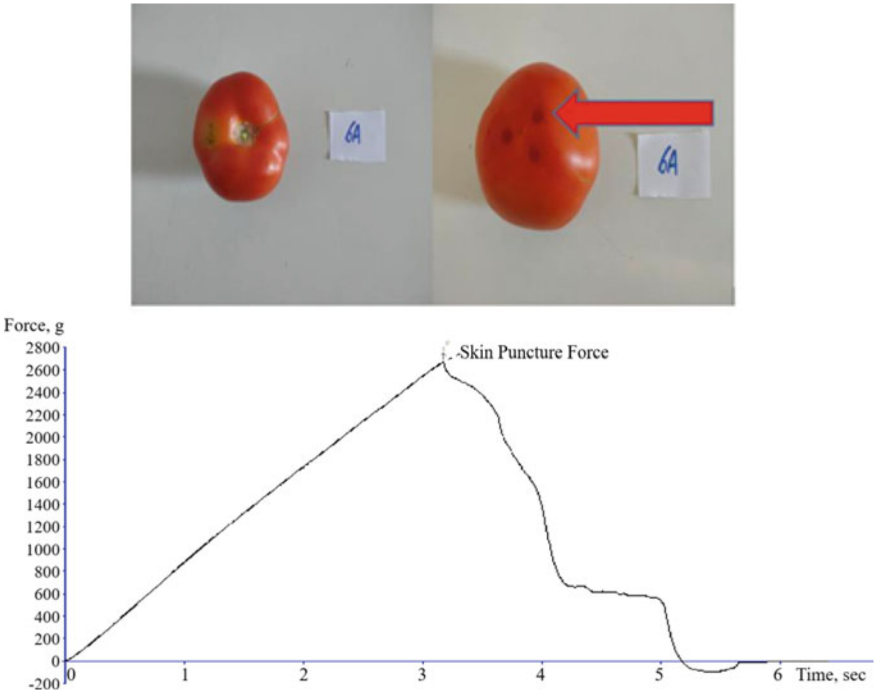

Fig. 3 Example of a penetrated tomato and its damage (showed by arrow) and maximum peaks obtained during trials

4 Possible Gripper Design

Let's consider one of the options for the structure of a gripping device that can be used for harvesting tomatoes. A specific design solution has been identified in this work as the one DOF (degree of freedom) mechanism, which is represented in Fig. 4. It is made up of two four-bar mechanisms, ABCL and EFGH. This mechanism is an extension of a design solution that was addressed previously in [43]. This mechanism provides a symmetrical bending of the palm around the revolute joint at point L after adequate dimensional synthesis. The revolute joint in the L joins the palm's two parts. A motor is installed at point E and can actively bend the palm. However, to achieve a passive adjustable palm bending, turn off this actuator and use the k stiffness of a spring attached at point L. Depending on your grasping requirements, you can choose between active and passive palm operation modes. The proposed palm also serves as a base for three fingers that can be attached to it at positions D1, D2, and I. The bending of the palm also results in the rotation of the fingers, which aids in the grasping of an object. The design of the proposed gripper is shown in Fig. 5 [44]. The proposed design of the gripping device allows us to satisfy the requirements formed above. In particular, the design allows the use of electric actuators and the

Table 2 Gripper requirements

Metrics	Value	Comment
Harvesting rate	30 kg/hour	To provide productivity comparable to manual labor [41]
Accuracy	1 mm	Sufficient accuracy based on the size of the tomatoes
Payload	500 g	According to the maximum weight of large types of tomatoes (Beefsteak and Heirloom)
Workspace	150 mm × 150 mm × 150 mm	According to the maximum size of large types of tomatoes (Beefsteak and Heirloom)
Measured force of sensor	1–30 N	According to the tomato stiffness range [23, 39, 40]
Type of sensors	Piezoresistive, piezoelectric	Suitable for tomatoes
Energy source of actuators	Electrical preferable (other suitable options can be used)	Compromise between functionality and energy consumption, enabling its implementation in current agricultural robotics [42]
Control	Position control, force feedback	Control algorithms with the stiffness of the object for the handling of fruits [42]
Material	Non-toxic material	Since tomatoes are a food product

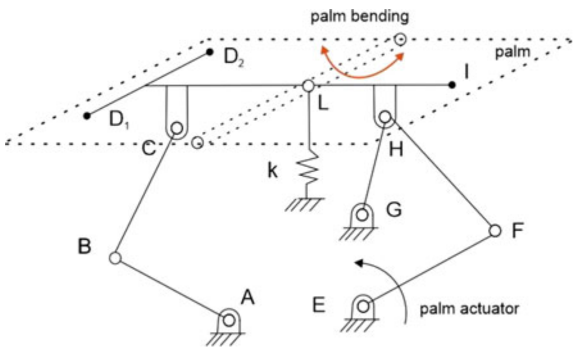

Fig. 4 Kinematic model of the driving mechanism for the proposed palm [44]

installation of the necessary sensors to implement force feedback. All-round fruit gripping allows for stable gripping of tomatoes weighing 500 g. The gripper will be non-toxic to products if food-grade plastic is used or has a special coating.

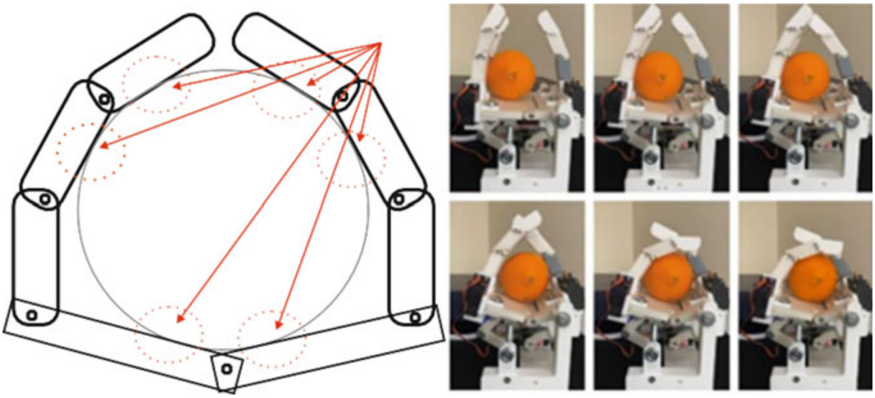

(a) (b)

Fig. 5 An example of grasping configuration while holding a cylindrical object, **a** scheme, **b** real environment

5 Conclusions

Presently, extensive research and various commercial solutions exist for robotic tomato harvesting; however, widespread implementation remains limited. As a result, manual labor is still widely employed for tomato harvesting. An ongoing challenge is the effective integration of recognition and control algorithms, as well as equipment, into real-world environments. Laboratory studies often fall short in addressing all the complexities of real-life conditions. The field of tomato harvesting requires increased automation to overcome existing limitations in the application of robotic systems. This paper delves into current literature, conducting preliminary testing to identify primary design requirements and constraints for achieving a human-like, gentle, and adaptable harvesting process for large tomatoes by proposing a possible design concept. Future investigations will center on designing a novel robotic gripper based on the proposed human-like concept.

Acknowledgements This paper has been funded by the PNRR Next Generation EU TECH4YOU–ECS 00000009, CUP H23C22000370006.

References

1. Kawamura, N., Namikawa, K., Fujiura, T., Ura, M.: Study on agricultural robot (Part 1). J. Japan. Soc. Agric. Mach. **46**, 353–358 (1984). (in Japanese)
2. Kondo, N., Shibano, Y., Mohri, K., Fujiura, T., Monta, M.: Request to cultivation method from tomato harvesting robot. Acta Hortic. **319**, 567–572 (1992)
3. Buemi, F., Massa, M., Sandini, G., Costi, G.: The AGROBOT project. Adv. Space Res. **18**(1–2), 185–189 (1996)
4. Jin, Z.M., Sun, W., Zhang, J., Shen, C., Zhang, H.Y., Han, S.Q.: Intelligent tomato picking robot system based on multimodal depth feature analysis method. In: IOP Conference Series Earth and Environmental Science, vol. 440, p. 042074 (2020)
5. Miah, I., Sultan, S., Wangchuk, J., Savitha R.: Development of solar power agriculturally based fruit picking robot. ESP J. Eng. Technol. Advancements **3**(1) JETA-V3I1P108 (2023)
6. Kawamura, N., Namikawa, K., Fujiura, T., Ura, M., Ogawa, Y.: Prototype production of the hand part of a fruit harvesting robot. J. Jpn. Soc. Agric. Mach. **49**, 116 (1987). (in Japanese)
7. Su, L., Liu, R., Liu, K., Li, K., Liu, L., Shi, Y.: Greenhouse tomato picking robot chassis. Agriculture **13**, 532 (2023)
8. Zhu, T., Xiang, J.: Chassis design of tomato picking robot in the greenhouse. J. Phys. Conf. Ser. **2136**, 012047 (2021)
9. Zu, L.L., Han, M.Z., Liu, J.Q., Liu, P.Z., Li, T., Su, F.: Design and experiment of nondestructive post-harvest device for tomatoes. Agriculture **12**, 1233 (2022)
10. Ota, T., Iwasaki, Y., Nakano, A., Kuribara, H., Higashide, T.: Development of yield and harvesting time monitoring system for tomato greenhouse production. Eng. Agric. Environ. Food **12**(1), 40–47 (2019)
11. Li, Z., Liu, J., Li, P., Li, W.: Analysis of workspace and kinematics for a tomato harvesting robot. In: Proceedings International Conference on Intelligent Computation Technology and Automation, Changsha, China, pp. 823–827 (2008)
12. Wu, J.H., Zhang, Y., Zhang, S.H., Wang, H.J., Liu, L., Shi, Y.G.: Simulation design of a tomato picking manipulator. Teh. Vjesn. **28**, 1253–1261 (2021)
13. Ishii, K., Matsuo, T., Takemura, Y., Sonoda, T., Sanada, A., Tominaga, M., Nishida, Y., Yasukawa, S., Shirahashi, K., Fujinaga, T., Arita, D., Kawajiri, K., Ohshima, K., Okada, M.: Report on the 8th tomato-harvesting competition toward smart agriculture. In: Proceedings of International Conference on Artificial Life and Robotics, pp.486–490 (2023)
14. Ohshige, T., Tominaga, M., Fujinaga, T., Takemura, Y., Ahn, J.: Development of harvesting robot for tomato robot competition 2022 and its evaluation. In: Proceedings of International Conference on Artificial Life and Robotics, pp. 477–480 (2023)
15. Yaguchi, H., Nagahama, K., Hasegawa, T., Inaba, M.: Development of an autonomous tomato harvesting robot with rotational plucking gripper. In: Proceedings of the 2016 IEEE/RSJ International Conference on Intelligent Robots and Systems (IROS), Daejeon, Korea, pp. 652–657, 9–14 October 2016
16. Guo, T., Zheng, Y., Bo, W., Liu, J., Pi, J., Chen, W., Deng, J.: Research on the bionic flexible end-effector based on tomato harvesting. J. Sens. **2022**, Article ID 2564952 (2022)
17. Elgeneidy, K., Lightbody, P., Pearson, S., Neumann, G.: Characterising 3D-printed soft fin ray robotic fingers with layer jamming capability for delicate grasping. In: 2019 2nd IEEE International Conference on Soft Robotics (RoboSoft), Seoul, Korea (South), pp. 143–148 (2019)
18. Russo, M., Ceccarelli, M., Corves, B., Hüsing, M., Lorenz, M., Cafolla, D., Carbone, G.: Design and test of a gripper prototype for horticulture products. Robot. Comput. Integ. Manuf. **44**, 266–275 (2017)
19. Liu, J., Li, Z., Li, P., Mao, H.: Design of a laser stem-cutting device for harvesting robot. In: Proceedings of the IEEE International Conference on Automation and Logistics Qingdao, China, pp. 2370–2374 September 2008
20. Stella, F., Della Santina, C., Hughes, J.: How can LLMs transform the robotic design process? Nat. Mach. Intell. **5**, 561–564 (2023)

21. Yeshmukhametov, A., Koganezawa, K., Buribayev, Z., Amirgaliyev, Y., Yamamoto, Y.: Development of continuum robot arm and gripper for harvesting cherry tomatoes. Appl. Sci. **12**, 6922 (2022)
22. Fujinaga, T., Yasukawa, S., Ishii, K.: Development and evaluation of a tomato fruit suction cutting device. In: Proceedings of the 2021 IEEE/SICE International Symposium on System Integration (SII), Fukushima, Japan, pp. 628–633, 11–14 January 2021
23. Fu, J., Yu, Z., Guo, Q., Zheng, L., Gan, D.: A variable stiffness robotic gripper based on parallel beam with vision-based force sensing for flexible grasping. Robotica, pp. 1–19, Published online 2023. https://doi.org/10.1017/S026357472300156X
24. Taqi, F., Al-Langawi, F., Abdulraheem, H., El-Abd, M.: A cherry-tomato harvesting robot. In: Proceedings of the 2017 18th International Conference on Advanced Robotics (ICAR), Hong Kong, China, pp. 463–468, 10–12 July 2017
25. Vu, Q., Ronzhin, A.A.: A model of four-finger gripper with a built-in vacuum suction Nozzle for harvesting tomatoes. In: Smart Innovation, Systems and Technologies, pp. 149–160. Spinger, Berlin/Heidelberg, Germany (2020)
26. Jun, J., Kim, J., Seol, J., Kim, J., Son, H.: Il towards an efficient tomato harvesting robot: 3D perception, manipulation, and end-effector. IEEE Access **9**, 17631–17640 (2021)
27. Ling, X., Zhao, Y., Gong, L., Liu, C., Wang, T.: Dual-arm cooperation and implementing for robotic harvesting tomato using binocular vision. Rob. Auton. Syst. **114**, 134–143 (2019)
28. Ling, P.P., Ehsani, R., Ting, K.C., Chi, Y-T., Ramalingam, N., Klingman, M.H., Draper, C.: Sensing and end-effector for a robotic tomato harvester. In: 2004 ASAE/CSAE Annual International Meeting, Ottawa, Ontario, Canada. American Society of Agricultural and Biological Engineers, St. Joseph, Michigan (2004)
29. Kondo, N., Monta, M., Shibano, Y., Mohri, K.: Two finger harvesting hand with absorptive pad based on physical properties of tomato. Environ. Control. Biol. **31**(2), 87–92 (1993)
30. Chiu, Y.C., Yang, P.Y., Chen, S.: Development of the end-effector of a picking robot for greenhouse-grown tomatoes. Appl. Eng. Agric. **29**(6), 1001–1009 (2013)
31. Zhang, F., Chen, Z., Wang, Y., Bao, R., Chen, X., Fu, S., Tian, M., Zhang, Y.: Research on flexible end-effectors with humanoid grasp function for small spherical fruit picking. Agriculture **13**, 123 (2023)
32. Wang, G., Yu, Y., Feng, Q.: Design of end-effector for tomato robotic harvesting. IFAC-PapersOnLine **49**(16), 190–193 (2016)
33. Rong, J., Wang, P., Wang, T., Hu, L., Yuan, T.: Fruit pose recognition and directional orderly grasping strategies for tomato harvesting robots. Comput. Electron. Agric. **202**, 107430 (2022)
34. Feng, Q., Zou, W., Fan, P., Zhang, C., Wang, X.: Design and test of robotic harvesting system for cherry tomato. Int. J. Agric. Biol. Eng. **11**, 96–100 (2018)
35. Kondo, N., Yata, K., Iida, M., Shiigi, T., Monta, M., Kurita, M., Omori, H.: Development of an end-effector for a tomato cluster harvesting robot. Eng. Agric. Env. Food. **3**, 20–24 (2010)
36. Gladyszewska, B., Ciupak, A.: Changes in the mechanical properties of the greenhouse tomato fruit skins during storage. Tech. Sci. **12**(12), 1–8 (2009)
37. Williams, S.H., Wright, B.W., Truong, V.D., Daubert, C.R., Vinyard, C.J.: Mechanical properties of foods used in experimental studies of primate masticatory function. Am. J. Primatol. **67**(3), 329–346 (2005)
38. Babarinsa, F.A., Ige, M.T.: Young's modulus for packaged Roma tomatoes under compressive loading. Int. J. Sci. Eng. Res. **3**(10), 314–320 (2014)
39. Jimenez, C.E.: Diseno de un organo aprenhensor para la recollecciòn de productos ortofruticolas", Master Thesis. University of Malaga, ETSII (1998)
40. Carbone, G. (eds): Grasping in Robotics. Mechanisms and Machine Science, vol 10. Springer, London. https://doi.org/10.1007/978-1-4471-4664-3_1
41. Samuel, D.V.K.: Manually operated tomato harvesting tool for greenhouse. Acta Hortic. **710**, 491–496 (2006)
42. Navas, E., Fernández, R., Sepúlveda, D., Armada, M., Gonzalez-de-Santos, P.: Soft grippers for automatic crop harvesting: a review. Sensors **21**, 2689 (2021)

43. Carbone, G., Rossi, C., Savino, S.: Performance comparison between FEDERICA hand and LARM hand. Int.J. Adv. Rob. Syst. **12**(7). 2015. https://doi.org/10.5772/60523
44. Rodinò, S., Lago, F., Malyshev, D., Carbone, G.: Design of a movable palm for a 3-fingers robotic hand. Int. J. Mech. Control **24**(1), 177–188 (2023)

Evaluating the Potential of Passive Exoskeletons in Modern Industries: A Comprehensive Analysis of the Impact on User Well-Being and Efficiency

Samuele Tonelli, Serenella Terlizzi, Cecilia Scoccia, Grazia Iadarola, Marianna Ciccarelli, Susanna Spinsante, and Giacomo Palmieri

Abstract This study investigates the application of passive exoskeletons in modern industries to enhance worker well-being and efficiency, especially in tasks prone to musculoskeletal issues. A specific protocol has been outlined to assess a passive exoskeleton (PAEXO back) through both objective and subjective analyses. The objective analyses focused on quantification on muscle activity, kinematic movements, and heart rate. Additionally, a preliminary study of skin conductance was carried out, since this parameter can directly disclose stress and exertion levels during task execution. On the other hand, the subjective analysis involved the use of questionnaires to quantify users' impressions, aiming to understand the impact of using an exoskeleton on task performance. The results indicate that the PAEXO back exoskeleton demonstrates promise and could prove beneficial for workers engaged in strenuous tasks, reducing the risk of musculoskeletal injuries and enhancing ergonomics. Nonetheless, there is the necessity to refine the protocol and extend the familiarization period to facilitate the transition of the study into a real workplace scenario.

Keywords Passive exoskeletons · Manufacturing · Human factor · Musculoskeletal disorders

S. Tonelli · S. Terlizzi · C. Scoccia (✉) · M. Ciccarelli · G. Palmieri
Department of Industrial Engineering and Mathematical Sciences, Polytechnic University of Marche, 60131 Ancona, Italy
e-mail: c.scoccia@staff.univpm.it

G. Iadarola · S. Spinsante
Department of Information Engineering, Polytechnic University of Marche, 60131 Ancona, Italy
e-mail: g.iadarola@staff.univpm.it

D. Pisla et al. (eds.), *Advances in Service and Industrial Robotics*, Mechanisms and Machine Science 157, https://doi.org/10.1007/978-3-031-59257-7_56

1 Introduction

The ongoing digital and technological transformation of production and logistics systems is emerging prominently with the advent of Industry 5.0. The social role of Industry 5.0 is placed at the centre of attention and in particular a human-centred approach in the design and management of production systems is promoted [1, 2]. The wellbeing of employees assumes a central role, especially in industrial contexts where manual activities remain fundamental, e.g. manufacturing industry. Many human factors have to be taken into account as the performance of activities is influenced by individual abilities, physical capabilities, gender, and age [3]. Furthermore, proper workstation design and environmental conditions are crucial to ensure workers' physical and mental efficiency [4]. In the ever-evolving landscape of technological innovation, active and passive exoskeletons emerge as a groundbreaking solution, offering support and assistance in various fields [5]. Industrial exoskeletons have recently gained increased attention as a form of personal protective equipment, aimed at minimizing work-related musculoskeletal disorders. There is a clear need for biomechanical risk assessment methodologies in scenarios where exoskeletons are used, so many researchers are investigating methods to evaluate how lifting support exoskeletons can reduce muscle activity [6] and fatigue in general. For this purpose, the authors developed a method for testing exoskeletons by means of a laboratory trial involving eight participants and consisting of objective and subjective evaluations. Currently, the most commonly used systems are: optoelectrical systems, inertial sensors and surface electromyography (sEMG) [7]. Beyond these conventional methods, a preliminary study explored skin conductance (SC), also known as electrodermal activity (EDA), which is associated to internal body temperature regulation. Stimuli activate the sympathetic nervous system, increasing sweat gland activity and SC. Therefore, the analysis of this parameter can directly reveal stress and exertion during task execution [8]. The objective analysis includes a motion test to assess joint angles and a fatigue test to estimate exertion. The latter is combined with the perceived fatigue questionnaire, which together with the post-experimental questionnaire accounts for the subjective analysis.

2 Materials and Methods

To conduct this analysis, a passive exoskeleton produced by Ottobock (Duderstadt, Germany) was used: the PAEXO back, designed to reduce the load on the lower back when lifting heavt objects. It operates based on a biomechanical principle: it absorbs force (from back and shoulders) during bending and releases it (to the thighs) during lifting, thereby facilitating the burden.

2.1 Tools for Objective and Subjective Analysis

This analysis is a combination of objective and subjective evaluations. To objectively quantify the effects of wearing the exoskeleton, several aspects were observed. Muscular activity is quantified by recording the electromyografic signals through the surface electrodes (sEMG) of the BTS FREEEMG 1000 system. This device has a sampling frequency of 1000 Hz and it is capable of acquiring the signals in real time and transmitting them wirelessly to the BTS EMG-analyser software. The electrodes were placed on the following muscles of interest: Erector Spinae Longissimus (ESL), Erector Spinae Ileocostalis (ESI) and the Semitendinosus (ST). The resulting data were then processed using a 4th-order Butterworth bandpass filter (with a cut-off frequency of 20–450 Hz), rectified and normalized with respect to the maximum contraction achieved during the task. Finally, the Root Mean Square (RMS) value of each signal was calculated, using a 2-second moving window with 1.8-second overlap. Using the Empatica E4 wristband worn on the non-dominant hand, heart rate (HR) and SC were recorded with sampling rates of 1 Hz and 4 Hz respectively. In particular, the SC signal was split into its two components: the Skin Conductance Level (SCL), indicating slow changes associated with thermoregulation and individual factors; and the Skin Conductance Response (SCR), reflecting rapid responses to external stimuli, driven by the Sympathetic Nervous System and appearing as sporadic peaks shortly after stimulus administration. Finally, to investigate whether joint angles change during the performance of a task with or without the exoskeleton, hip and knee flexion and extension angles have been analysed. Data acquisition was carried out using the Optitrack Motion Capture system at a sampling rate of 360 Hz. For the subjective evaluations, two questionnaires were administered to the participants. The first employs Borg Rating of Perceived Exertion (RPE) 0–10 scale to assess the subjects' perceived fatigue during task execution. The second questionnaire, on the other hand, is filled in at the end of the execution of both trials (with and without exoskeleton), and it consists of 16 different questions, to be rated on a 0–10 scale, and divided into four categories: Confidence (CO), Cognitive Load (CL), Functionality (FU) and Physical Effort (PE).

2.2 Testing Protocol

For the purpose of this analysis, eight male participants were involved, without orthopaedic problems, being 28.0 years old in average, and having a mean height of 178.4 cm, a mean mass of 72.9 kg and a mean body mass index (BMI) of 22.9.

The testing protocol steps are illustrated in Fig. 1. Initially, each subject is given a period of time to become familiar with the exoskeleton and the test procedure is explained. Subsequently, the choice of the trial is randomized, that is whether to start with or without the exoskeleton (exo or noexo). For the objective analysis, the first step is the fatigue test, which involves the acquisition of EMG, HR and SC signals.

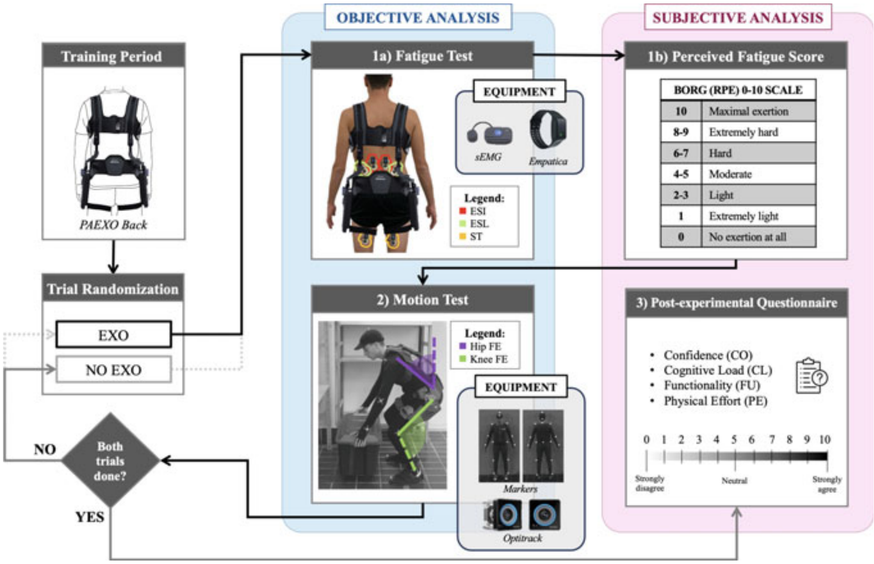

Fig. 1 Block diagram of the testing procedure: training period, trial randomization, objective analysis (1a. Fatigue Test; 2. Motion Test) with the employed equipment, subjective analysis (1b. Perceived Fatigue Score, 3. Post-experimental Questionnaire)

Specifically, this test involves the cyclic repetition of a task that includes lifting and stowing a box. The initial weight of the box is 6 kg, but it is gradually increased to 12 kg and then to 20 kg. The exercise is repeated for 5, 4 and 3 min for each weight respectively and between each stage there is a 2-minute break. On the other hand, for the subjective analysis, the Percieved Fatigue scores are recorded during task execution. The second step of the objective analysis is the motion test. The subject is provided with a suit with markers on it, in order to acquire joint angles with the motion capture system. At this stage, the previous exercise is repeated for 100 s for each weight. Once the test has been performed with and without the exoskeleton, the subject is asked to complete the post experimental questionnaire.

3 Results and Discussion

The muscular activity related to PAEXO back exoskeleton is summarized in Fig. 2a. The most relevant result regards the ST, since for this muscle the plot shows a reduced muscular contraction while wearing the exoskeleton. On the other hand, from a postural point of view, Fig. 2b shows a significant reduction in the maximal hip flexion angle while using the exoskeleton, which indicates the maintenance of a better posture. However, no significant influence was found on the HR. By way of example, the SC signals acquired for the subjects s2 and s8 are shown in Fig. 3,

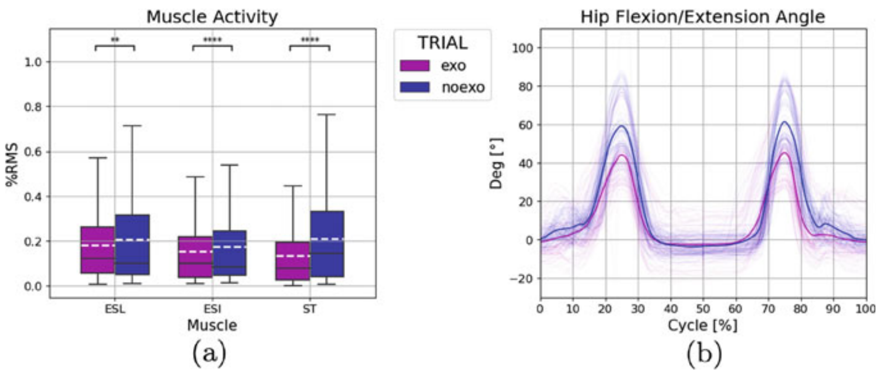

Fig. 2 Box plots of muscle activity (**a**), where the dotted lines represent the mean and the solid lines represent the median, stars indicate statistically significant differences resulting from Mann-Whitney-Wilcoxon two-sided test (*$p < 0.05$, **$p < 0.01$, ***$p < 0.001$, ****$p < 0.0001$); hip joint angles within a cycle of lifting and stowing the box (**b**)

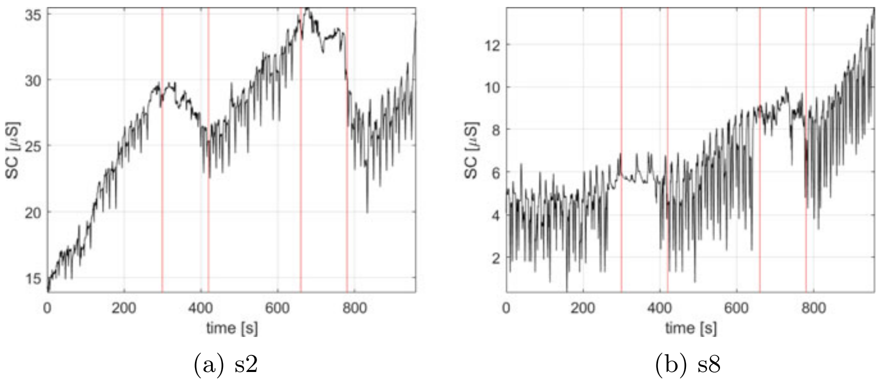

Fig. 3 SC signals for subject s2 (**a**) and subject s8 (**b**)

where the intervals between the red lines represent the windows of 2-minute break. Moreover, Table 1 shows, for each subject and each phase of the testing protocol, the average of SCL component and the average of SCR peaks per minute. As suggested in literature, an increase from relaxed condition to stimulation should appear in SCL component [9] as well as in terms of SCR peaks [10]. In this case study, an increase in the SCL component can be appreciated when proceeding from the initial phase to the final phase of activity. In particular, the growth is noteworthy for the subjects s1, s3, s6, s8, being at least equal to 60%. This outcome suggests that as the weight of the lifted box is increased when passing from one phase to the other, subjects experience an increase in sweating and, thus, in the physical effort. The only two exceptions occur with subjects s4 and s7, showing a decline in the SCL component during the final phase. Subject s4 stands out as an outlier displaying a consistent gradual decrease in the SCL component. Conversely, subject s7 con-

Table 1 Results of SC for each phase and each subject

Subject	Average of SCL [μS]					Average of SCR peaks/min				
	6 kg	Break	12 kg	Break	20 kg	6 kg	Break	12 kg	Break	20 kg
s1	13.59	24.03	25.71	25.47	25.52	8	6	7	5	8
s2	21.96	28.02	29.63	33.61	27.43	8	7	7	5	7
s3	0.14	0.14	0.14	0.15	1.46	0	0	0	0	4
s4	15.67	15.52	10.20	9.54	9.53	9	9	9	7	8
s5	2.75	2.97	3.35	3.16	3.22	8	8	10	8	8
s6	14.07	15.77	18.00	22.25	22.42	7	5	9	5	8
s7	3.60	5.54	6.71	7.78	2.61	4	5	7	8	6
s8	4.59	5.67	6.41	8.76	9.59	7	3	7	6	8

sistently exhibits an increasing trend in the SCL component throughout all phases, except the last one. This may be attributed to the limited acquisition time, potentially insufficient to induce a significant variation in SC amplitude for this specific subject. On the other hand, the number of SCR peaks per minute during the activity phases is compared to the number of peaks during the break phases. In fact, differently from SCL component, SCR component can reflect a rapid response to a stimulation [8]. The increase during the activity phases in comparison to the break phases in terms of number of peaks can be observed in the subjects s1, s2, s3, s5, s6, s8. Specifically, subjects s1, s6, and s8 consistently show more peaks during all activity phases than during breaks. Once again, when analyzing the number of SCR peaks, the sole exceptions are subjects s4 and s7. In conclusion, regarding the subjective analysis, the outcomes of the Perceived Fatigue Score questionnaire are depicted in Fig. 4. The regression line makes it evident that task execution without the exoskeleton yielded higher scores in comparison to performing the task while wearing the exoskeleton. This trend is consistent with the overall findings in muscle activity, highlighting a reduction in fatigue associated with the use of the exoskeleton. On the other hand, Table 2 shows the scores given in the 4 categories by the subjects involved in the experiment, giving a comprehensive grade of 5.5/10. Notably, the lowest score pertains to Confidence (CO), registering a value of 5.0, while the highest is linked to Functionality (FU), scoring 5.8. These findings suggest that, although participants initially encountered some adjustments in using the exoskeleton, the perception of its effectiveness indicates significant potential for fulfilling its intended design purpose.

4 Conclusions and Future Works

This study delves into the application of passive exoskeletons, with a specific focus on the PAEXO back, within modern industries to enhance worker well-being and efficiency, particularly in tasks susceptible to musculoskeletal issues. Through a

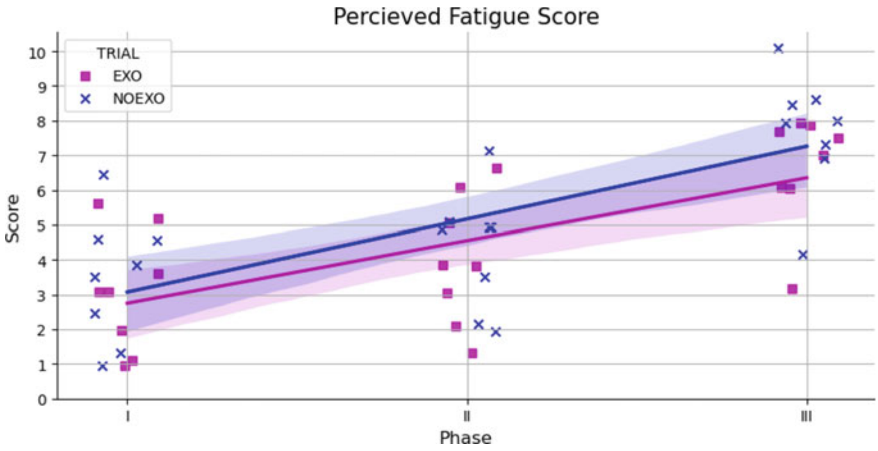

Fig. 4 Scatter plot and regression line (95% confidence interval) of the Perceived Fatigue Score across the three different phases (I, 6 kg; II, 12 kg; III, 20 kg)

Table 2 Post-experimental questionnaires in four categories: Confidence (CO), Functionality (FU), Cognitive Load (CL) and Physical Effort (PE)

Subject	Post-experimental questionnaire				
	CO	FU	CL	PE	TOT
s1	4.5	6.0	5.5	6.0	5.5
s2	6.0	6.2	5.6	6.3	6.0
s3	6.5	6.2	5.0	6.3	6.0
s4	2.0	3.8	6.2	4.7	4.2
s5	3.0	3.8	4.7	3.3	3.7
s6	7.0	7.6	5.2	8.0	6.9
s7	5.0	5.6	4.7	5.3	5.2
s8	6.0	7.0	7.2	5.3	6.4
TOT	5.0	5.8	5.5	5.7	5.5

The last row shows the average score of the four categories

comprehensive protocol encompassing both objective biomechanical assessments and subjective user feedback, the research sheds light on the potential benefits and areas for refinement in the integration of passive exoskeletons into modern industries. The results shows promise in reducing injuries and improving ergonomics for strenuous tasks. Objective analyses revealed a notable reduction in muscular contraction, especially in the Semitendinosus (ST) muscle, and improved hip flexion angles. This observation might be perceived as a limitation of the device, restricting freedom of motion. However, on a positive note, this limitation promotes improved posture and results in a reduction in torque, leading to less muscular effort. Moreover, the inclusion of skin conductance analysis provided valuable information about stress and exertion levels during task execution. The observed increase in SCL and SCR components suggests a physiological response to the weight of the lifted box, highlighting the potential of skin conductance as an additional parameter for assessing exoskeleton performance. Subjective evaluations, captured through questionnaires, consistently demonstrated a decrease in perceived fatigue scores when utilizing the exoskeleton. Despite experiencing initial unfamiliarity, participants expressed confidence in the functionality of the exoskeleton, underscoring their perception of its effectiveness. In conclusion, the PAEXO back exoskeleton demonstrates promise in enhancing worker efficiency in strenuous tasks within industrial settings and reducing the risk of musculoskeletal injuries. While the study highlights positive outcomes, the authors acknowledge the necessity to refine the testing protocol and extend the familiarization period to facilitate a smoother integration of passive exoskeletons into real workplace scenarios. The comprehensive insights gained from this research contribute to the ongoing discourse on human-centric approaches in the design and implementation of Industry 5.0, emphasizing the importance of employee well-being in the evolving landscape of technological innovation.

Acknowledgements This research has received funding from the project Vitality—Project Code ECS00000041, CUP I33C22001330007—funded under the National Recovery and Resilience Plan (NRRP), Mission 4 Component 2 Investment 1.5—'Creation and strengthening of innovation ecosystems,' construction of 'territorial leaders in R&D'—Innovation Ecosystems—Project 'Innovation, digitalization and sustainability for the diffused economy in Central Italy—VITALITY' Call for tender No. 3277 of 30/12/2021, and Concession Decree No. 0001057.23-06-2022 of Italian Ministry of University funded by the European Union—NextGenerationEU.

References

1. Ashta, G., Finco, S., Battini, D., Persona, A.: Passive exoskeletons to enhance workforce sustainability: literature review and future research agenda. Sustainability **15**(9), 7339 (2023)
2. De Looze, M.P., Bosch, T., Krause, F., Stadler, K.S., O'sullivan, L.W.: Exoskeletons for industrial application and their potential effects on physical work load. Ergonomics **59**(5), 671–681 (2016)
3. Kranenborg, S.E., Greve, C., Reneman, M.F., Roossien, C.C.: Side-effects and adverse events of a shoulder-and back-support exoskeleton in workers: a systematic review. Appl. Ergonom. **111**, 104042 (2023)
4. Papetti, A., Ciccarelli, M., Scoccia, C., Palmieri, G., Germani, M.: A human-oriented design process for collaborative robotics. Int. J. Comput. Integrated Manuf. **36**(12), 1760–1782 (2023)
5. Govaerts, R., De Bock, S., Provyn, S., Vanderborght, B., Roelands, B., Meeusen, R., De Pauw, K. The impact of an active and passive industrial back exoskeleton on functional performance. Ergonomics, 1–22 (2023)
6. Van Sluijs, R.M., Rodriguez-Cianca, D., Sanz-Morére, C.B., Massardi, S., Bartenbach, V., Torricelli, D.: A method to quantify the reduction of back and hip muscle fatigue of lift-support exoskeletons. Wearable Technol. **4**, e2 (2023)
7. Li-Baboud, Y.S., Virts, A., Bostelman, R., Yoon, S., Rahman, A., Rhode, L., Ahmed, N., Shah, M.: Evaluation methods and measurement challenges for industrial exoskeletons. Sensors **23**(12), 5604 (2023)
8. Iadarola, G., Bruschi, V., Cecchi, S., Dourou, N., Spinsante, S.: Low-cost monitoring for stimulus detection in skin conductance. Acta IMEKO **12**(3), 1–6 (2023)

9. Iadarola, G., Poli, A., Spinsante, S. Compressed sensing of skin conductance level for IoT-based wearable sensors. In: 2022 IEEE International Instrumentation and Measurement Technology Conference (I2MTC), pp. 1–6. IEEE (2022)
10. Amidei, A., Poli, A., Iadarola, G., Tramarin, F., Pavan, P., Spinsante, S., Rovati, L.: Driver drowsiness detection based on variation of skin conductance from wearable device. In: 2022 IEEE International Workshop on Metrology for Automotive (MetroAutomotive), pp. 94–98. IEEE (2022)

Technological Analysis of Types of Milking Systems and Robots: A Review

Denis Chikurtev, Ava Chikurteva, and Elena Blagoeva

Abstract Automated milking systems are sophisticated pieces of equipment that find a very large application on modern farms. They carry out milking processes completely autonomously, thanks to a robotic arm that is equipped with numerous sensors and auxiliary devices. In this paper, the components of automated milking systems are analyzed in terms of their technological characteristics, focusing mainly on the robots used. Typically, these systems use specialized robots that have a different design structure from industrial robots and are equipped with attachments to perform different operations. As a result of the technological analysis of the systems and robots used in automated milking systems, we can summarize that the development of robotics in the livestock sector has made a significant contribution to improving milking and animal care processes. The main issues that need to be further investigated are related to improved methods for collecting animal data and milk parameters, methods and algorithms for better udder and teat recognition and localization of cows, providing improved mobility and control of robotic arms, improving additional attachments and adding additional functionality and modularity to robotic arms.

Keywords Automated milking systems · Milking robots · Intelligent animal husbandry · Smart farms

D. Chikurtev (✉) · A. Chikurteva · E. Blagoeva
Institute of Information and Communication Technologies, Bulgarian Academy of Sciences, Sofia, Bulgaria
e-mail: denis.chikurtev@iict.bas.bg

A. Chikurteva
e-mail: ava.chikurteva@iict.bas.bg

E. Blagoeva
e-mail: elena.blagoeva@iict.bas.bg

D. Pisla et al. (eds.), *Advances in Service and Industrial Robotics*, Mechanisms and Machine Science 157, https://doi.org/10.1007/978-3-031-59257-7_57

1 Introduction

The development of technology and robotics in the field of animal husbandry and agriculture is giving a big boost to the farm sector globally. Thanks to robotic and automated solutions, production output is increased, raw material and resource costs, energy and time are reduced. They play a key role in solving problems regarding food security, energy efficiency and ecology. In this study, automated milking systems are considered as an essential element in modern and technologically advanced farms.

The aim of the paper is to investigate the types of automated milking systems, their main components, the technologies used and more specifically the robotic solutions in them. This will evaluate the effectiveness and applicability of the systems in practice and define problems for future research.

Automated milking systems (AMS) are usually composed of a milking cage, a robotic manipulator, a vacuum milking system, an udder and teat cup cleaning and disinfection system, a sensor system for cow and teat recognition, an information and communication system for animal identification, and milking data collection and analysis [1, 2]. The sophisticated design of the AMS also leads to the need to carefully plan the logistics and installation of the facility on farms [3].

The paper is structured in the following order, Sect. 2 discusses research on the different sub-systems of automated milking systems. In Sect. 3, the structure of the AMS is presented in detail and the classification of the different types of AMSs according to the technologies used is proposed. Section 4 describes the principle of operation and the applications of AMSs. Finally, a conclusion is presented where the current problems and topics for future research are defined.

2 Related Studies

Automated milking systems or Robotic Milking Systems (RMS) are designed to provide autonomous and continuous milking of cows on farms. Compared to conventional milking, they have significant advantages and are clearly the better choice for farmers [4].

In study [5], the authors made a detailed comparison between automated milking and non-automated milking. With this they show many benefits and advantages of automated milking systems. Milk quality is improved, cow health is monitored, milking time and staff occupancy is reduced. There is also one major issue to consider–the cost of automated milking systems. Furthermore, the authors define three types of automated milking systems according to their design: integrated AMS, AMS with industrial robot and rotary AMS. Each type of system has its application, depending on the needs of individual farms.

In [6], factors that influence milk production are investigated. The authors applied multivariable generalized mixed linear regressions to identify risk factors and the interaction between these factors and the amount of milk produced, using AMC.

The results of this study show that in terms of traffic, those AMCs with free traffic, lead to increased milk yield compared to those with forced traffic. The study also confirms the hypothesis that the use of one robot per pen is associated with reduced robot production per day compared to pens using 2 robots. Retrofitted farms had significantly less production in the first 4 years of installation compared to production after 4 years of installation. This indicates that it takes time for both cows to adapt to these systems and for farmers to learn to adjust milking and management parameters. In contrast, newly built farms did not see a significant change in production over time after installation, which may indicate that these systems are sophisticated and adaptable. Finally, the authors conclude that, overall, retrofitted farms do not produce significantly more or less milk than newly constructed farms. Similar results were achieved in another publication where the authors investigated milking parameters using AMS [7].

With regard to cow adaptation, the authors in [8], investigated factors that influence cows and respectively milk yield. It is clear from the study that stimulating cows to voluntarily go for milking, through the use of AMS, leads to increased quantity and quality of production. In addition, AMCs also have a positive impact on the farmers' psyche and health [9], with a reduction in stress. In another study, the relationships between selected psychological factors and milk parameters were investigated in detail by using AMS [10]. Here, the authors concluded that the natural physiological variability of udder and teat structure, as well as the course of lactation, significantly influences individual composition and milk flow during milking. As well as that the ability to regulate milk flow by adjusting the appropriate negative pressure during handling, given the observed variability of the individual mammary gland lobes, increases milking efficiency and as a result reduces the risk of mastitis in cows.

The results and research so far have been achieved thanks to another very useful feature of automated milking systems–the collection of data on multiple parameters for both milk and cow health. In [11], by analyzing data from AMS collected over a period of 3 years, the authors concluded that dairy cows are affected by heat stress. When the temperature-humidity index is increased, a decrease in milking time and a decrease in time spent in the milking parlor is observed. Another aspect that directly affects milking is herd formation. When cows are herded and AMS is used the human workload is significantly reduced and milking frequency is increased [12]. Another study looked for the relationship between milking interval and milk production rate. Here the authors found that reducing milking interval can significantly improve milk production rate [13].

An important factor in the milking process and the quality and functionality of the vacuum system. In [14], the influence of vacuum milking on milk production and udder health of cows is reviewed. Overall, the study showed that the management of vacuum systems is important for milk quality and quantity and cow health. These factors are also related to udder cleaning and disinfection. Different cleaning methods and techniques are presented in [15] and it is clearly seen that AMSs achieve better results in terms of milk cleanliness. In addition, the consumption of water and detergents is reduced, which reduces the financial costs and leads to an improvement in environmental parameters.

In another study [16], the authors focus on the energy efficiency of AMSs. Their study shows that the transition from pneumatic to electric actuators in AMS robots results in improved overall efficiency due to a reduction in the energy consumed by the air compressor.

According to the review, we can say that technological developments and scientific advances are the means to improve milk yield by implementing improved devices and methods to improve the systems and functions of automated milking systems.

3 Structure and Classification of AMS

The main manufacturers of automated milking systems covered in the study are Lely, Gea, DeLaval, Milkomax, SAC. They produce different types of systems tailored to the needs of the farms, in terms of the number of animals to be milked per day [17]. Specifically, we will consider the Astronaut-A5, DairyRobot-R9500, VMS-V310, M2ERLIN and Gemini UP Robot models. These system models are of the integrated AMC type–systems that are equipped with all the necessary modules to perform fully autonomous milking.

The main elements of each milking system are:

- **Milking boxes**: the place where the cow is milked and fed;
- **Identification system**: recognizes the cow and decides whether it should be milked and what the milking parameters should be;
- **Sensor system**: to recognize the udder, teats and measure milk parameters;
- **A robotic arm**: handles the preparation, milking and cleaning processes;
- **Milking and cleaning system**: performs the cleaning, milking and teat disinfection;
- **Software management system**: provides management of other systems, collects, processes, analyses and visualizes data.

The proposed classification of AMS is based on the device and different technological solutions used in modern automated milking systems. The proposed classification is based on the one proposed in [18]. Here, the authors consider the type of cow traffic, which in this case is not part of the AMS but refers to the logistics of a farm. Regarding milking boxes for integrated AMCs, we can define single and double, and their service is performed by one or two handlers, respectively.

The robotic arm used in these systems is usually specifically designed for them and is of the rigid robot type. Here the classification should be made according to whether the arm is equipped with embedded additional attachments or it is a gripper, that grasps and operates with the equipment (Fig. 1). Attention should also be paid to the type of actuator, as this directly affects the accuracy and control of the arm. Regarding the position of the arm, in all systems it is laterally positioned, and hidden so as not to disturb the cows. In all the systems considered, the robotic arm has an upper base that translates parallel to the cow's length, as well as translating in height, and the other arm units are rotary (Fig. 2). In [19], an approach for automated milking

Fig. 1 Robotic arm with integrated utensils–DairyRobot-R9500 (left) and robotic arm with gripper–DeLaval VMS V310 (right)

Fig. 2 Robotic arm used in Astronaut-A5

with a collaborative robot in a laboratory environment is presented, where due to many degrees of freedom of the robot, complex end-effector trajectory calculations are required.

Another different component is the cleaning and disinfection system, here the main difference is in cleaning and milking stimulation. In some systems brushes are used (Astronaut-A5, M2ERLIN) and in others cleaning is done by specially designed cups (DairyRobot-R9500, Gemini UP Robot, DeLaval VMS V310). Both types use water or soapy water. For disinfection, in some systems the robotic arm has a built-in nozzle for spraying disinfectant, while others carry this out via the cups.

For udder teat recognition, most systems use 3D cameras with computer vision and apply object recognition based on machine learning. Sensors built into the vacuum milking system are used to determine milk parameters. In terms of the information system for collecting and processing data for each cow, all AMSs offer a graphical application with charts and tables, remote control and monitoring.

The classification proposed is presented in Fig. 3. It refers to integrated AMSs, to serve small and medium farms.

We can define the following advantages and disadvantages for the different systems, according to the proposed classification, Table 1.

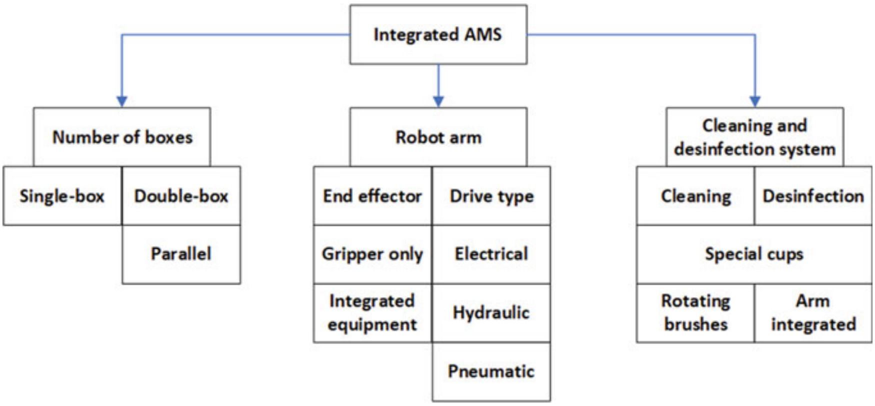

Fig. 3 Classification of AMC according to technological solutions

Table 1 Advantages and disadvantages of the different AMS sub-systems

	Advantage	Disadvantage
Box number		
Single box	Cheap price, easy install	Low capacity
Double box	High capacity	More complex, high price
End effector system		
Gripper only	Simple, easy service	More complex operations
Integrated equipment	Faster operation	Complex, advances service
Drive type		
Electrical	Quiet, accurate, energy efficient	High price
Hydraulic	Reliable	Mid energy efficient
Pneumatic	Reliable	Low energy efficient
Cleaning		
Special cups	Faster cleaning	Complex, advanced service
Rotating brushes	Better pre-milking stimulation	Complex, advanced service
Disinfection		
Special cups	Faster spraying	Complex, advanced service
Arm integrated	Simple, easy service	Slower spraying

4 Principle of Operation of AMS

In general, all AMSs operate in the same way. In Fig. 4, we have presented the workflow of operations for a complete milking of one cow. The process itself encompasses multiple operations to ensure maximum yield of quality and clean production, good cow health and optimum milking speed.

The AMS orchestrates a meticulously designed milking routine, commencing with cow identification as the animal enters the milking station. Identification sensors enable individualized milking processes, ensuring tailored care for each cow. The system incorporates a robotic arm equipped with advanced sensors for teat detection, attachment of milking cups, and the initiation of the milking process.

Sensor Integration and Milking Process: Key sensors within the system encompass teat-cleaning sensors, facilitating pre-milking disinfection for maintaining hygiene. Teat detection sensors enable precise cup attachment, ensuring an airtight seal for efficient and gentle milking. The system monitors milk flow, adjusting pressure and duration based on individual cow attributes. Additionally, sensors track milk quality parameters such as fat content and protein levels.

Fig. 4 Workflow of milking operations

Cow Welfare and Health Monitoring: Apart from milking, the system continuously monitors cow behavior, employing sensors to track activity levels and rumination patterns. These metrics aid in detecting deviations from normal behavior, potentially indicating health issues or heat cycles. All dairy farmers try to prevent mastitis. Apart from causing a great deal of pain to the cow, mastitis also means a lower milk yield, higher medical costs and more work. The milk quality control system helps detect mastitis at an early stage. The optional MQC-C function regularly takes measurements of each cow's somatic cell count. This ensures constant monitoring of cow health. Any deviations that could be of concern are shown immediately in the management platform. By taking action at an early stage, it ensures good well-being levels and high milk yield.

Autonomous milking systems can be installed indoors and outdoors. Their outdoor application refers to the rearing of herds outdoors. In these settings, difficulties arise in terms of access to water and electricity, as well as maintenance of the facilities [20]. As here the access of the cows is improved and uninterrupted, they are closer to the AMS. In an indoor installation, problems related to access to water and electricity are reduced, but the distance between the cows and the milking systems increases. In this case, the cows have to be further stimulated or forced to visit the milking robot.

5 Conclusion

The general appearance of the different models of automated milking systems at first glance looks quite the same. Going into a detailed study of the different solutions and systems used, it is apparent that quite different solutions and methods are used. It can be noted here that in order to find an optimized method or system, multi-criteria analysis and performance evaluation of the different solutions must be applied.

As a major challenge we can note the need for machine learning based analysis of the collected data in order to improve decision making. This is also related to the improvement of sensors and data collection methods from different systems.

Future research should be directed at finding improved methods for collecting animal and milk parameter data, methods and algorithms to better detect and locate udders and teats of cows, provide improved mobility and control of robotic arms, improve additional attachments and add additional functionality and modularity to robotic arms.

Acknowledgements This research is carried out as part of the project funded from the Bulgarian Ministry of Education and Science under the National science program "INTELLIGENT ANIMAL HUSBANDRY", grant agreement # D01-62/18.03.2021.

References

1. Zagidullin, L.R., Khisamov, R.R., Kayumov, R.R., Shaidullin, R.R., Zinnatov, F.F., Sadykov, N.F.: Dairy robotic milking system. In: BIO Web of Conferences, vol. 71, p. 01004. EDP Sciences (2023). https://doi.org/10.1051/bioconf/20237101004
2. Simões Filho, L.M., Lopes, M.A., Brito, S.C., Rossi, G., Conti, L., Barbari, M.: Robotic milking of dairy cows: a review. Semina: Ciênc. Agrár. **41**(6), 2833–2850 (2020). https://doi.org/10.5433/1679-0359.2020v41n6p2833
3. Rodenburg, J.: Robotic milking: technology, farm design, and effects on work flow. J. Dairy Sci. **100**(9), 7729–7738 (2017). https://doi.org/10.3168/jds.2016-11715
4. Shortall, J., Shalloo, L., Foley, C., Sleator, R.D., O'Brien, B.: Investment appraisal of automatic milking and conventional milking technologies in a pasture-based dairy system. J. Dairy Sci. **99**(9), 7700–7713 (2016). https://doi.org/10.3168/jds.2016-11256
5. Jiang, H., Wang, W., Li, C., Wang, W.: Innovation, practical benefits and prospects for the future development of automatic milking systems. Front. Agr. Sci. Eng. **4**(1), 37–47 (2017). https://doi.org/10.15302/J-FASE-2016117
6. Tremblay, M., Hess, J.P., Christenson, B.M., McIntyre, K.K., Smink, B., van der Kamp, A.J., Döpfer, D.: Factors associated with increased milk production for automatic milking systems. J. Dairy Sci. **99**(5), 3824–3837 (2016). https://doi.org/10.3168/jds.2015-10152
7. Sitkowska, B., Piwczyński, D., Aerts, J., Waśkowicz, M.: Changes in milking parameters with robotic milking. Arch. Anim. Breed. **58**(1), 137–143 (2015). https://doi.org/10.5194/aab-58-137-2015
8. Brouček, J., ToNGeL', P.: Adaptability of dairy cows to robotic milking. Slovak J. Anim. Sci. **48**(2), 86–95 (2015)
9. King, M.T.M., Matson, R.D., DeVries, T.J.: Connecting farmer mental health with cow health and welfare on dairy farms using robotic milking systems. Anim. Welf. **30**(1), 25–38 (2021). https://doi.org/10.7120/09627286.30.1.025
10. Kuczaj, M., Mucha, A., Kowalczyk, A., Mordak, R., Czerniawska-Piątkowska, E.: Relationships between selected physiological factors and milking parameters for cows using a milking robot. Animals **10**, 2063 (2020). https://doi.org/10.3390/ani10112063
11. Boďo, Š, Lüttmerding, G., Gálik, R., Kunc, P., Knížková, I., Gürdil, G.A.K.: Analysis of selected data from robotic milking regarding to heat stress of dairy cows. Acta Technol. Agriculturae **25**(2), 92–96 (2022). https://doi.org/10.2478/ata-2022-0015
12. Drach, U., Halachmi, I., Pnini, T., Izhaki, I., Degani, A.: Automatic herding reduces labour and increases milking frequency in robotic milking. Biosys. Eng. **155**, 134–141 (2017). https://doi.org/10.1016/j.biosystemseng.2016.12.010
13. Penry, J.F., Crump, P.M., Hernandez, L.L., Reinemann, D.J.: Association of milking interval and milk production rate in an automatic milking system. J. Dairy Sci. **101**(2), 1616–1625 (2018). https://doi.org/10.3168/jds.2016-12196
14. Besier, J., Lind, O., Bruckmaier, R.M.: Dynamics of teat-end vacuum during machine milking: types, causes and impacts on teat condition and udder health—a literature review. J. Appl. Anim. Res. **44**(1), 263–272 (2016). https://doi.org/10.1080/09712119.2015.1031780
15. Wang, X., Demirci, A., Graves, R.E., Puri, V.M.: Conventional and emerging clean-in-place methods for the milking systems. In: Raw Milk, pp. 91–115. Academic Press. https://doi.org/10.1016/B978-0-12-810530-6.00005-5
16. Höhendinger, M., Krieg, H.-J., Dietrich, R., Rauscher, S., Stumpenhausen, J., Bernhardt, H.: Impacts of divergent moving drives on energy efficiency and performance of various AMS in operative conditions. Agriculture **11**, 806 (2021). https://doi.org/10.3390/agriculture11090806
17. John, A.J., Clark, C.E.F., Freeman, M.J., Kerrisk, K.L., Garcia, S.C., Halachmi, I.: Review: milking robot utilization, a successful precision livestock farming evolution. Animal **10**, 1484–1492 (2016). https://doi.org/10.1017/S1751731116000495

18. Sharipov, D.R., Yakimov, O.A., Gainullina, M.K., Kashaeva, A.R., Kamaldinov, I.N.: Development of automatic milking systems and their classification. In: IOP Conference Series: Earth and Environmental Science, vol. 659(1), p. 012080. IOP Publishing. https://doi.org/10.1088/1755-1315/659/1/012080
19. Wang, C., Ding, F., Ling, L., Li, S.: Design of a teat cup attachment robot for automatic milking systems. Agriculture **13**, 1273 (2023). https://doi.org/10.3390/agriculture13061273
20. Cogato, A., Bršˇci´c, M., Guo, H., Marinello, F., Pezzuolo, A.: Challenges and tendencies of automatic milking systems (AMS): A 20-years systematic review of literature and patents. Animals **11**, 356 (2021). https://doi.org/10.3390/ani11020356

Part VII
Mobile Robots and Innovative Robot Design

Mobile Exploration Robot with Hybrid Locomotion System

Antonio Ioan Banabic and Mihai Olimpiu Tătar

Abstract The authors of this paper present an innovation in mobile robot modelling utilising a hybrid locomotion technology. The advantages of both wheeled and walking mobility are combined in the proposed locomotion system. The four-bar mechanism of the robot leg allows for improved stability and stiffness of the entire locomotion system without obstructing any of the three modes of mobility—on wheels, with legs, or combined. The paper describes the conceptual model, the structural scheme of the robot and analyses the possibilities of locomotion using wheels and legs.

Keywords Hybrid · Mobile robot · Locomotion

1 Introducere

The definition of exploration, in the field of robotic exploration extends beyond simply traversing known terrain to include discovery in unexplored spaces, be they remote planets, hazardous environments or confined spaces. The need for versatile robotic systems is becoming increasingly evident as we approach the frontiers of exploration. Wheeled robots work well on flat surfaces, but can struggle when navigating uneven terrain. This has led to the discovery of new methods of locomotion.

Their simplicity, adaptability to a wide range of shapes and sizes, and their high load capacity make conventional wheels popular. However, obstacles arise when these wheeled robots encounter uneven terrain, such as bumps, cracks and debris. By introducing complexity into the control mechanisms, active steering and timing

A. I. Banabic · M. O. Tătar (✉)
Technical University of Cluj-Napoca, Memorandumului, Nr. 28, 400114 Cluj-Napoca, Romania
e-mail: Olimpiu.Tatar@mdm.utcluj.ro

A. I. Banabic
e-mail: Antonio.Banabic@campus.utcluj.ro

D. Pisla et al. (eds.), *Advances in Service and Industrial Robotics*, Mechanisms and Machine Science 157, https://doi.org/10.1007/978-3-031-59257-7_58

become essential to maintain optimal robot performance. In contrast, legged locomotion systems offer a solution to the limitations of wheeled robots on uneven surfaces by providing the advantage of actively choosing position of the legs and controlling force distribution. However, there are significant drawbacks associated with legged locomotion systems, such as complicated control systems and high energy consumption [1–7].

Robotics specialists have focused on creating hybrid locomotion systems to address these problems. These innovative systems offer a complete solution that combines efficiency, adaptability and improved mobility, integrating the advantages of both wheeled and standing locomotion [8–10].

The study is further organized as follows: the conceptual model of the robot is described in the second section, and the analysis of the robot's movement is offered in the third section. The paper's conclusions are given at the end.

2 Conceptual Design

Our objective was to design a robot that could operate in a variety of locomotion modes.

It is necessary to employ a mechatronic mindset to design such a robot. The 3D model of the robot proposed in this paper is shown in Fig. 1. It is formed of four spatial mechanisms attached to a central platform that function as legs. At the end of these mechanism are four wheels that are mounted independently. Two different material types were used in the robot design: ABS and aluminium [11, 12]. A DC motor that generates the necessary torque for motion powers each wheel. A motor serves in achieving each wheel orientation. Each leg and each wheel's have two degrees of freedom thanks to the leg-wheel assembly.

A finite element simulation was carried out in order to determine the state of stress and deformations within the robot. The obtained results allow the dimensioning of the main resistance elements of the robot. For this purpose the total weight of the robot was calculated. For the simulation to function properly, motors, wheels, plates covering the robot frame and screws were removed. Knowing the total mass, 7.2 kg,

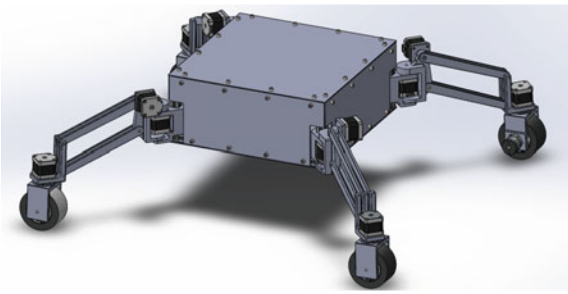

Fig. 1 The 3D model of the robot

the system was fixed to the wheel support and a force of 80 N was applied to the top of the frame.

The outcome of the finite element simulation is displayed in Fig. 2. The maximum stresses that occur following the application of 80 N force is $1.148e + 08$ N/m^2, stresses that are below the maximum value that the materials can withstand. For aluminium these are: $2.1e + 11$ N/m^2 and for ABS: $2e + 09$ N/m^2, [11, 12].

Figure 3 shows the displacements resulting from the simulation. The maximum displacement is 1.735 mm. The values obtained are quite low considering that several components that increase the rigidity of the structure were removed for the simulation.

Two degrees of freedom are available to each leg (M_1, M_2) and wheel (M_3, M_4) in the leg-wheel system. Figure 2 displays the assembly's kinematic system and 3D model. In Fig. 2, M_1, M_2 and M_3 represent stepper motors and M_4 represents the DC motor [13].

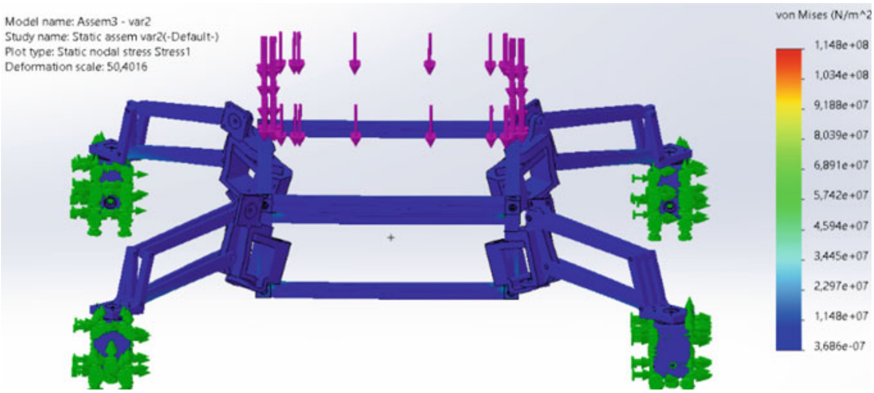

Fig. 2 Von Mises simulation

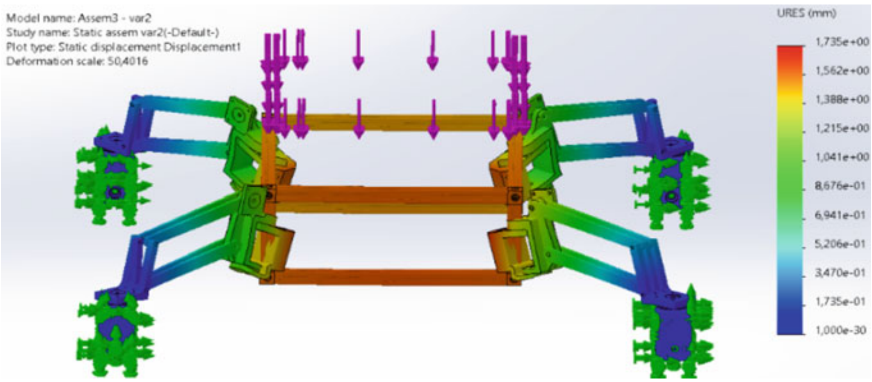

Fig. 3 Displacement simulation

For the kinematic analysis of the robot, the Denavit-Hartenberg method can be used, using the structural diagram of the leg in Fig. 4b [14].

The robot dimensions are: min/max length 591/815 mm, min/max width 597/821 mm, and min/max height 212/293 mm, depending on how its legs are arranged. Total mass is 7.2 kg. Figure 5 shows the volume of the robot during normal operation but also during transport. During operation the robot occupies a volume of 0.198 m^3 and during transport it occupies a volume of 0.074 m^3.

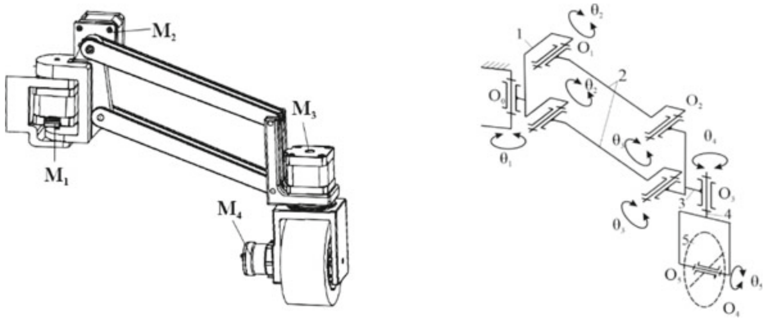

(a) (b)

Fig. 4 The leg-wheel structure of the assembly **a** 3D model; **b** structural diagram

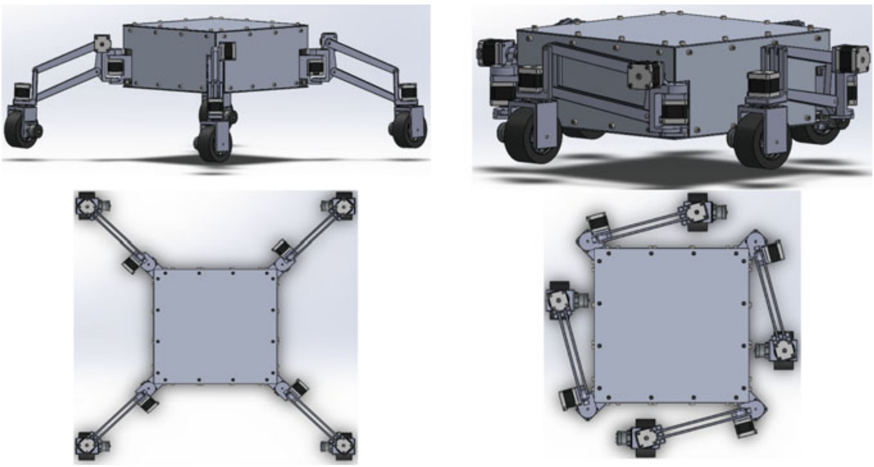

(a) (b)

Fig. 5 Changing the volume of the robot:: **a**Volume during operation (815 mm × 821 mm × 296 mm); **b** Volume during transport (591 mm × 597 mm × 212 mm)

3 Robot Locomotion

The robot is capable of three different types of locomotion because of this structure:

- locomotion on wheels—this involves using wheels to move the robot on flat terrain with its legs locked in place;
- walking locomotion—the wheels are locked in place, and the robot uses its legs to move over on uneven surfaces;
- hybrid locomotion—means that the robot is capable of moving both on wheels and with legs.

Locomotion on wheels

The drive motors M_1 and M_2 are positioned in a consistent manner to accomplish this kind of locomotion (the joints of the legs are locked). As a result, the robot will travel in three different directions: in Fig. 6a, b, around the CIR (Centre of Instantaneous Rotation), as shown in Fig. 6c, and diagonally, as shown in Fig. 6d [13]. The notation $\varphi_1, \varphi_2, \varphi_3, \varphi_4$ indicated the wheels orientation relative to the horizontal.

However, the robot can move in the plane with 3DOF. Thus, by holding the drive motor's location M_2 constant, we are able to lock the joints O_1, $O_1\prime$, O_2, $O_2\prime$. . The robot moves as a synchronous drive robot (the robot platform will be oriented in the same direction), as can be seen in Fig. 7.

While moving, the robot must maintain its stability at all times. This is achieved if the centre of gravity remains within the quadrilateral made by the wheels touching

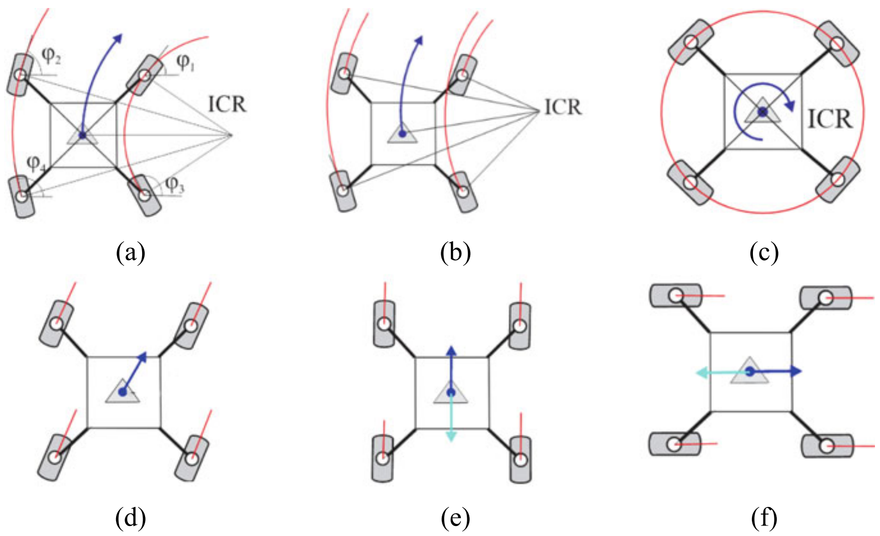

Fig. 6 Modes of wheel position

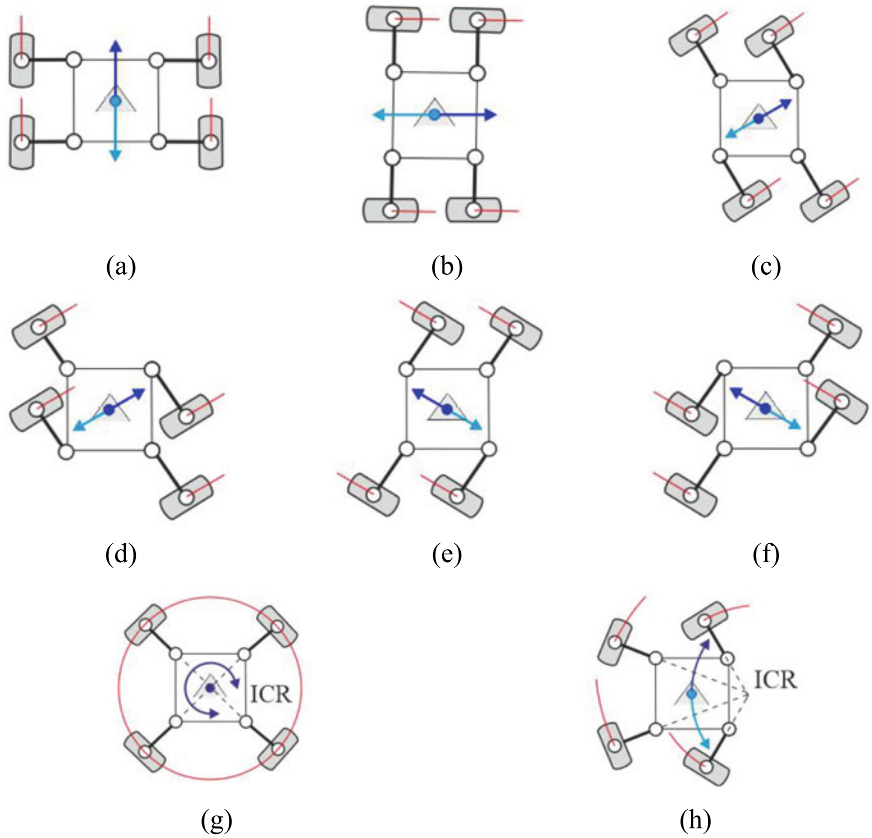

Fig. 7 Directions of motion for robot **a** forward–backward; **b** left–right; **c**–**f** diagonally; **g** rotation around CIR (CG = CIR); **h** rotation around CIR

the ground. Thus, in Fig. 8, several ways of positioning the legs and the polygons resulting from the contact of the wheels with the travel surface can be seen [13].

Legged locomotion

In walking mode, there are several ways to use the joints to achieve this movement. A first method is to lock the axes of the M_3 and M_4 motors and use the other motors to move the foot. Another method is to hold the M_4 motor shaft steady and use the M_1, M_2 and M_3 motors. In these situations, the robot operates like a quadruped robot [13].

The motor axis which drive the legs when walking is seen in Fig. 9. The motor axis M_4 remains constant and the leg can move it to 1, 2 and 3 positions. To guarantee the stability of the robot, it is necessary to keep the centre of gravity (CG) inside the triangle formed by the three legs in touch with the ground when modifying the points of contact with the walking surface (Fig. 9b).

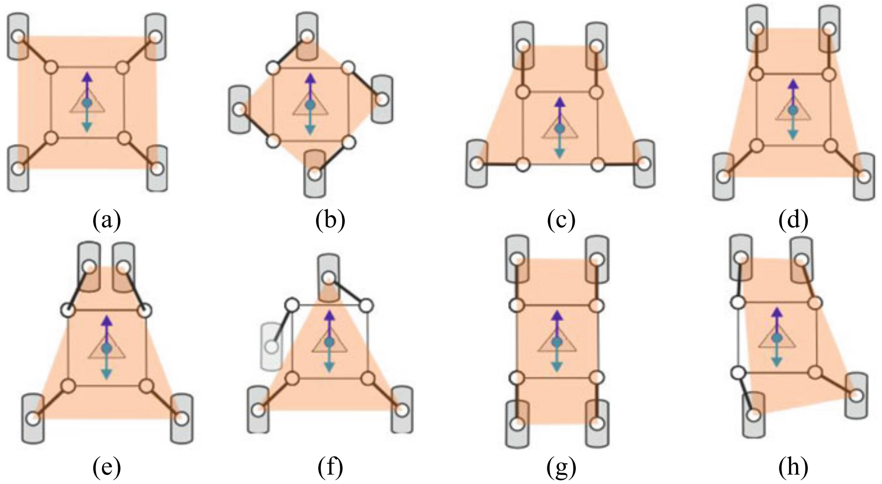

Fig. 8 Possible positions of the legs and the polygon made by them in X-position **b** with $\varphi_1 = 90°$ at each leg; **c**, **d** Y-shaped; **e** quasi-tripod; **f** tripod (with one leg raised); **g** with legs outstretched **h** with legs positioned asymmetrically

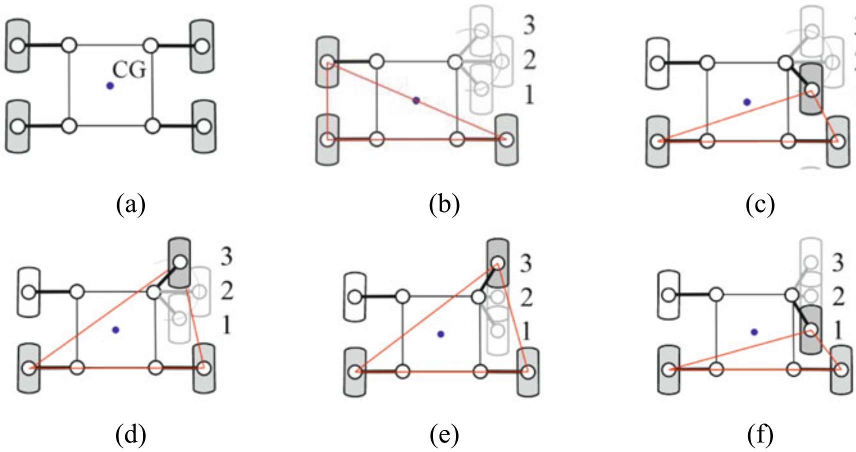

Fig. 9 Walking mode setup of the robot **a** diagram of robot in walking mode; **b**, **d**, **e** stable configuration; **c**, **f** unstable configuration

The obstacle's maximum height, $h_{\max}$ [mm], can vary depending on the robot's mode of locomotion. For wheeled locomotion $h_{\max}$ will be at most equal to the radius of the wheel, $r = 45$ mm. If the obstacle exceeds this value, the robot will not be able to move forward.

If this happens, the robot can move forward in walking mode. In this case, the distance between the raised wheel's contact point and the plane formed by the three

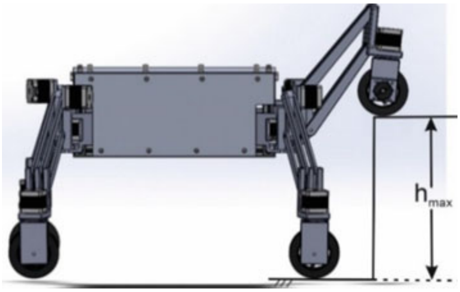

Fig. 10 Robot in walking mode

remaining feet on the ground is the maximum obstacle height ($h_{\max}$). In this mode $h_{\max}$ will be 286 mm (Fig. 10).

Hybrid locomotion

In this mode, all motors will be used, combining the efficiency of travel on flat surfaces with agility and the ability to overcome obstacles specific to locomotion with legs.

4 Conclusions

In this paper, a model of an exploration robot with a hybrid locomotive system was proposed. A 3D model of the robot was made, which was subjected to a finite element simulation to determine the maximum stresses and displacements. The structure of the leg-wheel assembly was presented, as well as the modes of locomotion that the robot can achieve. The proposed model can be considered as an effective model of a hybrid locomotion robot designed for exploration that offers greater mobility and high adaptability to different types of terrain. The robot will be physically built and tested in the following phase.

References

1. Taheri, H., Mozayani, N.: A study on quadruped mobile robots. Mech. Mach. Theory **190**, 1–17 (2023)
2. Rubio, F., Valero, F., Llopis-Albert, C.: A review of mobile robots: concepts, methods, theoretical framework, and applications. Int. J. Adv. Robot. Syst. **16**(2) (2019)
3. Ramirez, J.P., Hamaza, S.: Multimodal locomotion: next generation aerial–terrestrial mobile robotics. Adv. Intell. Syst. (2023)
4. Martz, J., Al-Sabban, W., Smith, R.N.: Survey of unmanned subterranean exploration, navigation, and localisation. IET Cyber Syst. Robot. **2**(1), 1–13 (2020)
5. Cirebea, C.I.: Research concerning of the mobile robots for inspection and exploration, Ph.D.Thesis, Technical University of Cluj-Napoca, Romania, 2012 (in Romanian)

6. Campion, G., Bastin, G., Dandrea-Novel, B.: Structural properties and classification of kinematic and dynamic models of wheeled mobile robots. IEEE Trans. Robot. Autom. **12**(1), 47–62 (1996)
7. Trojnacki, M., Dąbek, P.: Mechanical properties of modern wheeled mobile robots. J. Autom. Mobile Robot. Intell. Syst. **13**(3), 3–13 (2019)
8. Cordes, F., Kirchner, F., Babu, A.: Design and field testing of a rover with an actively articulated suspension system in a Mars analog terrain. J. Field Robot. **35**(7), 1149–1181 (2018)
9. Kameduła, M., Kashiri, N., Tsagarakis, N.G.: Wheeled motion kinematics and control of a hybrid mobility CENTAURO robot. Robot. Auton. Syst. **128** (2020)
10. De Santos, P.G., Garcia, E., Estremera, J.: Quadrupedal locomotion: an introduction to the control of four-legged robots, vol. 1. Springer, London (2006)
11. Rexroth Homepage. https://store.boschrexroth.com. Accessed in 03 Jan 2024
12. Omnexus homepage. https://omnexus.specialchem.com/selection-guide/acrylonitrile-butadiene-styrene-abs-plastic. Accessed 04 Jan 2024
13. Banabic, I.A.: Studies and research on exploratory robots, Technical University of Cluj-Napoca, coordinator Tătar, O.M. (2023) (in Romanian)
14. Handra-Luca V., Brisan C., Bara M., Brad S.: Introducere in modelarea robotilor cu topologie speciala, Editura Dacia Cluj-Napoca (2003) (in Romanian)

3D Printed Harmonic Drive for Legged Mobile Robots

D. G. Buleandra, A. O. Băneasă, and R. C. Donca

Abstract This paper will present the design and construction of a harmonic drive used in the actuation of a legged mobile robotic platform. The main advantage of this type of application is the minimal backlash, which is important for the precise positioning of the platform, also allowing high reduction ratios, in a compact form. The design also takes advantage of some of the latest additive manufacturing techniques, which have become easily accessible in the last few years. Most components are made from polymer materials, constructed using commercially available 3D printers.

Keywords Harmonic drive · Additive manufacturing · Legged robotics

1 Introduction

The field of legged robotics poses a particularly interesting challenge when it comes to mechanical drives. The drive has to be lightweight and compact enough to fit inside the leg mechanism of a mobile robot, as well as capable of delivering the substantial amount of torque needed for the movement of the part. It also has to be capable of extremely precise and repeatable movements to allow for the precise control of the motion of the legged robot.

Depending on the application, several constructive options are suitable for the design of a drive that can meet the requirements. For this particular application, the type of drive that was selected is the harmonic drive, also known as a strain wave gear drive. Harmonic drives are typically made up of three main constructive elements.

D. G. Buleandra · A. O. Băneasă (✉) · R. C. Donca
Mechatronics and Machine Dynamics Department, Technical University of Cluj-Napoca, Cluj, Romania
e-mail: Baneasa.Eu.Andrei@campus.utcluj.ro

D. G. Buleandra
e-mail: buleandra.fl.debora@student.utcluj.ro

R. C. Donca
e-mail: radu.donca@campus.utcluj.ro

D. Pisla et al. (eds.), *Advances in Service and Industrial Robotics*, Mechanisms and Machine Science 157, https://doi.org/10.1007/978-3-031-59257-7_59

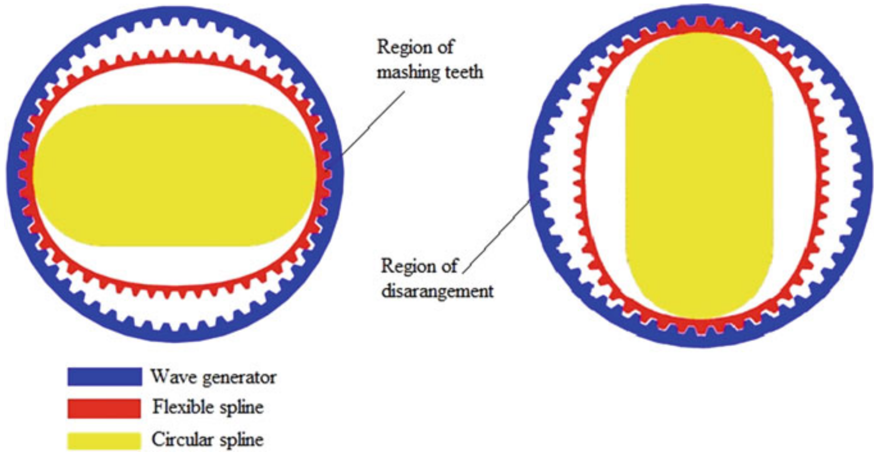

Fig. 1 Illustration of a strain wave gear

The wave generator can be found attached to the input shaft and has an elliptical shape. This will be deforming the second element, the flexible spline. The flexspline has teeth on its outer diameter, which engage with the teeth on the inside of the final element, the rigid circular spline. As the flexspline is deformed by the wave generator, its teeth will steadily engage with the circular spline in two diametrically opposed areas, providing the revolution of the circular spline in the reverse direction as the input shaft. The way this mechanism functions can be seen in more detail in Fig. 1.

The gear ratio is given as the ratio between the difference between the number of teeth of the circular spline and the number of teeth of the flexible spline and the number of teeth of the flexible spline [1]:

$$\text{gear ratio} = \frac{\text{no. teeth of the flexspline} - \text{no. teeth of the circular spline}}{\text{no. teeth of the flex spline}} \tag{1}$$

Because of this, the closer the number of teeth of the two splines are, the higher the reduction ratio is, meaning, it is possible to obtain very high reduction ratios by simply designing the flexible spline with a number of teeth that is just shy of the number of teeth of the circular spline. In fact, this is generally considered to be one the greatest advantages of this design, as it is quite common to get gear ratios of anywhere between 30:1 and 320:1.

Some other advantages of harmonic drives, when compared to traditional planetary drives, include their reduced weight. They can also generate high repeatability when repositioning inertial masses, due to extremely low backlash and the fact that the input and output shafts are coaxial. All these make it suitable not just for walking robotic platforms, but also for applications in industries such as aerospace and automotive.

In applications where high temperatures and high stress of the components is not expected, additive manufacturing technologies based on polymeric materials can be employed. As this is the case for most legged platforms, the design proposed here has most of its components made using this technology. The main advantages are the reduced weight, reduced cost and the short amount of time required to make the finished product [2] as compared to other designs, which will be discussed in the next chapter.

2 State of the Art

In the field of legged mobile robots, a great number of mechanisms have been used over the years in order to increase the torque output of various electrical drives which are constrained by size and weight limitations specific to the application.

The most obvious solution is to directly drive each joint using one motor. Unfortunately, this means that there is no mechanical amplification of torque. To overcome this, engineers need to resort to clever designs to achieve the desired leg motion. A good example of this can be seen in the design of Minitaur, which uses a 5 bars mechanism, directly driven by two electric motors. Although simple, robust and lightweight, this topology only has two degrees of freedom which may prove to hinder the platform's performance [3].

A significant number of designs rely on various versions of the traditional planetary gear drive. These can be integrated together with the motor and electronics into a single unit, allowing for modular design. This is possible in part due to the possibility of designing the drives to have high reduction ratios while still being compact. One good example of this is MIT's Cheetah [4], which takes advantage of a planetary drive with a gear ratio of 1:5.8 that is part of a bigger module also including the motor and an encoder. One significant disadvantage of planetary drives is that there is inherit backlash in the mechanism, reducing the accuracy. This can be mitigated through precise machining of the components and advanced control techniques, but these increase the complexity of the unit [5].

A novel approach is the series elastic actuator. Unlike traditional robotic joints, this design includes a flexible element, such as a linear compression spring. The connection between the driving mechanism and the flexible element is usually obtained using a variation of a chain and pulley mechanism. This is where harmonic drives can come in handy, as they are used as a torque multiplier, which is necessary for ensuring the deflection of the flexible element embedded in the leg design. By pre-loading the flexible element, the combination of harmonic drive and flexible component results in a backlash free design. One such design has been prototyped by researchers at the Swiss Federal Institute of Technology (ETHZ) for the ScarlETH project [6].

3 Dimensioning of the Harmonic Drive

Starting with the gear ratio, the number of teeth of the flexible spline and the circular spline can be chosen. For a gear ratio of 100:1, the number of teeth of the circular spline is $z_1 = 101$ and the number of teeth of the flex spline is $z_2 = 100$. Choosing a standardized module of $m = 0.45$, we can calculate the reference diameters of the two components.

$$D1 = z1 \cdot m = 101 \cdot 0.45 = 45.55\ \text{mm} \tag{2}$$

$$D_2 = z_2 \cdot m = 100 \cdot 0.45 = 45\ \text{mm} \tag{3}$$

The geometry of the teeth depends on the tooth profile. From a geometric point of view, both the involute profile and the triangular profile can be used. We chose a triangular profile, using recommended values for the pressure angle, reference top height coefficient and the usable height coefficient of the profile. We determined the specific deformation of the flexible spline $k_D = 0.87$.

To achieve a more compact design, we decided to put the wave generator on the rotor casing of the DXW A2208 brushless motor. This is possible because, for these types of motors, the output shaft is directly mounted on the out-runner rotor. The width of the flexible spline and the width of the wave generator will be equal to the usable width of the casing.

We chose a cam-type wave generator because it ensures adequate support for the flexible spline on its entire perimeter. This helps to achieve and maintain an optimal deformation shape. Using rolling bodies (bearing balls) between the outer surface of the cam and the flexible spline, the sliding friction is replaced by rolling friction. We can determine the perimeter of the cam knowing the inner radius of the not deformed flexible spline and the distance between the two components (Fig. 2).

The elliptic perimeter can be approximated by the equation:

$$L_c = 2 \cdot \pi \cdot \sqrt{\frac{a^2 + b^2}{2}} \tag{4}$$

To simplify the structure of the flexible spline, we decided to use another output component [7]. For half the width of the flexible spline, it will engage with the circular spline and for the other half, it will engage with the output component. To generate an output angular velocity equal to the angular velocity of the flexible spline, the geometry of the output spline will be similar to the geometry of the circular spline. It will have the same diameters and tooth profile, but the number of teeth will be equal to the number of teeth of the flexible spline.

To eliminate the sliding friction between the fixed component and the output component, we added a bearing channel on the surfaces between them. The geometry of the entire drive can be seen in Fig. 3.

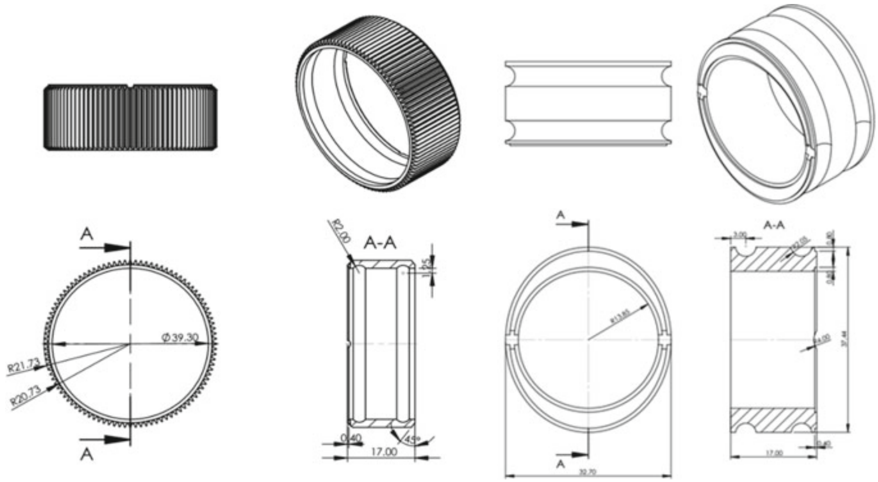

Fig. 2 The geometry of the flexspline (left) and the cam (right)

Fig. 3 Exploded view of the harmonic drive

4 Practical Realization

The practical realization of the components was achieved using the Anycubic Photon 3D printer. The technology behind this type of printing is known as stereolithography. A razor-thin layer of liquid polymer is exposed to UV light by a computer-controlled screen. The liquid polymer is sensitive to UV light and as such, solidifies when exposed to it. The pixels of the screen are activated in the shape of the slice it needs to create. The print is slowly raised out of the resin tank as new layers are added [8]. The final result is shown in Fig. 4.

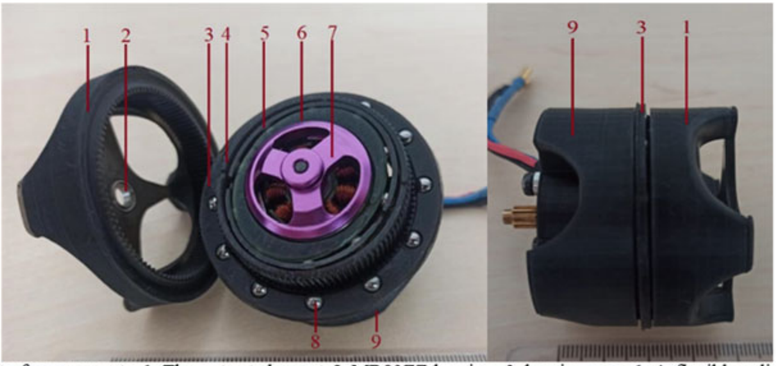

List of components: 1. The output element, 2. MR83ZZ bearing, 3. bearing cage 1, 4. flexible spline, 5. bearing cage 2, 6. the cam, 7. the brushless motor, 8. 2mm bearing balls, 9. the exterior circular spline (the fixed component)

Fig. 4 Final assembly of the harmonic drive

5 Results

In order to test the performance of our design, we created a simple test setup. This is made up of a flange onto which the drive is rigidly mounted. The two shafts are connected through a coupling to torque transducers [9]. This coupling also allows for additional load to be placed onto the output shaft. This was used to measure the input and output torque of the system. Both the input and output shafts of the drive are equipped with rotary encoders with a 20-bit resolution [10], which translates to a precision of around one and a quarter arc second, allowing for precise measurement of the position, and therefore the speed of the two shafts. This is also useful in determining the real backlash of the drive. Figure 5 presents a schematic overview of the setup used.

The obtained gear ratio is equal to the desired gear ratio of 100:1. A load was added to the output shaft in order to measure the input and output torque. The speed of the motor was steadily increased until there was observed tearing of the flexspline. We determined a maximum output torque of approximately 68.4 Nm. The values of the input and output torque depending on motor speed are represented in Fig. 6.

The efficiency can be calculated by simply dividing the output torque values to the corresponding input torque values. We obtained an efficiency of 65.04%. The common values for efficiency of commercially available harmonic drives are between 68 and 82% at an ambient temperature of 200 °C, with a maximum obtained efficiency of 89% at 500 RPM and 400 °C [11].

The backlash measured has an average value of approximately 225 arc seconds. Comparing with commercially available harmonic drives, the backlash is approximately 15 to 20 times higher [12]. Considering that additive manufacturing techniques were used, which are better suited to rapid prototyping rather than mass production, this result is to be expected (Fig. 7).

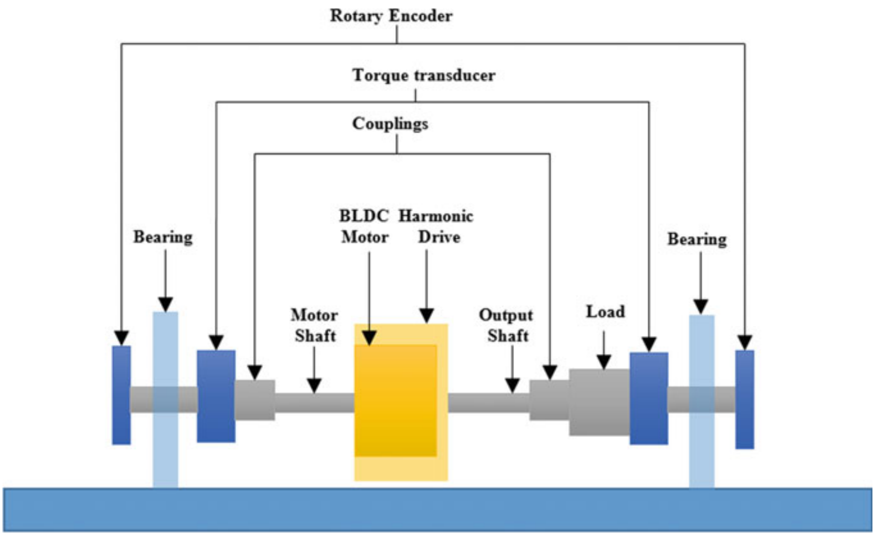

Fig. 5 Schematic representation of the test setup

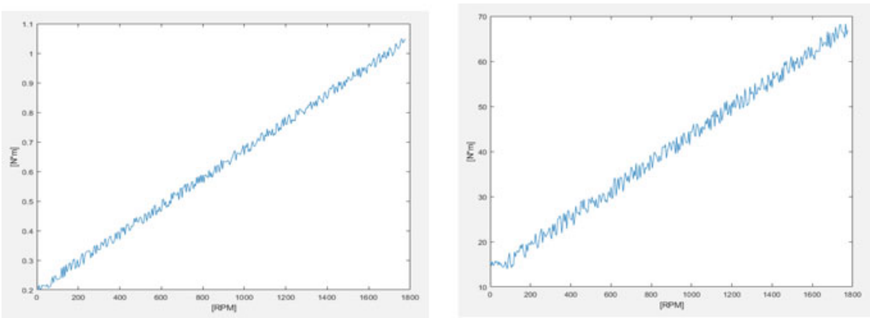

Fig. 6 Input torque depending on motor speed (left) and Output torque depending on motor speed (right)

Due to its geometry, the main cause of destruction of the flexible element is the variable bending stress and tooth wear. The material used must respond well to bending and stress concentrators and elongate as much as possible. In order to test the reliability of our design, the drive was driven at 1500 RPM, with no supplementary load, for 100 h. This equates to a total of 9 million deformations of the flexspline and about 1172 km travelled. The backlash was measured at different angular positions both before and after the test. The obtained values can be observed in Fig. 8.

The average backlash value stayed consistent after testing and the amount of wear is insignificant. However, it is plain to see that wear did occur, as the values of the backlash measured around certain positions increased. This suggests that although wear is present, it is consistent across the entirety of the flexspline. The cause for

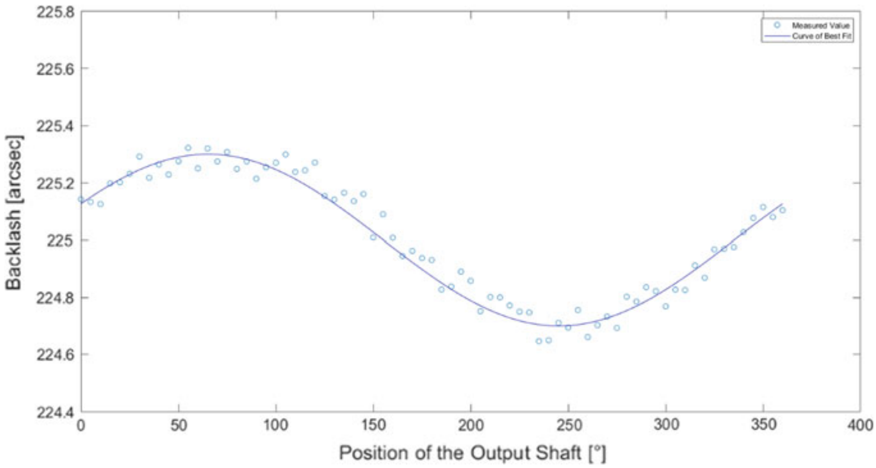

Fig. 7 Measured backlash of the harmonic drive

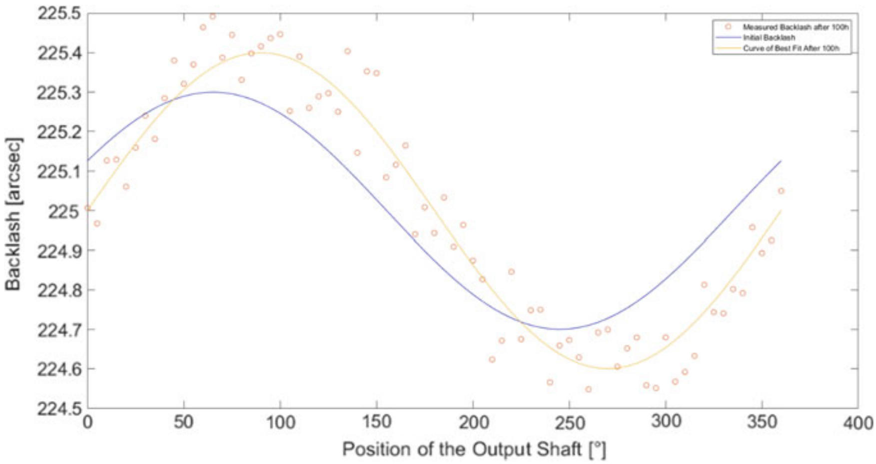

Fig. 8 Backlash before test (blue) and backlash after test (orange)

increased backlash is the wear of tooth crest and surface, while the accumulation of debris in the wave generator and tooth slot can decrease its value [13].

6 Conclusions

This paper presents the design of a harmonic drive which has most of its constructive elements made from polymeric materials and created using 3D printing technology. This type of drive is suitable for light weight robotics applications, as part of the driving mechanisms that allow for locomotion of legged robotic platforms. The prototype created by the authors provides the proof of concept that such mechanisms can be obtained using currently available additive manufacturing technologies.

References

1. Yu, Z., Gong, J.: Introducing kinematic fundamentals of strain wave gear for robotic arm joint (2019)
2. Berger, U.: Aspects of accuracy and precision in the additive manufacturing of plastic gears. Virt. Physic. Prototyp. **10**(2), 49–57 (2015). https://doi.org/10.1080/17452759.2015.1026127
3. Kenneally, G., De, A., Koditschek, D.E.: Design principles for a family of direct-drive legged robots. IEEE Robot Autom. Lett. **1**(2), 900–907 (2016)
4. Wensing, P.M., Wang, A., Seok, S., Otten, D., Lang, J., Kim, S.: Proprioceptive actuator design in the MIT Cheetah: impact mitigation and high-bandwidth physical interaction for dynamic legged robots. IEEE Trans. Rob. **33**(3), 509–522 (2017). https://doi.org/10.1109/TRO.2016.2640183
5. Chu, J.: Mini cheetah is the first four-legged robot to do a backflip. MIT News. Available at: https://news.mit.edu/2019/mit-mini-cheetah-first-four-legged-robot-to-backflip-0304. Accessed on 2024/02/10
6. Hutter, M., Remy, C., Hoepflinger, M., Siegwart, R.: High compliant series elastic actuation for the robotic leg ScarLETH. (2011). https://doi.org/10.1142/9789814374286_0059
7. Harmonic Drive Technologies: Pancake Component Gear Sets. Available at: https://www.harmonicdrive.net/_hd/content/LegacyLit/HDABFRPancakeBroch.PDF. Accessed on 2024/02/10
8. Quan, H., Zhang, T., Xu, H., Luo, S., Nie, J., Zhu, X.: Photo-curing 3D printing technique and its challenges. Bioact. Mater. **5**(1), 110–115 (2020). ISSN 2452–199X. https://doi.org/10.1016/j.bioactmat.2019.12.003
9. Vetek: Rotating torque transducer 10nm, USB. Available at: https://www.vetek.com/rotating-torque-transducer-10nm-usb-easytork-10nm-en/article. Accessed on 2024/02/10
10. Zettlex Inductive Encoders: Incoder inductive angle encoder 58mm: Zettlex. Available at: https://www.celeramotion.com/zettlex/product/incoder-58mm/. Accessed on 2024/02/10
11. Gravagno, F., Pennestri, E., Mucino, V.: The mechanical efficiency of harmonic drives: a simplified model. J. Mech. Des. (2020). https://doi.org/10.1115/1.4048412
12. Wang, B., Liu, J., Wang, C.: Measurement and analysis of backlash on harmonic drive. Mater. Sci. Eng. **542**, 012005 (2019)
13. Ishikawa, S.: Tooth profile of spline of Strain Wave Gearing. United States of America Patent Number 4.823.638. (1989)

Modeling, Parameter Estimation and Control Design of 4WIS4WID Mobile Robot: Simulation and Experimental Validation

Branimir Ćaran, Marko Švaco, Filip Šuligoj, and Bojan Jerbić

Abstract This paper introduces a systematic modeling approach for a mobile robot structure equipped with four-wheel-independent steering and four-wheel-independent driving (4WIS4WID). The mathematical model provided in this study forms the basis for the development of conventional PID controllers for both the steering and driving systems. Additionally, a non-linear kinematic trajectory tracking control law is proposed for accurate trajectory tracking. To ensure the effectiveness of the model, all relevant parameters are estimated, and the driving and steering subsystems are rigorously validated through simulations. These simulations are instrumental in identifying the optimal controller gains required for precise trajectory tracking. Subsequently, the chosen controller gains are implemented on a physical 4WIS4WID mobile robot, and the paper presents the results obtained from both simulation and experimental trials. During the experimental phase, the robot's movements are recorded using the OptiTrack motion capture system, enabling the verification of kinematic parameters, and providing insights for future research endeavors.

Keywords 4WIS4WID mobile robot · Kinematic and dynamic modeling · Parameter estimation · Non-linear trajectory tracking · Experimental validation

1 Introduction

In the last few years, there has been a growing interest in four-wheel-independent steering and four-wheel-independent driving (4WIS4WID) mobile robot structure [1]. This surge is attributed to electric motors, known for their high maneuverability. The application of this structure has been extensively examined across diverse sectors, including automotive and robotics industry [2–5]. Most of the research has been

B. Ćaran (✉) · M. Švaco · F. Šuligoj · B. Jerbić
Faculty of Mechanical Engineering and Naval Architecture, University of Zagreb, Zagreb, Croatia
e-mail: branimir.caran@fsb.hr

B. Jerbić
Croatian Academy of Sciences and Arts, Zagreb, Croatia

D. Pisla et al. (eds.), *Advances in Service and Industrial Robotics*, Mechanisms and Machine Science 157, https://doi.org/10.1007/978-3-031-59257-7_60

based on automotive applications due to electrification and requirements for high maneuverability. Robotics applications of this structure are still in research process, most robotics applications of this structure are based on agriculture [6, 7] and service robots [8].

Mathematical modeling and parameter estimation of 4WIS4WID structure are crucial segments before experimental validation of robot behavior and its control systems for driving and steering [9–11]. Despite simulations, mathematical model gives opportunity for stability and controllability analysis, controller design and model based control, such as the use of the model predictive control (MPC) method to realize the robot's trajectory tracking control.

In this paper, systematic modelling of kinematics and dynamics for 4WIS4WID robot structures has been presented. A derived model of robot has been parsed into driving and steering subsystems whose parameters have been estimated offline and simulation were validated with experimental data. With the given model of the robot, control systems for steering and driving subsystems have been designed using conventional PID controllers and non-linear kinematic model for trajectory tracking has been developed. With model and controllers, simulations were performed to find the best possible gains for non-linear kinematic control law. Gain values with fastest response and minimal overshoot were chosen for simulation and experimental validation.

2 System Description

Mobile robot used for experimental validation is developed in Regional Center of Excellence for Robotic Technologies (CRTA). Main purpose of this robot is to drive on vertical surfaces and perform NDT [8, 12]. Robot is equipped with additional actuators for performing NDT (nondestructive testing) inspection, but driving on vertical surfaces and performing NDT are not in the scope of this paper.

As shown in Fig. 1a, mobile robot is equipped with four steering motors and four driving motors *Dynamixel XH430-W210-T* found one actuator system with motor and driver in one case [13]. Mobile robot is equiped with a single board computer (*Raspberry Pi*) and communication with motors is done via USB to TTL converter. The mobile robot is controlled with the Robot Operating System (ROS), and its communication is primarily wireless. The single-board computer on the mobile robot transmits joint states to the master PC, which in turn calculates the required velocities for the robot to follow a predefined trajectory. Simultaneously, the master PC communicates with an OptiTrack PC to record and analyze the ground truth pose of the robot.

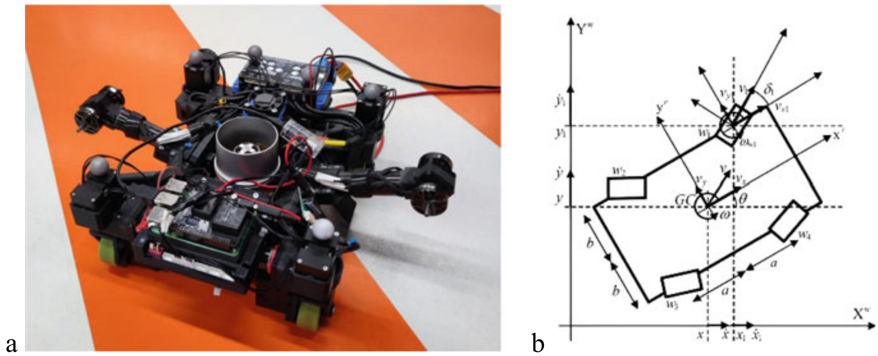

Fig. 1 4WIS4WID experimental robot (**a**) and robot schematic (**b**) [9]

3 Kinematic and Dynamic Model

In this section kinematic and dynamic models of four-wheel independent steering four-wheel independent driving mobile robot are presented. The kinematic model allows controlling the robot and calculating its position, while the dynamic model is responsible for all the forces and moments with which the actuators act on the robot.

3.1 Kinematic Model

A mobile robot configuration is shown in Fig. 1b. Global coordinates x, y and θ represent the pose of the robot in world reference frame; $2a$ and $2b$ are length and width between wheels respectively; wheels are denoted as w_i with the radius r and steering angle δ_i. The position of each wheel is defined as: $(x_{w1}, y_{w1}) = (a, b)$, $(x_{w2}, y_{w2}) = (-a, b)$, $(x_{w2}, y_{w2}) = (-a, -b)$ and $(x_{w4}, y_{w4}) = (a, -b)$. v and v_i are respectively robot linear speed $v = \sqrt{{v_x}^2 + {v_y}^2}$ and linear speed of each wheel $v_i = \sqrt{{v_{xi}}^2 + {v_{yi}}^2}$. ω is angular velocity of mobile robot and ω_i is steering velocity of each wheel.

Under the assumption that there are no motions of pitch and roll and mass is concentrated in the centroid of the mobile robot without considering slipping conditions, relationships between mobile robot velocity and each wheel velocity can be obtained by the rigid body constraints as $v_{xi} = v_i cos(\delta_i) = v_x - y_{wi}\omega$ and $v_{yi} = v_i sin(\delta_i) = v_y + x_{wi}\omega$.

By substituting the parameters of the robot in equations for v_{xi} and v_{yi} the relationship between wheel velocity and mobile robot velocity can be represented as:

$$\begin{bmatrix} 1 & 0 & -b \\ 0 & 1 & a \\ 1 & 0 & -b \\ 0 & 1 & -a \\ 1 & 0 & b \\ 0 & 1 & -a \\ 1 & 0 & b \\ 0 & 1 & a \end{bmatrix} \begin{bmatrix} v_x \\ v_y \\ \omega \end{bmatrix} = \begin{bmatrix} cos(\delta_1) & 0 & 0 & 0 \\ sin(\delta_1) & 0 & 0 & 0 \\ 0 & cos(\delta_2) & 0 & 0 \\ 0 & sin(\delta_2) & 0 & 0 \\ 0 & 0 & cos(\delta_3) & 0 \\ 0 & 0 & sin(\delta_3) & 0 \\ 0 & 0 & 0 & cos(\delta_4) \\ 0 & 0 & 0 & sin(\delta_4) \end{bmatrix} \begin{bmatrix} v_1 \\ v_2 \\ v_3 \\ v_4 \end{bmatrix} \tag{1}$$

We can introduce the pseudo-inverse of matrix where K=4a^2 + 4b^2. Premultiply Eq. 1. with $\boldsymbol{P}^{+}$ relationship can be obtained as:

$$\begin{bmatrix} v_x \\ v_y \\ \omega \end{bmatrix} = \begin{bmatrix} \frac{\cos(\delta_1)}{4} & \frac{\cos(\delta_2)}{4} & \frac{\cos(\delta_3)}{4} & \frac{\cos(\delta_4)}{4} \\ \frac{\sin(\delta_1)}{4} & \frac{\sin(\delta_1)}{4} & \frac{\sin(\delta_1)}{4} & \frac{\sin(\delta_1)}{4} \\ W_1 & W_2 & W_3 & W_4 \end{bmatrix} \begin{bmatrix} v_1 \\ v_2 \\ v_3 \\ v_4 \end{bmatrix} \tag{2}$$

where $W_i = (-y_{wi}\cos(\delta_i) + x_{wi}\sin(\delta_i))/(4{x_{wi}}^2 + 4{y_{wi}}^2)$.

Combining the three states of the robot body, wheel rotating angle and wheel steering angle, there are 11 state variables that represent the states and pose of 4WIS4WID mobile robot $\boldsymbol{q} = \begin{bmatrix} x & y & \theta & \varphi_1 & \varphi_1 & \varphi_1 & \varphi_1 & \delta_1 & \delta_2 & \delta_3 & \delta_4 \end{bmatrix}^T$.

After some calculations, kinematic model of mobile robot can be obtained as velocity vector $\dot{\boldsymbol{q}}$ in world coordinate frame; φ_i denotes the angle of driving wheel; c_i and s_i are $\cos(\theta + \delta_i)$ and $\sin(\theta + \delta_i)$ respectivly.

$$\dot{\mathbf{q}} = \begin{bmatrix} \dot{x} \\ \dot{y} \\ \dot{\theta} \\ \dot{\varphi}_1 \\ \dot{\varphi}_2 \\ \dot{\varphi}_3 \\ \dot{\varphi}_4 \\ \dot{\delta}_1 \\ \dot{\delta}_2 \\ \dot{\delta}_3 \\ \dot{\delta}_4 \end{bmatrix} \begin{bmatrix} \frac{c_1}{4} & \frac{c_2}{4} & \frac{c_3}{4} & \frac{c_4}{4} & 0 & 0 & 0 & 0 \\ \frac{s_1}{4} & \frac{s_2}{4} & \frac{s_3}{4} & \frac{s_4}{4} & 0 & 0 & 0 & 0 \\ W_1 & W_2 & W_3 & W_4 & 0 & 0 & 0 & 0 \\ r^{-1} & 0 & 0 & 0 & 0 & 0 & 0 & 0 \\ 0 & r^{-1} & 0 & 0 & 0 & 0 & 0 & 0 \\ 0 & 0 & r^{-1} & 0 & 0 & 0 & 0 & 0 \\ 0 & 0 & 0 & r^{-1} & 0 & 0 & 0 & 0 \\ 0 & 0 & 0 & 0 & 1 & 0 & 0 & 0 \\ 0 & 0 & 0 & 0 & 0 & 1 & 0 & 0 \\ 0 & 0 & 0 & 0 & 0 & 0 & 1 & 0 \\ 0 & 0 & 0 & 0 & 0 & 0 & 0 & 1 \end{bmatrix} \begin{bmatrix} v_1 \\ v_2 \\ v_3 \\ v_4 \\ \omega_1 \\ \omega_2 \\ \omega_3 \\ \omega_4 \end{bmatrix} = \mathbf{Jv} \tag{3}$$

3.2 Dynamic Model

Dynamic model of 4WIS4WID mobile robot has been derived in [9]. In our research we modified and expanded the existing dynamic model with individual dynamics of eight DC motors. In contrast, we consider friction in the model of the DC motors but not in the dynamics model of the robot. Thus, dynamic model is:

$$\dot{\boldsymbol{v}} = -\underbrace{\overline{\boldsymbol{M}}^{-1}\overline{\boldsymbol{V}}}_{\boldsymbol{A}}\, v(t) + \underbrace{\overline{\boldsymbol{M}}^{-1}\overline{\boldsymbol{N}}}_{\boldsymbol{B}}\, \tau(t) \tag{4}$$

where $\overline{\boldsymbol{M}} = \boldsymbol{J}^{\mathrm{T}}\boldsymbol{M}\boldsymbol{J}$, $\overline{\boldsymbol{V}} = \boldsymbol{J}^{\mathrm{T}}\boldsymbol{M}\dot{\boldsymbol{J}}$ and $\overline{\boldsymbol{N}} = \boldsymbol{J}^{\mathrm{T}}\boldsymbol{N}$.

Matrix $\boldsymbol{M}$ is mass matrix and matrix $\boldsymbol{N}$ is transformation matrix from control variables $\boldsymbol{\tau} = \left[\tau_{\varphi 1}\ \tau_{\varphi 2}\ \tau_{\varphi 3}\ \tau_{\varphi 4}\ \tau_{\delta 1}\ \tau_{\delta 2}\ \tau_{\delta 3}\ \tau_{\delta 4}\right]^{\mathrm{T}}$ and output variables $\dot{\boldsymbol{v}}$. Matrices in Eq. 4. are defined as

$$\boldsymbol{M} = \mathrm{diag}\big(m, m, I, I_\varphi, I_\varphi, I_\varphi, I_\varphi, I_\delta, I_\delta, I_\delta, I_\delta\big) \tag{5}$$

$$\boldsymbol{N} = \begin{bmatrix} \frac{c_1}{r} & \frac{c_2}{r} & \frac{c_3}{r} & \frac{c_4}{r} & 0 & 0 & 0 & 0 \\ \frac{s_1}{r} & \frac{s_2}{r} & \frac{s_3}{r} & \frac{s_4}{r} & 0 & 0 & 0 & 0 \\ T_1 & T_2 & T_3 & T_4 & 0 & 0 & 0 & 0 \\ 1 & 0 & 0 & 0 & 0 & 0 & 0 & 0 \\ 0 & 1 & 0 & 0 & 0 & 0 & 0 & 0 \\ 0 & 0 & 1 & 0 & 0 & 0 & 0 & 0 \\ 0 & 0 & 0 & 1 & 0 & 0 & 0 & 0 \\ 0 & 0 & 0 & 0 & 1 & 0 & 0 & 0 \\ 0 & 0 & 0 & 0 & 0 & 1 & 0 & 0 \\ 0 & 0 & 0 & 0 & 0 & 0 & 1 & 0 \\ 0 & 0 & 0 & 0 & 0 & 0 & 0 & 1 \end{bmatrix} \tag{6}$$

where $m = m_r + 4m_w$; m_r is mass of mobile robot; m_w is mass of the each wheel; I_θ, I_φ and I_δ are rotating moment of inertia of mobile robot, wheel and steering system respectively; inertia of robot is defined as $I = I_\theta + 4m_w\big(a^2 + b^2\big)$. Dynamic model of DC motor is also used for this purpose. Dynamic models of mobile robot and DC motors are decoupled.

$$u_a = L_a\frac{\mathrm{d}i_a}{\mathrm{d}t} + R_a i_a + K_m\omega_{DC} \tag{7}$$

where u_a, i_a, L_a and R_a are armature voltage, current, inductance and resistance respectively. K_m is back EMF constant. As torque vector $\boldsymbol{\tau}$ is input to mobile robot dynamic model and current of DC motor and torque are related with constant K_t. Torque of each motor can be presented:

$$\tau_{DC} = K_t i_a \tag{8}$$

4 Parameter Estimation

To achieve effective controller design and adequate simulations, comprehensive understanding of all parameters in the mathematical model of the mobile robot is important. The kinematic parameters can be measured and extracted from the computer-aided design (CAD) model of the robot. Kinematic parameters that are crucial for this type of robot are robot length $2a = 0.225\,\mathrm{m}$, width of mobile robot $2b = 0.225\,\mathrm{m}$ and wheel radius $r = 0.0254\,\mathrm{m}$.

Not all parameters of a dynamic robot model can be simply calculated. The mass and the inertia of the robot can be measured and calculated as well as the resistance, inductance, and back EMF force constant. Steering and driving friction and inertia parameters cannot be easily calculated, they need to be estimated.

In the following subsections, the results of the experiments that were carried out to estimate the necessary parameters of the system will be given together with the simulations in which the estimated parameters were used. Parameter estimations were done by minimizing the sum of squared error function.

4.1 DC Motor Parameters

For a successful parameter estimation of the steering and driving systems, it is necessary to know all the parameters of the motor. The motors on the robot are *Dynamixel XH430-W210-T* for which some of the parameters can be found in the datasheet [13]. Figure 2 shows experiment and simulation of DC motor step response. It is important to note that output speed of DC motor is filtered and filter that performed closest to the DC motor filter was 2nd order Bessel low-pass filter with cut off frequency $\omega_c = 32.8\mathrm{rad/s}$. From experiment, DC motor parameters were estimated (Table 1).

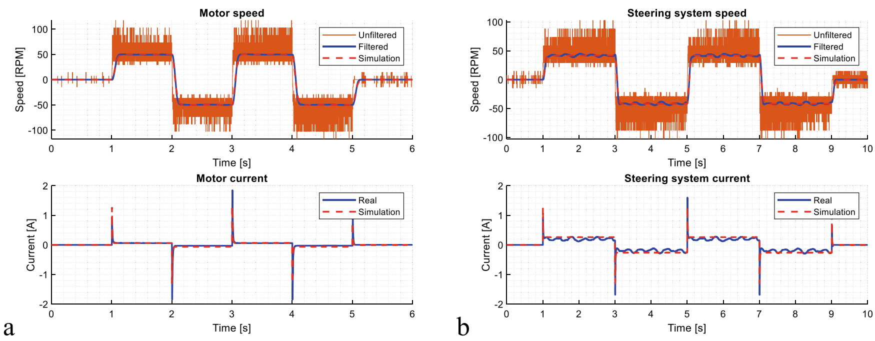

Fig. 2 DC motor response (**a**) and steering system response (**b**)

Table 1 DC motor parameters

Parameter	$R_a[\Omega]$	$L_a[H]$	$K_e[\frac{\mathrm{Vs}}{\mathrm{rad}}]$	$K_t[\frac{Nm}{A}]$	$b_{DC}[\frac{Nms}{rad}]$	$I_{DC}[kgm^2]$
Value	9.23	$3 \cdot 10^{-3}$	0.0103	0.0067	$3.6 \cdot 10^{-7}$	$5 \cdot 10^{-8}$

4.2 Steering System Parameters

The most important parameters for steering system are friction and inertia. Both those parameters were estimated in a similar way as for the DC motor. Figure 2 shows results from the experiment and simulation with estimated parameters. Estimated friction and inertia are $b_\delta = 1.9 \cdot 10^{-7} \frac{Nms}{rad}$ and $I_\delta = 6 \cdot 10^{-8}\mathrm{kgm}^2$.

5 Dynamic and Kinematic Control Design

In this section the control scheme of 4WIS4WID mobile robot is presented. The control scheme contains non-linear kinematic controller, four PI velocity controllers and four P position controllers for DC motors as shown in Fig. 3. In the next subsections simulation and experimental validation of PID velocity and position controllers.

5.1 Velocity Controller

After the DC motor parameters have been estimated and the obtained mathematical model has been verified, it is necessary to design the velocity controller. A PI controller was selected for the speed controller, and simulations were performed for 3 sets of parameters, $\{P_1 = 1, I_1 = 10\}$, $\{P_2 = 1.5, I_2 = 30\}$ and $\{P_3 = 1.5, I_3 = 51\}$. The parameters that gave the best response were selected, implemented in simulation model and verified on a real motor. Figure 2b shows simulation and real motor responses with chosen parameters for PI controller.

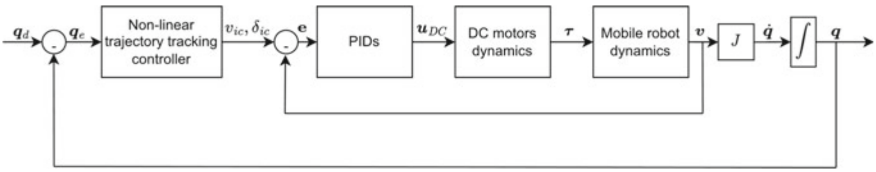

Fig. 3 Control scheme of 4WIS4WID mobile robot

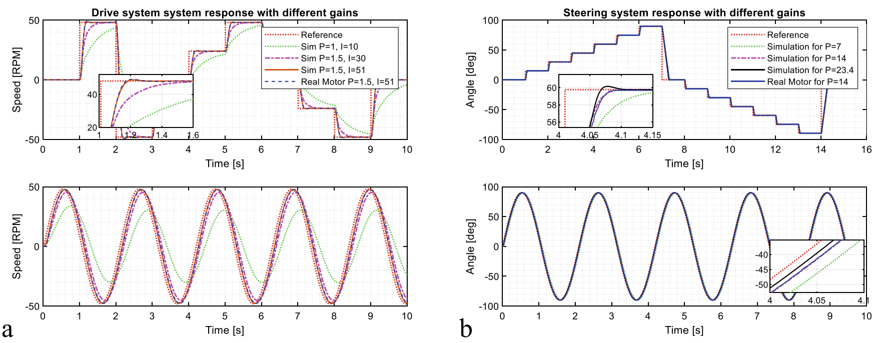

Fig. 4 Drive system response with PI controller (**a**) steering system response with P controller (**b**)

5.2 *Steering Position Controller*

Same as for velocity controller, position controller is designed for steering system of the mobile robot. The steering system uses P controller for controlling the steering angle of each wheel. Simulations were performed for different P gains of controller, $P_1 = 7$, $P_2 = 14$ and $P_3 = 23.4$, Controller with $P_2 = 14$ performed best with fast response and no overshoot which is important for steering system and thus that parameter was used for real motor experiment. Simulation and real motor response are shown in Fig. 4b.

5.3 *Non-linear Kinematic Controller*

Mobile robot reference is defined as $\boldsymbol{q}_d = \left[x_d(t)\ y_d(t)\ \theta_d(t)\right]^{\mathrm{T}}$ and objective is to let the robot track $\dot{\boldsymbol{q}}_d$ and that error between real robot state and reference state approach zero. Trajectory tracking error needs to be rotated in mobile robot reference coordinate frame and then can be defined as

$$\begin{aligned}\boldsymbol{q}_e = \begin{bmatrix} x_e \\ y_e \\ \theta_e \end{bmatrix} &= R(\theta)\begin{bmatrix} x_d - x \\ y_d - y \\ \theta_d - \theta \end{bmatrix} \\ &= \begin{bmatrix} \cos\theta & \sin\theta & 0 \\ -\sin\theta & \cos\theta & 0 \\ 0 & 0 & 1 \end{bmatrix}\begin{bmatrix} x_d - x \\ y_d - y \\ \theta_d - \theta \end{bmatrix}\end{aligned} \tag{9}$$

and error dynamic can be calculated as $\dot{\boldsymbol{q}}_e = \dot{\boldsymbol{q}}_d - \dot{\boldsymbol{q}} = \left[\dot{x}_e\ \dot{y}_d\ \dot{\theta}_d\right]^{\mathrm{T}}$. After some calculations, $\dot{\boldsymbol{q}}_e$ can be presented as

$$\dot{\boldsymbol{q}}_e = \begin{bmatrix} y_e\dot{\theta} + \dot{x}_d - v_x \\ -x_e\dot{\theta} + \dot{y}_d - v_y \\ \dot{\theta}_d - \omega \end{bmatrix} = \begin{bmatrix} y_e\dot{\theta} + \frac{1}{4}\sum_{i=1}^{4} v_{id}\cos\delta_{id} - \frac{1}{4}\sum_{i=1}^{4} v_i\cos\delta_i \\ -x_e\dot{\theta} + \frac{1}{4}\sum_{i=1}^{4} v_{id}\sin\delta_{id} - \frac{1}{4}\sum_{i=1}^{4} v_i\sin\delta_i \\ \sum_{i=1}^{4} v_{id}W_{id} - \sum_{i=1}^{4} v_i W_i \end{bmatrix} \tag{10}$$

where $v_{id} = \sqrt{\dot{x}^2 + \dot{y}^2}$, $\delta_{id} = \text{atan2}(\dot{y}, \dot{x})$, $W_{id} = (-y_{wi}\cos(\delta_i) + x_{wi}\sin(\delta_i))/\left(4x_{wi}^2 + 4y_{wi}^2\right)$, $v_{xid} = \dot{x} - y_{wi}\dot{\theta}_d$ and $v_{yid} = \dot{y} + x_{wi}\dot{\theta}_d$.

To derive non-linear tracking controller, we define the Lyapunov function as

$$V = \frac{1}{2}\left(x_e^2 + y_e^2 + \theta_e^2\right) \geq 0 \tag{11}$$

By taking time derivative, Lyapunov function becomes

$$\dot{V} = x_e\dot{x}_e + y_e\dot{y}_e + \theta_e\dot{\theta}_e \tag{12}$$

Control laws for velocities and angle of mobile robot motors can be defined as

$$v_{ic} = k_1\sqrt{a_i^2 + b_i^2} \tag{13}$$

$$\delta_{ic} = k_2 + \text{atan2}(b_i, a_i) \tag{14}$$

where $a_i = v_{id}\cos\delta_{id} + k_x x_e - k_\theta y_{wi}\theta_e$ and $b_i = v_{id}\sin\delta_{id} + k_y y_e - k_\theta x_{wi}\theta_e$, k_x, k_y and k_θ are positive constants. Constants k_1 and k_2 can be defined as

$$(k_1, k_2)\begin{cases} (+1, 0), |\delta_{id} - \delta_i| \leq \frac{\pi}{2} \\ (-1, \pi), otherwise \end{cases}$$

Inserting control law from Eq. into Eq. derivative of Lyapunov functions becomes

$$\dot{V} = -4k_x x_e^2 - 4k_y y_e^2 - 4k_\theta\theta_e^2 \tag{15}$$

Using appropriate k_x, k_y and k_θ, tracking error is asymptomatically stable for all $t > 0$ and $q_e \neq 0$.

6 Simulations and Experimental Results

Before implementing desired PID parameters and non-linear controller on real mobile robot, simulations were performed on various trajectories using MATLAB. The simulation parameters are chosen to be as close as possible to the real robot. Non-linear trajectory tracking control gains were chosen $k_x = k_y = 3$ and $k_\theta = 1$. Responses of the mobile robot for trajectory $x_d = y_d = 0.05t$ with $\theta_d = \text{atan2}(\dot{y}_d, \dot{x}_d)$ and for the $x_d = 0.5\cos(0.15t)$, $y_d = 0.5\sin(0.15t)$ with $\theta_d = \text{atan2}(\dot{y}_d, \dot{x}_d)$ are presented in Figs. 5 and 6. Responses and similarity of the simulation and experiment are satisfied. Small inequality in response can be improved with better friction model, *Columb*, *Stribeck* or *LuGre* friction models. It is important to note that robot response is not the same as *OptiTrack* recordings, reason to that are kinematic parameters, *a, b* and *r* which will be part of future research as different approach for calibration must be researched.

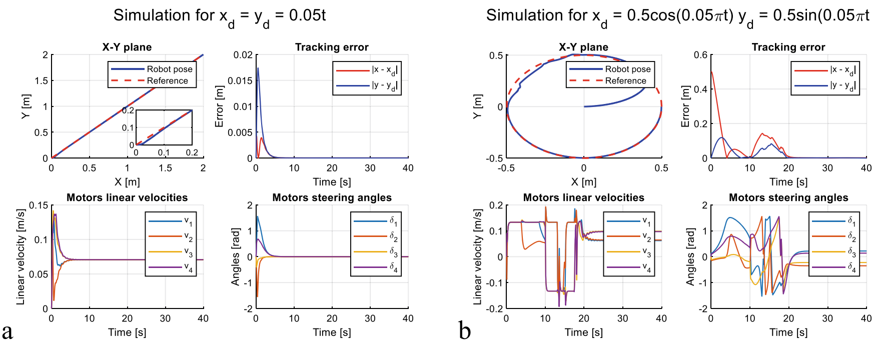

Fig. 5 Mobile robot responses in simulation using derived mathematical model and estimated parameters

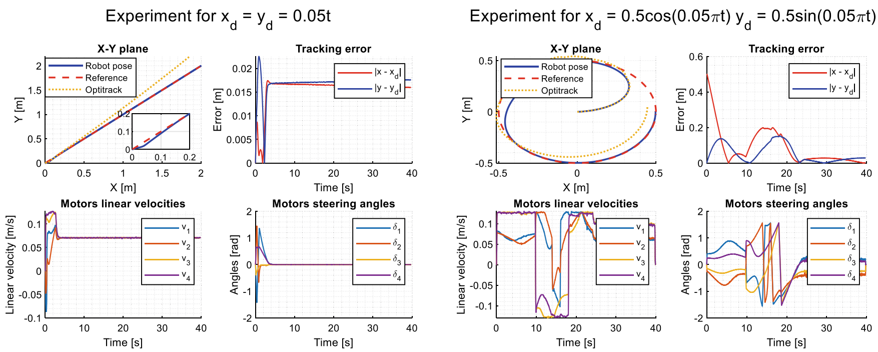

Fig. 6 Real mobile robot responses

7 Conclusion

The robot trajectory tracking presented in Figs. 5 and 6 show a satisfactory matching which indicates that systematic modeling of kinematics and dynamics and controller design for the 4WIS4WID mobile robot can be improved with good parameter estimation. Given mathematical model with good parameters is basis for the future research where kinematic model parameters needs to be calibrated and dynamic model needs to be expanded with potential energy for driving on vertical surfaces.

Acknowledgments We would like to acknowledge the project CRTA—Regional Center of Excellence for Robotic Technologies funded by the ERDF fund and Autonomous System for Assessment and Prediction of infrastructure integrity (ASAP) project funded by European Regional Development Fund's Competitiveness and Cohesion Operational Program, grant number KK.01.1.1.04.0041.

References

1. Li, Z., et al.: Experimental characterization and comparison of three typical omnidirectional mobile robots. In: 2023 International Conference on Advanced Robotics and Mechatronics (ICARM), Sanya, China: IEEE, pp. 1162–1168. https://doi.org/10.1109/ICARM58088.2023.10218777
2. Wang, B., Li, S., Guo, J., Chen, Q.: Car-like mobile robot path planning in rough terrain using multi-objective particle swarm optimization algorithm. Neurocomputing **282**, 42–51 (2018). https://doi.org/10.1016/j.neucom.2017.12.015
3. Zheng, H., Yang, S.: A trajectory tracking control strategy of 4WIS/4WID electric vehicle with adaptation of driving conditions. Appl. Sci. **9**(1), 168 (2019). https://doi.org/10.3390/app9010168
4. Bae, B., Lee, D.-H.: Design of a four-wheel steering mobile robot platform and adaptive steering control for manual operation. Electronics **12**(16), 3511 (2023). https://doi.org/10.3390/electronics12163511
5. Li, T.-H.S., Lee, M.-H., Lin, C.-W., Liou, G.-H., Chen, W.-C.: Design of autonomous and manual driving system for 4WIS4WID vehicle. IEEE Access **4**, 2256–2271 (2016). https://doi.org/10.1109/ACCESS.2016.2548081
6. Tu, X., Gai, J., Tang, L.: Robust navigation control of a 4WD/4WS agricultural robotic vehicle. Comput. Electron. Agric.**164**, 104892 (2019). https://doi.org/10.1016/j.compag.2019.104892
7. Hayat, A.D., Hassan, A., Hajar, M., Ali, E.A.: Fuzzy logic controller for 4WD/4WS autonomous agricultural robotic. In: 2022 IEEE 3rd International Conference on Electronics, Control, Optimization and Computer Science (ICECOCS), Fez, Morocco: IEEE, pp. 1–6 (2022). https://doi.org/10.1109/ICECOCS55148.2022.9983035
8. Božić, M., Ćaran, B., Švaco, M., Jerbić, B., Serdar, M.: Mobile wall-climbing robot for NDT inspection of vertical concrete structures. E-J. Nondestruct. Test. **27**(9) (2022). https://doi.org/10.58286/27295
9. Lee, M., Li, T.S.: Kinematics, dynamics and control design of 4WIS4WID mobile robots. J. Eng. **2015**(1), 6–16 (2015). https://doi.org/10.1049/joe.2014.0241
10. Yoon, Y., Gur, B.: Parameter estimation and control of nonholonomic mobile robots: a model-based approach. In: 2018 6th International Conference on Control Engineering & Information Technology *(CEIT)*, Istanbul, Turkey: IEEE, pp. 1–6 (2018). https://doi.org/10.1109/CEIT.2018.8751792

11. Stöger, C., Müller, A., Gattringer, H.: Parameter identification and model-based control of redundantly actuated, non-holonomic, omnidirectional vehicles. In: Madani, M., Peaucelle, D., Gusikhin, O. (eds.) Informatics in Control, Automation and Robotics, vol. 430, in Lecture Notes in Electrical Engineering, vol. 430, Springer International Publishing, Cham, pp. 207–229 (2018). https://doi.org/10.1007/978-3-319-55011-4_11
12. Bozic, M., Jerbic, B., Svaco, M.: Development of a mobile wall-climbing robot with a hybrid adhesion system. In: 2021 44th International Convention on Information, Communication and Electronic Technology (MIPRO), Opatija, Croatia: IEEE, pp. 1136–1142 (2021). https://doi.org/10.23919/MIPRO52101.2021.9596717
13. 'ROBOTIS e-Manual', ROBOTIS e-Manual [Online]. Available: https://emanual.robotis.com/docs/en/dxl/x/xh430-w210/. Accessed on Dec 17 2023

Autonomous Mobile Robotic System for Measuring the Electrical Conductivity of Soil

Franci Ovčak, Sebastjan Šlajpah, Marko Munih, and Matjaž Mihelj

Abstract The paper presents an innovative application for optimizing and digitizing modern agriculture by integrating advanced farming techniques and robotic solutions. The main focus lies in developing a mobile platform with sensors that measure soil resistivity, a key parameter for optimizing fertilizer application. The platform utilizes advanced localization and navigation techniques, enabling autonomous and precise data collection. The system efficiently determines optimal sampling points in the field while avoiding obstacles and field boundaries. The results demonstrate the effectiveness of the proposed methodology in achieving precise and automated agricultural operations, facilitating sustainable and data-driven farming practices.

Keywords Outdoor mobile robot · Localization · Soil analysis · ROS

1 Introduction

Modern agriculture strives for optimization and digitalization. Precision farming includes innovative cultivation methods based on collected data. Robotic solutions for agriculture allow the automation of demanding agricultural operations such as picking, harvesting, weed control, mowing, pruning, sowing, spraying, thinning, phenotyping, monitoring, sorting, and packaging. In autonomous soil sampling, which is typically still done manually, specific solutions already exist [1, 2]. However, these platforms are often designed for a single task and do not include other systems

F. Ovčak (✉) · S. Šlajpah · M. Munih · M. Mihelj
Faculty of Electrical Engineering, University of Ljubljana, Tržaška cesta 25, 1000 Ljubljana, Slovenia
e-mail: franci.ovcak@fe.uni-lj.si

S. Šlajpah
e-mail: sebastjan.slajpah@fe.uni-lj.si

M. Munih
e-mail: marko.munih@fe.uni-lj.si

M. Mihelj
e-mail: matjaz.mihelj@fe.uni-lj.si

D. Pisla et al. (eds.), *Advances in Service and Industrial Robotics*, Mechanisms and Machine Science 157, https://doi.org/10.1007/978-3-031-59257-7_61

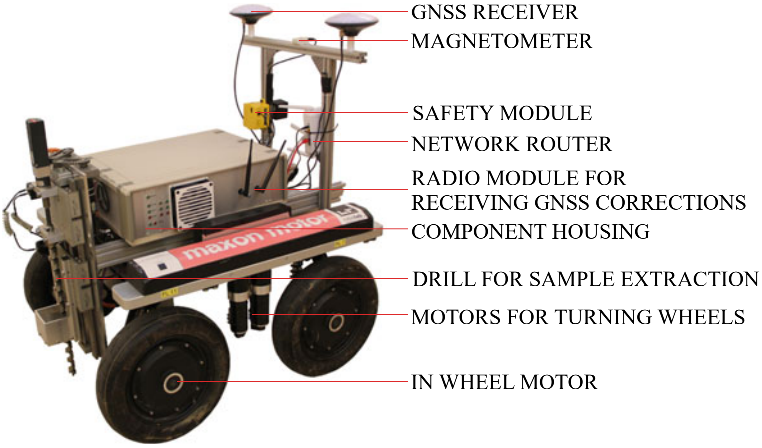

Fig. 1 Arrangement of elements on the mobile platform

for soil analysis. Soil composition is a pivotal factor in guiding decision-making and optimizing various aspects of agricultural practices, such as applying fertilizers, pesticides, irrigation, and crop cultivation. The electrical resistance of the soil, an essential indicator for determining its physical and chemical properties (moisture, salinity, organic matter, nutrient levels), can be accurately measured. For this reason, we propose an approach to monitoring soil resistivity using a four-wheel mobile robotic platform, onto which we mounted electrodes and a soil resistivity meter. We have further upgraded the platform with the equipment for autonomous sampling. Using the robotic operating system (ROS), we implemented algorithms for localization and navigation. We developed an HMI (Human Machine Interface) as a web user interface to control and display real-time data.

2 Mobile Platform

The mobile platform, illustrated in Fig. 1, is a four-wheeled vehicle with four-wheel independent steering (4WAS). The platform is equipped with an Asus mini PC running the Ubuntu 18.04 and ROS Melodic operating systems, Beckhoff controller to control individual motors, a network router for connecting the modules, a receiver for Global Navigation Satellite System (GNSS) signals, a soil resistivity meter, an Inertial Measurement Unit (IMU) and a power supply system.

2.1 GNSS RTK Receiver

In most cases, localisation accuracy using a GNSS module is limited to a few meters due to atmospheric conditions, signal reflections from surrounding objects, and clock errors [3]. GNSS signal data is corrected using Real-Time Kinematic GNSS (RTK GNSS) technology to determine the mobile platform's position with centimetres level accuracy.

The mobile platform includes two Mosaic-X5 GNSS modules connected to its multi-band antenna (Fig. 1). The antennas are mounted on the platform's rear left and right sides. These antennas significantly improve noise resistance and increase the maximum number of satellites the module can receive at any given moment, which contributes to improved convergence and positioning accuracy [4].

2.2 Wheel Encoders

Each of the four-wheel motors is equipped with a dual-channel incremental encoder. With quadrature decoding, we achieve a resolution of $N = 16{,}000$ pulses per revolution. The sampling frequency of the encoders is set to 50 Hz ($\Delta t = 0.02$ s). To calculate the speed of the mobile platform, we take the average speed of all four wheels.

2.3 Inertial Measurement Unit (IMU)

The unit contains a 6-axis MPU-9250 Inertial Measurement Unit (IMU), which includes a 3-axis gyroscope, a 3-axis accelerometer and a magnetometer, enabling the measurement of absolute orientation by detecting the Earth's magnetic field. The data from the sensors are processed by an integrated STM32 microcontroller, which then sends them to the target device via a USB interface.

2.4 Soil Resistivity Meter

One of the most efficient and reliable methods for measuring soil fertility is by measuring soil resistivity [5], as this method is fast, accessible, and reliable. For this purpose, we developed a PCB board for measuring specific resistivity based on the open-source project *OhmPi* [6]. The measurement system consists of a measurement circuit and electrodes mounted on the rear side of the platform. Figure 2 shows the configuration with four evenly distributed electrodes attached to holders.

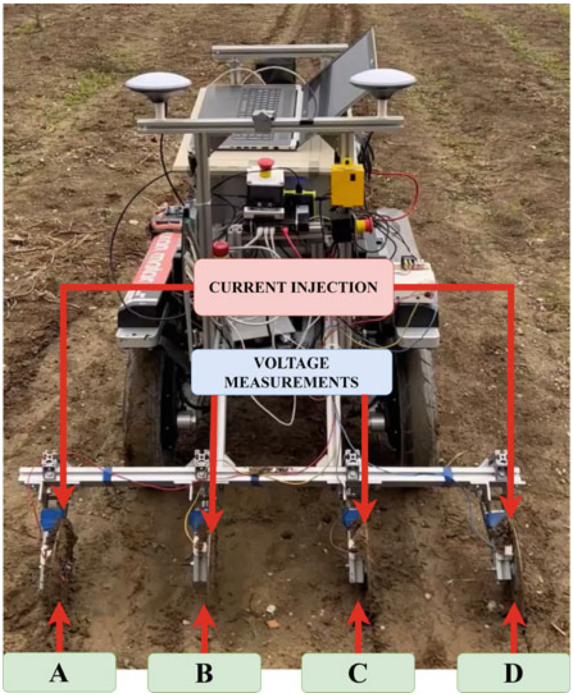

Fig. 2 Electrodes attached to the mobile platform

The electrodes are insulated from one another, ensuring that a current only flows between them when they are in contact with the soil. The outer electrodes impose a current, and the generated voltage is measured across the two inner electrodes. The specific resistance of the soil is calculated using the following equation:

$$\rho_{\mathrm{a}} \approx 2\pi \mathrm{a}\frac{\mathrm{U}}{\mathrm{I}}, \tag{1}$$

where a is the distance between electrodes, I is the injected current, and U is the voltage between the inner electrodes.

The soil has its electrical potential, which can cause measurement inaccuracies. We address this issue using the two-pulse method, where the first pulse generates a current in one direction and the second in the opposite direction. Finally, the actual voltage is obtained by averaging the two measurements:

$$\mathrm{U} = \frac{1}{2}\left(\mathrm{U}_k + \mathrm{U}_{k+1}\right). \tag{2}$$

2.5 Kinematics

The kinematic model of the presented platform is summarized from [8]. In the article, the authors simplify the kinematic model as a single-track system assuming pure rolling and a small steering angle. Additionally, we further simplified the model by neglecting the influence of slip angles ($\beta \approx 0$) as the mobile platform moves at relatively low speeds. Thus, the kinematic model is of the following form:

$$\dot{X} = v_m \cos(\varphi), \tag{3}$$

$$\dot{Y} = v_m \sin(\varphi), \tag{4}$$

$$\dot{\varphi} = \frac{v_m}{L} \left(\tan\left(\delta_f\right) - \tan\left(\delta_r\right)\right), \tag{5}$$

where v_m represents the speed of the platform, φ the orientation of the platform, δ_f the angle of the front middle wheel, δ_r the angle of the rear middle wheel, and L the wheelbase. To increase the maneuverability, we employ counterphase steering method, $\delta_f = -\delta_r$.

3 Localization

To identify the most efficient data fusion approach, we developed a two-stage filtering framework, illustrated in Fig. 3. Initially, an Unscented Kalman Filter (UKF), adapted from [7], integrates data from the IMU and two GNSS sensors. This stage aims to provide a precise estimate of the mobile platform's orientation, which is critical for accurately merging GNSS positions in the subsequent stage, thereby enhancing the overall accuracy.

In the second stage, we combine orientation data obtained from the UKF with positions from the GNSS sensors and odometry information. This odometry data is derived from changes in position, which are calculated based on wheel encoders and the rotation of the wheels using Eqs. (3), (4) and (5). To assess the effectiveness of this approach, we examined three data fusion methods: (1) the Extended Kalman Filter (EKF), (2) Dynamic weighting, and (3) the Particle filter, evaluating their performance in enhancing navigation and localization accuracy.

3.1 Localization Validation

Validating localization algorithms poses a challenge in environments with high GNSS signal covariances, such as when a platform moves beneath a tree, primarily because of the absence of an absolute reference for comparison or validation. To address this issue, data collection was carried out in an open field where the accurate position of the platform was known. Subsequently, noise was intentionally added during post-processing for further analysis.

To assess the performance of the UKF in the first stage, we compared the estimated platform orientation with the orientation calculated from the positions of two GNSS receivers. In the absence of artificial noise applied to the data, the UKF filter demonstrated adequate accuracy, as shown in Fig. 4 (area outside artificial noise). When we intentionally introduced artificial noise by adding Gaussian noise to GNSS data, ($R_{\text{gps}} = \text{diag}([1, 1, 1]\,\text{m})$) between $t = 110$ s and $t = 185$ s, we observed minimal deviation in the estimated orientation compared to the actual orientation. The accuracy of this filter, while not paramount, is sufficiently reliable for its primary purpose: to achieve a reasonably accurate orientation that enables the effective combination of both GNSS positions in the second stage.

Two testing methods were employed to validate the second stage. In the first method, Gaussian noise with $\sigma = 1$ m was introduced, while in the second method, a unidirectional component (offset) of magnitude 0.3 m was added to this noise. The

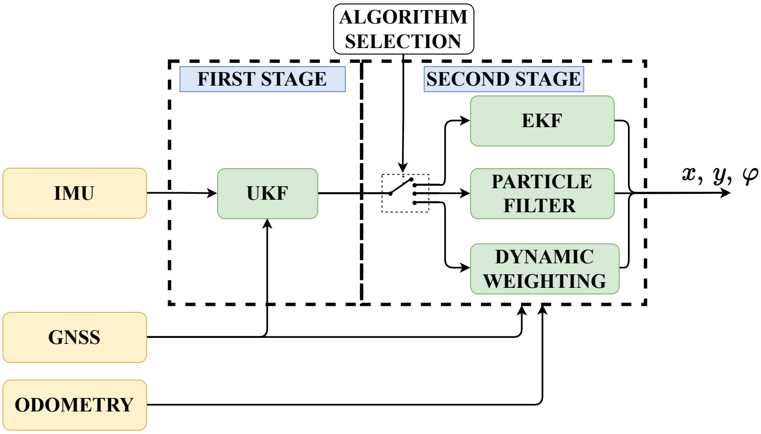

Fig. 3 Block diagram of the use of filters for the purpose of localization

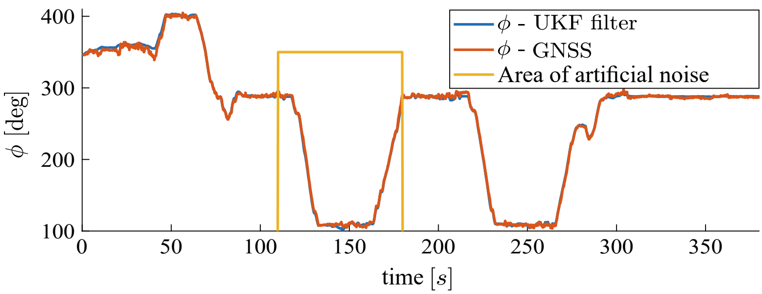

Fig. 4 UKF filter operation considering correction

Table 1 Root mean square error of position for the three methods in the 2nd stage of localization

Method	Gaussian noise position (m)	Gaussian noise + offset Position (m)
EKF	0.11	0.17
Dynamic weighting	0.10	0.25
Particle filter	0.10	0.20
GNSS left	1.25	1.29
GNSS right	1.24	1.31

Table 2 Root mean square error of orientation for the three methods in the 2nd stage of localization

Method	Gaussian noise φ (°)	Gaussian noise + offset φ (°)
EKF	0.81	0.95
Dynamic weighting	0.83	0.83
Particle filter	1.65	1.05
GNSS left/right	100.84	104.21

accuracy of the filter was assessed by calculating the Root Mean Square (RMS) error between the actual position and position given by the filter, with results detailed in Table 1. For orientation accuracy, we calculated the mean error between the actual orientation and the orientation provided by the filter results, shown in Table 2. All three methods utilized in the second stage, significantly enhance localization compared to direct GNSS signals, rendering them suitable for localization purposes. Notably, the Extended Kalman Filter (EKF) exhibited slightly superior accuracy, while the particle filter showed a higher error in estimating orientation when compared to the other two methods.

4 Navigation

To facilitate the navigation of the mobile platform, we employ the *Teb Local Planner* algorithm, which uses the *Time Elastic Band* method [9]. Originally, it was designed for platforms without holonomic constraints, such as differential drive platforms. The authors adapted the algorithm to accommodate car-like platforms, incorporating considerations for their kinodynamic constraints [10].

4.1 Planning Soil Sampling

To plan a path for collecting soil measurements, we developed an algorithm that determines navigation points for guiding the mobile platform. The user initiates the process by defining the agricultural area in the user interface and selecting the side of the field along which the robot should move.

The algorithm then calculates navigation points using the chosen side as a reference to create a line moving a specified distance d, representing the sampling step, towards the farthest point from the selected side. This process iterates until no further intersections are found. Subsequently, upon user command, the action server processes these points, considering the platform's orientation, and sequences them for the navigation system.

5 Measurement and Analysis of Soil Resistivity

To combine and filter multiple resistance measurements, we partitioned the field into segments measuring $0.5\,\mathrm{m} \times 0.5\,\mathrm{m}$ and assigning each measurement to the nearest segment. Each segment may contain one or more measurements, and the soil's electrical resistivity within the segment is determined based on the median of all measurements it encompasses. Linear interpolation was employed to address missing values between individual segments.

Sampling was conducted in fields on the grounds of the Biotechnical Faculty of the University of Ljubljana. Due to the dampness of the soil at the time of measurement, recorded resistivity levels were relatively low (Fig. 5). Resistance measurements were collected along two 30 m parallel strips of land, with the mobile platform's speed ranging from $0.1\,\mathrm{m\,s^{-1}}$ to $0.5\,\mathrm{m\,s^{-1}}$. Throughout the measuring process, we did not maintain a constant speed and occasionally stopped the platform, which resulted in some sections having more measurements than others. Electrodes were inserted about two to three centimetres into the soil during testing, with springs mounted on each electrode holder ensuring constant contact with the soil.

6 Conclusion

Our research demonstrates that employing a mobile platform equipped with sensors for measuring soil electrical conductivity facilitates precise and automated data collection in agriculture. Integrating localization and navigation technologies facilitates autonomous navigation. Implementing a two-stage filter allows us to compensate for poor GNSS data temporarily, enabling the mobile platform to navigate under trees or near tall structures that impair GNSS signal quality. By calculating navigation points specifically tailored to the requirements of soil resistance measurement, we

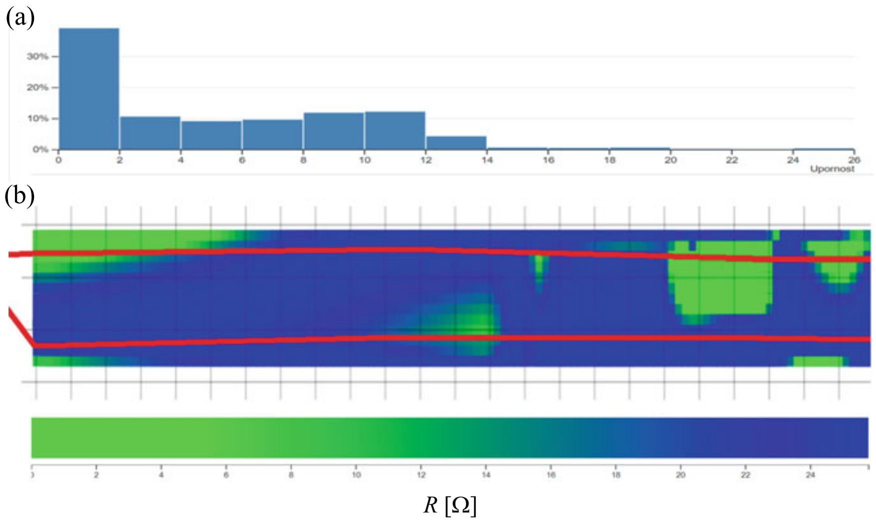

Fig. 5 Sampling at a field at the Biotechnical Faculty, UL: **a** histogram of soil resistivity distribution; **b** soil resistivity (green/blue fields) and path of the vehicle (red line), black squares represent 1m × 1m

can sample an average Slovenian agricultural land of 0.6 ha in approximately 2 h, maintaining a speed of 0.5 ms^{-1} and a 2 m interval between sampling points.

References

1. Väljaots, E., Lehiste, H., Kiik, M., Leemet, T.: Soil sampling automation using mobile robotic platform. 16 volume Agronomy Res. (2018). https://dspace.emu.ee/xmlui/handle/10492/4000
2. Schumacher, D.: Autonomous robots enter fields to collect precise soil samples, help farmers improve yields, reduce environmental impact, save money (2019)
3. European GNSS Agency: PPP-RTK market and technology report (2019). https://www.euspa.europa.eu/sites/default/files/calls_for_proposals/rd.03_-_ppp-rtk_market_and_technology_report.pdf
4. Hamza, V., Stopar, B., Sterle, O.: Testing the performance of multi-frequency low-cost GNSS receivers and antennas. Issue 21 Sensors (2021). https://www.mdpi.com/1424-8220/21/6/2029
5. Corwin, D., Lesch, S: Application of soil electrical conductivity to precision agriculture. Issue 3 of Agronomy Journal (2003). https://acsess.onlinelibrary.wiley.com/doi/abs/10.2134/agronj2003.4550
6. Clement, R., Fargier, Y., Dubois, V., Gance, J., Gros, E., Forquet, N.: An open source data logger for dedicated applications of electrical resistivity imaging at the small and laboratory scale. Volume 3 HardwareX (2020). https://www.sciencedirect.com/science/article/pii/S2468067220300316
7. Van Der Merwe, R.: Sigma-point Kalman filters for probabilistic inference in dynamic state-space models. Univ, Oregon Health Sci. (2004)
8. Tan, X., Liu, D., Xiong, H.: Optimal control method of path tracking for four-wheel steering vehicles. Volume 11 Actuators (2022). https://www.mdpi.com/2076-0825/11/2/61

9. Rosmann, C., Feiten, W., Wosch, T., Hoffmann, F., Bertram, T.: Efficient trajectory optimization using a sparse model. In: European Conference on Mobile Robots (2013). https://ieeexplore.ieee.org/document/6698833
10. Rosmann, C., Hoffmann, F., Bertram, T.: Kinodynamic trajectory optimization and control for car-like robots. In: International Conference on Intelligent Robots and Systems (2017). https://ieeexplore.ieee.org/document/8206458

Design and Test Validation of Humanoid Tripod-Based Limbs

Marco Ceccarelli, Earnest Ofonaike, Steven Beaumont, Léo Neves, and Matteo Russo

Abstract A tripod-based design with linear actuators is presented with features and performance suitable for humanoid limbs as based on a tripod mechanism architecture. Design compact solutions are developed for arm and leg structures with low-cost Arduino-based controlled operation and market components for a revised version of LARMbot humanoid robot. A general design is then specified in an arm structure with a gripper on a wrist joint and in a leg structure with a foot on an ankle joint. Performance characteristics are characterized in lab tests with suitable large motion range, high payload capacity, and limited power consumption.

Keywords Humanoid robots · Design · Tripod design · LARMbot humanoid · Experimental robotics · Performance analysis

1 Introduction

Most of the current humanoid robots, both in research and applications, even with market solutions, are designed with a mechanical that are strongly inspired to the human anatomy. Since the first humanoid robot "WABOT-1" developed in the early 1970s at Waseda University in Tokyo, Japan [1], the limbs are designed with bulky solutions that include actuators and sensors. Examples of today's humanoid robots can be indicated in ASIMO [2], WABIAN [3], HRP [4], Johnnie and Lola [5],

M. Ceccarelli (✉) · E. Ofonaike · M. Russo
University of Rome Tor Vergata, 00133 Rome, Italy
e-mail: marco.ceccarelli@uniroma2.it

E. Ofonaike
e-mail: earnestugonna.ofonaike@alumni.uniroma2.eu

M. Russo
e-mail: matteo.russo@uniroma2.it

S. Beaumont · L. Neves
SeaTech-School of Engineering, University of Toulon, Toulon, France
e-mail: steven.beaumont.24@seatech.fr

D. Pisla et al. (eds.), *Advances in Service and Industrial Robotics*, Mechanisms and Machine Science 157, https://doi.org/10.1007/978-3-031-59257-7_62

HUBO [6], ATLAS [7], and BHR [8], just to cite few in a growing robot population worldwide.

Today, humanoid robots are still investigated also in design solutions with the aim to increase robot capabilities such as walking on various terrains, fall protection, and interaction with the environment, with solutions that can span from very sophisticated and complex one up to very simple low-cost solutions, even in the form of toys. In addition, a growing interest is addressed to propose solutions with low-cost and user-oriented design even if with structure of limited capabilities. Within this research line LARMbot humanoid has been developed since the beginning of 2000s' up to design a prototype in 2016 [9, 10]. The LARMbot humanoid is characterized by a peculiar low-cost efficient design that is based on parallel mechanism architectures [9]. The used parallel mechanism architecture in the form of a tripod is inspired to the muscle-skeleton anatomy in nature [11].

In this paper, expanding previous designs and experiences reported in [12–15], a tripod-based mechanism provided of specific 3-SPR joint mechanism [16] is redesigned with solutions and features that have been adjusted for leg and arms, in consideration of the similarity of the human limbs in term of the muscle-skeleton anatomy The proposed prototype solutions are tested successfully to validate the design feasibility and to characterize the operation performance as lightweighted efficient limbs for the in humanoid LARMbot.

2 Design and Operation Requirements

Following the experiences in recent years with the humanoid LARMbot [12–15], a reconsideration of the structure and functionality of the limbs was recognized necessary in order to achieve a synergistic structure that overall has functional characteristics and load capacity of similar magnitude in all its components. The structure of the torso was fundamental as based on a serial-type spinal column system with a parallel architecture cable actuation with high movement and load capacities which were limited by the serial structures especially of the arms. After positive experiences with a tripod structure for the legs with parallel architecture, the possibility is considered feasible in developing such a structure that can be valid for both the arms and the legs with characteristics of similar efficiency in terms of facilitating a synergy of movement and action between all components of the humanoid LARMbot with similar characteristics.

The conceptual idea is summarized in the sketches of Fig. 1 where the functionality of the limb extremity, either arm or leg, is represented by the possibility of movement in space in three directions with 3 DOFs preserving the characteristic of an operation with antagonistic and collaborative components to ensure compactness and lightness of the limb. In the sketches of Fig. 1, the structure of a mobile platform is emphasized with a solution that can be easily connected to the corresponding part of the trunk in which the bases of the linear actuators are connected. The actuated tripod realizes the

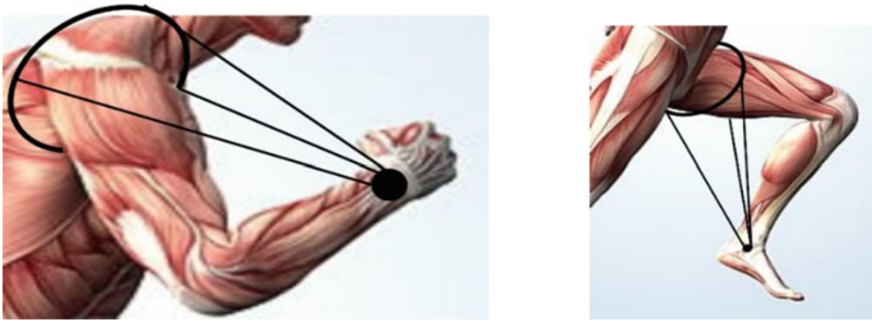

(a) (b)

Fig. 1 Schemes for design and operation features for: **a** arm **b** leg

translational motion of a limb point, leaving the mobile platform for the additional wrist or ankle joint for the terminal element as hand, Fig. 1a, or foot Fig. 1b.

3 The Tripod-Base Designs

The new LARMbot humanoid limb is designed as the conceptual design in Fig. 1 with a tripod architecture whose actuated links converge in a point giving tetrahedron shape of the full limb consisting of three links connecting the base plate (shoulder or waist) to the mobile platform (wrist or ankle), Fig. 2 [12–15]. The link convergence is ensured by a specially designed joint with the kinematic structure 3-SPR in the zoomed view in Fig. 2 [16].

The linear actuated links are connected by universal joints at the frame-base plate and revolute joints of the converging joint mechanism connect each link to the mobile platform. Figure 2 represents the kinematic scheme of the tripod structure with its design and operation prismatic parameters. The shoulder base plate is designed with an equilateral triangular shape whereas the wrist mobile platform is designed to host a extremity-link frame. The tripod limb shows 3-DoFs that are operated as translational degrees of freedom, to enable the swing of the limb.

Figure 3 shows the implementation of the conceptual design in Figs. 1 and 2 with similar but differentiated construction solutions for the arm in Fig. 3a and for the leg in Fig. 3b in which it can be noted how the same linear actuators are connected to the structures that specifically create the shoulder or pelvis and the wrist or ankle joint, respectively. It should also be noted that the prototypes are designed and obtained also with a dimensional similarity with sizes indicated in Fig. 4.

Figure 5 shows how the mobile platform of the tripod is designed with a shape suitable for the ankle joint, hosting the corresponding rotary actuator while maintaining the design peculiarity of compactness and lightness. The wrist joint for the arm is designed similarly. The prototypes are all built using commercial actuators

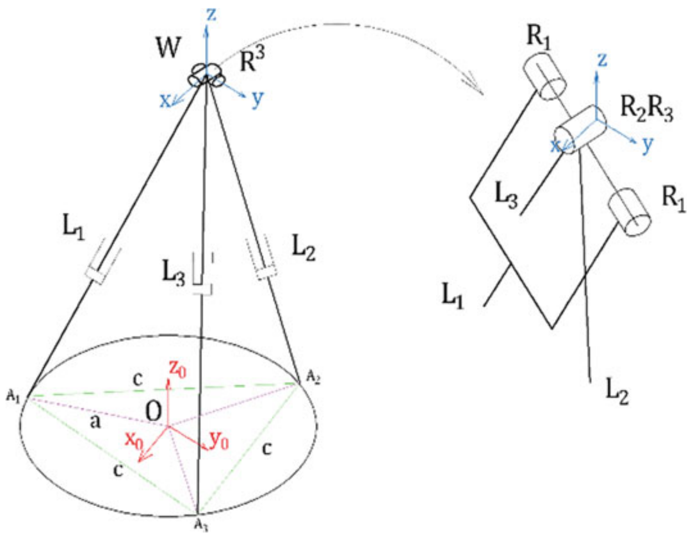

Fig. 2 Kinematic design of a tripod—based structure with the extremity link-converging joint

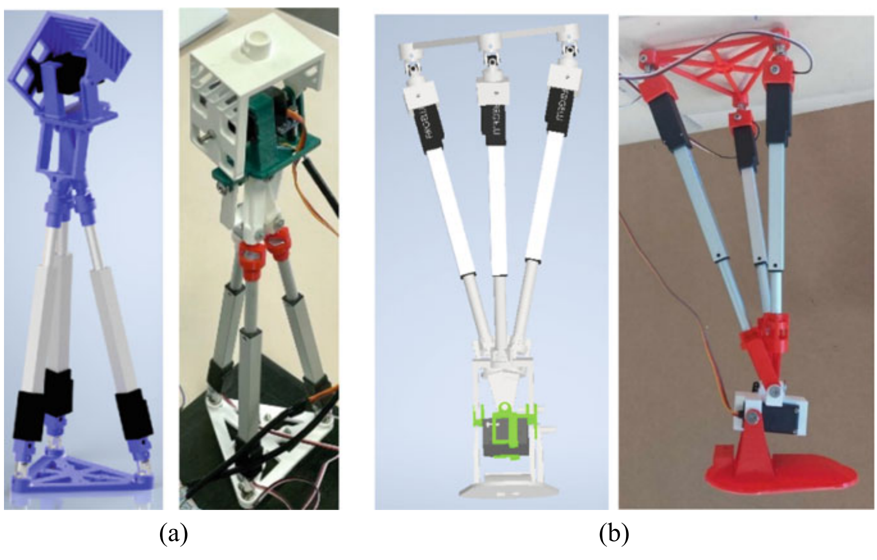

Fig. 3 CAD design and prototype of the tripod—based limb: **a** arm; **b** leg

and constructing the structural parts through 3D printing to create the joints and connections necessary for the LARMbot humanoid robot body application with correspondingly end extremities.

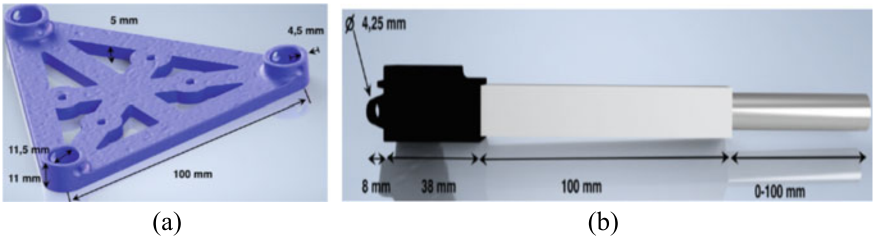

Fig. 4 Main components of the tripod–based limb arm in Fig. 3a: **a** base frame; **b** linear actuator

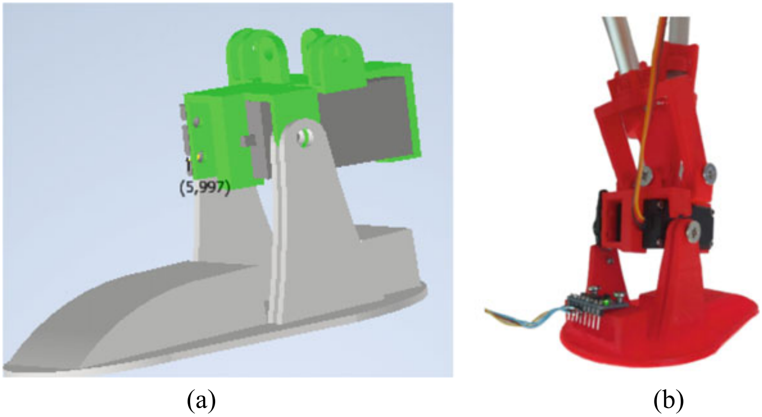

Fig. 5 Foot of the tripod—based leg: **a** CAD design; **b** prototype

The prototype designs in Figs. 3, 4 and 5 are elaborated in CAD solutions in SolidWorks software both to define the mechanical structures and to validate design and operation features by simulation. Figures 3, 4 and 5 show CAD solutions against prototype constructions in which the main limb tripod structure is completed by specific revolute actuators for wrist and ankle joints, respectively.

4 Prototypes and Lab Test Results

Figures 6 and 7 show snapshots of laboratory experiments to validate and characterize the motion and manipulative capabilities of the prototypes for the leg and arm.

In particular, Fig. 6 shows an air walking experiment in which one can appreciate the wide range of motion up to 60 ° combined with the ankle movement to allow the foot to exercise the typical rolling movement of human walking.

Figure 7 similarly shows a movement experiment of the arm tripod prototype simulating extensive manipulation with a two-finger gripper installed on the movable body of the wrist joint. Experiments were carried out both with unloaded and loaded

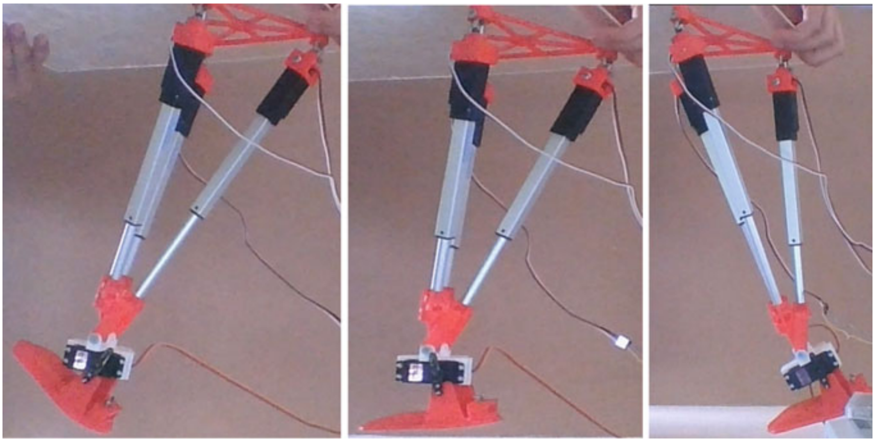

Fig. 6 A snapshot of a lab test of the walking capability of the tripod–based leg prototype

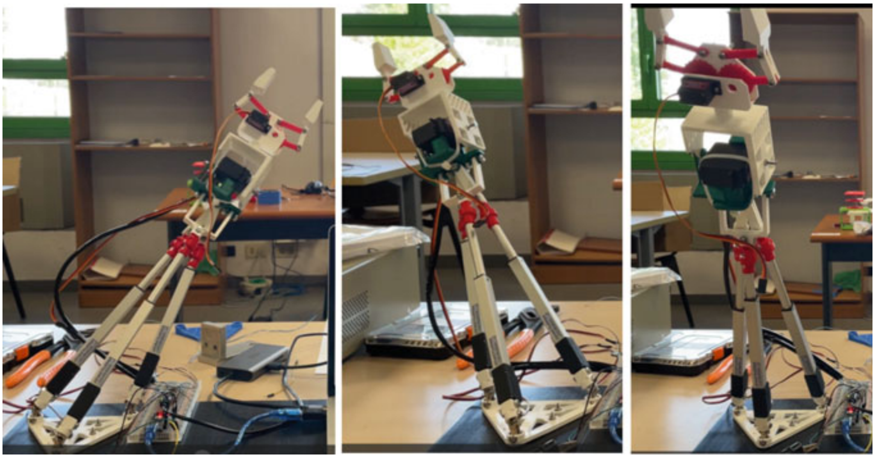

Fig. 7 A snapshot of a lab test of the manipulation capability of the tripod–based leg arm

limbs to also evaluate the ability to move and manipulate objects and load. The experiments shown in Figs. 6 and 7 were also characterized from a numerical point of view by acquiring motion characteristics using IMU sensors installed on the extremities on the foot or gripper body together with a monitoring of the power consumed in the execution of the motion. Illustrative results are displayed in Figs. 8, 9 and 10.

Figure 8 reports results acquired in the performance analysis via simulation and during tested movement of the robotic arm acquired in terms of values of the angles of the manipulation movement, showing that the movement is performed as prescribed with adequately smooth movements and small variations essentially due to the backlash assembly tolerances.

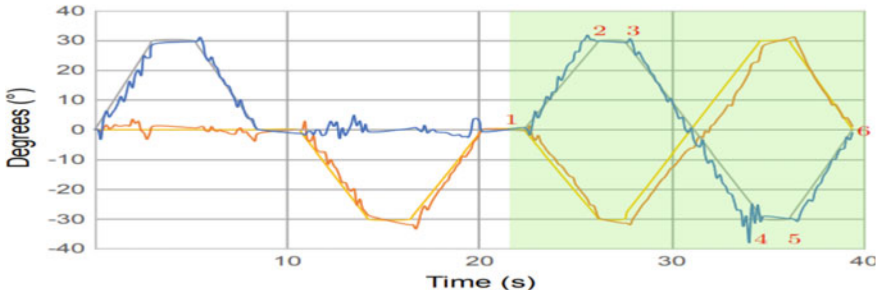

Fig. 8 A numerical result in terms of acquired angles of the gripper extremity of the tripod-based arm prototype during a test like in Fig. 6. (rotation around X: blue line is from test and grew line is from simulation; rotation around Y: orange line is from test and yellow line is from simulation)

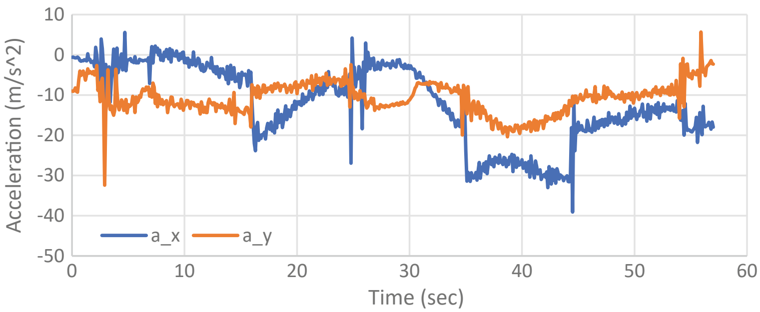

Fig. 9 A numerical result in terms of acquired acceleration of the foot extremity of the tripod-based leg prototype during a test like in Fig. 7 (in blue is x-component; in orange is y-component)

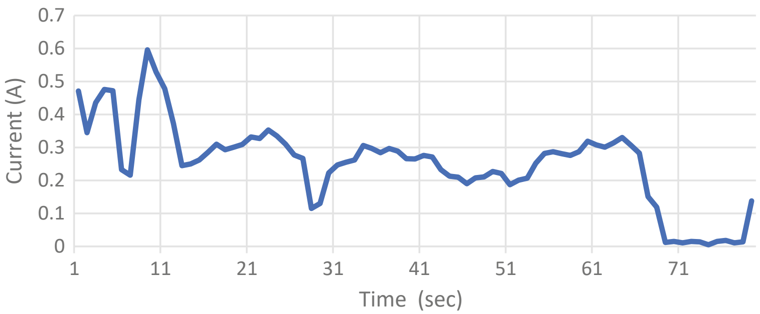

Fig. 10 A numerical result in terms of acquired power current of the actuators of the tripod-based leg prototype during a test like in Fig. 7

Figure 9 shows the accelerations acquired during the walking in the air experiment of Fig. 6, showing that the tested movement was performed with the due cyclicality and adequate smooth movement while presenting peaks probably due to the of inversion of the movement. Finally, Fig. 10 shows the power consumed in terms of supply current during the movement of the experiment in Fig. 7 with an overall power consumption of approximately 5.0 W.

In addition, it is to note that both prototypes are built with a total weight of about 750 g at a cost of about 230 euro, including all the components, with a capability to handle about 2.5 kg of payload as grasped object or locomoted body, respectively. All the tested features well fit the expected outcomes of the designed tripod-based limbs for application on the structure of a new LARMbot humanoid.

5 Conclusions

The tripod structure inspired by the human musculoskeletal nature of the limbs was used to redesign the legs and arms of the LARMbot humanoid robot with a common structural feature that are particularized only in the terminal element as ankle and wrist joints, respectively. The parallel structure used in the design of all modules for the humanoid LARMbot has structural and functional advantages compared to the usual serial structures which can be summarized in high load capacity and wide mobility. Prototypes were built with the same commercial components for the actuators, sensors, and control unit using specific structural parts produced via 3D printing in PLA. The functionality of these prototypes was successfully tested satisfying the expected functional characteristics in terms of wide movement capacity and load capacity with low energy consumption managed by nano-Arduino based control for user-oriented operation towards potential users with no specific skills in Humanoid Robotics.

References

1. Lim, H.-O., Takanishi, A.: Biped Walking Robots Created at Waseda University: WL and WABIAN Family. Philos. Trans. Roy. Soc. Math. Phys. Eng. Sci. **365**, 49–64 (2007)
2. Sakagami, Y., Watanabe, R., Aoyama, C., Matsunaga, S., Higaki, N., Fujimura, K.: The intelligent ASIMO: system overview and integration. IEEE/RSJ International Conference on Intelligent Robots and Systems, Lausanne, 2002, pp. 2478–2483. https://doi.org/10.1109/IRDS.2002.1041641
3. Ogura, Y., et al.: Development of a new humanoid robot WABIAN-2. In: Proceedings 2006 IEEE International Conference on Robotics and Automation, 2006. ICRA 2006., Orlando, FL, USA, pp. 76–81. https://doi.org/10.1109/ROBOT.2006.1641164
4. Kaneko, K., Kanehiro, F., Kajita, S., et al.: Humanoid Robot HRP-2. Proceedings of the IEEE International Conference on Robotics and Automation, New Orleans, LA, 26 April-1 May 2004, pp. 1083–1090 (2004). https://doi.org/10.1109/ROBOT.2004.1307969

5. Buschmann, T., Gienger, M.: TUM robots (e.g. Johnnie, Lola). In: Goswami, A., Vadakkepat, P. (eds.) Humanoid Robotics: A Reference. Springer, Dordrecht (2017). https://doi.org/10.1007/978-94-007-7194-9_13-1
6. Oh, J.-H., Hanson, D., Kim, W.-S., Han, Y., Kim, J.-Y., Park, I.-W.: Design of android type humanoid robot albert HUBO. In: 2006 IEEE/RSJ International Conference on Intelligent Robots and Systems, Beijing, pp. 1428–1433. https://doi.org/10.1109/IROS.2006.281935
7. Kuindersma, S., Deits, R., Fallon, M., et al.: Optimization-based locomotion planning, estimation, and control design for the atlas humanoid robot. Auton. Robot. **40**, 429–455 (2016). https://doi.org/10.1007/s10514-015-9479-3
8. Huang, Q., Yu, Z.G., Chen, X.C., Zhang, W.M., Yang, T.Q., Liao, W.X., Ceccarelli, M.: Historical developments of BHR humanoid robots. Adv Histor Stud **8**, 79–90 (2019). https://doi.org/10.4236/ahs.2019.81005
9. Ceccarelli, M., Cafolla, D., Russo, M., Carbone, G.: LARMBot humanoid design towards a prototype. MOJ Int. J. Appl. Bion. Biomech. **1**(2), 00008. https://doi.org/10.15406/mojabb.2017.01.00008
10. Ceccarelli, M.: A History of LARMbot humanoid. In: Proceedings of 2024 IFToMM symposium on history of machines and mechanism, Ankara, April 2024, paper no. 23 (in print)
11. Ceccarelli, M., Russo, M., Morales-Cruz, C.: Parallel architectures for humanoid robots. Robotics **9**(4), 75 (2020). https://doi.org/10.3390/robotics9040075
12. Cafolla, D., Wang, M., Carbone, G., Ceccarelli, M., LARMbot: a new humanoid robot with parallel mechanisms. In: Parenti-Castelli, V., Schiehlen, W. (eds.), ROMANSY 21 - Robot Design, Dynamics and Control, CISM International Centre for Mechanical Sciences 569, pp. 275–283. https://doi.org/10.1007/978-3-319-33714-2_31
13. Russo, M., Cafolla, D., Ceccarelli, M.: Design and experiments of a novel humanoid robot with parallel architectures. Robotics **7**(4), 79 (2018). https://doi.org/10.3390/robotics7040079
14. Fort, A., Laribi, M.A., Ceccarelli, M.: Design and performance of a LARMbot PK arm prototype. Int. J. Humanoid Robot. **19**(2), 2250009 (16 pages) (2022). https://doi.org/10.1142/s0219843622500098
15. Couprie, R., Ceccarelli, M., Laribi, M.A.: Design and performance of LARMbot Arm V3. In: Doroftei, I., Nitulescu, M., Pisla, D., Lovasz, E.C. (eds.), Proceedings of SYROM 2022 & ROBOTICS 2022. IISSMM 2022 (2023)
16. Russo, M., Ceccarelli, M., Takeda, Y.: Force transmission and constraint analysis of a 3-SPR parallel manipulator. In: Proceedings of the Institution of Mechanical Engineers, Part C: Journal of Mechanical Engineering Science, vol. 232. 095440621775019 (2017). https://doi.org/10.1177/095440621775019

Soft Grasping Delicate Parts by Robotic Effectors

Stefan Havlik and Jaroslav Hricko

Abstract This paper deals with the problem of reliable grasp of delicate objects by robotic effectors when handling or any physical interaction with the environment. The principal condition for such a task is to prevent any damage to the object by contact forces. The brief comparison of hard and soft contacts/grasps with regard to the load capacity of a gripper is discussed. In the case when contact forces are limited a more reliable grasp be reached if all contacts between grasp elements/fingers and object surface are soft. This condition should be respected in the design of effectors for manipulation with biomaterials or living organisms e.g. in medical operations, for handling fragile objects in optoelectronics, or in agriculture for harvesting soft fruits or plants. The grippers for these purposes are usually task-oriented tools and should be designed as relatively simple devices. An illustrative example of the gripper with an artificial "soft contact surface" is shown.

Keywords Grasping objects · Soft contact · Modelling contact · Robotic gripper

1 Introduction

The standard task of robotics is performing manipulation operations with mostly rigid objects [1]. New and further widespread applications of robotics in service areas include a wide class of operations where it is necessary to handle various soft or delicate objects. There are activities in several domains, for example: robot-assisted medical surgeries [2, 3], harvesting fruits [4] or handling foods in the food industry. The common requirement for all these applications is that specific effectors for grasping objects are needed e.g. that are able to perform operations without damaging objects.

S. Havlik (✉) · J. Hricko
Institute of Informatics, Slovak Academy of Sciences, Banská Bystrica, Slovakia
e-mail: havlik@savbb.sk

J. Hricko
e-mail: hricko@savbb.sk

D. Pisla et al. (eds.), *Advances in Service and Industrial Robotics*, Mechanisms and Machine Science 157, https://doi.org/10.1007/978-3-031-59257-7_63

There are several approaches to grasping delicate parts. The most frequently used is approach based on using soft fingers [3], or rather soft actuators, directly as fingers [4, 5]. Most frequently used are pneumatic actuators [4] or actuators using shape memory alloys. For some operations are specific grippers with proximity and force sensing capabilities that enable them to avoid hard impact at the moment of the first contact with the environment [6]. The gripper control system processes sensory data in order to detect post-grasp potential slip and to achieve grasp stability. The specific example, where sensors extend the capabilities of the robot control system in surgeries is in [2]. Another possible solution is a fusion of visual and tactile data processing by a convolutional neural network [7, 8].

However, the complex solutions are not applicable in cases of small/micro grippers, where integration of various sensors is hardly possible and not adequate from technical or economic reasons. The aim of this article is to point out the possibilities of achieving a stable grasp of the object by creating soft contact between the gripper and the object surface. One of the solutions is creation of flexible surfaces on parts of gripping elements that are in contact with the object. Solutions of such contact layers built on mechanical metamaterials/structures come into consideration when designing dimensionally small/micro effectors.

2 Soft Grasp of Objects

2.1 The Reliable Grasp

The basic problem when handling or performing any operation with an object is its reliable grasp by grippers. The kinematic structure of a gripper depends on the shape of the objects considering gravitational and inertial forces, as well as possible external load (force/moment) acting on the object. In general, the shapes of objects require solutions of the structure and geometry with several contacts and gripping elements—fingers. The gripping elements ensure the required accuracy of a grasped object with respect to the defined coordinates of the object positioning system.

Consider a shape-complex object grasped by a gripper with several contact/gripping elements, as shown in Fig. 1. Introduce the common O(x, y, z) gripper reference system for expression vectors of forces acting on the object and positions of contacts. Denote external load acting on the gripper that includes the external load, gravitational and possible inertia forces by common symbols: $\boldsymbol{F_{ex}} = [f_x, f_y, f_z]^T$ the 3×1 vector of external force components and $\boldsymbol{M_{ex}} = [m_x, m_y, m_z]^T$ the 3×1 vector of moment components. Positions of the particular contact points C_i, $i = 1, \ldots n$, is given by position vectors $\boldsymbol{r_i} = [r_{xi}, r_{yi}, r_{zi}]^T$ (see Fig. 1). In each i-th contact point between the gripper fingers and the grasped object denote the contact force that represent the three-component vector $\boldsymbol{P_i} = [p_{xi}, p_{yi}, p_{zi}]^T$. *Rem.*: We are tentatively considering “hard” and the one-point contacts between the object and fingers, i.e. the friction is very small/negligible.

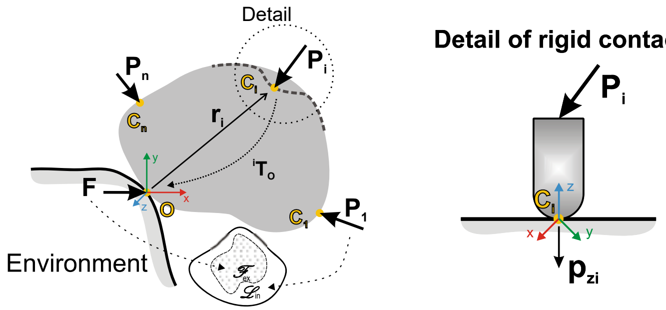

Fig. 1 Grasping a shape-complex object

As obvious, the grip stability determines the number and spatial arrangement of grip points in relation to the shape of the object. Expressing the cumulative effects of contact forces created by action of all fingers/gripping elements will be in vector form

$$\boldsymbol{F}_{int} = \sum_{i=1}^{n} \boldsymbol{P}_i; \qquad \boldsymbol{M}_{int} = \sum_{i=1}^{n} \boldsymbol{r_i} \times \boldsymbol{P_i} \tag{1}$$

Then, for the reliable grasp of an object when acts an external load (force and moment) it must be still valid (1)

$$\boldsymbol{F}_{ex} < \boldsymbol{F}_{int}; \qquad \boldsymbol{M}_{ex} < \boldsymbol{M}_{int}. \tag{2}$$

Rewrite the cumulative effects of contact forces in (1) by the common equation in form

$$\boldsymbol{L_{int}} = \begin{bmatrix} \boldsymbol{F_{int}} \\ \boldsymbol{M_{int}} \end{bmatrix} = \sum_{\boldsymbol{n}} \begin{bmatrix} \boldsymbol{P_i} \\ \boldsymbol{R}_{i0}.\boldsymbol{P_i} \end{bmatrix}, \quad \text{where } \boldsymbol{R_{iO}} = \begin{bmatrix} 0 & r_{zi} & -r_{yi} \\ -r_{zi} & 0 & r_{xi} \\ r_{yi} & -r_{xi} & 0 \end{bmatrix} \tag{3}$$

When introduce absolute values of contact forces P_{ai} in each contact point and arrange them into the vector of contact forces $\boldsymbol{P_a} = [P_a1, \ldots P_{ai}, \ldots P_{an}]^T$, the above relation leads to rewriting into form

$$\boldsymbol{L_{int}} = \boldsymbol{H}.\boldsymbol{P_a} \tag{4}$$

where $\boldsymbol{H}$ is the $6 \times$ n grasp force matrix which represents cumulative effect of all fingers. The columns of this matrix transform effects/contributions of particular contact forces into O(x, y, z) reference system. Rem.: The possible (pseudo)inversion of $\boldsymbol{H}$ gives actual values of contact forces when acts an external load.

Then, when maximal forces in contact are given, the condition (2) and (4) determine maximal external loads that the gripper can bear. Thus, the allowable load/capacity is the relevant characteristic for construction of a gripper.

2.2 Soft Grasp

Consider now the case when the contacts of finger elements and object surface are soft. As shown below, the soft/elastic contact of two bodies in addition to the normal force transmits tangential/frictional forces as well as moments.

For the following analysis we introduce the contact reference systems $C_i(x, y, z)$ in each contact of the gripper element (see Fig. 2). The mechanical interaction of two bodies are expressed as vectors of force and moment components $\boldsymbol{P_i} = [p_x, p_y, p_z, m_x, m_y, m_z]^T$, where component p_z represents normal force with respect to the object surface. As previously, $\boldsymbol{r_i}$ are position vectors of contacts. Then, in the case of soft grasp, the capacity of a gripper will be

$$\boldsymbol{L}_{int} = \sum_{i=1}^{n} \boldsymbol{T}_{io}.\boldsymbol{P}_i \tag{5}$$

where: $\boldsymbol{T_{io}}$ is the 6×6 matrix, which transmits acting of contact force and moment components expressed in the $C_i(x, y, z)$ reference system into common O(x, y, z) gripper references in form

$$\boldsymbol{T}_{i0} = \begin{bmatrix} \boldsymbol{S}_{iO} & \emptyset \\ \boldsymbol{R}_{iO}.\boldsymbol{S}_{iO} & \boldsymbol{S}_{iO} \end{bmatrix} \tag{6}$$

$\boldsymbol{S_{iO}}$ is the (3×3) rotation matrix of the contact reference system in C_i into O gripper references, Ø is the 3×3 zero matrix.

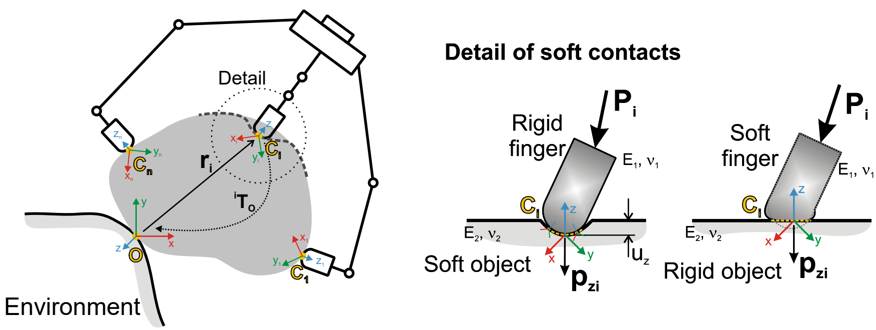

Fig. 2 A graphical illustration of the grasp with soft contacts

2.3 Modelling Soft Contacts

Modelling contacts of two bodies is the subject of extensive studies in various research areas. The majority of studies are based on general Hertzian and Hunt-Crossey models, as most suitable for viscoelastic cases [9, 10]. These models describe contact geometry and physical interactions between specific forms of two bodies.

Our main goal in connection with grasping of delicate objects is the creation of such a contact between the gripping element and the object that ensures the required transfer of other contact forces at the limited normal force acting on the object. Three types of soft contacts were studied: soft object-rigid finger, soft object-soft finger and rigid object-soft finger surface. As a general tool for performing mechanical interaction, i.e. calculations of force-deflections the COMSOL Multiphysics was used. Two marginal types of soft contacts with deflections and forces are shown in Fig. 3.

For calculation the following data of materials are given: rigid parts—aluminium E = 70 GPa, soft parts—rubber like material E = 2.5 MPa, both parts are flat materials of 10 mm of thickness.

Compare now both types of soft contacts from the point of view of possible tangential forces that the contact is able to keep. The contact in Fig. 3a represents a relatively flat contact surface and tangential/slip resistance gives only friction between two materials. For given materials, this friction force is approximately 20% of the normal force (the friction coefficient $\mu = 0.2$). In contact Fig. 3b, the relatively rigid body is partially buried inside the surface of the opposite soft body and the corresponding friction force is highly increased by the form of elastic deflection. Simulation shows that the value of friction within the range $\mu = 0.4 \div 0.5$ can be reached. See some similar experimental results in [10].

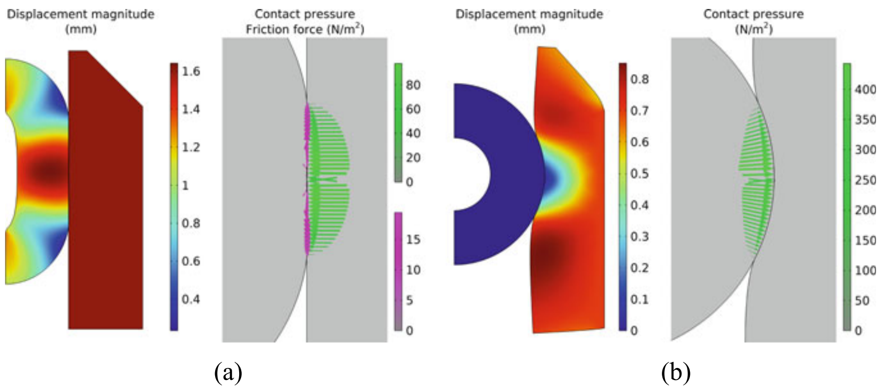

Fig. 3 **a** Contact of the soft object-rigid finger, **b** contact of the rigid object-soft finger

3 Design of the Gripper with Soft Contact Area

Following the above study, one possibility is the creation of an elastically compliant surface on the inner side of grasping elements/fingers that come into contact with a grasped object. This new perspective concept was adopted in the design of the experimental gripper for grasping small delicate objects. In principle, the additional elastically compliant surface represents the deposition of layers in the form of artificial meta-material (AMM) with the required flexural characteristics. Such a layer consists of higher number of small mechanically flexible cells arranged into a more complex structure according to the shape of the grasping element/finger. The properties of the surface thus determine the deflection characteristics of particular cells. When talking about grasping objects with a limited contact force, the suitable solutions are flexible structures of the mechanisms that exhibit approximately constant force within a given range of elastic deflection. The compliant constant force mechanisms are widely applied in building various devices [11].

To create the AMM layer we decided to use the compact structure of flexible cells in Fig. 4. As to flexural properties, two principal requirements given for the cell are satisfied:

- The deformable structure exhibits dominant compliance in the direction of normal force; the cross-deflection effects in other directions are minimal.
- The change of normal force is minimal within a given range of deflection. According to the performed flexural analysis, the value is approximately stable within the range of elastic surface deflection of 0.5–1.25 mm; as shown in Fig. 4.

As depicted above the research includes solving and elaborations of following tasks:

- Study, analysis and tests of properties on enlarged physical models. Designs of suitable structures for flexible cells and layers are part of the solution.
- Specific solutions and task-oriented design of grasping devices. Part of the research is the design of a suitable AMM technology for the creation of flexible layers.

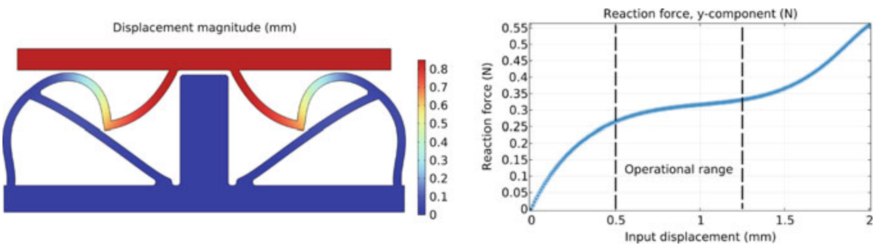

Fig. 4 Compliant constant force cell of the layer (left), force to displacement curve (right)

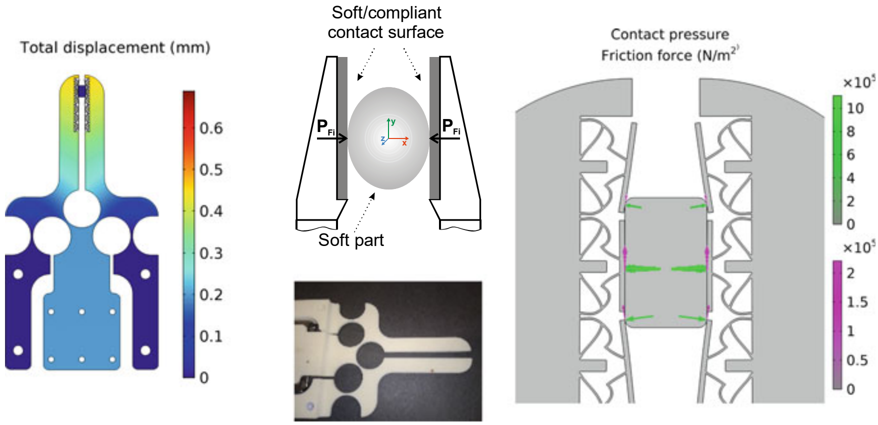

Fig. 5 Experimental compliant gripper, displacement field (left), photography of the physical sample (middle), the contact pressure and friction forces in the case of grasping object (right)

For further elaboration of the proposed concept of an experimental gripper with soft layers on fingers we decided to use the previously designed and manufactured gripper with the flexural structure [12, 13], as shown in the model in Fig. 5. The physical sample is made from nylon (polyamide) by 3D printing technology in magnification scale 20:1, comparing to our original design. Its main dimensions are 154.2 × 80 mm^2 and the minimal thickness of compliant joints is 1 mm. An actuator for this laboratory sample the linear card motor will be used. The maximal dimensions of grasped objects will not be more than 4 mm.

4 Conclusion

This article shows the conditions that must be met for reliable grasping of delicate objects by robotic grippers when the contact forces on the grasping object are limited. The main attention is paid to development of grasping methods through the so-called "soft contacts". For this purpose, the solution with soft layers on the surface of the gripping elements that come into contact with an object is proposed. It indicates possible solution of the soft cell with specific flexural properties that can be arranged into layers, as the artificially created meta-materials (AMM).

The proposed solution presents the initial stage of elaboration employing calculations and simulations. The physical models of grippers on an enlarged scale are prepared. As a part of future research, the design of specific AMM and appropriate technologies will be addressed.

The contribution points to the possibilities of solving relatively simple gripping devices/effectors suitable for handling delicate objects.

Acknowledgements The Slovak Scientific Grant Agency VEGA under contract No. 2/0135/23—"Intelligent sensor systems and data processing" supported this work. It was supported by project APVV-20-0042—"Microelectromechanical sensors with radio frequency data transmission".

References

1. Monkman, G.J., Hesse, S., Steinmann, R., Schunk, H.: Robot Grippers. Wiley, Weinheim (2006). ISBN 978-3-527-40619-7
2. Park, Y.-J., Lee, E.-S., Choi, S.-B.: A cylindrical grip type of tactile device using magneto-responsive materials integrated with surgical robot console: design and analysis. Sensors **22**, 1085 (2022). https://doi.org/10.3390/s22031085
3. Baghbani Kordmahale, S., Qu, J., Muliana, A., et al.: A hydraulic soft microgripper for biological studies. Sci. Rep. **12**, 21403 (2022). https://doi.org/10.1038/s41598-022-25713-1
4. Galley, A., Knopf, G.K., Kashkoush, M.: Pneumatic hyperelastic actuators for grasping curved organic objects. Actuators **8**, 76 (2019). https://doi.org/10.3390/act8040076
5. Haibin, Y., Cheng, K., Junfeng, L., Guilin, Y.: Modeling of grasping force for a soft robotic gripper with variable stiffness. Mech. Mach. Theory **128**, 254–274 (2018). https://doi.org/10.1016/j.mechmachtheory.2018.05.005
6. Hricko, J., Havlik, S.: Exchange of effectors for small mobile robots and UAV. Mech. Mach. Sci. **67**, 308–315 (2019). https://doi.org/10.1007/978-3-030-00232-9_32
7. Ruan, W., Zhu, W., Zhao, Z., Wang, K., Lu, Q., Luo, L., Yeh, W.-C.: RFCT: multimodal sensing enhances grasping state detection for weak-stiffness targets. Mathematics **11**, 3969 (2023). https://doi.org/10.3390/math11183969
8. Cui, S., Wang, R., Wei, J., Li, F., Wang, S.: Grasp state assessment of deformable objects using visual-tactile fusion perception. In: Proceedings of the 2020 IEEE International Conference on Robotics and Automation (ICRA), Paris, France, 31 May–31 August 2020 (2020), pp. 538–544. https://doi.org/10.1109/ICRA40945.2020.9196787
9. Popov, V.L., Heß, M., Willert, E.: Handbook of Contact Mechanics. Springer, Berlin (2019). ISBN 978-3-662-58708-9. https://doi.org/10.1007/978-3-662-58709-6
10. Wijayarathne, L., Sima, Q., Zhou, Z., Zhao Y., Hammond, F.L.: Simultaneous trajectory optimization and force control with soft contact mechanics. In: 2020 IEEE/RSJ International Conference on Intelligent Robots and Systems (IROS), Las Vegas, NV, USA, pp. 3164–3171 (2020). https://doi.org/10.1109/IROS45743.2020.9341030
11. Lan, C.-C., Wang, J.-H., Chen, Y.-H.: A compliant constant-force mechanism for adaptive robot end-effector operations. In: 2010 IEEE International Conference on Robotics and Automation, Anchorage, USA, pp. 2131–2136 (2010). https://doi.org/10.1109/ROBOT.2010.5509928
12. Hricko, J.: Experimental platform for performance tests of compliant robotic devices. In: Advances in Intelligent Systems and Computing: Advances in Robot Design and Intelligent Control. RAAD 2015, vol. 371, pp. 37–45 (2015). https://doi.org/10.1007/978-3-319-21290-6
13. Hricko, J., Havlik, S.: Small-size robotic tools with force sensing. In: Modern Machinery Science Journal: 20th International Workshop on Robotics in Alpe-Adria-Danube Region–2011, special edition, pp. 73–77 (2011). ISSN 1805-0646

A 3D Printed Reconfigurable Multi-fingered Gripper

Boštjan Baras and Miha Deniša

Abstract This paper presents a novel reconfigurable gripper designed for versatile and cost-efficient automation. The gripper is characterized by its under-actuated fingers and modular design, enabling it to adapt to a wide range of objects and tasks. Central to our design is the robotic finger module, which utilizes a single motor within a 3D-printed frame, ensuring both efficient functionality and ease of assembly. The gripper's adaptability is further enhanced by a reconfigurable board that supports multiple finger configurations, such as two-finger and three-finger setups. Evaluation tests were conducted to assess the gripper's adaptability and durability. Using a series of 3D-printed objects, the tests focused on the finger's response time and ability to withstand repetitive use, highlighting its capability to efficiently handle diverse objects. Its adaptability and open-source nature make it a valuable asset for a wide range of uses.

Keywords Grippers · Adaptive systems · Additive manufacturing · Open source hardware · Mechanical design · Under-actuated systems

This research has received funding from the program group P2-0076 Automation, robotics, and biocybernetics supported by the Slovenian Research Agency and from DIGITOP funded by Ministry of Higher Education, Science and Innovation of Slovenia, Slovenian Research and Innovation Agency and European Union—NextGenerationEU.

B. Baras · M. Deniša (✉)
Humanoid and Cognitive Robotics Lab., Department of Automatics, Biocybernetics, and Robotics, Jožef Stefan Institute, Ljubljana, Slovenia
e-mail: miha.denisa@ijs.si

B. Baras
e-mail: bb1625@student.uni-lj.si
URL: https://abr.ijs.si/

B. Baras
Faculty of Electrical Engineering, University of Ljubljana, Ljubljana, Slovenia

D. Pisla et al. (eds.), *Advances in Service and Industrial Robotics*, Mechanisms and Machine Science 157, https://doi.org/10.1007/978-3-031-59257-7_64

1 Introduction

To address the challenges posed by evolving market demands, the manufacturing sector must transition from classical production lines, which traditionally rely on standard automation approaches. These conventional methods often involve repetitive, fixed tasks using specialized machinery. However, the shift towards high-mix low-volume production [1] requires more adaptive and flexible systems. This is particularly crucial as approximately 80% of EU manufacturers are small and medium-sized enterprises (SMEs). For these SMEs, new manufacturing paradigms that are cost-effective and easily integrable are vital for maintaining competitiveness and efficiency.

One of the key areas of automatic production lines is grasping, which is greatly affected by the need to shift towards high-mix low-volume production. The main areas of research in the field of robotic grippers focus on enhancing their capabilities, versatility, and integration into various industrial and non-industrial applications.

Our approach focuses on a cost-efficient reconfigurable gripper. With this in mind, under-actuated fingers [2] preset themselves as a viable solution, as they enable grasping of various objects while opting for a low number of actuators. Two main approaches are used in an under-actuated finger design: tendon driven [3] and mechanical linkage systems [4]. While under-actuated fingers with a mechanical linkage systems are more complex, they provide more functionality and can exert a higher force. The main design used for adaptive grippers in a three-finger design with actuated reconfiguration [3, 5]. These grippers offer actuated adaptation of finger poses, but their span of reconfiguration is limited while having a more complex design with additional actuators.

To keep the cost low, we opted for a manual reconfiguration, as the reconfiguration is done sporadically in a high-mix low-volume manufacturing scenario. The gripper design allows for the integration of two key elements: a mounting board and robotic fingers. Each robotic finger is designed as single module that includes finger joints and an actuator to alter the angles between them. These modules encompass a system for attachment to the board along with other auxiliary elements. The board design permits the attachment of at least three robotic fingers simultaneously, with the capability to position the fingers in a variety of orientations. The robotic gripper facilitates configurations of basic standard grippers, such as the classic two-finger and three-finger grippers.

The various configurations of the gripper complement each other. If one configuration cannot grasp a certain object, another configuration is capable of doing so. This versatility allows the same gripper to handle different objects that would typically require separate grippers. The gripper design emphasizes cost-effectiveness and simplicity in manufacturing, aligning with the goal of creating an open-source gripper. It is designed for 3D printing, utilizing cost-effective materials, and can be assembled using basic workshop tools.

Evaluation was carried out on individual fingers and on the reconfigurable gripper design as a whole.

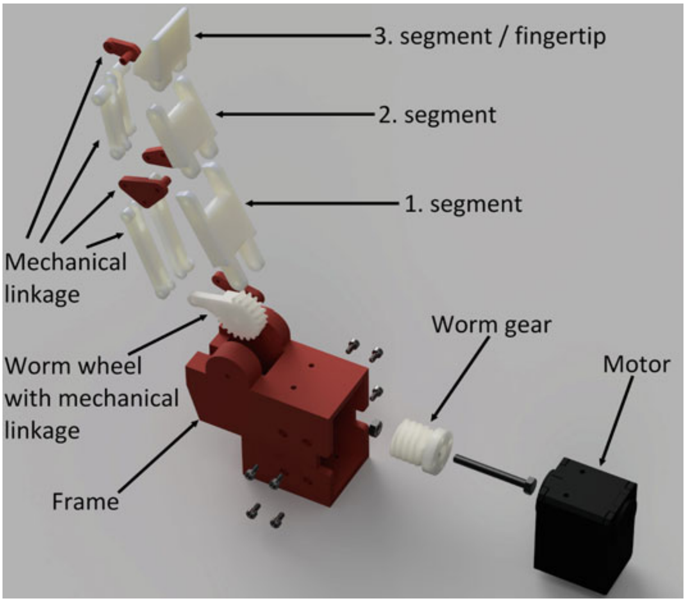

Fig. 1 Exploded view of the finger model with the marked main components

2 Robotic Finger Module

As mentioned, our design calls for configurations with varying numbers of fingers. This means that each finger should be able to function as an individual unit. Another aspect we wish to attain is the affordability of the gripper. With these restrictions in mind, we opted for a under-actuated finger design with a single motor.

As the open source gripper model from Robotiq [5] includes fingers close to our desired specifications, their design was used as a starting point. While their model [6] was used as a basis, our finger was modeled from scratch. 3D modeling was conducted using the Autodesk Fusion 360 software. The under actuation design could be transferred, but the rest of the finger needed a different design, i.e. the base of the finger with a motor, the base for attaching the finger to the gripper plate, torsion springs, etc. The exploding view of the model can be seen in Fig. 1.

The frame, which is a central element of the 3D model, supports the finger, motor, and the gear connection between the motor and the finger. The gear transmission utilizes a worm gear and wheel system, chosen for its simple axis of rotation alteration, compact size, substantial torque enhancement, and suitability for 3D modeling and printing. The worm wheel was customized based on a standard design from the McMaster-Carr catalog, with modifications including teeth placement only where needed, appropriate thickness adjustment, and the addition of a mechanical guide. A corresponding worm gear was also chosen from the catalog and modified to be shorter than its original version, along with a mounting system for direct motor attachment. The frame is designed to precisely fit the gear pair and the motor, ensuring proper component alignment and integration. It underwent various modifications to accommodate two different motor models and to adjust for assembly tolerances. Torsion springs are incorporated in the model to enable the fingers to return to a fully extended position. The design includes designated areas for installing these springs, contributing to the effective and realistic movement of the fingers.

The chosen motor is the Dynamixel XL430-W250-T [7], selected for its ideal mix of maximum torque, size, and cost. This motor has a maximum torque of 1.5 Nm, dimensions of 28.5 mm × 46.5 mm × 34 mm, an absolute 12-bit encoder, and costs approx. €50. Its various mounting options were effectively used for integrating the motor into the frame and for creating a mechanism to change the model's configuration.

Dynamixel XL430-250-T motors have a resolution of 4096 pulses per revolution, with operations based on pulse counting. Motor rotation is represented by the count of pulses from the origin. Torque is read in the motor program using *Present Load*, returning a value between -1000 and 1000. This number indicates the current torque as a fraction of the maximum torque, calculated as $M = \frac{x}{1000} \cdot M_{\max}$ where x is the returned value and $M_{\max} = 1.5$ Nm. The sign of the value indicates the direction of the torque. Most control functions accept desired torque as a percentage. When 100% is input, the function waits for a *Present Load* value of at least 250, representing a quarter of the maximum torque. However, it's noted that this torque reading is an estimate based on other internal motor variables [7].

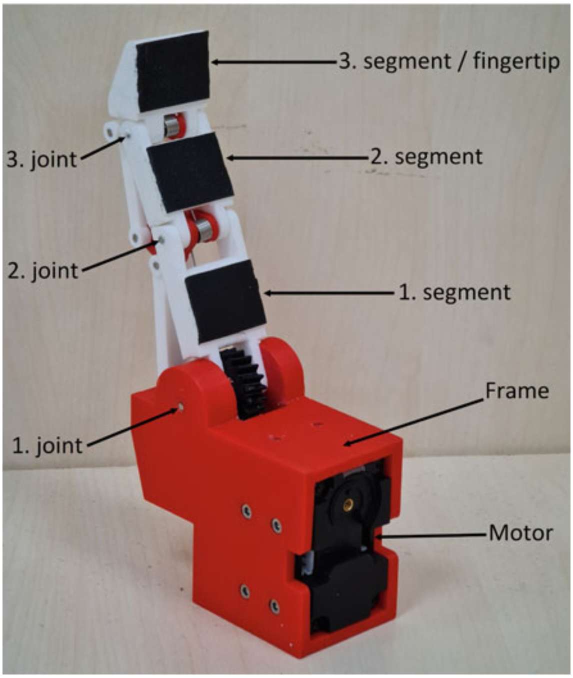

Fig. 2 Robotic finger and its fundamental components

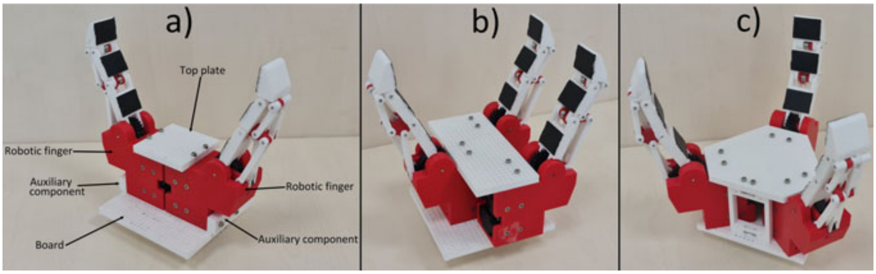

Fig. 3 Three basic configurations: **a** two-finger, **b** classic three-finger, and **c** circular three-finger. Main components of the gripper are marked in (**a**)

The fully assembled finger module can be seen in Fig. 2. Compared to the design, seen in Fig. 1, additional rubber strips can be seen, which were added to increase the friction while grasping objects.

3 Reconfigurable Modular Robotic Gripper

To enable various configurations of the finger modules, a reconfiguration mounting board was designed. The board should have a large number of holes, through which screws would be inserted and then screwed into the threads of the robotic finger motors. Considering the dimensions of the robotic fingers and the expected loads, the board dimensions selected were 10 cm $\times$ 10 cm with a thickness of 6 mm. From the motor specifications, we determined that the aforementioned threads should be arranged in a rectangle with the shorter side being 12 mm, the longer 16 mm, and the diagonal 20 mm (distances measured between the axes of the threads). The greatest common divisor of these values is 4, so we arranged the holes on the board in a square pattern, with the distance between adjacent holes always being 4 mm. The board also enables the gripper to be mounted to a robot arm.

The board provides a mechanical connection between the robotic arm and the robotic fingers. However, it is still necessary to create a plate that will be located between the fingers and the object that the gripper will grasp. Without this top plate, gaps can appear between the fingers, weakening the quality of the gripper's grasp.

In some configurations the robotic finger is attached through the board with only two screws instead of four, which could lead to overloading of the threads inside the motor. By adding auxiliary components, we enabled an additional option for attaching the fingers to the board, thereby relieving the load on the motor threads and allowing the assembly of new configurations. All the gripper components can be seen in Fig. 3.

Different auxiliary components were printed to allow for different configurations. Some configurations, typically used in robotics, can be seen in Fig. 3.

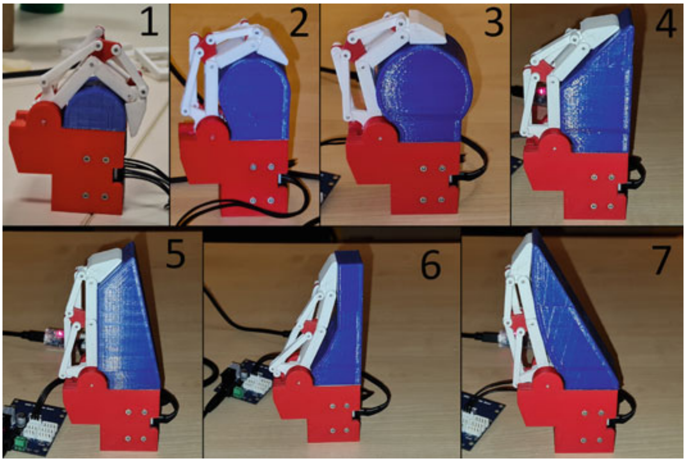

Fig. 4 Seven different test objects used for evaluation

4 Evaluation

We focused on measuring characteristics of the robotic finger that are ascertainable through motor-provided data, specifically angle and torque, due to the difficulty in measuring many parameters and the need for special equipment [8]. Our primary interests were assessing the finger's durability, to evaluate the quality of 3D printed elements, and its adaptability and response time during grasping.

Seven different 3D printed test objects were used to assess the adaptability of the robotic finger, seen in Fig. 4. These objects, selected to test a wide range of finger positions during grasping, were attached to the threads of the robotic finger, originally designed for base attachment. From Fig. 4, it is evident that the robotic finger adequately adapted to all 7 test objects. During the grasp of the first test object, the worm gear moved to its extreme angle relative to the first finger joint, but this did not affect the finger's shape during grasping. However, we infer that the finger would not have adapted to an object smaller than test object 1. In grasping the other six test objects, the finger performed within our expectations.

For each test object, we repeatedly closed and opened the robotic finger a hundred times at 100% torque. We measured the average time the finger need to clasp the object, denoted as closing time, and the average time needed to fully extend again, denoted as opening time. The results of this measurement are shown in Table 1. As expected, the closing time was longer for objects requiring the motor to rotate through a larger angle.

We also recorded the torques and differences in motor rotation between the finger's open position and its position when gripping the object.

While evaluating with the test object 1 and 2, the worm gear wore out to the point where the finger no longer moved when the motor rotated. This can be seen in

Table 1 Average closing and opening times for each test object

Object #	1	2	3	4	5	6	7
Opening time [s]	6.92	4.39	3.62	3.16	2.61	3.43	1.65
Closing time [s]	7.00	4.43	2.67	3.21	2.65	4.49	1.67

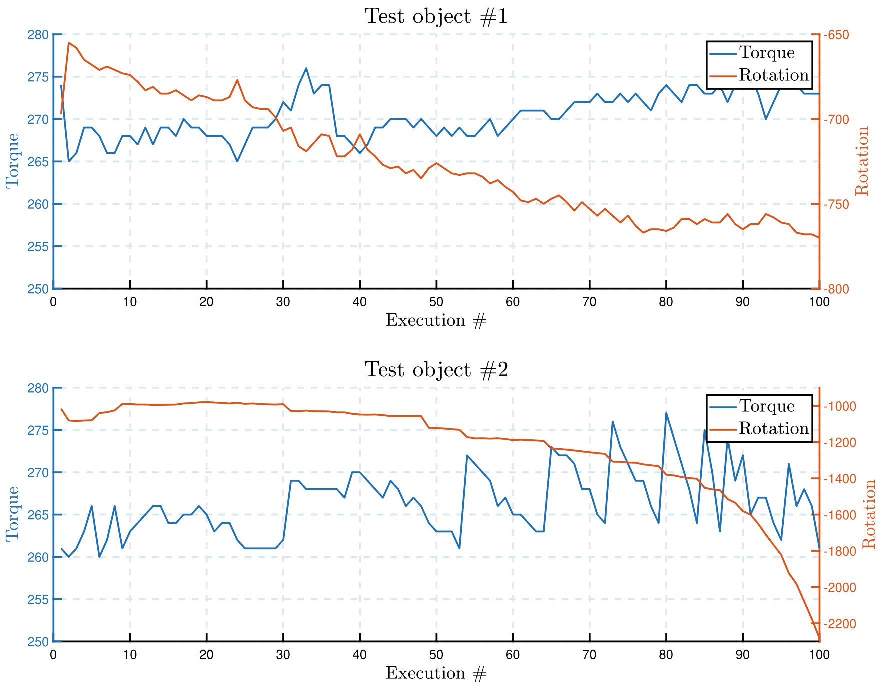

Fig. 5 The motor's torque and rotation during the grip test

Fig. 5, which shows the motor's torque and rotation during the grip test, measured in values from 0 to 1000 for torque, as described previously, and in counted motor pulses for rotation. The figure indicates that while torque stayed relatively stable, motor rotation decreased greatly. This change suggests worm gear deformation, as each 360° motor rotation moves the worm gear by one tooth. The inspection of the gear confirmed its deformation.

To validate our overheating hypothesis, we modified the test to include a 30 s cooling period after every ten cycles. Using a new worm gear, we repeated the test across all seven objects. Figure 6 shows the motor's torque and rotation during the adapted evaluation for the first two test objects. After 700 cycles, the finger functioned correctly with only minor, non-critical wear on the gear teeth. This outcome, much improved from the original test, supported our overheating hypothesis.

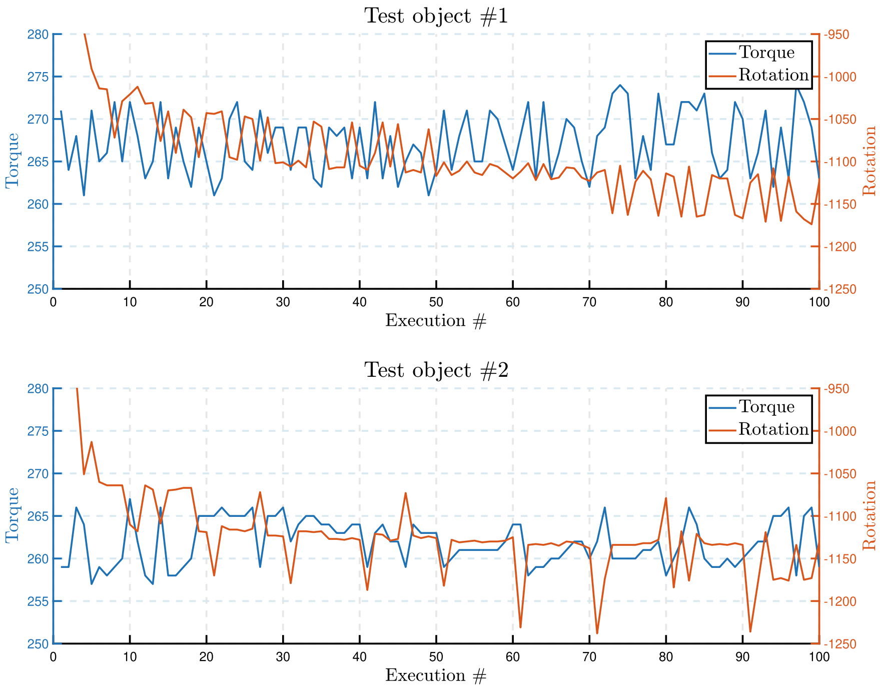

Fig. 6 The motor's torque and rotation during the grip test with a cooling period

5 Conclusion

This research introduces a reconfigurable gripper that enhances the adaptability and cost-effectiveness of automation in various sectors. Our design's primary feature is the under-actuated finger module, which efficiently achieves versatility in grasping different objects while maintaining simplicity and affordability. The use of a single motor per finger, combined with a 3D-printed framework, exemplifies our commitment to creating a gripper that is both functional and accessible.

The modular nature of the gripper, facilitated by the reconfigurable board, allows for adjustments to various finger configurations, such as two-finger and three-finger setups. This adaptability is vital in meeting the diverse needs of high-mix low-volume production environments. Furthermore, compared to actively reconfigurable grippers, we opt for a manual reconfiguration to lower the cost and increase the adaptability. While manual reconfiguration is slow, it is appropriate for high-mix low-volume production, where changes are not needed each cycle, but rather every few days at most.

Through testing with multiple 3D-printed objects, we have demonstrated the finger's ability to adapt to a range of shapes and sizes, confirming its effectiveness and reliability. The evaluation also highlighted areas for improvement, such as gear wear, overheating, and relatively long clasping times providing valuable insights for future development.

References

1. Hu, S.J., Ko, J., Weyand, L., ElMaraghy, H.A., Lien, T.K., Koren, Y., Bley, H., Chryssolouris, G., Nasr, N., Shpitalni, M.: Assembly system design and operations for product variety. CIRP Annals **60**(2), 715–733 (2011)
2. Birglen, L.: The kinematic preshaping of triggered self-adaptive linkage-driven robotic fingers. Mech. Sci. **2**(1), 41–49 (2011)
3. Ma, R., Dollar, A.: Yale openhand project: optimizing open-source hand designs for ease of fabrication and adoption. IEEE Robot. Autom. Mag. **24**(1), 32–40 (2017). https://doi.org/10.1109/MRA.2016.2639034
4. Telegenov, K., Tlegenov, Y., Shintemirov, A.: A low-cost open-source 3-d-printed three-finger gripper platform for research and educational purposes. IEEE Access **3**, 638–647 (2015). https://doi.org/10.1109/ACCESS.2015.2433937
5. Sadun, A.S., Jalani, J., Jamil, F.: Grasping analysis for a 3-finger adaptive robot gripper. In: 2016 2nd IEEE International Symposium on Robotics and Manufacturing Automation (ROMA), pp. 1–6 (2016).https://doi.org/10.1109/ROMA.2016.7847806
6. Ilg, M.: 3-finger-gripper. https://github.com/manuelilg/3-finger-gripper, [Online]. Accessed 19 Jan 2023
7. Robotis e-Manual, https://emanual.robotis.com/docs/en/dxl/x/xl430-w250/, [Online]. Accessed 19 Apr 2023
8. Bicchi, A., Salisbury, J., Brock, D.: Contact sensing from force measurements. Int. J. Robot. Res. 249–262 (1993). https://doi.org/10.1177/027836499301200304

Author Index

D. Pisla et al. (eds.), *Advances in Service and Industrial Robotics*, Mechanisms and Machine Science 157, https://doi.org/10.1007/978-3-031-59257-7